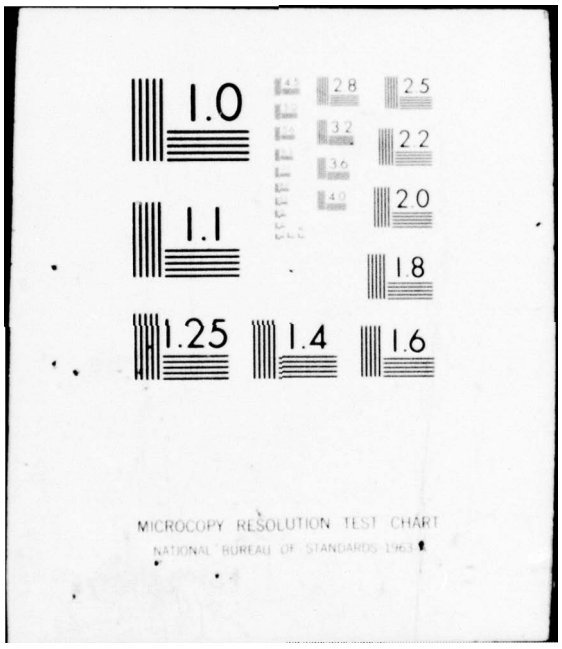
AD-A040 012 ARMAMENT DEVELOPMENT AND TEST CENTER EGLIN AFB FLA F/G 17/7
PROCEEDINGS OF THE BIENNIAL GUIDANCE TEST SYMPOSIUM (8TH) HELD --ETC(U)
MAY 77

UNCLASSIFIED ADTC-TR-77-3-VOL-1 NL

1 OF 8
AD
A040012




1.0
1.1
1.25
1.4
1.6
2.8
2.5
3.2
2.2
3.6
2.0
4.0
1.8
MICROCOPY RESOLUTION TEST CHART
NATIONAL BUREAU OF STANDARDS 1963

AD A040012

VOLUME 1

ADTC-TR 77-3



EIGHTH GUIDANCE TEST SYMPOSIUM PROCEEDING

DDC
MAY 27 1977
C

DDC FILE COPY

APPROVED FOR PUBLIC RELEASE;
DISTRIBUTION UNLIMITED.

UNCLASSIFIED

SECURITY CLASSIFICATION OF THIS PAGE *(When Data Entered)*

REPORT DOCUMENTATION PAGE		READ INSTRUCTIONS BEFORE COMPLETING FORM
1. REPORT NUMBER ADTC TR 77-3 (Vol I)	2. GOVT ACCESSION NO.	3. RECIPIENT'S CATALOG NUMBER
4. TITLE *(and Subtitle)* Eighth Guidance Test Symposium Proceedings t.p. takes precedence		5. TYPE OF REPORT & PERIOD COVERED Symposium Proceedings 6. PERFORMING ORG. REPORT NUMBER TR 77-3 (Vol I)
7. AUTHOR(s) As indicated on individual papers.		8. CONTRACT OR GRANT NUMBER(s)
9. PERFORMING ORGANIZATION NAME AND ADDRESS 6585th Test Group/GD Holloman AFB, New Mexico 88330		10. PROGRAM ELEMENT, PROJECT, TASK AREA & WORK UNIT NUMBERS
11. CONTROLLING OFFICE NAME AND ADDRESS 6585th Test Group/GD Holloman AFB, New Mexico 88330		12. REPORT DATE May 1977 13. NUMBER OF PAGES 732
14. MONITORING AGENCY NAME & ADDRESS*(if different from Controlling Office)*		15. SECURITY CLASS. *(of this report)* Unclassified 15a. DECLASSIFICATION/DOWNGRADING SCHEDULE

16. DISTRIBUTION STATEMENT *(of this Report)*

DISTRIBUTION STATEMENT A
Approved for public release;
Distribution Unlimited

17. DISTRIBUTION STATEMENT *(of the abstract entered in Block 20, if different from Report)*

18. SUPPLEMENTARY NOTES

19. KEY WORDS *(Continue on reverse side if necessary and identify by block number)*

Gyroscopes, accelerometers, modeling, guidance, inertial, navigators

20. ABSTRACT *(Continue on reverse side if necessary and identify by block number)*

These proceedings contain papers included in the Eighth Biennial Guidance Test Symposium. This symposium, hosted by the Central Inertial Guidance Test Facility, is directed toward the exchange of information, stimulation of new ideas, and discussion of recent developments in the field of guidance testing. The papers presented in these proceedings include such topics as aircraft inertial navigators, strapped-down guidance systems, component evaluation, and analysis techniques. The included papers were those presented in the

DD FORM 1 JAN 73 1473 EDITION OF 1 NOV 65 IS OBSOLETE

UNCLASSIFIED

SECURITY CLASSIFICATION OF THIS PAGE *(When Data Entered)*

unclassified sessions of the symposium. Papers presented in the classified portion of the meeting are being published as Volume II.

t.p.

(14) ADTC-TR-77-3-Vol-1

VOLUME I

(11) May 77

(6)

PROCEEDINGS OF THE

EIGHTH BIENNIAL GUIDANCE TEST SYMPOSIUM (8th)

(12) 711p.

held at

HEADQUARTERS 6585TH TEST GROUP,
ARMAMENT DEVELOPMENT TEST CENTER,
HOLLOMAN AIR FORCE BASE, NEW MEXICO,

ACCESSION for
NTIS White Section ✓
DDC Buff Section
UNANNOUNCED
JUSTIFICATION
BY
DISTRIBUTION/AVAILABILITY CODES
Dist. AVAIL. and/or SPECIAL
A

hosted by

CENTRAL INERTIAL GUIDANCE TEST FACILITY

11 - 13 MAY 1977.

404038

4/8

FOREWORD

The Eighth Biennial Guidance Test Symposium was held at Holloman Air Force Base 11 - 13 May 1977. These symposiums are hosted by the Central Inertial Guidance Test Facility (CIGTF). These meetings bring together approximately 450 people from industry, educational institutions, foreign governments, the Department of Defense, and other Government agencies. The goal is to provide a forum for the exchange of technical information and the stimulation of new ideas related to the testing of guidance systems and components.

Many excellent papers were received for presentation at this meeting, but due to the time available only a portion of those submitted could be included. The Paper Review Committee, headed by Dr Fred F. Kuhn of the Central Inertial Guidance Test Facility, included: Colonel Robert S. Ziernicki, HQ USAF; Lt Col James W. Cox, Air Force Armament Laboratory; Major Dino Lorenzini, Space and Missile Systems Organization; Dr Harold L. Pastrick, US Army Missile Command; Mr William Laubendorfer, Aeronautical Systems Division; Mr Thomas E. Sanders, Naval Air Development Center; Mr Nick Schneider, Naval Weapons Center; Colonel Leonard R. Sugerman, USAF (Retired), Physical Science Laboratory, New Mexico State University; and Mr Duane R. McKanna (Retired), formerly of HQ USAF.

In addition to those listed above and the contributing authors, a large number of people contributed to the success of this meeting; and I wish to express my appreciation to each for his efforts. Any suggestions you may have for future such meetings may be given to me or our Symposium Manager, Mr Fred P. Ray, Jr.

This document is published only for the exchange and stimulation of ideas. Its publication does not constitute Air Force approval of the document's findings or conclusions.

Richard H. Boivin

RICHARD H. BOIVIN, Lt Col, USAF
Director, Guidance Test Division

ABSTRACT

These proceedings contain papers included in the Eighth Biennial Guidance Test Symposium. This symposium, hosted by the Central Inertial Guidance Test Facility, is directed toward the exchange of information, stimulation of new ideas, and discussion of recent developments in the field of guidance testing. The papers presented in these proceedings include such topics as aircraft inertial navigators, strapped-down guidance systems, component evaluation, and analysis techniques. The included papers were those presented in the unclassified sessions of the symposium. Papers presented in the classified portion of the meeting are being published as Volume II.

TABLE OF CONTENTS

FOREWORD

ABSTRACT

TABLE OF CONTENTS

PROCEEDINGS

Simulation of Dual-System Sled Testing - Dr Herbert R. Lotze and Major Bruce T. Kujawski

On the Isolation of Errors During Flight Testing and its Application to GPS - Peter A. Grundy and G. Jeffrey Geier

The Role of System Simulations in a Radar Flight Test Program - Charles C. Ormsby, Gregory L. Mealy, and James D. Shields

Designing Weapon System Test Trajectories for Guidance Error Source Observability - S. M. Archer, C. L. Bowman, and N. N. Gurwell

Slab Calibration for Strapdown Systems - A. A. Morgan

Sled and Flight Testing of Advanced Tactical Inertial Navigation Systems (ATIGS)

a. Captive Flight Tests of the Advanced Tactical Inertial Guidance System, Model X-0 (ATIGS X-0)- Merritt D. Mullen

b. Sled Tests of the ATIGS Laser Gyro Strap-Down Inertial Guidance System - Donald F. Walker

Calibration and Field Testing of a High-Quality Strapped Down Inertial Navigation System - George R. Taylor, Donald J. Pasik, and John W. Fish

Laboratory Calibration of a Precision Strapdown Inertial Navigation System Having a Non-Orthogonal Instrument Configuration - Patrick J. Donoghue and Leland B. Cotter

Flight Testing a Redundant Strapdown Inertial System - Thomas L. Shuck, Robert A. Booth, Jerold P. Gilmore, Thomas P. Schamp, T. T. Chien, and Ronald J. Hruby

Micron Configured to Meet Standard Medium Accuracy Navigator Specification - J. C. Pinson

Theoretical and Experimental Determination of the g^2 and g^4 Error Torques of a Free-Rotor Gyroscope - S. L. Zedekar and Capt J. E. Justin

Gyro Performance Evaluation from Linear Random Vibration Testing - Robert Thede and 1Lt Michael DeLorenzo

Multiple Accelerometer Testing as a Technique to Eliminate Undesirable Test Bed Characteristics - Robert H. Fall

An Examination of Low Power Spectral Density (PSD) Noise Performance of a Dry Tuned Gimbal Two-Degree-of-Freedom Gyroscope, and Methods for Further Noise Reduction - Robert B. Irvine and John W. Ritter

Stellar Update Demonstration for Upper Stage Boosters - G. R. Quasius, J. O. Boutelle, D. E. Sanders, and S. P. Kau

New Methods and Results in High Acceleration Terminal Homing Guidance and Control System's Testing - Dr Harold L. Pastrick and Jess B. Huff

A New Technique for Detecting Guidance Coefficient Instabilities - Edward M. Duiven, Charles M. Ermer, Kevin S. Tait, and C. Julian Vahlbert

An Advanced Software Mechanization for Calibration and Alignment of the Advanced Inertial Reference Sphere (AIRS) - D. J. Sifter and V. D. Henderson

The Application of CS/RT to the Omega 2041 Source Selection - Capt Paul E. Ronan and Harold W. Underwood

Test Evaluation of Two High Performance Strapdown IMU's - Joseph C. Blondin, James A. Jennings, and Stewart P. Weinstein

EIGHTH BIENNIAL GUIDANCE TEST SYMPOSIUM

SIMULATION OF DUAL-SYSTEM SLED TESTING

AUTHORS: DR HERBERT R. LOTZE
MAJOR BRUCE T. KUJAWSKI

CENTRAL INERTIAL GUIDANCE TEST FACILITY
6585TH TEST GROUP
HOLLOMAN AIR FORCE BASE, NEW MEXICO

I. INTRODUCTION

The state-of-the-art in guidance systems technology has been advancing at an incredible rate. The ever increasing accuracy of the systems now being developed is challenging our ability to test their accuracy. We are faced with the task of investing considerable time, effort and resources in the development of adequate test facilities or to develop alternate techniques which allow system evaluation with existing facilities. In particular, the high speed sled test track at Holloman Air Force Base, New Mexico, is the best surveyed and best instrumented facility available for testing precision inertial guidance systems. Yet systems now being designed will surpass the accuracy of the track reference system if all the design goals are met. One technique proposed to overcome the gap in accuracy is dual-system sled testing.

Dual-system testing implies the testing of two (usually identical) systems, one against the other, in order to determine the accuracy of both. Such an approach trades sophistication of equipment for sophisticated analysis. Although considered feasible for some time, a detailed study of dual-system testing parameters and effectiveness is required to validate its practicality.

It is expected that dual-system testing will generate solutions for error coefficients which could not be recovered using conventional test methods unless the accuracy of the reference system can be improved by two or more orders of magnitude. There is no intent to suggest all development of reference systems should cease; only that we may be able to extract adequate information about the systems without requiring the classic minimum of one order of magnitude superiority of reference instrumentation over test system.

The purpose of this study was to demonstrate the practical aspects of dual-system testing and to develop the analysis tools required to implement such a concept. The study was limited to the coefficient recovery process while recognizing other significant problems need addressing before the concept can become a procedure. A secondary purpose was to identify additional topics which must be addressed.

The approach used in the study was based on digital simulation. Although the system models were kept as general as possible, the numerical computations used values typical of the next generation Minuteman Guidance System (MX). Where actual values were not available, an "educated guess" was made based on recent developments in component technology. Two systems were simulated under the influence of a typical rocket sled acceleration profile; the resultant outputs were then used as inputs to the dual-system analysis procedure in order to recover original error coefficients. These steps are defined more precisely in the next section.

II. DEFINITION OF THE PROBLEM

A. Acceleration Profile

The first task, that of defining a typical sled acceleration profile, was hampered by the non-technical problem of there not being a typical profile. Each test program with its unique hardware and unique test objectives also has a unique acceleration profile. The profile selected was typical of a Minuteman II sled test program on the assumption the MX guidance system would not be too much different. The selected profile was represented by 52 straight line segments of the form

$$a_i(t) = a_{0i} + \dot{a}_i t, \quad i = 1, 2, \ldots, 52.$$

This form is a compromise between a larger number of segments, higher order polynominal segments, and computation time vs accuracy. A plot of the acceleration profile, along with the resultant velocity and position, is presented in Figure 1. Note that in addition to matching an actual sled test profile in acceleration, velocity, and position the coefficients were adjusted to maintain continuity in acceleration.

B. Error Equations

The basic simulation of the system(s) to be tested was accomplished in the velocity error domain. The velocity error observed by the system includes errors due to the SFIR (Specific Force Integrating Receiver, i.e. accelerometer), SFIR misalignments, platform misalignment and platform drift due to TGG (Third Generation Gyro) errors. These are:

$$\begin{aligned}
\Delta v_x &= \Sigma k_{xj} f_{xj} + \beta_{xz} v_y - \beta_{xy} v_z \\
&\quad + \alpha_z v_y - \alpha_y v_z \\
&\quad + (\int a_y \phi_z dt)_x - (\int a_z \phi_y dt)_x \\
\Delta v_y &= \Sigma k_{yj} f_{yj} + \beta_{yx} v_z - \beta_{yz} v_x \\
&\quad + \alpha_x v_z - \alpha_z v_x \\
&\quad + (\int a_z \phi_x dt)_y - (\int a_x \phi_z dt)_y \\
\Delta v_z &= \Sigma k_{zj} f_{zj} + \beta_{zy} v_x - \beta_{zx} v_y \\
&\quad + \alpha_y v_x - \alpha_x v_y \\
&\quad + (\int a_x \phi_y dt)_z - (\int a_y \phi_x dt)_z
\end{aligned}$$

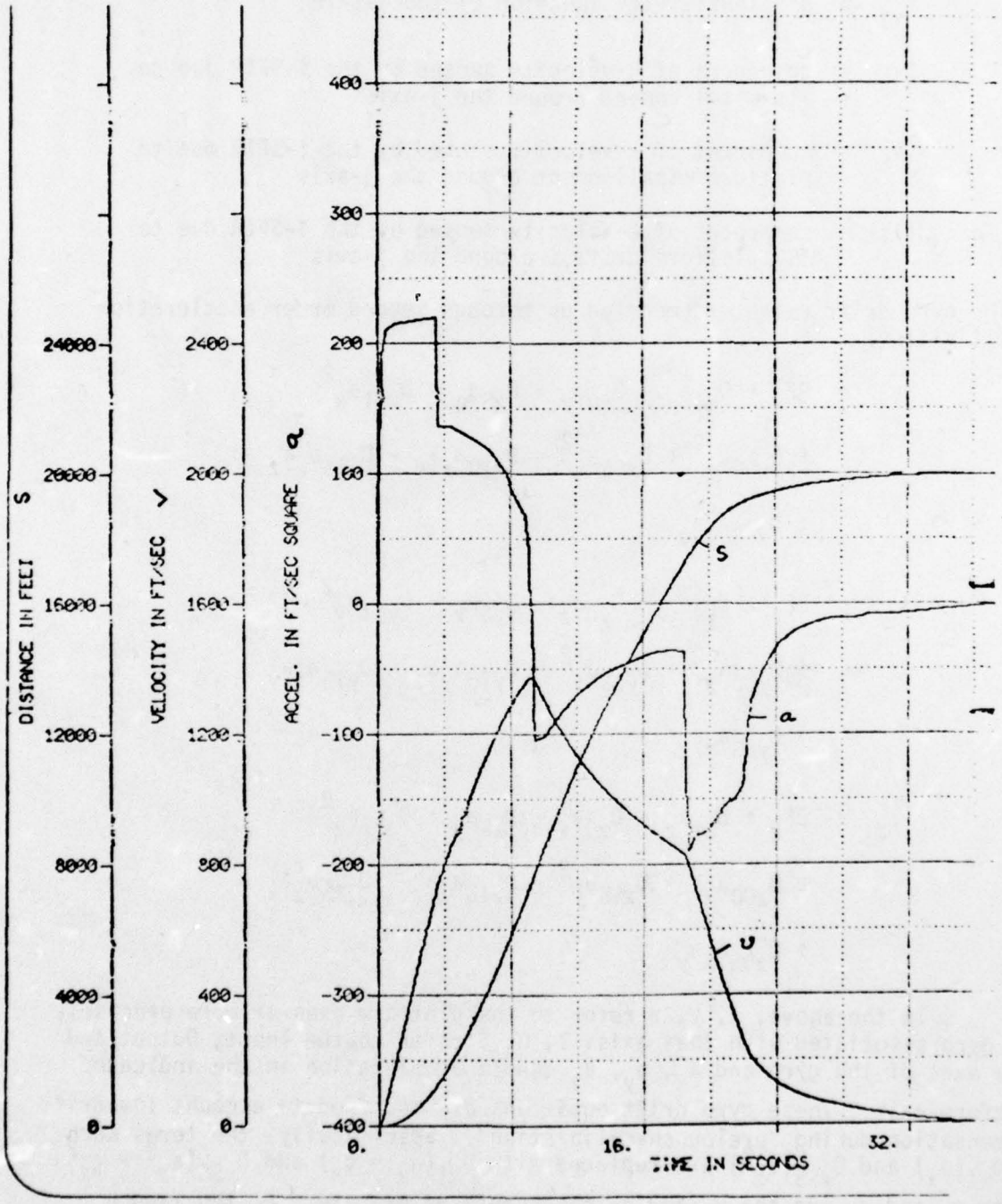


FIGURE 1. ACCELERATION, VELOCITY AND DISTANCE OF SLED VS TIME

where

k_{ij} = j^{th} coefficient of the SFIR sensing in i-direction

f_{ij} = j^{th} sensitivity function of the i-SFIR

$\beta_{ij}v_k$ = component of k-velocity sensed by the i-SFIR due to its misalignment around the j-axis

$\alpha_j v_k$ = component of k-velocity sensed by the i-SFIR due to platform misalignment around the j-axis

$(\int a_k \phi_j dt)_i$ = component of k-velocity sensed by the i-SFIR due to TGG platform drift ϕ around the j-axis

The gyro drift rates are modeled up through second order acceleration sensitivities.

$$\dot{\phi}_x = DF_x + D_{xI}a_x - D_{xO}a_y - D_{xS}a_z + D_{xII}a_x^2 + D_{xOO}a_y^2 + D_{xSS}a_z^2 - D_{xIO}a_xa_y - D_{xIS}a_xa_z + D_{xOS}a_ya_z$$

$$\dot{\phi}_y = DF_y + D_{yI}a_y - D_{yO}a_z - D_{yS}a_x + D_{yII}a_y^2 + D_{yOO}a_z^2 + D_{ySS}a_x^2 - D_{yIO}a_ya_z - D_{yIS}a_xa_y + D_{yOS}a_xa_z$$

$$\dot{\phi}_z = DF_z + D_{zI}a_z - D_{zO}a_x - D_{zS}a_y + D_{zII}a_z^2 + D_{zOO}a_x^2 + D_{zSS}a_y^2 - D_{zIO}a_xa_z - D_{zIS}a_za_y + D_{zOS}a_xa_y$$

In the above, x, y, z refer to the platform axes or more precisely the gyro associated with that axis; I, O, S refer to the Input, Output and Spin axes of the gyro and a_x, a_y, a_z denote acceleration in the indicated platform axis. These gyro drift equations are modified to account for drift, compensation during "prelaunch-calibration". Specifically, the terms such as $D_{xI}(a_x)$ and $D_{xSS}(a_z^2)$ are replaced with $D_{xI}(a_x - g_x)$ and $D_{xSS}(a_z^2 - g_z^2)$ where g_x and g_z are the x- and z- components of gravity. At the launch

pad $g_x = 0$ by definition of the local tangent plane and $a_z = g_z$. Clearly $D_{xSS}(a_z^2 - g_z^2)$ vanishes at the launch pad. Note that g_z varies along the track and g_x grows proportional to D_x/R where D_x is distance along track and R is the earth radius. Both variations are assumed small compared to the nominal input for the respective axis.

The assumed error model for the SFIR includes bias, scale factor error, and input axis and cross axis non-linearities. Note a linear cross axis sensitivity is indistinguishable from SFIR misalignment.

Incorporation of the above component error models into the system error model results in the set of equations depicted in Figures 2, 3, and 4. These equations containing 48 unknown coefficients represent the error model for but one of the systems under test. For dual-system test simulation it is necessary to combine two such sets of equations, one for each system, in such a way that the differenced output leads to a solution for the unknown coefficients of each system. This is the problem of defining a consistent set of platform orientations.

C. Platform Orientations

The platform orientations have a very significant effect on the accuracy of the results, number of sled runs required, and computational effort required. One scheme is to rotate one platform 45 degrees about the down-track (x) axis to place an equal component of gravity in the y- and z-axes. This effects recovery of more TGG coefficients per run, however due to high correlation of the inputs, the accuracy of the coefficients is greatly reduced.

After considerable trial and error, the following scheme for selecting platform orientations was selected (Table 1). Each orientation has two axes in the local tangent plane (LTP), that is, all rotations are 0, $\pm$90, or 180 degrees. Reserving x, y, z for platform axes and using 1, 2, 3 to denote down-track, cross-track, and vertical, the group code xly2z3 represents a platform orientation with x down-track (fore or aft), y cross-track (right or left), and z vertical (up or down). Clearly, in order to maintain a right-handed coordinate system only two may be selected independently. Thus group 1, code xly2z3 contains 2x2=4 orientations, each system can be positioned in 6x4=24 unique orientations, and two systems present 24x24=576 possibilities. Fortunately not all are required to obtain a solution.

The approach to defining the required orientations was to look for a set which would effectively extract SFIR coefficients assuming no TGG errors. This leads to the selection of pairs of parallel and anti-parallel orientations with each axis along-track. Any such set of six orientation pairs will identify the 24 SFIR coefficients and misalignment errors in the absence of TGG errors. The presence of gyro errors may camouflage results somewhat requiring the selection of alternate orientations.

$$
\begin{aligned}
\Delta v_x = {} & k_{x0}t + k_{x1}v_x + k_{x2}\int a_x^2 dt + k_{x3}\int (a_y^2 + a_z^2)dt \\
& + (\beta_{xz} + \alpha_z)v_y - (\beta_{xy} + \alpha_y)v_z \\
& + DF_z\int a_y t dt + D_{zI}(\int a_y v_z dt - g_z \int a_y t dt) \\
& - D_{z0}(\int a_y v_x dt - g_x \int a_y t dt) - D_{zS}(\int a_y v_y dt - g_y \int a_y t dt) \\
& + D_{zII}(\int a_y \int a_z^2 dt dt - g_z^2 \int a_y t dt) \\
& + D_{z00}(\int a_y \int a_x^2 dt dt - g_x^2 \int a_y t dt) \\
& + D_{zSS}(\int a_y \int a_y^2 dt dt - g_y^2 \int a_y t dt) \\
& - D_{zI0}(\int a_y \int a_x a_z dt dt - g_x g_z \int a_y t dt) \\
& - D_{zIS}(\int a_y \int a_y a_z dt dt - g_y g_z \int a_y t dt) \\
& + D_{z0S}(\int a_y \int a_x a_y dt dt - g_x g_y \int a_y t dt) \\
& - DF_y\int a_z t dt - D_{yI}(\int a_z v_y dt - g_y \int a_z t dt) \\
& + D_{y0}(\int a_z v_z dt - g_z \int a_z t dt) + D_{yS}(\int a_z v_x dt - g_x \int a_z t dt) \\
& - D_{yII}(\int a_z \int a_y^2 dt dt - g_y^2 \int a_z t dt) \\
& - D_{y00}(\int a_z \int a_z^2 dt dt - g_z^2 \int a_z t dt) \\
& - D_{ySS}(\int a_z \int a_x^2 dt dt - g_x^2 \int a_z t dt) \\
& + D_{yI0}(\int a_z \int a_y a_z dt dt - g_y g_z \int a_z t dt) \\
& + D_{yIS}(\int a_z \int a_x a_y dt dt - g_x g_y \int a_z t dt) \\
& - D_{y0S}(\int a_z \int a_x a_z dt dt - g_x g_z \int a_z t dt)
\end{aligned}
$$

Gyro Drift Error $\int a_y \phi_z dt$

Gyro Drift Error $-\int a_z \phi_y dt$

FIGURE 2

SYSTEM X-AXIS VELOCITY ERROR MODEL

$$\Delta v_y = k_{y0}t + k_{y1}v_y + k_{y2}\int a_y^2 dt + k_{y3}\int (a_x^2 + a_z^2)dt$$

$$+ (\beta_{yx} + \alpha_x)v_z - (\beta_{yz} + \alpha_z)v_x$$

$$+ DF_x\int a_z t dt + D_{xI}(\int a_z v_x dt - g_x \int a_z t dt)$$

$$- D_{x0}(\int a_z v_y dt - g_y \int a_z t dt) - D_{xS}(\int a_z v_z dt - g_z \int a_z t dt)$$

$$+ D_{xII}(\int a_z \int a_x^2 dt dt - g_x^2 \int a_z t dt)$$

$$+ D_{xSS}(\int a_z \int a_z^2 dt dt - g_z^2 \int a_z t dt)$$

$$+ D_{x00}(\int a_z \int a_y^2 dt dt - g_y^2 \int a_z t dt)$$

$$- D_{xI0}(\int a_z \int a_x a_y dt dt - g_x g_y \int a_z t dt)$$

$$- D_{xIS}(\int a_z \int a_x a_z dt dt - g_x g_z \int a_z t dt)$$

$$+ D_{x0S}(\int a_z \int a_y a_z dt dt - g_y g_z \int a_z t dt)$$

Gyro Drift Error $\int a_z \phi_x dt$

$$- DF_z\int a_x t dt - D_{zI}(\int a_x v_z dt - g_z \int a_x t dt)$$

$$+ D_{z0}(\int a_x v_x dt - g_x \int a_x t dt) + D_{zS}(\int a_x v_y dt - g_y \int a_x t dt)$$

$$- D_{zII}(\int a_x \int a_z^2 dt dt - g_z^2 \int a_x t dt)$$

$$- D_{zSS}(\int a_x \int a_y^2 dt dt - g_y^2 \int a_x t dt)$$

$$- D_{z00}(\int a_x \int a_x^2 dt dt - g_x^2 \int a_x t dt)$$

$$+ D_{zI0}(\int a_x \int a_x a_z dt dt - g_x g_z \int a_x t dt)$$

$$+ D_{zIS}(\int a_x \int a_y a_z dt dt - g_y g_z \int a_x t dt)$$

$$- D_{z0S}(\int a_x \int a_x a_y dt dt - g_x g_y \int a_x t dt)$$

Gyro Drift Error $-\int a_x \phi_z dt$

FIGURE 3

SYSTEM Y-AXIS VELOCITY ERROR MODEL

$$
\begin{aligned}
\Delta v_z = {} & k_{z0}t + k_{z1}v_z + k_{z2}\int a_z^2 dt + k_{z3}\int (a_x^2 + a_y^2)dt \\
& + (\beta_{zy} + \alpha_y)v_x - (\beta_{zx} + \alpha_x)v_y \\
& + DF_y \int a_x t dt + D_{yI}(\int a_x v_y dt - g_y \int a_x t dt) \\
& - D_{y0}(\int a_x v_z dt - g_z \int a_x t dt) - D_{yS}(\int a_x v_x dt - g_x \int a_x t dt) \\
& + D_{yII}(\int a_x \int a_y^2 dt dt - g_y^2 \int a_x t dt) \\
& + D_{ySS}(\int a_x \int a_x^2 dt dt - g_x^2 \int a_x t dt) \\
& + D_{y00}(\int a_x \int a_z^2 dt dt - g_z^2 \int a_x t dt) \\
& - D_{yI0}(\int a_x \int a_y a_z dt dt - g_y g_z \int a_x t dt) \\
& - D_{yIS}(\int a_x \int a_x a_y dt dt - g_x g_y \int a_x t dt) \\
& + D_{y0S}(\int a_x \int a_x a_z dt dt - g_x g_z \int a_x t dt) \\
& - DF_x \int a_y t dt - D_{xI}(\int a_y v_x dt - g_x \int a_y t dt) \\
& + D_{x0}(\int a_y v_y dt - g_y \int a_y t dt) + D_{xS}(\int a_y v_z dt - g_z \int a_y t dt) \\
& - D_{xII}(\int a_y \int a_x^2 dt dt - g_x^2 \int a_y t dt) \\
& - D_{xSS}(\int a_y \int a_z^2 dt dt - g_z^2 \int a_y t dt) \\
& - D_{x00}(\int a_y \int a_y^2 dt dt - g_y^2 \int a_y t dt) \\
& + D_{xI0}(\int a_y \int a_x a_y dt dt - g_x g_y \int a_y t dt) \\
& + D_{xIS}(\int a_y \int a_x a_z dt dt - g_x g_z \int a_y t dt) \\
& - D_{x0S}(\int a_y \int a_y a_z dt dt - g_y g_z \int a_y t dt)
\end{aligned}
$$

Gyro Drift Error $\int a_x \phi_y dt$

Gyro Drift Error $-\int a_y \phi_x dt$

FIGURE 4

SYSTEM Z-AXIS VELOCITY ERROR MODEL

ORIENTATION GROUP	GROUP CODE	ORIENT NO.	ROTATIONS (DEGREES) AZ	PITCH	ROLL
1	X1Y2Z3	1	0	0	0
		2	180	0	0
		3	180	180	0
		4	0	180	0
2	X1Y3Z2	1	0	0	90
		2	0	0	- 90
		3	180	0	- 90
		4	180	0	90
3	X2Y1Z3	1	- 90	0	0
		2	90	0	0
		3	- 90	0	180
		4	90	0	180
4	X2Y3Z1	1	90	0	90
		2	- 90	0	90
		3	- 90	0	- 90
		4	90	0	- 90
5	X3Y1Z2	1	0	- 90	- 90
		2	0	- 90	90
		3	0	90	90
		4	0	90	- 90
6	X3Y2Z1	1	0	90	0
		2	180	90	0
		3	0	- 90	0
		4	180	- 90	0

TABLE 1. LTP AXES ROTATION SCHEME

Some rules for selection and subsequent adjustment of orientations are as follows: The orientation for system 1 and system 2 may but need not necessarily be from the same group (Table 1). Within its group there are 4 orientations for each system allowing the choice of 1 in 16 orientations once the groups are selected. Within a group the same set of coefficients is always excited, only the sign of the excitation differs.

D. Simulation Set-Up

Although primarily a tool in this study, the dual-system simulation is an essential element. The major simulation steps, depicted in Figure 5 are as follows: The acceleration profile is integrated to obtain velocity and again integrated to obtain sled position. Separate coordinate transformations (T_1 and T_2) are applied, one for each system. Thirty-six sensitivity functions are generated in the system coordinate frame. The sum of the products of error coefficients and sensitivity functions is formed and transformed back into the LTP coordinate system. Finally, the differences in error functions are output from the simulation and constitute inputs to the coefficient recovery algorithm.

Note only the vertical and down-track error functions, denoted Dv_z and Dv_x are differenced. The cross track components v_{y1}, v_{y2} sensed by the two systems are processed as single-system test data which has some advantages in the coefficient recovery process.

III. ERROR COEFFICIENT RECOVERY

A. Cross Track Data

The basic premise of dual-system testing is to form the difference of two systems' outputs to eliminate errors of the reference system. However, the cross-track velocity is precisely known to be zero plus the integral of Coriolis effects. Therefore, there is little advantage to differencing cross-track outputs and furthermore, coupling of coefficients which results from combining the output of two systems may actually be avoided.

Consider the case with both systems orientated x down-track, y cross-track, and z vertical-down, (Group 1, Orientation 3, Table 1). Then the cross-track output is precisely as given in Figure 3 for Δv_{y1} and Δv_{y2}. The output error Δv_{y1} is fit in the least squares sense to the coordinate functions of time, t, down-track velocity, v_{DT}, and $\int a_{DT}^2 dt$, that is

$$\Delta v_{y1} = Y01 \cdot t + Y11 \cdot v_{DT} + Y31 \cdot \int a_{DT}^2 dt$$

Comparison with the equation of Figure 3, ignoring gyro terms, and recognizing $v_z = g \cdot t$, $v_x = v_{DT}$, $\int a_x^2 dt = \int a_{DT}^2 dt$, and $\int a_z^2 dt = g^2 t$ leads one to

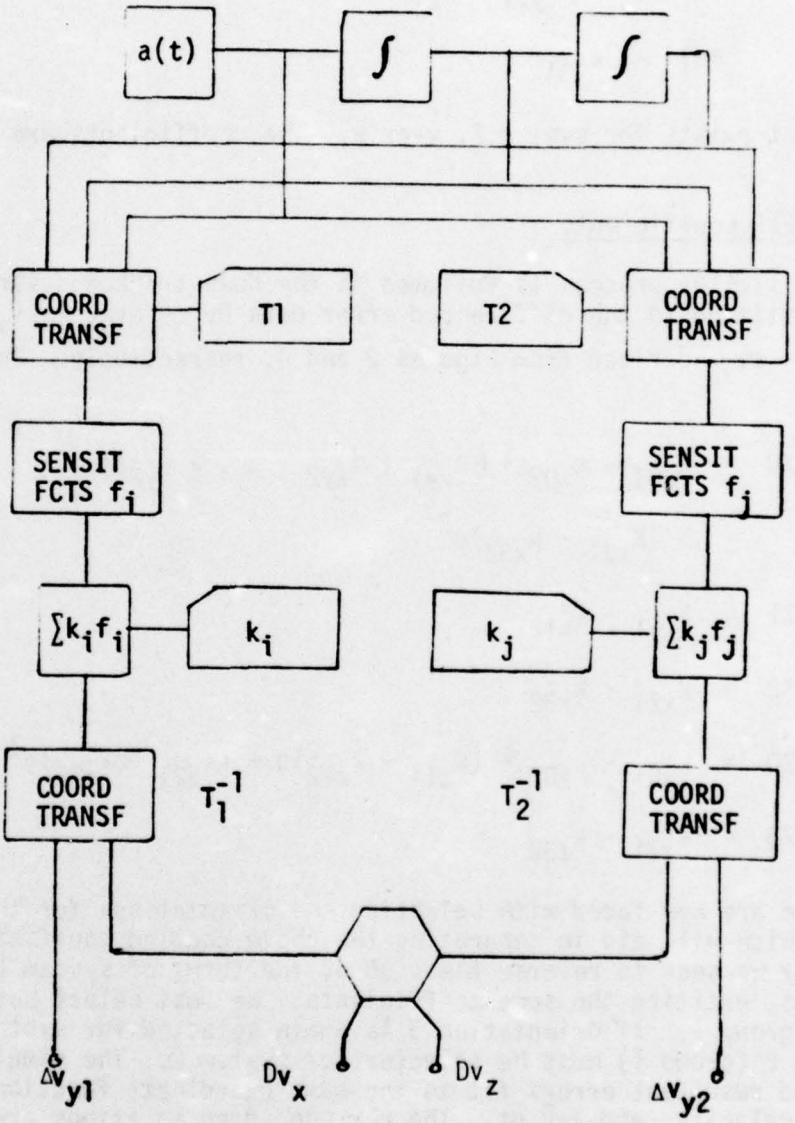


FIGURE 5. SIMULATION FLOW CHART

$$Y01 = k_{y01} + (\beta_{yx1} + \alpha_{x1})g + k_{y31}g^2$$

$$Y11 = -(\beta_{yz1} + \alpha_{z1})$$

$$Y31 = k_{y31}$$

A similar set exists for system 2, y-axis. The coefficients are beginning to emerge.

B. SFIR Coefficients

A similar process is followed in the down-track and vertical directions fitting to the differenced error data $Dv_x = \Delta v_{x1} - \Delta v_{x2}$ and $Dv_z = \Delta v_{z1} - \Delta v_{z2}$ derived from Figures 2 and 4, respectively. The results are:

$$X0 = k_{x01} - k_{x02} + (-\beta_{xy1} + \beta_{xy2} - \alpha_{y1} + \alpha_{y2})g + (K_{x31} - k_{x32})g^2$$

$$X1 = k_{x11} - k_{x12}$$

$$X2 = k_{x21} - k_{x22}$$

and:

$$Z0 = k_{z01} - k_{z02} + (K_{z11} - k_{z12})g + (K_{z21} - k_{z22})g^2$$

$$Z3 = k_{z31} - k_{z32}$$

We are now faced with selecting the orientations for the second sled test which will aid in separating the above coupled coefficients. Specifically we seek to reverse the sign of the terms of system 2 along the x and z axes, exciting the same coefficients. We must select both orientations from group 1. If orientation 3 is again selected for system 1, orientation 2 (group 1) must be selected for system 2. The simulation is repeated and resultant errors fit to the same coordinate functions of time, down-track velocity, and $\int a_{DT}^2 dt$. The corresponding equations are

$$X0' = k_{x01} + k_{x02} + (\beta_{xy1} - \beta_{xy2} + \alpha_{y1} - \alpha_{y2})g + (k_{x31} + k_{x32})g^2$$

$$X1' = -k_{x11} + k_{x12}$$

$$X2' = k_{x21} + k_{x22}$$

$$Y01' = k_{y01} + (\beta_{yx1} + \alpha_{x1})g + k_{y31}g^2$$

$$Y02' = k_{y02} + (\beta_{yx2} + \alpha_{x2})g + k_{y32}g^2$$

$$Y11' = -(\beta_{yz1} + \alpha_{z1})$$

$$Y12' = -(\beta_{yz2} + \alpha_{z2})$$

$$Y31' = k_{y31}$$

$$Y32' = k_{y32}$$

$$Z0' = k_{z01} + k_{z02} + (k_{z11} - k_{z12})g + (k_{z21} + k_{z22})g^2$$

$$Z3' = k_{z31} + k_{z32}$$

By inspection of these and the previous set of equations it is easily seen that the signs of the coefficients are as required for separation, except the equations for X1 and X1' provide no additional information for the separation of k_{x11} and k_{x12}. Likewise, the equations for Z0 and Z0' contain a double sign reversal making separation not completely possible. Furthermore, since platform misalignments may be expected to vary from sled test to sled test, the equations containing these terms are not entirely useful.

Selection of additional pairs of dual-system sled orientations with y-axis down-track and then a pair with z-axis down-track, six sled runs in total provides sufficient information to extract all coefficients except explicit scale factor errors.

The reason scale factor errors are always obtained as the difference in coefficients can be explained as follows: Neglecting bias and non-linearities, the output of any instrument can be related to its input by the relation

$$\text{out} = \frac{1}{SF}[\text{in}]$$

We determine a measure of the input quantity by multiplying the instrument output by the appropriate scale factor, SF. Suppose our knowledge of the scale factor is in error by the amount $k_1 \cdot SF$, i.e., we use $(1+k_1) \cdot SF$ instead of SF, then our measurement is given by

$$\text{meas} = \text{in} + k_1 \cdot [\text{in}]$$

Using two instruments to sense the same input:

$$\text{meas}_1 = \text{in} + k_{11} \cdot [\text{in}]$$

$$\text{meas}_2 = \text{in} + k_{12}\cdot[\text{in}]$$

Differencing to eliminate the input gives

$$\text{meas}_1 - \text{meas}_2 = (k_{11} - k_{12})\cdot[\text{in}]$$

If instrument 1 is a test specimen and instrument 2 is a precision reference, then $k_{12} << k_{11}$ and $\text{meas}_2 = \text{ref} \simeq \text{in}$, therefore

$$\text{meas}_1 - \text{ref} = k_{11}[\text{ref}]$$

If the available reference is of insufficient accuracy or the instruments are nearly identical the above is not useful. We are led to a second test of the instruments with one of the sensors reversed, say #2, then:

$$\text{meas}_1 = \text{in} + k_{11}\cdot[\text{in}]$$

$$\text{meas}_2 = -\text{in} + k_{12}\cdot[-\text{in}]$$

Summing to eliminate the input yields

$$\text{meas}_1 + \text{meas}_2 = (k_{11} - k_{12})\cdot[\text{in}]$$

which still provides a difference in scale factor error. Note this algebraic sum is really a numerical difference since $\text{meas}_2 \simeq -\text{in} \simeq \text{meas}_1$.

A remedy to the separation problem is to look at the ratio of measurements as well as sums and differences. Consider

$$R = \frac{\text{meas}_2}{\text{meas}_1} = \frac{1 + k_{12}}{1 + k_{11}}$$

from which

$$k_{11} = \frac{1 - R}{R} + \frac{k_{12}}{R}$$

Suppose we have $X1 = k_{11} - k_{12}$ computed from the difference of measurements then, with some algebra

$$X1 = \frac{1 - R}{R} + \frac{k_{12}}{R} - k_{12}$$

$$k_{12} = \frac{X1R}{1 - R} - 1$$

and

$$k_{11} = \frac{X1}{1 - R} - 1$$

In practice it is expected that the ratio R will be computed from pre- and post-run calibration data where neglecting higher order non-linear terms is a reasonable approximation. Even so, the value of R may be close to 1 causing great difficulty in estimating k_{11} and k_{12}.

C. TGG Coefficients

The procedure for recovery of gyro coefficients is not unlike the procedure for recovery of SFIR coefficients and in fact is carried out simultaneously. As with the SFIR coefficients, certain gyro coefficients appear explicitly in the solution, notably DF, D_{II} and D_{OO}, and are recoverable from single sled tests. The remainder appear in combination with like coefficients of its dual-system and therefore require judicious choice of system orientations for satisfactory isolation.

The platform orientations previously selected for recovery of SFIR coefficients is the starting point for TGG coefficient recovery. The first observation is that the down-track and vertical dual-system error functions contain common terms due to drift of the horizontal (cross-track) gyro; therefore, only the down-track and cross-track errors will be analyzed.

Recall sled test one has both systems orientated x-axis down-track z-axis down. Fitting the function $\int a_z t dt = v_z t - S_z$ to the error Dv_x derived from the equation in Figure 2 yields

$$GX1 = - DF_{y1} + DF_{y2}$$

Fitting the function $\int a_z v_x dt$ yields

$$GX2 = D_{yS1} - D_{yS2} + (D_{yOS1} - D_{yOS2})g$$

where the identity $\int a_z \int a_x a_z dtdt = g \int a_z v_x dt$ has been used. Fitting to $\int a_z \int a_x^2 dtdt$ yields

$$GX3 = -D_{ySS1} + D_{ySS2}$$

The cross axis terms are evaluated separately as single system data would be processed. In order to reduce correlation of the sensitivity functions which leads to an ill-conditioned least squares matrix the following observations are made: $\int a_x t dt = v_x t - S_x$ and $\int a_z v_x dt = gS_x$ both contain terms proportional to S_x, therefore instead of fitting to $\int a_x t dt$, the function $v_x t$ alone is used. Then S_x is used only once in the fitting process greatly reducing the correlation. The same arguments apply to $\int a_y t dt$ and $\int a_z t dt$. However in the vertical direction $v_z t$ will yield only one-half the expected coefficient since $v_z t = gt^2$, whereas $\int a_z t dt = \frac{1}{2} gt^2$.

Following the above procedure the six tests identified as appropriate for SFIR coefficient recovery provide information on the TGG coefficients defined in Tables 2a, 2b, and 2c. Note the column headings correspond to Table 1 group designation followed by the orientation number for system 1 and system 2, separated by a comma.

Our inspection of the table reveals all 60 TGG coefficients have been excited but several are still coupled. The next task is to identify additional tests which will aid in separation of coefficients. In particular, the following coefficients cannot be separated (i = x, y, z).

$$D_{iSS1} - D_{iSS2} \text{ in GX3}$$

$$- D_{iI1} - D_{iIS1}g \text{ in GY31}$$

$$- D_{i01} - D_{iI01}g \text{ in GY41}$$

as well as three of the four terms in GX2.

Additional information can be obtained from additional tests in orientations within the same groups in order to specifically excite the same coefficients. The following orientations are selected.

GROUP	SYSTEM 1 ORIENTATION	SYSTEM 2 ORIENTATION
1	1	3
5	1	3
4	1	3

The solutions found from these additional sled tests are as follows:

From GP1: 1, 3: $GX2 = - D_{ySS1} - D_{ySS2} + (D_{yOS1} - D_{yOS2})g$

$GX3 = + D_{ySS1} + D_{ySS2}$

$GY31 = - D_{xI1} + D_{xIS1}g - DF_{z1}/g$

$GY41 = + D_{z01} + D_{zI01}g$

From GP5: 1,3: $GX2 = - D_{zS1} - D_{zS2} + (+ D_{zOS1} - D_{zOS2})g$

$GX3 = + D_{zSS1} + D_{zSS2}$

$GY31 = - D_{yI1} + D_{yIS1}g - DF_{x1}/g$

$GY41 = + D_{x01} + D_{xI01}g$

	GP1: 3, 3	GP1: 3, 2
GX1	$-DF_{y1} + DF_{y2}$	$+DF_{y1} - DF_{y2}$
GX2	$+D_{ySI} - D_{yS2} + (D_{yOS1} - D_{yOS2})g$	$+D_{ySI} + D_{yS2} + (D_{yOS1} - D_{yOS2})g$
GX3	$-D_{ySS1} + D_{ySS2}$	$+D_{ySS1} - D_{ySS2}$
GY11	$-\frac{1}{2}DF_{x1}$	$+\frac{1}{2}DF_{x1}$
GY21	$+DF_{z1}$	$-DF_{z1}$
GY31	$-D_{xI1} - D_{xIS1}g + DF_{z1}/g$	$-D_{xI1} - D_{xIS1}g + DF_{z1}/g$
GY41	$-D_{z01} + D_{zI01}g$	$-D_{z01} + D_{zI01}g$
GY51	$-D_{xII1}$	$+D_{xII1}$
GY61	$+D_{z001}$	$-D_{z001}$
GY12	$-\frac{1}{2}DF_{x2}$	$+\frac{1}{2}DF_{x2}$
GY22	$+DF_{z2}$	$-DF_{z2}$
GY32	$-D_{xI2} - D_{xIS2}g + DF_{z2}/g$	$+D_{xI2} - D_{xIS2}g + DF_{z2}/g$
GY42	$-D_{z02} + D_{zI02}g$	$+D_{z02} + D_{zI02}g$
GY52	$-D_{xII2}$	$+D_{xII2}$
GY62	$+D_{z002}$	$-D_{z002}$

TABLE 2a

GYRO COEFFICIENTS RECOVERABLE
FROM SLED TESTS 1 AND 2 (SCHEME 1)

	GP5: 3, 3	GP5: 3,2
GX1	$-DF_{z1}+DF_{z2}$	$+DF_{z1}-DF_{z2}$
GX2	$+D_{zS1}-D_{zS2}+(+D_{zOS1}-D_{zOS2})g$	$+D_{zS1}+D_{zS2}+(+D_{zOS1}-D_{zOS2})g$
GX3	$-D_{zSS1}+D_{zSS2}$	$+D_{zSS1}-D_{zSS2}$
GY1i	$-\frac{1}{2}DF_{y1}$	$+\frac{1}{2}DF_{y1}$
GY21	$+DF_{x1}$	$-DF_{x1}$
GY31	$-D_{yI1}-D_{yIS1}g+DF_{x1}/g$	$-D_{yI1}-D_{yIS1}g+DF_{x1}/g$
GY41	$-D_{xO1}+D_{xIO1}g$	$-D_{xO1}+D_{xIO1}g$
GY51	$-D_{yII1}$	$+D_{yII1}$
GY61	$+D_{xOO1}$	$-D_{xOO1}$
GY12	$-\frac{1}{2}DF_{y2}$	$+\frac{1}{2}DF_{y2}$
GY22	$+DF_{x2}$	$-DF_{x2}$
GY32	$-D_{yI2}-D_{yIS2}/g+DF_{x2}/g$	$+D_{yI2}-D_{yIS2}g+DF_{x2}/g$
GY42	$-D_{xO2}+D_{xIO2}g$	$+D_{xO2}+D_{xIO2}g$
GY52	$-D_{yII2}$	$+D_{yII2}$
GY62	$+D_{xOO2}$	$-D_{xOO2}$

TABLE 2b

GYRO COEFFICIENTS RECOVERABLE
FROM SLED TESTS 4 AND 5 (SCHEME 1)

	GP4: 3, 3	GP4: 3, 2
GX1	$-DF_{x1} + DF_{x2}$	$+DF_{x1} - DF_{x2}$
GX2	$+D_{xS1} - D_{xS2} + (+D_{xOS1} - D_{xOS2})g$	$+D_{xS1} + D_{xS2} + (+D_{xOS1} - D_{xOS2})g$
GX3	$-D_{xSS1} + D_{xSS2}$	$+D_{xSS1} - D_{xSS2}$
GY11	$-\frac{1}{2}DF_{z1}$	$+\frac{1}{2}DF_{z1}$
GY21	$+DF_{y1}$	$-DF_{y1}$
GY31	$-D_{zI1} - D_{zIS1}g + DF_{y1}/g$	$-D_{zI1} - D_{zIS1}g + DF_{y1}/g$
GY41	$-D_{yO1} + D_{yIO1}g$	$-D_{yO1} + D_{yIO1}g$
GY51	$-D_{zII1}$	$+D_{zII1}$
GY61	$+D_{yOO1}$	$-D_{yOO1}$
GY12	$-\frac{1}{2}DF_{z2}$	$+\frac{1}{2}DF_{z2}$
GY22	$+DF_{y2}$	$-DF_{y2}$
GY32	$-D_{zI2} - D_{zIS2}g + DF_{y2}/g$	$+D_{zI2} - D_{zIS2}g + DF_{y2}/g$
GY42	$-D_{yO2} + D_{yIO2}g$	$+D_{yO2} + D_{yIO2}g$
GY52	$-D_{zII2}$	$+D_{zII2}$
GY62	$+D_{yOO2}$	$-D_{yOO2}$

TABLE 2c

GYRO COEFFICIENTS RECOVERABLE
FROM SLED TESTS 7 AND 8 (SCHEME 1)

From GP4: 1, 3: $GX2 = -D_{xS1} - D_{xS2} + (D_{xOS1} - D_{xOS2})g$

$GX3 = +D_{xSS1} + D_{xSS2}$

$GY31 = -D_{zI1} + D_{zIS1}g - DF_{y1}/g$

$GY41 = +D_{yO1} + D_{yIO1}g$

The GYn1 terms above apply to system 1. There are an equal number of GYn2 terms for system 2.

Processing the above equations leaves six g^2-terms still coupled. Three additional tests are required to separate these coefficients. The required orientations are:

SYSTEM 1 ORIENTATION	SYSTEM 2 ORIENTATION
GP3:1	GP4:1
GP6:4	GP1:1
GP2:1	GP5:1

With these orientations, the following equations are obtained, respectively:

$GX2 = -D_{xO1} - D_{xS2} + (D_{xOS1} + D_{xOS2})g$

$GX2 = -D_{yO1} - D_{yS2} + (D_{yOS1} + D_{yOS2})g$

$GX2 = -D_{zO1} - D_{zS2} + (D_{zOS1} + D_{zOS2})g$

It would appear that recovery of these coefficients are rather expensive, requiring three additional runs to separate six additional coefficients. In fact, these runs also provide substantiating data on coefficients already extracted, thereby substantiating their validity.

D. Rate of Recovery

Although there are several factors usually considered in the efficiency of a computational algorithm, in the case of dual-system sled testing the principal factor is number of sled runs. Several schemes for selecting dual-system orientations were investigated. These schemes differ in the sequence of runs using the same set of orientations. The results of the various schemes are displayed in Figure 6. It can be seen scheme 1 has a higher recovery rate, however, the total number of runs required to recover all coefficients is the same for both schemes.

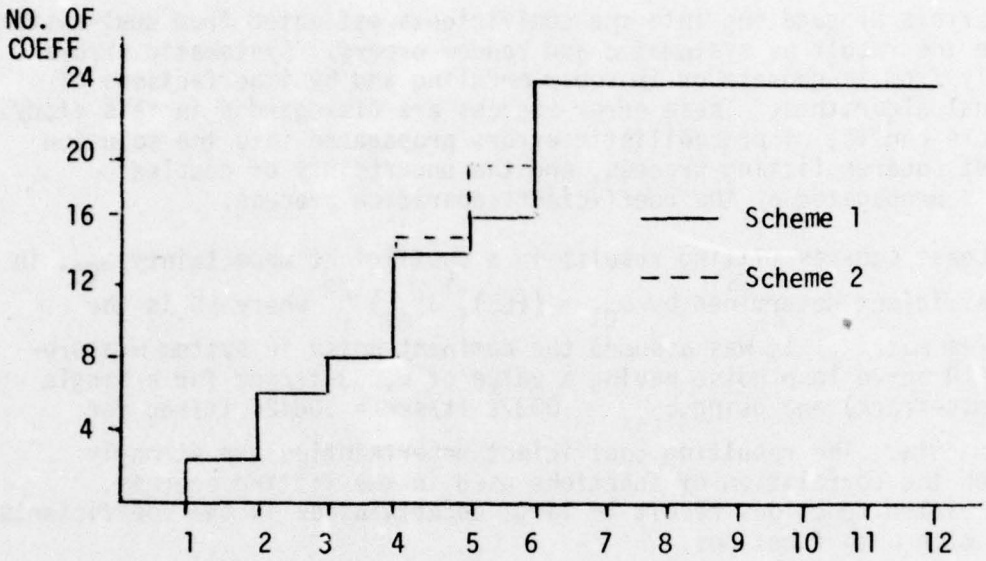


FIGURE 6a. NUMBER OF SFIR COEFFICIENTS RECOVERED VS NUMBER OF SLED RUNS

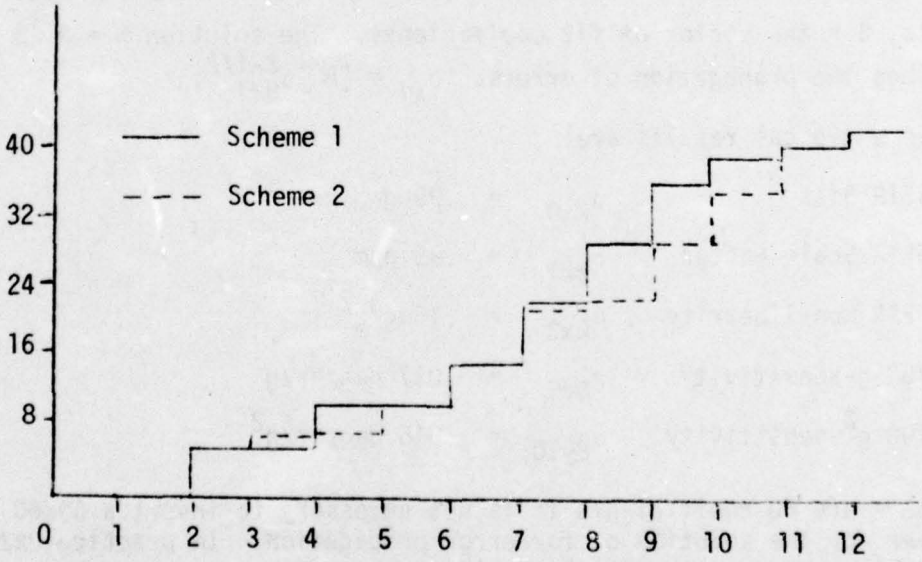


FIGURE 6b. NUMBER OF TGG COUPLED COEFFICIENTS RECOVERED VS NUMBER OF SLED RUNS

E. Smallest Recoverable Coefficients

Errors propagating into the coefficients estimated from dual-system testing are the result of systematic and random errors. Systematic errors arise mainly from inadequate or improper modeling and by imperfections of computational algorithms. These error sources are disregarded in this study. Random errors consist of probabilistic errors propagated into the solution by the least squares fitting process, and the uncertainty of coupled coefficients propagated by the coefficient separation process.

Least squares fitting results in a coefficient uncertainty, σ_{Ci}, in the ith coefficient determined by $\sigma_{Ci} = ((LS)^{-1}_i \sigma^2_{res})^{1/2}$ where LS is the least squares matrix. It was assumed the dominant noise in system measurements is SFIR servo loop noise having a value of 0.003 ft/sec for a single system (cross-track) and using $\sigma_{res} = .003\sqrt{2}$ ft/sec = .00424 ft/sec for dual system data. The resulting coefficient uncertainties are strongly dependent on the correlation of functions used in the fitting process. Highly correlated functions result in large uncertainties in the coefficients associated with both functions.

The separation of coupled coefficients may be viewed as a process of matrix inversion. That is, the set of equations relating error model coefficients to least squares fit coefficients being a set of linear equations can be represented in matrix form: $AX = B$, X = the vector of error model coefficients, B = the vector of fit coefficients. The solution $X = A^{-1}B$ also describes the propagation of errors: $\sigma_{xi} = [A^{-1}\sigma^2_B]^{1/2}_i$.

Some typical results are:

SFIR Bias	σ_{kx0}	=	.99μg
SFIR Scale Factor	σ_{kx1}	=	.95 ppm
SFIR Non-linearity	σ_{kx2}	=	.16μg/g^2
TGG g-sensitivity	σ_{DyS}	=	.037 deg/hr/g
TGG g^2-sensitivity	σ_{DyI0}	=	.045 deg/hr/g^2

Although there are 60 coefficients it is not necessary to invert a 60x60 matrix either for the solution or for error propagation. In practice 2x2 or 3x3 partitions may be used for both steps.

The benefit of dual-system testing in the form of reduced uncertainty in the recovered coefficients depends on the quality reference system we are trying to overcome. The ratio of coefficient uncertainty from dual-system results to the uncertainty from single system recovery is

$$R = \left(\frac{2\sigma_{sys}^2}{\sigma_{ref}^2 + \sigma_{sys}^2}\right)^{1/2}$$

If the system and reference are equally accurate, no advantage is gained. (This assumes we take care to separate reference errors from system errors, otherwise we allow systematic errors to accumulate.)

IV. CONCLUSIONS

The investigation of dual-system sled tests leads to the following conclusions:

Valid procedures exist for recovering error coefficients from dual-system tests.

The dual-system approach is applicable to down-track and vertical directions. Cross-track data should be evaluated by applying standard single-system procedures.

Six properly chosen sled tests yield 24 SFIR coefficients (6 SFIRs) and 12 misalignment angles.

Twelve (six additional) tests yield 60 gyro drift coefficients (6 TGGs). Most gyro coefficients (90%) are recovered after nine sled tests.

Dual-system tests and single-system tests yield, on the average, the same number of coefficients per sled run. Platform orientations selected for dual-system tests are also applicable to single-system tests.

Dual-system tests require pre-launch calibration data to determine the ratio of SFIR coefficients. Ratios near unity may prevent recovery of both scale factor errors. The recovery of other SFIR error coefficients and TGG coefficients are not affected by this limitation should it occur.

Extensions to this study will be required to answer additional questions before dual-system sled testing is a practical test approach.

Can an external reference such as space/time data be incorporated to advantage?

Is there a dependence on the acceleration profile, and, if so, how can an advantage be made from this dependence.

What effect does random vibration and relative motion between platforms have on the effectiveness of dual-system sled testing for component error coefficient recovery?

V. REFERENCE

The research described herein is being published in more complete detail as an ADTC Technical Report with the same title. Inquiries should be addressed to: 6585th Test Group/GDP, Holloman AFB NM 88330.

EIGHTH BIENNIAL GUIDANCE TEST SYMPOSIUM

ON THE ISOLATION OF ERRORS DURING FLIGHT TESTING AND ITS APPLICATION TO GPS

AUTHORS: PETER A. GRUNDY
G. JEFFREY GEIER

INTERMETRICS, INC.
CAMBRIDGE, MASSACHUSETTS

ON THE ISOLATION OF ERRORS DURING FLIGHT TESTING AND ITS APPLICATION TO GPS*

Peter A. Grundy, G. Jeffrey Geier
Intermetrics, Inc.
Cambridge, Mass.

ABSTRACT

The testing and checkout of current navigation systems is an increasingly complex task. The multiplicity of sensor subsystems, the sophisticated level of navigation algorithms, the integrated nature of the system itself, all conspire to decrease the direct observability of any particular error source which may cause poor system performance.

Extensive test standards and procedures have been developed to qualify each of the system components prior to the initiation of field testing. These tests normally entail driving the system with simulated inputs or with those inputs which can be generated in a laboratory environment. These tests do not provide a complete system checkout due to: 1) possible lack of fidelity of simulator models to the real world; and 2) failure to exercise the full range of possible environmental conditions.

This paper attempts to develop a methodical, generalized data analysis procedure for the isolation of errors from processing of flight test recorded data. A "top-down" analysis of a generalized navigation system is outlined. The system consists of one or more sensor packages with appropriate interfaces, a minicomputer or microprocessor, the navigation software which operates on the sensor data to compute the navigation solution (position, velocity, etc.), and possibly, feedback paths from the software to the sensors.

The error isolation problem is then disassembled into two functionally separate procedures: 1) analysis of the quality of sensor output data, and 2) analysis of the processing algorithm performance.

The first procedure is implemented through resource to optimal estimation techniques. We define an Error Isolation Filter computer program which analyzes sensor performance and provides a measure of the adequacy of postulated sensor models. As a by-product, the outputs of this computer program can be utilized for sensor calibration or possibly, as a higher accuracy reference trajectory for evaluation of real-time navigation system performance.

---

*This work was sponsored in part by General Dynamics Electronics Division, San Diego, California, under US Air Force Contract F04701-75-C-0001 for the development of the Phase 1 NAVSTAR GPS Control and User Segments.

The second procedure is implemented by a computer program which executes the real-time software in the post-test environment. We define a Post-Flight Processor which is able to duplicate the onboard processing by operating on flight recorded data. This computer program offers the ability to analyze intermediate computation variables, evaluate the impact of different computation parameters or algorithms, or introduce compensation for off-nominal error source performance.

The specification of variables to be recorded during the test flight flows naturally from the requirements of the two above defined computer programs.

The above outlined error isolation procedures are illustrated by application to the Global Positioning System (GPS) User Segment Test Program. We present a discussion of the test environment, the capabilities incorporated into the data analysis computer and the envisioned data analysis procedure.

1. INTRODUCTION

The testing and evaluation of a navigation system is an integral part of a new system development. The test program exhibits system design and/or implementation errors, and provides an assessment of system performance. This latter function would ideally include both evaluation of total system navigation error and quantification of individual significant error sources for error budget construction.

We can visualize the test program as being divided into three sequential phases, as defined in Figure 1.

- Test Planning
- Error Isolation ("shakedown")
- Performance Evaluation

The test planning activity defines the procedures to be implemented to fulfill the test program objectives. The error isolation activity constitutes the first period of actual testing and is characterized by an intensive system shakedown effort, where design deficiencies, "bugs", and component malfunctions are isolated, identified and corrected. The test program then gradually moves into the performance evaluation period, where uncorrupted test data is collected and analyzed.

The usual approach to the Error Isolation process relies on the use of some external reference data. The computed navigation solution is differenced with a reference trajectory to generate error plots. An experienced analyst then "eyeballs" the error curves, and postulates possible causes of the observed poor performance. The analyst may make use of data processing aids in his effort. He may use a simulator to attempt to recreate the observed performance by exercising suspected error characteristics. He may exercise detailed data analysis programs (e.g., regression analysis) to attempt to quantify individual error sources. In general, the analyst will encounter severe observability problems due to data recording limitations during the test flight and to the correlation of error sources contributing to the total system error. The error tracing effort will usually be a tedious and drawn out procedure, absorbing significant time of senior experienced personnel.

The primary purpose of this paper is to describe a methodical, generalized error isolation procedure which can efficiently lead to the identification of the cause or causes of observed poor system performance. We will first analyze a

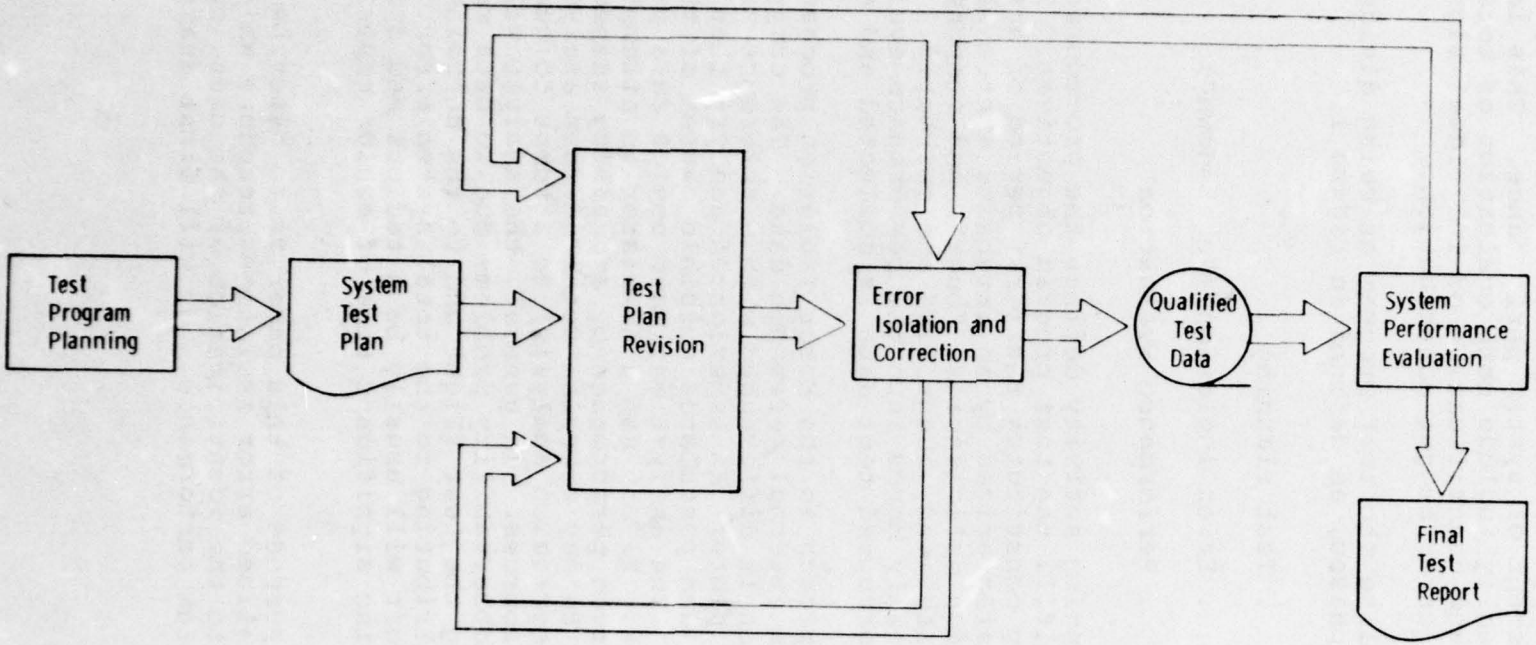


Figure 1 Test Program Phase Sequencing

generalized navigation system model. The model will then be disassembled into functionally distinct components, and the analysis procedures to be applied to each will be derived. Finally, we will particularize the proposed methodology by illustrating its application to the checkout of the NAVSTAR Global Positioning System (GPS) User Segment.

2. ERROR ISOLATION PROCEDURE DEVELOPMENT

2.1 Generalized Navigation System Model

The top-level view of the navigation system model is shown in Figure 2. The system is assumed to consist of from one to n sensor subsystems, a computation medium, and a display unit. For test program purposes, a tape unit would be added to record desired test data. A software module is assumed to be resident in the computation medium; the module accepts data from the sensors in order to compute the navigation solution and generates appropriate display and tape records. In addition, the software may "close the loop" by generating commands to the sensors, as indicated by the feedback paths in the figure.

The differentiation between sensor and computation medium is functional, rather than related to hardware vs. software, measurement vs. computation, or other concepts, and the boundary between these two "black boxes" will yield to the test procedure designer's viewpoint.

To illustrate these ideas, consider an inertial navigation system (INS). We may consider the INS to be composed of three different modules: 1) the Inertial Measurement Unit (IMU), with associated Power Supply; 2) the Airborne Computer, whose software implements the INS navigation equations; and 3) the Time Base Generator (TBG).

In one analysis approach, the IMU would constitute Sensor #1, providing as outputs accelerometer readings and gimbal angles. The TBG would constitute Sensor #2, providing time marks. The navigation software resident in the airborne computer would then combine these two data sources to generate the navigation solution and feedback signals to the IMU in the form of gyro torque commands.

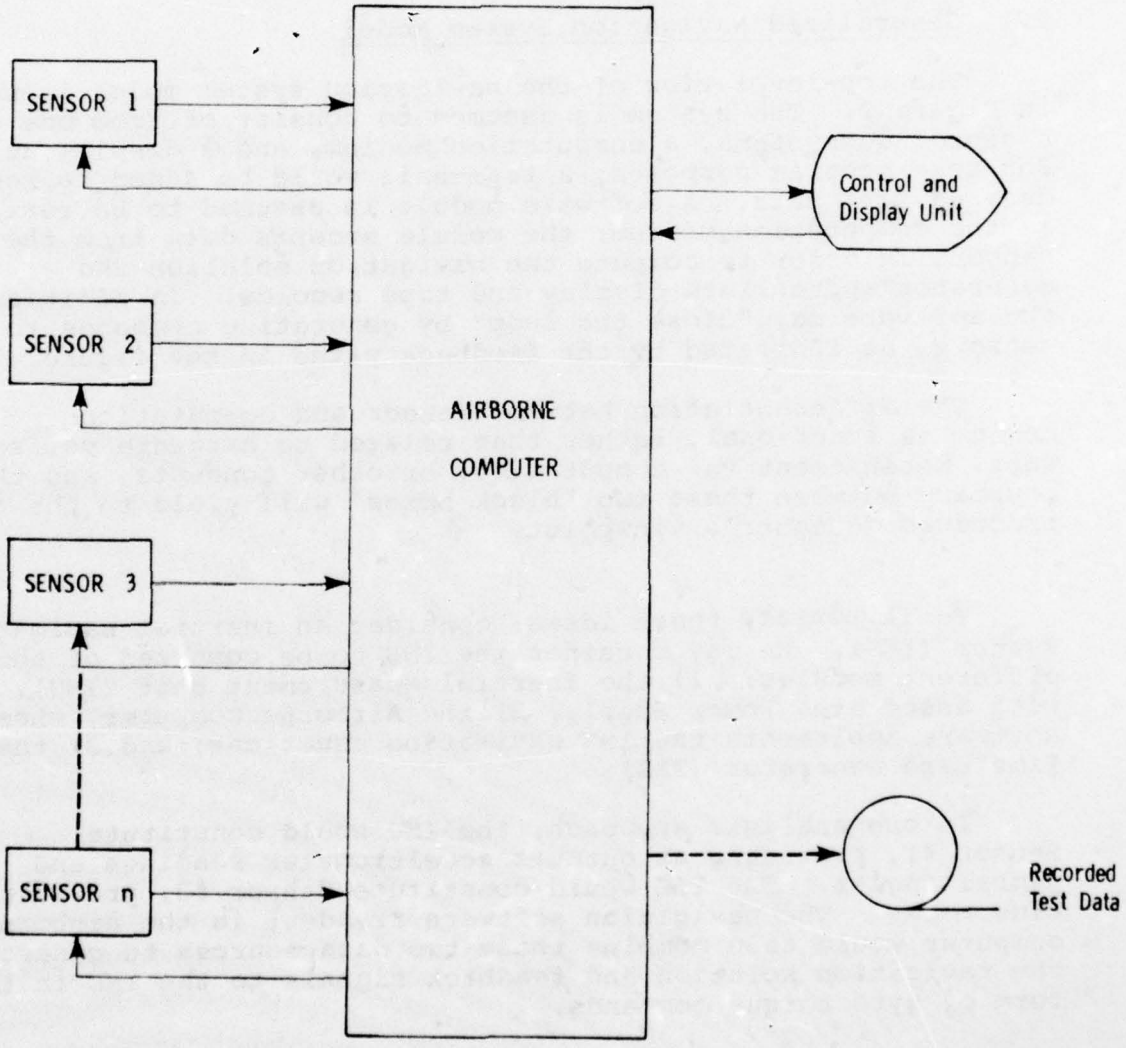


Figure 2 Navigation System Model
Top-Level Diagram

Alternately, the sensor boundary could be drawn to include all three components. The INS sensor would then generate outputs of aircraft position, velocity, and attitude. The sensor could constitute the navigation system by itself, in which case this analysis approach would view the navigation software as a direct pass-through of display data. On the other hand, the INS outputs could be combined with other sensor outputs in a further algorithm, (e.g., Kalman filter), which would then generate the navigation solution, and, possible, corrections to the INS computed solution. Note that, in this case, the INS navigation equations and the Kalman filter algorithm could very well be resident on the same computer, without obviating the chosen sensor boundary.

The above error model is included to provide a formal structure in which to treat the error isolation problem. The following sections will provide the motivation for drawing the sensor/software boundary, and address specialized procedures to be applied to each component.

2.2 Functional Partition

Modern estimation theory provides a mathematical framework for the development of analysis tools for the evaluation of navigation system test data. Optimal filters and smoothers can be designed which incorporate high order state vectors, appropriately modeled time-varying error sources, and do not encounter numerical difficulties in the presence of highly correlated error sources. The application of optimal estimation techniques offers significant advantages over the commonly used regression and other analysis procedures.

To apply optimal estimation to recorded test data, a stochastic linearized error model of the form

$$\dot{\underline{x}} = F\underline{x} + \underline{w} + \underline{u} \qquad (1)$$

must be developed for the system under test, where

- $\underline{x}$ State vector comprised of all the dynamics and static random error sources
- F Fundamental matrix of the state differential equation
- $\underline{w}$ White noise disturbance vector
- $\underline{u}$ Known deterministic forcing function

This requirement defines the separation of sensor vs. software components. Software errors tend to be deterministic, highly

non-linear error sources, and would therefore not be appropriately represented by a model of the form of Equation (1).

Note that the above statement represents a necessary but not sufficient condition for component separation. That is, if high confidence exists that a software module represents an errorless implementation of a correct algorithm (e.g., one validated in a previous test program), it may well be included within the sensor boundary, as long as it does not prevent the sensor performance from being described by a model of the form of Equation (1).

The component boundary specification is then driven by additional considerations, such as

- Data accessibility
- Error Model detail
- Computational burden, etc.

Having drawn the component boundary, we define two functionally distinct error isolation procedures: 1) analysis of the quality of sensor data, by application of optimal estimation techniques to the sensor outputs, and 2) analysis of the navigation algorithm performance.

The two distinct procedures are implemented by recourse to two data processing computer programs:

1. Error Isolation Analysis Filter (EIAF) - an "optimal" filter and/or smoother program, which combines the sensor data with available reference system data in order to generate "optimal" estimates of operating sensor error sources.

2. Post-Test Processor (PTP) - a program which re-executes the operational system software over the sensor generated data. The availability of this program allows observation of intermediate computation variables, "tuning" of algorithm parameters, and evaluation of alternate computational modules using actual flight data.

From this differentiation of analysis procedures, the following critical rule can be derived

"All dynamic data crossing the sensor/software boundary is to be recorded for post-flight analysis."

The minimum set of flight recorded data is thus required to include all sensor outputs and all feedback signals sent from the software to the sensors.

2.3 Error Isolation Analysis Filter

The EIAF combines sensor data with available reference data in a high order filter/smoother to generate "optimal" estimates of the sensor operating error sources. The key issues in the formulation of this computer program lie in the areas of

- Data Requirements
- Sensor Models
- Solution Validation

Primary inputs to the EIAF consist of sensor outputs and feedback signals. The sensor outputs constitute the basic processing data from which the error source estimates are derived. In addition, if the sensor data does not constitute a sufficient data set (in the sense that it provides observability of the desired error sources), external tracking data is required. In such a case, a time synchronization medium (such as IRIG time reference) is a necessary addition to the input data.

The software generated feedback signals to the sensors constitute an external disturbance to the propagation of the linearized sensor error model comprised in Equation (1). The known disturbance vector $\underline{u}$ in that equation provides the means by which the EIAF can compensate the effect of these external forcing functions and maintain the integrity of its error propagation model.

The EIAF implements a Kalman filter/smoother to process the available input data. The Kalman filter will generate the "optimal" (in the minimum variance sense) set of error model parameters (modeled error sources) to fit the set of observations generated by comparing sensor outputs against each other or against an available reference data set.

The discrete form of the optimal estimation equations is included in Table 1. In applying this technique to navigation sensor testing, a critical step is the selection of an appropriate set of state variables. The choice of states depends on the objectives of the test, observability of error sources, and the accuracy of reference data.

If the test requirements dictate that only an evaluation of total sensor error is required, the state vector dimension will be small, as only errors in the output quantities need be estimated. On the other hand, if a detailed sensor analysis is required, the state dimension will grow, as multiple individual error sources must now be estimated.

Table 1
Discrete Optimal Estimator Equations

Discrete Representation of Continuous Process (Equation 1)

State Propagation

$$\underline{x}_{i+1} = \Phi_i \underline{x}_i + \underline{w}_i + \underline{u}_i$$

State Transition Matrix

$$\dot{\Phi}(t,t_i) = F(t)\Phi(t,t_i) \; ; \quad \Phi(t_i,t_i) = I$$

Random Disturbance

$$\underline{w}_i = \int_{t_i}^{t_{i+1}} \Phi(t_{i+1},t)\underline{w}(t)dt$$

$$E[\underline{w}_i]=0; \quad E[\underline{w}_i \underline{w}_i^T]=Q_i$$

$$\dot{Q}(t,t_i) = F(t)Q(t,t_i) + Q^T(t,t_i)F(t) + N(t);$$

$$Q(t_i,t_i)=0$$

with $E[\underline{w}(t_1)w(t_2)^T] = N(t_1)\delta(t_1-t_2)$

Deterministic Forcing Functions

$$\underline{u}_i = \int_{t_i}^{t_{i+1}} \Phi(t_{i+1},t)\underline{u}(t)dt$$

Linearized Observations

$$z_i = g_i(\underline{x}_i) + v_i$$

Non-Linear Observation function Taylor Series Expansion

$$g_i(x_i) = g_i(\hat{\underline{x}}_i) + \underline{h}_i^T(\underline{x}_i-\hat{\underline{x}}_i) + \ldots$$

Measurement Gradient Vector

$$\underline{h}_i = \left.\frac{\partial g_i}{\partial \underline{x}_i}\right|_{\underline{x}_i = \hat{\underline{x}}_i}$$

Additive Measurement Random Error

$$E[v_i]=0 \; ; \quad E[v_i^2] = r_i$$

Kalman Optimal Estimator Equations

State, Covariance Propagation

$$\hat{\underline{x}}_{i+1} = \Phi_i \hat{\underline{x}}_i + \underline{u}_i$$

$$P_i = E[(\hat{\underline{x}}_i-\underline{x}_i)(\hat{\underline{x}}_i-\underline{x}_i)^T]$$

$$P_{i+1} = \Phi_i P_i \Phi_i + Q_i$$

Measurement Update (for each scalar measurement)

$$\hat{\underline{x}}_i^+ = \hat{\underline{x}}_i + \underline{k}_i \Delta z_i$$

$$\Delta z_i = z_i - g_i(\hat{\underline{x}}_i)$$

$$P_i^+ = P_i - \underline{k}_i \underline{h}_i^T P_i$$

$$\underline{k}_i = P_i \underline{h}_i / (\underline{h}_i^T P_i \underline{h}_i + r_i)$$

Frazer Two-Filter Smoother Equations

$$\hat{\underline{x}}_s = P_s(P_f^{-1} \hat{\underline{x}}_f + P_b^{-1} \hat{\underline{x}}_b)$$

$$P_s = (P_f^{-1} + P_b^{-1})^{-1}$$

Note: Subscripts s, f, b indicate smoother, forward filter, backward filter computed solutions

If the test environment and sensor characteristics are such that error sources are known to be highly correlated, these sources should be excluded from the error state and only their linear combination estimated. While the filter will not encounter numerical difficulties in the face of high state correlations, computation time will be wasted due to the unnecessarily large state dimension. A related issue is that, if other error sources have an error effect comparable to desired error coefficients, it will become necessary to include them in the state vector. Otherwise, process noise will have to be exercised to cover the effect of the neglected states. The noise input will then prevent the recovery of the desired error sources.

A similar consideration applies to treatment of reference system data. If the reference system is significantly more accurate than the sensors under test, reference system error sources can be neglected. Otherwise, reference system errors will have to be included in the state vector.

An alternate approach would be to delete the reference trajectory data from the estimation process entirely. Even though the natural reaction is to utilize all the available data, the test procedure designer should carefully weigh whether the increase in error source observability is worth the increased computational burden. Many navigation systems today provide, by themselves, high error source observability, such that the improvement, if any, afforded by consideration of reference system data clearly is not cost-effective. The role to be played by the reference instrumentation solution is then that of an outer bound check on the estimation process. Consistency between the estimator and reference solutions provides the first confidence level in the EIAF returned estimates.

A critical issue in the implementation of this error isolation procedure is the validation of the EIAF solution. As the program contains a high order model and utilizes a large segment, if not all, of the available data, it will usually generate the highest accuracy estimates obtainable. The check on the EIAF solution validity must therefore rely on internal filter consistency. We have in the past utilized hypothesis testing techniques with satisfactory results. The hypothesis to be tested is that the actual sensor errors are consistent with the EIAF model. As an example, we can compare actual observation residuals with the EIAF computed measurement residual variance. The measurement residual can be expressed as

$$\Delta z = z - \underline{h}^T \hat{\underline{x}} \qquad (2)$$

The measurement residual variance, as computed by the Kalman filter, is given by

$$\sigma_z^2 = \underline{h}^T P \underline{h} + r \tag{3}$$

If the filter model is appropriate, we would expect the measurement residuals to have zero mean and variance equal to σ_z^2. We can therefore monitor the performance of parameters such as

$$\overline{\Delta z} = \frac{1}{n} \sum_{i=1}^{n} \Delta z_i$$

$$J = \frac{1}{n} \sum_{i=1}^{n} \Delta z_i^2 / \sigma z_i^2 \tag{4}$$

in order to establish confidence in the program solution. Any deviation of these parameters from their expected values would indicate a need to re-evaluate the filter model.

Note that, as the series of observation residuals is theoretically uncorrelated, the sums of n successive ratios $\Delta z^2/\sigma z^2$ should exhibit a Chi-Square distribution with n degrees of freedom. Thus, by application of standard statistical techniques, we can compute confidence levels for the observed values of the parameter J in Equation (4), and, by association, obtain similar confidence levels for the returned filter estimated.

2.4 Post-Test Processor

The functional partition of the error isolation process, addressed in Section 2.2, directed the implementation of different data processing computer programs for analysis of the functionally distinct navigation system components. The previous section briefly discussed the application of optimal estimation techniques to the evaluation of navigation sensor data. This section will address characteristics of the computer program to be applied to analysis of navigation software performance.

The PTP is a computer program capable of re-executing the operational software in the post-flight environment. As a non-real-time program, it allows detailed evaluation of intermediate computation variables, repeated execution of the software with different system parameters, input of compensation

values for isolated sensor error sources, and evaluation of the performance of alternate computation modules operating over actual flight data.

A top-level view of the PTP structure is shown in Figure 3. An initialization module sets up the initial PTP state to a condition compatible with that of the real-time software at the selected time. A cyclic loop is then entered, where sensor data is first read from the flight data tape and desired compensations are applied to it. The data is then passed to the "operational software" module, which computes the new navigation solution. An output module then displays the regenerated solution and/or comparisons of it vs. the recorded onboard computed values or vs. a set of reference trajectory values.

Based on the deterministic nature of computation, it can be stated that, given a sufficient representation of the state of onboard computation at one point in time, a PTP will be able to regenerate the computation state at any future point in time based solely on the sensor inputs and operator inputs, if any, through the control unit. Alternately, as stable navigation systems intrinsically deweight the value of old data, it will usually be possible to approximately regenerate the computation state at any point in time as long as it is sufficiently far from the time of PTP execution initiation, even though a sufficiently complete computation state representation was not recorded. The PTP will therefore, by being able to reproduce the values of internal computation variables, reduce the test data recording requirements while actually increasing the analyst's visibility into the computation process. The test procedure designer may still, however, wish to record some amount of intermediate computation results in order to check the validity of PTP solution reconstruction.

By being able to re-execute the operational software over actual flight data, the PTP serves as an ideal platform from which algorithm tuning and parametric analysis can be undertaken on the basis of a single or limited number of test flights.

A useful feature easily incorporated into the PTP structure is related to the compensation of sensor errors. The usual case is that, if it is determined that a sensor exhibited abnormal error behavior during a test flight, the test data is lost in terms of its usefulness for further system checkout. The PTP offers the capability to apply compensations for identified error coefficients to the flight recorded data prior to processing by the operational software. In this fashion, utilization of test data can be improved, with consequent reduction on test fligt requirements.

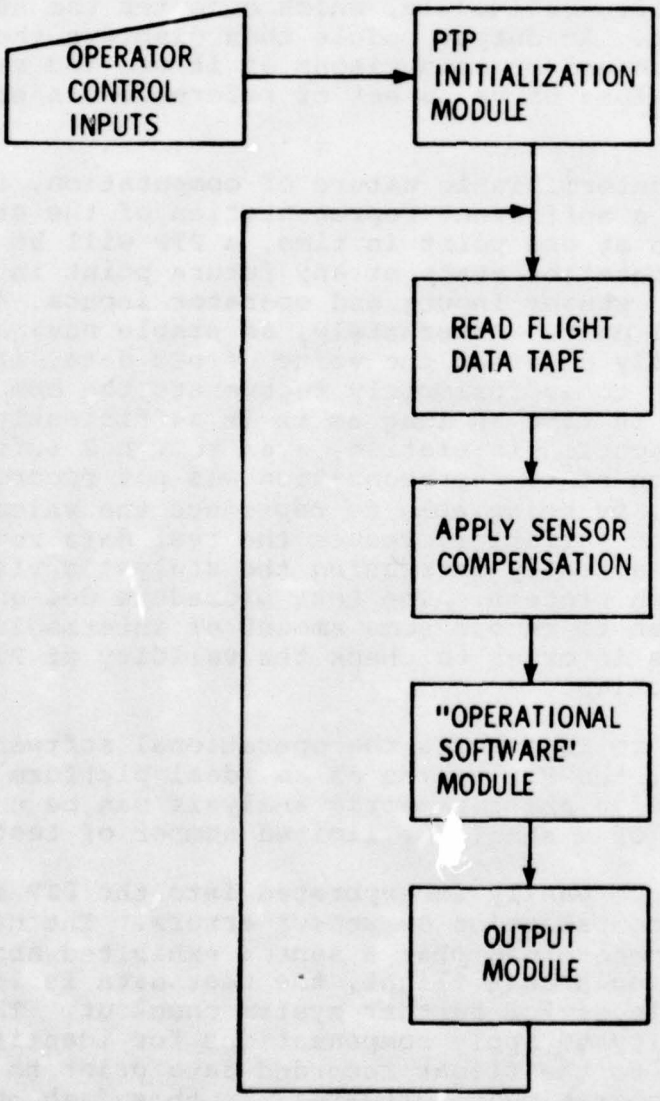


Figure 3 - PTP Top-Level Structure

2.5 Data Processing Overview and Summary

We have analyzed a generalized navigation system model with the purpose of motivating an error isolation procedure which operates on flight recorded data. A classification of system components into two distinct groups has been developed, based on their susceptibility to be represented by a linearized stochastic model of the form of Equation (1). Two distinct analysis procedures have been described in terms of the test data processing computer programs which implement them. In the course of this discussion, we have identified the data recording requirements for implementation of this analysis approach. The identified data recording requirements can be listed as follows:

System Navigation Solution

Sensor Outputs

Sensor Feedback

Operator Inputs

The utilization of the EIAF and PTP program in a generalized error isolation procedure is illustrated in Figure 4. It is assumed that, prior to execution of this procedure, some gross or "quick-look" evaluation (e.g., comparison of navigation solution to reference trajectory) has taken place to establish abnormal system performance.

The inputs to the process consist of a flight recorded data tape and a tape of reference trajectory data. The EIAF is first executed to establish validity of the sensor data. If so, detailed examination of intermediate PTP computation variables is undertaken to search for possible software errors. If none are found, then tuning of the navigation algorithms or parameters is required.

If anomalous sensor errors, or software errors, are discovered, the PTP can be executed with appropriate compensation to establish the validity of the new solution. If abnormal performance persists, the process can be re-entered at the appropriate point until all anomalies have been eliminated.

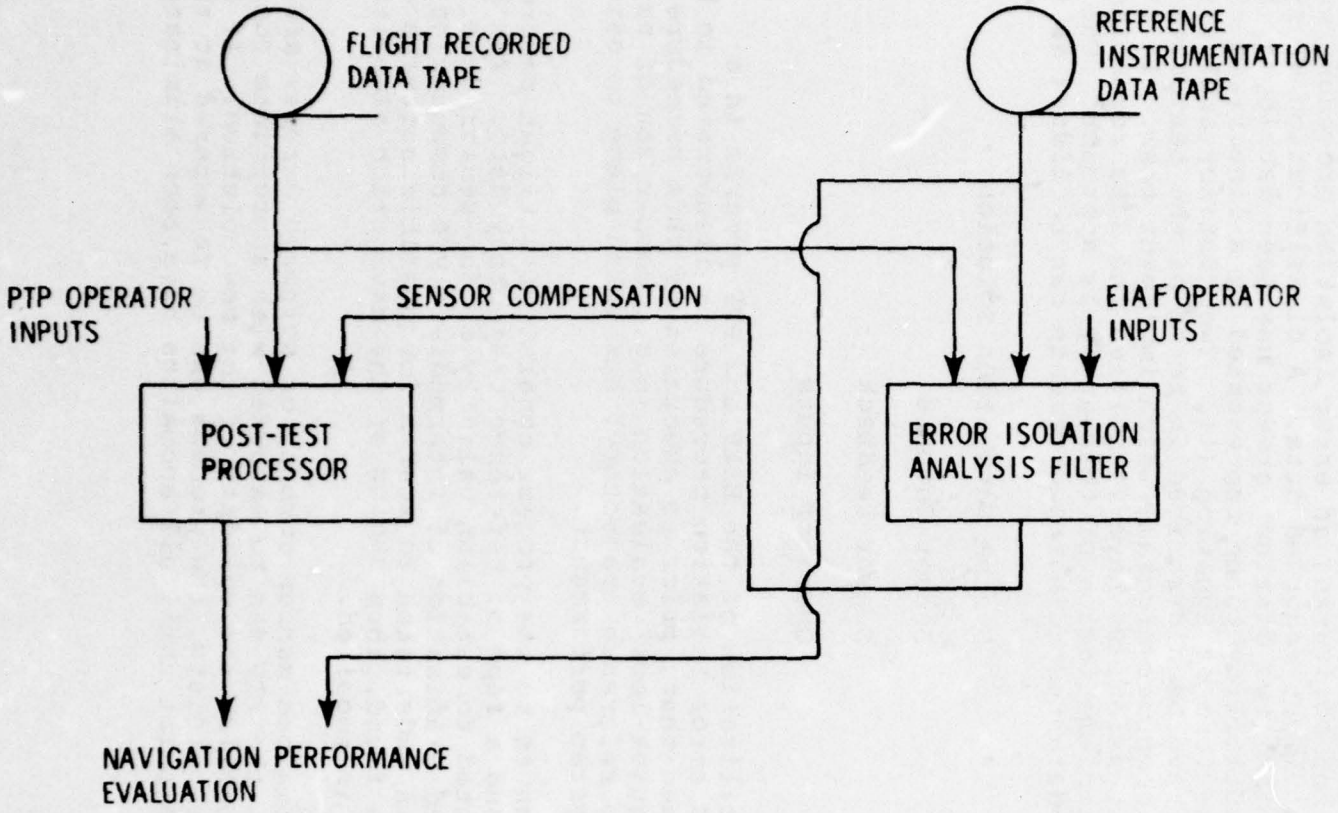


Figure 4 - Error Isolation Procedure Overview

3. GPS USER SEGMENT ERROR ISOLATION PROCEDURES

The NAVSTAR Global Positioning System (GPS)[1] is being developed by the Department of Defense to provide a world-wide, continuous navigation capability suited to the needs of a wide class of potential users. The system will enter its test phase in the near future.

Extensive preparations have been undertaken to ensure a successful GPS test program. The following sections deal with one phase of that effort: the development of error isolation procedures for the User Segment (US). As an introduction, a brief description of the system concept and the test environment is included.

3.1 GPS Description

The GPS concept envisions a constellation of 24 satellites placed in 12-hour orbits, such that direct line-of-sight coverage is afforded world-wide by at least 4 satellites at any point in time. The satellites will continuously transmit signals from which suitably equipped users can derive range, range-rate (delta-range) and satellite positional information. Ranges to the satellite are obtained from precise measurements of the phase delay of a user-borne clock synchronized to the GPS transmitted signal. Range-rates are obtained by measurement of the integrated doppler shift of the received signal over a specified interval. Normally, three range measurements to known points would be sufficient for user position fixing. In GPS, however, a fourth measurement is required in order to separate a user clock error relative to GPS time from the signal time-of-travel (which contains the ranging information).

The satellites are tracked by a network of Control Stations[2] placed at various surveyed locations within the United States. An Upload Station regularly uploads to the satellite updated satellite ephemeris and satellite clock correction parameters for transmission to users. Thus, perturbations of satellite orbits and drift of satellite clocks are prevented from compromising the system accuracy.

The constellation of satellites is denoted as the GPS Space Segment. The network of ground tracking stations is denoted as the GPS Control Segment. The User Segment then consists of the required equipment for a user to receive the satellite signals and utilize them to compute its navigation solutions.

Various versions of User Equipment (UE) are being developed by different contractors. The baseline UE development effort (as addressed here) includes two GPS receiver sets, X and Y.

X sets are four channel receivers capable of simultaneously tracking, and taking measurements to, four different satellites. Y sets are single-channel receivers which track satellites in sequential fashion.

Both aided and unaided UE configurations are being developed, where the denomination indicates the presence or absence of an Inertial Measurement Unit (IMU) as an aiding sensor to GPS.

The GPS UE navigation software [3] blends the GPS signals with available additional sensor data in Kalman-type estimators to generate navigation solutions and estimates of the user clock phase and frequency offsets from the GPS reference clock.

3.2 GPS Test Environment

The GPS system concept will be tested at the U.S. Army Yuma Proving Grounds (YPG), in Yuma, Arizona. The initial test configuration, the Inverted Range (IR), consists of four ground transmitters (GT), located on the range, which simulate the GPS navigation signals as would be generated by the satellites [4]. This GT configuration is monitored and controlled by the Inverted Range Control Center (IRCC) in order to maintain synchronization of the GT time references.

As GPS satellites are launched and activated, they will be incorporated into the test program. The UE versions will thus be required to operate with an all-GT configuration, an all-satellite configuration, and a hybrid configuration consisting of both GTs and satellites, as shown in Figure 5.

Several trajectories and vehicle types will be utilized during the test program. The latter will include transport and high performance aircraft, helicopters, and ground vehicles.

The primary YPG reference instrumentation system consists of a network of laser trackers, which provide measurements of range, azimuth and elevation to the test vehicle at a high rate, and associated data processing algorithms. Two reference trajectory solutions can be generated for each test flight: 1) a Real-Time Estimate (RTE), representing a coarse, fast-turnaround solution, and 2) a Best Estimate of Trajectory (BET), representing a fine solution, but with attendant delays in its availability.

The test and evaluation of the various GPS segments will be accomplished separately. That is, the GPS Monitor Stations will monitor the performance of the Control and Space Segments. They will track the GPS signals during the user tests and generate post-test estimates of what the actual satellite ephemeris and clock drifts were. This solution will be of a higher accuracy than the predicted ephemeris and clock model

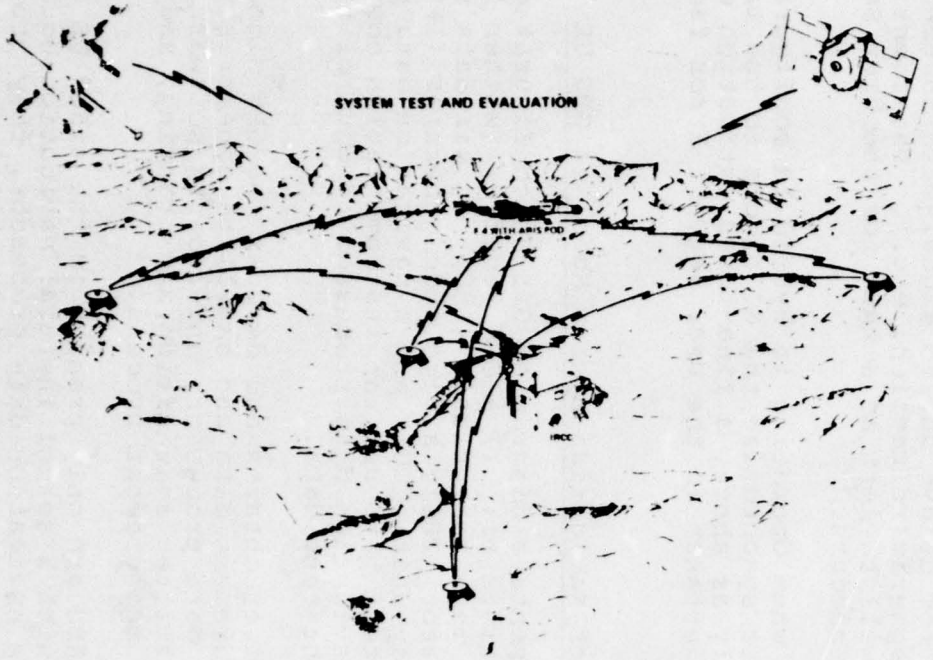


Figure 5 - Hybrid Inverted Range Configuration

parameters transmitted to the user during the test period. The higher accuracy estimates will be used to back-out Control Segment errors from the UE navigation solution, thus separating the effect of Control and User Segment errors.

A similar consideration will apply to the Inverted Range. The IRCC will monitor the GT signals and observe the GT clock drift. However, due to the fixed IR geometry, it is expected that GT clock phase offsets from the IRCC reference time will not be separable from delays due to signal-path induced errors (multipath, tropospheric refraction, etc.). The identification of these offsets will be left as a task for the User Segment Error Isolation procedure.

In addition, when operating in hybrid IR configuration, it will be required to syncnronize the GT clocks to the master GPS clock. Analogously as above, a fine-tuned estimation of this offset will be undertaken in the User Segment Error Isolation Process.

3.3 Application of Navigation System Model to GPS UE

Figure 6 presents a diagram of GPS UE configuration. The configuration consists of: 1) a GPS receiver (either X or Y set); an inertial measurement unit (IMU); an air data unit (ADU); a time base generator (TBG); a time code generater (IRIG), a control and display unit (CDU); and a navigation data processor. In addition, for test purposes, an instrumentation computer is attached to the navigation data processor to control the recording of flight test data.

The GPS receiver obtains and decodes the GPS signals. It provides the measurement data and satellite ephemeris parameters to the navigation data processor, and accepts software generated commands for transmitter acquisition and tracking, and for sequencing of the measurement process.

The IMU and ADU are only present in the aided UE configurations. Together with a set of inertial navigation equations implemented in the navigation data processor, they provide a stand-alone baro-inertial navigation capability.

The TBG provides the basic navigation cycle timing. The TBG is a distinct unit from the user time reference used for synchronization to GPS time; this latter unit is an integral part of the GPS receiver configuration.

The IRIG provides the link between UE and the range instrumentation. It therefore allows comparison of UE navigation solution with a reference trajectory through use of a common time base.

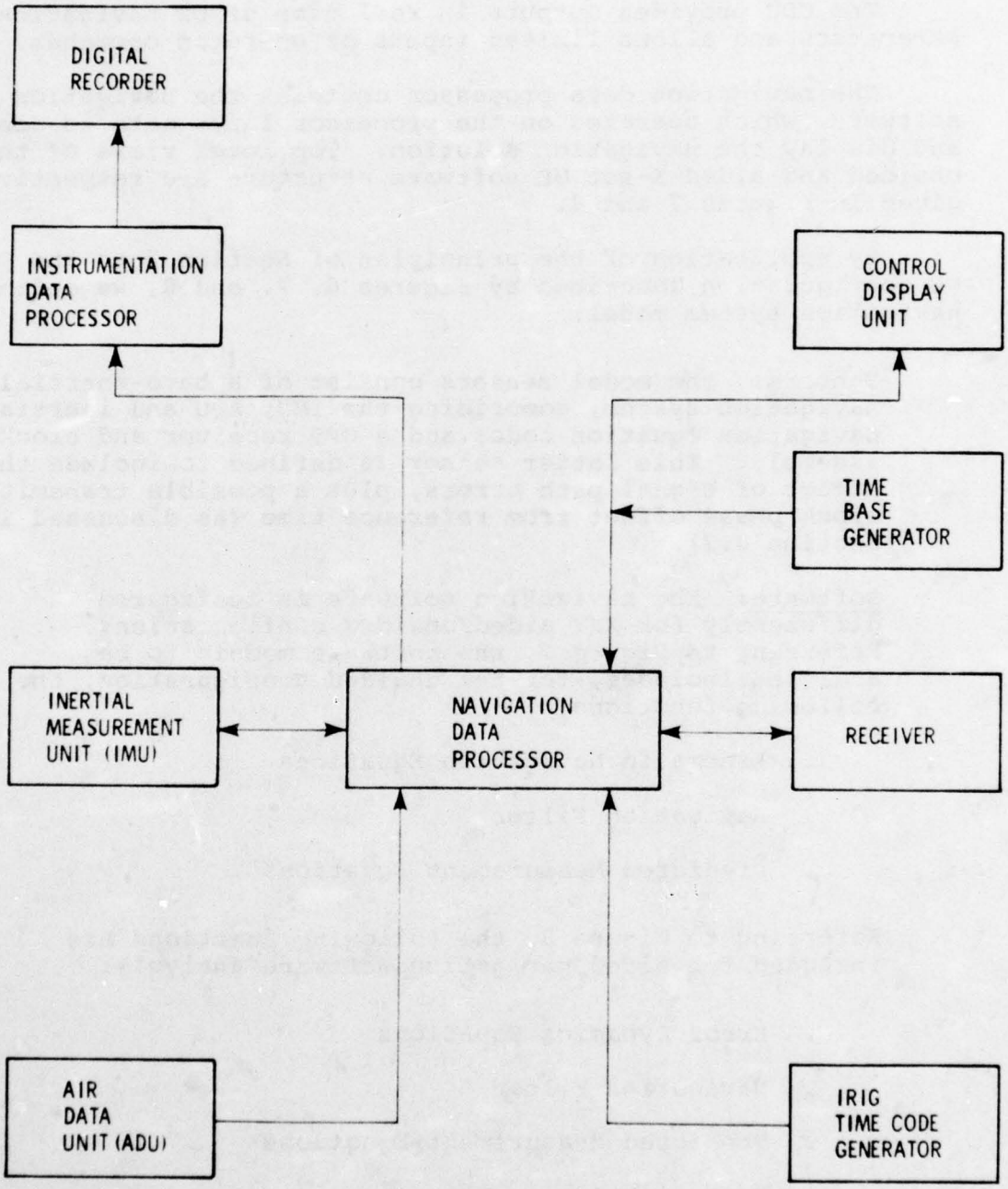


Figure 6 GPS UE Configuration

The CDU provides outputs in real time of UE navigation parameters and allows limited inputs of operator commands.

The navigation data processor contains the navigation software, which operates on the processor input data to compute and display the navigation solution. Top level views of the unaided and aided X-set UE software structure are respectively given in Figures 7 and 8.

By application of the principles of Section 2 to the GPS UE configuration described by Figures 6, 7, and 8, we define the navigation system model:

Sensors: the model sensors consist of a baro-inertial navigation system, comprising the IMU, ADU and inertial navigation equation code; and a GPS receiver and clock assembly. This latter sensor is defined to include the effect of signal path errors, plus a possible transmitter clock phase offset from reference time (as discussed in Section 3.2).

Software: the navigation software is configured differently for X/Y aided/unaided configurations. Referring to Figure 7, the software module to be analyzed includes, for the unaided configuration, the following functions:

- Kinematic Navigation Equations
- Navigation Filter
- Predicted Measurement Equations

Referring to Figure 8, the following functions are included for aided navigation software analysis:

- Error Dynamics Equations
- Navigation Filter
- Predicted Measurement Equations
- Rectification Equations

In accordance with the error isolation methodology, we must therefore define an EIAF computer program to analyze the quality of the baro-INS and GPS receiver and clock data, and a PTP to re-execute the above identified software functions by operating on the recorded data.

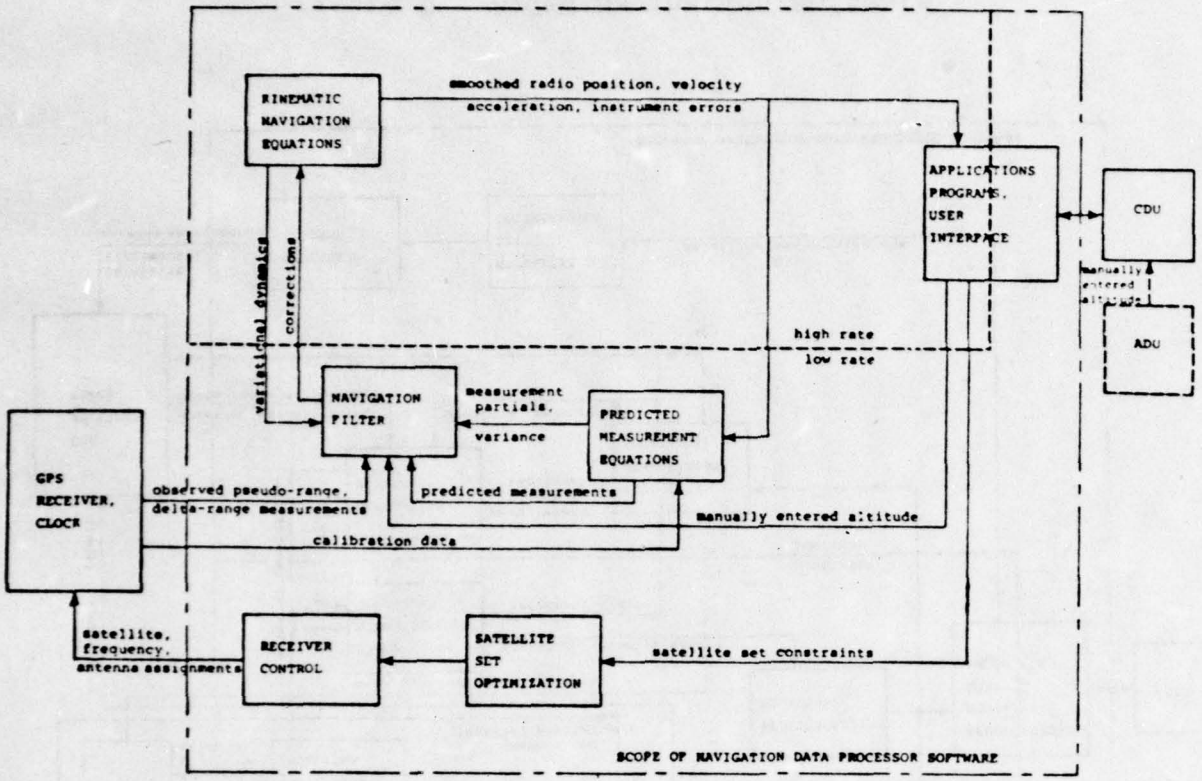


Figure 7 - Unaided Navigation Software

BEST AVAILABLE COPY

BEST AVAILABLE COPY

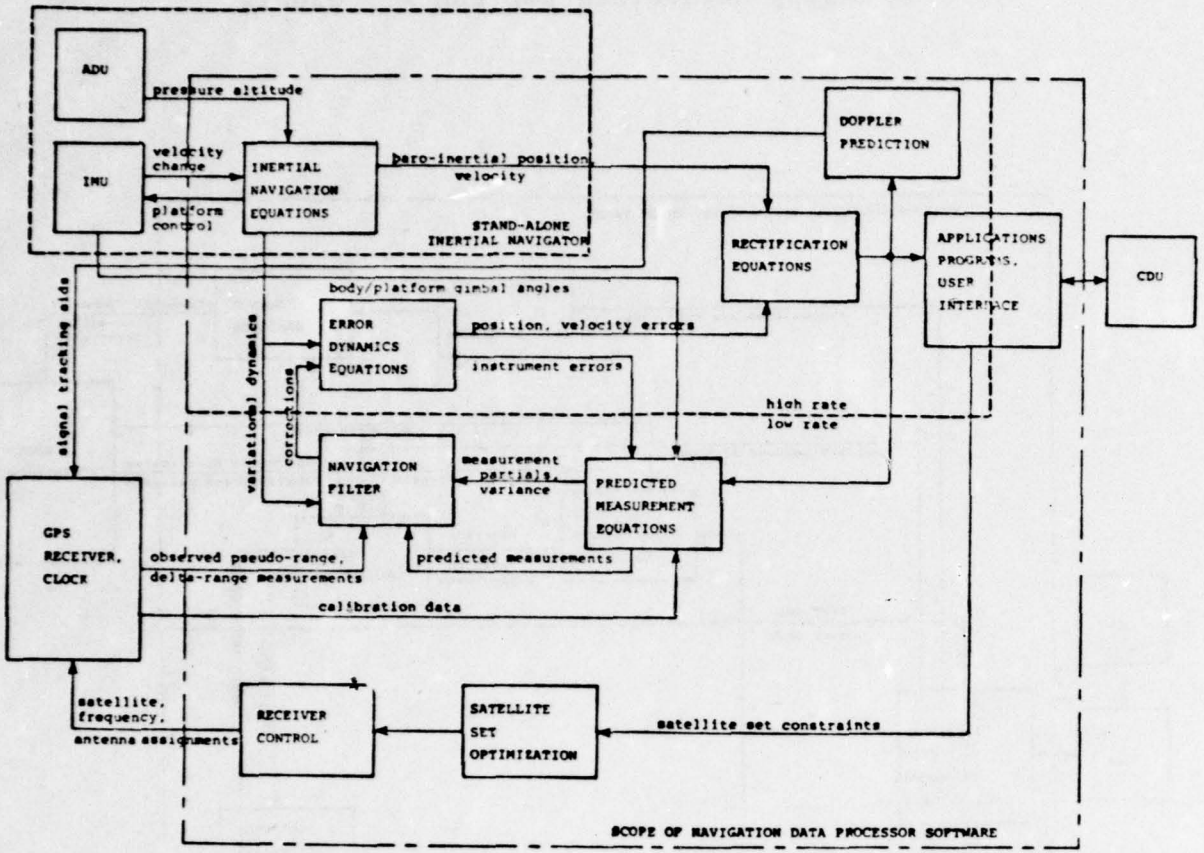


Figure 8 - Aided Navigation Software

As a first step to implementation of this procedure, we need to specify the test data to be recorded in flight. Keeping in mind the considerations of Section 2, the data recording specification listed in Table 2 has been generated.

The primary inputs to the error isolation process are comprised of data block #2, containing the baro-INS outputs (aided) and timing information; data block #6 containing the raw GPS measurements; data block #8 containing the satellite position and clock correction descriptors; data block #9, containing manually-entered baro-altitude measurements (unaided); data block #14, containing operator control inputs; and data blocks #24-28 (unaided) or #30-36 (aided) containing the UE software data base at execution initiation.

In addition, data blocks #2, 7, 8, 10, and 11 contain either UE navigation solution parameters or intermediate computation variables for evaluation of inflight performance.

3.4 GPS User Segment Error Isolation Filter

A top-level view of the EIAF processing is given in Figure 9. The program accepts as inputs, the recorded flight data tape, a BET tape containing reference trajectory data, and a Control Segment compensation tape used to back-out satellite position and timing errors from the GPS measurements. The input data is processed by a Kalman filter/smoother to generate "optimal" estimates of the operating error sources. Although contained in the same program, two different error models are mechanized, corresponding to aided and unaided system configurations.

The aided state vector is listed in Table 3. The first eleven states represent a model of baro-INS output errors. States 14 and 15 model the user clock errors relative to the GPS master clock. States 16 through 19 represent pseudo-range errors to the four currently active transmitters; the main error effects modeled by these states consist of signal-path induced errors, possible receiver channel specific biases, and, in IR operation, possible transmitter clock phase offsets. The remaining six state elements model IMU error sources, and are included for the purpose of allowing undisturbed observation of delta-range errors during maneuvering flight.

This system state representation has been selected to yield error isolation down to the subsystem level; thus, a detailed model of IMU error sources, for example, has not been included in the state formulation.

For the unaided configuration, all baro-INS related states are deleted, and the state vector is reduced to six elements (states 14 through 19 in Table 3).

Table 2 Data Recording Specification

BLOCK NUMBER	BLOCK DESCRIPTION
1	Spare (not to be used)
2	Solution data plus filter estimates - solution inputs and outputs
3	IMU data
4	CDU output data
5	Aided alignment velocity data
6	Measurement data
7	Measurement incorporation process data - filter covariance square root matrix following measurement
8	Satellite position data
9	Manually-entered baro altitude data
10	Range measurement data recording statistics
11	Delta range measurement data recording statistics
12	Extension of block 2
13	Spare
14	CDU mode selection
15	Receiver data group IV - satellite or antenna changing directives
16	Receiver data group V - track aiding information
17	Fault data
18	Bombing mission data
19	Fault data
20	Satellite data for channel 1
21	Satellite data for channel 2
22	Satellite data for channel 3
23	Satellite data for channel 4
24	Unaided data base
25	Unaided data base
26	Unaided data base
27	Unaided data base
28	Unaided data base
29	Reserved for test
30	Aided data base
31	Aided data base
32	Aided data base
33	Aided data base
34	Aided data base
35	Aided data base
36	Aided data base

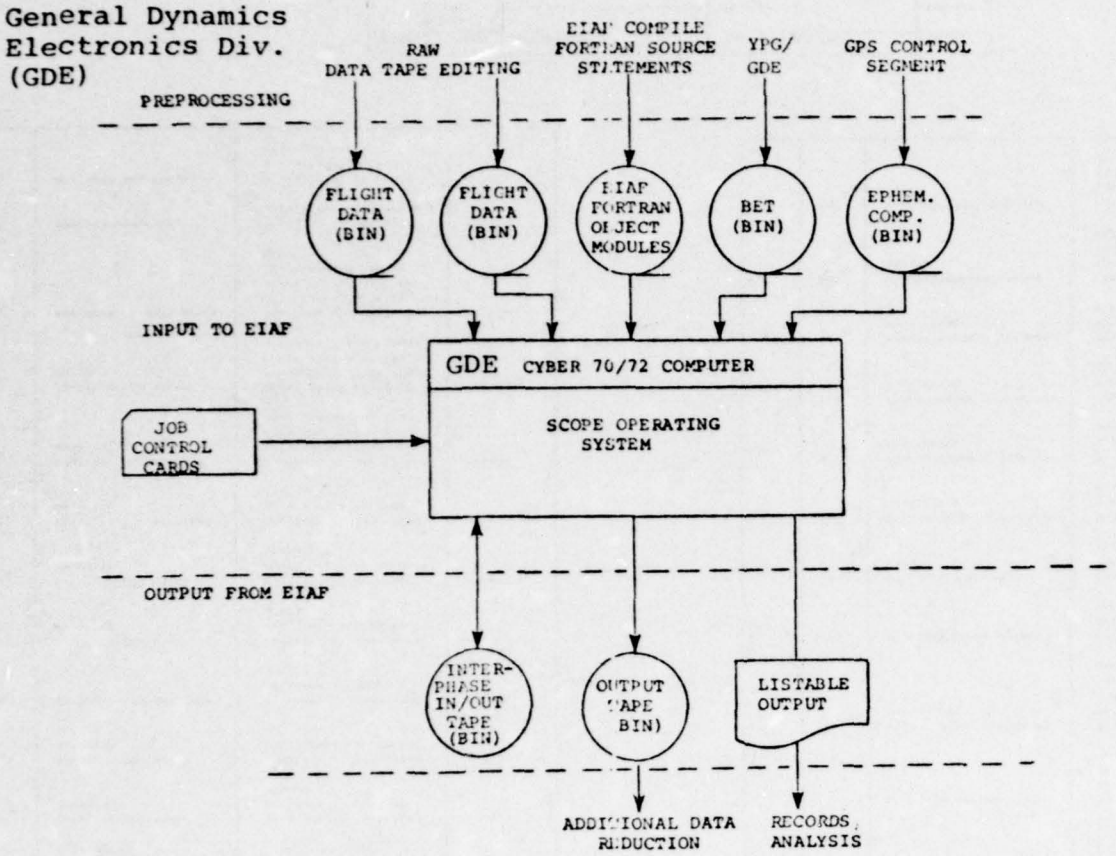


Figure 9 - EIAF Computer System Interface

BEST AVAILABLE COPY

Table 3 EIAF State Vector

STATE	SYMBOL	DEFINITION	SIGN CONVENTION	UNITS
x_1	$\delta\lambda$	Error in INS east longitude	Positive if indicated position is east of actual	radians
x_2	δL	Error in INS north latitude	Positive if indicated position is north of actual	radians
x_3	δh	Error in INS altitude	Positive if indicated altitude is above actual	meters
x_4	δv_e	Error in INS east velocity	Positive if indicated east velocity exceeds actual	meters/sec
x_5	δv_n	Error in INS north velocity	Positive if indicated north velocity exceeds actual	meters/sec
x_6	δv_z	Error in INS vertical velocity	Positive if indicated up velocity exceeds actual	meters/sec
x_7	θ_e	Platform tip about east	Positive if platform is rotated positive about east axis from its steady-state attitude	radians
x_8	θ_n	Platform tip about north	Positive if platform is rotated positive about north axis from its steady-state attitude	radians
x_9	θ_z	Platform azimuth error	Positive if platform is rotated positive about the up axis from the computed wander angle	radians
x_{10}	δh_b	Baro-altitude error	Positive if measured altitude exceeds actual	meters
x_{11}	δa_z	Vertical acceleration	Positive if it induces a positive vertical velocity error	meter/sec^2

STATE	SYMBOL	DEFINITION	SIGN CONVENTION	UNITS
x_{12}	ZA_x	Vertical accelerometer misalignment about X	Positive if accelerometer is rotated positive about platform X axis from the normal to the geoid	radians
x_{13}	ZA_y	Vertical accelerometer misalignment about Y	Positive if accelerometer is rotated positive about platform Y axis from the normal to the geoid	radians
x_{14}	CPO	UE clock phase offset	Positive if measured pseudo-ranges exceed actual	secs
x_{15}	CFO	UE clock frequency offset	Positive if measured pseudo-delta-ranges exceed actuals	secs/sec
x_{16}	$\delta\rho r_1$	Pseudo-range 1 measurement error	Positive if measured pseudo-range exceeds actual	secs
x_{17}	$\delta\rho r_2$	Pseudo-range 2 measurement error	Positive if measured pseudo-range exceeds actual	secs
x_{18}	$\delta\rho r_3$	Pseudo-range 3 measurement error	Positive if measured pseudo-range exceeds actual	secs
x_{19}	$\delta\rho r_4$	Pseudo-range 4 measurement error	Positive if measured pseudo-range exceeds actual	secs
x_{20}	ASF_x	X accelerometer scale factor	Positive if a positive specific force induces a positive velocity error	ND
x_{21}	ASF_y	Y accelerometer scale factor	Positive if a positive specific force induces a positive velocity error	ND

STATE	SYMBOL	DEFINITION	SIGN CONVENTION	UNITS
x_{22}	YA_z	Y accelerometer misalignment about Z	Positive if Y accelerometer is rotated positive about Z platform axis	radians

The EIAF program outputs include a tape of estimated states and their associated covariance. In addition, a time history of computed measurement residual statistics is generated. Analysis of these parameters will expose the validity of the program error model when compared with actual test data. Note that one of the assumptions of the model is that delta-range measurement errors are purely random (no delta-range error states are included in the state vector). Analysis of delta-range computed residual mean values will indicate whether this assumption is justified.

3.5 GPS User Segment Post-Test Processor

The different UE software configurations have dictated the generation of a series of PTP programs compatible with GPS UE X/Y aided/unaided versions. The additional consideration of target host machine has directed a duplication of PTP versions for each configuration. It would ideally be desired to host the PTP on a similar computer to that which hosts the operational software, as computational precision and round-off considerations would not affect comparison of PTP and UE solutions. However, core and peripheral unit limitations on normal airborne computers would then unnecessarily constrain PTP capabilities. It has therefore been decided to generate two PTP versions for each UE configuration: one resident on a flight-type computer, and one resident on a more powerful general purpose machine. The flight computer resident version is capable of exactly regenerating the onboard computed solution, given the required data. The general purpose computer resident version is capable of regeneration only to the level allowed by thedifferent precision machine capabilities; however, it allows for the use of a Control Segment compensation tape to back-out satellite position and clock errors from the UE navigation solution. Top-level views of the PTPs processing are given in Figure 10.

Both program versions allow the operator to access internal computation variables during the run, provide error source compensation values, modify desired program parameters, and provide comparisons of the UE generated navigation solution with that computed by the PTP.

3.6 GPS Error Isolation Overview

The interactive use of the PTP and EIAF programs in the GPS error isolation procedure is illustrated in Figure 11. Inputs to the process consist of the UE flight recorded data tape, and desired operator interventions.

It is assumed that, prior to implementation of this procedure, a quick-look evaluation of system performance has been accomplished, and that anomalous navigation accuracy has been

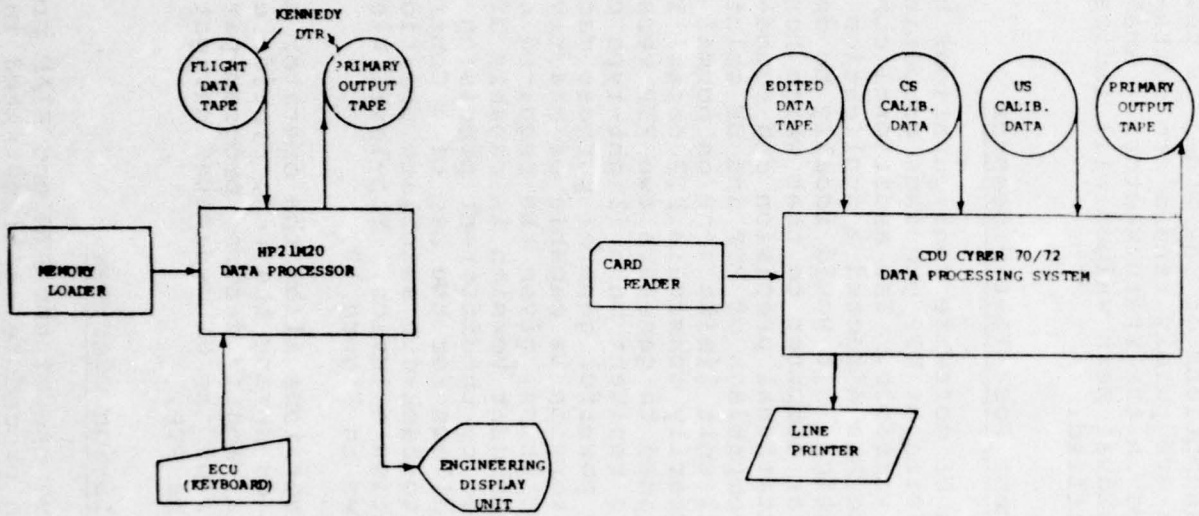
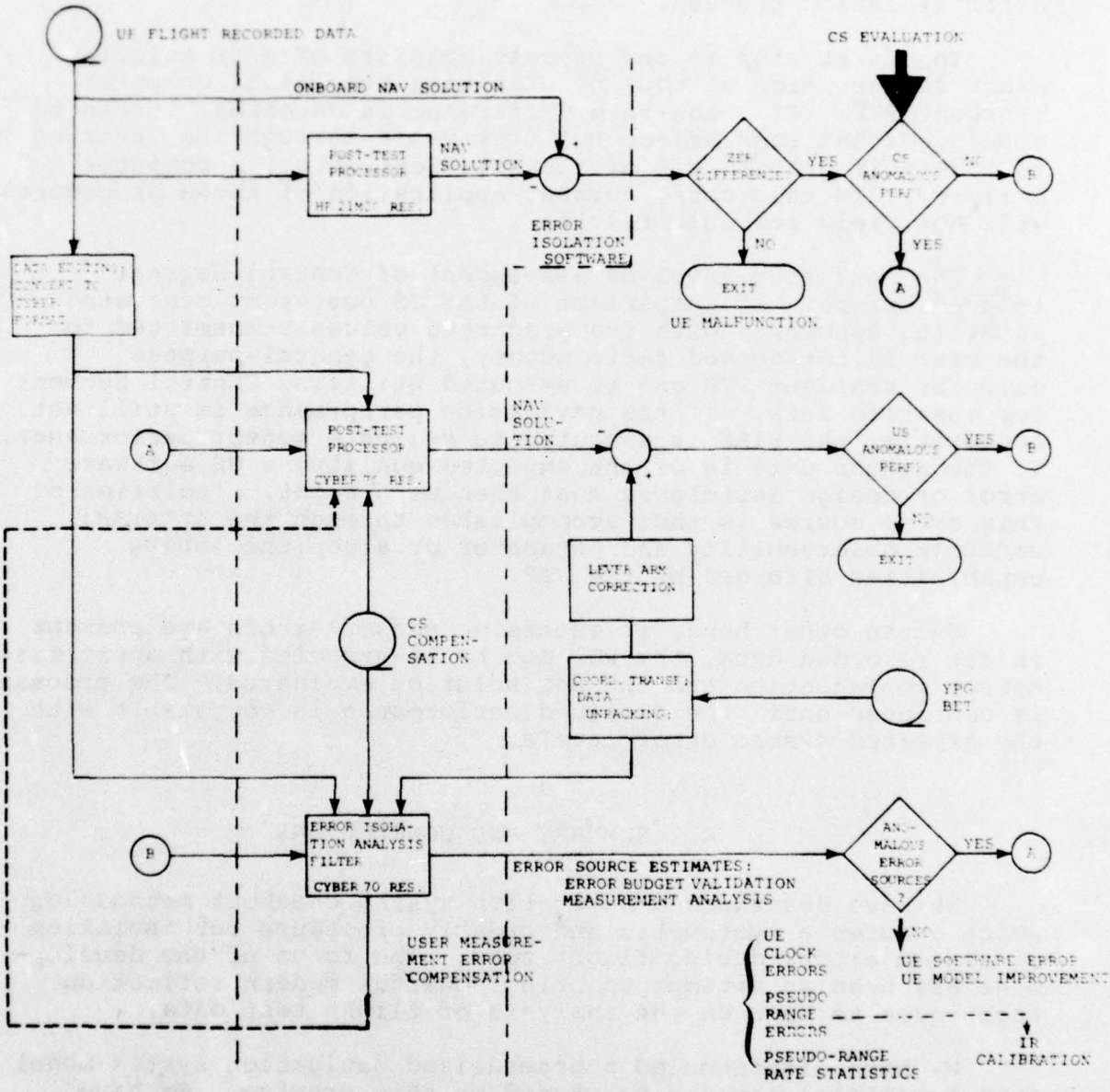


Figure 10 - PTP Target Environments

BEST AVAILABLE COPY



Note: Anomalous ≙ inconsistent with UE model

Figure 11 - Post-Test Analysis Overview (If Anomalous System Navigation Performance Observed)

established. It is therefore desired to identify and remove the cause of the observed poor performance by recourse to the error isolation process.

The first step in the process consists of a UE solution exact regeneration attempt by utilizing the flight computer resident PTP. If a non-zero difference is detected, it can be concluded that some effect not observable through the recorded test data is driving one of the solutions (e.g., a computer failure). In this case, further application of these procedures will not yield reliable results.

The next step involves assessment of Control Segment induced errors. If comparison of the CS post-test generated satellite ephemeris with the predicted values transmitted to the user is not deemed satisfactory, the general-purpose computer resident PTP can be executed utilizing Control Segment compensation data. If the navigation performance is still not acceptable, the EIAF is executed to evaluate sensor performance. If the sensor data is of the expected quality, a UE software error or design deficiency must then be present. Isolation of this error source is then accomplished through the internal variable observability and parameter or algorithm tuning capabilities afforded by the PTP.

On the other hand, if excessive sensor errors are present in the recorded data, the PTP can be re-executed with appropriate sensor compensation and the new solution evaluated. The process is continued until the obtained performance is compatible with the expected system error levels.

4. SUMMARY AND CONCLUSIONS

We have described a navigation system checkout methodology which imposes a systematic and orderly procedure for isolation of system errors during flight test. The focus of the development has been an attempt to bring powerful modern estimation techniques to bear on the analysis of flight test data.

We have disassembled a generalized navigation system model into functional components, based on this premise. We have defined as "sensors" those system components whose error characteristics are appropriately described by a linearized, stochastic model. We have, on the other hand, recognized that software error responses cannot be modeled with linear equations, and thus, require different analysis techniques. We believe that most, if not all, navigation system implementations are compatible with this viewpoint.

Based on the above distinction, we have formulated error isolation procedures for each of the system's two functional components. The procedures are implemented through two computer programs: an Error Isolation Analysis Filter (EIAF), for analysis of sensor data, and a Post-Test Processor (PTP), for analysis of navigation software performance. In the course of the procedure formulation, we have identified data recording requirements to support the approach.

The EIAF analyzes the sensor performance through recourse to optimal estimation. The estimator model can be formulated to yield any level of analysis detail desired by the tester. Given the right error source excitation, the program will yield high accuracy estimates of the desired error coefficients. In addition, the technique is capable of implementing self-consistency checks to yield confidence levels on the formulated error models.

The PTP supports analysis of the navigation software performance by providing high observability into the computation process and the capability for parametric design and tuning over actual flight data.

We recognize that application of these procedures will not result automatically in a successful test program. The real-world continuously offers surprises which only the flexibility of the man-in-the loop approach can conquer. The above described procedures do, however, represent powerful tools in the checkout process, and their appropriate application will result in a significantly faster, more cost-effective and reliable effort.

Finally, we have illustrated the methodology by describing its application to the checkout of the NAVSTAR GPS User Segment, which is about to enter its test program phase. The complexity of the User Equipment configurations and the potential high accuracies involved, require the implementation of powerful analysis techniques, in order to reach a successful program completion. The developed error isolation programs described offer that promise.

REFERENCES

1. Smith, D., and Criss, W., "GPS Navstar Global Positioning System", Aeronautics and Astronautics, Vol. 14, No. 4, April 1976, pp. 26-32.

2. Schaibly, J.H., Harkins, M.D., Fees, W.A., and Murch, W.G., Simulated and Projected Performance of the Navstar GPS Control Segment", AIAA Guidance and Control Conference, San Diego, California, August 1976.

3. Klein, D.W., Roy, K.J., Copps, E.M., Kosmala, A.L., Gilman, A.S., and Rose, R.C., "Navigation Software Design for the User Segment of the Navstar GPS", AIAA Guidance and Control Conference, San Diego, California, August 1976.

4. Harrington, R.L., Dolloff, J.T., "The Inverted Range: GPS User Test Facility", IEEE 1976 Position, Location and Navigation Symposium, San Diego, California, November 1976.

EIGHTH BIENNIAL GUIDANCE TEST SYMPOSIUM

THE ROLE OF SYSTEM SIMULATIONS IN A RADAR FLIGHT TEST PROGRAM

AUTHORS: CHARLES C. ORMSBY
GREGORY L. MEALY
JAMES D. SHIELDS

THE ANALYTIC SCIENCES CORPORATION
READING, MASSACHUSETTS

THE ROLE OF SYSTEM SIMULATIONS IN A RADAR FLIGHT TEST PROGRAM

by

Charles C. Ormsby
Gregory L. Mealy
James D. Shields

THE ANALYTIC SCIENCES CORPORATION
Reading, Massachusetts 10867

ABSTRACT

A wide variety of simulation tools have been employed at TASC to aid in the initial concept formulation, design and testing phases of radar system development. The cost of simulation development and usage increases dramatically as simulation complexity increases. For this reason, the objectives of a proposed simulation and the benefits to be derived from it must be carefully assessed and weighed against the projected costs. This paper discusses the utility of simulations in the design, test and evaluation of airborne radar systems. Results of correlation guidance (i.e., map matching) radar sensor studies are presented to illustrate the application of simulation techniques. Simulation development techniques which increase simulation utility by maximizing computational efficiency are illustrated for the case of the APQ-144 radar in a ground imaging mode. Two techniques, used extensively in simulation models developed at TASC, which reduce the computational requirements associated with Monte Carlo performance analysis by a factor of approximately ten thousand (for an example case in which 100 Monte Carlo trials are simulated) are discussed.

1. INTRODUCTION

With the steadily rising cost of flight testing developmental hardware, it is clear that test hardware designs, software specifications and flight test experimental plans must be carefully controlled to minimize the cost of achieving test objectives. System simulations can offer an effective tool for the control of flight test costs and can magnify the benefits derived from test data by offering a structured framework within which test results can be interpreted.

A wide variety of simulation tools have been employed to aid in the initial concept formulation, design and testing phases of radar system development. Simulations can vary in complexity from the simple digital implementation of the basic radar range equations and formulas for detection probability to hybrid computer simulations employing some of the radar system components in the analog portion of the simulation. The cost of simulation development and usage increases dramatically as simulation complexity increases. For this reason, the objectives of a proposed simulation and the benefits to be derived must be carefully assessed and weighed against the projected costs. In Section 2 of this paper, the utility of simulations in the design, test and evaluation of airborne radar systems is discussed. In particular, results of correlation guidance (i.e., map matching) radar sensor studies are presented to demonstrate the application of simulation techniques. Section 3 describes examples of techniques which have been used to overcome the huge computational burden normally associated with the simulation of a ground-imaging radar system.

2. SIMULATION OBJECTIVES

A useful distinction can be made between simulations whose principal objective is the analysis of integrated system performance (e.g., the performance of an entire weapon system including the radar, inertial system, data processing system, etc.) and simulations which focus on the performance of the radar system in its role within the context of the overall system. Figure 2-1 illustrates the complementary roles played by simulations satisfying these two objectives. One can view these simulations as being used in an iterative fashion. The integrated system simulation first generates the initial system context (often with covariance analysis (Ref. 1) and error budget techniques, Fig. 2-2). Examples of parameters included in the system context would be the statistics of:

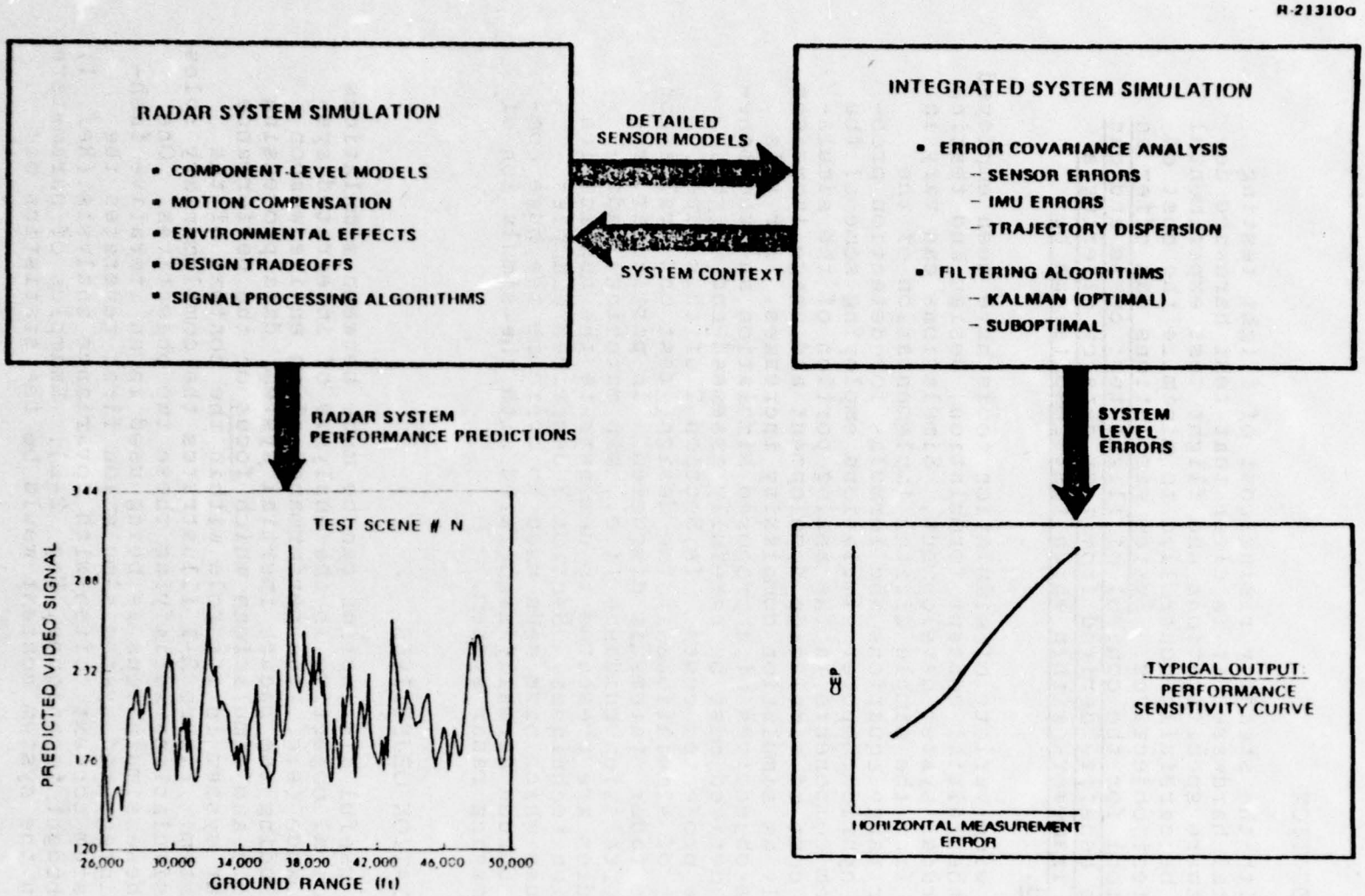


Figure 2-1 Complementary Role of Integrated System and Sensor Level Simulations

- Radar system position uncertainties
- Velocity uncertainties
- Antenna pointing errors

Once these uncertainties (both differences from pre-mission nominals and real time estimation errors) are combined with knowledge of the nominal range of operating parameters, the radar simulation can generate data indicating the measurements performance levels attained by the radar. The statistics of the measurements are returned to the integrated system simulation and position, velocity and pointing error uncertainties are updated. The radar simulation then uses this information to predict subsequent radar system performance and the process continues.

Integrated system and radar system simulations are useful throughout the entire period of system development. The development period can be broken down as follows:

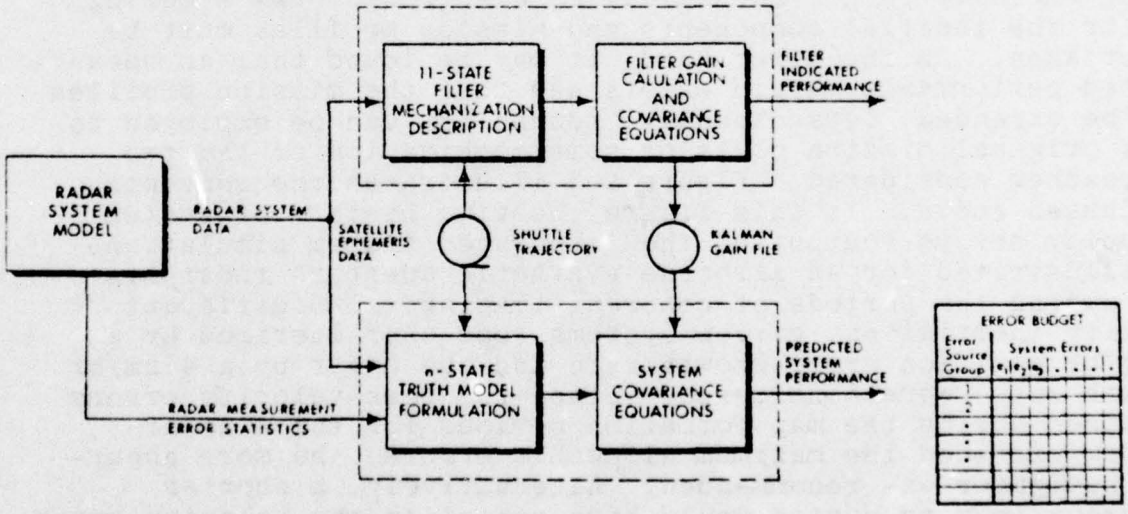


Figure 2-2 Overview of System-Level Covariance Analysis Methodology

- Initial Design
- Flight Test Planning
- Flight Testing
- Test Data Reduction and Simulation Validation
- Extrapolation of Flight Test Results and Finalization of System Design.

It should be noted that these periods often overlap (e.g., data reduction will occur during the flight test period) and therefore the conclusions reached in one phase can (and should) influence the conduct of the concurrent phase(s).

Initial Design

In the initial design phase, it may be found that the system context predicted by the integrated system simulation is not consistent with the radar technology being employed (e.g., position and/or pointing uncertainties are so large that the radar scan or data processing capabilities are exceeded). Clearly a reassessment of the radar technology being employed (e.g., mechanical or electronic beam steering) and/or the inertial components and mission profiles must be undertaken. On the other hand, it may be found that an unexpected performance margin exists and that the mission profiles can be expanded, less expensive technology can be employed to meet original mission goals or some combination of the two approaches considered. Figure 2-3 illustrates the concepts discussed above. In this figure the time history of system velocity errors (output of the integrated system simulation) is illustrated for an airborne synthetic aperture radar system during the periods of coherent imaging. Two different quality inertial navigation systems (one characterized by a 1 nm/hr position error growth rate and the other by a 4 nm/hr growth rate) were considered. Since the peak velocity errors attained during the map formation periods for the 4 nm/hr system exceeded the maximum allowable errors, the more accurate navigator was recommended. Alternatively, a shorter coherent imaging period would have satisfied the velocity error requirement at the expense of lower resolution images.

The use of radar and integrated system simulations in the design process does not eliminate the need for an analytical design effort. Rather, it affords a verification of the design process and provides a tool for the evaluation of design trade-offs in the integrated system.

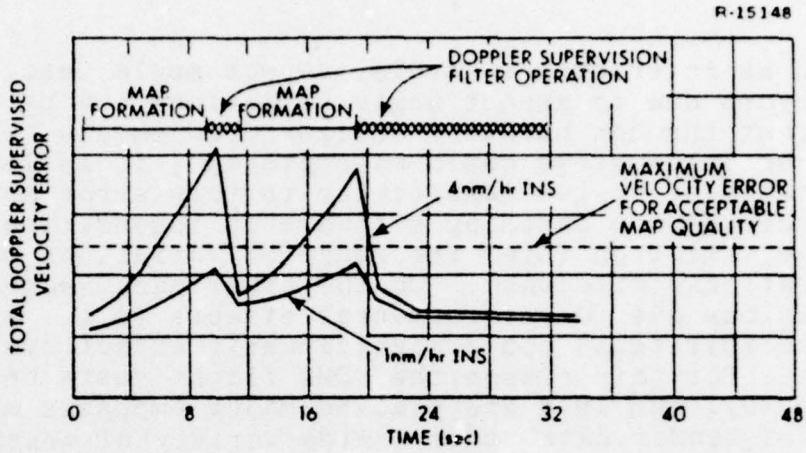


Figure 2-3 Evaluation of INS Requirements for an Airborne Synthetic Aperture Radar System

Flight Testing Planning

The development of radar system flight test plans is greatly enhanced by the availability of radar simulations capable of predicting performance for a variety of flight test conditions. The ability to generate detailed, quantitative flight test performance estimates makes it possible to isolate those parameter variations which greatly affect system performance. Since one of the primary purposes of a flight test program is to verify that the system design is capable of satisfying mission requirements, regions of high system sensitivity* should be singled out for extensive testing.

The test program for the Pulse Doppler Map Match (PDMM) system offers a typical example for a correlation guidance sensor. PDMM is a synthetic aperture radar sensor which, during its approach to a target, images an area of terrain containing a uniquely shaped, high contrast ratio edge. A template matching scheme is employed to locate this edge in the sensed image and the vehicle's position is updated based on the measured range and range-rate (both available in the SAR image) to a point having known coordinates. To assess the impact of these error sources on PDMM performance, TASC has developed† a Synthetic Aperture Radar Simulation (SARSIM). Investigations employing SARSIM have indicated that the reliability and accuracy of the edge correlation process depends on edge shape, contrast ratio and imaging

*In some cases system sensitivity can be reduced through redesign; in others the sensitivity is to environmental effects over which the designer has little or no control.

†Air Force Contract No. F04701-75-C-0084.

errors such as interference levels, aspect angle, etc. Although errors due to aspect angle variations can be controlled to some extent through hardware design improvements (i.e., improved inertial systems could be employed), it is less costly to decrease system sensitivity to this error source by insuring that the map matching software is insensitive to aspect angle variation (over the range of variations expected during operational missions). On the other hand, edge contrast ratio variations due to environmental effects (e.g., snow cover or precipitation) could significantly affect system performance. For this reason, the PDMM flight tests being planned for 1977 and 1978 are placing major emphasis on the collection of sensor data under a wide variety of weather and seasonal conditions.

Radar sensor simulations can aid in the process of specifying the quantities which should be measured during flight testing. TASC is currently in the process of specifying a test plan for the flight testing of a low altitude radar correlation guidance system. As shown in Fig. 2-4, this system mixes correlation data from the APQ-144 scanning radar and the APN-194 radar altimeter (terrain profile matching) to create a position update for an aircraft navigation system. As a part of this program*, a simulation of an advanced version of the APQ-144 radar was developed. Further discussion of this simulation will be given in Section 3. This simulation has been used to predict system performance under a wide variety of conditions and is being used as the primary tool for identifying the data to be collected during the proposed flight test program.

Flight Testing

Once the flight test program is planned, specific performance prediction for key tests should be made using the system simulation. Simulation predictions should be made for one of the early tests of the flight program to generate data to be used for both model validation and test hardware checkout. The process of investigating any discrepancies between simulation-predicted and actual system performance will not only build confidence that the model predictions are meaningful, but also provide a methodology for confirming that the hardware under test and the instrumentation configuration are functioning properly. If modifications to

*Air Force Contract No. F33615-76-C-1352.

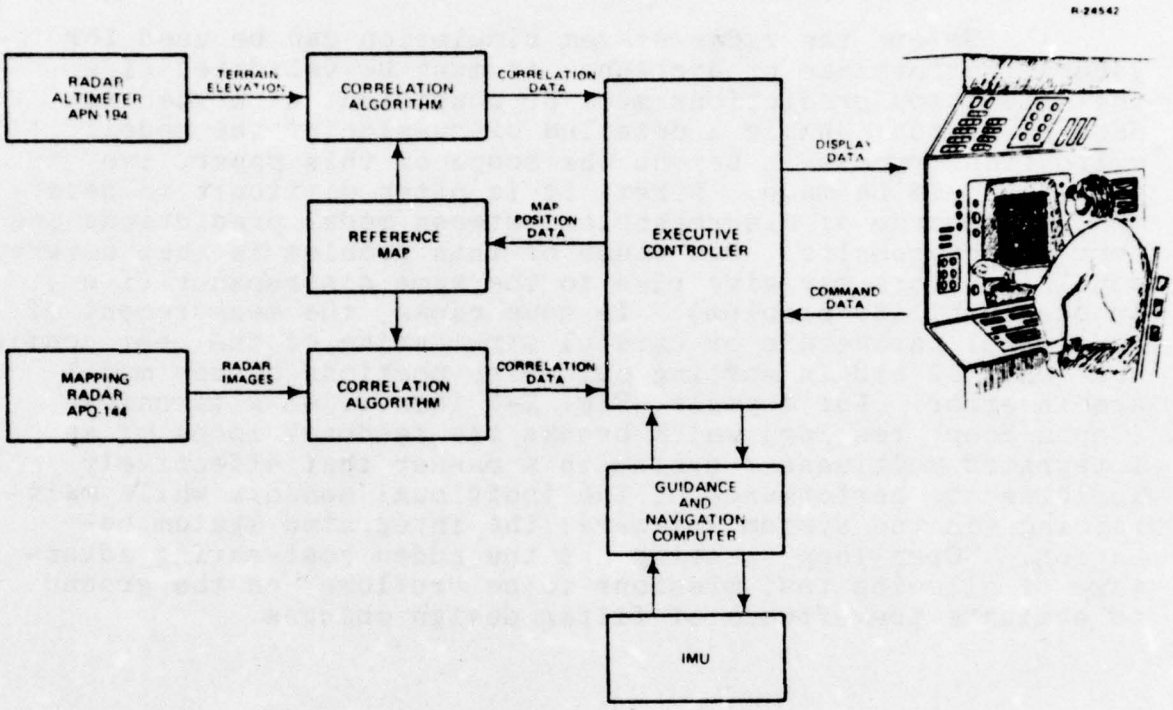


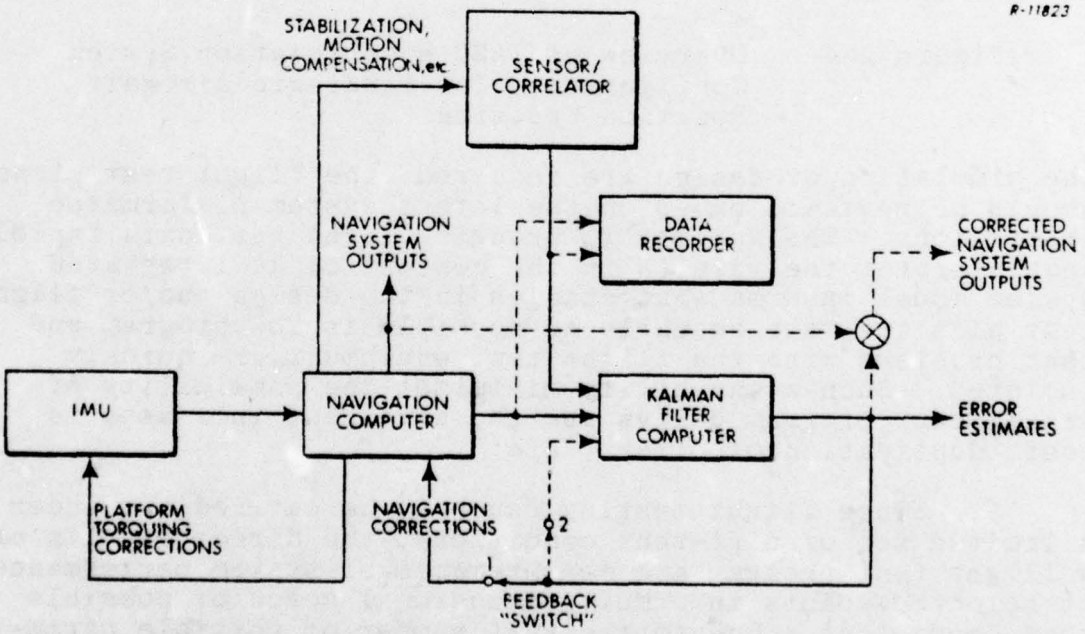
Figure 2-4 Overview of TASC's Correlation System Configuration for Strategic Aircraft Position Updating

the simulation or design are required, the flight test plans should be reviewed based on the latest system performance predictions. The ability to process flight test data rapidly and interpret the results in the context of an integrated system model insures that changes in the design and/or flight test plan are made as early as possible in the program and that problems with the flight test equipment are quickly isolated. Such a capability minimizes the possibility of significant program delays and the attendant increases in cost, duplication of effort, etc.

Since flight testing can only be carried out under a limited set of different conditions, the direct results of a flight test program are measurements of system performance at selected points in a multidimensional space of possible test conditions. Due to the vast number of possible parameter combinations, even the results of an extensive flight test program contain data at only a fraction of the points of interest. Therefore, one of the primary functions of the system simulation is to tie the flight test data to an integrated theoretical framework so that system performance at other points in this multidimensional space can be predicted.

Simulation Validation

Before the radar system simulation can be used for general performance predictions, it must be validated (i.e., the simulation predictions must be consistent with the test data obtained). While a detailed discussion of the model validation process is beyond the scope of this paper, two points should be made. First, it is often difficult to determine the source of discrepancies between model predictions and test flight results. One cause of this problem is that several modeling errors may give rise to the same discrepancy (i.e., an observability problem). In some cases, the measurement of additional parameters or careful structuring of the test configuration will aid in sorting out which portions of the model are in error. For example, Fig. 2-5 identifies a technique ("open loop" testing) which breaks the feedback loops of an integrated multisensor system in a manner that effectively isolates the performance of the individual sensors while maintaining (in the system software) the integrated system behavior. "Open loop" testing has the added cost-saving advantage of allowing test missions to be "reflown" on the ground to evaluate the effects of filter design changes.



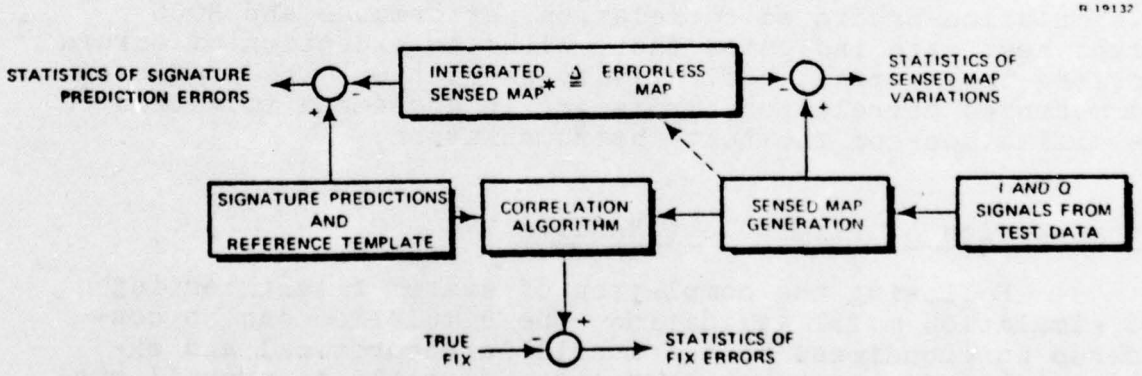
Dotted lines show data collection paths and feedback procedures for "open loop" test configuration.

Figure 2-5 Example of "Open Loop" Test Design and Data Collection

Another approach is to isolate the possible problems by adding tests which specifically exclude the possiblity of certain error sources contributing to the test results. The possibility that errors in the flight test instrumentation are the cause of the discrepancies must also be considered. The isolation of a single critical instrumentation problem early in the test program (based on the analysis of discrepancies between model prediction and preliminary flight test results) can itself pay for the simulation development.

Second, specific attention should be directed toward the planning of data collection procedures so that model validation can be effectively carried out. To accomplish this, a detailed plan for the model validation procedure is required. Figure 2-6 illustrates the procedure which TASC has proposed for the validation of its PDMM fix accuracy performance model. The outputs of this process can be used to assess the accuracy of simulation models for signature prediction errors, scintillation/clutter statistics, hardware biases and correlator performance.

Figure 2-7 illustrates the results obtained using a similar procedure for validating a simulation of the Range Only Correlation System (ROCS) based on flight test data collected by Goodyear Aerospace. The figure illustrates the difference between preflight signature predictions (produced by a simulation of the ROCS sensor) and the average flight



*Integration refers to the summation of maps generated at different frequencies (i.e., nonconherent integration)

Figure 2-6 Procedure for Validation of PDMM Accuracy Predictions (Ambiguity Consideration Excluded)

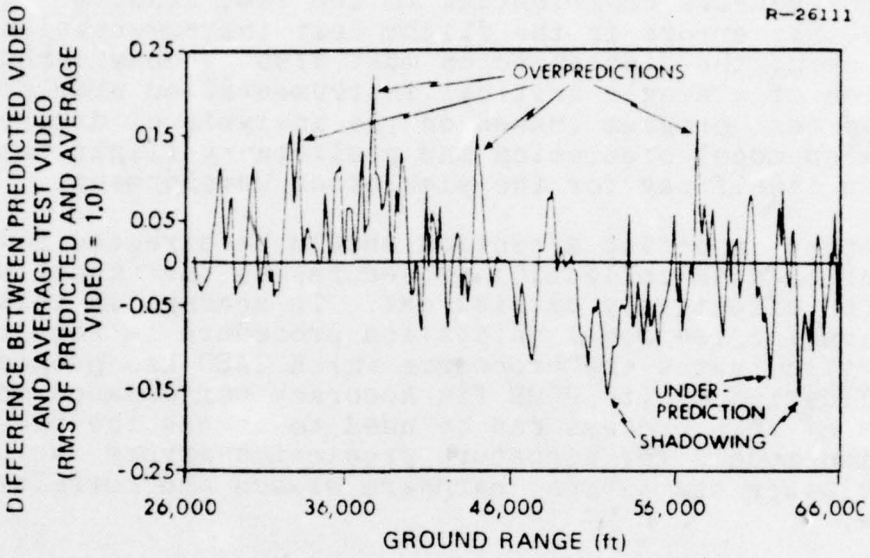


Figure 2-7 Difference Between Predicted and Average Test Video Signal Resulting from Scene Reflectivity Prediction Errors

test video data. These differences are believed to arise from the misprediction of scene reflectivity (receiver noise effects are assumed to have been averaged out). A comparison of simulation-predicted correlation performance and ROCS flight test data indicates that, with the exception of errors ascribed to imperfect reflectivity prediction, the predicted and measured correlation errors are in agreement to within the limitations of the test instrumentation.

Extrapolation of Flight Test Results

Following the completion of system flight testing and simulation model validation, the simulation can be considered an embodiment of the available theoretical and experimental information which relates directly to overall system performance. (Clearly, the simulation will not explicitly contain the detailed theory concerning the functioning of individual components, but it will contain the abstract models which relate component or subsystem performance to system level performance.) The validated simulation can therefore be used with much greater confidence to predict system performance for a specific operational mission than can techniques based on the average flight test performance or the identification of test results which were obtained under conditions "most nearly approximating" the proposed operational mission.

When the operational mission includes conditions which are significantly outside the realm of the test environment (or design changes are considered), the availability of a system model is even more important. The framework offered by the simulation model often allows the addition of a theoretical model to account for the new conditions without affecting the bulk of the system performance simulation. In this way, the extrapolated predictions need only be parameterized over the region of uncertainty of the added theoretical model. By way of example, the aircraft and helicopter flight tests for the PDMM and ROCS sensors will not evaluate plasma effects (which will be present if these sensors are used in reentry environments). Once the validated models for these sensors have been modified to account for the effects of plasma attenuation, interference and phase distortions, the resulting predictions will be as good as the plasma models utilized. In this case, the results of "plasma experiments" specifically conducted to measure these effects can be utilized to validate the added theoretical models.

3. SIMULATION DEVELOPMENT

Figure 3-1 illustrates the basic components of a correlation-updating sensor simulation. The complexity and computational requirements of such a simulation are typically dominated by the radar sensor model (depending on the level of detail, a model of the reference data preparation process can also make a major contribution).

In this section, a simulation of the APQ-144 radar developed by TASC for a low altitude correlation updating application (see Fig. 2-4) will be used to illustrate several techniques which can be employed to reduce these requirements for a ground imaging radar simulation. This simulation was developed to aid in the design, performance analysis, and flight testing of a correlation system based on the APQ-144 radar. It has been designed specifically to perform the functions outlined in the previous section of this paper. While the simulation development techniques discussed here may not be direcly applicable to the simulation of other radar systems it is expected that similar concepts can be applied.

Before discussing the specific simulation development techniques, a review of the APQ-144 radar system and an assessment of the simulation requirements will be given. Table 3-1 summarizes the characteristics of the APQ-144 radar system when operating in the ground imaging mode. To insure reasonable

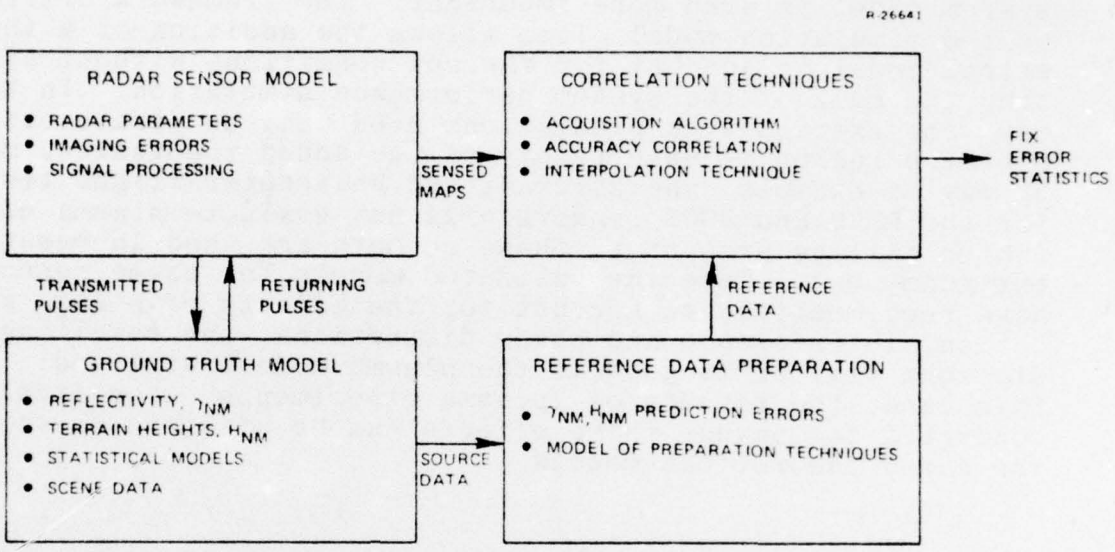


Figure 3-1 Overview of Correlation Updating Simulation

TABLE 3-1

APQ-144 RADAR CHARACTERISTICS
(GROUND IMAGING MODE)

PARAMETER	VALUE
Scan Limits	±10 or ±45 deg
Scan Rates	20 or 74 deg/sec
Azimuth Beam Width	~1.3 deg (3 dB one way)
Pulse Repetition Frequency (PRF)	2022 pulses per second
RF Frequency	16.2 GHz
Elevation Beam Pattern	$\csc^2$ cos
Maximum Power	65 kW

simulation fidelity, the model used to specify the ground truth data (i.e., reflectivities and terrain heights) must have greater resolution than the sensor being simulated. Based on the range resolution offered by the APQ-144 and using a ground truth model specifying reflectivities and terrain heights on a somewhat finer grid (a factor of two offers good simulation fidelity) leads to the processing of between 250 and 500 ground reflectors for each transmitted pulse (a much greater number would be needed for a high altitude/longer range application). Using a pulse repetition frequency of 2022 pulses per second, the fastest scan rate and smallest scan limits (i.e., 74 deg/sec and ±10 deg) leads to approximately 550 pulses per scan and a resulting total processing burden of between 138 and 275 thousand reflectors per scan. Since the correlation configuration being considered for the APQ-144 utilizes three scans, a Monte Carlo analysis based on 100 trials would require the processing of 40 to 80 million reflectors. At the conclusion of this processing, reasonably good statistics would be available for one terrain signature under a particular set of imaging conditions (i.e., imaging geometry, environmental conditions, attitude errors, etc.). Clearly, this approach to radar system simulation is unacceptable even at low altitudes, limited scan angles and fast scan rates. Two improvements to this approach will be described which together reduce this computational load to a reasonable level.

The first technique effectively moves the reflector processing (i.e., ground imaging) outside of the Monte Carlo loop (i.e., it allows the reflector processing to be done just once for a given imaging geometry). If the reflector statistics are assumed to have a Rayleigh distribution (Refs. 2 through 5), the predetection video signal for the ℓth pulse and k^{th} range gate can be expressed as

$$V_{k\ell} = \mathrm{Re}\left\{ \sum_n K_n \, R_\ell(\gamma_n) \, e^{j\phi_{\ell n}} \right\} \qquad (3\text{-}1)$$

where environmental and receiver noise effects have been temporarily neglected and

$\sum_n$ represents the sum over the reflectors (subscripted by n) which contribute to the kth range gate

K_n represents a gain dependent on radar parameters, reflector location, antenna parameters, slant range, imaging geometry, etc.

$R_\ell(\gamma_n)$ is a Rayleigh distributed random number which models the statistical characteristics of the magnitude of the return from the nth reflector

γ_n is the reflectivity associated with the nth reflector

$\phi_{\ell n}$ models the phase of the nth reflector and is assumed to be uniformly distributed from zero to 2π

Equation 3-1 can be rewritten as

$$V_{k\ell} = \sum_n K_n \gamma_n^{\frac{1}{2}} N_{\ell n}(0,1) \qquad (3\text{-}2)$$

where $N_{\ell n}(0,1)$ is a zero mean, normally distributed number with unit variance. (Note that the real part of $R_\ell(\gamma_n)e^{j\phi_{\ell n}}$ is normally distributed.) Equation 3-2 can be further simplified by noting that the sum of many normally distributed random numbers is also normal and therefore

$$V_{k\ell} = \left(\sum_n K_n^2 \gamma_n\right)^{\frac{1}{2}} N_\ell(0,1) \qquad (3\text{-}3)$$

The coefficient, $(\sum_n K_n^2 \gamma_n)^{\frac{1}{2}}$, represents the square root of the signal power returning on the ℓth pulse for the kth range bin (i.e., $P_k^{\frac{1}{2}}$). Based on Eq. 3-3, a deterministic simulation can be developed which calculates the mean power returned for each pulse (associated with each range bin) and stores these powers for later use within the Monte Carlo simulation. In the Monte Carlo simulation, sample video signals can be generated using Eq. 3-3.

A more general version of Eq. 3-3 which incorporates environmental effects and receiver gain variation can be written as

$$V_{k\ell} = G_k \left\{ (A_k P_k)^{\frac{1}{2}} N_{S\ell}(0,1) + (N_{C_k} + N_J + N_R)^{\frac{1}{2}} N_{I\ell}(0,1) \right\} \quad (3\text{-}4)$$

where

A_k is an attenuation factor which models the signal propagation losses for the kth range bin (e.g., radome, weather, etc.)

N_{C_k} is the power associated with the clutter interference in the kth range bin (including both ground clutter through unmodeled sidelobes and weather clutter).

N_J is the jamming power level

N_r is the receiver noise power level

G_k is a receiver gain which may vary with range (i.e., time after pulse transmission) and therefore may be different from range bin to range bin (e.g., Sensitivity Time Control (STC))

The correlation of one return with subsequent returns (depending on the degree of frequency agility employed) can easily be simulated by creating a correlated sequence of random numbers, $N_\ell(0,1)$, having a pulse-to-pulse correlation coefficient given by (Ref. 6)

$$\rho(\Delta f) \approx \frac{\sin(2\pi\Delta f/B)}{(2\pi\Delta f/B)} \quad (3\text{-}5)$$

where

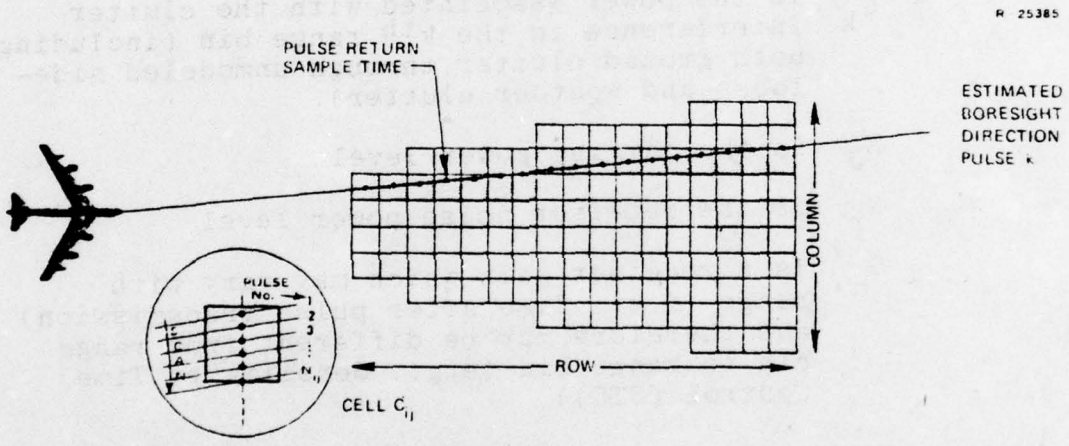
Δf is the frequency difference between the two pulses under consideration

B is the receiver bandwidth

The second technique employed to lower the computational burden reduces the number of transmitted pulses which must be simulated by deriving an integrated power for each

cell of the map generated by the digital scan converter. Figure 3-2 illustrates the sampling logic and pulse-return assignment logic used by the digital scan converter. If a pulse-by-pulse simulation of the APQ-144 were to be conducted, it would be necessary to:

- Set the range gate limits based upon the pulsewidth and estimated range to C_{ij} (plus an error related to range gate timing)
- Set the true antenna azimuth direction for the ℓth pulse of N_{ij} pulses to be simulated.



- SENSED CELLS, C_{ij}, STABILIZED DURING SCAN
- RANGE GATES (i.e., SAMPLING TIMES) CONTROLLED SO THAT CENTER OF PULSE RETURN CENTERED ON SENSED CELL
- PULSE INTEGRATION DEPENDENT ON ESTIMATED BORESIGHT DIRECTION

Figure 3-2 Imaging Control by APQ-144 Digital Scan Converter

- Weight each of the reflectors within the range gate limits by the azimuth beam pattern for the ℓth pulse
- Repeat this for each of the N_{ij} pulses and sum the results.

This procedure can be symbolically represented by

$$C_{ij} = \underbrace{\sum_{\ell=1}^{N_{ij}}}_{\substack{\text{pulse} \\ \text{sum}}} \left\{ \underbrace{\sum_{n} \gamma_n G_A^2 (\delta\phi_{\ell n})}_{\substack{\text{reflector} \\ \text{sum}}} \right\} \qquad (3\text{-}6)$$

where

$G_A^2(\phi)$ is the two-way antenna gain pattern (azimuth)

γ_n represents a reflector within the range gate limits

$\delta\phi_{\ell n}$ is the azimuth direction of the nth reflector relative to the antenna boresight on the ℓth pulse

Equation 3-6 can be rewritten as follows:

$$C_{ij} = \sum_{n} \gamma_n \left\{ \sum_{\ell=1}^{N_{ij}} G_A^2(\delta\phi_{\ell n}) \right\} \qquad (3\text{-}7)$$

The inner sum can be viewed as a convolution of the two-way beam pattern as illustrated in Fig. 3-3. Since the nominal configuration for the APQ-144 correlator uses a ±10 degree scan, N_{ij} is approximately the same for each cell within the jth column of the sensed map (sensed map cells with approximately the same range from the aircraft, see Fig. 3-2). Therefore, a convolved beam pattern, $G_{\Sigma j}(\phi)$, can be computed just once for each column, j, of the sensed map, tabulated over the range of interest (e.g., over a range of ϕ for which $G_{\Sigma j}(\phi) \geq 0.01\, G_{\Sigma j}(0)$) and then used for each sensed cell at that range as follows

$$C_{ij} = \sum_{n} \gamma_n \, G_{\Sigma_j} (\phi_n - \phi_{ij})$$

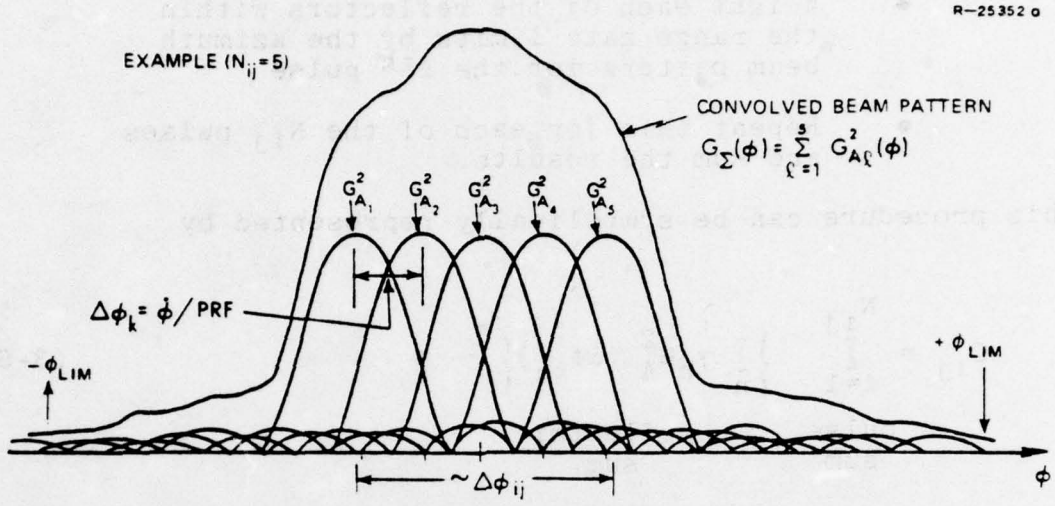


Figure 3-3 Illustration of Beam Pattern Convolution for $N_{ij} = 5$

where ϕ_{ij} is the azimuth angle to the center of C_{ij} and ϕ_n is the azimuth angle to the nth reflector. Calculation of C_{ij} now involves only one computation for every reflector within the range and azimuth limits associated with C_{ij} instead of one computation per reflector assigned to the (i,j) cell for each transmitted pulse.

Since approximately 100 pulses are integrated for each cell, C_{ij}, a reduction in computational burden of approximately 100 has been achieved through the use of this technique.

By combining both techniques a reduction in computational burden of approximately ten thousand has been achieved (100 each for the examples cited). The number of reflectors processed for 100 Monte Carlo trials has been reduced from 40 to 80 million to 4 to 8 thousand. The utility of the resulting simulation has been vastly improved and a wide range of imaging geometries, scene signatures and environmental conditions can now be reasonably simulated.

4. SUMMARY

The objective of this paper has been to outline the general role of simulations in a radar flight test program and to illustrate this role through the use of examples taken from the simulation and flight testing of radar sensors

used for correlation guidance. Since the efficiency of radar simulations can seriously impact their utility, a discussion of the development of a ground imaging radar simulation, created to aid in the design and flight testing of a viable sensor configuration, has been presented.

A central theme of this paper is that the simulation of radar sensors leads to an improved understanding of the relative importance of different system error sources, thus allowing limited design and testing resources to be effectively concentrated on those error sources which pose the greatest threat to successful program completion. Since simulations are initially developed through the integration of theoretical analyses of numerous system components, they offer the only "general" theory with which to predict and explain system performance (both prior to and after system testing). Performance predictions generated in advance of testing allow the development of efficient test plans which explore all of the crucial areas of system operation. As test data is collected, discrepancies between model predictions and test results force a reexamination of simulation model assumptions, test equipment and test procedures. Past experience has shown that the development and use of simulations provides insights into the characteristics and consequences of the major system error sources. Therefore, hardware problems which do arise are often uncovered more quickly than would have been the case in the absence of simulation experience. Finally, after testing has been completed, the successfully validated simulation models can be used to extend system performance predictions to important cases not covered by the test program and for predicting the improvements in system performance which could be obtained through design modifications.

Simulation development techniques which increase simulation utility by maximizing computational efficiency are illustrated for the case of the APQ-144 radar in a ground imaging mode. The two techniques discussed in this paper reduce the computation requirements associated with Monte Carlo performance analysis by approximately ten thousand (for an example case in which 100 Monte Carlo trials are simulated).

REFERENCES

1. Gelb, A., Editor, Applied Optimal Estimation, M.I.T., Press, Cambridge, Mass., April 1974.

2. Ament, W., MacDonald, F., and Sheubrodge, R., "Radar Terrain Reflections for Several Polarizations and Frequencies," Trans. of the 1959 Symposium on Radar Returns, Part II, 11 and 12 May 1959.

3. Guinerd, N.W., Ransone, J.T., Loing M.B., and Hearton L.E., NRL Terrain Clutter Study Phase I, Naval Research Laboratory Report No. 6487, 10 May 1967.

4. Long, M.W., Radar Reflectivity of Land and Sea, D.C. Heath & Co., Lexington, Mass., 1975.

5. Linell, T., "An Experimental Investigation of the Amplitude Distribution of Radar Terrain Return," 6th Conf. of the Swedish National Committee on Scientific Radio, 13 March 1963.

6. Ray, H., "Improving Radar Range and Angle Detection with Frequency Agility," Microwave Journal, May 1966.

EIGHTH BIENNIAL GUIDANCE TEST SYMPOSIUM

DESIGNING WEAPON SYSTEM TEST TRAJECTORIES FOR GUIDANCE ERROR SOURCE OBSERVABILITY

AUTHORS: S. M. ARCHER
C. L. BOWMAN
N. N. GURWELL

LOGICON, INC.
SAN PEDRO, CALIFORNIA

ABSTRACT

The area of experimental design has long been a subject of much concern to statisticians and engineers alike. Here, a weapon system flight test reentry trajectory is designed in order to improve guidance system performance evaluation. The evaluation is performed from a simulated post flight analysis of the measurements made by radar/camera ground sensors and a reentry vehicle inertial measurement unit. A result of this evaluation is the covariance matrix of the error in estimating the various reentry guidance system error sources. The measure of the improvement provided by a trajectory design is a weighted trace of this covariance matrix, where the weights are the relative importance of the principal error contributors of the operational trajectory. Two modified constrained optimization techniques are developed to solve this problem. The results show that significant improvement in the observability of guidance system error parameters can be attained.

INTRODUCTION

This paper considers the problem of weapon system flight test trajectory design for the purpose of improving operational system performance evaluation. It is shown that the observability of the principal reentry guidance system errors can be substantially enhanced by trajectories designed for this purpose.

The principal weapon system reentry vehicle inertial measurement unit (IMU) error sources were determined from error analyses performed on a candidate operational trajectory. Using this identification of the principal error contributors and their corresponding weights, a search for a reentry trajectory which minimized the weighted trace of the measured principal error source covariance matrix was performed. The measurements are a difference between those of the reentry IMU and radar/camera ground sensor position measurements with existing geometry near the impact at Kwajalein. The ground sensors are modeled as having bias and scale factor errors. The covariance analysis of the IMU and ground sensor error parameters, simulating post flight data processing, was performed using an extended Kalman filter. The refinement of the reentry trajectory assumed a standard boost and freeflight as launched from SAMTEC and was restricted to satisfy energy, vehicle, and instrumentation constraints during reentry.

To obtain a solution to this input design problem, the standard Cramer-Rao lower bound on the covariance of an unbiased estimator was used, however the usual "eigenvalue" input design solution was not applicable. As a result, two modified constrained optimization techniques were developed and each used to obtain an improved trajectory. Both of the improved trajectories showed a significant improvement in the estimation of the principal reentry IMU error sources.

The discussion of these investigations is presented in four sections. In Section 1, the assumed operational system is described, Section 2 documents the identification of the principal weapon system performance contributors, Section 3 describes the flight test reentry trajectory design process, and Section 4 presents the performance attained with the derived trajectories.

1. OPERATIONAL SYSTEM DESCRIPTION

The operational system considered consists of an aerodynamically controlled reentry vehicle and a full three degree-of-freedom stabilized reentry inertial measurement unit (RIMU) deployed from a Minuteman III booster with a NS-20 guidance system. The NS-20 is modeled with the error sources shown in Table 1 and error source uncertainties corresponding to current accuracy estimates.

At launch, the RIMU is assumed coarsely aligned in azimuth using the azimuth gimbal resolver, and is aligned about the level axes using the platform accelerometers. The RIMU navigates from launch and is updated by comparison of the RIMU navigated state with that of the more accurate NS-20 at the end of Stages I and II and prior to deployment, using a Kalman filter.

The reentry navigation system is reinitialized at reentry with a state vector mapped from the estimated state at deployment and navigates through the reentry phase of the mission. The RIMU platform axes are aligned to a downrange, crossrange, and up orientation at launch and the accelerometer and gyro input axes are as shown in Figure 1.

RIMU Error Models

The RIMU is modeled with accelerometer, gyro, gimbal mass unbalances, and platform compliance errors.

Accelerometer Error Model

The acceleration error for each accelerometer is modeled by:

$$\Delta A_i = K_o + K_i A_i + K_s |A_i + K_o| + K_d \text{sign}(A_i + K_o)$$

$$+ K_2 A_i^2 + K_3 A_i^3 + K_{ip} A_i A_p + K_{io} A_i A_o$$

$$+ K_p A_p + K_o A_o + \beta A_p + \gamma A_o$$

The coefficients for the error model and their description are:

K_o - bias

K_i - scale factor

Table 1. NS-20 Error Sources

Error Source

- IMU Preflight
  - Q-Matrix
    - Reference Errors
      - Level Detector Bias
      - Level Detector Random
      - ϕ-Matrix Error
      - ϕ-Parameter Error
      - OER
    - PIGA Errors
      - Output Stability
      - Input Axis Uncertainty
      - Pulse Count Timing
  - Long Term Drift
    - PIGA Scale Factor Drift
    - PIGA Input Axis Drift
  - Platform
    - Level Alignment
    - Azimuth Alignment
      - Random
      - Bias
    - Compliance
      - Random DR/CR
      - Bias DR/CR

Error Source (Cont'd)

- Gyro
  - Biasing Routine
    - X-Channel
    - Y-Channel
    - Z-Channel
  - Spin Axis Mass Imbalance, δC
  - Motor Torque Deflection, δD
  - Gas Bearing Compliance
    - Incompressibility Effects, δB
    - Compressibility Effects, δE
  - Spin Axis G^2, δF
- PIGA
  - Short Term Bias Stability
  - Nonlinearity
- IMU Inflight
  - Gyro Random Drift
  - Internal Temperature Change
  - PIGA
    - Bias Shift
    - Scale Factor Shift
    - Input Axis Shift
    - FMET Pulse Quantization
  - Platform Limit Cycles
    - Level
    - Azimuth

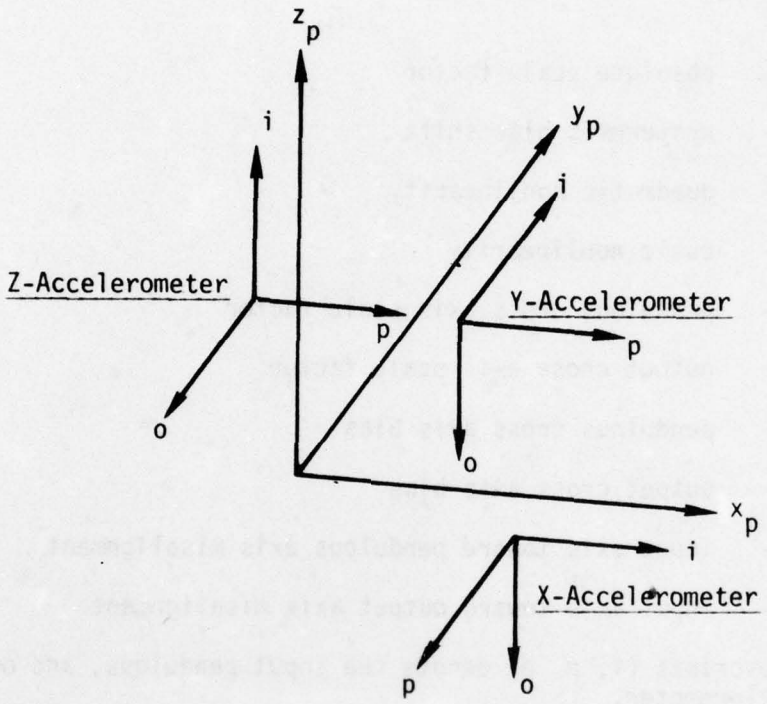


Figure 1a. RIMU Accelerometer Orientations

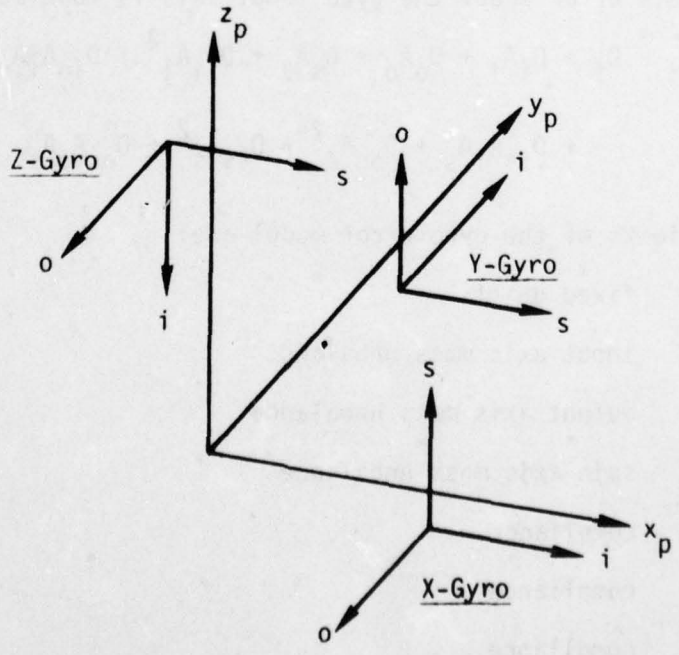


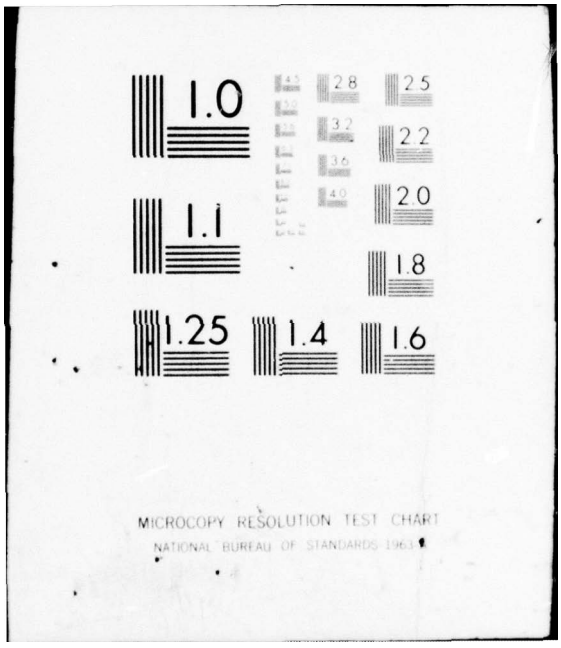
Figure 1b. RIMU Gyro Orientations

AD-A040 012 ARMAMENT DEVELOPMENT AND TEST CENTER EGLIN AFB FLA F/G 17/7
PROCEEDINGS OF THE BIENNIAL GUIDANCE TEST SYMPOSIUM (8TH) HELD --ETC(U)
MAY 77

UNCLASSIFIED ADTC-TR-77-3-VOL-1 NL

2 OF 8
AD
A040012




1.0
1.1
1.25
1.4
1.6
1.8
2.0
2.2
2.5
2.8
3.2
3.6
4.0
MICROCOPY RESOLUTION TEST CHART
NATIONAL BUREAU OF STANDARDS 1963

K_s - absolute scale factor

K_d - hysteresis bias shift

K_2 - quadratic nonlinearity

K_3 - cubic nonlinearity

K_{ip} - pendulous cross axis scale factor

K_{io} - output cross axis scale factor

K_p - pendulous cross axis bias

K_o - output cross axis bias

β - input axis toward pendulous axis misalignment

γ - input axis toward output axis misalignment

and the subscripts (i, p, o) denote the input pendulous, and output axes of the accelerometer.

Gyro Error Model

The drift rate error about the gyro input axis is modeled by:

$$\dot{\Phi}_i = D_f + D_i A_i + D_o A_o + D_s A_s + D_{ii} A_i^2 + D_{io} A_i A_o$$

$$+ D_{is} A_i A_s + D_{oo} A_o^2 + D_{ss} A_s^2 + D_{os} A_o A_s$$

The coefficients of the gyro error model are:

D_f - fixed drift

D_i - input axis mass unbalance

D_o - output axis mass unbalance

D_s - spin axis mass unbalance

D_{ii} - compliance

D_{io} - compliance

D_{is} - compliance

D_{oo} - compliance

D_{ss} - compliance

D_{os} - compliance

where the subscripts (i, o, s) denote the input, output and spin axes of the gyro.

Gimbal Mass Unbalance Model

The gimbal mass unbalances give rise to misalignments about the platform x, y, and z axes of the forms:

Misalignment about x axis
$$\begin{cases} \theta_{xy} = -K_{xy} A_y \\ \theta_{xz} = K_{xz} A_z \end{cases}$$

Misalignment about y axis
$$\begin{cases} \theta_{yx} = K_{yx} A_x \\ \theta_{yz} = -K_{yz} A_z \end{cases}$$

Misalignment about z axis
$$\begin{cases} \theta_{zx} = -K_{zx} A_x \\ \theta_{zy} = K_{zy} A_y \end{cases}$$

Where the A_x, A_y, A_z are in platform coordinates.

Platform Compliance Model

Deformation of the platform caused by g loading causes the accelerometers to be misaligned with respect to their theoretical input axes. The errors in acceleration caused by this deformation are modeled as:

$$\Delta A_i = K_{ijk} A_j A_k$$

where

A_i is the acceleration error along the ith axis caused by the A_j and A_k accelerations.

Platform Alignment

The platform is misaligned at launch by the angles ϕ_x, ϕ_y, ϕ_z about the platform axes. The acceleration error due to the platform misalignment is given by

$$\overline{\Delta A}(t) = \begin{pmatrix} \phi_x \\ \phi_y \\ \phi_z \end{pmatrix} \times \overline{A}(t)$$

where $\overline{A}$ and $\overline{\Delta A}$ are in platform coordinates.

Trajectory

The operational trajectory assumed for this analysis is a northerly launch azimuth, 4250 nmi range, -27.5 degree reentry angle boost trajectory with a mixture of yaw maneuvers and coasts for the reentry trajectory depicted in Figure 2. The impact point is approximately 2 nmi downrange and 4 nmi crossrange from the ballistic impact point.

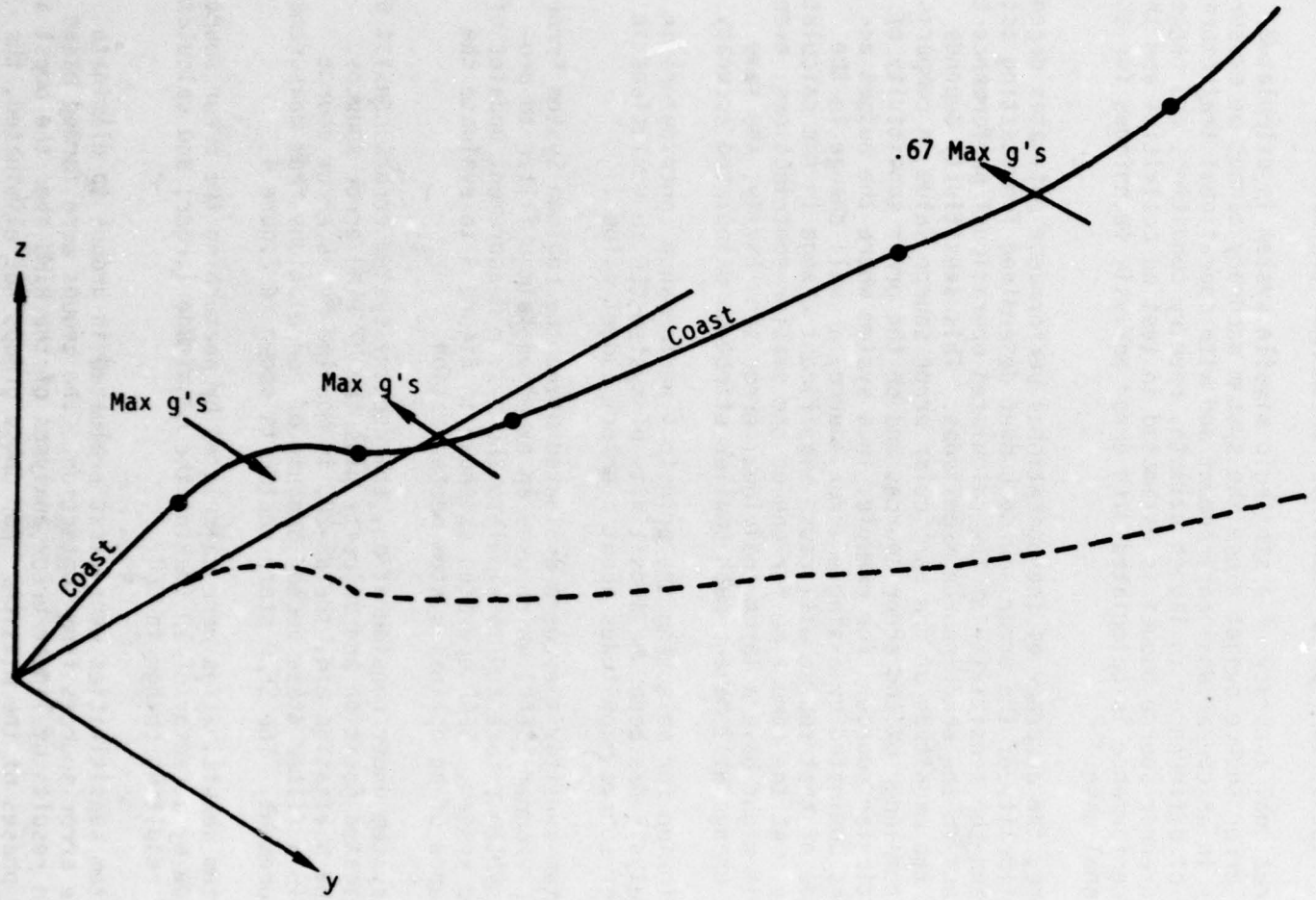


Figure 2. Operational Analysis Trajectory

2. IDENTIFICATION OF PRINCIPAL PERFORMANCE CONTRIBUTORS

The operational accuracy of a strategic missile system is calculated from an error source budget since the system accuracy cannot be measured directly in an operational environment and with operational trajectories because of differences in launch azimuth, reentry conditions and range. Thus, an error source budget is estimated in testing activities and the system performance is calculated with error analysis techniques for the operational case.

Therefore, the accuracy of the operational performance estimates depends on the fidelity of the error source budget determined from testing activities and the sensitivity of the calculated operational performance to variations in the error source magnitudes. This sensitivity depends both on the magnitude of the particular error source value in comparison to the remainder of the error sources and on the error sensitivity of the particular source. For example, in a system where the budget accuracy is dominated by a single error source, a small change in the magnitude of that source will cause significant change in the calculated accuracy. At the same time for one of the smaller contributions, even though it might have a large individual error sensitivity, the same percent change will have a much smaller effect on calculated accuracy.

The criterion for selecting the principal performance contributors in this analysis has been the sensitivity of system CEP to variations in the error source magnitudes about a priori budget values.

The system sensitivities were evaluated using the Logicon System Error Analysis Program (SEAP) which uses an extended Kalman filter to propagate system errors and to simulate the system measurement updates of an aided system. SEAP operates as shown in Figure 3 to evaluate the performance of an optimal system mechanization.

In the system under consideration, the reentry system errors consist of the navigated position and velocity plus the 87 RIMU error sources, while the navigation aid, the NS-20, is modeled by 78 error source states in a filter state vector because of correlations from measurement to measurement. The SEAP state vector is shown in Figure 4.

The system sensitivities were calculated by perturbing the error source magnitude by a factor of 10 (making the magnitude larger) and calculatng ing the resulting change in CEP.

The system sensitivities were first evaluated in groups to eliminate possible error sources from contention. The groups were formed based upon the results of linear error analyses of the RIMU over the boost and reentry phases of the mission. For those groups not eliminated, the

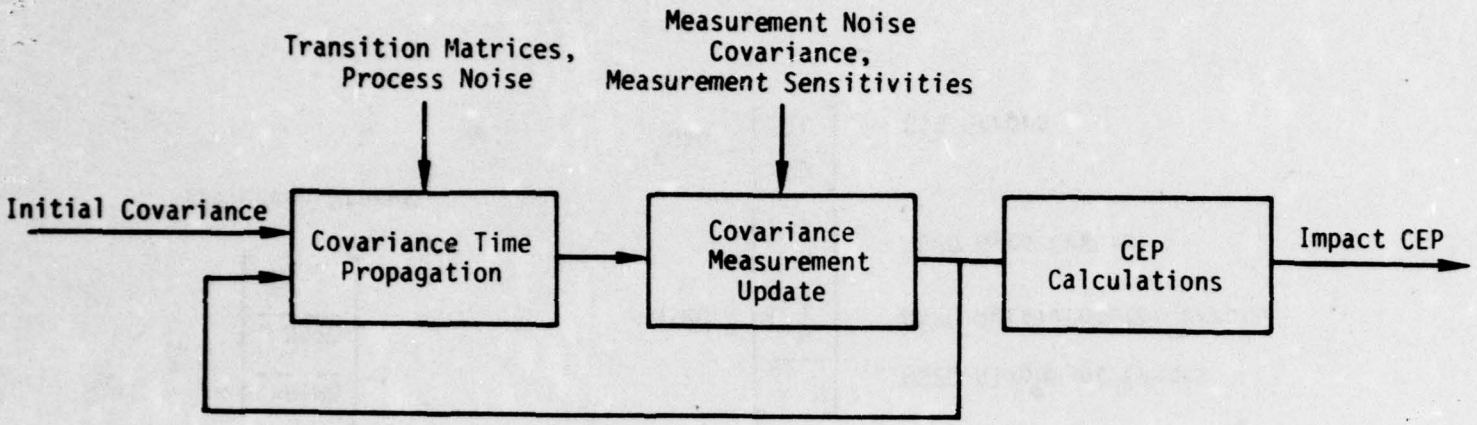


Figure 3. System Error Analysis Program

$$\underline{X} = \begin{bmatrix} \underline{S} \\ \hline \underline{E}_{RIMU} \\ \hline \underline{E}_{NS20} \\ \hline \underline{E}_{G\&G} \end{bmatrix}$$

179 Error States

$$\underline{S} = \begin{bmatrix} \delta\overline{P} \\ \hline \delta\overline{V} \end{bmatrix}$$ ECI Position Error

$$\underline{E}_{RIMU} = \begin{bmatrix} \overline{\delta\phi}^{R} \\ \hline \underline{E}_{A}^{R} \\ \hline \underline{E}_{G}^{R} \end{bmatrix}$$ RIMU Alignment Errors; RIMU Accelerometer Errors; RIMU Gyro Errors

$$\underline{E}_{NS20} = \begin{bmatrix} \overline{\delta\phi}^{N} \\ \hline \underline{E}_{A}^{N} \\ \hline \underline{E}_{G}^{N} \end{bmatrix}$$ NS20 Alignment Errors; NS20 Accelerometer Errors; NS20 Gyro Errors

$$\underline{E}_{G\&G} = \begin{bmatrix} \delta GM \\ \hline ETC \end{bmatrix}$$ G&G Errors

Figure 4. System State Vector

contributing error sources were determined using subdivisions of the groups and finally individual system CEP sensitivities were determined. For the system and a priori error budget under consideration, the system sensitivity magnitudes are dominated by 15 error sources. The 15 error sources with the largest sensitivities and their sensitivities are given in Table 2. These significant sensitivities arise during the reentry phase since the effects during boost are estimated by the inflight measurements. Error sources, such as azimuth alignment which might be expected to appear among the largest contributors do not because they are estimated by the inflight measurements.

Table 2. Principal Performance Contributors

Source Number	Description	% CEP Change at Impact*
1	Gimbal Mass Imbalance About Z by Y	71.0
2	Y-Gyro D_{II}	37.4
3	X-Accelerometer Bent to Y by Y	30.6
4	Z-Gyro D_{SS}	26.5
5	Z-Gyro D_{IS}	14.3
6	X-Accelerometer Bent to Y by X	7.7
7	X-Gyro D_{SS}	7.1
8	Gimbal Mass Imbalance About X by Y	5.9
9	Y-Gyro D_{IO}	5.8
10	X-Accelerometer Bent to Z by Z	5.8
11	Y-Gyro D_{OO}	5.7
12	Y-Gyro Fixed Drift	5.4
13	X-Gyro Fixed Drift	4.2
14	Z-Gyro D_{II}	3.7
15	Z-Gyro D_{OS}	3.7

* 1000% increase in uncertainty

3. FLIGHT TEST REENTRY TRAJECTORY DESIGN

Flight Test System

The system assumed for the flight test experiment is the reentry vehicle deployed from a Minuteman I booster on a SAMTEC to Kwajalein trajectory. For this analysis the reentry vehicle impact is assumed to be in the lagoon where adequate ground sensor coverage is possible. The flight test boost trajectory has a -26.5 degree reentry angle.

The boost guidance system is the NS-10 guidance set and the RIMU is a less mature version of the operational RIMU with some error source magnitudes budgeted larger than those for the operational version. The flight test RIMU error model form is identical to the operational model described earlier.

In this analysis, the emphasis has been to design trajectory maneuvers to facilitate the identification of the RIMU error source magnitudes. To this end a single set of sensors has been chosen. Figure 5 shows the locations of the sensors and the assumed impact point. To reduce computer expenditures in this exploratory study, the three sensors are each assumed to be a composite of a radar (for range measurement) and a camera (for angle measurements) located at the sites shown in Figure 5. Ground sensor measurement accuracy is assumed to be 20 ft 1σ in range and $.003^{o}$ 1σ in azimuth and elevation angles. The initial estimate of the reentry vehicle state at reentry is assumed to be derived from the ground sensor data.

The assumed vehicle is a bank-to-turn vehicle so that the controls available are normal acceleration, a_n, and bank angle, ϕ. The acceleration due to aerodynamic drag on the vehicle is partially a function of the normal acceleration. The vehicle is subject to constraints on normal acceleration magnitude, integral of acceleration, and impact Mach number.

The Identification Problem

The RIMU and ground sensor state error variables are taken to be of the bias form, i.e.,

$$\underline{\theta} = \begin{pmatrix} \theta_{RIMU} \\ \theta_{SENSOR} \end{pmatrix}, \quad \underline{\dot{\theta}} = 0$$

where the vector θ_{RIMU} contains the RIMU error parameters to be identified and the vector θ_{SENSOR} contains the ground sensor non-random error parameters.

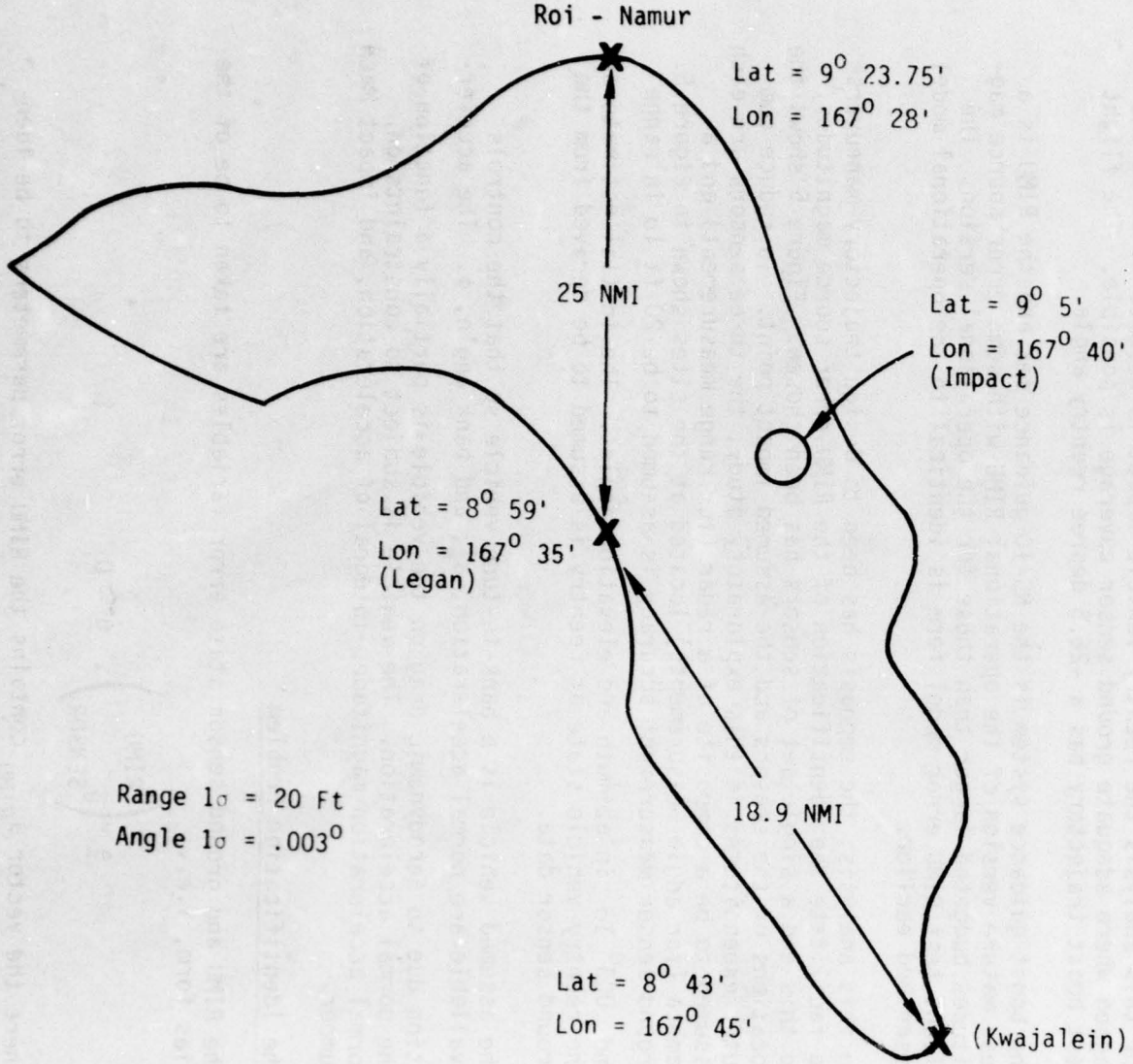


Figure 5. Ground Sensor Geometry

The measurement equation is

$$\underline{Z}(t) = H(t, \underline{u})\ \underline{\theta} + \nu(t)$$

where

$$E(\nu(t)\ \nu^T(t')) = R(t)\delta(t - t')$$

It is instructive to examine the form of the RIMU observables. The RIMU error sources can be divided into gyro and non-gyro errors. In platform coordinates, the RIMU acceleration errors can be shown to be of the following forms. For the input non-gravitational acceleration, $\bar{A}(t)$, the error in RIMU sensed acceleration is $\Delta\bar{A}(t)$, where:

Non-Gyro Errors

$$N_1: \quad \Delta\bar{A}_i(t) \propto \theta_i$$

$$N_2: \quad \Delta\bar{A}_i(t) \propto \theta_i A_k(t)$$

$$N_3: \quad \Delta\bar{A}_i(t) \propto \theta_i A_k(t) A_\ell(t)$$

Gyro Errors

$$G_1: \quad \Delta\bar{A}_i(t) = \theta_i t B_i \bar{A}(t)$$

$$G_2: \quad \Delta\bar{A}_i(t) = \theta_i \int_0^t A_i(\tau)d\tau\ B_i \bar{A}(t)$$

$$G_3: \quad \Delta\bar{A}_i(t) = \theta_i \int_0^t A_k(\tau)A_\ell(\tau)d\tau\ B_i \bar{A}(t)$$

where A_k and A_ℓ are the k and ℓ components of the acceleration $\bar{A}$ and

$$B_i = \begin{bmatrix} 0 & \delta_{j3} & -\delta_{j2} \\ -\delta_{j3} & 0 & \delta_{j1} \\ \delta_{j2} & -\delta_{j1} & 0 \end{bmatrix}$$

is a misalignment matrix corresponding to a rotation about a predefined jth axis for the ith error source.

If a velocity measurement is to be made, the observable for the ith RIMU error source is

$$\overline{\Delta V}_i(t) = \int_0^t \overline{\Delta A}_i(\tau)d\tau$$

and for a position measurement

$$\overline{\Delta R}_i(t) = \int_0^t \int_0^\tau \overline{\Delta A}_i(s)ds d\tau$$

The non-gravitational acceleration in platform coordinates is a function of the normal acceleration and bank angle control.

$$\overline{A}(t) = \overline{F}(a_n(t), \phi(t))$$

At the time of maneuver initiation on the flight test trajectory, the vehicle drag is nearly along the platform negative z-axis and yaw maneuvers will produce platform y-accelerations while pitch maneuvers produce x-accelerations.

Figure 6 indicates the output channel sensitivities to various combinations of input accelerations. Figure 7 depicts the non-gravitational acceleration in platform coordinates for the flight test trajectory equivalent to the assumed operational trajectory (a yaw-maneuvering trajectory). For the yaw-maneuvering trajectory, drag and the yaw-accelerations produce primarily a_y and a_z inputs to the RIMU error dynamics. From Figure 6 it can be seen that for ten of the error sources, including the five most important, little separation in the output channel can be achieved by the yaw-maneuvering trajectory. On this trajectory error sources 6 and 15 have virtually no output. In contrast, for a combined a_x, a_z (pitching maneuver), a threeway channel separation can be achieved for five of the error sources. This observation, coupled with the realization that a pitch-up maneuver tends to extend flight time and thus the number of measurements, suggests that pitching maneuvers may be advantageous. It is also clear that more output channel separation would be achieved by the use of maneuvers which induce accelerations along all three platform axes.

Input Design Techniques

The problem under investigation here is to improve the identification of the RIMU error sources by varying the test flight trajectory, and as such, is a type of input design problem. This problem area has been the subject of much statistical and engineering literature. A common

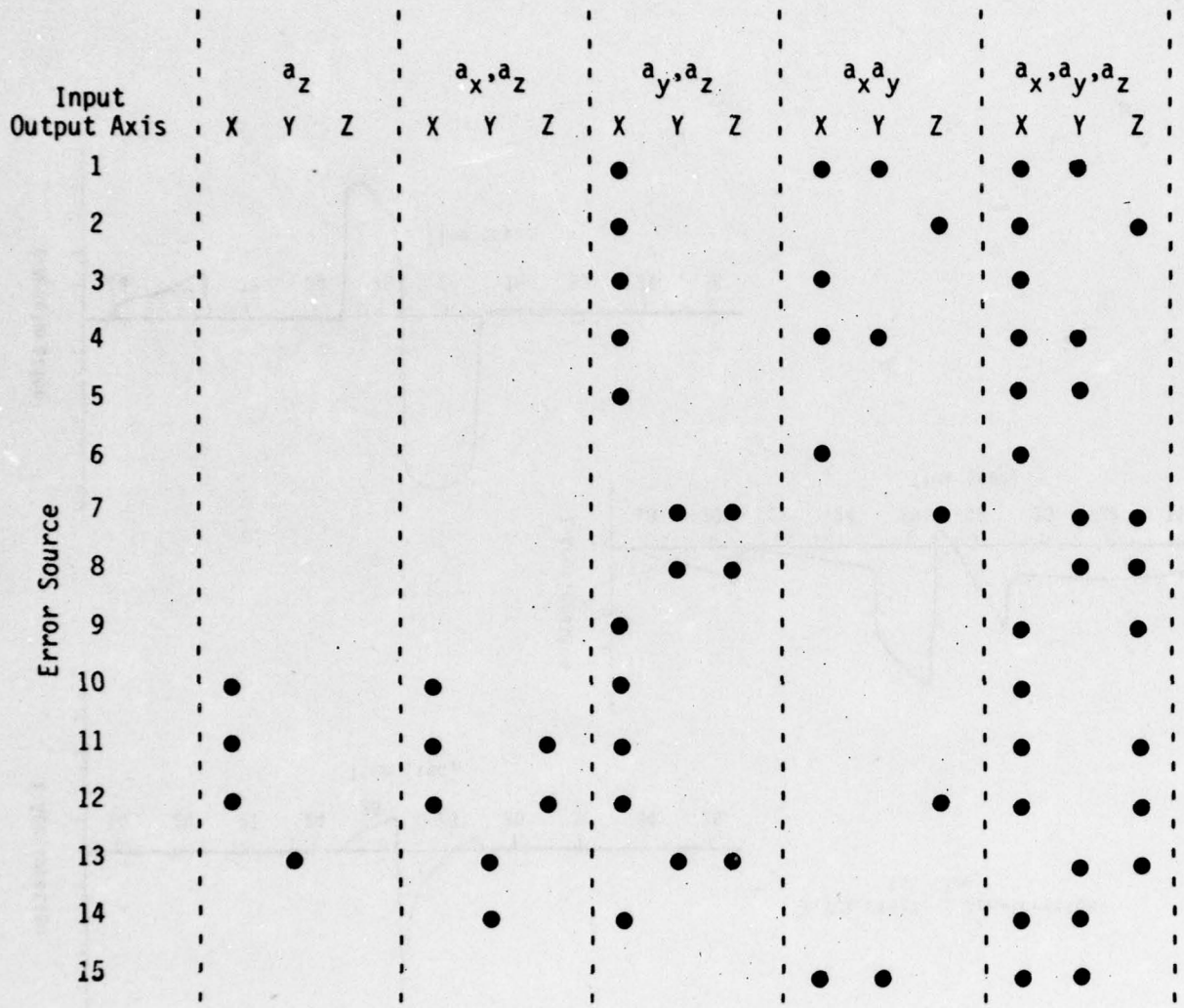


Figure 6. Input Design Problem Output Sensitivities To Inputs (Platform Coordinates)

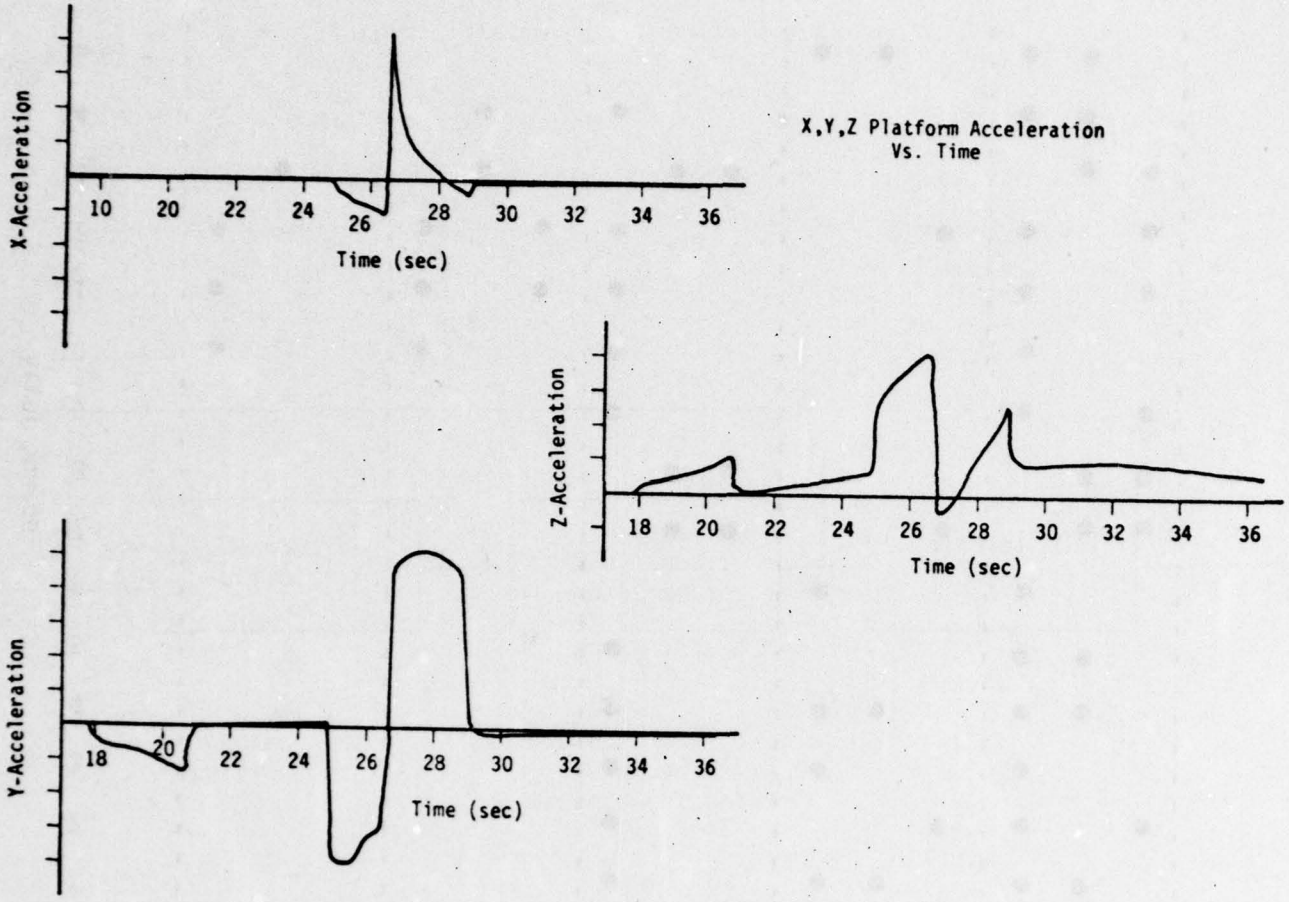


Figure 7. Accelerations in Platform Coordinates
Yaw-Maneuvering Trajectory

approach, which is somewhat independent of the estimator invoked, is to use the Fisher information matrix, M, as a measure of the information on θ provided by a feasible input. The reason for its use is that it is computationally attractive and its inverse, termed the Cramer-Rao lower bound, provides a "good" lower bound on the covariance of θ for all regular unbiased estimators. (Here, regular refers to certain modest regularity assumptions on the distribution of the observations, Rao [1].) The solution then sought to the input design problem is an input which optimizes some objective functional of M or M^{-1}, for example a weighted trace or determinant, Mehra-Gupta [2].

A general problem considered in the literature is of the form

$$\dot{X} = F(t,\theta)X + G(t,\theta)u \quad ; \quad Y = H(t,\theta)X + \nu \tag{1}$$

where

- X is the state vector
- u is the input control vector
- θ is the vector of unknown parameters
- ν is a white noise vector with zero mean and covariance R.

Making use of the additive type control, various objective functionals can be expressed as

$$J(u) = |< Tu, u >|$$

where u belongs to some Hilbert space $\mathcal{H}$ and $||u|| \leq 1$ and T is some normal, compact bounded linear operator on $\mathcal{H}$. An optimal input u then is $\sup_{u\in\mathcal{H}} J(u)$, which is satisfied by the u corresponding to the largest eigenvalue (in absolute value) of T (see Rudin [3] , Gupta and Hall [4]).

The problem considered here does not fall into the form of (1) since it is not linear in the control u. Consequently, it cannot be solved by applying the above technique. In fact, here H is a function of u and is sufficiently nonconvex in u so as not to guarantee convergence to an optimal input of any general optimization algorithm. As a result, optimization techniques, based on certain necessary conditions for solution, are used in the present problem.

Commonly, a linear functional of the information matrix M is chosen for the objective functional, since for the general problem (1), M is a quadratic function of u. The drawback with maximization of diagonal elements of M is that the off-diagonal elements can become large, in which case the diagonal elements of M^{-1} can increase. This fact, in conjunction with the nonconvexity of H in u for the problem here, caused

the choice of a weighted trace of the covariance matrix as the objective functional to be minimized. This functional is defined in the next section.

Trajectory Performance Criterion

The performance function chosen for the trajectory design problem here is

$$J = \text{tr}\,(W^T W P_f) = W P_f W^T$$

where P_f is the final covariance of the RIMU error parameters after estimation, and W is a row vector of weights derived in the identification of the operational principal performance contributors which describe the relative importance of the error parameter estimates. Table 3 gives the weights, which are derived from the sensitivities of Table 2. Since the Fisher information matrix and its inverse for a trajectory can be computed with less effort than the covariance P_f, the following performance function based on the Cramer-Rao lower bound is used in the optimization process.

$$J_{CR} = W M^{-1} W^T$$

where

$$M = M_o + \int_0^t H^T(t,u) R^{-1} H(t,u)\,dt$$

Once a trajectory design is found using J_{CR}, the estimation process is then used to calculate the actual J.

A comparison of the relative improvement shown by the J_{CR} and J performance measures for a 15-state system is given in Table 4 for the yaw-maneuvering trajectory and two trajectories developed in this study. The difference between J_{CR} and J is caused by numerical effects since J_{CR} was calculated with double precision and J with single precision. These results show that the trajectories have a consistent relative performance with respect to J_{CR} and J, and thus J_{CR} is an adequate alternate performance measure for trajectory design purposes.

Table 3. Performance Criterion Weights

Error Source	Weight
1	.302
2	.159
3	.130
4	.113
5	.061
6	.033
7	.030
8	.025
9	.025
10	.025
11	.024
12	.023
13	.018
14	.016
15	.016

Table 4. Cramer-Rao/Estimator Comparison
(15-State System)

Trajectory	J_{CR}*	$\bar{J}$*
Yaw-Maneuvering Trajectory	1.00	1.00
Design A	.703	.692
Design B	.578	.570

* Normalized to the Yaw-Maneuvering Trajectory

Trajectory Selection Algorithms

Two techniques using the C-R lower bound performance index have been used in attempting to arrive at a trajectory design in the present case. The first method is a combination of engineering judgement and the use of gradients of J_{CR} with respect to the control variables a_n, and ϕ to iterate for refinement of the trajectory. This method involves estimating the gradient at a point and then pivoting in a modified direction of steepest descent until no further improvement or a boundary is attained. At this point, another gradient is taken and the process is repeated.

The second method is a modified method of local variations. This method does not require the calculation of a gradient. It is based on a progressively finer partitioning of the set of feasible inputs. From an initial input and an initial step size, one pivots to adjacent vertices of the partition which decrease the value of the objective functional. When such an improvement is no longer possible the step size is cut down and the algorithm pivots on this finer partition. Under certain conditions, the method is known to converge to points with a zero gradient. This algorithm is defined as follows:

Step 0: Select an initial feasible control $u_o \epsilon R^n$. Select an initial step size $r > 0$. Select m directions of variation $d_j \epsilon R^n$ such that for any point $X \epsilon R^n$

$$x = \sum_{j=1}^{m} \lambda_j d_j \text{ where } \lambda_j \geq 0.$$

Step 1: Set $i = 0$. Compute $J_{CR}(u)$.

Step 2: Set $j = 0$.

Step 3: Set $j = j + 1$. If $j = m + 1$, then $j = 1$.

Step 4: Set $u = u_i$ and $K = K + 1$. If $K = m + 1$, then $r = r/4$ and go to Step 2.

Step 5: If $u + rd_j$ is a feasible control, compute $J(u + rd_j)$. Otherwise, go to Step 3.

Step 6: If $J(u + rd_j) < J(u)$, set $u_{i+1} = u + rd_j$, $i = i + 1$, and $K = 0$ and go to Step 4. Otherwise, go to Step 3.

Here an input control u is specified as a set of normal acceleration and bank angle commands at selected time intervals during reentry. Thus, with n/2 selected intervals, a control function u(t) is determined through the vehicle simulation from an input control $u \epsilon R^n$. The set of feasible input controls are defined as those which generate trajectories which satisfy the given constraints. The efficiency of this algorithm depends on the choice of the $d_j \epsilon R^n$. Here, m = (3/2)n d_j's were chosen such that n of them were directed "nearly" along the boundary of the set of feasible controls, in an effort to encourage pivoting along the boundaries. The remaining n/2 were chosen so as to satisfy the requirement given in Step 0 above. The purpose of this requirement in the algorithm is to enable convergence to a "desired" solution, such as indicated in the following theorem.

Theorem: If $\{u \mid J(u) \leq J(u_0)\}$ is feasible and bounded and J(u) is continuously differentiable, then every accumulation point u* of $\{u_i\}$ generated by the above algorithm satisfies $\nabla J(u^*) = 0$.

The proof of this theorem uses the mean value theorem to show that $\langle \nabla J(u^*), d_j \rangle \geq 0$ for all d_j. Consequently, due to the requirement on the d_j's, $\nabla J(u^*) = 0$.

The problem considered here is a constrained minimization problem, so the solution is not expected to satisfy $\nabla J(u^*) = 0$ and in fact $\{u \mid J(u) \leq J(u_0)\}$ is not contained in the set of feasible trajectories. But the accumulation points of the above algorithm are expected to be "good" candidates for a solution which is as much as can be said here due to the nonconvexity of J(u).

Trajectory Development

An improved trajectory was developed using each of these techniques and the method of development of the trajectories is outlined below.

Modified Steepest Descent: After an initial try at optimizing starting from the yaw-maneuvering trajectory shown in Figure 5, a second trajectory developed by considering the output channel sensitivities of Figure 6 was used as a starting point. This trajectory has the approximate gradients of J_{CR} shown in Table 5. From the gradient data for this trajectory it is clear that the largest payoff would be derived from perturbations in the bank angle in the middle of the trajectory. Several small increments were made in the direction indicated by the gradient after which a new gradient was evaluated and the process repeated. In the process, a low g normal acceleration was applied for the final trajectory phase.

Table 5. Approximate J_{CR} Gradient
For Modified Steepest Descent

Time	$\Delta J/\Delta A_N$† - g^{-1}	$\Delta J/\Delta \phi$† - deg^{-1}
17.0	-.00418	---*
18.0	-.00414	-.00009
19.0	-.00413	-.00015
20.0	.00020	.00065
21.0	.00006	---*
22.0	.00096	-.00787
23.0	.00116	-.00824
24.0	---**	-.00737
25.0	---**	-.00290
26.0	-.00026	-.00295
27.0	-.00011	-.00209
28.0	.00002	---*
29.0	-.00004	---*
30.0	-.00007	---*
31.0	-.00011	---*
32.0	-.00012	---*
33.0	-.00012	---*
34.0	-.00010	---*
35.0	-.00006	---*
36.0	-.00004	---*

* Zero sensitivity for $A_N = 0$

** No perturbations evaluated at Max g's

† Relative to J = 1.0

Once the neighborhood of the energy constraint was reached, use of the steepest descent perturbations caused energy constraint violations, so the design was refined along less steep directions.

The acceleration in platform coordinates for the final trajectory version, Design A, is presented in Figure 8. The trajectory commands for the Design A trajectory are given in Table 6.

Modified Method of Local Variations: The modified method of local variations was initialized at an initial trajectory where the commanded normal acceleration, A, and bank angle, ϕ, are as defined in Table 7.

The initial step size was r_0 = (5g's, 3^0). Six time segments were chosen for the commands, so the dimension used was n = 12. A total of m = 18 pivoting directions were chosen. The commands for the trajectory, Design B, which resulted soon after the step size was cut down is shown in Table 8.

When other more adhoc initial trajectories were tried, about half of the Design B improvement in the cost functional was generally easy to accomplish and the corresponding trajectories were approaching a trajectory with high g's and "near" yaws as in the Design B trajectory. The acceleration in platform coordinates for the Design B trajectory is shown in Figure 9.

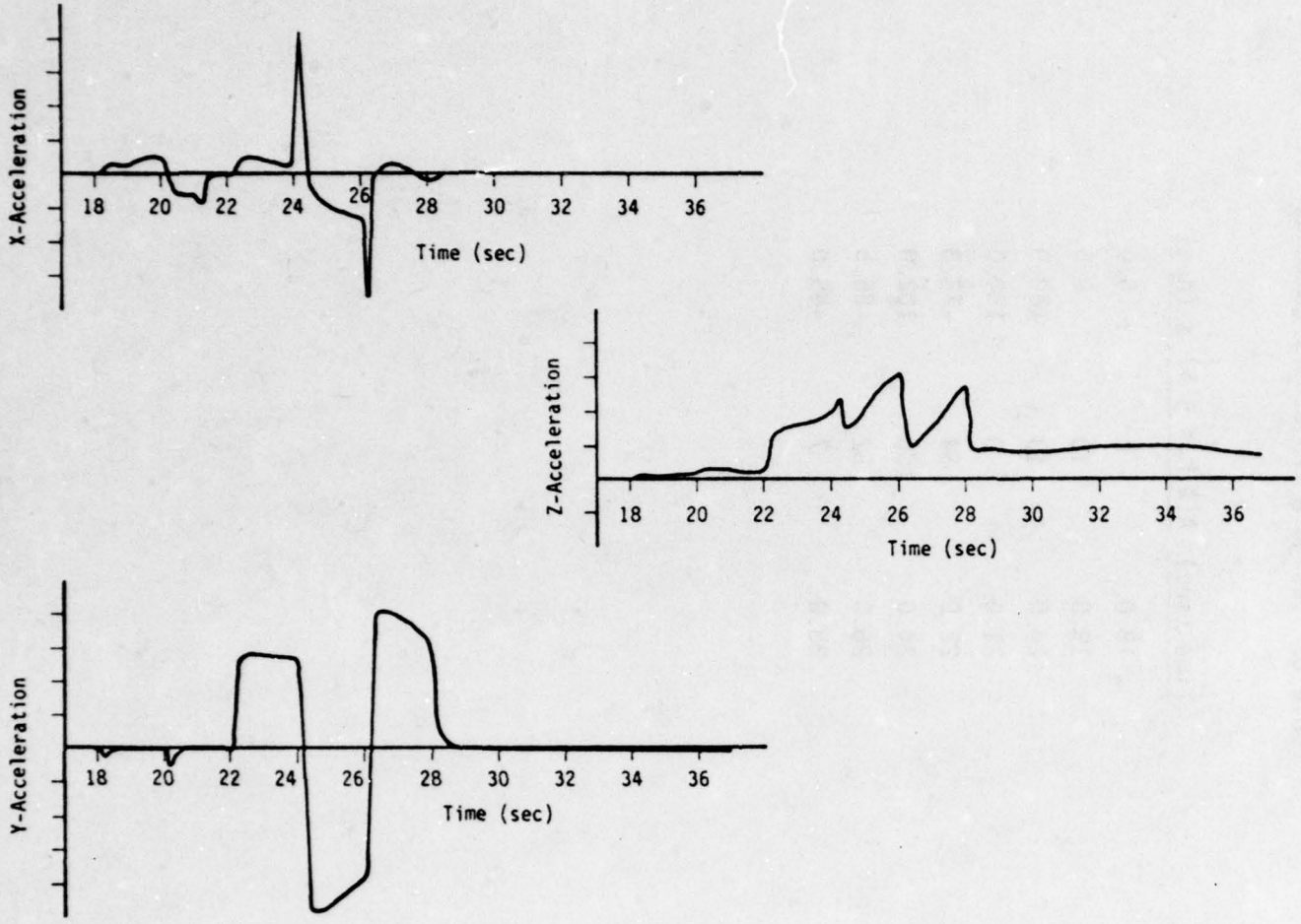


Figure 8. Accelerations in Platform Coordinates
Design A Trajectory

Table 6. Design A Trajectory Commands

Time (sec)	A(% Max g's)	ϕ (deg)
18.0	6	0.0
19.0	10	0.0
20.0	13	180.0
21.0	0	180.0
22.0	64	-78.8
24.0	100	102.0
26.0	82	-86.5
28.0	7	-85.0

Table 7. Local Variations Initial Trajectory Commands

T (sec)	A(% Max g's)	ϕ(deg)
20	0	-90
22	80	-90.
23	80	-90.
24	100	90.
26	80	-90.
28	0	-90

Table 8. Design B Trajectory Design

T (sec)	A(% Max g's)	ϕ (deg)
21.6	0	-69.5
22	62	-69.5
23	67	-74
24	100	108
25	100	103
26	91	-86
28	13	-84
30	0	-84

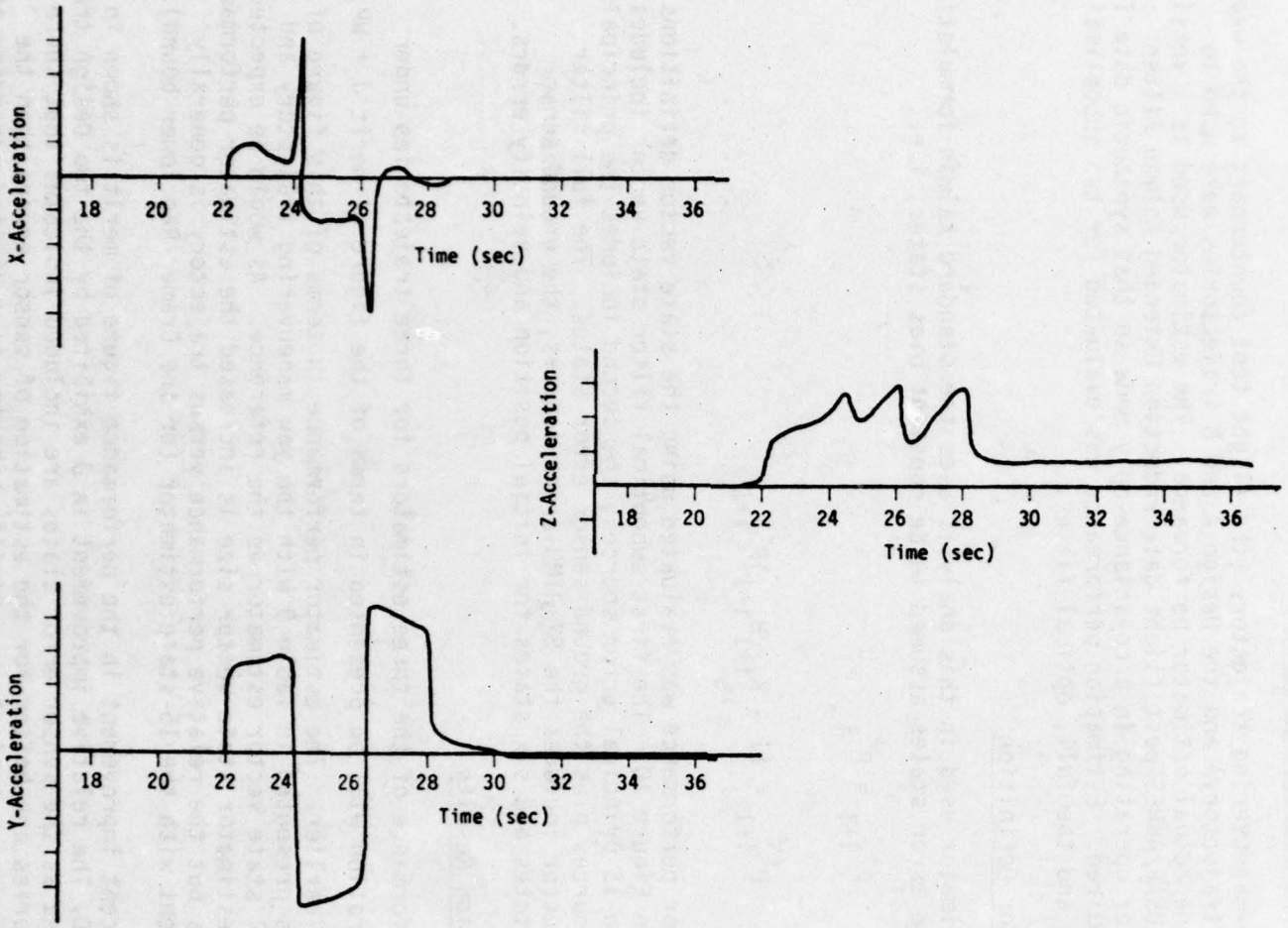


Figure 9. Acceleration in Platform Coordinates
Design B Trajectory

4. ESTIMATION PERFORMANCE

The yaw-maneuvering trajectory (the flight test counterpart to the weapon system trajectory) and the Design A and B trajectories were used to determine actual estimator performance. The estimator used is a version of the USAF/ABRES post flight data reduction Extended Kalman Filter estimator operating in a covariance-only mode so that synthetic data is not required. Estimation performance was evaluated for two suboptimal filters and the full, optimal filter.

Estimator Definition

The estimator used in this analysis uses the standard Kalman formulation with the error states assumed to be constant bias states, i.e.,

$$P^-_{i+1} = P^+_i$$

$$P^+_{i+1} = (I - K_{i+1}H_{i+1})P^-_{i+1}$$

Estimator performance was evaluated using the state vector definitions shown in Figure 10. The first suboptimal filter state vector includes only the 15 principal error sources, the second includes the principal error sources plus the ground sensor error states. The full filter state vector includes the 87 RIMU error sources, the ground sensor error states and six states for initial position and velocity errors.

Estimation Results

The performance of the three estimators for three trajectories under consideration will be presented in terms of the figure of merit $J = WP_fW^T$ defined earlier. The estimator performance in terms of this figure of merit is presented in Table 9 with the yaw maneuvering trajectory and the full state vector estimator as the reference. As would be expected, as the estimator state vector size is increased the estimator performance degrades but the relative performance versus trajectory is generally consistent with the 15-state estimator (or the Cramer-Rao lower bound).

The percent improvement in the performance figure of merit is shown in Table 10. The relative improvement in J exhibited by the two Design trajectories as the sensor error states are included indicates that these trajectories are better for the estimation of sensor errors than the yaw-maneuvering trajectory. Similar behavior is exhibited regarding the estimation of the error sources not included in the 15-state model. In this case, however, Design A turns out to be a better trajectory than Design B for the estimation of the secondary RIMU error sources.

$$\underline{X}_1 = \begin{bmatrix} \underline{\theta} \end{bmatrix} \qquad \underline{X}_2 = \begin{bmatrix} \underline{\theta} \\ \underline{S} \end{bmatrix} \qquad \underline{X}_3 = \left.\begin{bmatrix} \underline{\theta} \\ \underline{S} \\ \overline{P}_o \\ \overline{V}_o \\ \overline{\phi}_o \\ \underline{\Psi} \end{bmatrix}\right\} \text{105 states}$$

15 states

27 states

$\underline{\theta}$ is vector of principal error sources (15)

$\underline{S}$ is vector of ground sensor error sources (12)

$\overline{P}_o$ is initial position error vector (3)

$\overline{V}_o$ is initial velocity error vector (3)

$\overline{\phi}_o$ is initial alignment error vector (3)

$\underline{\Psi}$ is vector of secondary error sources (69)

Figure 10. Estimator State Vector Definitions

Table 9. Estimator Performance Results

$J = WP_f W^T$ Versus Trajectory and Estimator*

Trajectory \ Estimator	Principal Error Sources	Principal Sources Plus Sensor Errors	Full RIMU State Vector Plus Sensor Errors
Yaw Maneuvering	.315	.339	1.00
Design A	.218	.222	0.408
Design B	.180	.185	0.461

* Normalized to Yaw-Maneuvering Trajectory and Full Estimator State Vector

Table 10. Estimator Performance Results

Percent Improvement in J versus Trajectory and Estimator

Trajectory \ Estimator	Principal Error Sources	Principal Sources Plus Sensor Errors	Full RIMU State Vector Plus Sensor Errors
Yaw Maneuvering	----	----	----
Design A	30.9	34.5	59.2
Design B	43.0	45.4	53.9

Table 11 shows the percent change in the estimated 1σ error source magnitudes from the a priori values versus trajectory for the principal error sources. The estimation improvements on an individual error source basis of the Design A and B trajectories over the yaw-maneuvering trajectory are not as large as indicated by the figure of merit based on the covariances. This indicates that some of the improvement indicated by J is in the form of correlations set up between error sources and thus additional experimental sources of information would be required to obtain improvements in the 1σ estimates equivalent to those indicated by the performance measure J. In addition, Table 11 shows that error sources 12 and 13 are not significantly estimated. These are fixed gyro drift error terms which contribute primarily to alignment errors at reentry through drift during freeflight and have small observability during reentry.

Table 13. Error Source Magnitude Estimation
Percent Change In 1σ Values From A Priori

Error Source	Trajectory		
	Yaw Maneuvering	Design A	Design B
1	21.4	40.7	36.9
2	50.6	52.1	47.4
3	7.1	11.6	11.0
4	24.5	46.0	44.1
5	12.9	6.9	7.4
6	4.0	2.3	6.4
7	51.3	54.4	47.7
8	43.2	52.8	52.2
9	2.4	1.6	2.0
10	3.3	1.7	1.7
11	6.3	5.1	4.3
12	0.0	0.0	0.0
13	0.0	0.0	0.0
14	2.4	3.3	3.5
15	2.5	3.3	7.0

Conclusions

An approach to the design of flight test trajectories for the observation of guidance system errors has been formulated. Using this approach, trajectories which improve the ability to estimate the principal error sources over that possible with a flight test analog of the weapon system trajectory have been designed and show a 52% to 59% improvement.

In this study the trajectory optimization efforts were terminated when reasonable improvements were found so that further improvement in the design of the trajectories with the given constraints is certainly possible. This effort has concentrated only on the reentry portion of the flight test trajectory for one ground sensor type and future efforts are planned to investigate other facets of the problem. Other areas for study include the inclusion of tracking and booster guidance system data during boost, variations in reentry guidance system orientation, relaxation of vehicle constraints, and variations in the geometry and types of ground instrumentation. It is to be expected that, even when these variations in the problem definition are considered, other sources of data would still be required to obtain good individual error source estimates. Thus a complementary combination of flight and ground tests would be required to obtain good error source magnitude estimates for the prediction of operational system accuracy.

Acknowledgement

The work described in this paper was performed for the Air Force Space and Missile Systems Organization under Contract Number F04701-75-C-0112. The authors wish to express their appreciation to Major J. T. Pearson and Captain J. A. Davis of the ABRES Program Office for their support.

BIBLIOGRAPHY

1. C. R. Rao, Linear Statistical Inference and Its Applications, Wiley, 1965.

2. R. K. Mehra and H. K. Gupta, "Status of Input Design for Aircraft Parameter Identification", AGARD Specialists Meeting NASA Langely Research Center, Hampton, Virginia, November 1974.

3. W. Rudin, Functional Analysis, McGraw-Hill Book Co., 1973.

4. N. K. Gupta and W. E. Hall, Jr., "Input Design for Identification of Aircraft Stability and Control Derivatives", NASA CR-2493, Systems Control Inc., Palo Alto, California, February 1975.

EIGHTH BIENNIAL GUIDANCE TEST SYMPOSIUM

SLAB CALIBRATION FOR STRAPDOWN SYSTEMS

AUTHOR: A. A. MORGAN

HONEYWELL, INC.
AVIONICS DIVISION
ST. PETERSBURG, FLORIDA

ABSTRACT

To achieve accuracy, certain non-ideal characteristics of inertial sensor outputs which are known to be stable must be measured and compensated. For strapdown inertial systems, this calibration process involves a series of measurements taken in a test facility. Once the strapdown system is installed in the missile or aircraft, full calibration is not feasible.

It is usually too costly to duplicate strapdown calibration test equipment at remote facilities. Returning the system to the factory to resolve out-of-specification performance may be operationally unsatisfactory. Building the system to allow a no-test sensor replacement adds cost, and the procedure compromises performance and reliability. For these reasons, less expensive and operationally simpler techniques for providing calibration measurements have been examined. The result has been the definition of an attractive process called slab calibration.

Slab calibration features low cost test equipment, simple manual operations, and relatively sophisticated data processing. The tests are accomplished on a nearly level flat granite slab with the inertial sensor assembly mounted in a holding fixture which has six calibrated nearly orthogonal surfaces. The holding fixture is placed on each surface with both static and turn tests made, collecting and processing the sensor outputs in a support computer. Considerations in developing the process have included handling, safety, surface wear, accuracy, procedural simplicity and redundancy. Data processing involves a maximum likelihood batch process estimator which results in a display of coefficients, standard deviations, and residuals.

Intended for the more rugged tactical missile strapdown systems, slab calibration was first applied in July 1976 on the Honeywell H700-2 system, which features the GG1328 ring laser gyro and the Sundstrand QFLEX accelerometer. This paper describes the test equipment, procedures, accuracy, data collection and processing software, and the results of the evaluation tests.

TABLE OF CONTENTS

		Page
Abstract		ii
Section		
	INTRODUCTION	1
	SLAB CALIBRATION	3
	TECHNICAL DETAIL	6
	STATUS AND CONCLUSIONS	15

INTRODUCTION

Any inertial system, regardless of precision, must be calibrated. This may be accomplished by adjustments during the sensor build process, special trimming during the system assembly cycle, or a final trim after installation in the vehicle. Because the installed system must remain in one position, this latter option is mostly unavailable for strapdown inertial systems. Whether the output of the calibration process is a variety of mechanical/electrical adjustments or the determination of compensation coefficients in a flight computer is a trade of considerable importance affecting cost, performance, and operations.

Accuracy of computer compensation is only limited by the quality of the calibration testing and of the inertial sensor assembly (ISA). Its reliability is as good as that of the flight computer, and its costs involve those of establishing the coefficients, and the costs of time and memory within the flight computer. The strapdown compensation equations are typically a computer burden of the same magnitude as the attitude algorithm; significant, but acceptable. Since no disassembly is required for either the calibration measurements or corrections, reliability and accuracy are enhanced. This widens the tolerance of acceptable sensor trending, avoiding unnecessarily identifying units as failed. Possibly the greatest benefit from the use of computer compensation is derived from the simplifying of processes and testing associated with the build and assembly of the ISA. Machining tolerance can be widened, and costly and vulnerable trim circuitry can be eliminated.

Although the requirement for system trimming establishes the primary need for calibration testing, experience has shown that performance monitoring is the most frequent use, with an important secondary role of supporting the repair cycle. Repair of a failed strapdown system involves detection, identification, replacement, calibration, and verification. In many cases the test equipment needed for identification is exactly the same as that needed for calibration and for verification. Also, the best verification tests are the same ones used in calibration, allowing this operation to be simultaneous. From the standpoint of mechanical design and assurance of correct and complete identification of the problem, it is not feasible to replace a sensor without moving the ISA to some sort of test facility. Once this happens, calibration becomes a minor, but essential part of the subsequent tests, greatly enhancing the confidence in the newly assembled unit as well as improving the accuracy.

Calibration is accomplished by conducting a series of tests in which the physical inputs to the ISA are varied sufficiently to excite and isolate each of the model terms. These physical inputs are the acceleration from gravity and ISA turning rates including Earth rotation. In the past, the emphasis has been on tests in which as few terms as possible are allowed to influence the data of a single test, and in which the term sought is the dominant effect in the data. Such data was often referred to optical surfaces. The approach allowed simple computations, clarity and traceability of data, and often a very protracted and tedious data collection process. This resulted from the need for repeated optical setups, demanding a highly skilled operator.

Precision multiaxis tables with arc-second positioning and constant turn rate control can remove the optical requirement (if there are no optical surfaces on the ISA). Aside from installation, removal, and calibration of essential ISA optical surfaces, fully automatic calibration testing can be accomplished on such tables. These tables also may protect sensitive devices, such as gas bearing gyros, from a potentially damaging handling environment. Such features as linearity testing on both the accelerometer and gyro can be included in the sequence. The process can be accurate and efficient. The major difficulty with the precision tables is availability and cost. The strapdown system manufacturer has such tables, as does many of his users; but not all users have made this investment. It should be noted that investment in such a facility involves not only the cost of the table, but the interface equipment, the support computer and software, the control equipment, the operator, and the cost of maintenance. Maintenance includes assuring the calibration of the table.

The choice between a cumbersome procedure demanding highly skilled operators and a more automatic process with expensive test equipment has led to such concepts as the normalized sensor. In this case, the calibration parameters are carried with the sensor, and the sensor is designed to retain the same characteristics, whether tested as a single unit or a part of an ISA. If we disregard the arguments stated above about the strapdown repair cycle, this approach has clear operational advantages. The weakness is added cost, to perform calibration six times instead of once, added parts and machining, and the lack of a valid confidence check after assembly. Experience has shown that, while many strapdown systems are built to avoid the need for system calibration, this requirement almost always becomes important. For these systems, the price is paid twice.

The solution has been to reexamine the test facility to determine what is essential to the calibration task. The result was an observation that in spite of the great capability of the precision tables, calibration testing usually required only a

series of static positions and a series of constant rate turns. The most common sequence was to place each sensor axis up and down, for a total of six static positions, with plus and minus turn rates about each axis. Although simple, this sequence of tests proved adequate for most strapdown systems, including the precision H-408 system used for AGENA guidance, the rugged H-478F system, and the ATIGS X0 system. The major requirement for these tests were very precise angles between positions, a stable base during static testing, a good north reference, a constant turn rate, and an accurate starting and stopping reference for the turns. A technique has been found to remove the constant turn rate requirement for some strapdown ISAs, allowing the use of much simpler test equipment and processes. These are described next.

SLAB CALIBRATION

The ISA is mounted in a holding fixture having six calibrated, nearly orthogonal, surfaces. Testing takes place on a nearly level granite slab to which a precision edge, surveyed in respect to north, is attached. Power and communication with the laboratory support computer are provided through a cable slung conveniently overhead. Inertial data is collected in the computer during testing, with instructions to the operator and communication between the operator and computer provided by the control and display console. The output is stored on cassette tapes and hard line printer. This test facility is shown in Figures 1 and 2.

The process involves having the operator sequentially place the holding fixture against the reference edge with each of its six faces against the slab. Static inertial data is collected with the holding fixture establishing precise angular relations between these positions. While on each surface, between static data collection, the operator manually slides the holding fixture on the table through one revolution and ties the same surface against the reference edge. The contribution of Earth rate to the gyro data is removed using the gyro output and initial conditions based on the reference edge azimuth. The sequence is directed by the computer, with the operator designating the beginning and ending of operations. Unless there is a specific need to relate optical surfaces, cubes, or porro prisms to the inertial sensors, there is no need for the optical measurements. Accurate calibration can be accomplished by one operator in less than one hour.

Slab calibration is intended for the more rugged strapdown systems, and would be inappropriate for ISAs with sensors, such as gas bearing gyros, that might not tolerate the handling. Accuracy goals have been directed toward tactical missile



FIGURE 1. SLAB CALIBRATION H700-2 STATIC TESTING



FIGURE 2. SLAB CALIBRATION H700-2 TURN TESTING

guidance system requirements. The first tests were made in July 1976 on the H700-2* inertial sensor assembly, with 40 additional calibrations performed through the year end. These tests were directed toward wringing out a newly designed inertial system, with evaluation of slab calibration being a secondary interest.

Three engineers, experienced in inertial system testing, performed the operations at different times. Training requirements were minimal, with successful calibrations achieved on the first attempt. The physical requirements, including installing the ISA into the holding fixture, tipping the holding fixture onto each of its six faces, and turning the holding fixture were judged to be easy and safe for one man. Experienced with calibration processes involving 4 to 8 hours of testing, the operators commented favorably about the quickness and simplicity of slab calibration. The operations were found to be as safe, and no more difficult, than the handling of an ISA with automatic calibration test equipment.

The surprise from the data has been the remarkable alignment stabilities. This includes alignment between the holding fixture and the accelerometers, between accelerometers, between gyros, and the stability of the slab leveling. Over consistent data sets, each of these has remained within 1 or 2 arc-seconds 1σ. These reflect combined stabilities of the H700-2 ISA and the test equipment. Alignment between the gyro and accelerometer triads (mechanically separate) had a standard deviation of 5 arc-seconds, reflecting real motion. Gyro scale factor repeated to 14 PPM 1σ. Intentionally limited in accuracy by the test duration, gyro drift repeated to 0.02 degree/hour. Accelerometer bias repeated to 15 μG 1σ on two axes, and 32 μG on the third. An accelerometer channel scale factor problem was identified that was not satisfactorily resolved during the 1976 testing. There were electrical/mechanical adjustments made to the ISA during the testing period, with the given standard deviations calculated from 7 to 16 sequential calibrations. These numbers are the averages of the standard deviations on three axes. The results are not only very encouraging for slab calibration, but also indicate the excellent performance of the H700-2.

---

* The Honeywell H700-2 strapdown system features the Honeywell GG1328 ring laser gyro and the Sundstrand QFLEX accelerometer. This system is being used on the Advanced Tactical Inertial Guidance System (ATIGS) program by the Naval Weapons Center at China Lake and on the Simplified Inertial Guidance Demonstration (SIG-D) program by MICOM at Huntsville. Most of the reported testing was on an internal development unit.

TECHNICAL DETAIL

Primary elements of the process include the holding fixture, the slab and its reference edge, the support computer and the data collections software, the data regression software, the ISA, and the operator. Some of the trades and technical approaches are discussed below.

Slab. The flat granite slab serves as a bearing for the turn tests, and a level reference for static testing. Accelerometer data is used to establish slab level, removing any need to explicitly calibrate or adjust the slab. The process depends on slab stability during the procedures. Because of surface wear between the steel legs of the holding fixture and slab, a resulting flat on flat condition desensitized the test equipment to the large number of depressions ($\sim$1/16 inch) noted in the slab. A large gradual bowl shaped depression of 140 μ inches was measured in the center of the slab. For the 14-inch holding fixture, this could result in a maximum tipping of 2 arc-seconds. Since the static testing is confined to a small region, this error is much reduced. There was some chattering during the turns due to the fourth holding fixture leg. This was resolved by careful attention to cleaning the surface before the tests.

Reference Edge. The purpose of the edge is to provide a north reference for Earth rate compensation and to provide a starting and stopping reference for the one revolution turns. The sensitivity at 45 degrees latitude is 0.01 degree/hour/milliradian azimuth error. Laboratory references can establish azimuth to several arc-seconds. For a 14-inch holding surface, a 140 μ inch inability to repeat the positioning of the holding fixture legs against the edge from before to after the turn would result in a 10 μ radian error in measuring the rotation. This would result in a 1.6 PPM gyro scale factor error. An added feature of the edge is a device to positively grip the holding fixture during static tests.

Holding Fixture. The need is to hold the ISA, providing six nearly orthogonal precision surfaces. Wear characteristics of the surfaces, calibration of the surfaces, and stability are important concerns.

The design is also intended to provide handling ease, with sufficient handles, room to move the cables, and relatively light weight. Calibration of the holding fixture is a straightforward optical process, that need be repeated infrequently. Although the overdetermined plane is undesirable, a fourth leg was included on each surface to provide handling ease and symmetry. This leg is adjusted to within 50 μ inches of the plane of each surface before the holding fixture is calibrated. Because there is no redundancy in the optical data set which provides holding

fixture surface calibration, there was concern about unnoticed errors. Repeating these measurements (four times) and careful procedures guards against this problem. Another approach was to estimate the alignment between the surfaces based on the compensated gyro turn data. The first time this was done, a 1 arc-minute optical reading error was discovered, and traces to its source. When the optical data was corrected, the gyro data agreed with the optical measurements to 4 arc-seconds 1σ. Whether this indicated gyro error, or a remaining error in the optical data was not resolved.

Another trade involved the alignment of the ISA within the holding fixture. The input axes of the H700-2 inertial sensors have equal projection on the cylindrical axis of the package. It is convenient from a handling standpoint, and from the ease of sighting a porro prism, which is to be mounted parallel to the cylindrical axis, to mount the ISA with its cylindrical axis normal to a holding fixture face. This configuration, called symmetric mounting, is less accurate than the case in which the input axes are normal to the holding fixture faces, called in-line mounting. The analytic comparison for a one hour test is given in Table 1.

TABLE 1. COMPARISON BETWEEN IN-LINE AND SYMMETRIC MOUNTING ACCURACY

	Symmetric Mounting (Average 1σ)	In-Line Mounting (Average 1σ)
Accelerometer		
Bias (μg)	33.6	10
Scale Factor (PPM)	11	6
Scale Factor Imbalance (PPM)	51	12
Nonorthogonality (μrad)	9	10
Gyro		
Drift (deg/hr)	0.05	0.05
Scale Factor (PPM)	22	22
Nonorthogonality (μrad)	16	16
Gyro to Accel Alignment (μrad)	16	16

Optical Measurements. While not needed for the inertial sensor calibration, optical surfaces and porro prisms are often referred to the sensor axes. The reason may be to refer the ISA to some external device such as an antenna, telescope, or star seeker, or to provide an initial azimuth reference. The slab calibration test setup can be very convenient for making these measurements. Capability to handle sightings or mirrors, optical

cubes, and porro prisms has been included in the processing software.

Interface. The interface between the ISA and the support computer is through a cable slung overhead. Since the support computer for the H700-2 is essentially the same design as the flight computer, the interface is especially simple. Because of carefully chosen sequences, cable twisting has not been a problem.

Data Collection. During the static tests, the computer collects the sum of the output counts ($\Delta\theta$s and ΔVs) from the six sensors. These are displayed each minute, with the total, multiplied by nominal scale factors, displayed at the end of the selected collection period. The RMS deviation from a constant rate input is calculated from the high frequency data to indicate the quality of the test. During the turn, gyro data is collected, and compensated for Earth rate using a simple first order algorithm.

1. Initialize Earth rate, Ω, based on position against edge.
2. Set accumulators $\Sigma\theta$ and ϕ to 0.
3. During turn, using gyro output $\Delta\theta$, compute

$$\Omega \leftarrow \Omega + \Omega \times \Delta\theta$$

$$\phi \leftarrow \phi + \Omega\, \Delta t$$

$$\Sigma\theta \leftarrow \Sigma\theta + \Delta\theta$$

4. After turn,

$$\Sigma\theta \leftarrow \Sigma\theta - \phi$$

This may be accomplished at between 10 and 50 Hz, with 10 Hz used currently. There is no problem from varying turn rates with the ring laser gyro because of its excellent scale factor linearity and lack of sensitivity to angular dynamics. This may not be true for spinning mass gyros. It is expected that looser accuracy requirements for tactical missile systems with miniature spinning mass gyros will make these operations tolerable; but this remains to be evaluated.

An additional feature that will be included in the data collection will be to monitor the progress of the test to determine failure induced by either the ISA or the operators. These will include correctness of positions, maximum turn rates, continuity of data, and any lifting during the turn.

Calculations. After the static data and turn data is collected, the compensation coefficients are computed. Figure 3 shows a typical data set, Figure 4 shows the calculated coefficients,

BEST AVAILABLE COPY

```
LIST DATA.
```

TITLE AND TEST CONDITION CODE

```
101024,12/6/76,61(3,5,2)A1(2,6,7,S2,SL1,F1,P2
1,1,1
22,1,1,180
1,2,1
-8.4687,-9.5691,6.6548,-19.2077,-18.7404,-18.8976
2,28.3,207.9877,208.0978,208.16
1,2,1
-8.5207,-9.5819,6.6745,-19.2077,-18.741,-18.8976
1,2,3
-3.7836,-4.8849,-13.5523,13.4034,13.671,-26.8568
2,22.3,-147.0532,-147.2214,293.5386
1,2,3
-3.8511,-4.918,-13.5478,13.4032,13.6711,-26.8564
1,-3,2
-1.6644,-12.7218,-7.8328,23.5728,-23.0908,-.2837
2,26.8,-254.1753,254.8113,-.7046
1,-3,2
-1.7219,-12.7257,-7.7109,23.5739,-23.0911,-.2929
1,-3,-1
14.5412,-5.4237,4.0488,19.3841,19.3543,19.1668
2,29.8,-207.3931,-207.7706,-209.0367
1,-3,-1
14.4807,-5.45,4.167,19.3841,18.9547,19.1659
1,-3,-2
3.7793,12.5371,7.6765,-23.3227,23.3713,.2862
2,25.6,254.2005,-254.8038,.7075
1,-3,-2
3.7609,12.5814,7.6828,-23.3237,23.3715,.2863
1,2,-3
5.8382,4.6952,13.2561,-13.224,-13.4423,27.1199
2,24.2,147.1066,147.1087,-293.582
1,2,-3
5.8884,4.7568,13.4548,-13.2237,-13.44155,27.1198
1,2,1
-8.456,-9.4699,6.7032,-19.2075,-18.7406,-18.8978
1,2,1
-8.5015,-9.4425,6.7228,-19.2081,-18.7416,-18.898
1,-2,1
2.3788,1.2257,-14.9953,-19.1997,-18.735,-18.9132
1,-2,1
2.378,1.2377,-14.9596,-19.1997,-18.7351,-18.9131
```

GYRO DATA (DEG/HR)

ACCEL DATA (FT/SEC^2)

TURN DATA

HOLDING FIXTURE POSITIONING CODE

FIGURE 3. TYPICAL SLAB CALIBRATION DATA SET

I01024,12/6/76,G1(3,5,2)A1(2,6,7)S2,SL1,F1,P2

		U	V	W
ACCEL				
BIAS	MG	1.6455	1.3143	-0.1337
(SIGMA)		0.0424	0.0370	0.0174
SF	PCNT	3.2255	2.1056	2.6852
(SIGMA)		0.0012	0.0011	0.0011
SFB	PCNT	0.2318	0.3256	0.4841
(SIGMA)		0.0069	0.0059	0.0024
ORTH	MR	-0.1093	0.1934	-0.0453
(SIGMA)		0.0091	0.0087	0.0083
GYRO				
DRIFT	DEG/HR	1.0235	-0.0729	-0.0655
(SIGMA)		0.0522	0.0522	0.0522
SF	PCNT	0.0233	0.0076	0.0043
(SIGMA)		0.0022	0.0022	0.0022
ALIGN	MR	5.2855	9.1063	0.4121
(SIGMA)		0.0157	0.0157	0.0157
ORTH	MR	0.1056	0.3773	0.3320
(SIGMA)		0.0157	0.0157	0.0157
ALIGNMENT				
HOLD	MR	-4.1551	-7.5692	0.1148
(SIGMA)		0.0090	0.0121	0.0100
BASE	MR	0.0234	0.2884	
(SIGMA)		0.0120	0.0111	

FIGURE 4. COEFFICIENT SUMMARY PAGE
(H700-2 SYMMETRIC TEST, CAL NO. 24)

BEST AVAILABLE COPY

BEST AVAILABLE COPY

INPUT					RESIDUALS				SIGMA
U	V	W			U	V	W		RSS
-18.7	-18.5	-18.5	F/S/S		0.008	0.015	0.015	MG	0.7
-18.7	-18.5	-18.5	F/S/S		0.008	-0.004	0.015	MG	0.6
12.9	13.3	-26.3	F/S/S		0.002	0.006	-0.016	MG	0.7
12.9	13.3	-26.3	F/S/S		-0.004	0.009	-0.004	MG	0.4
22.7	-22.7	-0.3	F/S/S		-0.011	0.009	-0.019	MG	0.8
22.7	-22.7	-0.3	F/S/S		0.022	-0.000	0.005	MG	0.8
18.6	18.4	18.6	F/S/S		0.001	-0.017	0.037	MG	1.4
18.6	18.4	18.6	F/S/S		0.001	-0.005	0.010	MG	0.4
-22.7	22.7	0.3	F/S/S		-0.000	0.004	-0.012	MG	0.4
-22.7	22.7	0.3	F/S/S		-0.000	0.010	-0.009	MG	0.5
-12.9	-13.3	26.3	F/S/S		-0.004	-0.000	-0.011	MG	0.5
-12.9	-13.3	26.3	F/S/S		0.006	0.022	-0.014	MG	0.9
-18.7	-18.5	-18.5	F/S/S		0.014	0.009	0.009	MG	0.6
-18.7	-18.5	-18.5	F/S/S		-0.004	-0.022	0.003	MG	0.7
-18.7	-18.5	-18.5	F/S/S		-0.015	-0.025	0.012	MG	1.0
-18.7	-18.5	-18.5	F/S/S		-0.015	-0.028	0.015	MG	1.2
-9.5	-9.5	6.8	D/HR		0.011	-0.017	-0.061	D/HR	0.3
208	208	208	DEG	13 D/S	0.031	0.279	-0.074	MR	1.5
-9.5	-9.5	6.8	D/HR		-0.041	-0.030	-0.042	D/HR	0.3
-4.8	-4.8	-13.4	D/HR		-0.000	-0.017	-0.054	D/HR	0.3
-147	-147	294	DEG	16 D/S	0.053	0.125	0.032	MR	0.7
-4.8	-4.8	-13.4	D/HR		-0.063	-0.050	-0.050	D/HR	0.5
-2.7	-12.6	-7.7	D/HR		0.032	0.001	-0.085	D/HR	0.4
-254	255	0	DEG	13 D/S	0.006	-0.010	0.106	MR	0.5
-2.7	-12.6	-7.7	D/HR		-0.025	-0.003	0.037	D/HR	0.2
13.5	-5.3	4.1	D/HR		0.059	-0.024	0.009	D/HR	0.3
-207	-208	-209	DEG	12 D/S	0.030	0.282	-0.074	MR	1.5
13.5	-5.3	4.1	D/HR		-0.001	-0.044	0.127	D/HR	0.6
2.7	12.6	7.7	D/HR		0.035	-0.040	0.060	D/HR	0.4
254	-255	0	DEG	14 D/S	0.006	-0.007	0.105	MR	0.5
2.7	12.6	7.7	D/HR		0.017	0.004	0.066	D/HR	0.3
4.8	4.8	13.4	D/HR		0.002	-0.031	-0.109	D/HR	0.5
147	147	-294	DEG	15 D/S	0.055	0.125	0.031	MR	0.7
4.8	4.8	13.4	D/HR		-0.008	0.031	0.089	D/HR	0.5
-9.5	-9.5	6.8	D/HR		0.024	0.032	-0.013	D/HR	0.4
-9.5	-9.5	6.8	D/HR		-0.022	0.109	0.007	D/HR	0.5
1.4	1.4	-14.9	D/HR		-0.022	-0.051	-0.015	D/HR	0.3
1.4	1.4	-14.9	D/HR		-0.023	-0.039	0.021	D/HR	0.2

```
STOP,
?
```

FIGURE 5. RESIDUAL DISPLAY
(H700-2 SYMMETRIC TEST, CAL NO. 24)

and Figure 5 displays the residuals, indicating how well the model fits the data.

Maximum likelihood batch process estimation is used to obtain the coefficients. The language and the results are similar to a Kalman filter, with some computational conveniences not enjoyed by the real time process. The ISA coefficients and all other parameters to be estimated are called the state, x. The estimate of the state uncertainty is expressed as the state covariance, P, and the estimate of the measurement uncertainty is the measurement covariance, Q. In this case, the measurement includes, not just the inertial sensor output, $\tilde{y}$, but its estimate, $\hat{y}$, based on the test conditions. The steps are outlined below.

1. Initialize P based on estimated initial state uncertainty.
   Invert P.
   Zero data accumulator, D.

2. Collect inertial measurement, $\tilde{y}$.

3. Compensate $\tilde{y}$, using current state estimate $\quad \tilde{y} \leftarrow \tilde{y} - f(\tilde{y}, x)$

4. Predict measurement based on test condition, u. $\quad \hat{y} = g(u, \hat{x})$

5. Calculate the measurement residual $\quad \Delta y = \tilde{y} - \hat{y}$

6. Calculate the sensitivity $\quad H = -\frac{\partial \Delta y}{\partial x}$

7. Calculate the measurement covariance, Q.

8. Update the inverse state covariance $\quad P^{-1} \leftarrow P^{-1} + H' Q^{-1} H$

9. Update the data accumulator $\quad D \leftarrow D + H' Q^{-1} \Delta y$

Return to step 2 for more measurements, Otherwise

10. Invert the inverse state covariance $\quad P = (P^{-1})^{-1}$

11. Calculate the state correction $\quad \Delta x = P D$

12. Update the state estimate $\quad \hat{x} \leftarrow \hat{x} + \Delta x$

At this point, the data set can be reprocessed to remove the consequence of nonlinearities, or the state estimates can be displayed. An important final step is to reprocess the data, only making the calculations necessary to obtain the residuals of step 5. This allows inconsistent data to be identified. With each coefficient, the square root of the diagonal of the

state covariance is displayed, indicating the expected uncertainty of the result.

The accelerometer and gyro data are processed separately. The state elements for accelerometer processing include the following (with output mnemonics in parenthesis):

Alignment parameters

Slab leveling angles	(BASE)
Holding fixture to accelerometers	(HOLD)
Porro prism to accelerometers	(PORRO)
Optical cube to accelerometer	(CUBE)
Accelerometers to accelerometers	(ORTH)

Accelerometer parameters

Bias	(BIAS)
Scale Factor	(SF)
Scale Factor Imbalance	(SFB)

With the exception of the slab leveling angles, each of these state parameters has three terms, for a possible total of 20. The optical terms are optional, with either the PORRO or the CUBE model allowed. Data on a single mirror is displayed under CUBE. The processing program has been designed to allow a larger model.

The gyro model includes the alignment parameters:

Gyro to accelerometer	(ALIGN)
Gyro to gyro	(ORTH)

and the gyro parameters:

Fixed drift	(DRIFT)
Scale Factor	(SF)
Scale Factor Imbalance	(SFB)
Mass Imbalance along the Spin Axis	(MUSA)
Mass Imbalance along the Input Axis	(MUIA)

Because the H700-2 system employs ring laser gyros, the MUSA, MUIA and SFB have not been included in the gyro data processing. Each parameter has three terms resulting in a possible 21 state element.

Alignment between the holding fixture surfaces and between the reference edge and north are input parameters that are not estimated with the data set. The alignment parameters included in the state are initialized in a manner that allows small numbers

to be displayed. The basic measurements include:

Static testing. 1 g vertical is transformed through the alignment parameters to the accelerometer frame, and subtracted from the compensated accelerometer data.

Vertical and north components of Earth rate are transformed through the alignment parameters to the gyro frame, and subtracted from the compensated gyro data.

Turn tests. One revolution about the normal to the slab is transformed to the gyro frame, and subtracted from the compensated gyro data which has had Earth rate removed during data collection.

Optical surfaces. The elevation angle of the line of sight from the theodolite to the mirror is subtracted from the predicted elevation angles computed from the alignment state elements.

Porro prism. Using the azimuth and elevation of the line of sight (LOS) from the theodolite to the prism to construct the LOS vector in the Earth reference frame, use the state alignment parameters to transform to a frame common to the porro axis, and take the dot product.

These calculations provide the necessary residuals. The equations and derivatives to obtain the necessary sensitivities are a straightforward task. The processing program has included some added capabilities, including the ability to process accelerometer and gyro data in unknown orientations based on the knowledge that the magnitude of the input is 1 g and 1 Earth rate, and the ability to handle data from almost any multiaxis table. These features are not used in slab calibration processing.

Uncertainties can be estimated for each of the state elements, providing the needed initial condition for the state covariance. The measurement covariance is constructed from estimates of unmodeled effects causing errors in the calculated residuals. These include quantization, position to position alignment errors from holding fixture compliance and calibration errors, gyro random walk, errors during turn from lack of a true axis and Earth rate compensation errors, linear and angular motion during static testing, and optical measurement errors.

Currently the processing resides in a computer separate from the data collection computer. Because of the short data set (Figure 3), manual data transfer has been acceptable for this evaluation period. The display of residuals has provided quick identification of data transfer errors. Eventually the entire

process will reside in a single computer. This will include the conversion of the output parameters into the flight computer format.

STATUS AND CONCLUSIONS

Slab calibration has been analyzed, simulated, and tested, indicating performance compatible with tactical missile navigation requirements. The process has been found to be a suitable one man operation, employing simple, safe, and efficient procedures. Stability of the test hardware and excellent visibility of the data have been demonstrated. The evaluation is not yet complete, with a precision rate table calibration comparison test series planned in 1977. It is also hoped that this process will be applied to a strapdown system with spinning mass gyros. Because of the low cost and availability of the test equipment, it is expected that this process will become extensively used, making strapdown system calibration practical at remote sites.

EIGHTH BIENNIAL GUIDANCE TEST SYMPOSIUM

CAPTIVE FLIGHT TESTS OF THE ADVANCED TACTICAL INERTIAL GUIDANCE SYSTEM, MODEL X-0 (ATIGS X-0)

AUTHOR: MERRITT D. MULLEN

NAVAL WEAPONS CENTER
CHINA LAKE, CALIFORNIA

INTRODUCTION

The Advanced Tactical Inertial Guidance System--ATIGS--is an advanced development program of the Naval Air Systems Command with the Naval Weapons Center, China Lake, as the development activity. The purpose of the program is to demonstrate the feasibility of using laser gyros in strapdown inertial guidance systems for midcourse guidance of long-range, tactical, air-to-surface missiles. Through the use of laser gyros in a strapdown mechanization, and by taking advantage of advanced digital computer technology, ATIGS would be characterized by high accuracy and reliability, compactness, low power requirements, and low cost of ownership. Since ATIGS performs the function of missile autostabilization as well as midcourse navigation and steering, there is no need for a separate autopilot system. ATIGS is designed to interface with, and control, a terminal guidance system and, if required by the mission, a midcourse position updating system.

The current ATIGS systems, designated ATIGS X-O, were built by Honeywell under contract to the Naval Weapons Center. The first X-O system was delivered in May 1974 and a second, identical system, in July 1975. These systems, which use the Honeywell GG1300 laser gyro, are the subject of this report and are described in greater detail below. A second-generation system, designated ATIGS X-2, is currently under build by Honeywell for delivery in mid-1977. The X-2 system uses the smaller GG1328 gyro and closely approaches the design goals for a production system. Table 1 lists the design parameters for the various systems. Both X-O and X-2 were designed as missile-ready prototypes, to be free-flight tested in the Air-Launched, Low-Volume Ramjet (ALVRJ), a developmental, long-range, supersonic missile. Current plans show the first ATIGS-guided ALVRJ shots occuring in early 1979.

Table 1. ATIGS Design Parameters.

		System Model		
	Units	X-O	X-2	Goal
Diameter	in.	12.5	9	-
Length	in.	12	12	-
Volume	cu.in.	1470	716	500
Weight	lbs.	60	35	25
Power	watts	200	115	65
Price (2000 units)	$	-	-	15000
CEP (6 mins)(1)	ft.	76(2)	-	500
Gyros used		GG1300	GG1328	-

(1) Exclusive of initialization errors.
(2) Rocket sled results.

The two X-O units have been extensively tested--in the laboratory, in captive flight, and on the high-speed test track at Holloman Air Force Base. To date, the two units have logged some 119 hours of captive-flight navigational time on 53 individual flights. This paper describes the ATIGS X-O system and the test procedures and conditions, and reviews the navigational performance demonstrated by ATIGS during captive flight. A brief review of the navigational performance achieved during the sled tests conducted at Holloman Air Force Base is also given (reference 6 provides a detailed error analysis of the Holloman tests).

SYSTEM DESCRIPTION

HARDWARE

ATIGS X-O is a strapdown inertial navigator and midcourse missile guidance system using Honeywell laser gyros, Sundstrand Q-flex accelerometers, and a Delco digital computer. The ATIGS X-O system was designed to be installed in the ALVRJ missile for free-flight testing.

Figure 1 is a drawing of the ATIGS X-O system, illustrating the mounting of the three gyros, the digital computer, power supply, and velocity measuring unit (VMU). The VMU contains three strapdown accelerometers with rebalance loops and analog-to-digital conversion electronics, yielding velocity pulses at its output. ATIGS X-O characteristics are listed in Table 2.

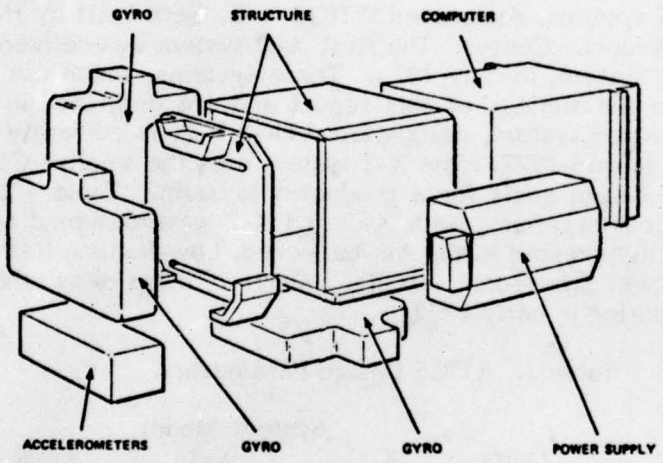


Fig. 1. ATIGS X-O Assembly.

Table 2. ATIGS X-O Characteristics.

Size:	12 in. long, 12.5 in. dia.
Volume:	1470 cu.in.
Weight:	60 lbs.
Power:	200 watts
Computer:	Delco Magic 362, 8000 words, 16 bits/word
Gyros:	3 Honeywell GG1300
Accelerometers:	3 Sundstrand Q-flex
Angular Rate Maximum:	131 deg/sec
Linear Acceleration Maximum:	25 g's
Gyro Output Scale Factor:	2^{-17} rad/pulse
VMU Output Scale Factor:	2^{-4} or 2^{-6} fps/pulse (selectable)

The feature of the ATIGS system that represents an advance in inertial system technology is its use of the laser gyro. The laser gyro is a potentially low-cost strapdown sensor with the attributes of: a high input rate capability (400 deg/sec), high g-capability, direct digital output, high resolution (1.57 arc sec/pulse), and the potential for simple built-in test capability. The angular rate maximum of 131 deg/sec (Table 2) is a result of the pulse width and duty cycle chosen for the ATIGS X-O system and is not a limitation inherent to the laser gyro (the GG1328 gyro used in ATIGS X-2 is specified to operate to 400 deg/sec and actually is capable of about 800 deg/sec).

SOFTWARE

Flight program functions and computational flow are shown in Figure 2. The program is organized into modules with sequencing and timing controlled by an executive module. The attitude reference and coordinate transformation modules are each processed at a 100 Hz rate and the basic navigational equations are processed at 10 Hz.

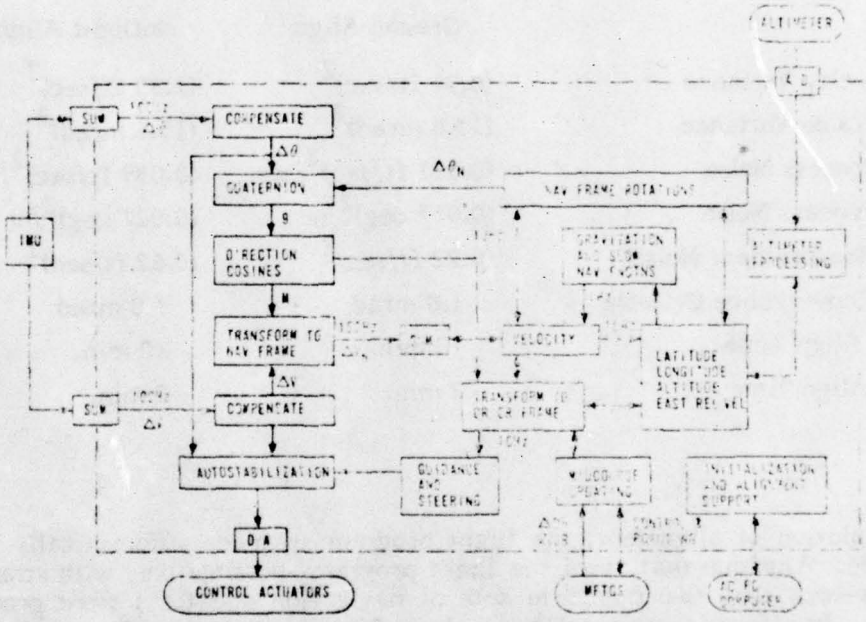


Fig. 2. Flight Program Computational Flow.

Initialization and Alignment

As a missile navigator, ATIGS is designed to be initialized and aligned in flight from digital data supplied by an aircraft inertial navigator. Initialization and alignment begin immediately upon application of system power or when re-initialized by the operator. At that time, latitude, longitude, roll, pitch, and yaw are transferred from the aircraft navigation system to ATIGS, initializing the alignment algorithm. Since initial attitude values are available from the aircraft navigator, ATIGS does not require a coarse alignment scheme, and proceeds directly into fine alignment. The alignment algorithm uses a five-state Kalman filter which processes north and east velocity

measurements (received from the aircraft navigator) to derive estimates of system north and east velocities and north, east, and vertical attitude errors. Standard Kalman algorithms are used, and the error estimates are used to update the actual ATIGS velocities and attitudes. Note that ATIGS arrives at its own estimates of velocity and attitude (based on velocity measurements); however, ATIGS position is slaved to aircraft navigator position until alignment is complete. Table 3 lists the various parameters used by the alignment filter. During captive flight testing, both in-air and ground alignments were used. The only difference between a ground alignment and an in-air alignment was in the values of the filter parameters as indicated in Table 3. In the case of a ground alignment, since position is constant and the velocity is known to be zero, alignment can proceed independently of the aircraft navigator. Alignment time was allowed to vary from 2 to 10 minutes depending on how quickly the algorithm met the convergence criteria. In actual practice, ground alignments always required the maximum time, 10 minutes, whereas an in-air alignment was complete in 2 minutes. The shorter in-air alignment was achieved by flying an S-turn maneuver, which quickened the convergence process.

Table 3. Alignment Parameter Values.

	Ground Align	Inflight Align
Initial Velocity Variance	$(0.31 \text{ ft/sec})^2$	$(1.33 \text{ ft/sec})^2$
Initial Attitude Variance	$(15.6 \text{ mrad})^2$	$(15.6 \text{ mrad})^2$
Velocity Process Noise	$(0.017 \text{ ft/sec})^2/\text{sec}$	$(0.039 \text{ ft/sec})^2/\text{sec}$
Attitude Process Noise	$(0.017 \text{ deg})^2/\text{hr}$	$(0.027 \text{ deg})^2/\text{hr}$
Velocity Measurement Noise	$(0.22 \text{ ft/sec})^2$	$(0.62 \text{ ft/sec})^2$
Azimuth Convergence Criteria	1.0 mrad	1.0 mrad
Maximum Align Time	10 min.	10 min.
Minimum Align Time	2 min.	2 min.

Navigation

Upon completion of alignment, the flight program switches automatically to the navigation mode. A unique feature of the flight program--possible only with strapdown mechanizations--was that two complete sets of navigation equations were processed simultaneously. In effect, there were two independent navigators, although both used the same sensor data. This scheme allowed one navigator to be re-aligned in flight and to accept position updates, while the other navigated continually throughout the flight based on the initial ground alignment and was not updated. Both navigators used barometric altimeter data to stabilize the vertical channel. Because of the dual navigation feature, on most of the flight test series, it was possible to collect both missile-type (short-term navigation following in-air alignment) and aircraft-type (long-term navigation following ground alignment) navigation data.

Midcourse Updates

ATIGS was designed to interface with a Midcourse Fix and Terminal Guidance System (MFTGS) which will supply position updates at points along the cruise portion of the flight and also provide target acquisition and track in the terminal phase. The MFTGS tested during captive flight tests of ATIGS X-O was the microwave radiometry (MICRAD) system developed at the Naval Weapons Center. This system operated in two modes, the "fixer" and the "seeker". The fixer mode provided midcourse position updates to ATIGS by correlating a stored reference with the radiometric scene viewed below the vehicle and determining downrange and crossrange displacement from the reference center. The seeker mode, which was implemented on the last flight test series, provided terminal tracking of a target on the ground. On those flights where MICRAD was not installed, ATIGS could receive position updates from the aircraft navigator. This was done by the pilot depressing the aircraft fix-designate button as he flew over a known checkpoint whose coordinates had been entered in the aircraft navigator computer. The updating method, in both the MICRAD and aircraft cases, was a simple position reset.

TEST CONFIGURATION

For captive flight testing, ATIGS was installed in an Air Force Weapons Evaluation Test Pod (AFWET) and mounted under the starboard wing (station 7) of an A-7C attack aircraft. Figure 3 shows the interconnection of the various components.

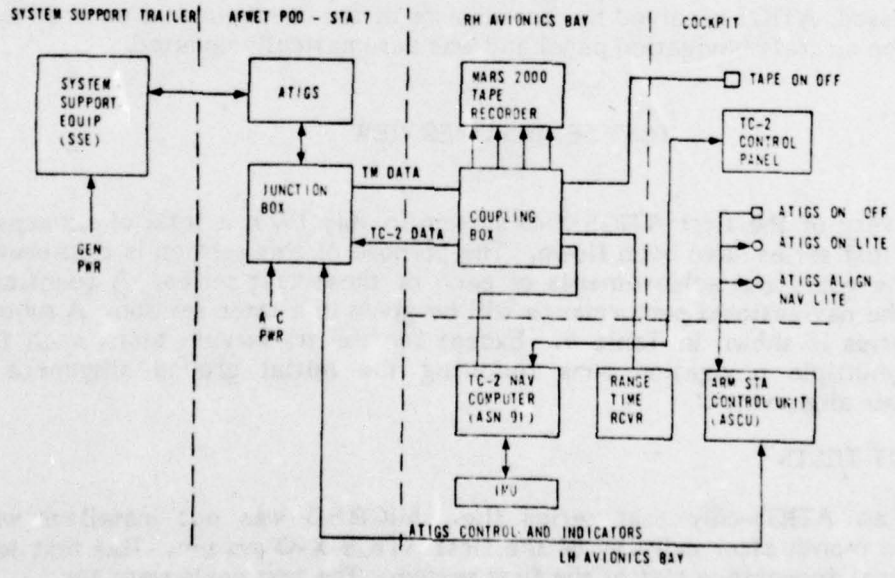


Fig. 3. ATIGS Flight Test Configuration.

BEST AVAILABLE COPY

SYSTEM SUPPORT EQUIPMENT

The System Support Equipment (SSE) provides all the equipment necessary to operate, monitor, and test the ATIGS system independently of the aircraft. During flight testing, the SSE was installed in the system support trailer and used on the flight line for pre-flight checkout of the system and post-flight data dump((Fig. 4).

AIRCRAFT NAVIGATION SYSTEM

The aircraft navigation system consisted of an ASN-90 Inertial Measurement Unit (IMU) and an ASN-91 Navigational/Weapons Delivery Computer. As described in the previous section, the ASN-91 computer provided initialization and in-air alignment support of ATIGS as well as providing barometric altitude and position updates when the MICRAD system was not installed.

COCKPIT CONTROLS

In order to minimize wiring changes to the aircraft, available aircraft armament panel switches and lights were used to control ATIGS. From the cockpit, the pilot could

1. turn ATIGS on or off,
2. re-initialize alignment, and
3. designate midcourse updates (when MICRAD was not installed).

Once an alignment was initialized, ATIGS sequenced automatically through initialization, alignment, and into the navigate mode. A light indicated when alignment was complete and the system was navigating. When the MICRAD system was not installed, the pilot provided position updates to ATIGS by performing the standard "flyover update" procedure normally used to update the aircraft navigator. When the "designate" button was pressed, ATIGS received the coordinates of the checkpoint as entered by the pilot through the aircraft navigation panel and was automatically updated.

TEST SERIES OVERVIEW

Since delivery of the first ATIGS X-O system in May 1974, a total of six separate captive flight test series have been flown. The purpose of this section is to present an overview of the goals and achievements of each of those test series. A quantitative discussion of the navigational performance will be given in a later section. A summary of the test series is shown in Table 4. Except for the tri-service tests, each flight consisted of multiple navigation runs following the initial ground alignment and subsequent in-air alignments.

INITIAL FLIGHT TESTS

This was an ATIGS-only test series (i.e., MICRAD was not installed) which commenced one month after delivery of the first ATIGS X-O system. This test series served as the final acceptance test of the first system. The test goals were to:

(1) Detect and correct any hardware, software, or interface problems that might occur in a captive flight environment.

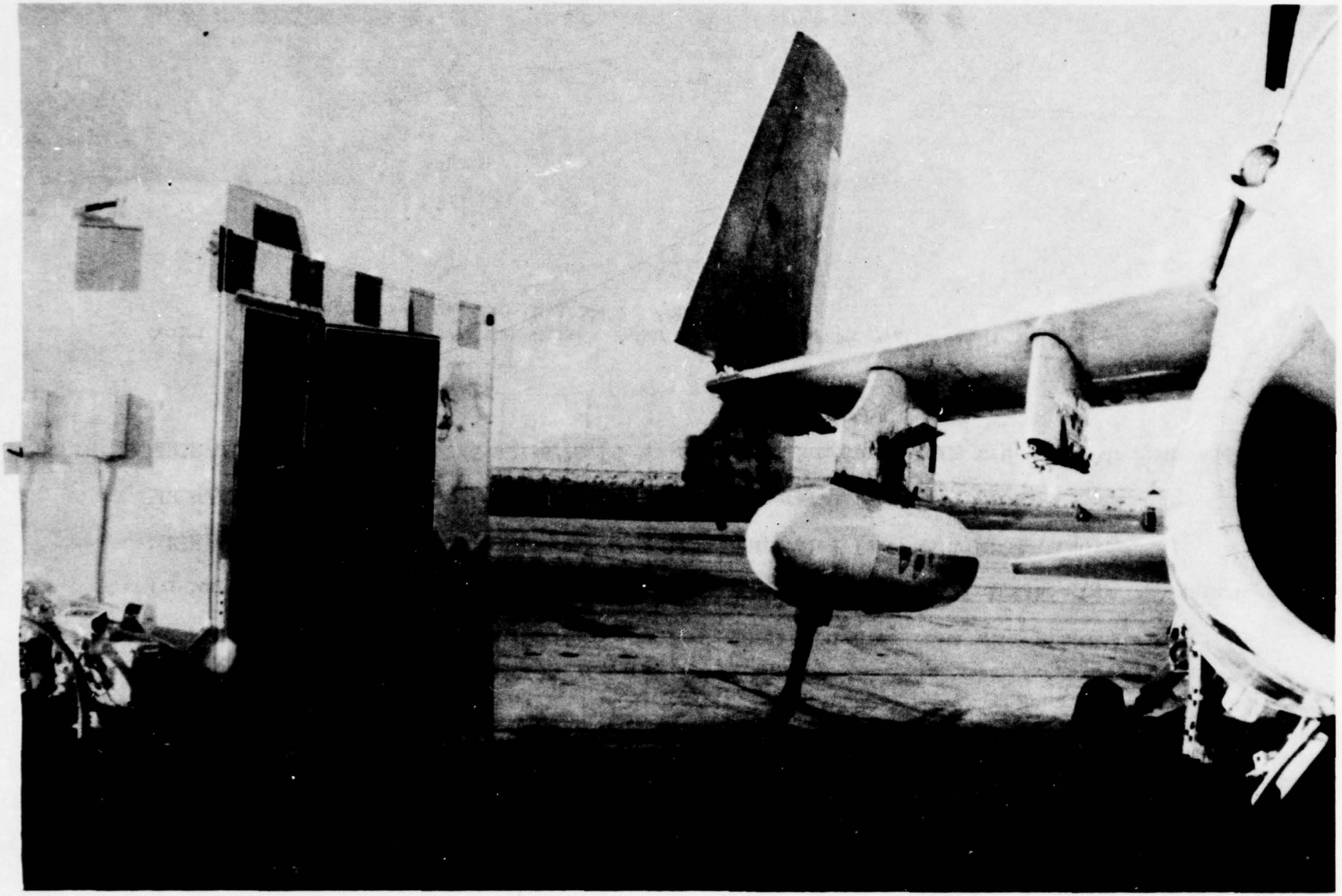


Fig. 4. ATIGS in Pod, Showing System Support Equipment Trailer.

Table 4. ATIGS X-O Captive Flight Tests.

Test Series	Unit No.(1)	Test Dates Start	End	No. Flts.	No. Hrs.	Comments
Initial	1	6/20/74	7/12/74	22	43	First Flight Tests.
MICRAD I	1	1/9/75	1/24/75	6	11	First Integrated Tests with MICRAD Fixer.
Tri-Service	1	3/4/75	3/24/75	8	28	Long-Term (3-4 hrs.) Aircraft-type Navigation.
MICRAD II	1	5/21/75	6/4/75	7	17	Integrated Tests with MICRAD Fixer.
MICRAD III	2	1/15/76	2/17/76	5	14	Integrated Tests with MICRAD Fixer.
MICRAD IV	2	7/2/76	7/16/76	5	6	First Integrated Tests with MICRAD Fixer and Seeker.

Note: (1) Unit No. refers to the serial number of the unit under tests. Unit SN 1 was delivered 5/21/74, and Unit SN 2, 7/21/75.

(2) Demonstrate the ability to achieve accurate in-air alignments.

(3) Demonstrate the ability of ATIGS to accept midcourse position updates from the aircraft navigator.

(4) Provide an initial measurement of system navigational accuracy.

All of the above goals were met. From the first flight, the system consistently exceeded the specified performance goals. A minor design error was discovered in the system flight computer and was repaired prior to flight 7. Of particular significance was the demonstration of the in-air alignment algorithm. By flying an S-turn maneuver during alignment, the alignment algorithm met the 1.0 milliradian azimuth convergence criteria and completed alignment within the 2-minute minimum alignment time.

TRI-SERVICE FLIGHT TESTS

Because of the excellent results achieved on the initial flight test series, interest was generated in the Department of Defense for fully investigating the potential of laser gyros for aircraft inertial navigation. As a result, a series of flight tests were flown where ATIGS was operated as an aircraft navigator. Navigation flights followed ground gyrocompass alignments and were of 3 to 4 hours duration. The navigator operated in a pure inertial mode throughout. The goal of the tests was to determine long-term navigational accuracy of the system. A series of 8 flights showed ATIGS to be a 2 nm/hr navigator (by comparison, the A-7 aircraft navigator, which was trimmed for maximum performance, yielded 0.8 nm/hr on these same flights). Considering that ATIGS was designed as a 10 nm/hr missile navigator and was operated in the relatively rough environment of a wing pod, it is felt that the flights adequately demonstrated the viability of the strapdown, laser-gyro navigator as a candidate for low-cost aircraft navigation.

ATIGS/MICRAD TESTS (MICRAD I, II, III)

In the Fall of 1974, the MICRAD fixer system was integrated with ATIGS X-O and, following laboratory checkout, the integrated systems were installed in the AFWET pod for flight test. The purposes of these tests were to

(1) Demonstrate the ability of ATIGS to navigate with sufficient accuracy (following an in-air alignment) to place MICRAD within the fix reference area.

(2) Demonstrate the ability of ATIGS to provide proper data and control signals to MICRAD.

(3) Demonstrate the ability of MICRAD to successfully scan the reference area, achieve a correlation, and calculate downrange and crossrange position offsets for updating ATIGS.

(4) Demonstrate the ability of ATIGS to apply the MICRAD data to achieve a position update and to subsequently navigate to the next MICRAD fix area.

Although the ability of MICRAD to accurately update ATIGS was demonstrated early in the test series, a number of software and hardware problems, primarily in the MICRAD system, prevented achievement of consistent results. For this reason, additional test series were flown, providing data for improving the reliability of the system.

ATIGS/MICRAD TESTS (MICRAD IV)

These tests were a follow-on to the earlier ATIGS/MICRAD flights with the addition of the MICRAD seeker to the integrated system. By providing the capability of acquisition and track of a surface target, the seeker adds the terminal guidance function to the midcourse guidance provided by ATIGS and the MICRAD fixer systems. The goal of this test series was to demonstrate, in captive flight, the full missile guidance sequence of

(1) In-air alignment of ATIGS

(2) ATIGS navigation and guidance to a midcourse fix area

(3) MICRAD fixer correlation on reference area and updating of ATIGS position

(4) ATIGS navigation to target acquisition point and pointing of MICRAD seeker antenna at target

(5) MICRAD acquisition and track of target.

Of the five flights in this series, the first three were necessary to work out hardware and software problems in the integrated systems. With the problems fixed, the last two flights were virtually 100% successful. Of a total of 12 passes, there were 11 successful MICRAD updates and 12 successful acquisitions and tracks of the target.

FLIGHT TEST PROCEDURES

GENERAL

All flights began and ended at NAF, China Lake. Depending on the purpose of the particular test series, various trajectories were flown, ranging in duration from one to over four hours. Trajectories for each test series are shown in Figures 5 through 8. Except for the final test series (MICRAD IV), the trajectories were flown at normal A-7 cruise speeds, which varied from about 300 to 360 knots. In-flight navigational performance was determined by comparing ATIGS (and aircraft navigator) position to known locations on the ground (checkpoints) marked by use of the standard A-7 low-altitude flyover update procedure. Using this procedure, the pilot flew over the checkpoint at a minimum safe altitude (usually less than 500 feet AGL) and depressed a "designate" button when on top. Accuracy is estimated to be about 300 feet. In addition to marking checkpoints, this procedure was used to provide position updates to both ATIGS and the aircraft navigator on certain flights. Checkpoints were available at approximately ten-minute intervals. A final checkpoint was taken at the flight line at the end of each flight. On flights where MICRAD was installed, position errors were determined photographically at each MICRAD fix by use of a camera mounted in the pod. Accuracy of this method is about 200 feet. Because of the dual navigator feature

of the ATIGS flight program, both updated, short-term navigational data and pure-inertial, long-term data were available on most of the test series.

ATIGS was normally turned on 2 1/2 hours prior to each flight for system checkout and warmup, and remained on until the end of the flight. During the pre-flight period, ATIGS performance was monitored with the SSE, mounted in the trailer alongside the aircraft. During this time, an "auto-cal" procedure was performed on the A-7 navigator. This procedure provided a trim of aircraft navigator gyro biases. By minimizing aircraft navigator errors, the amount of error transfered to ATIGS during in-air alignments was also minimized. After engine start and prior to taxiing, the aircraft navigator was switched to the navigate mode and a final ten-minute ground alignment of ATIGS was performed. Aircraft parking locations are known to 0.1 arc-seconds of latitude or longitude and initial position may be entered into the A-7 navigator (and transferred to ATIGS) to the nearest arc-second (about 100 feet). Once ATIGS alignment was complete, the aircraft was cleared to taxi and takeoff usually occurred within five minutes.

Depending on the requirements of the particular test series, various in-flight procedures were used, and these are discussed in greater detail below. All essential navigational and functional data were recorded in flight on the MARS-2000 tape recorder installed on the aircraft. In addition, a limited amount of "quick-look" data was stored in ATIGS memory for rapid assessment following each flight. Upon return of the aircraft to the flight line following the flight, a final checkpoint was taken and ATIGS and the aircraft were shut down. The trailer was brought alongside the aircraft and the system support equipment was connected for post-flight data dump and checkout. The MARS-2000 tape was removed and taken to the central computing facility for data reduction. The ATIGS system remained on the aircraft between flights of each test series.

INITIAL FLIGHT TESTS

The initial flight series was ATIGS-only (MICRAD was not used) with position updates provided by the aircraft navigator (low-altitude flyover update procedure) at the checkpoints shown in Figure 5. Both east-west and north-south trajectories were flown. In keeping with the concept of a missile navigator, most flights included multiple, short navigational runs following in-air transfer alignments from the aircraft navigator. A typical flight began with a ground alignment and short (10 to 14 minutes) navigation run to the first enroute checkpoint where a fly-over fix was taken. Following the first fix, an in-air transfer alignment was accomplished followed by another navigation run. Normally, several in-air alignments and navigation runs were done with the final run terminating with the last fix taken after the aircraft parked. Four of the 22 flights included lengthy (1 hour) navigation runs following the ground alignment. During this test series only, in-air alignments could be initiated only by cycling power to ATIGS. Alignment commenced immediately upon reapplication of system power. Thus, both sections of the ATIGS dual navigator received in-air alignments although only one section received position updates. A problem with this procedure was that the power interruption caused a transient in the accelerometer thermal control unit resulting in undesirable shifts in accelerometer bias. On the later flight test series, the system was modified so that alignments could be initiated without cycling power. In addition to eliminating the accelerometer thermal transient, the new procedure allowed the updated navigator to be aligned in flight without affecting the un-updated navigator, which navigated continously throughout the flight based on the ground alignment.

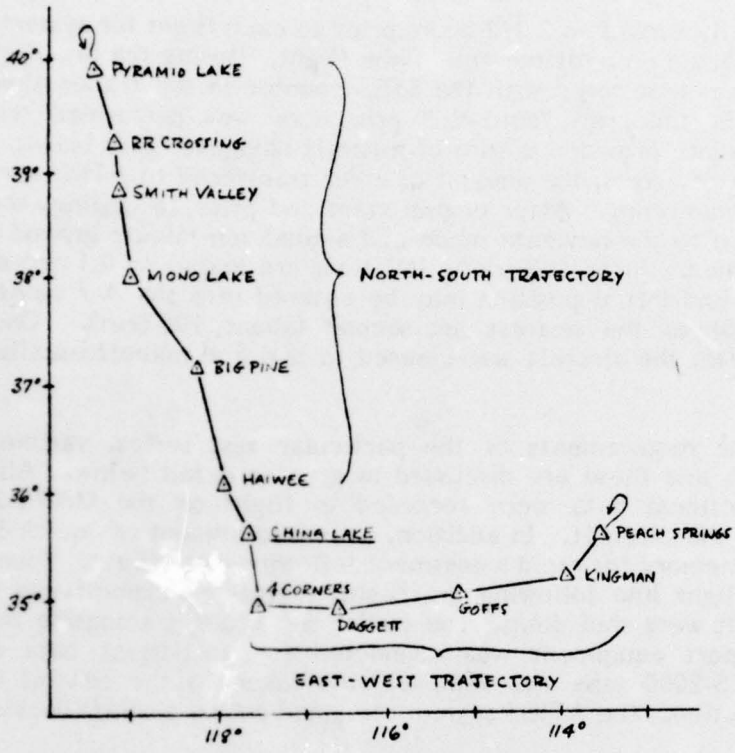


Fig. 5. Flight Trajectories for Initial Flight Tests.

TRI-SERVICE FLIGHT TESTS

All flights in this series consisted of long-term, pure-inertial navigation runs following ground alignment. No in-air alignments were performed. As shown in Figure 6, two flight paths were used, of 3- and 4-hours duration respectively. Each of the paths were flown both clockwise and counterclockwise. Checkpoints were used as position references to determine navigational errors following the flight but were not used to update the navigator.

ATIGS/MICRAD TESTS (MICRAD I, II, III)

The integrated ATIGS/MICRAD tests series used the MICRAD "fixer" to apply position updates to the ATIGS navigator. The aircraft fly-over update procedure was used to update the aircraft navigator and supply checkpoints to ATIGS, but ATIGS could only be updated by MICRAD. The first five flights took place in the Owens Valley with Little Lake and Lone Pine as MICRAD fixes, and Big Pine and Mono Lake as checkpoints (Fig. 7). The procedure was to update the aircraft navigator at one of the checkpoints north of the MICRAD fixes, followed by an in-air alignment of ATIGS (by updating the aircraft navigator just prior to ATIGS alignment, ATIGS initial position error was

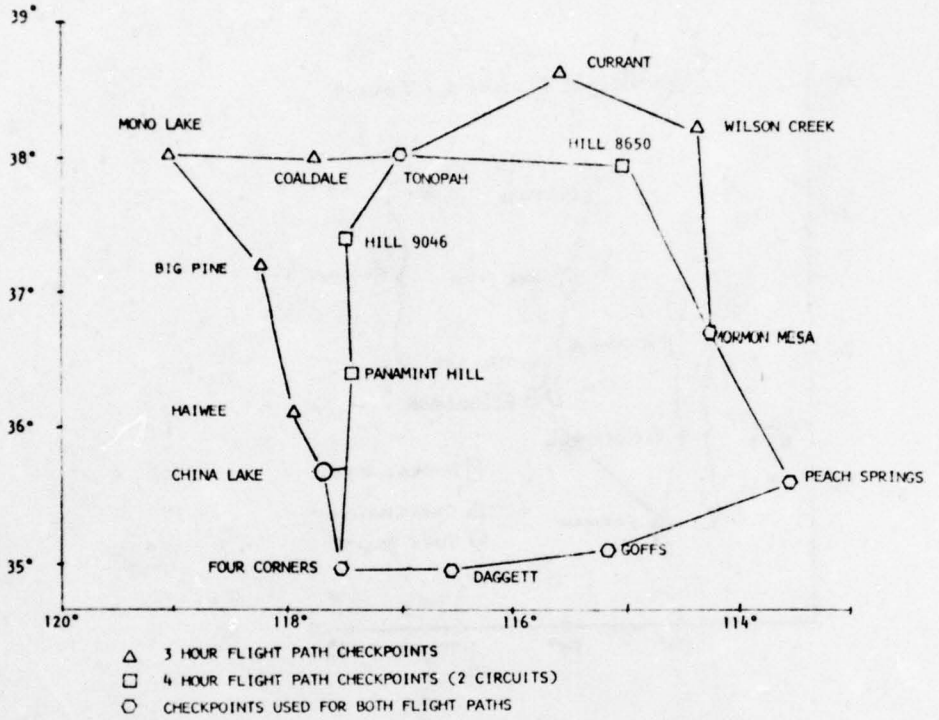


Fig. 6. Flight Trajectories for Tri-Service Flight Tests.

reduced). The aircraft proceeded southbound obtaining MICRAD updates at Lone Pine and Little Lake, then turned and proceeded northbound over the two fix areas, for a total of four MICRAD updates. The whole procedure was repeated three times for a total of 12 MICRAD fixes. Flights 6 through 18 took place in the San Joaquin Valley, using Gorman Vortac as a checkpoint and Bakersfield and Porterville as MICRAD fixes. Procedures were similar to the Owens Valley flights, with Gorman used to update the aircraft navigator just prior to in-air alignment of ATIGS. The aircraft would then fly Bakersfield, Porterville, Porterville, Bakersfield, obtaining two northbound and two southbound MICRAD fixes. The aircraft would then return to Gorman, update the aircraft navigator, re-align ATIGS and repeat the procedure for a total of three passes (12 MICRAD updates). The MICRAD updating procedure was (1) for ATIGS to command MICRAD to start scan as the fix area was entered (based on ATIGS navigation), (2) for MICRAD to scan the area, correlate with a stored reference, and determine downrange and crossrange displacement from the fix center, and (3) for ATIGS to convert the MICRAD data to latitude and longitude corrections and to update the navigational equations. Prior to the third ATIGS/MICRAD test series, an ATIGS-controlled steering needle was added to the cockpit which enabled the pilot to follow ATIGS guidance over the MICRAD fix area rather than by following a visual ground track. Although ATIGS navigational accuracy could be determined in both cases, the closed-loop guidance provided by the steering needle provided real-time demonstration of ATIGS ability to place the aircraft in the MICRAD fix reference area.

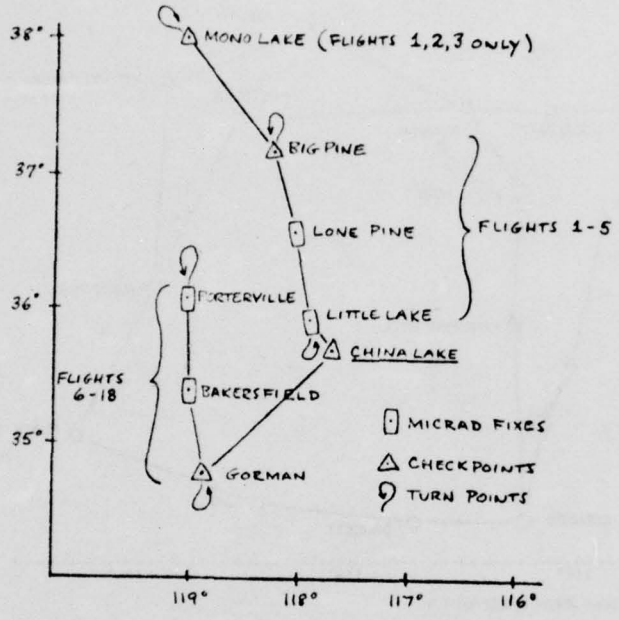


Fig. 7. Flight Trajectories for ATIGS/MICRAD (MICRAD I, II, III) Flight Tests.

ATIGS/MICRAD TESTS (MICRAD IV)

The final flight test series was the first integrated tests to include the full MICRAD system, both midcourse updating (fixer) and terminal guidance (seeker). The procedures on this test came closest to simulating an actual missile flight. The trajectory is shown in Figure 8. A pass commenced with a low-altitude flyover update of the aircraft navigator (to reduce initial position error transferred to ATIGS), followed by an in-air alignment of ATIGS. During alignment the aircraft climbed to 6000 feet AGL. When alignment was complete, a 180 degree turn was executed and the aircraft accelerated to 565 knots. The pilot then followed the steering needle to the MICRAD fix reference area, where the MICRAD updating sequence (scan, correlate, update) was initiated by ATIGS. After leaving the fix area, the pilot commenced a climb to 22,000 feet MSL and turned to set up a 40 degree dive on the target. At 28,000 feet slant range, the MICRAD seeker antenna was uncaged and the updated ATIGS navigator pointed the antenna at the prestored coordinates of the target on the ground. At 22,000 feet slant range, MICRAD acquired and tracked the target until the pilot commenced pull up. A total of six passes were flown on each flight. In addition to the usual digital data, a video camera was boresighted to the pod and the terminal portion of each flight was recorded as well as displayed in the cockpit. A cursor on the TV screen representing seeker antenna position showed the accuracy of the initial pointing, acquisition, and track.

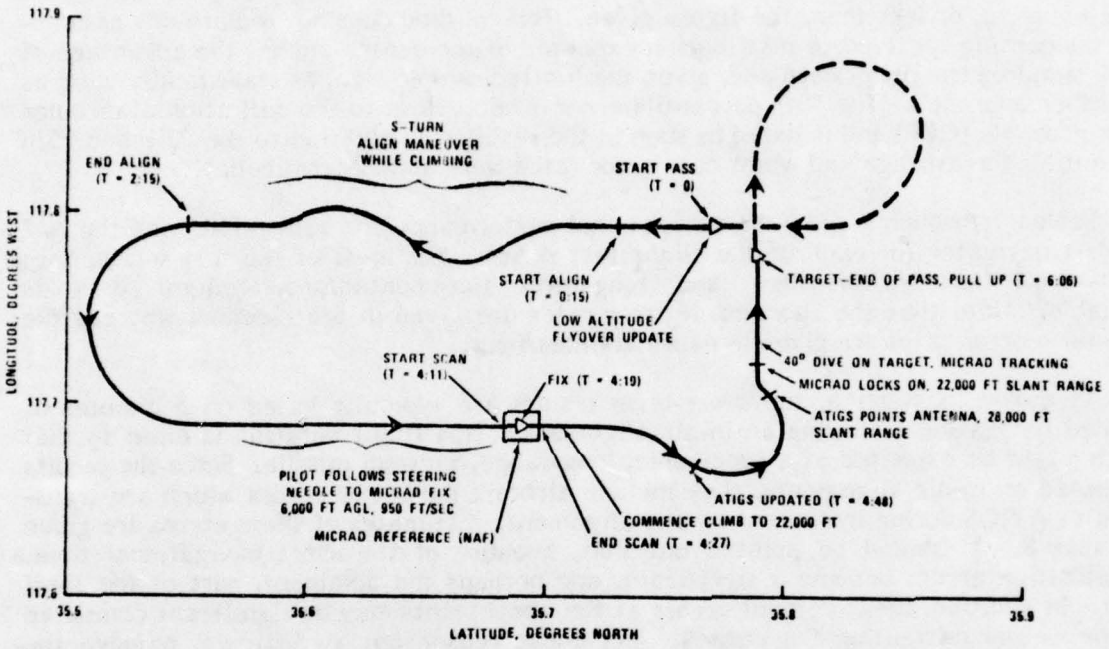


Fig. 8. Flight Trajectory for ATIGS/MICRAD (MICRAD IV) Flight Tests.

RESULTS

Navigational performance was measured by noting the position error at each checkpoint or MICRAD fix and applying the procedures of reference 4 to determine radial position error rates. Basically, the procedure was as follows:

(1) Divide the radial position error at each checkpoint or MICRAD fix by the navigational time to that point. For the updated navigator, time was from the last update (or from the end of the last alignment if an update had not yet occurred). For the unupdated navigator, time was from the end of ground alignment.

(2) List the radial position error rates obtained in step (1) above in ascending order.

(3) From the list, find the 50th and 90th percentile error rate (interpolating if necessary).

Thus, the 50th (or 90th) percentile simply means that 50 (or 90) percent of the errors were equal to, or less than, the figure given. This method does not require any assumption concerning the type of distribution expected of the errors and has the advantage of being simple, straightforward and, given the limited sample size, as statistically valid as any other approach. The 50th percentile error is equivalent to the definition of circular error probable (CEP) and is listed as such in the results. In addition to the CEP and 90th percentile, the average and worst case error rates were also determined.

Tables 5 through 7 show the navigational performance for both ATIGS and the A-7 aircraft navigator for each of the flight test series. For most of the test series, both short-term (updated/air-align) and long-term (un-updated/ground-align) data is available. Note that the short-term error rates are given in feet/second, whereas the long-term error rates are given in nautical miles/hour.

As shown in Table 5, the short-term results are typically based on 5 minutes of unaided navigation following an in-air alignment. This flight duration is close to that which might be expected of a supersonic, long-range, tactical missile. Since the results are based on in-air alignments, they include aircraft navigator errors which are transfered to ATIGS during initialization and alignment. Estimates of those errors are given in Table 8. It should be pointed out that, because of the short navigational time, initialization errors become a significant, and perhaps the dominant, part of the total error. In addition, measurement errors at the checkpoints may be significant compared to the actual navigational accuracy. For these reasons, it is difficult to judge the performance of ATIGS, per se, based on the data in Table 5. The data is useful, however, in giving a realistic picture of the errors that might be expected when the system is operated as a missile navigator.

Table 6 gives a better picture of the performance of ATIGS as an independent navigator. Since the data is based on ground alignments, initial position and velocity errors are known to be zero, and initial attitude errors are those resulting from the sensor errors during alignment. Initial azimuth error is estimated to be approximately 300 arc-sec and initial level error, 20 arc-sec. Because of the longer navigation times, errors in the actual measurement of position at the checkpoints should have a negligible effect on the overall results. In comparing the data for the various test series, it should be remembered that, except for the tri-service test series, the primary purpose of the tests was to demonstrate performance as a missile navigator. Consequently, long-term performance suffered somewhat because of less optimal trajectories and operating procedures. On the tri-service test series, the system was tested specifically as a long-term aircraft navigator and, thus, performance is more representative of that condition.

Table 7 shows the performance of the A-7 aircraft navigator--both long-term, pure-inertial navigation as demonstrated during the tri-service tests and short-term (i.e., 23 minutes) navigation between updates as demonstrated on the MICRAD tests. Because of the affect on ATIGS performance following in-air alignments, care was taken to insure best performance from the aircraft navigator (adequate warmup, AUTO-CAL before each flight, etc.). Thus, the results shown here may be significantly better than the performance of a typical A-7 navigator.

Table 5. ATIGS X-O Short-Term Navigational Performance - Updated Navigator Following In-Air Transfer Alignment.

Test Series	Unit No.	Test Date	No. Flts.	No. Hrs.	Error Rate (ft/sec)				Time (sec)	Data Based On		
					Ave.	CEP	90th	Worst		Flts.	Runs	Pts.
Initial[1]	1	6/74	22	43	7.8	8.3	16.7	20.4	2683	15	25	114
MICRAD I	1	1/75	6	11	8.5	8.7	13.2	20.9	516	2	5	8
Tri-Service	1	3/75	8	28	(No updated Nav/In-air align data available)							
MICRAD II	1	5/75	7	17	9.7	9.5	11.5	12.5	333	2	6	6
MICRAD III	2	1/76	5	14	5.7	4.7	9.9	10.0	402	3	9	19
MICRAD IV	2	7/76	5	6	6.4	6.3	9.3	10.1	148	2	12	23
Total, Unit 1	1	--	43	99	9.0	9.1	12.0	20.9	438	4	11	14
Total, Unit 2	2	--	10	20	6.1	5.2	9.6	10.1	263	5	21	42
Total, All	-	--	53	119	6.8	6.9	10.0	20.9	307	9	32	56

Notes: (1) Data on initial flight test series is <u>un-updated</u> navigation following in-air align. As this is non-standard with respect to the remaining data, it is not included in the totals (except for total flights and flight hours).

(2) Time is average navigation time between checkpoints or MICRAD fixes; Flts. = flights; Runs = navigation runs; Pts. = checkpoints or MICRAD fixes.

Table 6. ATIGS X-O Long-Term Navigational Performance - Pure Inertial Navigator Following Ground Alignment.

Test Series	Unit No.	Test Date	No. Flts.	No. Hrs.	Error Rate (NM/HR)				Time (Hrs.)	Data Based On	
					Ave.	CEP	90th	Worst		Flts.	Pts.
Initial	1	6/74	22	43	5.9	6.3	9.0	9.4	1.0	4	25
MICRAD I	1	1/75	6	11	2.5	2.4	3.1	3.3	1.3	1	3
Tri-Service	1	3/75	8	28	2.6	2.1	4.9	6.5	3.5	7	107
MICRAD II	1	5/75	7	17	6.0	6.0	9.2	11.9	2.5	5	25
MICRAD III	2	1/76	5	14	2.4	2.4	3.8	4.1	2.6	2	10
MICRAD IV	2	7/76	5	6	(No pure inertial/ground align data available)						
Total, Unit 1	1	--	43	99	3.6	4.4	7.4	11.9	2.5	17	160
Total, Unit 2	2	--	10	20	2.4	2.4	3.8	4.1	2.6	2	10
Total, All	-	--	53	119	3.6	4.2	7.4	11.9	2.5	19	170

Note: (1) Time is average navigation time per flight; Flts. = flights; Pts. = Checkpoints.

Table 7. A-7 Aircraft Navigator Performance.

Updated Navigation - Short-Term Performance Between Updates

Test Series	Test Date	No. Flts.	No. Hrs.	Error Rate (ft/sec) Ave.	CEP	90%	Worst	Time (min)	Data Based On Flts.	Pts.
Initial	6/74	22	43	(Data not available)						
MICRAD I	1/75	6	11	3.8	3.1	7.4	11.4	18.7	2	12
Tri-Service	3/75	8	28	(A-7 not updated this series; see below)						
MICRAD II	5/75	7	17	1.9	1.4	3.7	5.5	31.2	2	10
MICRAD III	1/76	5	14	1.4	1.2	2.0	4.6	33.3	3	14
MICRAD IV	7/76	5	6	3.7	3.9	5.2	5.3	7.2	2	11
Total	--	53	119	2.7	2.0	4.9	11.4	23.0	9	47
		Pure-Inertial Navigation - Long-Term Performance								
				Error Rate (nm/hr)				(hrs)		
Tri-Service	3/75	8	28	0.9	0.8	1.4	2.0	3.5	8	120

Note: (1) Time is average navigation time between checkpoints (updated Nav) or average navigation time per flight (pure-inertial Nav); Flts. = flights; Pts. = checkpoints.

Table 8. Estimated Initialization Errors Received by ATIGS from A-7 Navigator During In-Air Transfer Alignments.

	CEP	90th	Units
Position[1]	404	726	feet
Velocity[2]	2.0	4.9	ft/sec
Level[3]	6		arc-sec
Azimuth[3]	360		arc-sec

Notes:

(1) Position error assumes 300 ft error following latest update of A-7 Nav, plus 135 sec of error build up (at rates given for velocity error) between update and end of ATIGS alignment.

(2) Velocity error assumes A-7 position error rates observed during flight tests to be indicative of velocity error during ATIGS alignment.

(3) Attitude errors are simply one-sigma estimates for the A-7 Navigator. It is assumed that equivalent errors are transferred to ATIGS during alignment.

HOLLOMAN TRACK TESTS

During March through June 1976, ATIGS X-O unit number 1 was at Holloman Air Force Base for a series of rocket sled tests designed to investigate system performance (particularly the laser gyros) when exposed to accelerations similar to those expected during actual missile firings. A full description of those tests and analysis of the results is given in references 5, 6, and 7. To complete the picture of ATIGS performance as demonstrated during captive flight testing, a review of the navigational performance of ATIGS during sled testing is given below. For a detailed examination of ATIGS sensor errors during the tests, see references 6 and 7.

TRAJECTORY

The trajectory (acceleration, velocity, and position) is shown in Figure 9. Four runs were made. Each run consisted of a boost phase, a "cruise" phase (a coasting period to allow the sled to decelerate to water brake entry velocity), a water brake phase, and finally a coasting phase until the sled stops. Average values for each phase of the four runs were:

Phase	Duration (sec)	Velocities (ft/sec)	Acceleration (g's)	Cumulative Distance (ft)
Boost	3.5	0-864	14.6	1200
Cruise	7.0	864-550	-1.4	5700
Waterbrake	2.5	570-197	-5.8	6300
Coast	32.0	197-0	-0.2	10197

The sled was in motion for an average of 45 seconds. The Holloman track is oriented in a north-south direction and all runs were made from south to north.

PROCEDURES

Three hours prior to each run, with the sled positioned at the launch point, the system was turned on for warmup and checkout. Navigational data, as well as direct sensor and other functional data, could be monitored in the blockhouse. Once turned on, the system remained on until the end of the sled run. At 13 minutes prior to launch, a final 10-minute gyrocompass alignment of ATIGS was started (the same alignment algorithm used during captive flight tests). This allowed a 3-minute navigational time prior to launch during which pre-launch drifts could be observed. After launch, the sled was in motion for about 45 seconds, and ATIGS was allowed to run an additional 125 seconds for a total navigation time of 350 seconds.

RESULTS

Table 9 tabulates the position and velocity errors observed on each of the four runs at three significant points during the run: at launch, after the sled had stopped at the end of the run, and just prior to shutdown. At all three times, the sled was stopped at a known position on the track so errors could be calculated exactly. A study of Table 9 shows the only significant error to be a change in cross-track (east) velocity error of about -0.44 ft/sec (average) induced during the time the sled is in motion. This in turn,

results in growth in crosstrack position error during the time the sled is stopped at the end of the run. The last two lines of the table give the radial velocity and position errors averaged over the four runs. These can be compared with the original error budget for ATIGS X-O as follows:

	Nav Time (sec)	Position (ft)	Velocity (ft/sec)
Error Budget (CEP values)	330	420	2.54
Sled Runs (average)	352	92	0.65

The original error budget assumed zero initial condition errors, which was the case for the sled runs (except for initial attitude error remaining after the gyrocompass alignment). As reported in reference 6, most of the errors observed during the sled runs appears due to a cross-axis sensitivity in the accelerometers, with very little error attributable to the laser gyros.

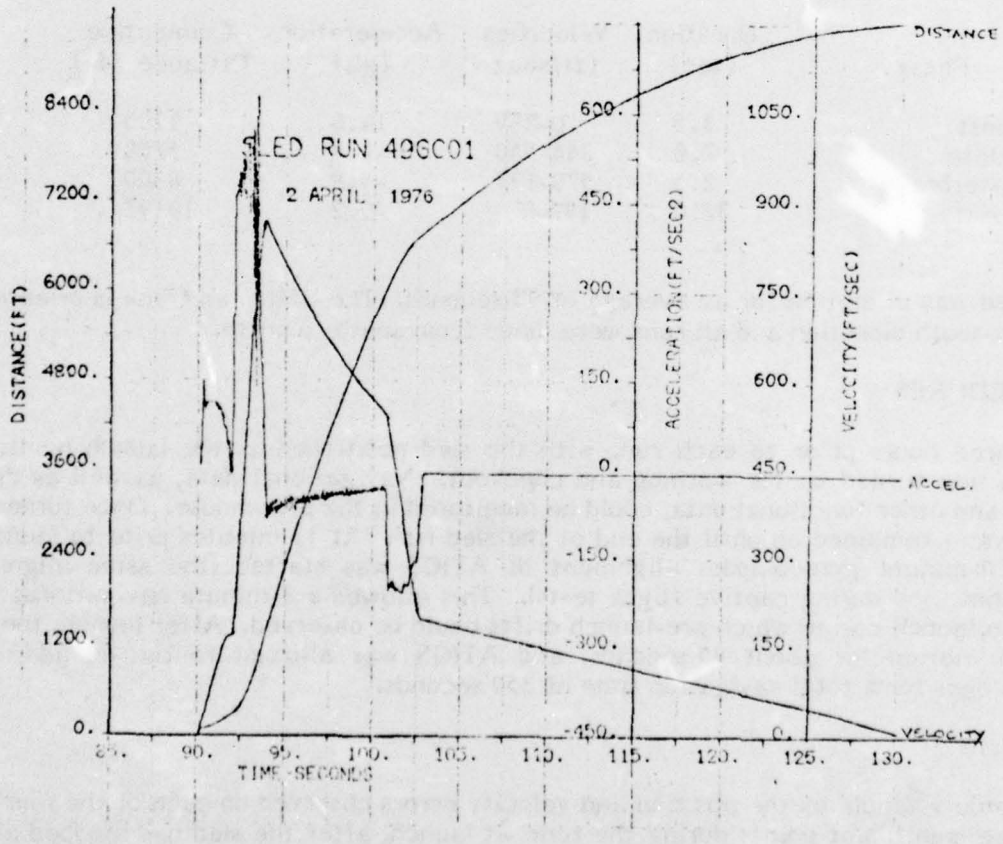


Fig. 9. ATIGS X-O Sled Run Trajectory.

Table 9. Sled Run Error Summary.

	Sled Run	Launch	Event Stop	End
Nav Time (sec)	1	181	220	354
	2	179	230	349
	3	180	227	349
	4	180	223	354
Down-Track Velocity (ft/sec)	1	-0.14	-0.11	-0.32
	2	-0.05	+0.04	+0.04
	3	+0.10	+0.17	-0.17
	4	+0.08	+0.17	-0.18
Cross-Track Velocity (ft/sec)	1	+0.34	-0.03	-0.02
	2	-0.04	-0.51	-0.53
	3	-0.14	-0.58	-0.94
	4	-0.04	-0.51	-0.76
Down-Track Position (ft)	1	-15	-22	-54
	2	-15	-12	+3
	3	+15	+12	+12
	4	+15	+5	+5
Cross-Track Position (ft)	1	+12	+28	+15
	2	-12	-12	-79
	3	-27	-28	-132
	4	-12	-8	-100
Average Radial Velocity (ft/sec)	1-4	0.17	0.44	0.65
Average Radial Position (ft)	1-4	22	23	92

SUMMARY

Table 10 is a summary of results observed in captive flight and rocket-sled testing of the ATIGS X-O missile guidance system. Tests conducted to date have demonstrated:

(1) Better-than-required navigational performance in captive flight as a short-term missile navigator.

(2) Long-term flight performance approaching the requirements for an aircraft navigator.

(3) Accurate in-air alignment of the ATIGS inertial platform from the aircraft navigator.

(4) Integrated operation with the MICRAD midcourse updating system.

(5) Integrated operation with the MICRAD terminal system.

(6) Operation under the high-g sled environment with no significant degradation of performance.

Remaining to be demonstrated is ATIGS guidance of an actual missile in free flight.

Although designed for guidance of long-range tactical missiles, ATIGS X-O has considerably bettered the 10 nmi/hr error rate requirement for a missile navigator and has come close to the 1 nmi/hr error rate typically expected of aircraft navigators. Because of this, strapdown laser-gyro system development is now proceeding along two paths: ATIGS X-2, the smaller tactical missile navigator described in the introduction, and RLGN (Ring Laser Gyro Navigator), a higher accuracy aircraft quality navigator.

Table 10. Summary of ATIGS X-O Navigational Performance During Captive Flight and Sled Testing.

Captive Flight	
Number of Flights	53
Number of Flight Hours	119 hours
Radial Position Error Rates	
Short-Term Navigation[a]	6.9 ft/sec CEP
Long-Term Navigation[b]	2.1 nmi/hr CEP
Rocket Sled	
Number of Runs	4
Boost Acceleration	15 g's
Radial Errors After 350 sec. of Navigation	
Position	92 ft
Velocity	0.65 ft/sec

Notes:

a. 5-minute Nav Runs after in-air alignment.

b. 3 1/2 hour Nav Runs after ground alignment.

REFERENCES

1. Naval Weapons Center. "ATIGS--First Flight Test Results", by Merritt D. Mullen. China Lake, California, NWC, May 1975. 87 pp. (NWC TN 404-211).

2. Naval Weapons Center. "ATIGS--Tri-Service Test Plan", by W. F. Ball. China Lake, California, NWC, February 1975. 26 pp. (NWC TN 404-201).

3. Naval Air Development Center. "Evaluation of the ATIGS Tri-Service Navigation Tests", by Micaela Di Pasquo. Warminster, Penn., September 1975. 47 pp. (NADC-75086-60).

4. Dynamics Research Corporation. "Guidelines for Evaluation of the Navigation Accuracy of the Carrier Aircraft Inertial Navigation System (CAINS)". Wilmington, Mass., September 1972. 8 pp. (DRC R-137U).

5. Armament Development and Test Center. "Test Plan--Advanced Tactical Inertial Guidance System (ATIGS)", by Keith Miles and Walter E. Davis. Holloman Air Force Base, New Mexico, 6585th Test Group, May 1976. 18 pp.

6. Armament Development and Test Center. "Advanced Tactical Inertial Guidance System (ATIGS) Final Report". Holloman Air Force Base, New Mexico, 6585th Test Group, January 1977.

7. Armament Development and Test Center. "Sled Tests of the ATIGS Laser Gyro Strapdown Inertial Guidance System", by Donald F. Walker. Holloman Air Force Base, New Mexico, 6585th Test Group, January 1977.

EIGHTH BIENNIAL GUIDANCE TEST SYMPOSIUM

SLED TESTS OF THE ATIGS LASER GYRO STRAP-DOWN INERTIAL GUIDANCE SYSTEM

AUTHOR: DONALD F. WALKER

CENTRAL INERTIAL GUIDANCE TEST FACILITY
6585TH TEST GROUP
HOLLOMAN AIR FORCE BASE, NEW MEXICO

ABSTRACT

This paper presents the methods and results of the first sled test of a strap-down inertial guidance system which uses a triad of laser gyros. Four sled tests were conducted on the Advanced Tactical Inertial Guidance System (ATIGS) on the high speed test track located at Holloman AFB, New Mexico. The ATIGS was developed at the Naval Weapons Center, China Lake, California.

The ATIGS consisted of the following components: Three Honeywell GG1300 AE ring laser gyros, three Sundstrand Q-flex accelerometers, and a Delco Magic Model 362 computer. The computer processed the accelerometer and gyro output data through software to produce system output velocities in a computational coordinate frame appropriate for comparison with the reference data derived from the test track.

The ATIGS was mounted in a dual rail sled vehicle. Launch parameters were input to the system for alignment several minutes before the sled run. After alignment the system was switched to the flight mode. ATIGS outputs were telemetered and the raw gyro and accelerometer outputs were recorded on sledborne analog magnetic recorders.

A two-stage firing sequence employing five Little John solid rockets boosted the sled vehicle at a typical maximum acceleration of 15g's to a velocity of 865 ft/sec. A water brake of -6.7g's for a duration of two seconds provided deceleration.

Telemetered data from the flight computer was available but occurred only at low frequency of about 10 Hz. The analysis methods therefore used the raw, high frequency accelerometer and gyro data recorded on the sled. This data was processed through a ground based CDC 7600 to simulate the flight computer computation.

In order to separate accelerometer errors from gyro errors, two different analysis procedures were utilized. The first method compared raw, untransformed accelerometer data to a reference function derived from test track data. Past experience has demonstrated the validity of this technique for test environments involving elastic or otherwise predictable test pallet angular motion during sled runs. The resulting difference velocities were modeled by means of regression analysis for accelerometer error coefficients and system angular motion. The second method was aimed at investigating the gyro errors. The system output velocities (namely, accelerometer data transformed to the computational coordinate frame through the use of the gyro data in a strap-down algorithm) were compared to reference test track data in the same frame. The resulting system velocity errors were again entered into regression analysis, where the model used was designed to describe both acceleration and gyro errors.

Four sled runs, five centrifuge tests (counter-rotating mode), and twelve system calibrations were performed. The ATIGS system operated

reliably and its instrument coefficients (gyro and accelerometer) remained stable across the dynamic test environments imposed during the three-month test effort (17 March - 23 June 1976).

The predominant system error source appeared to be the accelerometers. An asymmetrical cross-axis sensitivity was observed in the accelerometer data from both sled and centrifuge tests. No specific gyro errors, except for a residual fixed drift (.04 deg/hr), could be identified. ATIGS system velocity errors could be modeled to within .05 ft/sec (one sigma) from sled test data. Improved test and analysis techniques were developed for evaluating strap-down guidance systems.

TABLE OF CONTENTS

		PAGE
	ABSTRACT	iii
	TABLE OF CONTENTS	v
	LIST OF TABLES	vi
	LIST OF FIGURES	vii
1.	INTRODUCTION	1
2.	TEST DESCRIPTION	1
	2.1 ATIGS Calibrations	1
	2.2 Sled Test Description	3
3.	SLED ANALYSIS PROCEDURES AND DATA	6
	3.1 Gyro and Accelerometer Compensation	7
	3.2 Attitude Quaternion Generation	7
	3.3 Reference System Derivation	9
	3.4 Analysis and Model Derivations	9
	3.5 Error Models	9
4.	SLED TEST RESULTS	13
	4.1 Gyro Data	13
	4.2 Accelerometer Velocity Errors	13
	4.3 System Velocity Error	18
	4.4 Linear Regression Analysis	18
5.	CONCLUSIONS	41
	REFERENCES	42

LIST OF TABLES

TABLE		PAGE
I	SLED GYRO DATA SUMMARY	17
II	ACCELEROMETER DV ERROR SUMMARY	20
III	ATIGS ΔV ERROR SUMMARY	22
IV	X-SYSTEM MODEL COEFFICIENTS (6 TERM MODEL)	26
V	Y-SYSTEM MODEL COEFFICIENTS (6 TERM MODEL)	27
VI	Z-SYSTEM MODEL COEFFICIENTS (6 TERM MODEL)	28
VII	X-ACCELEROMETER MODEL COEFFICIENTS (9 TERM MODEL)	33
VIII	Y-ACCELEROMETER MODEL COEFFICIENTS (9 TERM MODEL)	34
IX	Z-ACCELEROMETER MODEL COEFFICIENTS (9 TERM MODEL)	35
X	X-SYSTEM MODEL COEFFICIENTS (9 TERM MODEL)	36
XI	Y-SYSTEM MODEL COEFFICIENTS (9 TERM MODEL)	37
XII	Z-SYSTEM MODEL COEFFICIENTS (9 TERM MODEL)	38

LIST OF FIGURES

FIGURE		PAGE
1	ATIGS SYSTEM	2
2	SLED AND BOOSTER AT TRACK	4
3	SLED RUN PROFILE	5
4	QUATERNION VECTOR	8
5	ANALYSIS OF ATIGS DATA	10
6	X GYRO ANGLE	14
7	Y GYRO ANGLE	15
8	Z GYRO ANGLE	16
9	ACCELEROMETER VELOCITY ERROR (DV)	19
10	ATIGS VELOCITY ERROR (ΔV)	21
11	ACCELEROMETER RESIDUALS	24
12	ATIGS SYSTEM RESIDUALS	25
13	ACCELEROMETER RESIDUALS (6 TERM MODEL)	30
14	ACCELEROMETER RESIDUALS (9 TERM MODEL)	31
15	ATIGS SYSTEM RESIDUALS (9 TERM MODEL)	32
16	THREE COORDINATE FUNCTIONS USED IN MODEL	39
17	CONTRIBUTION OF THREE COORDINATE FUNCTIONS	40

1. INTRODUCTION

Rocket sled and centrifuge testing of the Advanced Tactical Inertial Guidance System (ATIGS) were performed at Holloman Air Force Base for the Air Force Space and Missiles Systems Organization (SAMSO). The ATIGS test effort is a subtask of the Small Hardened Inertial Platform (SHIP) project, JON 627ANP01. The ATIGS test item and on-site technical support for the three month test effort (March through June 1976) were provided by the Naval Weapons Center (NWC), China Lake, California.

Emphasis has been placed on the development of a strap-down inertial navigator using Ring Laser Gyros (RLG) to achieve the low cost and high reliability requirements of Air Force weapon systems. A strap-down navigator provides advantages over a conventional system in that it does not require gimbals or slip rings. The gimbals are replaced mathematically by software in an on-board digital computer. Also, body-mounted inertial sensors provide the flexibility for midcourse guidance and autostabilization, eliminating the requirement for separate autopilot rate gyros and accelerometers.

Honeywell, Inc. developed the ATIGS (X-0) system, a strap-down RLG navigator, under contract to the Naval Weapons Center. Extensive laboratory and flight tests of this system were performed by NWC. Captive flight evaluations were made using an A-7E aircraft as a test vehicle. Results from the Navy tests in June 1974 and March 1975 are 4 nmi/hr average radial error in the first test series and 2.2 nmi/hr radial error in the second. The Air Force sponsored rocket-sled and centrifuge testing at Holloman to further define the dynamic performance of the RLG strap-down system.

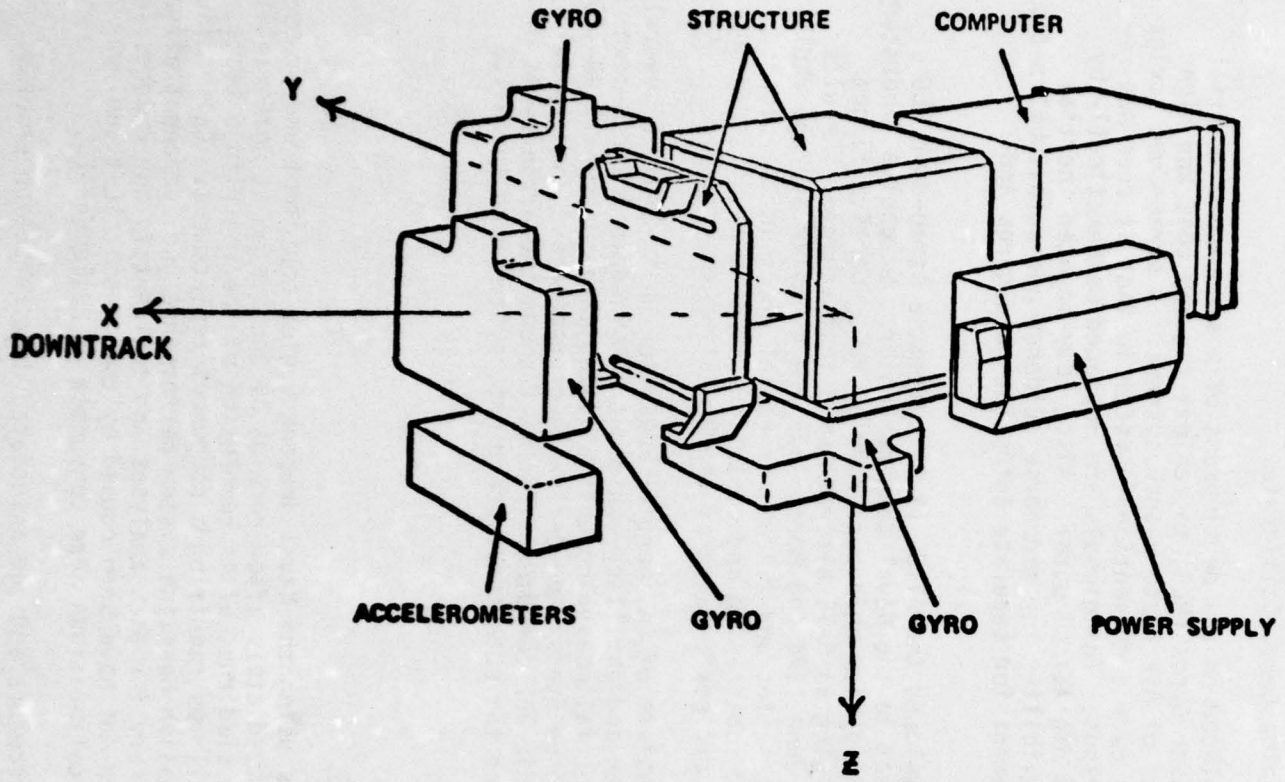
The basic ATIGS consists of an inertial measuring unit (IMU), a general purpose digital computer and ancillary equipment combined in a strap-down configuration. The inertial measuring unit utilizes three Honeywell GG-1300 ring laser gyros and three Sundstrand Q-flex accelerometers. The digital computer is a Delco Magic 362 computer. Figure 1 shows the arrangement of the ATIGS components and the orthogonal coordinate system used for ATIGS mechanization.

2. TEST DESCRIPTION

2.1 ATIGS Calibrations

ATIGS calibrations using the Naval Weapons Center equipment and procedures were performed immediately after receipt of the system at Holloman Air Force Base, after each sled run, after completion of the centrifuge tests, and after any ATIGS failures requiring a component replacement. Calibration data were used to establish baseline system performance and component alignments which were necessary for data analyses and to identify any changes in component outputs which may have been caused by the dynamic test environments. A total of 12 calibrations were conducted at Holloman AFB.

The calibration procedure and the associated data reduction program



ATIGS SYSTEM

Weight: 50 lbs.
Size: 12" long by 13" diameter
Volume: 1592 cubic inches

FIGURE 1. ATIGS SYSTEM

provide the accelerometer biases, scale factors, scale factor imbalances and orthogonalities as well as the gyro fixed drifts, scale factors, and misalignment angles.

Detailed pre-sled setup calibration data taken on the Y-accelerometer at one g-forces around its null point showed anomalous behavior. The Y-accelerometer hysteresis-type behavior was attributed to problems in the accelerometer electronics. Since the electronics could not readily be modified to eliminate this problem, the decision was made to perform the sled and centrifuge tests with the understanding that this hysteresis could induce ATIGS errors under test conditions where the Y-accelerometer operated about its zero-g point.

2.2 Sled Test Description

The sled test portion of the ATIGS evaluation program was divided into three phases; environmental sled runs, ATIGS test site integration, and ATIGS sled runs.

Phase I tests were conducted to establish the acceleration and vibration environment to be experienced by the test item. For these four sled runs, a dummy mass, constructed to duplicate ATIGS weight and center of gravity, was mounted and wired for linear and angular vibration limits, proper operation of test instrumentation was ascertained to include performance of the Test Vehicle Recorders (TVR), primary and secondary power supplies, and the basic sapce-time velocity reference system.

During Phase II, following delivery, the ATIGS was subjected to a complete laboratory functional checkout and the count down procedures were developed and verified. The ATIGS was then calibrated and mounted within the sled (down-track axis) to reduce the hysteresis errors. Figure 2 is a photograph of the complete sled with the booster train. The system was subjected to a complete functional check in the sled with test instrumentation checkout including measuring raw gyro and accelerometer signals. The ATIGS was again calibrated using localized calibration parameters in the calibration routines. Following completion of all laboratory checks, the sled was positioned on the track for tracksite functional checks.

Following satisfactory completion of all Phase I and Phase II activities, four high-speed rocket sled runs were conducted. Each test consisted of a detailed prelaunch countdown allowing 2.5 hours for ATIGS warm-up with continuous monitoring of gyros, accelerometer, and system outputs. ATIGS down-track alignment to within $\pm$ 6 arc-seconds in azimuth and elevation was obtained prior to each run using an attached mirror cube and reference theodolites. The ATIGS system was switched from the alignment to navigate mode three minutes prior to sled launch.

Figure 3 is a typical sled run profile achieved by using five "Little John" motors, each producing 3200 pounds of thrust. Over 600 feet of water braking were used to achieve the desired deceleration. The average maximum deceleration was -6.7 g's.

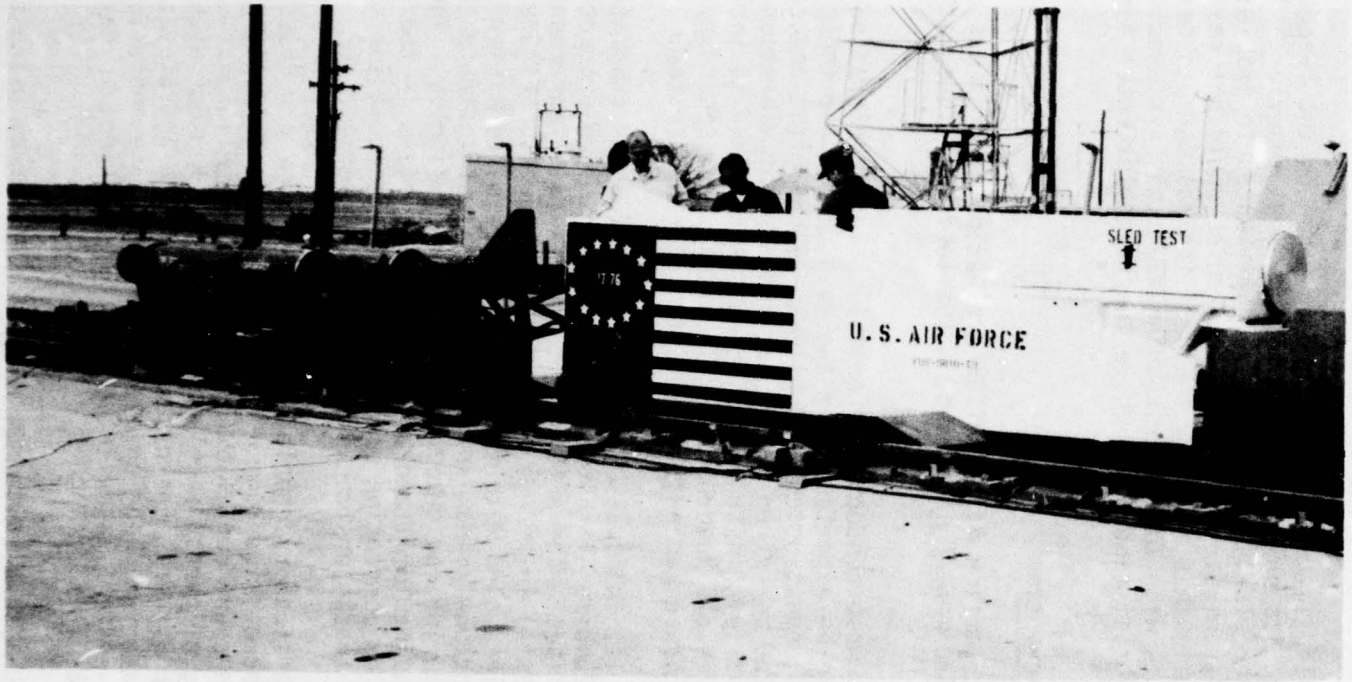


FIGURE 2

Sled and Booster at Track

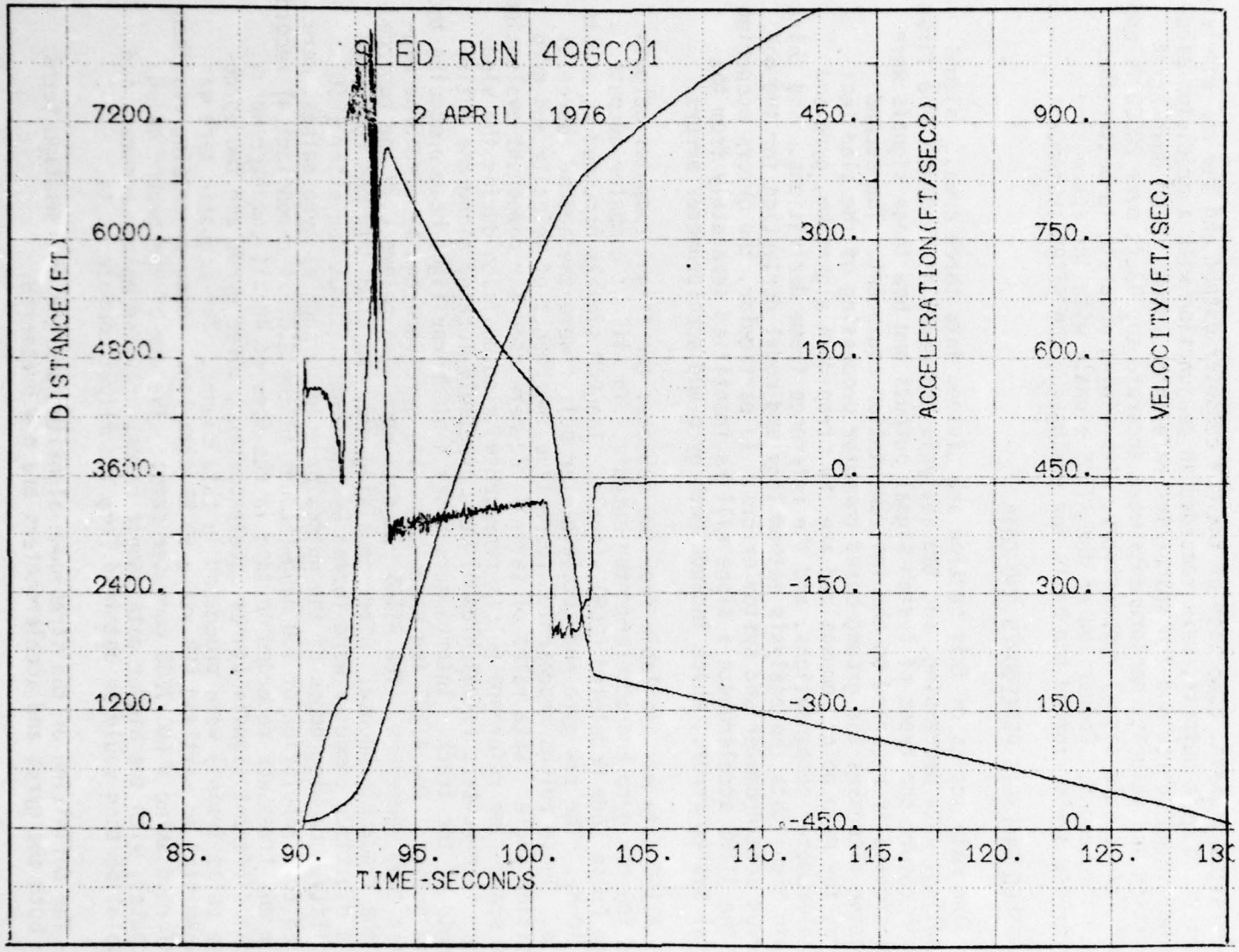

SLED RUN 49GC01
2 APRIL 1976
DISTANCE(FT)
7200.
6000.
4800.
3600.
2400.
1200.
0.
ACCELERATION(FT/SEC2)
450.
300.
150.
0.
-150.
-300.
-450.
VELOCITY(FT/SEC)
900.
750.
600.
450.
300.
150.
0.
85.
90.
95.
100.
105.
110.
115.
120.
125.
TIME-SECONDS

FIGURE 3

ATIGS signals, comprised of the PCM computer output and the raw accelerometer and gyro outputs, were recorded in conjunction with a precision sled-borne timing source and the space-time reference system. Sled down-track position and velocity measurements were accurate to .03 ft over 20000 ft and .004 ft/sec (one sigma) respectively, with timing accurate to better than one microsecond. Comparison of the ATIGS signals with the space-time reference system formed the basis for evaluating the ATIGS system.

3. SLED ANALYSIS PROCEDURES AND DATA

The main topics of this section are divided into three areas: signal handling, data processing, and the analysis and model derivation. The first topic covers the types of system signal outputs and how these signals were electronically recorded on the instrumentation equipment. The second section discusses the ground-based computer processing of the sled test data; the main points emphasized are the strap-down algorithm, gyro and accelerometer compensations, and the reference frame derivations. The third topic highlights the analysis methodology and model derivation for the observed accelerometer and system errors. In particular, the errors occurring in the ATIGS accelerometers alone will be identified separately from the total system errors, which include both gyro and accelerometer errors.

ATIGS data was available from two sources; the flight computer outputs and the raw gyro and accelerometer outputs. The flight computer outputs were Pulse Code Modulated (PCM) signals. The PCM signals occurred at a rate of 10 Hz. The raw gyro and accelerometer pulses were the second source of data. These pulses represented respective increments of velocity and gyro position angle. Data rates of several kHz were used for component evaluation. The space-time reference pulses represented sled position during the sled run. Interrupters (steel blades) were precisely located along the entire length of the track. Interrupters broke a sledborne light beam producing the data pulses. The ATIGS and space-time data were recorded by sledborne magnetic tape recorders. The ATIGS PCM data were also telemetered and recorded at the track blockhouse. After each sled run, the sled data was converted to a digitized computer word format by the General Input Converter (GIC) facility. Leading edges of the pulses or events, such as gyro pulses, were timed to a resolution of 500 nano-seconds at the GIC. A chronological record of event times was recorded on tape in the form of 48 bit computer words. Eight different signals (three accelerometers, three gyros and two space-time pulse trains) were processed in this manner. The magnetic tape was transmitted to Kirtland AFB via a 50 KB data link. Data processing was then performed using a CDC 7600 computer setup. The use of the ground based computer, with the higher data sample rates, provided better accuracy and resolution than could be obtained from the flight computer data.

The definition of the strap-down algorithm and the compensation terms for both the gyros and accelerometers are now presented.

The body-mounted accelerometers and gyros, in conjunction with math computations performed by the flight computer, eliminate the gimbals and slip rings of conventional navigation system. The digitized gyro data

served as a reference for the accelerometers by providing angle rate information. This angular rate information is used to build a coordinate transformation matrix or direction cosine matrix. The continual updating of this direction cosine matrix enables the acceleration pulses, increments of velocity, to be resolved into a computational navigation frame. These velocity increments are then accumulated in the standard navigation frame as north, east and down velocities. The basic algorithm can be expressed as

$$\int_{t}^{t+\Delta t} A_n \, d\tau = \int_{t}^{t+\Delta t} M A_r \, d\tau$$

A_n = (3x1) accelerations in navigation frame

A_r = (3x1) accelerations in body frame

M = (3x3) body to navigation transformation matrix

where for small time increments, we can write

$$\Delta V_n(t + \Delta t) = M(t + \Delta t)\Delta V_r(t + \Delta t)$$

The V's are then accumulated to update the navigation frame velocities.

$$V_n(t + \Delta t) = V_n(t) + V_n(t + \Delta t)$$

The gyro and accelerometer data were interpolated to a common time series on the ground based computer before entering the algorithm. A small Δt step size of 2500 microseconds was used. The step size kept the amount of data to a reasonable limit and also avoided errors caused by a low updating rate of the transformation matrix.

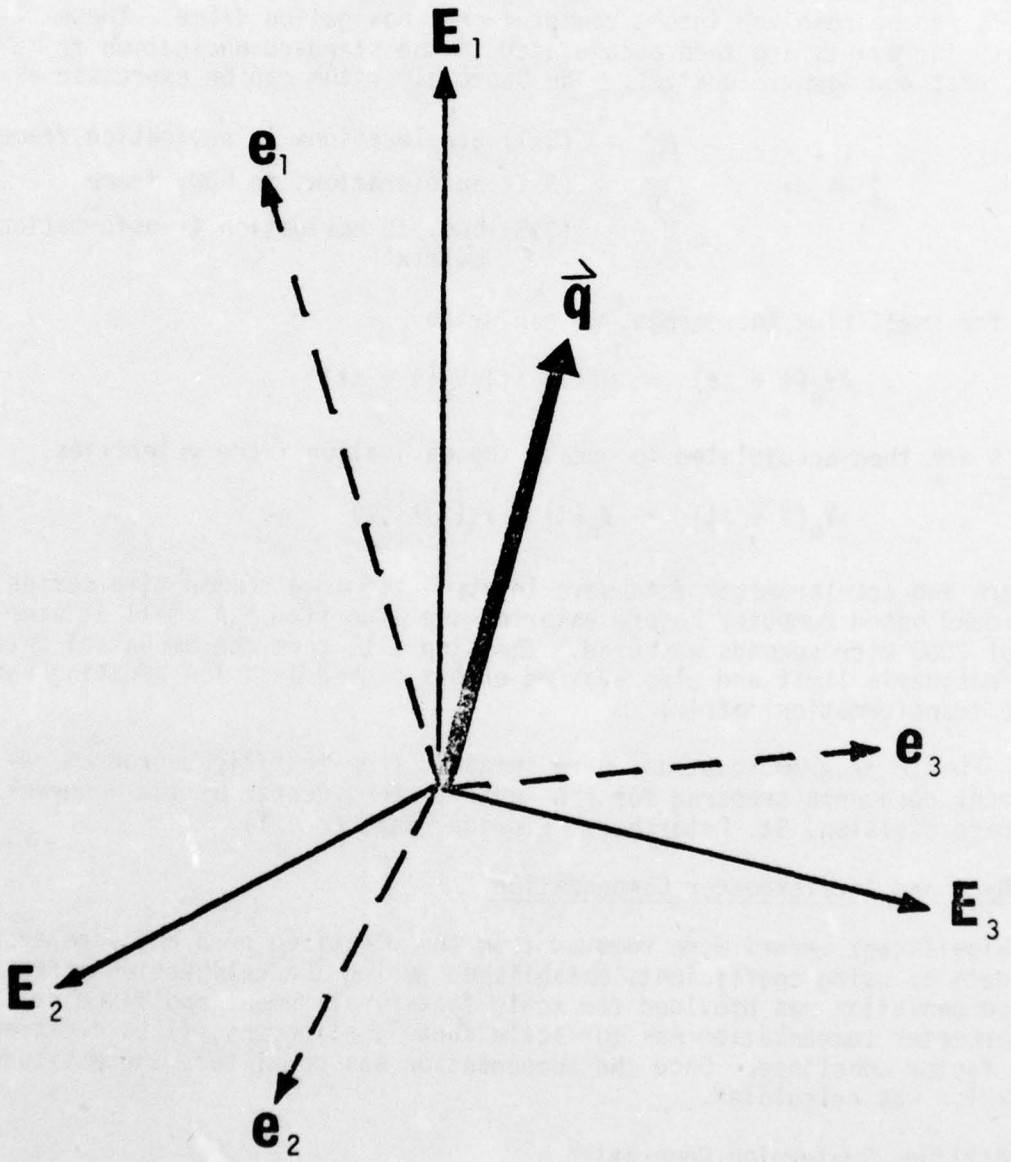
The basic program equations were obtained from the flight program requirement documents prepared for the Naval Weapons Center by the Honeywell Aerospace Division, St. Petersburg, Florida (Reference 1).

3.1 Gyro and Accelerometer Compensation

Significant errors were removed from the digitized gyro and accelerometer data by using coefficients established during the calibration process. Gyro compensation was provided for scale factor, alignment and fixed drift. Accelerometer compensation was for scale factor, alignment, fixed drift and scale factor unbalance. Once the compensation was completed, the attitude quaternion was calculated.

3.2 Attitude Quaternion Generation

One of the more interesting features of the ATIGS strap-down algorithm is the use of quaternions or four dimensional hypercomplex numbers. The orthonormal frames, a reference ($\vec{E}_1$, $\vec{E}_2$, $\vec{E}_3$) and a body fixed ($\vec{e}_1$, $\vec{e}_2$, $\vec{e}_3$), are presented in Figure 4. The quaternion vector, $\bar{q}$, lies along an axis of rotation about which the body could be rotated to become aligned with the reference system. The magnitude of $\bar{q}$ is $\sin\phi/2$ where ϕ is the angle through



REFERENCE SYSTEM
$(E_1\ E_2 E_3)$

BODY FIXED SYSTEM
$(e_1 e_2\ e_3)$

QUATERNION VECTOR $\vec{q}$

FIGURE 4

which the reference system must be rotated to become aligned with the body and is positive in the direction of a right-handed rotation.

The primary advantage of the quaternion is that the kinematic equations relating the angular velocity vector of a rigid body to its attitude have a simpler form when stated in terms of the quaternion. There are only four linear first order homogeneous differential equations to be solved instead of the nine Euler angle equations required for solution in the direction cosine equations.

3.3 Reference System Derivation

The digitized space-time pulses are processed through appropriate programs to provide a reference frame for comparison of the compensated accelerometer putputs and strap-down output data to the high speed test track. For this procedure a matrix, A_{MA}, transforming from a cube mirror to the ATIGS accelerometers, was solved for during the calibrations. Theodolite readings were also made before each sled run on the system mounted cube mirror to provide a matrix, A_{IM}, which gives the transformation from the launch coordinate to the mirror. The final known matrix, A_{RL}, was computed from track survey data and transformed data from test track rail coordinates to launch point tangent plane coordinates. The use of all these 3x3 matrices and appropriate computer programs established a reference frame that would be seen by an ideal navigation system.

3.4 Analysis and Model Derivations

The analysis methodology and test item model derivation used in this report are based upon past sled test project experience and are documented in Reference 2. The following discussion summarizes the techniques used in this report.

Two analysis procedures were utilized to separate accelerometer errors from gyro errors. Figure 5 illustrates the two approaches. The first approach compared untransformed, compensated accelerometer data to space-time reference data. The comparison was made in the velocity domain. The resulting difference velocities, or DV's, were modeled by means of regression analysis for accelerometer error coefficients and system angular mation. The second method investigated gyro errors. The system output velocities, derived from using gyro data to transform accelerometer data to the computational coordinate frame using the strap-down algorithm were also compared to space-time reference velocities. These ΔV velocity errors were also processed through regression analysis and modeled. This second model was formulated to describe the error sources of both the accelerometers and gyros.

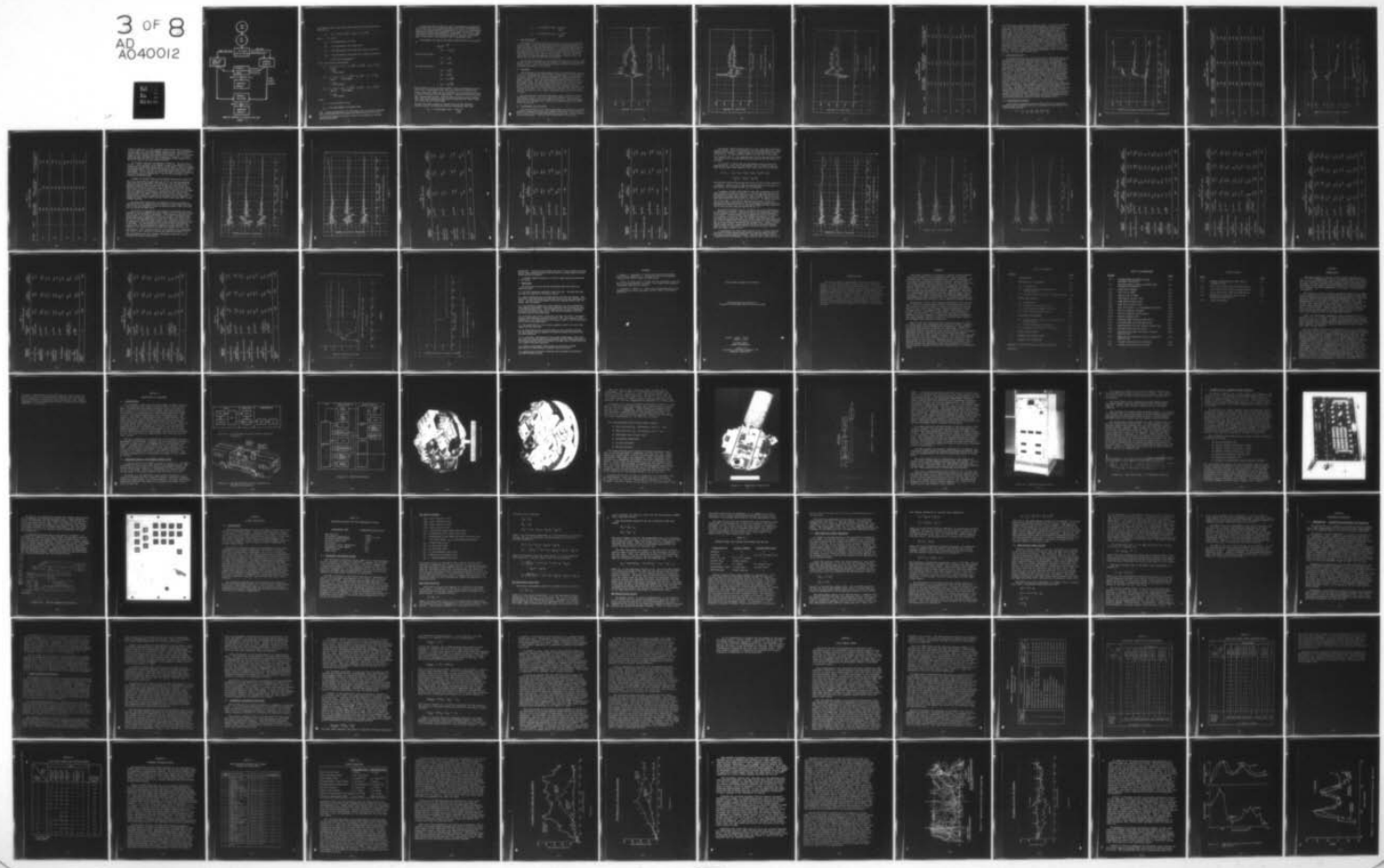
3.5 Error Models

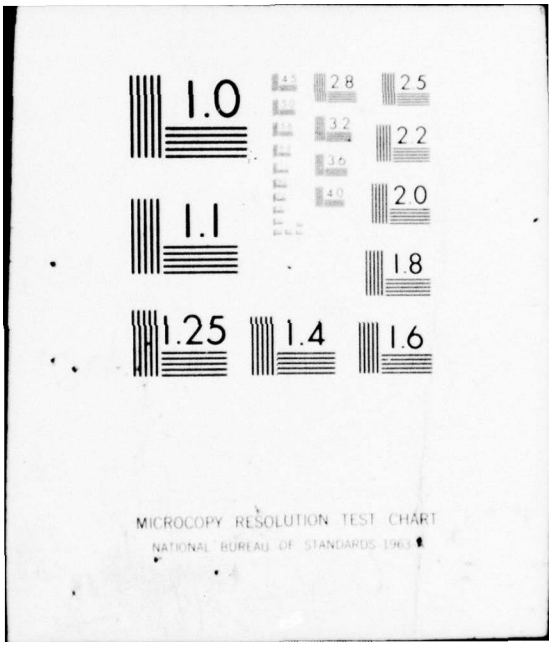
The formulation of the two separate models for the accelerometer errors and the system errors (which include gyro errors) are presented in the following section. The accelerometer errors δA_i are usually attributable to

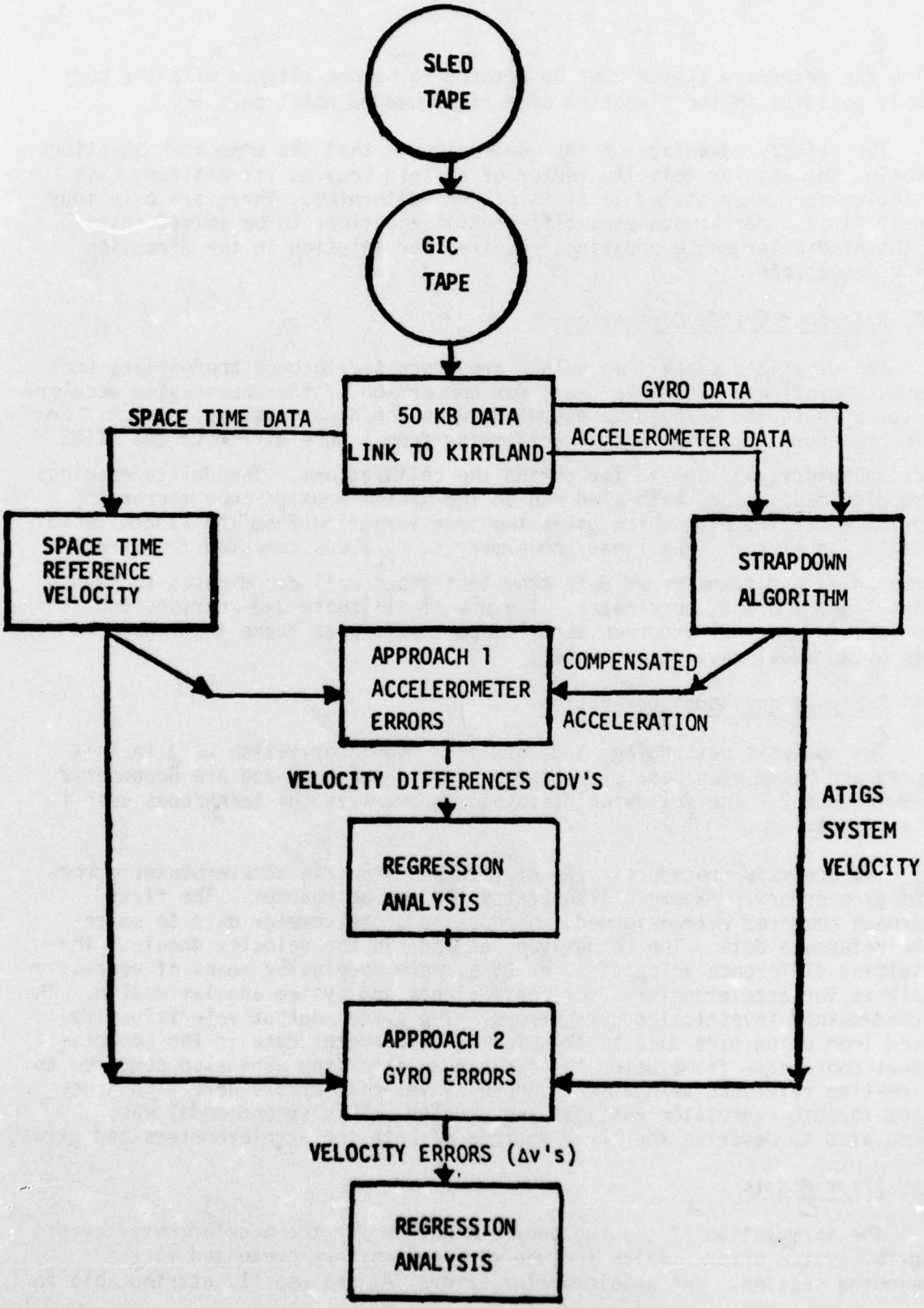
AD-A040 012 ARMAMENT DEVELOPMENT AND TEST CENTER EGLIN AFB FLA F/G 17/7
PROCEEDINGS OF THE BIENNIAL GUIDANCE TEST SYMPOSIUM (8TH) HELD --ETC(U)
MAY 77

UNCLASSIFIED ADTC-TR-77-3-VOL-1 NL

3 OF 8
AD
A040012




1.0
1.1
1.25
1.4
1.6
2.8
3.2
3.6
4.0
2.5
2.2
2.0
1.8
MICROCOPY RESOLUTION TEST CHART
NATIONAL BUREAU OF STANDARDS 1963



ANALYSIS APPROACHES TO EVALUATE ATIGS DATA

FIGURE 5

such effects as bias, scale factor, first order scale factor nonlinearity and time lag.

$$\delta A_i = K_{0i} + \delta SF_i A_i + K_{1i} A_i^2 + K_{2i} A_i^3 - \tau \dot{A}_i + 1/2 \tau^2 \ddot{A}$$

where i = X, Y, Z and

K_{0i} = ith accelerometer bias error

δSF_i = ith accelerometer scale factor error

K_{1i} = ith accelerometer first order scale factor nonlinearity

K_{2i} = ith accelerometer second order scale factor nonlinearity

τ = time lag of accelerometer

which in the velocity domain become

$$\delta V_x = \underbrace{K_x}_{\text{offset}} + K_{0x} t + \delta S \cdot F \cdot \hat{V}_x + K_{1x} \int \hat{A}_x^2 dt + K_{2x} \int \hat{A}_x^3 dt - \tau_x \hat{A}_x + 1/2 \tau_x^2 \dot{\hat{A}}_x + \underbrace{\theta_{0y} g t}_{\text{misalignment}}$$

$$\delta V_y = \underbrace{K_y}_{\text{offset}} + K_{0y} t + \underbrace{\theta_{0z} \hat{V}_x}_{\text{misalignment}} + K_{1y} \int \hat{A}_x^2 dt + K_{2y} \int \hat{A}_x^3 dt - \tau_y A_x + 1/2 \tau_y^2 \dot{\hat{A}}_x + \underbrace{\theta_{0x} g t}_{\text{misalignment}}$$

$$\delta V_z = \underbrace{K_z}_{\text{offset}} + K_{0z} t + \underbrace{\theta_{0y} \hat{V}_x}_{\text{misalignment}} + K_{1z} \int \hat{A}_x^2 dt + K_{2z} \int \hat{A}_x^3 dt - \tau_z \hat{A}_x + 1/2 \tau_z^2 \dot{\hat{A}}_x + \underbrace{0x g t}_{\text{misalignment}}$$

Where

K_i = ith accelerometer offset

θ_{0i} = ith accelerometer misalignment angle.

NOTE: We have assumed that δA is sufficiently small so that the accelerometer measured down-track acceleration and derived velocity ($\hat{A}_x$ and $\hat{V}_x$) could be used instead of the ideal A and V in the equations to generate coordinate functions.

It must be pointed out that the Y and Z accelerometers, mounted with a 30 roll about the x axis, changed attitude as the pallet fixture moved because of the sled acceleration and deceleration. The Y and Z accelerometers sensed these motions as sine components of the down-track velocity. These accelerometer motions then showed up as large errors. The x accelerometer also senses the sled motion but because the error involves a cosine term there is very little error observed in the X accelerometer value.

Accelerometer error due to test pallet angular motion can be expressed as

$$\theta_{Dynamic} = KA_x$$

$$\delta A_z = \sin\theta_{1z} A_x$$

thus for small angles

$$\delta A_z = \theta_{1z} A_x$$

$$\delta A_y = \theta_{1y} A_x$$

Then substituting for θ

$$\delta A_z = K_{1y} A_x^2$$

$$\delta A_y = K_{1y} A_x^2$$

$$\delta V_z = K_{1z} \int A_x^2 dt$$

$$\delta V_y = K_{1y} \int A_x^2 dt$$

which indicates that for the major portion of the Z accelerometer error and part of the Y accelerometer error, the $K_{1z}K_{1y}$ coefficients describe the dynamic pitch angle rather than the first order scale factor nonlinearity as K_{1x} does for the case of the X accelerometer. The terms $K\int A^3 dt$ and θgt were later removed from the model. These two terms provided very small contribution values to the total error and could be omitted from the linear regression without any significant change.

The gyro error model, because it involved fitting of the strap-down algorithm outputs, contained both gyro and accelerometer model terms.

$$\Delta V_x = \text{x accelerometer terms} - \underbrace{1/2 g w_{0y} t^2}_{\text{Drift}}$$

$$\Delta V_y = y \text{ accelerometer terms} - \underset{\text{Drift}}{w_{Oz} \int A_x t dt}$$

$$\Delta V_z = z \text{ accelerometer terms} + \underset{\text{Drift}}{w_{Oy} \int A_x t dt}$$

4. SLED TEST RESULTS

This section is divided into four main areas: gyro data, accelerometer velocity errors, system velocity errors, and linear regression analysis. A short discussion of the gyro data centers on the fact that three of the four sled runs produced repeatable results (Run #2 gyro data was questionable). The accelerometer velocity errors indicate the dynamic ATIGS motions, while the system velocity errors show how well the gyros perform in removing the accelerometer sensed errors due to dynamic motions. The final discussion topic covers the modeling performed on the respective velocity errors and demonstrates how well the model fits the test data.

The results from sled Run #1 are presented throughout this section. This run was selected as the main test case because it produced the best regression analysis results. Data from the remaining three sled runs are summarized in the appropriate tables in this section.

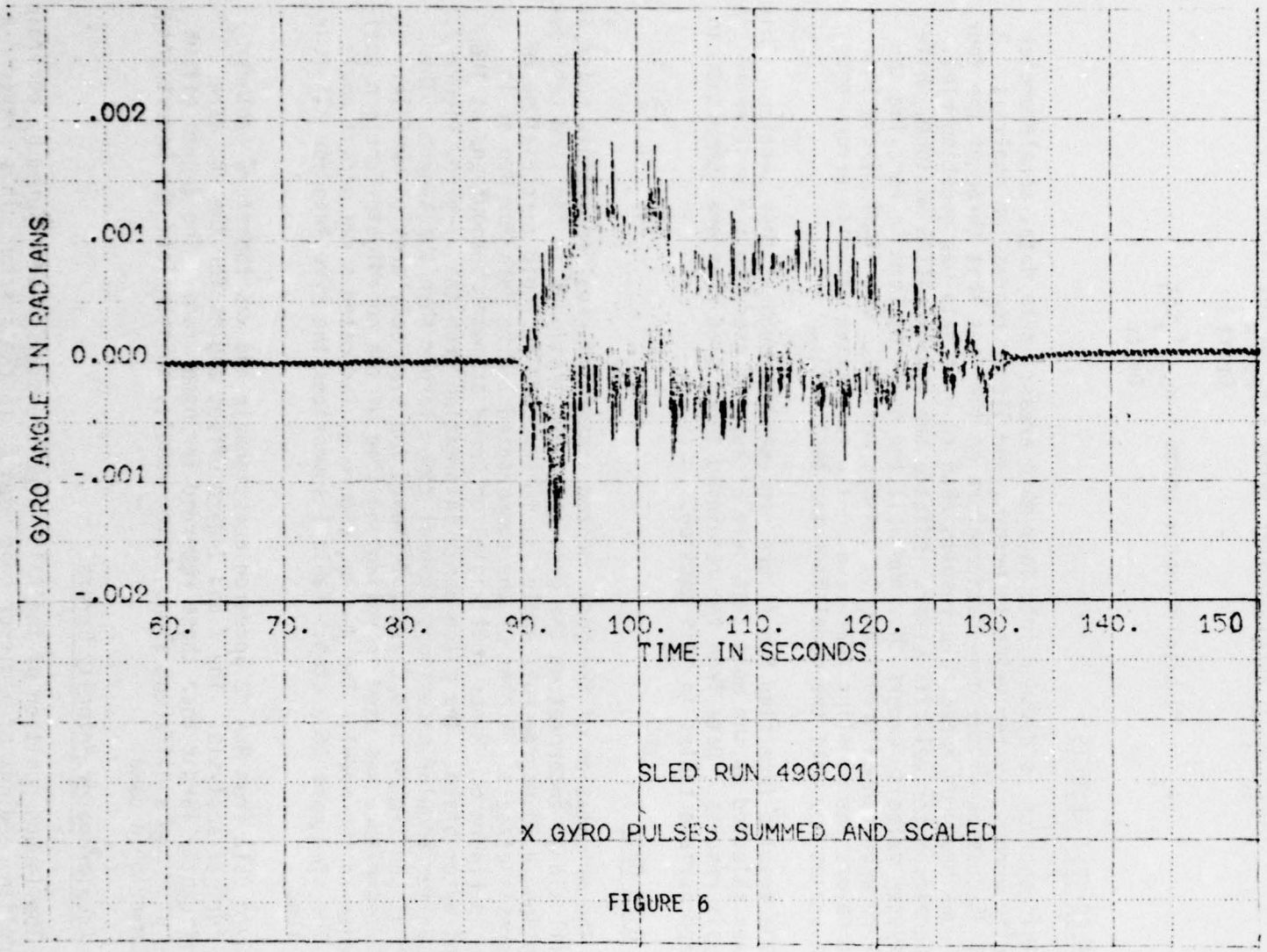
4.1 Gyro Data

The orientation of the body mounted sensors is recalled at this point as it will aid in interpreting the gyro data. As mentioned in the sled test description, a 30 degree roll angle was implemented to avoid Y-accelerometer hysteresis effects. A plot of the compensated X-gyro data for Run #1 is shown in Figure 6. Minor roll angles occurred at motor burnout and at the end of water brake. The pitch angle information from the Y-gyro, Figure 7, had maximum angular excursions several times larger than the X-gyro. The shape of the Y-gyro data closely followed the sled acceleration profile. This resemblance was used in validating some of the coordinate function coefficients in the model. The Z-gyro, Figure 8, indicated a yaw offset angle when the sled came to a stop. Table I summarizes the gyro data for all four sled runs.

Gyro data from Run #2 appeared questionable and was therefore excluded from further analysis. The X and Z-gyro offset angles for the run were significantly larger than those recorded for other runs. The Z-gyro offset angle also had a different sign. Later results substantiate the uncertainty in Run #2 gyro data.

4.2 Accelerometer Velocity Errors

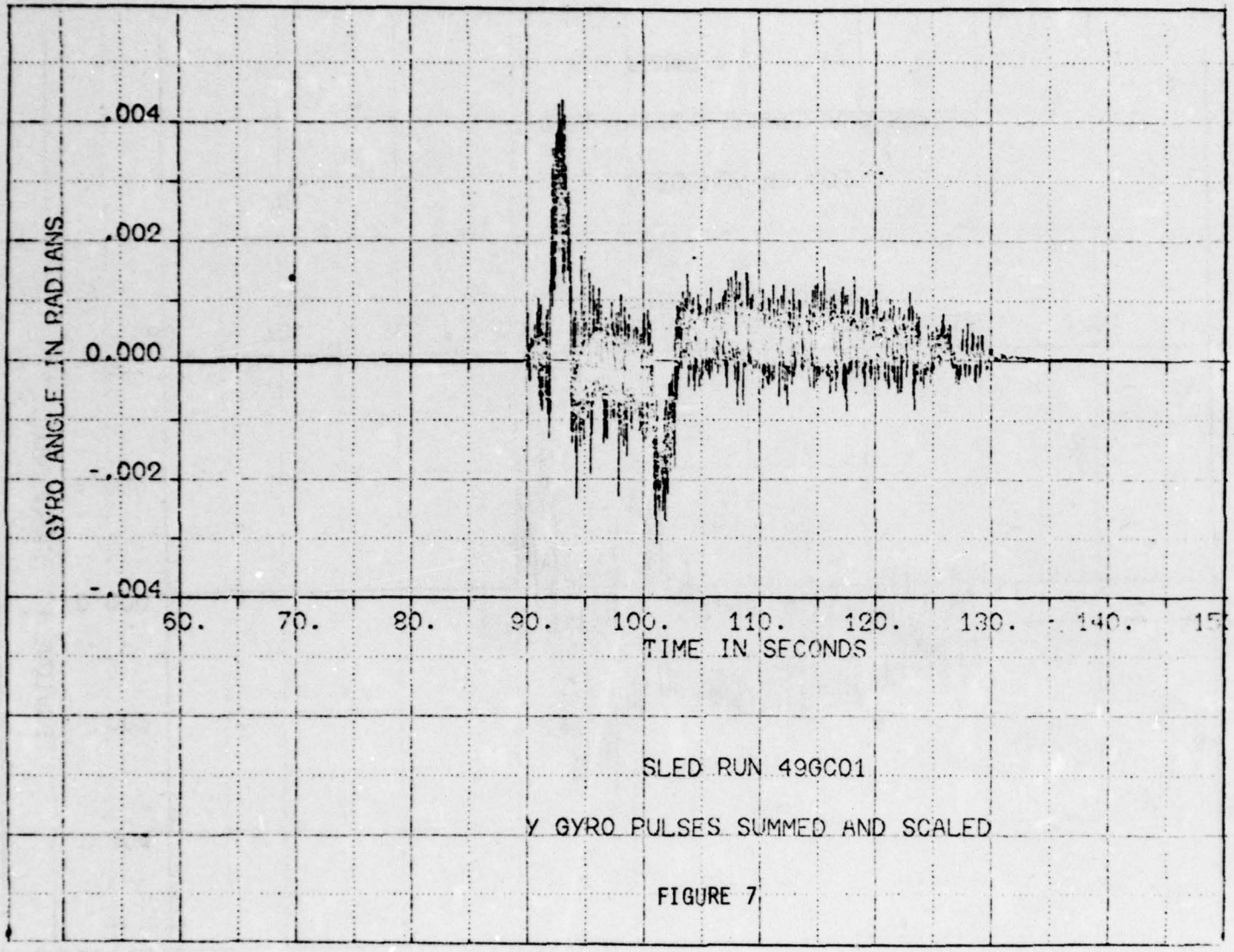
The launch position of the ATIGS accelerometers was measured by recording theodolite readings of a mirror cube mounted to the system. This provided a check on system self-alignment operation and also gave more accurate prelaunch yaw angle measurement. For Run #1 the X-accelerometer velocity error



SLED RUN 49GC01

X GYRO PULSES SUMMED AND SCALED

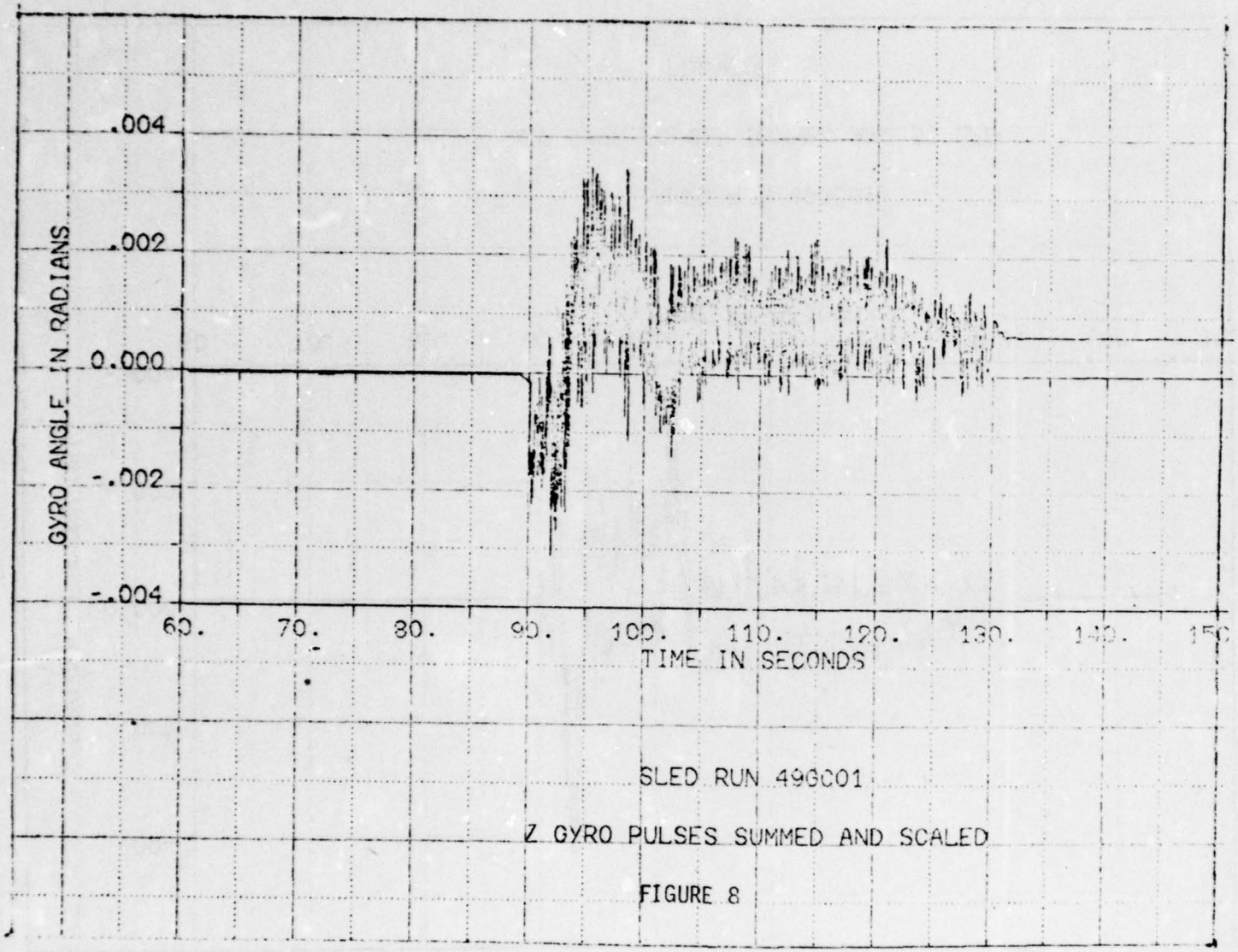
FIGURE 6



SLED RUN 49GC01

Y GYRO PULSES SUMMED AND SCALED

FIGURE 7



SLED RUN 49GC01

Z GYRO PULSES SUMMED AND SCALED

FIGURE 8

TABLE I

SLED GYRO DATA SUMMARY

SLED RUN	GYRO	VALUE AT BOOST IN MILLIRADIANS	VALUE AT WATER BRAKE IN MILLIRADIANS	VALUE AT SLED STOP POINT IN MILLIRADIANS
	X	-1.0	1.3	0.1
#1	Y	3.9	-2.0	0.0
	Z	-2.0	-0.5	0.7
	X	-0.5	1.8	1.0
#2	Y	4.0	-1.8	-0.7
	Z	-2.5	-1.0	-1.4
	X	-1.1	0.7	0.1
#3	Y	3.2	-1.5	-0.2
	Z	-2.7	0.7	0.4
	X	-0.5	1.4	0.5
#4	Y	4.3	-1.3	0.4
	Z	-1.7	0.7	1.5

(Figure 9) showed a system position change at launch. The remaining x-velocity error (DV_x) retained this constant slope throughout the sled run and after completion of sled motion. A check on the Y-gyro final offset angle was performed. The angle derived from the gravity component sensed by the X-accelerometer, at the end of each sled run, agreed closely with the Y-gyro offset angle in all runs except Run #2. The Y-accelerometer velocity error (DV_y) looked different for each sled run. This was probably caused by non-repeatable cross-track motion and vibration. The Y-accelerometer measured some of the sled-induced pitch angle and therefore had a positive DV_y value at the end of the sled run. The Z-accelerometer velocity error (DV_z), which was caused almost entirely by pitch motion, had a large positive value at launch and increased in value at water brake. This step-shaped error can be described by the coordinate function integral A_x squared where A_x is the down-track acceleration. A compilation of all sled run DV's values are found in Table II. This table displays repeatable accelerometer errors in DV_x and DV_z and shows the wider range of values in DV_y.

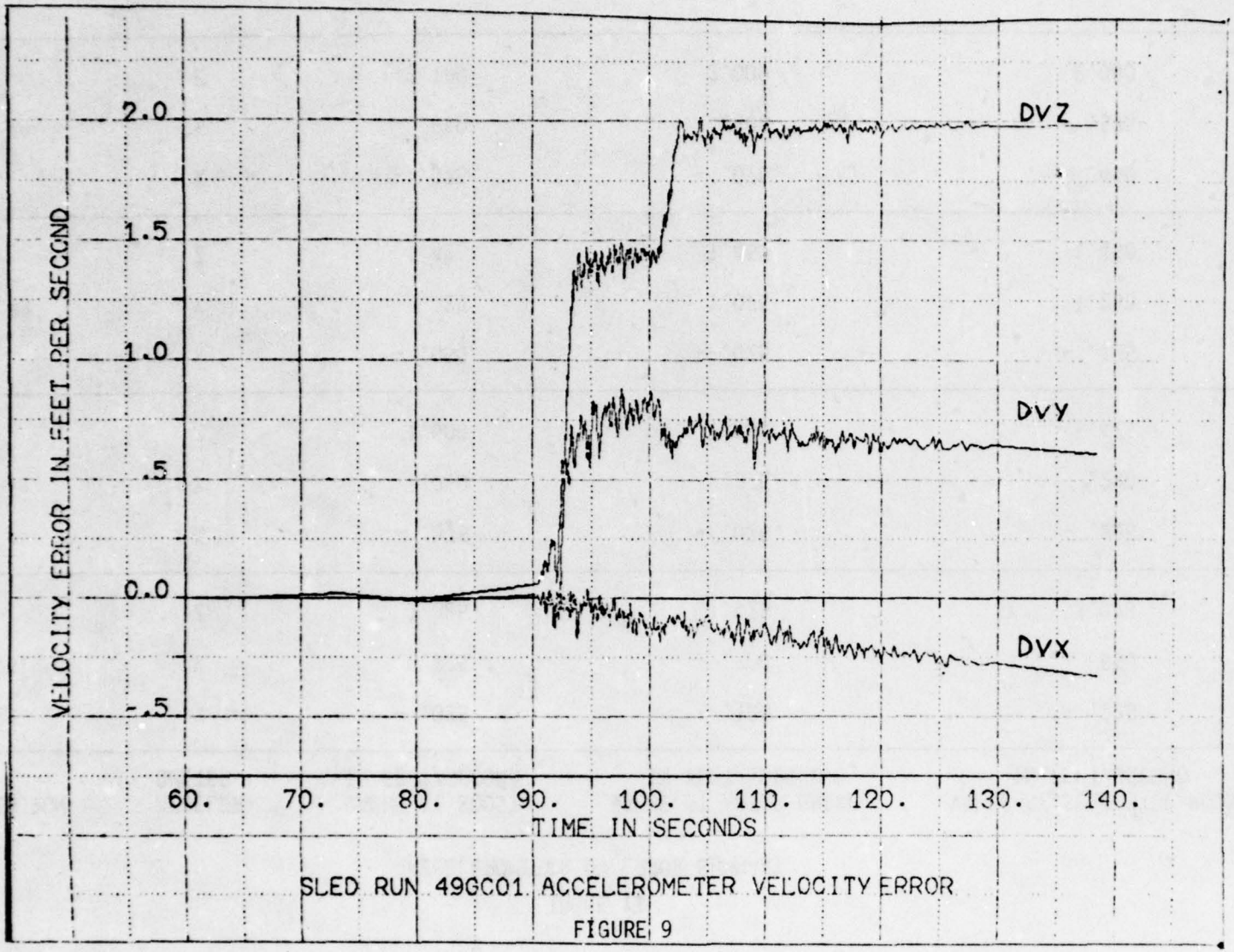
4.3 System Velocity Error

The system velocity errors (ΔV's) were formed by differencing space-time reference velocity from the computed system velocity. The system velocity was derived from raw sensor data and processed through the strap-down algorithm on a ground based computer. The ΔV's were consistently negative. Figure 10 for sled run #1 shows the negative V errors. A comparison of the accelerometer DV_x, which was essentially a sloping line, to the system ΔV_x shows that the accelerometers and/or gyros have introduced additional errors. The ΔV_x error resembles the velocity profile and is essentially zero after water brake. The gyros appear to have measured the final pitch offset angle correctly, as the ΔV_x had no major gravity component when the sled stopped. A reasonable explanation for the ΔV_x shape is that two accelerometer error terms were equal and nearly opposite in value. The error contribution from an X-accelerometer scale factor error could have been equal in magnitude but opposite in sign, to the DV error caused by a pallet pitch angle. The maximum Y-gyro angle is only .22 degrees. An X-accelerometer scale factor of the order of 230 ppm is large enough to counteract the pitch angle and provide a flat DV_x. The system ΔV_x would still contain the X-accelerometer scale factor error, and hence the velocity profile, because the Y-gyro had correctly measured the pallet motion. Actual ATIGS PCM data was processed to form a ΔV_x and it too contained the velocity error. The ΔV_y and ΔV_z errors are also negative in value as observed in Figure 10. Table III summarizes system V's for the ATIGS sled runs. The linear regression analysis presented next will tend to substantiate the postulate of major accelerometer errors.

4.4 Linear Regression Analysis

Each of the accelerometer velocity errors was fit in a linear least-squares regression procedure with the six coordinate functions shown in the following model equation.

$$\Delta V = \underset{0i}{K} + \underset{1i}{Kt} + \underset{2i}{K\hat{A}_x} + \underset{3i}{K\dot{\hat{A}}_x} + \underset{4i}{K\int\hat{A}^2} + \underset{5i}{K\hat{V}_x}$$



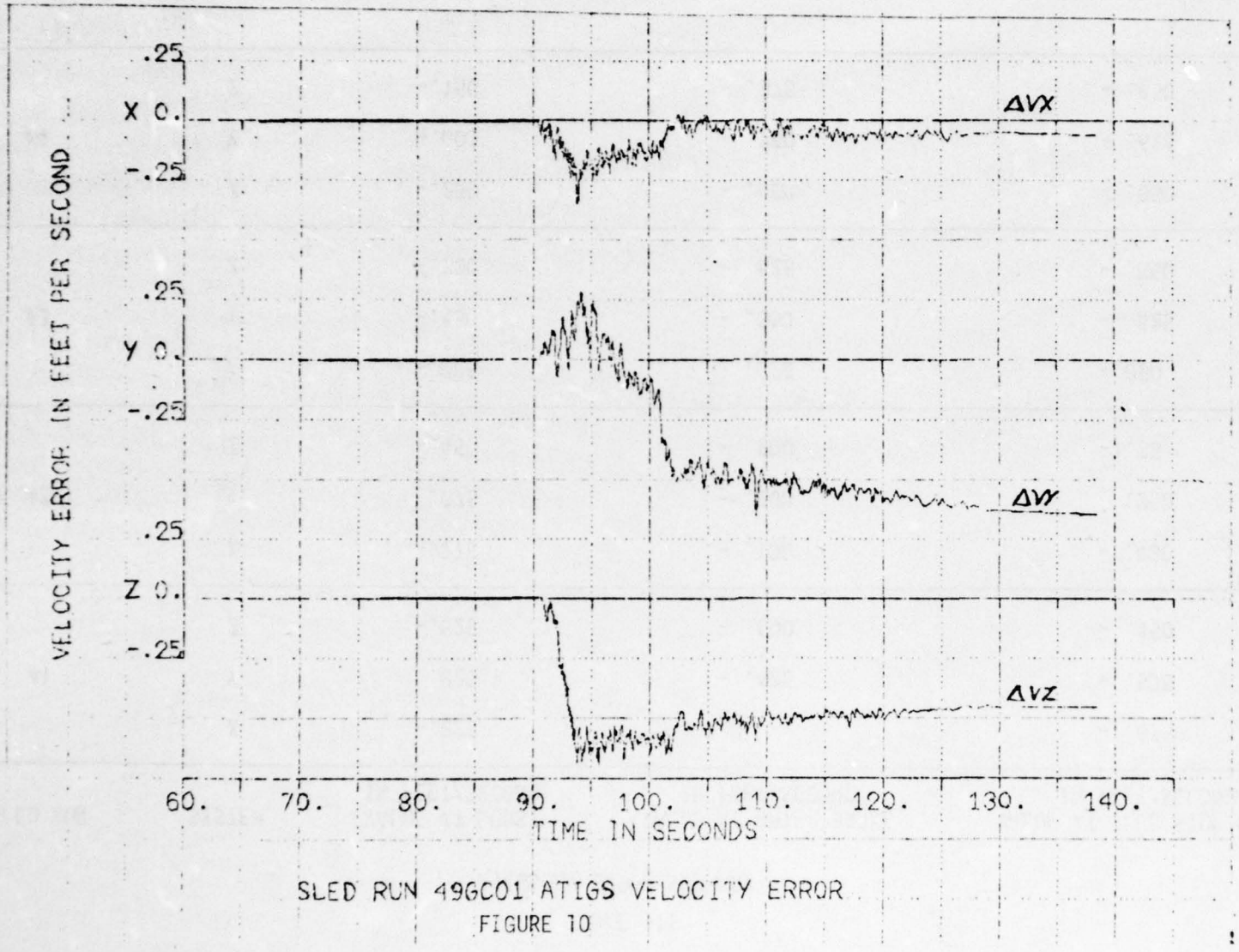
SLED RUN 49GC01 ACCELEROMETER VELOCITY ERROR

FIGURE 9

TABLE II

ACCELEROMETER DV ERROR SUMMARY

SLED RUN	ACCELER-OMETER	VALUE AT BOOST IN FEET/SECOND	VALUE AT WATER BRAKE IN FEET/SECOND	VALUE AT SLED STOP POINT IN FEET/SECOND
	X	- .025	- .100	- .225
#1	Y	.725	.700	.650
	Z	1.325	1.925	1.975
	X	- .075	- .025	- .225
#2	Y	.750	.375	.200
	Z	1.600	1.500	1.425
	X	- .050	- .025	- .425
#3	Y	.325	1.075	1.250
	Z	1.425	1.450	1.450
	X	- .075	- .075	- .450
#4	Y	- .550	.500	.575
	Z	2.150	2.000	2.000



SLED RUN 49GC01 ATIGS VELOCITY ERROR

FIGURE 10

TABLE III

ATIGS ΔV ERROR SUMMARY

SLED RUN	SYSTEM	VALUE AT BOOST IN FEET/SECOND	VALUE AT WATER BRAKE IN FEET/SECOND	VALUE AT SLED STOP POINT IN FEET/SECOND
	X	-.225	0.	- .075
#1	Y	.225	- .425	- .575
	Z	-.625	- .600	- .450
	X	-.275	- .100	- .450
#2	Y	.075	- .200	.950
	Z	-.450	- .800	-1.35
	X	-.225	.025	-.050
#3	Y	-.450	- .300	- .625
	Z	-.300	- .625	- .550
	X	-.250	- .050	- .050
#4	Y	-.600	- .750	- .625
	Z	-.150	- .375	- .450

Figure 11 shows the x, y, and z residual velocity errors after using this six term model for Run #1 accelerometer velocity errors. The X-accelerometer residual shows minor functional changes between the time interval of 95 seconds to 102.5 seconds (sled launched at 90 seconds). The Y and Z-accelerometer residuals displayed functional changes of .1 ft/sec to -.1 ft/sec during the same time interval. The Y-accelerometer residual appears to be the mirror image of the Z-accelerometer residual.

The system ΔV residuals are presented in Figure 12. The main item to observe in these residuals is the removal of some of the trends seen in the accelerometer DV residuals from 90 seconds to 100 seconds. These ΔV residuals indicate the removal by the ATIGS gyros of some of the angular motion-induced accelerometer errors. The same six coordinate functions were used in the system model. The $\int A^2$ function was left in the model to account for possible pitch and yaw gyro scale factor error. The ΔV_y and ΔV_z residuals still contained unaccounted trends.

A summary of the most important accelerometer coefficients reveals that the Y and Z accelerometer coefficients for $\int A^2$ are an order-of-magnitude larger than the X-accelerometer $\int A^2$ coefficient. This is because the δA^2 coordinate function, which was explained in the error model derivation, describes different error sources. The $\int A^2$ describes a first-order scale-factor error in the DV_x data but describes mostly pallet motion for the DV_x error and highest for the DV_y error. The DV_x error reflected low vibrational inputs in comparison to the dominant down-track velocity input and was described well by the model. The DV_y and the DV_z errors, however, contain large vibration effects in comparison to the sensed velocity components. No attempt was made to model these vibration effects; hence they remain in the residual functions.

The system model coefficients are presented in Tables IV through VI. Coefficients are not presented for Run #2 due to the questionable gyro data. An effort was now extended to remove the remaining trends in the ΔV residual data by changing the model terms.

At this point in the modeling, the assumption was made that the trends observed in the accelerometer and system residual plots, for the y and z axes, were due only to the ATIGS accelerometers. Past experience has shown that accelerometers can be sensitive to cross-axis g-inputs. The ATIGS accelerometers were already compensated for scale factor unbalance; however, this was only for the respective normal g-input axis. Based upon a postulate of an asymmetrical cross-axis g-sensitivity, a new coordinate function was tried in the model. This new function had to account for the slope changes observed on the Y and Z-accelerometer residuals and system residuals. The integral of the absolute value of the down-track acceleration ($\int |A_x|$) was then derived. Linear regression analysis was repeated for the accelerometer (DV) errors in the y and z-axes using the new coordinate function, $\int |A_x|$. The accelerometer error had a residual improvement on both the y and z-residuals; the slopes were decreased.

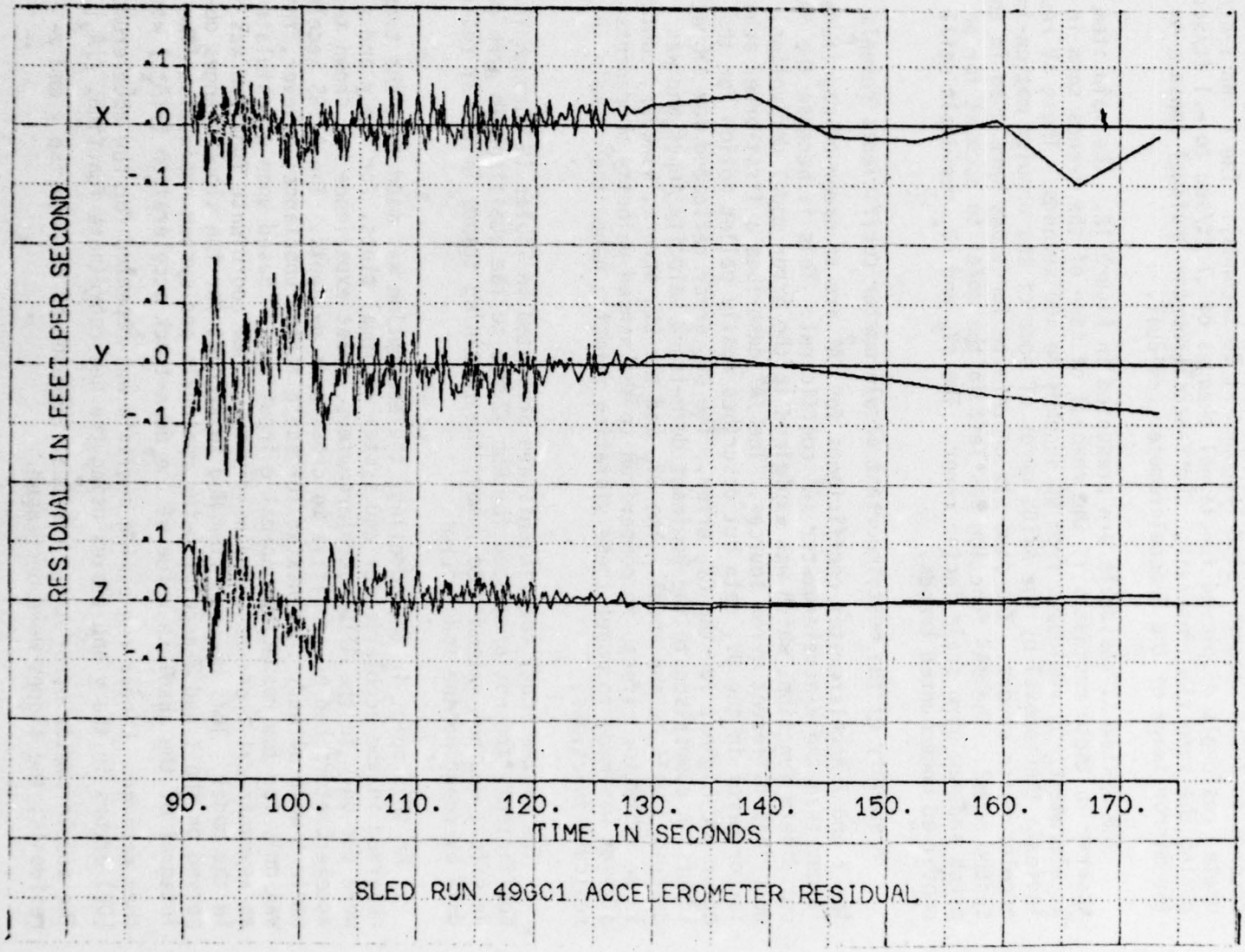

RESIDUAL IN FEET PER SECOND
X
Y
Z
.1
.0
-.1
90.
100.
110.
120.
130.
140.
150.
160.
170.
TIME IN SECONDS
SLED RUN 49GC1 ACCELEROMETER RESIDUAL

FIGURE 11

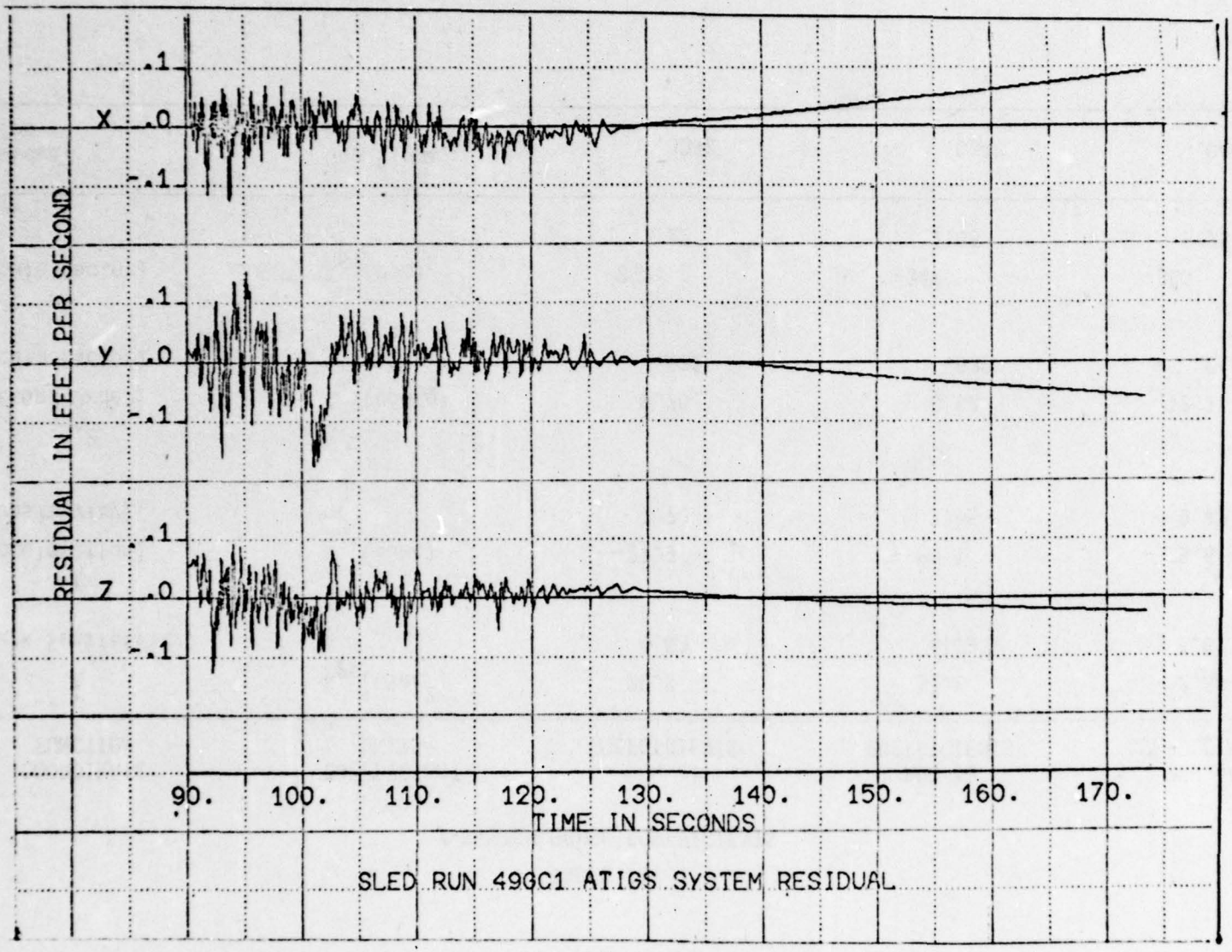

RESIDUAL IN FEET PER SECOND
X
Y
Z
.1
.0
-.1
90.
100.
110.
120.
130.
140.
150.
160.
170.
TIME IN SECONDS
SLED RUN 49GC1 ATIGS SYSTEM RESIDUAL

FIGURE 12

TABLE IV

X-SYSTEM MODEL COEFFICIENTS

COORDINATE FUNCTION	COEFFICIENT UNITS	RUN #1 COEFFICIENTS	RUN #3 COEFFICIENTS	RUN #4 COEFFICIENTS
$\dot{A}$	$K_{2i}(\mu Sec^2)$	26.7	37.2	2.84
(Jerk Sensitivity)	σ	4.53	4.83	5.67
A				
(Acceleration)	$K_{3i}(\mu Sec)$	-21.9	- 80.1	- 39.6
(Sensitivity)	σ	7.70	7.95	9.42
$\int A^2$				
(Second Order)	K_{4i}(ppm/g)	6.76	8.58	12.1
(Scale Factor)	σ	.632	.632	.846
V				
(Scale Factor)	K_{5i}(ppm)	-282.	-348.	-350.
	σ	7.22	7.05	8.75
Residual Value	One Sigma σR	.0342	.0347	.0422

TABLE V

Y-SYSTEM MODEL COEFFICIENTS

COORDINATE FUNCTION	COEFFICIENT UNITS	RUN #1 COEFFICIENTS	RUN #3 COEFFICIENTS	RUN #4 COEFFICIENTS
$\dot{A}$	$K_{2i}(\mu Sec^2)$	- 42.1	-65.8	-64.2
(Jerk Sensitivity)	σ	7.76	11.1	11.0
A	$K_{3i}(\mu Sec)$	- 34.5	18.6	-44.2
(Acceleration Sensitivity)	σ	13.2	18.3	18.2
$\int A^2$	K_{4i}(arc-sec/g)	- 10.0	- 9.35	-10.1
(Pallet Motion)	σ	.223	.296	.307
V	K_{5i}(arc-sec)	162.	-16.7	- 5.88
(Misalignment	σ	2.55	10.8	3.50
Residual Value	One Sigma σR	.059	.080	.082

TABLE VI

Z-SYSTEM MODEL COEFFICIENTS

COORDINATE FUNCTION	COEFFICIENT UNITS	RUN #1 COEFFICIENTS	RUN #3 COEFFICIENTS	RUN #4 COEFFICIENTS
$\dot{A}$	$K_{2i}(\mu Sec^2)$	-25.2	-56.5	-17.5
(Jerk Sensitivity)	σ	5.55	6.68	7.58
A	$K_{3i}(\mu Sec)$	22.7	99.2	10.4
(Acceleration Sensitivity)	σ	7.73	11.0	10.9
$\int A^2$	K_{4i}(Arc-Sec/g)	- 7.47	-10.1	- 7.39
(Pallet Motion)	σ	.131	.178	.184
V	K_{5i}(Arc-Sec)	-55.9	21.7	4.37
(Misalignment)	σ		2.01	2.10
Residual Value	One Sigma σR	.034	.048	.049

The residual functions from the new fit to the y and z DV's were significantly improved. Hence, the postulate of the new accelerometer error source appeared to be justified. Figure 13 shows the elimination of the slopes in in DV_y and DV_z. The new coordinate function was then used for the system ΔV's instead of the $\int A^2$. The assumption here was that the gyros had no major scale factor errors and hence there existed no need for the $\int A^2$ function in the model.

In an effort to improve both the accelerometer and the system error description (for y and z only), the function $\int A^2$ was returned to the new model and two higher order asymmetric error terms, $|A_x|$ and $|A_x|$ were used.

$$\Delta V_y \text{ or } _z = K_{0i} + K_{1i}t + K_{2i}\hat{A}_x + K_{3i}\hat{A}_x + K_{4i}\int\hat{A}_x^2 + K_{5i}\hat{V}_x$$

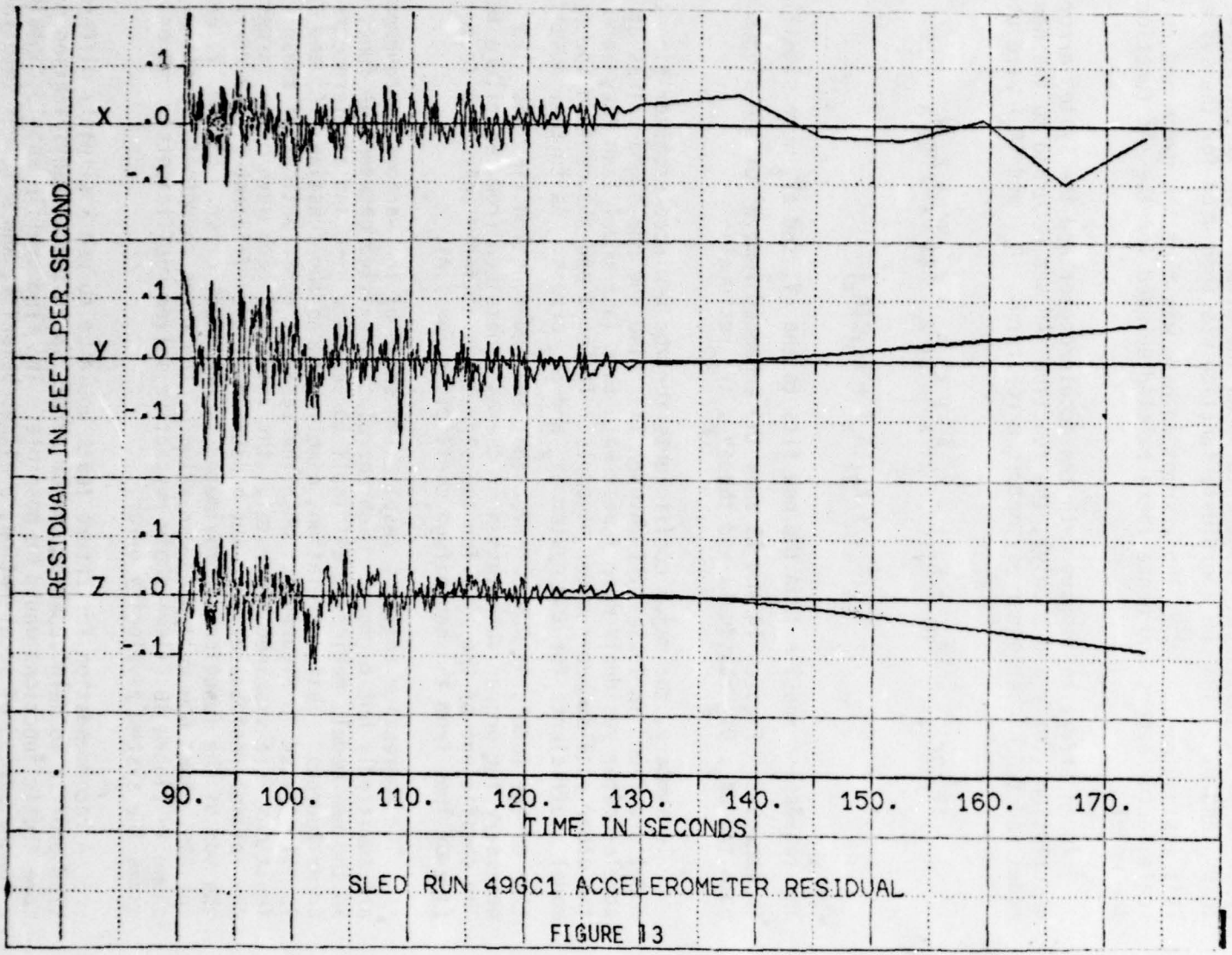
$$+ K_{6i}|\hat{A}_x| + K_{7i}|\hat{A}_x| + K_{8i}\int|\hat{A}_x|$$

The regression results from the new fits to the ΔV_y and ΔV_z were significantly improved. Figures 14 and 15 show the enhanced removal of the slopes in both the DV_y, DV_z residuals and the ΔV_y, ΔV_z residuals.

In summary, the major coefficients for the new accelerometer nine-term model are found in Tables VII through IX. Also the one sigma values of the accelerometer residuals were lowest with this last model than they were for the other accelerometer model attempts. Tables X and XII contain the final model coefficients for the system ΔV_y and ΔV_z errors. As further justification of the model, it was observed that the new function $\int|A|$ was also necessary for proper description of the ΔV's obtained from centrifuge tests. The coefficient of the $\int|A|$ for the sled tests differed only by a factor of five or less from the centrifuge coefficient for $\int|A|$.

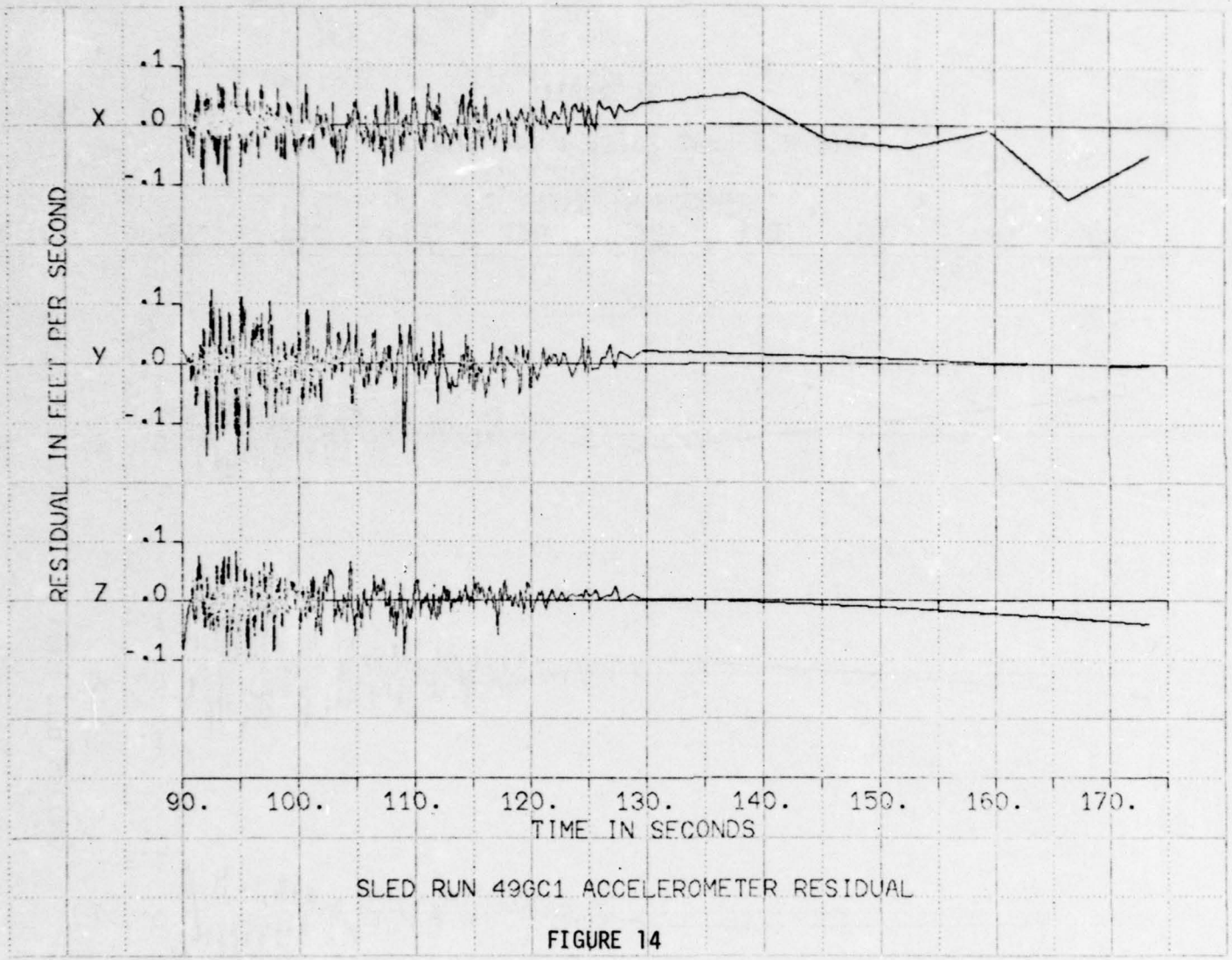
The regression analysis results, in spite of the various improvements, are admittedly not perfect. High correlation existed between two functions in the new model, making it difficult to separate gyro and accelerometer error sources. This correlation, namely between the function $\int|A|$ and $\int A^2$, is illustrated in Figure 16. When the residual contributions of these functions were examined separately, the values of each were often larger than the initial residual error. But because of the coefficient sign differences, the sum of the functions approximated the residual error. Figure 17, nevertheless, shows how well a summed value of the three coordinate functions, shown in Figure 16 (times their respective solved coefficients), approximates the system z-velocity error.

A recommendation for future tests would be to use a slightly different sled profile to help separate system errors so that the identification of more exotic functions would be possible. The sled profile should contain a longer period of acceleration, a higher velocity, and a longer interval of



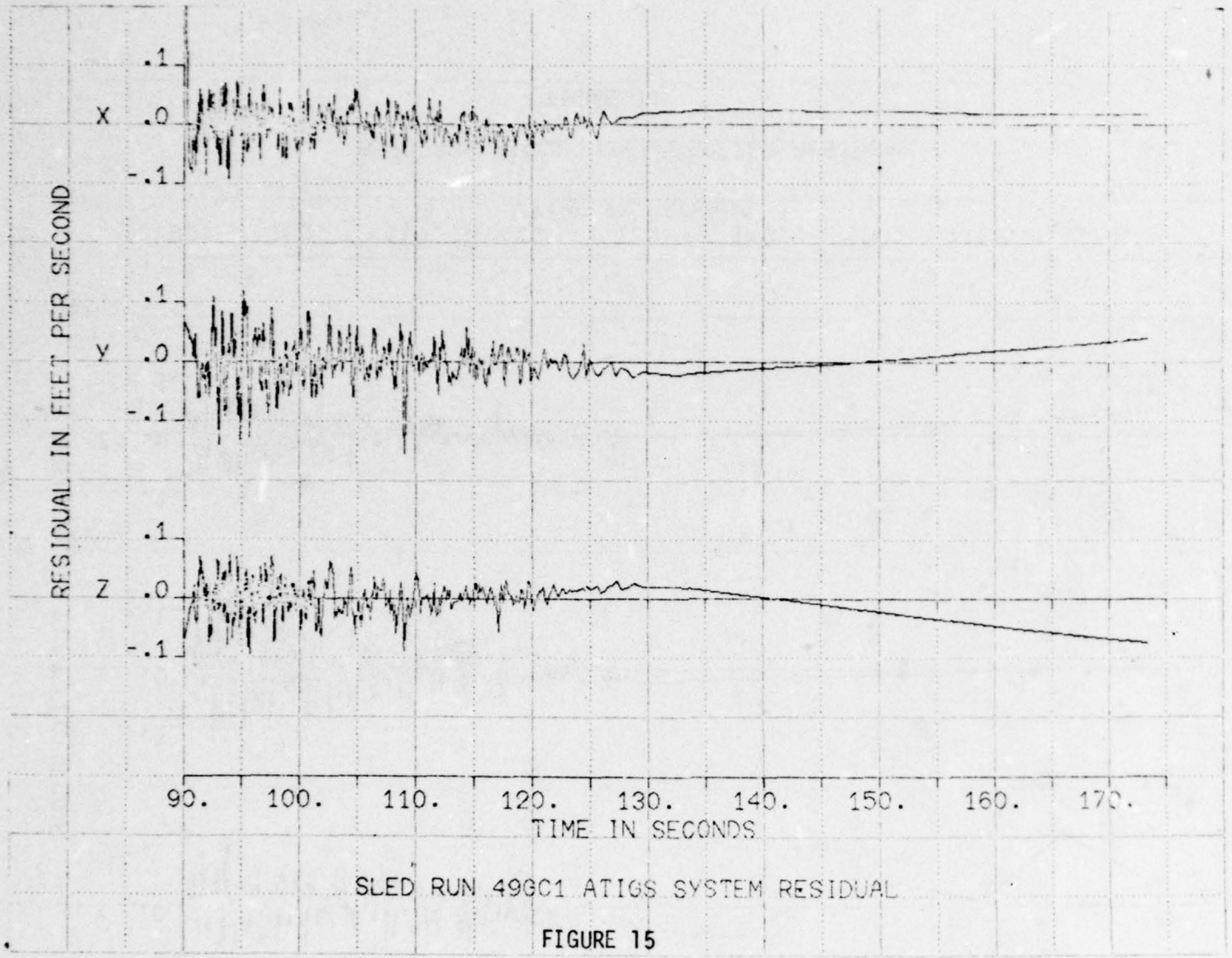
SLED RUN 49GC1 ACCELEROMETER RESIDUAL

FIGURE 13



SLED RUN 49GC1 ACCELEROMETER RESIDUAL

FIGURE 14



SLED RUN 49GC1 ATIGS SYSTEM RESIDUAL

FIGURE 15

TABLE VII

X-ACCELEROMETER MODEL COEFFICIENTS

COORDINATE FUNCTION	COEFFICIENT UNITS	RUN #1 COEFFICIENTS	RUN #2 COEFFICIENTS	RUN #3 COEFFICIENTS	RUN #4 COEFFICIENTS
$\dot{A}$	$K_{2i}(\mu Sec^2)$	38.6	30.5	37.2	49.5
(Jerk Sensitivity	σ (one sigma)	4.36	4.68	4.67	5.27
$\lvert\dot{A}\rvert$	$K_{6i}(\mu Sec^2)$	- 26.0	- 33.2	2.93	- 41.4
(Asymmetric Sensitivity)	σ	4.57	5.12	4.85	5.56
A	$K_{3i}(\mu Sec)$	- 18.1	-141.	- 56.3	- 87.9
(Delay)	σ	15.0	154.	14.4	17.1
$\lvert A\rvert$ (Asymmetrical)	$K_{7i}(\mu Sec)$	16.8	83.4	- 21.8	116.
(Sensitivity)	σ	16.2	16.5	15.4	18.3
V	K_{5i}(ppm)	-211.	- 94.1	-323.	-366.
(Misalignment)	σ	29.5	11.6	30.1	35.3
$\int\lvert A\rvert$ (Asymmetrical)	K_{8i}(ppm)	-338.	196.	-483.	-482.
(Sensitivity)	σ	75.2	30.9	83.8	95.1
$\int A^2$ (First Order)	$K_{4i}\frac{(ppm)}{g}$	43.9	- 9.18	60.4	66.2
(Scale Factor	σ	7.54	2.83	8.36	9.35
Residual Value	σ_R	.0307	.0335	.0315	.0370

TABLE VIII

Y-ACCELEROMETER MODEL COEFFICIENTS

COORDINATE FUNCTION	COEFFICIENT UNITS	RUN #1 COEFFICIENTS	RUN #2 COEFFICIENTS	RUN #3 COEFFICIENTS	RUN #4 COEFFICIENTS
$\dot{A}$	$K_{2i}(\mu Sec^2)$	- 29.4	- 54.4	- 25.9	- 31.3
(Jerk Sensitivity)	σ (One sigma)	6.97	6.79	6.49	7.78
$\lvert\dot{A}\rvert$ (Asymmetrical)	$K_{6i}(\mu Sec^2)$	- 91.1	-101.	- 40.6	- 89.9
(Cross-Axis Sensitivity)	σ	7.30	7.42	6.75	8.19
A	K_{3i}(Sec)	34.1	54.9	102.	99.4
(Acceleration Sensitivity)	σ	23.9	22.4	20.0	25.2
$\lvert A\rvert$ (Asymmetrical	K_{7i}(Sec)	-106.	172.	-576.	- 53.8
(Cross-Axis Sensitivity)	σ	25.9	22.4	20.0	26.9
V	K_{5i}(Arc-Sec)	176.	130.	-178.	-224.
(Misalignment)	σ	9.73	3.47	8.63	10.7
$\int\lvert A\rvert$ (Asymmetrical)	$K_{8i}\frac{\text{(Parts Y)}}{(10^6 \text{ Parts X})}$	967.	426.	31.4	232.
(Cross-Axis Sensitivity)	σ	120.	44.9	11.6	140.
$\int A^2$	$K_{4i}\frac{\text{(Arc-Sec)}}{g}$	- 11.76	1.02	24.6	6.21
(Pallet Motion)	σ	2.49	.847	2.40	2.84
Residual Value	σ_R	.0491	.0485	.0438	.046

TABLE IX

Z-ACCELEROMETER MODEL COEFFICIENTS

COORDINATE FUNCTION	COEFFICIENT UNITS	RUN #1 COEFFICIENTS	RUN #2 COEFFICIENTS	RUN #3 COEFFICIENTS	RUN #4 COEFFICIENTS
$\dot{A}$	$K_{2i}(\mu Sec^2)$	3.68	- 58.2	- 31.7	20.1
(Jerk Sensitivity)	σ (One Sigma)	4.01	7.37	4.85	4.82
$\lvert\dot{A}\rvert$	$K_{6i}(\mu Sec^2)$	20.6	5.57	7.69	19.0
(Cross-Axis Sensitivity)	σ	4.20	8.05	5.04	5.08
A	$K_{3i}(\mu Sec)$	-139.	-163.	107.	-136.
(Acceleration Sensitivity)	σ	13.8	24.3	15.0	15.6
$\lvert A\rvert$					
(Asymmetrical)	$K_{7i}(\mu Sec)$	-235.	-311.	-226.	-301.
(Cross-Axis Sensitivity)	σ	14.9	26.0	16.1	16.7
V	K_{5i}(Arc-Sec)	-165.	128.	31.5	69.5
(Misalignment)	σ	5.60	3.77	6.45	6.66
$\int\lvert A\rvert$					
(Asymmetrical)	$K_{8i}\frac{(\text{Parts Z})}{}$	-934.	1385.	-325.	-904.
(Cross-Axis Sensitivity)	σ (10^6 Parts X)	69.3	48.7	87.1	86.9
$\int A^2$	$K_{4i}\frac{(\text{Arc-Sec})}{g}$	57.4	6.13	33.0	52.6
(Pallet Motion)	σ	1.43	.919	1.79	1.76
Residual Value	σ_R	.0283	.0527	.0327	.0339

TABLE X

X SYSTEM MODEL COEFFICIENTS

COORDINATE FUNCTION	COEFFICIENT UNITS	RUN #1 COEFFICIENTS	RUN #3 COEFFICIENTS	RUN #4 COEFFICIENTS
$\dot{A}$	$K_{2i}(\mu Sec^2)$	37.3	45.4	37.2
(Jerk Sensitivity)	σ (One Sigma)	4.38	4.85	5.19
$\lvert\dot{A}\rvert$				
(Asymmetrical)	$K_{6i}(\mu Sec^2)$	- 19.1	19.1	42.0
(Sensitivity)	σ	4.59	5.03	5.47
A	$K_{3i}(\mu Sec)$	- 45.5	- 77.1	-117.
(Delay)	σ	15.1	14.9	16.8
$\lvert A\rvert$				
(Asymmetrical)	$K_{7i}(\mu Sec)$	62.6	23.3	159.
(Sensitivity)	σ	16.3	16.0	18.0
V	K_{5i}(ppm)	-551.	-606.	-619.
(Misalignment)	σ	29.6	31.4	34.7
$\int\lvert A\rvert$				
(Asymmetrical)	$K_{8i}\frac{\text{(Parts X)}}{(10^6 \text{ Parts X})}$	-790.	-840.	-836.
(Sensitivity)	σ	75.6	87.0	93.6
$\int A^2$				
(First Order)	$K_{4i}\frac{(ppm)}{g}$	81.8	88.0	89.3
(Scale Factor)	σ	7.57	8.68	9.20
Residual Value	σ_R	.0309	.0327	.0365

TABLE XI

Y SYSTEM MODEL COEFFICIENTS

COORDINATE FUNCTION	COEFFICIENT UNITS	RUN #1 COEFFICIENTS	RUN #3 COEFFICIENTS	RUN #4 COEFFICIENTS
$\dot{A}$	$K_{2i}(\mu Sec^2)$	- 26.1	- 18.5	- 20.4
(Jerk Sensitivity)	σ (One Sigma)	6.52	6.10	7.43
$\lvert A \rvert$ (Asymmetrical)	$K_{6i}(\mu Sec^2)$	- 71.7	- 57.4	- 76.2
(Cross-Axis Sensitivity)	σ	6.83	6.34	7.82
A	$K_{3i}(\mu Sec)$	121.	102.	- 79.8
(Acceleration Sensitivity)	σ	22.4	18.8	24.1
$\lvert A \rvert$ (Asymmetrical)	$K_{7i}(\mu Sec)$	-322.	-511.	-307.
(Cross-Axis Sensitivity)	σ	24.2	20.2	25.7
V	K_{5i}(Arc-Sec)	199.	- 47.0	- 33.5
(Misalignment)	σ	9.10	8.11	10.2
$\int \lvert A \rvert$ (Asymmetrical	$K_{8i} \frac{\text{(Parts Y)}}{}$	764.	493.	491.
(Cross-Axis Sensitivity)	σ (10^6 Parts X)	113.	110.	134.
$\int A^2$	$K_{4i} \frac{\text{(Arc-Sec)}}{g}$	- 22.5	- 10.8	- 11.9
(Pallet Motion)	σ	2.32	2.25	2.72
Residual Value	σ_R	.046	.0412	.0522

TABLE XII

Z SYSTEM MODEL COEFFICIENTS

COORDINATE FUNCTION	COEFFICIENT UNITS	RUN #1 COEFFICIENTS	RUN #3 COEFFICIENTS	RUN #4 COEFFICIENTS
$\dot{A}$	$K_{2i}(\mu Sec^2)$	.625	- 25.3	21.4
(Jerk Sensitivity)	σ (One Sigma)	4.02	4.65	4.53
$\lvert\dot{A}\rvert$ (Asymmetrical)	$K_{6i}(\mu Sec^2)$	- 2.62	1.12	1.56
(Cross-Axis Sensitivity	σ	4.21	4.23	4.77
A	$K_{3i}(\mu Sec)$	45.6	121.	- 5.55
(Acceleration Sensitivity)	σ	13.8	14.3	14.7
$\lvert A\rvert$ (Asymmetrical)	$K_{7i}(\mu Sec)$	-134.	-260.	-214.
(Cross-Axis Sensitivity)	σ	14.9	15.4	15.7
V	K_{5i}(Arc-Sec)	-129.	- 29.9	- 50.1
(Misalignment)	σ	5.60	6.18	6.25
$\int\lvert A\rvert$ (Asymmetrical)	$K_{8i}\frac{\text{(Parts Z)}}{(10^6 \text{ Parts X})}$	-746.	-214.	-777.
(Cross-Axis Sensitivity)	σ	69.3	83.5	81.6
$\int A^2$	$K_{4i}\frac{\text{(Arc-Sec)}}{g}$	9.92	.948	13.0
(Pallet Motion)	σ	1.43	1.72	1.66
Residual Value	σ_R	.0283	.0314	.0318

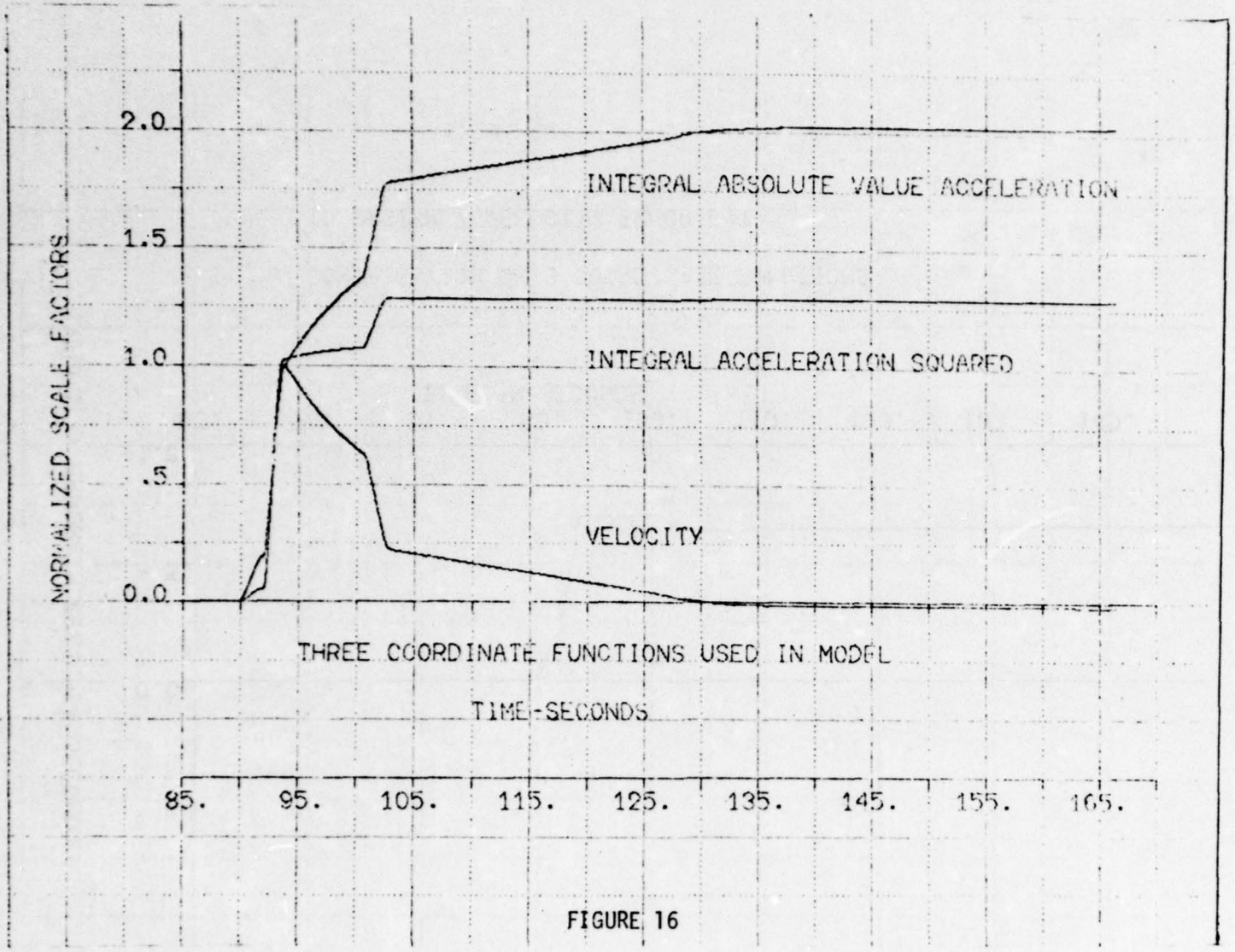
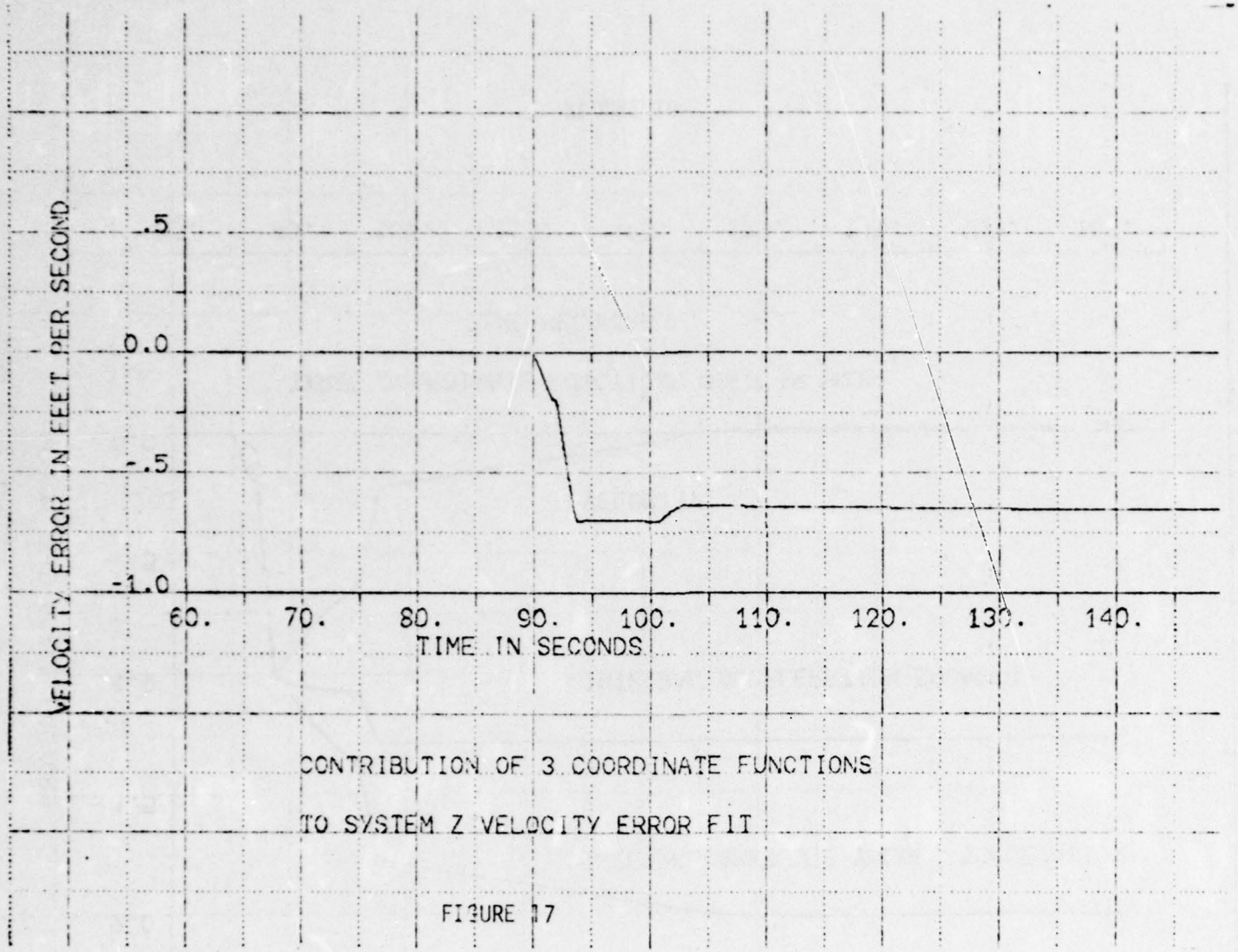

NORMALIZED SCALE FACTORS
2.0
1.5
1.0
.5
0.0
INTEGRAL ABSOLUTE VALUE ACCELERATION
INTEGRAL ACCELERATION SQUARED
VELOCITY
THREE COORDINATE FUNCTIONS USED IN MODEL
TIME-SECONDS
85.
95.
105.
115.
125.
135.
145.
155.
165.

FIGURE 16



CONTRIBUTION OF 3 COORDINATE FUNCTIONS

TO SYSTEM Z VELOCITY ERROR FIT

FIGURE 17

deceleration. This would allow greater separation of the coordinate functions during linear regression analysis and may result in a better model of accelerometer and gyro performance.

A further suggestion would be to utilize a better quality accelerometer in the system.

5. CONCLUSIONS

The conclusions derived from the three-month ATIGS test effort are summarized below.

5.1 The ATIGS system was subjected to four sled runs. The data from three sled runs was submitted to fine-grain analysis.

5.2 Twelve calibrations were performed during the ATIGS test program. The system was calibrated before and after each sled run and each centrifuge test series. The gyro and accelerometer coefficients remained stable across the dynamic test environments.

5.3 The predominant system error source appeared to be the accelerometers. Three unusual accelerometer errors were postulated which accounted for most of the observed ATIGS error. The postulated errors are due to asymmetrical cross-axis acceleration sensitivity. This error was observed in the data from both sled and centrifuge tests.

5.4 No specific gyro errors, except for a residual fixed drift (.04 deg/hr), based on centrifuge data, could be identified. This may be because of the existence of as yet undefined errors in the gyros and/or in the accelerometers (which affect the system output).

5.5 The system velocity errors could be modeled to within .05 ft/sec (one sigma) from sled test data.

5.6 No significant errors were attributable to the strap-down algorithm. The 100 Hz update rate was adequate for system navigation during both sled and centrifuge tests.

5.7 In retrospect, consideration of the unusual accelerometer errors indicates that the sled and centrifuge acceleration profiles require optimization. Sled maximum velocity should be increased (from 860 ft/sec to 1600 ft/sec) to aid in model error-term separation.

5.8 Improved accelerometers would enable the sled tests to center specifically on identification of possible laser gyro errors.

5.9 Improved test and analysis techniques were developed for evaluating strap-down guidance systems.

REFERENCES

1. Morgan, A., "Attachment IV Flight Program Requirements Document (Preliminary)", Honeywell, Inc., Aerospace Division, St. Petersburg, Florida, 23 May 1973 in support of ATIGS Program.

2. Ingold, N., Smith, Capt W., "Rocket Sled Test Evaluation of the Lance Gyro by Strap-Down Analysis Techniques", Sixth Guidance Test Symposium Proceedings, AFSWC TR-72-73, Volume I.

3. Cosentino, D., Walker, D., "Rocket Sled and Centrifuge Tests of the Advanced Tactical Inertial Navigation Systems (ATIGS)", Final Report, ADTC TR-77-7.

EIGHTH BIENNIAL GUIDANCE TEST SYMPOSIUM

CALIBRATION AND FIELD TESTING OF A HIGH-QUALITY STRAPPED DOWN INERTIAL NAVIGATION SYSTEM

AUTHORS: GEORGE R. TAYLOR
DONALD J. PASIK

RAYTHEON COMPANY
SUDBURY, MASSACHUSETTS

JOHN W. FISH
THE CHARLES STARK DRAPER LABORATORY, INC.
CAMBRIDGE, MASSACHUSETTS

ACKNOWLEDGMENT

The authors wish to acknowledge the patient managerial support of this test program on the part of the Raytheon Company and the Charles Stark Draper Laboratory. The original concept of deriving error feedback information from natural kinematic constraints on vehicle motion, as applied in the ZOSS and ZEUS filters described herein, was due to James B. Matthews of Raytheon. Special thanks are due to Sheldon Buck and John Mastroelli of CSDL for support of the gravimeter measurements. Thanks are also due to James B. Matthews of Raytheon and Professor Wallace Vander Velde of M.I.T. for concept and original development of the special calibration methods.

ABSTRACT

This paper presents the results of dynamic land navigation tests using modern filter techniques with a high accuracy strapped down inertial measurement unit. These tests were part of a continuing Raytheon program to develop a high accuracy autonomous strapped down navigation system. The major goal here was to demonstrate improved accuracy by combining the high-quality CSDL SIMU with computational improvements developed earlier using a ring laser gyro system. Calibration and field test methods and navigation results are summarized. Operating in a self-damped mode without external aids for either initial alignment or en route corrections, this Raytheon/CSDL system was capable of land navigation within 0.1 miles horizontal, and several hundred feet vertical, over a 240-mile six-hour course.

Performance at this level requires excellent prior calibration. Since the system could not be conveniently returned to the laboratory between tests, a number of calibration methods useful in the field were devised. These calibration methods are described in the paper in some detail, and examples are given. In particular, it is shown that accurate laboratory fixtures are not necessary to calibrate instrument alignments and scale factors, which are often the critical error sources for strapped down inertial navigators.

Many of the test conditions were similar to earlier tests of a Ring Laser Gyro strapped down navigation system, reported at the Seventh Biennial Guidance Test Symposium. Comparisons are drawn between the two series of field tests, and it is suggested that the remarkably good earlier results could probably have been further improved using the software refinements developed for the later series of tests. Data are also presented which suggest that the residual errors in the later test series are largely attributable to unmodeled gravity anomalies and deflections of the vertical. If this theory is correct, then a further navigation improvement would be obtained by allowing the navigation filters to track the irregularities in the gravity field.

TABLE OF CONTENTS

Section		Page
1	INTRODUCTION	1-1
2	DESCRIPTION OF EQUIPMENT	2-1
	2.1 Introduction	2-1
	2.2 Strapdown Inertial Measurement System (SIMS)	2-1
	2.3 Raytheon RAC-251 General Purpose Computer	2-12
3	FILTER DESCRIPTION	3-1
	3.1 Introduction	3-1
	3.2 Horizontal Navigation Filter	3-2
	3.3 Zero Side-Slip (ZOSS) Prefilter	3-7
	3.4 Zero Up-Slip (ZEUS) Filter	3-9
4	CALIBRATION TECHNIQUES	4-1
	4.1 Introduction: Calibration Requirements and Philosophy	4-1
	4.2 Field Calibration Techniques	4-2
	4.3 Laboratory Calibration Techniques	4-4
5	LOCAL DYNAMIC TESTS	5-1
6	EXTENDED NAVIGATION TESTS	6-1
7	SUMMARY AND CONCLUSIONS	7-1
APPENDIX:	SQUARE-ROOT KALMAN FILTER ALGORITHM	A-1
REFERENCES		

LIST OF ILLUSTRATIONS

Figure		Page
2-1	Raytheon/CSDL Strapdown System Equipment Laboratory	2-2
2-2	Raytheon Mobile Inertial Guidance and Navigation Laboratory	2-2
2-3	SIMS Block Diagram	2-3
2-4	Top View of SIMU	2-4
2-5	Bottom View of SIMU	2-5
2-6	SIMU Remote Control Unit	2-7
2-7	SIMU Phase Locked Loops	2-8
2-8	SIMS Local Control Unit	2-10
2-9	Data Bus Format - 2's Complement Notation	2-11
2-10	RAC-251 Computer Assembly	2-13
2-11	RAC-251 Computer Architecture	2-14
2-12	Control Display Unit	2-15
6-1	Extended ZOSS Longitude RMS Errors	6-5
6-2	Extended ZOSS Latitude RMS Errors	6-6
6-3	Massachusetts Gravity Anomaly Contour Map	6-9
6-4	Extended ZOSS Run #15 Errors	6-10
6-5	Indicated Altitude and Gravity Anomaly, ZOSS Run #15	6-12
6-6	Measured and Indicated Gravity Anomalies, ZOSS Run #17	6-13
6-7	1-Sigma Longitude Error Envelope	6-14
6-8	1-Sigma Latitude Error Envelope	6-15

LIST OF TABLES

Table		Page
5-1	Sudbury, Massachusetts Test Course Checkpoint List	5-3
5-2	Local Test Course ZOSS Latitude Errors	5-4
5-3	Local Test Course ZOSS Longitude Errors	5-5
5-4	Local Test Course ZOSS Altitude Errors	5-7
6-1	Massachusetts Turnpike Test Course Checkpoint Description	6-2
6-2	Filter Parameters	6-3

SECTION 1

INTRODUCTION

This paper updates a series of past reports (References [1], [2], [3]) on strapped down inertial navigation tests at Raytheon. For the currently described test series, as was often the case in the past, the test program was sponsored jointly by Raytheon and the Charles Stark Draper Laboratory (CSDL), the latter providing the strapdown inertial measurement unit (SIMU), its interfaces, and support.

The objective of the currently reported program was to demonstrate improved accuracy by combining the high-quality CSDL SIMU with the computational improvements developed during a prior test program using a ring laser gyro system (Reference [3]). The demonstration was successful: spherical errors on the order of 25 feet for a terrestrial navigator over a 17-mile, one-hour course; and spherical errors on the order of 500 feet over a 234-mile, six-hour course. These results compare with an expected free navigation performance of about half a nautical mile per hour for an inertial unit of the CSDL SIMU quality.

Thus, our improvement compared to free navigation was by a factor of 30 to 1 or better, a result similar to prior tests with the ring laser gyro system. However, to accomplish this improvement, careful prior calibration and improved computational filters were required; accordingly, these are described in more detail here than in past reports.

Not all readers will wish to scrutinize with equal intensity all sections of this paper. Accordingly, we have tried to organize the sections to appeal to special interests the reader may have. Section 2 describes the hardware of the navigation system, with special emphasis on the unusual - e.g., phase locked loops to interpolate pulse outputs from the inertial instruments. Section 3 describes the special filters used in the navigation system software, with further algorithmic details in the Appendix; the traditional bugaboos of strapped down navigation software - attitude update, velocity resolution, etc. - are regarded as solved problems, and are accordingly ignored in the current paper. Section 4 describes the calibration methods employed in the test program. Sections 5 and 6 describe the test results. The development activity in arriving at the results is not suppressed; i.e., errors discovered and subsequently corrected; computational and

procedural improvements developed during the test series; the pleasant problem of navigating so accurately that map errors have an important influence on test evaluations; and, finally, hypotheses of how the excellent results to date may be further improved in the future.

SECTION 2

DESCRIPTION OF EQUIPMENT

2.1 INTRODUCTION

The strapdown system used for these tests is shown in Figure 2-1. The equipment was mounted and evaluated in the Raytheon Mobile Guidance and Navigation Laboratory shown in Figure 2-2. This vehicle is a 35-foot long by 8-foot wide modified Thomas bus chassis on a ruggedized 1971 International Harvester frame. It has a five-speed transmission with a two-speed axle. The interior floor has a cargo holding area of approximately 250 square feet with cargo hold-down rails recessed into the floor. These provide for quick, easy installation of test equipment allowing speedy transition from lab to van (and back). Power is provided for by four 5 KW Onan 1ϕ 60 Hz 120 volt gas-powered generators and one 5 KW Katolight 3ϕ 400 Hz 120/208 volt gas-powered generator. Cooling is provided by four 1/2 ton Intertherm electric-powered air conditioners, and heating is provided by four 1500 watt electric heaters plus front and rear bus hot water heaters.

The major elements of the system are the Strapdown Inertial Measurement System (SIMS), computer and its associated peripherals. The SIMS is comprised of a Strapdown Inertial Measurement Unit (SIMU), a Remote Control Unit (RCU) and a Local Control Unit (LCU). The computer, a Raytheon RAC-251, has associated with it a Control and Display Unit (CDU). The computer peripherals consist of an Infoton CRT and a Centronics line printer. Each of these components will be described in detail in the sections to follow.

2.2 STRAPDOWN INERTIAL MEASUREMENT SYSTEM (SIMS)

A block diagram of the SIMS is shown in Figure 2-3. The SIMU is mounted to the vehicle structure by three mounting pads. The Remote Control Unit, also in a cylindrical package, is mounted on top of the SIMU. Electrical interfaces are routed through a single cable to the Remote Control Unit and then to the LCU.

The SIMU is a cylindrically shaped package measuring 13-1/2 inches in diameter by 5-1/2 inches in height, weighing 35 pounds containing three gyros, three accelerometers, and their associated electronic modules. Two views of the package are shown in Figures 2-4 and 2-5.

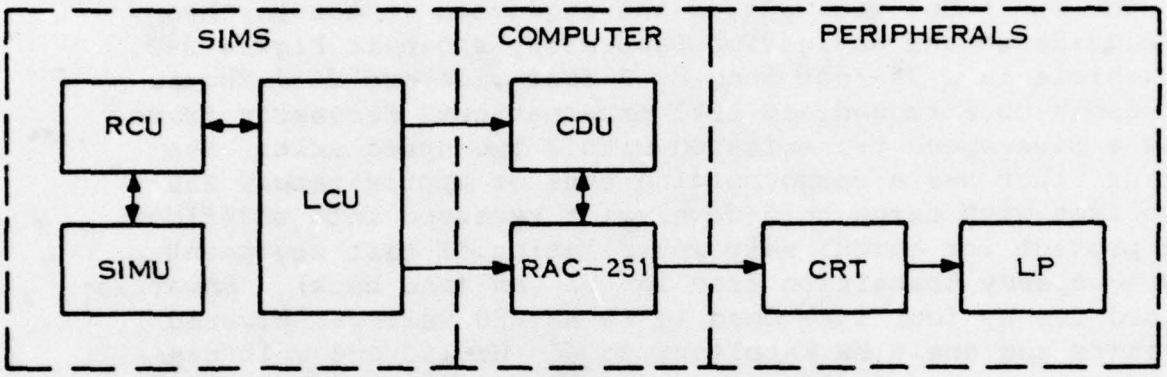


Figure 2-1 Raytheon/CSDL Strapdown System Equipment Laboratory

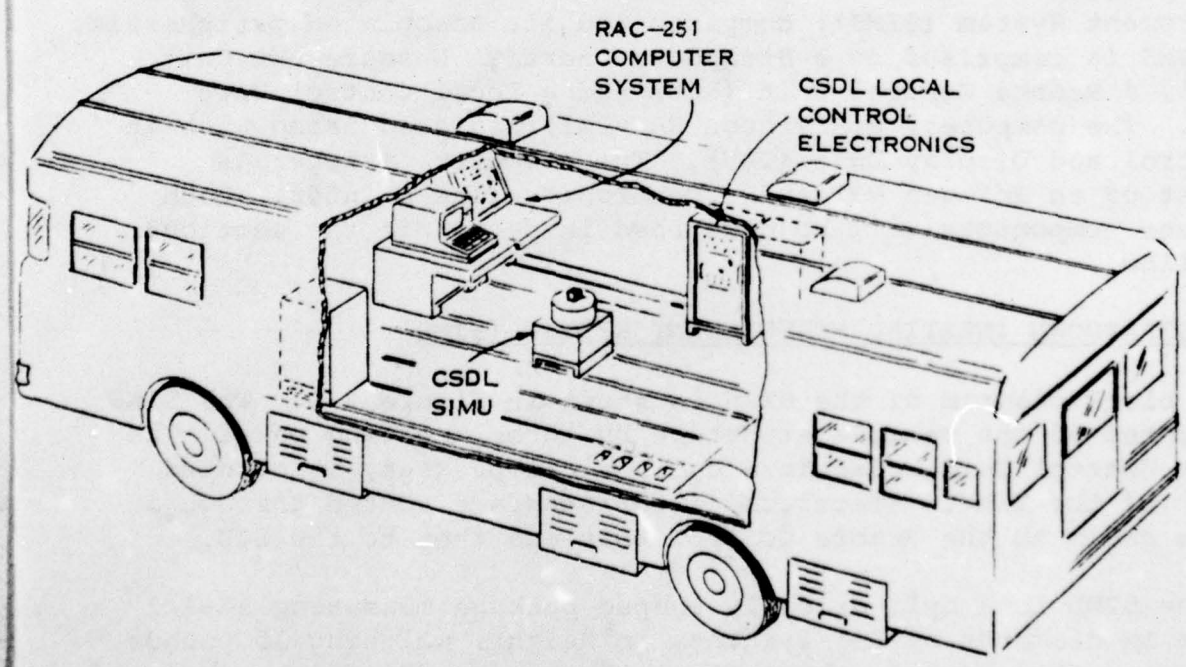


Figure 2-2 Raytheon Mobile Inertial Guidance and Navigation Laboratory

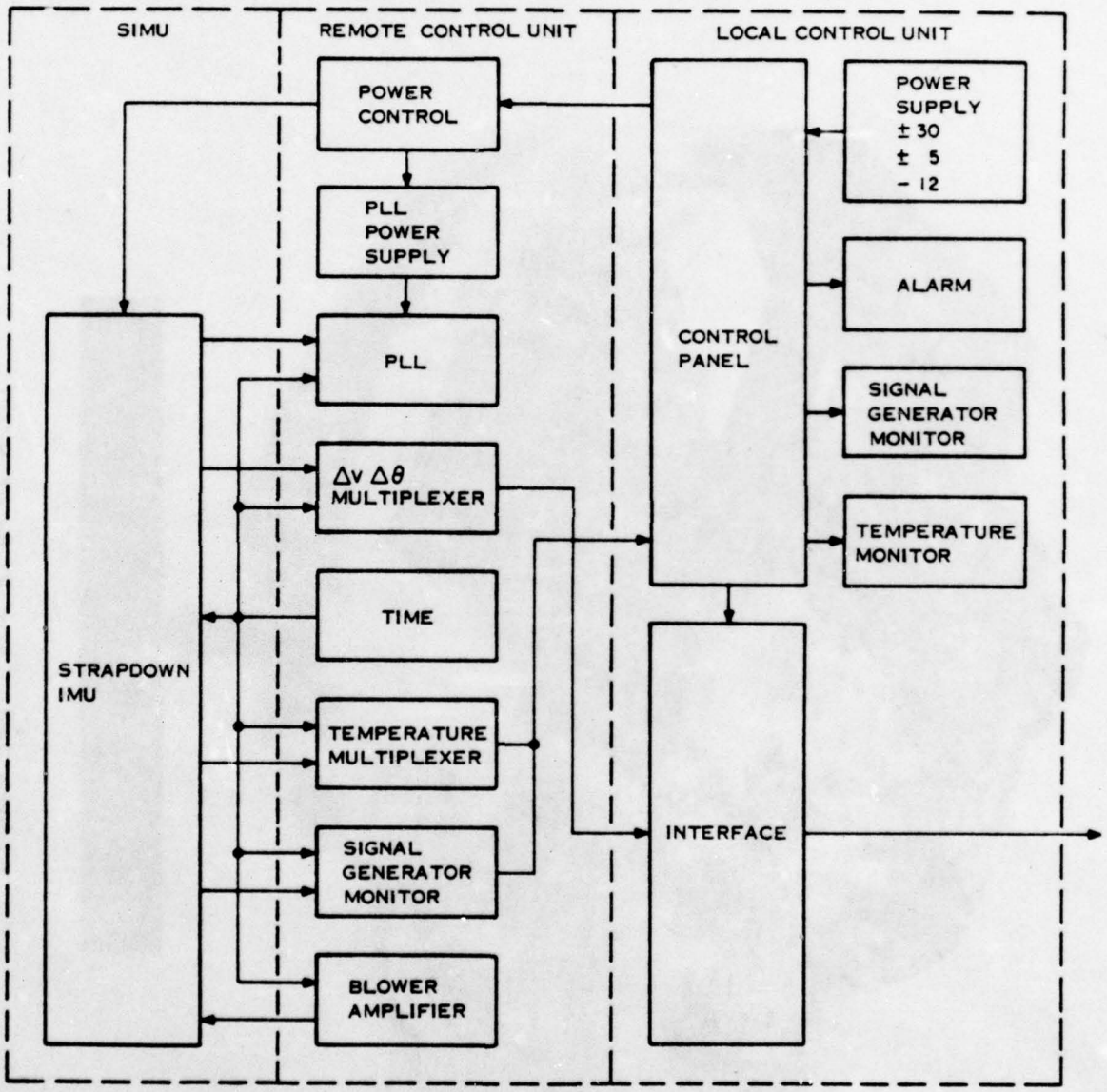


Figure 2-3 SIMS Block Diagram

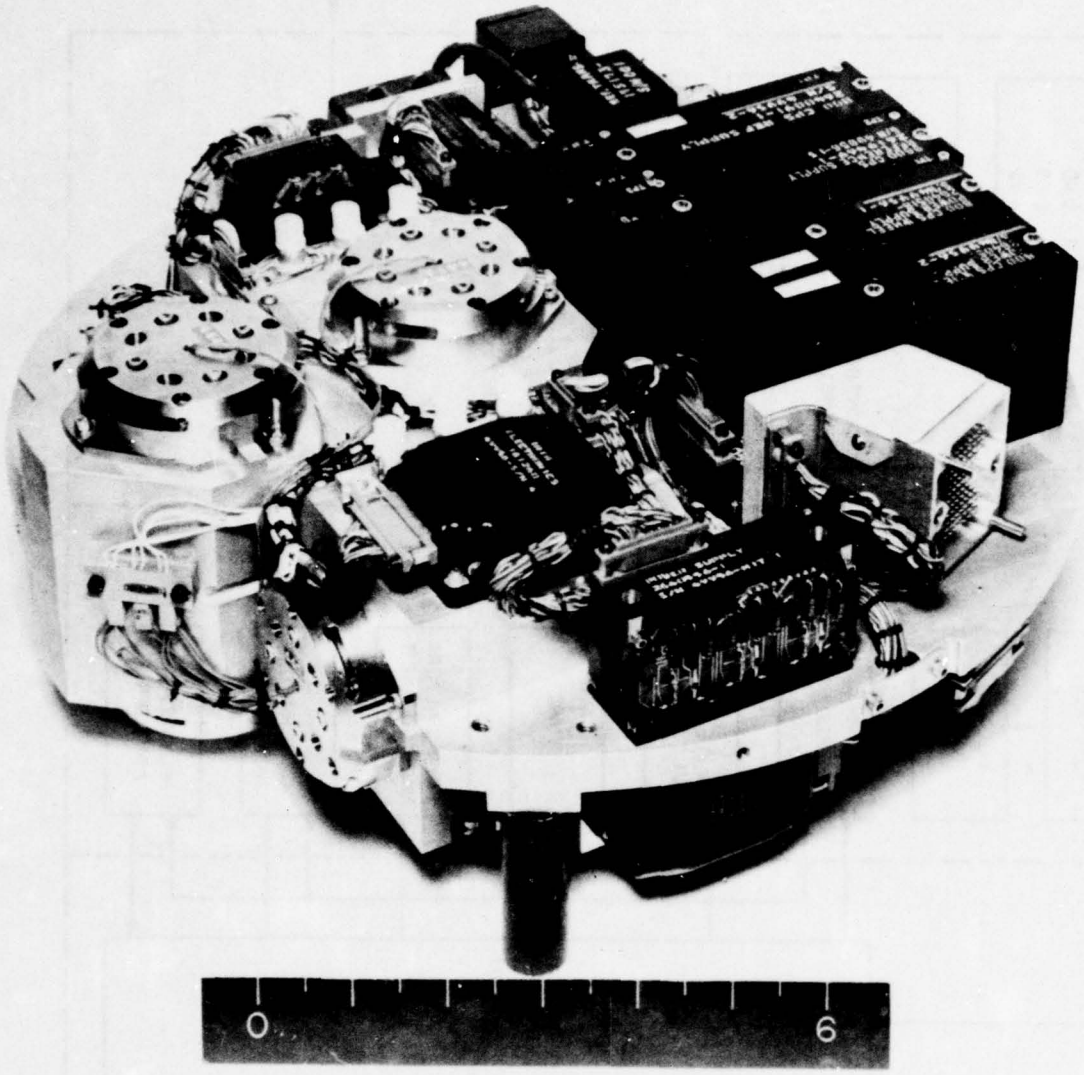


Figure 2-4 Top View of SIMU

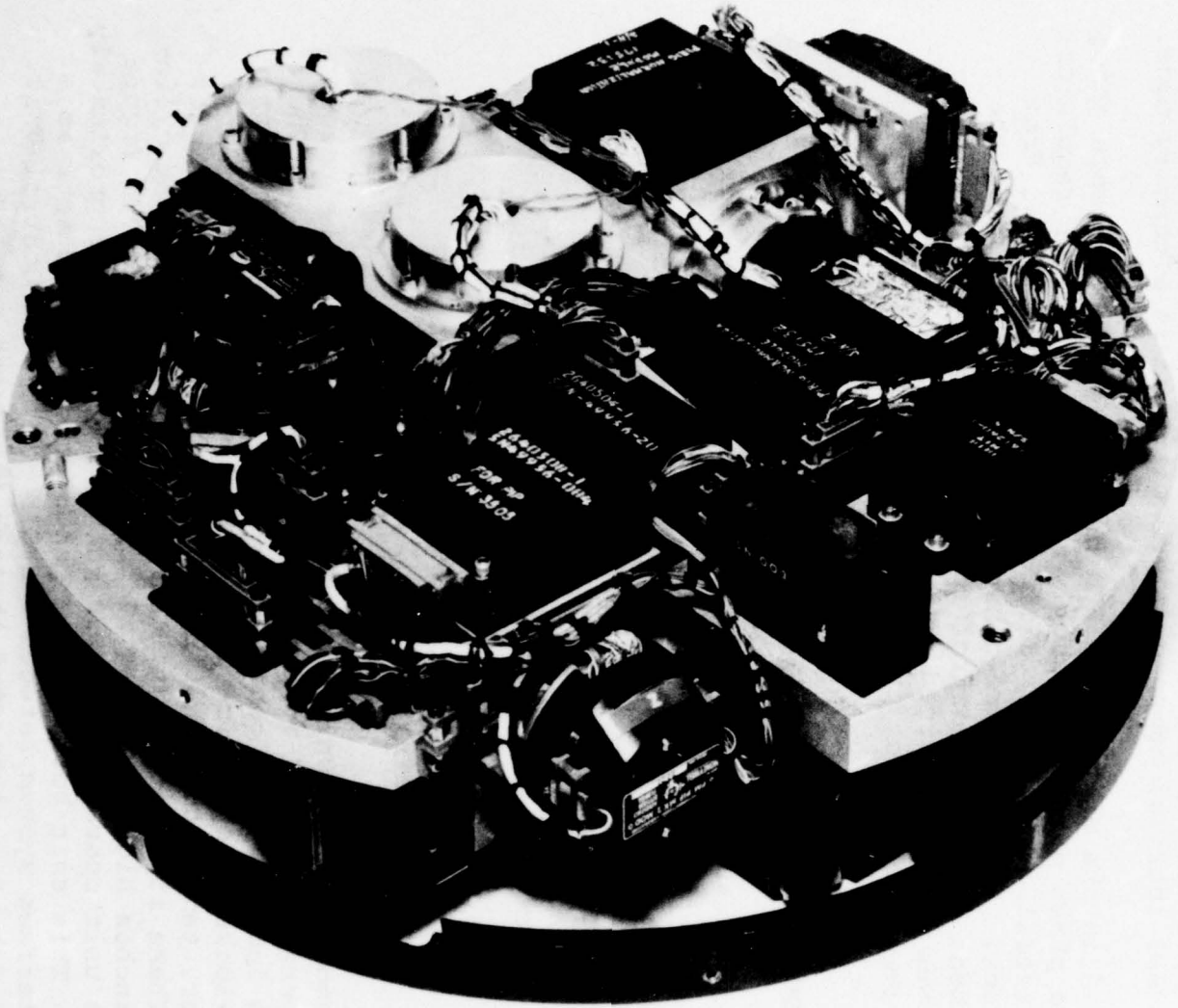


Figure 2-5 Bottom View of SIMU

The gyros used in this system are CSDL, 18 IRIG, Mod B instruments. The 18 IRIG is a single-degree-of-freedom, gas bearing, floated, integrating gyro. The accelerometer used in this system is the CSDL, Type 16 PM, PIP Mod B. The 16 PM, PIP is a single-degree-of-freedom torque to balance pendulous accelerometer. All inertial components are operated in a ternary mode.

Included in the unit are an 800 Hz and 9600 Hz reference generator, a two phase gyro wheel supply and a special power regulator for the inertial components. Timing signals are obtained from the RCU clock. A temperature sensor is located in each of the six instrument cases for control and external monitoring. An 800 Hz blower provides forced convection cooling for the modules. The power requirements for the SIMU are +30 Vdc,6A.

The SIMU provides the following output signals:

- Plus and minus ΔV_B (incremental velocity - six)
- Plus and minus $\Delta \theta_B$ (incremental angle - six)
- Instrument error signal (six)
- Instrument temperature
- 9.6 kHz reference
- 800 Hz reference

The Remote Control Unit consists of those subsystems necessary to operate the SIMU at distances less than 350 feet. These subsystems include power control, phase-locked loop power supply, six phase-locked loops, time generator, blower amplifier, ΔV-$\Delta \theta$ multiplexer, temperature multiplexer and signal generator multiplexer. These items are contained in a 13.5 inch diameter cylinder, 3.5 inches high, weighing 12 pounds and are shown in Figure 2-6. This unit operates from $\pm$30 Vdc and dissipates approximately 70 watts. This unit bolts to the top of the SIMU and acts as a buffer/interface system between the SIMU and Local Control Unit. It is cooled by air circulated through it by its own fan.

A phase-locked loop is used to interpolate the instrument case to float angles. They are used to improve the gyro resolution by a factor of four and the accelerometer resolution by a factor of eight. Figure 2-7 shows a block diagram of the SIMU phase-locked

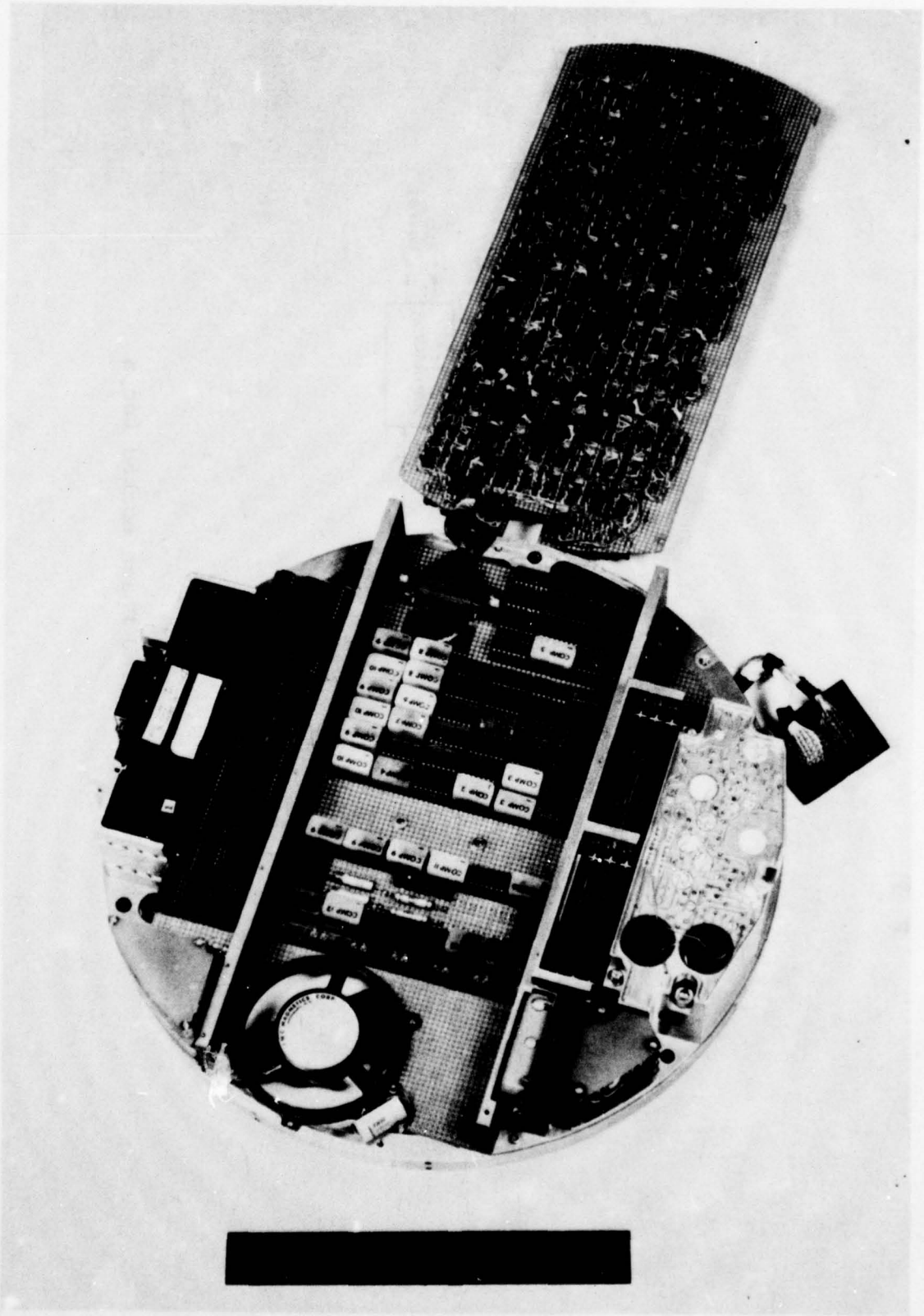


Figure 2-6 SIMU Remote Control Unit

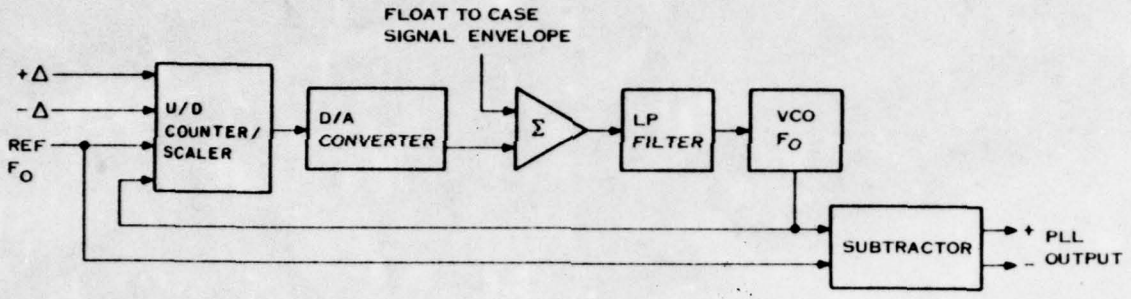


Figure 2-7 SIMU Phase Locked Loops

loops. A reference pulse train obtained from the clock is the same as the frequency at the center of the linear portion of the VCO characteristic. The up-down counter, analog-digital converter combination serves as the loop phase comparator. The error signal outputs from each instrument are transformer coupled in the remote control unit into six demodulators. The filtered demodulator outputs are fed directly into the error signal inputs of the phase locked loops. The error signal causes the VCO frequency to shift off center. The subtractor output pulses represent one-half the frequency difference between the reference and VCO frequencies. These difference pulses are fed to the phase comparator. The resulting phase comparator output tends to cancel the error signal input. The polarity and frequency of the difference pulses gives information on instrument float to case angle. They pass through dividers which give the 8:1 scaling for the accelerometers and 4:1 scaling for the gyros.

In normal operation the PLL switch on the Local Control Unit is set to normal. In this case $\pm\Delta$ pulses are prevented from entering the phase comparator. The net number of output pulses is zero. The outputs are transmitted by cable to up-down counters in the interface. The contents of the counters are sampled each 5 ms. This information is sent to the general-purpose computer along with information on the total number of whole instrument pulses. The fractional number of pulses for each instrument is obtained by subtracting successive float to case angle information every 5 milliseconds.

The PLL outputs, the inertial component ΔV, $\Delta\theta$ outputs, the instrument signal generator outputs and temperature monitor signals are multiplexed to the LCU minimizing the number of signal pairs.

The Local Control Unit is contained in a 48" high by 21" square pallet mounted module weighing about 300 pounds. Pictorially, it is shown in Figure 2-8. This module contains the Control Panel, Interface Unit, $\pm$5 Vdc and +12 Vdc Power Supplies, $\pm$30 Vdc Power Supplies and a Cathode Ray Oscilloscope.

This unit is powered by 117 Vac, 60 Hz at 7 A. It can also be operated from 117 Vac, 400 Hz with some slight modifications. Cooling the Local Control Unit is done by drawing ambient air in on the bottom sides and exhausting through the top rear of the unit. The cables from the Remote Control Unit, Data-Handling Equipment and the General Purpose Computer all connect to the Local Control Unit through a rear opening.

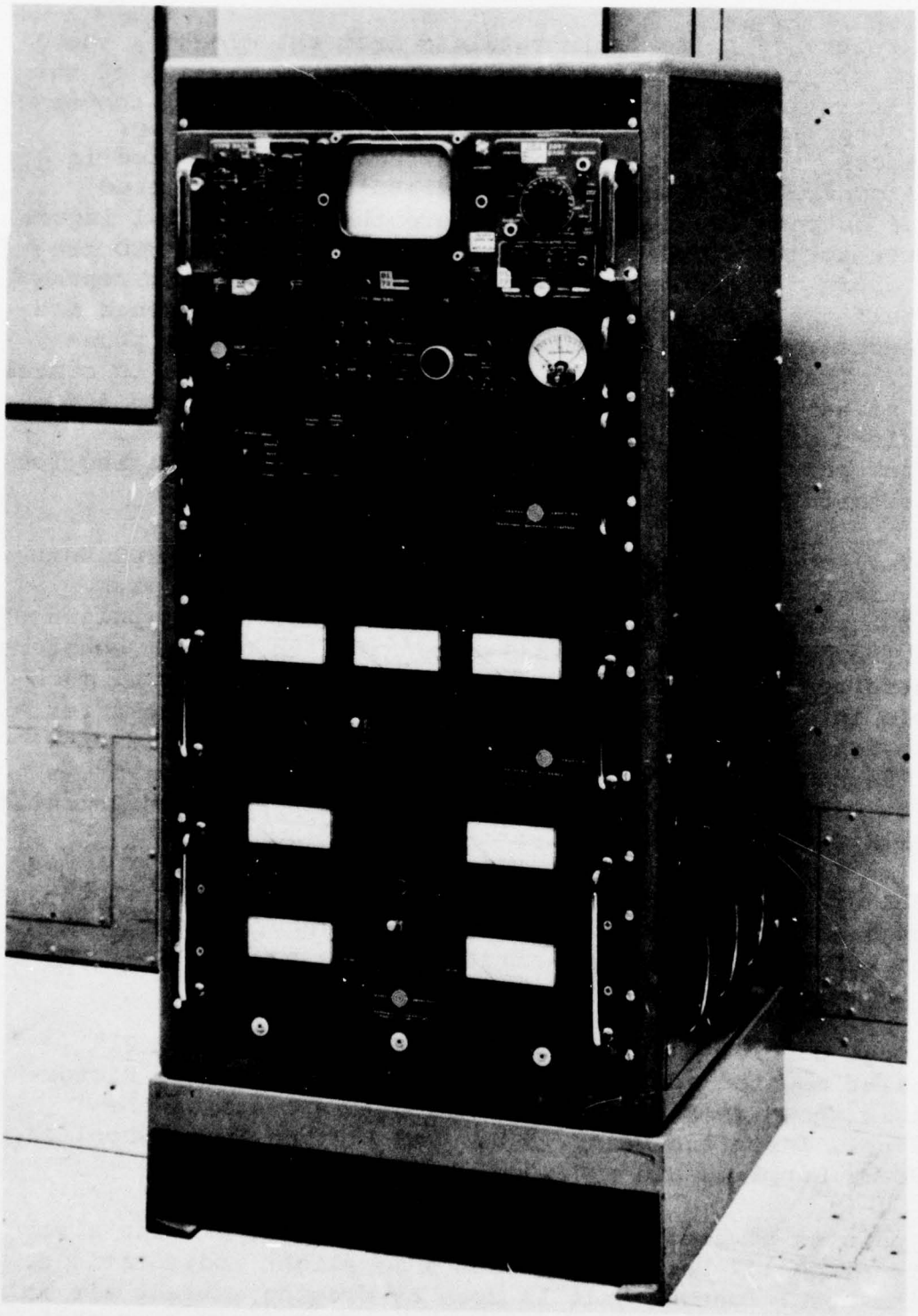


Figure 2-8 SIMS Local Control Unit

All signals and power to and from the Remote Control Unit and the SIMU pass through the LCU control drawer. The operator has control over the SIMU status and is able to monitor its performance.

The Local Control Unit contains two power supply chassis. The upper chassis contains the ±5 Vdc and the +12 Vdc power supplies, and the lower chassis contains the ±30 Vdc power supplies.

The interface is located below the Control Panel. It receives the inertial data and timing pulses from the Remote Control Unit, demultiplexes and distributes these pulses to various support equipment along with pulses from an external velocity sensor.

All connections to the Interface are made through a door in the back of the Local Control Unit. It incorporates a 32-bit parallel repeater bus designed for use with a Raytheon RAC-251 general purpose computer. This repeater bus has attached to it 12 up-down, inertial-data counters. They are sampled, latched and an interrupt is sent to the computer. When the computer acknowledges this interrupt, it returns a control word. This word is decoded in the Interface to transmit the desired data through the repeater bus. The interrupt occurs every 5 ms. The first interrupt pulse can be activated either manually or from an external command pulse by pushing the appropriate button on the front panel. Interrupt can be terminated by pushing the stop button. Figure 2-9 shows the data format and the data identification code for the repeater bus.

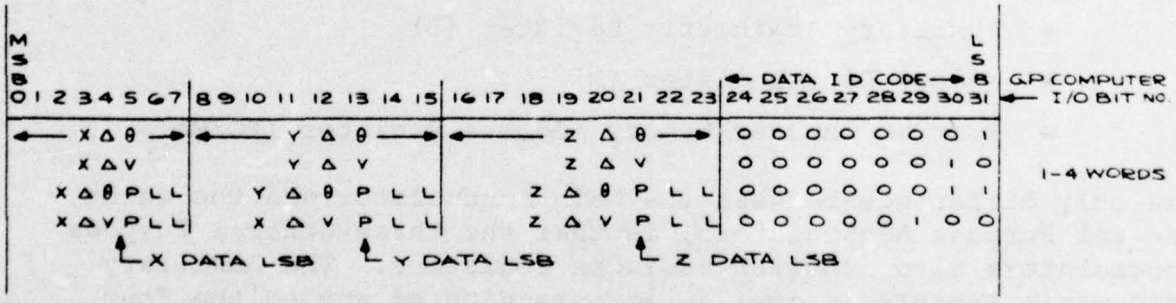


Figure 2-9 Data Bus Format - 2's Complement Notation

2.3 RAYTHEON RAC-251 GENERAL PURPOSE COMPUTER

The RAC-251 Computer and is power supply are packaged in two separate units. The computer measures approximately 9 x 19 x 28 inches, its power supply about 4 x 19 x 19. Total combined weight is about 100 pounds (65 and 35 lbs). Each unit is independently air cooled and shielded (Figure 2-10). Manual control, single-step operation, and visual display are provided in the front panel.

The RAC-251 is a general purpose, parallel-organized, multi-accumulator computer. The arithmetic unit is completely implemented with bipolar LSI arrays. The control unit utilizes micro-programming techniques and is implemented with bipolar read-only memory LSI devices. Full indexing is provided with three index registers which also function as general purpose accumulators. It contains 8K words of high speed core storage with a 2.5μ sec cycle time. Memory-referenced adds take 4μ sec; multiplies 15μ sec and divides 28μ sec. Except for the expanded I/O capability required for use in a strapdown navigation system, it is similar to the RAC-251 developed for the TPN-19 Air Traffic Control Program. The computer architecture is shown in Figure 2-11.

The arithmetic unit contains seven 32-bit hardware registers, specified as follows:

- Main Accumulator (A)
- General Purpose Accumulator A (XA)
- General Purpose Accumulator B (XB)
- General Purpose Accumulator C (XC)
- Auxiliary Arithmetic Register (B)
- Memory Data Register (B)
- Program Counter/Memory Address Register (PC/MA).

The only difference between the Main Accumulator and the three General Purpose Accumulators, is that the three General Purpose Accumulators also function as index registers. The Auxiliary Arithmetic Register serves as an extension of any of the four accumulators and automatically participates with the specified accumulator when a double word instruction such as long shift, multiply, etc., is executed. The Memory Data Register provides buffering between the memory and computer. The program counter and memory address register share a common 32-bit register.

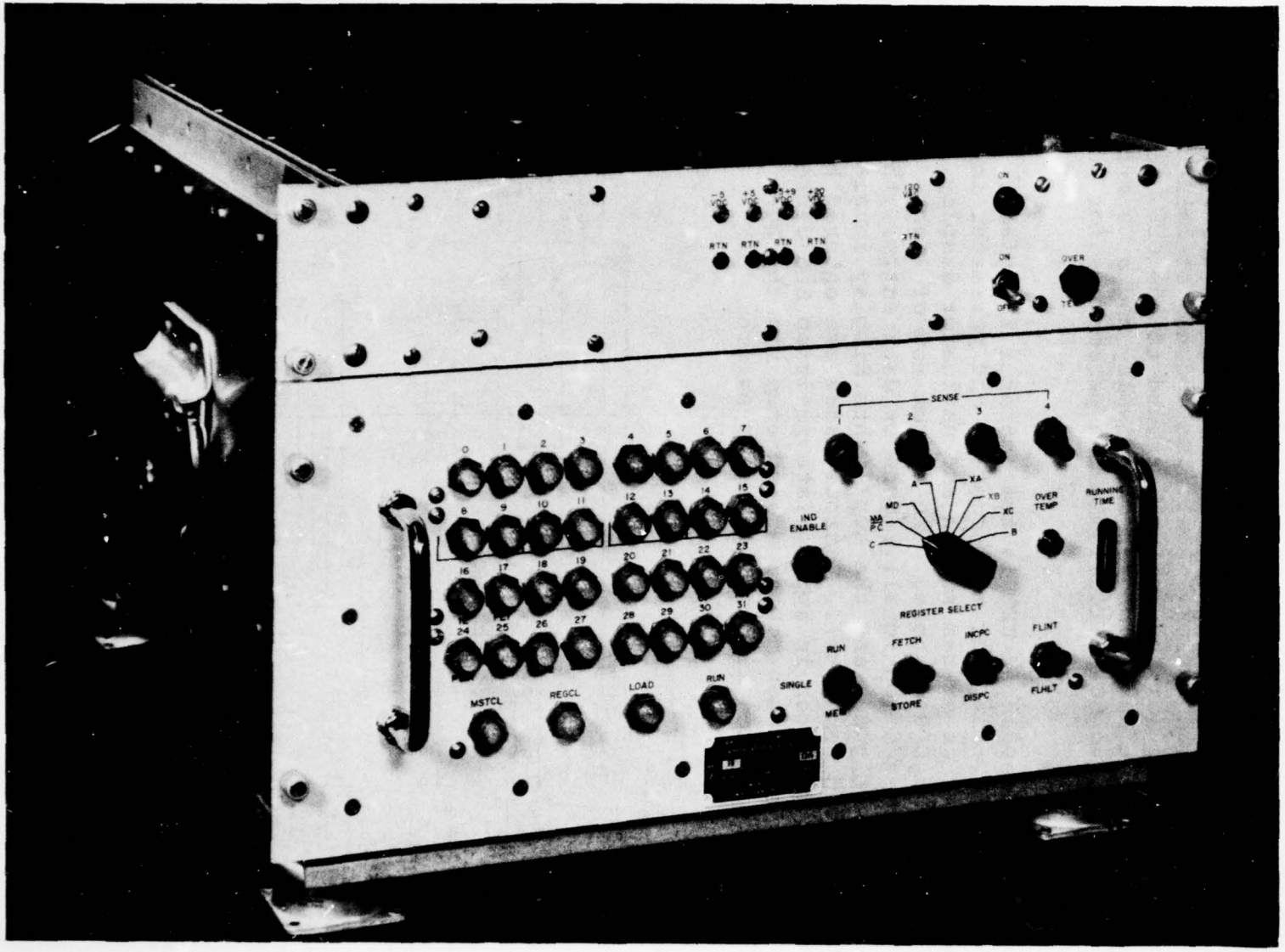


Figure 2-10 RAC-251 Computer Assembly

The RAC-251 is configured to accept and process (and control) the incremental gyro and accelerometer data. Under executive control it maintains all the reference frames, solving the navigation equations in real time. Real time updates of latitude, longitude, and speed (or heading) are issued to the CDU, as well as periodic printout on an Infoton CRT Display and a Centronics 101 Printer, of up to 60 critical mission parameters for post-test evaluation.

The Raytheon-developed CDU is the operator interface. It furnishes the capability for mode control and parameter input to the system as well as system status and navigator display. Figure 2-12 shows the CDU console. The bottom row of lights normally displays Ground Speed (optionally, mode or data entry), the middle lights display latitude, and the top lights display longitude (optionally heading or data). Various modes are entered by setting the selector switch in appropriate position and depressing the "Ex" (execute) button. Data are entered via the push button and buffers coordinated with the selector switch.

BEST AVAILABLE COPY

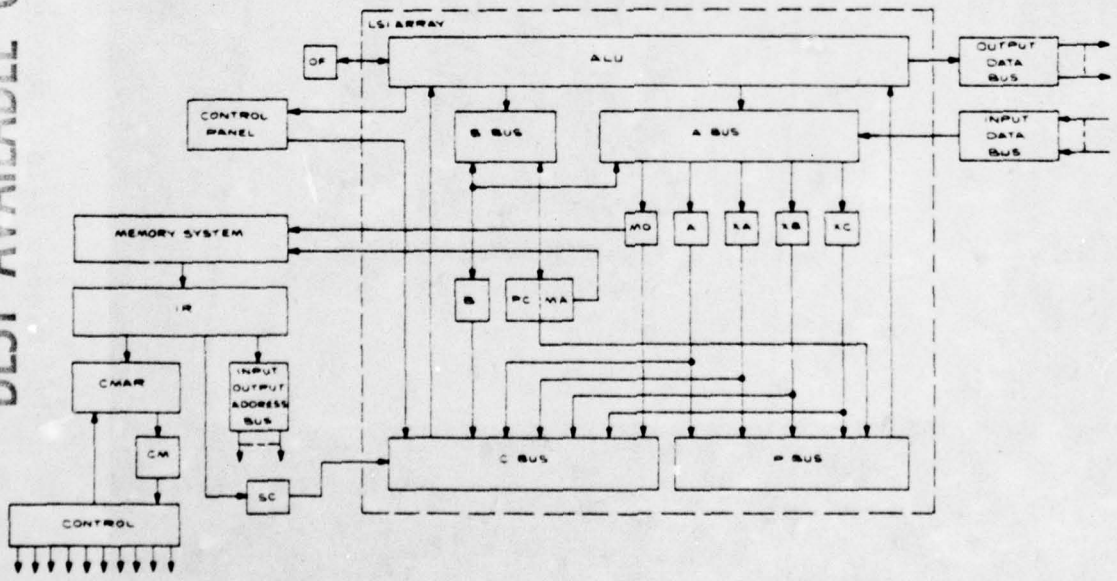


Figure 2-11 RAC-251 Computer Architecture

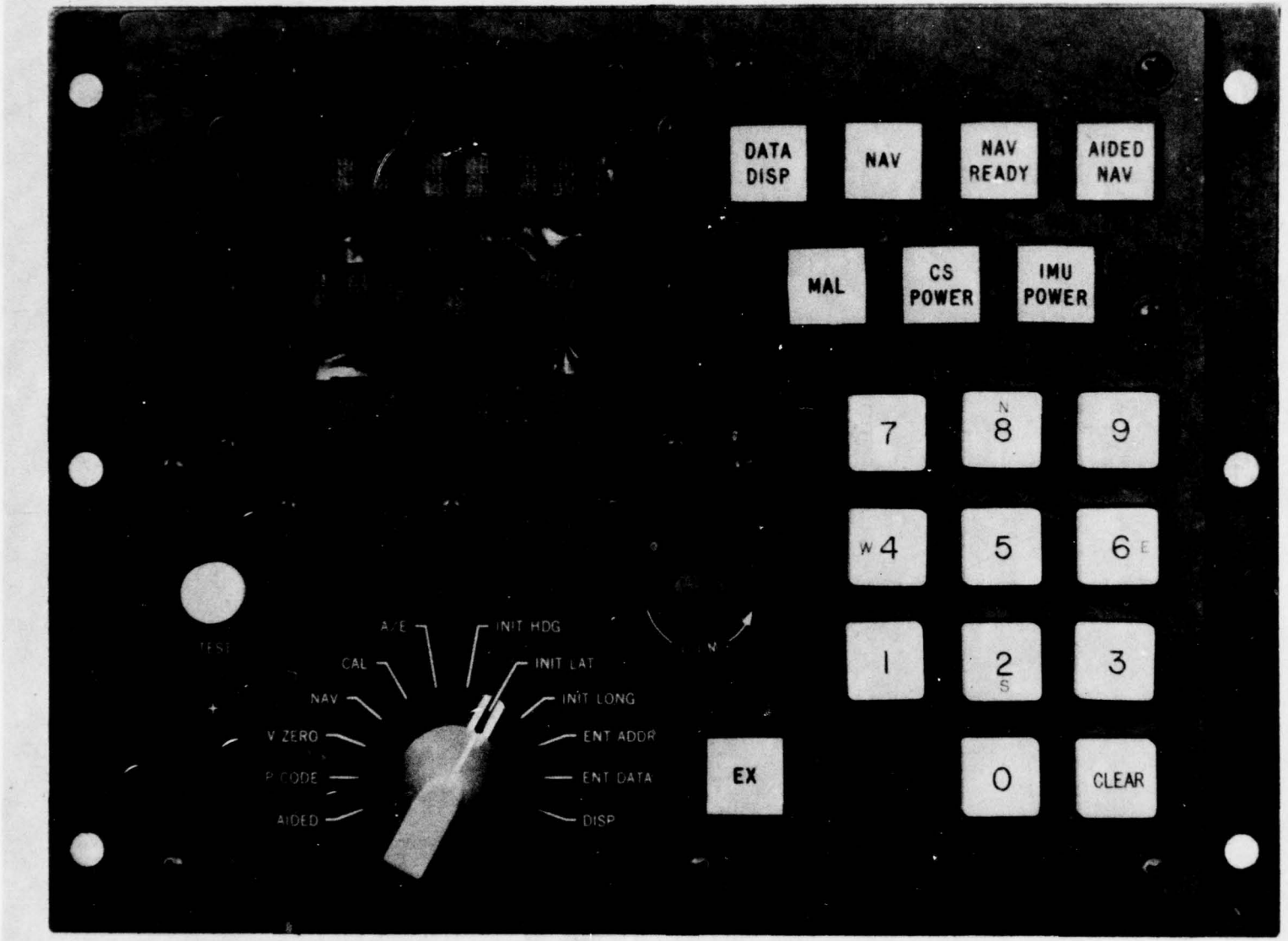


Figure 2-12 Control Display Unit

SECTION 3

FILTER DESCRIPTION

3.1 INTRODUCTION

This section describes the filter software used in the static and mobile navigation tests. Three filters were used together in the tests: a horizontal navigation filter (HNF) for controlling error effects in the north and east directions; a zero sideslip (ZOSS) prefilter, for obtaining accurate inputs to the horizontal navigation filter; and a zero-upslip (ZEUS) filter for the vertical channel. Each of these filters is described in further detail below.

The filters served to enhance the performance of the basic strapped-down navigation algorithms. The latter have been described in some depth in Reference [3], but for convenience are summarized here. The instrument pulses (three accelerometers and three gyro channels) were compensated to yield estimates of integrated acceleration and integrated angular rates respectively in ideal IMU coordinates. The angle changes were integrated, in the form of a direction cosine matrix, to yield current body attitude relative to an inertial coordinate system. The velocity changes were resolved into inertial coordinates and summed for half-second intervals. Every half second, the summed velocity changes were resolved to indicated local north-east-down coordinates, and augmented by the integral of the computed gravity. They were then doubly integrated in a navigation algorithm which indicated longitude, latitude, and altitude (and their rates) directly.

The repetition periods for the navigation algorithms and filters are summarized in Table 3-1. The filters occupied about 20 percent of the computation duty cycle, and their storage requirement was about 2,250 words for combined program and data, including all interface computations.

TABLE 3-1

REPETITION PERIODS FOR THE COMPUTATION BLOCKS

COMPUTATION UNIT	REPETITION PERIOD (SEC)
IMU Sampling	0.005
Instrument Compensation	0.005 to 0.020
Direction Cosine Update	0.010
Velocity Resolution	0.010
Navigation	0.5
Horizontal Filter Integration	1.0
Horizontal Filter Update	30.0
ZOSS Prefilter	1.0
ZEUS Filter	1.0

3.2 HORIZONTAL NAVIGATION FILTER

The horizontal navigation filter (HNF) was a 13-state Kalman filter, operating on errors in position, velocity, and orientation, and selected instrument errors. The filter algebra was a square root formulation, the technical details of which are deferred to Appendix A. In the present section, the state variables are defined, and the deterministic portions of the state equation and measurement equations are presented.

The HNF is similar to the filter described in Reference [3] where it was applied to navigation with a (much less accurate) ring laser gyro IMU. More details are provided here than in Reference [3]. It should be noted that the HNF operated in the error feedback mode, wherein errors discovered by the filter were immediately subtracted into the navigation variables and instrument compensation coefficients. This mode simplifies the filter algebra, since it bypasses the need for deterministic error propagation between updates. It may also enhance performance by preventing error growth to the point where assumptions of linearity are questionable.

HNF STATE VARIABLES

δR_N = north position error

δR_E = east position error

δV_N = north velocity error

δV_E = east velocity error

θ_N = orientation error about level north

θ_E = orientation error about level east

θ_D = orientation error about the local vertical axis (in other words, θ_D is the IMU azimuth error)

ω_X = X gyro bias error

ω_Y = Y gyro bias error

ω_Z = Z gyro bias error

B_X = X accelerometer bias error

A_B = IMU-to-van boresight error

B_Z = Z accelerometer bias error

This state vector is the same as was used for earlier tests reported in Reference [3], except that the Y accelerometer bias has been replaced by IMU boresight error. In the IMU orientation used for the mobile tests, the Y accelerometer was nominally vertical and therefore did not contribute directly to errors in the horizontal channels. It was therefore replaced in the filter by the IMU boresight error, which if uncorrected would have an important effect on the zero-sideslip (ZOSS) measurements to be described below.

HNF State Equations

Each state variable was modeled to be driven by zero-mean white noise. In addition to the noise, certain of the state variables derivatives were also deterministic functions of the state itself. In general notation,

$$\dot{X} = MX + N$$

where X is the state vector, M is the system matrix describing the deterministic error propagation, and N is the vector of noise sources. The non-zero elements of M are identified in the

following state equations

$$\dot{\delta R}_N = \delta V_N$$

$$\dot{\delta R}_E = \delta V_E$$

$$\dot{\delta V}_N = -g\ \theta_E - A_E\ \theta_D + C_{XN}\ B_X + C_{ZN}\ B_Z$$

where g is the gravity magnitude, A_E is the easterly acceleration, and C_{XN} and C_{ZN} are direction cosine elements of X-north and Z-north respectively.

$$\dot{\delta V}_E = g\ \theta_N + A_N\ \theta_D + C_{XE}\ B_X + C_{ZE}\ B_Z$$

$$\dot{\theta}_N = -\frac{1}{R}\ \delta V_E - \dot{\lambda}\ \sin L\ \theta_E + C_{XN}\ \omega_X + C_{YN}\ \omega_Y + C_{ZN}\ \omega_Z$$

where R is distance from the earth center, $\dot{\lambda}$ is the longitude rate relative to inertial space, and L is the latitude.

$$\dot{\theta}_E = \left(\frac{1}{R}\right)\delta V_N + \dot{\lambda}\ \sin L\ \theta_N + \dot{\lambda}\ \cos L\ \theta_D + C_{XE}\ \omega_X + C_{YE}\ \omega_Y + C_{ZE}\ \omega_Z$$

$$\dot{\theta}_D = \left(\frac{\tan L}{R}\right)\delta V_E - \dot{\lambda}\ \cos L\ \theta_E + C_{XD}\ \omega_X + C_{YD}\ \omega_Y + C_{ZD}\ \omega_Z$$

HNF Measurement Equations

The filter measurement equation in general form is given by

$$H = CX + \epsilon_M$$

where H is the scalar measurement, C is the measurement matrix (actually a row vector), X is the state, and ϵ_M is a zero-mean random error in the measurement process. Two specific measurement modes were used in the tests described here: the calibration mode, used in stationary periods prior to the mobile runs,

and on occasion for stops en route; and the zero-sideslip (ZOSS) mode, used when moving.

The measurement equations for the calibration mode were simply

$$\Delta V_N = \delta V_N + \epsilon_N$$

$$\Delta V_E = \delta V_E + \epsilon_E$$

The actual numbers used for the measurements were the indicated velocities north and east, as derived from the indicated latitude and longitude rates. Thus, the random noise (ϵ) components contained the effects of both accelerometer quantization and actual vibratory motions of the test van.

The ZOSS measurement was based on the fact that a rolling vehicle tends to have zero velocity in the direction parallel to its rear axle. Thus, any indicated velocity in that direction must be erroneous, and can be fed back through the filter. The specific measurement equation for the ZOSS mode was

$$\Delta V_S = (\cos AZ)\delta V_N - (\sin AZ)\delta V_E - V\,\theta_D - V\,A_B + \epsilon_S$$

where ΔV_S is the side-slip velocity error, AZ is the IMU azimuth, V is the ground speed of the test van (as derived from the navigation algorithm), and ϵ_S is the composite error in estimating sideways velocity. For test results reported earlier (Reference [3]), the number used for ΔV_S was simply the indicated velocity resolved through the indicated direction cosine matrix, the IMU having been carefully optically aligned to the test van. For the tests reported here, this method was deemed too crude; accordingly, a smoothing prefilter was developed which would allow for the boresight error between the IMU and the test van. The operation of the ZOSS prefilter is described in some detail below.

HNF Modeled Error Levels

The Kalman filter, in spite of appearances, is not adaptive to the actual level of errors encountered in operation; that is, given its initial conditions and noise parameters, the gains computed by the filter can be completely predicted from the mission profile and planned measurement schedule. Thus, to ensure that

the filter gains will be reasonable, it is imperative to use a realistic set of filter parameters describing the initial error statistics, the process noise powers, and the measurement noise.

For most of the test runs reported here (the exceptions being identified in the description of the test results), the state parameter initial 1-sigma values and noise powers are summarized in Table 3-2. Note that the process noise powers are stated in the familiar form of (state units)^2/(time unit), although as actually programmed for the square-root filter algebra, the square roots of these numbers were used.

TABLE 3-2

INITIAL SIGMAS AND PROCESS NOISE MODEL FOR THE HNF

State Variable	Initial 1-Sigma	Process Noise Power
Position	0	0
Velocity	0	$(5 \times 10^{-5}$ ft/sec$)^2$/sec
Level (θ_N, θ_E)	20×10^{-6} radians	0
Azimuth (θ_D)	0.0005 radians	0
Gyro Drift	0.2 merus	(0.1 meru)^2/hour
Accelerometer Bias	20 milligals	(5 mgal)^2/hour
IMU Boresight	0.0005 radians	0

Several comments about these numbers are appropriate. The initial sigmas for the instrument biases reflect our opinion about how well we could calibrate them in the field. The instrument noise powers are somewhat larger than observed in the laboratory, and allow for the comparatively poor thermal control in the field. Azimuth was always found by gyrocompassing (never optically), and the figure of 0.5 milliradians reflects the jitter observed in the gyrocompass azimuth loop after a typical ten-minute settling time. The IMU-to-van boresight error reflects our knowledge gained from early shakedown runs. The IMU was in fact bolted to the van nearly one degree off nominal. However, the filter discovered this fact during the first few runs, so that the figure of 0.5 milliradians reflects only our residual uncertainty in the boresight offset. In retrospect, it was probably a mistake to assign a zero noise power to the leveling

errors, since this does not allow for changing deflections of the vertical.

The velocity measurement noises used in the calibration (stationary) mode were 0.1 feet per second, reflecting the assumed level of vibration induced primarily by the test van's generators, and to some extent by the van's response to wind gusts. The measurement noise level for the ZOSS measurements was computed by the ZOSS prefilter, as described immediately below.

3.3 ZERO SIDE-SLIP (ZOSS) PREFILTER

As noted in the description of the horizontal navigation filter (HNF), the latter is ready for updates every 30 seconds. For mobile operations the update information is the indicated sideways velocity, which is known to be erroneous because the vehicle is rolling in the forward direction only. However, an instantaneous sample of the sideways velocity may be in dynamic error by as much as 0.5 ft/second. The purpose of the ZOSS prefilter is to smooth the sideways velocity errors during the 30-second interval, thus providing a more accurate estimate of the sideways velocity, and also an estimate of its RMS error for use by the HNF filter.

Since the velocity errors are fairly stable in local north-east-down coordinates, it is clear that the sideways velocity error ΔV_S may change drastically as the vehicle azimuth changes. Thus, the forward velocity error ΔV_F must also appear in the filter, and in vehicle-fixed coordinates it turns out that the two velocity errors are coupled by the deterministic relation

$$\dot{\Delta V}_F = - \dot{A} \, \Delta V_S$$

$$\dot{\Delta V}_S = \dot{A} \, \Delta V_F$$

where $\dot{A}$ is the vehicle azimuth rate. For the ZOSS prefilter, ΔV_F and ΔV_S form a two-element state vector, and the ZOSS prefilter is programmed in the conventional Kalman filter algebra.

The measurement inputs to the ZOSS prefilter, computed once per second, are derived from the indicated vehicle velocity and azimuth information. For the tests described here, the IMU X axis was nominally sideways, and the Z axis nominally along the van longitudinal axis, positive toward the rear. Thus, the X

and forward components of velocity were computed by

$$V_X = C_{XN} V_N + C_{XE} V_E$$

$$V_F = -C_{ZN} V_N - C_{ZE} V_E$$

where V_N is the north velocity component, V_E is the east velocity component, and C_{XN} (for example) is the direction cosine of the X IMU axis on the local level north direction. Were it not for the IMU boresight error (A_B), V_X would be the current sideways velocity error. The boresight error is taken into account by

$$V_S' = V_X - A_B V_F$$

Using the three immediately preceding equations, the ZOSS prefilter is updated once per second. The Kalman gain for the sideways velocity error (K_S) is computed in the usual manner, and the sideways velocity estimate is updated by

$$V_S \longleftarrow V_S + K_S(V_S' - V_S)$$

The smoothed V_S becomes the measurement input to the HNF, and the ZOSS prefilter covariance element for V_S becomes the measurement noise figure to the main filter. After the main filter update, the ZOSS prefilter is reset by setting V_S to zero and restarting the covariance matrix. The reset values for the latter were 1-sigma values of 0.5 ft/sec for forward velocity, and 0.15 ft/second for sideways velocity, which are typical conservative estimates of the residual velocity errors after the main (HNF) filter update.

The performance of the ZOSS prefilter depends primarily on the measurement noise associated with each of the individual sideways velocity measurements (V_S'). Following a series of test drives on straight (but typically bumpy) roads, and tests with severe turning rates, the sideways velocity noise was found to depend on accelerometer quantization, angular acceleration, and a term proportional to both angular rate and forward speed. This last term was attributed to a tendency for the van chassis to lag behind the wheels during turns, due to imperfect azimuth suspension. Thus, the measurement noise variance for the individual V_S' measurements was modeled as

$$R_S = R_Q + (K_L \ddot{A})^2 + (K_H V_F \dot{A})^2$$

where R_Q is the quantization variance $(0.03 \text{ ft/sec})^2$; K_L is the angular acceleration coefficient (50 ft-sec); and K_H is the azimuth hang-off coefficient (0.067 seconds). The beneficial effect of this model was to generate large covariances for V_S when the road was bumpy and during rapid turns, so that the main (HNF) filter would give comparatively little weight to the sideways velocity updates under those conditions. Conversely, the ZOSS prefilter under good road conditions produced smoothed velocity estimates which were an order of magnitude better than any instantaneous measurement, thus enabling comparatively accurate updates to the main filter.

3.4 ZERO UP-SLIP (ZEUS) FILTER

The zero up-slip (ZEUS) filter was conceived as an attempt to do for the vertical navigation what the ZOSS filter did for the horizontal navigation. The constraint idea for the ZEUS filter is analogous, namely that a rolling vehicle will on the average have an altitude rate proportional to its forward speed and to the tangent of its pitch angle. Thus, if the speed and pitch angle are known with moderate accuracy (which they are), then a fairly accurate independent estimate of altitude rate exists. As with the ZOSS filter, a boresight error between the IMU level axes and the road level must be dealt with. This boresight error (ϑ) was defined specifically as the vertical angle between the IMU Z axis and the line joining the ground contact points of the front and rear van wheels. The other elements estimated in the ZEUS filter were altitude error (δh); altitude error rate ($\dot{\delta h}$); and vertical acceleration error (δf).

The ZEUS filter was programmed as a Kalman filter in covariance form. The modeled state equations were

$$(\dot{\delta h}) = \dot{\delta h} + N_h$$

$$\ddot{\delta h} = -\delta f + G\,\delta h + N_V$$

$$\dot{\delta f}_D = N_f$$

$$\dot{\vartheta} = N_\vartheta$$

In the foregoing, G is the gravity gradient and the various N's are zero-mean white noise sources. The power of altitude noise (N_h) was set at (0.03 feet)^2/sec to allow for accelerometer quantization. The power of altitude rate noise (N_V) was assumed to be zero. The power of vertical force noise (N_f) was set at (20 milligals)^2/hour. The latter was a bastardized number used to represent the combined effects of Y accelerometer bias, and of changes in the local gravity anomaly which might be expected in mobile tests. The up-slip angle noise (N_φ) power was taken to be (1 milliradian)^2/hour. This term represents the comparatively long-term changes in the van chassis angle relative to the ground, attributable to changing tire pressure, shifting fuel load, thermal response of the springs, etc. The number used was strictly a guesstimate.

The measurement input to the ZEUS filter was the altitude rate error $\Delta\dot{h}$, computed from

$$\Delta\dot{h} = V_F(C_{ZD} + \varphi) - \dot{h}$$

where $\dot{h}$ was the altitude rate indicated by the navigation algorithm, V_F was the indicated forward speed component, and C_{ZD} was the direction cosine between the IMU Z axis and the local down direction (and, therefore, the sine of the angle of Z off level).

The noise variance (R) in the ZEUS filter measurement is modeled as

$$R = R_Q + (R_J\ V_F)^2$$

where R_Q is the accelerometer quantization noise (0.03 ft/sec)^2 in the indicated altitude rate, and R_J is the 1-sigma high frequency jitter in the van's pitch angle. The value used for R_J was 0.004 radians, a guesstimate based on "gut feeling" after riding in the test van for a few hours.

The initial 1-sigma values in the filter covariance were modeled as follows: Altitude: 20 feet. This reflects uncertainties in reading and interpreting the topographic maps. Altitude rate: 0.03 feet/second, due to accelerometer quantization. Vertical force: 5 milligals, reflecting primarily the error in the vertical accelerometer. For runs starting where an accurate gravity measurement was not available, a larger value would be needed. Up-slip angle: 1 milliradian. This represents our knowledge of the angle, rather than the angle itself. In

fact, early shakedown runs converged on a value of about +9 milliradians for the up-slip boresight angle. Thus, the 1 milliradian figure represents possible day-to-day changes depending on equipment loading, suspension wear, and so forth.

The ZEUS filter was programmed in the usual covariance form for the Kalman filters, and operated independently of other filters. It performed updates once per second, and always operated whether in the stationary or mobile mode. We (or one of us, to be exact) worried about its numerical stability when the van was stationary, since it would then be collecting no information about one of its state variables (namely, the up-slip angle). However, it was in fact found to be stable over at least several days of continuous stationary operation.

The ZEUS filter was a late addition to our software. As the test results section below shows, it had a surprisingly good ability to track the gravity anomalies en route, as well as to maintain a good estimate of altitude. It is considered possible that, with more realistically chosen coefficients, it would be useful in future gravity survey work.

SECTION 4

CALIBRATION TECHNIQUES

4.1 INTRODUCTION: CALIBRATION REQUIREMENTS AND PHILOSOPHY

The definition of an effective calibration program depends on a clear understanding of the mission accuracy requirements, and on the expected stability of the items being calibrated.

The nature of error propagation in inertial navigators is well understood, both in terms of detailed error propagation for specified missions and instrument configurations, and in terms of "rules of thumb" relating gyro and accelerometer accuracy levels to average navigation performance. Britting (Reference [4]) for example, gives excellent illustrations of instrument error propagation over long periods, for a stationary navigation system. For a frequently reorienting strapped down system, however, the changing geometry of the error sources gives a random-looking appearance to the navigation error growth. Thus, one reverts to the familiar rules of thumb that error growth on the order of one nautical mile per hour is associated with gyro drifts of one meru (= 1 milli-earth rate unit = 0.015°/hour), or with accelerometer biases of about 100 milligals.

Extensive past experience with the CSDL SIMU suggested that, in a laboratory ambient environment, the day-to-day gyro bias stability was 0.1 meru or better, and that the long-term stability of the accelerometers was better than 5 milligals. Thus, a reasonable if optimistic performance goal for the system was about 0.2 nautical miles per hour. The optimism in this goal owes to two factors. First, the instruments might not be as stable in the field as in the laboratory. Second, the dynamic environment of mobile tests would excite error sources - particularly alignments and scale factors - which, if not properly compensated, could contribute errors far in excess of the gyro and accelerometer biases.

Accordingly, the calibration plan was divided into two phases. Field calibration techniques were needed to monitor and compensate changes in the gyro and accelerometer drifts. Also, prior laboratory calibration methods were needed to accurately assess instrument alignments and scale factors.

A secondary goal of the test program was to free the system from any dependence on optical references. Accordingly, all navigation tests were initialized by gyrocompassing (see Reference [2] for technique). Furthermore, the calibration methods where feasible were made independent of the need for accurate positioning equipment or accurate optical references for determining orientation. As will be shown below, substantial independence from external references may be afforded by using the navigation software to assist in the calibration.

The philosophy in using the navigation software in calibration may be summarized as follows: Calibration errors manifest themselves as navigation errors. When the system is known to be stationary, the navigation software directly indicates navigation errors. With thoughtful use of orientations and prior rotations, these errors may be uniquely attributable to error sources in the inertial measurement system. What follows in this section is primarily an articulation of the foregoing statement.

4.2 FIELD CALIBRATION TECHNIQUES

The important constraint on our field calibration program was that the SIMU was to remain bolted to the mobile test van. Hence, only an azimuth freedom was available (namely, by moving the mobile test van) for reorienting the SIMU, and, furthermore, the azimuth could be controlled only approximately. With this limitation, the field calibration program was limited to estimating and correcting the bias outputs in the gyros and accelerometers. The SIMU was bolted to the van in such a manner that two of the gyros and accelerometer pairs were roughly horizontal, the other pair roughly vertical. Separate calibration methods were used in the horizontal and vertical channels.

The calibration procedure for a level gyro was as follows. First, allow the system to erect and align for about ten minutes, then switch to the free navigation mode. Reorient the van (if need be) to get the gyro approximately level north. With the van stopped, monitor the eastbound acceleration error for about ten minutes. Linear changes in the indicated acceleration are attributed to bias output in the level north gyro.

The analysis of this effect is as follows. Any bias output in the level north gyro will cause a proportional rotation error in the direction cosine matrix. For example, with excessive north gyro output, the level east axis will seem to sink below level at a uniform rate. When apparently below level, it will

seem to pick up an acceleration from the force counteracting gravity, proportional to the error angle - hence, an acceleration error trend proportional to the north gyro drift.

Several error sources in this method should be noted. First, instrument quantization and translational vibrations in the van impose noise on the acceleration trend. Second, measurement times exceeding ten minutes are unwise, since Schuler modulation of the acceleration error will occur. Third, the indicated level of the north gyro could be inaccurate (due, for example, to erection errors), so that an earth rate component would erroneously be picked up in the level north channel. Even with these limitations, we felt confident in our ability to resolve gyro bias to the nearest 0.1 meru.

It might be thought that a gyro near level east could be calibrated by analogous methods, looking at trends in southerly acceleration error. However, the prior alignment will have created an azimuth error just sufficient to negate the north-south acceleration trend; thus, any residual north-south acceleration trends will be due only to residual settling noise in the alignment algorithm.

Calibration of the vertical gyro is more challenging. If it were known to be the only (or dominant) mis-calibrated instrument, the navigation error propagation would be as follows: in free navigation following erection and alignment, errors in the vertical gyro would seem to drive the level east gyro toward level north. The east gyro would then pick up an earth rate component proportional to its error angle (and to the cosine of latitude), which would look like a ramp change in its drift output. This would look like a change in the rate of change of acceleration in the north-south channel. In practice, however, the foregoing method was swamped by error sources of the type described above for north gyro calibration.

The preferred method for calibrating the azimuth gyro was to monitor the SIMU azimuth indicated by the direction cosine matrix. This method involves "cheating" on our calibration philosophy in the respect that it relies on long-term stability of the actual azimuth of the test van. For the first four hours of free navigation, the indicated azimuth error rate is proportional to the azimuth (vertical) gyro drift, provided that no residual drift exists about the east axis. (Such drift would cause the vertical gyro to seem to tip toward north, and hence to pick up an erroneous earth rate component.) Thus, in the vertical gyro calibra-

tion, the horizontal navigation filter was activated for the first few minutes, to trim out any residual drift effects in the horizontal. Following this, the indicated azimuth trend was smoothed for one to two hours. Typical noise jitter in azimuth was on the order of 20 arc seconds, due both to gyro quantization and actual angular vibrations. Noting that 0.1 meru is worth only 4.4 arc seconds of drift in an hour, it is clear why such long smoothing times are necessary.

Field calibration of the accelerometers was comparatively easy. For the level accelerometers, the system was switched to free navigation and (if need be) reoriented so that the level accelerometers were roughly north and east. The average accelerations north and east were then monitored for a few minutes, yielding an acceleration resolution of about 5 milligals. The van was then reversed in azimuth (approximately), and the north and east accelerations were again estimated. The accelerometer biases were then computed as twice the acceleration differences (after azimuth reversal minus before). The explanation of the foregoing inference is deferred to the next section, where the effects of rotations are discussed in detail.

Calibration of the vertical accelerometer bias was performed automatically by the ZEUS filter, as discussed in Section 3.4. The filter converged to a precision of better than 1 milligal within 30 seconds. Its accuracy, of course, was directly related to the knowledge of gravity (and, hence, of both altitude and the gravity anomaly). With this method, a change of accelerometer scale factor would be wrongly corrected as a changed bias; this distinction, however, was unimportant since our test program involved keeping the van upright at all times.

4.3 LABORATORY CALIBRATION TECHNIQUES

The calibration of relative instrument alignments is discussed first. For the methods described here, the navigation software plays an important role in alignment calibration. On the other hand, there is no dependence on optical references, nor on precision laboratory fixtures for effecting the required rotations.

The primary laboratory data to be collected for the alignment tests is the difference in indicated acceleration before and after a specified rotation. Such differences represent simple combinations of alignment errors and accelerometer bias errors; thus, from a suitable set of such data, all the misalignments and biases may be solved.

The general method for predicting the effects of rotations is as follows: First, algebraically define approximate locations for the accelerometers prior to rotation, and accelerometer bias errors. Also, define an approximate value for the direction cosine matrix indicated in the navigation computer. From the foregoing, the indicated acceleration may be computed by resolving the actual accelerometer outputs through the indicated cosine matrix. Next, identify an actual rotation to perform on the IMU, and using this calculate the actual new orientation of the accelerometers. Also, considering the gyro misalignments, calculate the rotation inputs to the navigation computer, hence the apparent rotation indicated in the computer, hence the new indicated cosine matrix. Then the indicated acceleration after rotation is the actual accelerometer output resolved through the new indicated cosine matrix.

For selected rotations, it turns out that acceleration diferences are excited by only accelerometer bias and one pair of misalignment terms, all other error sources (namely, all other misalignments, errors in choosing both the pole and the angle of the rotation, errors in knowing the initial orientation, accelerometer scale errors, and in some cases gyro scale errors) being reduced to second order contributions. To prove the foregoing requires 20-odd pages of algebra articulating the analysis of the preceding paragraph. Rather than present this, we will give an intuitive description of why the method works.

Consider an IMU whose X,Y,Z axes are perfectly aligned to local north, east, down, and whose calibration is perfect except as noted below. Consider first the effect of a rotation of 180° about the level north axis. If the X accelerometer were misaligned toward Z through an angle A_{XZ}, then following the rotation its level would change by $2A_{XZ}$, and its output would therefore change by $2g\ A_{XZ}$. Furthermore, if the Z gyro were misaligned toward X by an angle G_{ZX}, then during the rotation the Z gyro would pick up pulses proportional to G_{ZX}. Thus, the apparent pole of the rotation would be below level north by an angle G_{ZX}, so that the computer would think that the X accelerometer had been rotated below horizontal by and angle of $2G_{ZX}$, thus inducing an apparent acceleration error of $2g\ G_{ZX}$. Thus, the net acceleration difference in the north direction would be

$$\Delta A_{NORTH} = 2g(A_{XZ} + G_{ZX})$$

For this same rotation, the errors in the east and down directions

are unaffected by misalignments. In the vertical, the only difference is induced by bias in the Z accelerometer,

$$\Delta A_{DOWN} = -2\ B_Z$$

In the east channel, the Y accelerometer bias effect is also doubled by resolving the bias in the west direction after rotation. A scale error S_X in the X gyro also causes the apparent rotation to differ from 180 by an amount of 180 S_X, hence causing the Y accelerometer to seem to be above horizontal by 180 S_X, thus causing an apparent acceleration error of 180g S_X. Thus, the east acceleration difference comes to

$$\Delta A_{EAST} = -2\ B_Y - 180g\ S_X$$

Next, go back to the original orientation and consider a rotation of 180° about the down axis. If the X accelerometer were misaligned toward Z by an angle of A_{XZ}, its error output of g A_{XZ} would be moved to south after the rotation, hence doubled in the acceleration difference. The same would obviously happen to its bias output B_X. Furthermore, if the X gyro were misaligned toward Z by an angle G_{XZ}, then it would pick up pulses from the rotation, so that the apparent pole of the rotation would not be straight down, but rather misaligned toward north by angle G_{XZ}. Thus the X accelerometer would apparently end up $2G_{XZ}$ below level south, thus developing an apparent acceleration of 2g G_{XZ}, with reversed sign since the error is resolved southbound. Thus, the net acceleration difference in the north channel is

$$\Delta A_{NORTH} = 2g(A_{XZ} - G_{XZ}) - 2\ B_X$$

The vertical channel is, of course, unaffected by the rotation. The effects in the east channel are precisely analogous to north, yielding

$$\Delta A_{EAST} = 2g(A_{YZ} - G_{YZ}) - 2\ B_Y$$

Thus, it is seen that the foregoing rotations give amply redundant information about accelerometer biases. Also, the rotation about level north gives the combined error by which the X accelerometer leans toward Z, and the Z gyro toward X - hence,

in general, the deviation from nominal 90° of a remote accelerometer-gyro pair. Furthermore, the rotation about the vertical gives the Z component of the alignment difference between the X accelerometer and the X gyro - hence, in general, one component of the angular separation of a nominally aligned accelerometer-gyro pair.

It should be clear, then, that if the rotation tests are repeated, permuting the initial orientations of (X Y Z) on the north, east, down coordinates, all the comparative alignments of all the instruments may be determined. After eliminating accelerometer biases, the yield in fact is 9 simultaneous equations in 12 unknown alignments. Since no external reference surface is involved, three degrees of freedom are available for assigning arbitrary alignment values; for example, one can say that the X accelerometer is by definition correctly aligned, as is the Z alignment component of the Y accelerometer. This yields 12 equations in 12 unknowns, and a unique solution.

It might be thought that the IMU orientations before and after the rotations are convenient orientations in which to calibrate the gyro g-sensitive drifts, thus killing two birds with one stone. This is true in principle, but bad in practice. The reason is that poorly calibrated gyros cause linearly changing acceleration errors in the horizontal channels, thus interfering with one's ability to infer acceleration differences induced by the rotations. For precisely this reason, the rotation tests afford an excellent opportunity to verify the prior gyro calibration. In fact, the alignment calibration may reveal that the gyro axes were not where they were assumed to be during the prior gyro drift calibration, in which case erroneous earth rate components on the gyro input axes had caused errors in computing the drift compensations. For the SIMU, we found alignment errors on the order of 1 milliradian in some cases, necessitating bias corrections on the order of 1 meru.

The sensitivity of the rotation tests depends of course on the stability of the accelerometer biases during the entire test series, and on the effects of quantization on the acceleration estimates. For the SIMU, the accelerometer biases were more than adequately stable (a fact verified by repeating the test sequence several times), and the quantization noise was small enough to yield acceleration estimates to the nearest 5 milligals with about 5-minute smoothing before and after each rotation. In the misalignment equations, 5 milligals is worth about 5 microradians or 1 arc second. Thus, we believe that the SIMU alignments were calibrated to at worst several arc seconds of error.

The SIMU instruments, being ternary torqued, were known to have small (i.e., 5 to 10 arc second) deadbands about their output axes. Which side of the deadband the input axis lay on depended on the sign of the instrument output. For our final alignment calibration test, we deliberately shimmed the SIMU off the nominal north-east-down orientation, to control the sign of the information being processed by each instrument during the rotations. Following this, the shims were changed to reverse the signs, hence to cause the instrument whose alignment was being checked to be on the other side of its deadband. In this manner, the theoretical width of the deadbands was verified, and subsequently the dynamic alignment compensations were programmed in the navigation system software.

Several methods were available for calibrating the gyro scale factors. Referring back to the east channel effect of a rotation about level north, it is seen that the acceleration difference was sensitive to (in the example) the X gyro scale factor as well as the Y accelerometer bias. It is clear that if the rotation had been 360° rather than 180°, the Y accelerometer would have apparently wound up below level by an angle of 360 S_X, thus giving an apparent acceleration error of (in radians) 2π g S_X, from which the scale error S_X can be inferred. It is clear that the Y accelerometer bias, which equally affects the eastbound acceleration before and after rotation, cancels from the difference. It is also true, but less clear, that errors in achieving a precise 360° rotation are unimportant.

The foregoing method was used to verify the gyro scale factors, but not for their original determination. The original calibration used an accurate laboratory turntable, which could be precisely (i.e., within an arc second or two) reset at a designated azimuth mark. The SIMU was placed on the table with the gyro to be tested held vertical, and the free navigation software was turned on following the usual erection and alignment algorithm. The azimuth indicated by the direction cosine matrix was smoothed for a few minutes, to average out quantization errors and to estimate any azimuth rate trend from imperfect bias compensation. Following this the table was rotated once (or several times) in azimuth, and reset accurately to the starting azimuth, after which the indicated azimuth was again smoothed. Clearly, a scale factor error S would manifest itself as an azimuth change of $2n\pi S$, from which the value of S could be inferred. We estimate that the overall error in the procedure was about 2 arc seconds out of 360°, or about 2 parts per million.

It is illuminating to compare the two methods of calibrating the scale factor. In the latter, a precision fixture was used to control the precise degree of rotation. In the former, we rely on the level (Y) accelerometer to tell the computer exactly how far off level it was following the rotation, thus in effect automatically indicating the true total rotation angle. Thus, even though precision in effecting the rotation may be poor, precision in measuring it can be excellent.

SECTION 5

LOCAL DYNAMIC TESTS

The major goal of this program was to develop a high performance real time autonomous land navigation system without periodic stopping constraints to perform velocity updates. As indicated in Reference [3] surprisingly accurate results had been obtained with the zero side-slip (ZOSS) mode tests using the Ring Laser Gyro Strapdown Inertial System. Here, the same type of tests were repeated using the much higher quality CSDL SIMS with the same basic Raytheon software/hardware system, as described in Sections 2 and 3.

After completion of the laboratory and field calibration tests described in Section 4, several dynamic free navigation test runs (totally unaided) were made around our local test course to determine performance levels. All tests were begun in the alignment and erection mode (A/E), automatically leveling and gyrocompassing for about ten minutes, switching to the free navigation mode, and traversing the local test course. This 17-mile course, which takes about one hour to traverse, is a mixture of smooth, relatively straight local highways and rough, winding bumpy New England paved country roads. The course is shown in Reference [3]. Dynamic free navigation performance in the 0.5 to 1.0 nautical mile per hour (NMPH) range was consistently obtained here. The CSDL SIMS appears to produce an order of magnitude better results than that obtained with the strapdown system tested using the Sperry laser gyros.

Once the baseline dynamic free navigation performance level was established, we turned our attention to testing in the ZOSS mode to try to determine the ultimate accuracy of the technique. A typical ZOSS test began in the A/E mode, leveling and gyrocompassing for ten minutes, transferring to the calibration mode for three to five minutes to fine trim any offsets, and finally transferring to the ZOSS mode, leaving shortly thereafter to traverse the test course. The level gyro drifts were checked daily using the field calibration procedure and corrected as required. Occasionally the azimuth gyro was calibrated and even more rarely the level accelerometers. We found the accelerometers to always be within 10 milligals (usually 5) of the original values taken at CSDL before going to the field. Gyro drift changes, on the other hand, were somewhat larger than would be expected from laboratory experience. The major reason for inertial instrument drift was

assumed to be thermal. The Mobile Test Van did not have adequate thermal control. We eventually installed a wooden shroud with a thermally controlled fan over the IMU to temper the environment seen by the CSDL SIMU.

The first ZOSS tests had the vertical channel clamped, as it had been for the tests with the laser gyro system. The results of the first few local ZOSS runs were consistent, with the radial closure error always less than 100 feet. But at a couple of checkpoints, latitude errors of 2 arc seconds (200 feet) were observed and another checkpoint had a longitude error of 3 arc seconds (225 feet) consistently. We had originally scaled our checkpoints from the appropriate Geological Survey maps to the nearest arc second (so we thought). After carefully rescaling the checkpoints, checking the locations, and accounting for uncertainty due to changes such as road relocation, it turned out the ZOSS navigator was a much better locator than we were. Table 5-1 lists the checkpoints and their corrected coordinates.

Although several modifications were made to the Kalman filter as the ZOSS mode evolved into its final configuration, none of these changes seemed to affect the local test results significantly. As we developed Kalman filter concepts we would test them on the local test course before proceeding to the extended test course. Tables 5-2 and 5-3 list the results for the latitude and longitude channels respectively for various test runs accrued over the course of the program representative of the data obtained. The errors are indicated to the nearest arc second (approximately 100 feet in latitude and 75 feet in longitude) as they were read from the CDU. These runs had a mix of stopping at a checkpoint to get a reading, and drive-bys estimating to the nearest arc second from the CDU. Actual location at each checkpoint was probably only good to about 25 feet as we attempted to physically use the same land mark each time; i.e., the course was not accurately surveyed in and marked, but scaled off the Geological maps as indicated above.

Section 6 describes the evolution of the ZOSS filter and the extended test results. As described therein, in December 1975 we added an altitude rate estimator routine to the navigator to uncouple the vertical error coupling from the horizontal channels. The navigation $\dot{R}$ equation (which had been clamped) was replaced with one based on the resolution of the ground speed to the vertical using the appropriate direction cosine matrix element with an offset factor. This new $\dot{R}$ was then integrated to yield R.

TABLE 5-1

SUDBURY, MASSACHUSETTS TEST COURSE

CHECKPOINT LIST

Checkpoint Number	Description	Latitude NORTH	Longitude WEST
0	Raytheon Boresight Facility Initialization Point	42°21'50"	71°26'01"
1	Raytheon Drive West @ Rte. 20	42°21'37"	71°26'00"
2	Old Boston Post Rd. East Ent. @ Rte. 20	42°21'25"	71°27'49"
3	Old Boston Post Rd. West Ent. @ Rte. 20	42°21'05"	71°29'20"
4	Farm Rd. @ Brook	42°20'32"	71°30'57"
5	Framingham Rd. @ Sherman St.	42°19'46"	71°31'58"
6	Framingham Rd. @ Newton St.	42°19'12"	71°31'44"
7	Framingham Rd. @ Old Boston Rd.	42°18'15"	71°30'56"
8	Old Boston Rd. @ Pleasant St.	42°17'54"	71°29'50"
9	Pleasant @ Redcoat/Bosworth	42°18'28"	71°28'26"
10	Belknap Rd. @ Grove St.	42°18'42"	71°26'48"
11	Edgell Rd. @ Water St.	42°19'43"	71°26'11"

TABLE 5-2

LOCAL TEST COURSE ZOSS LATITUDE ERRORS

Checkpoint \ Test Run	Arc Seconds								
	(#29) 11/10/75	(#30) 11/10/75	(ZOSS #11) 2/25/76	(ZOSS #12) 3/12/76	(ZOSS #13) 3/25/76	(ZOSS #14) 4/1/76	4/26/76	(ZOSS #15) 4/28/76	12/15/76
0	0	0	0	0	0	0	0	0	0
1	0	0	0	0	0	-1	0	0	0
2	0	0	0	0	0	0	0	0	+1
3	0	0	0	0	0	0	+1	0	0
4	0	0	0	0	0	+1	0	0	+2
5	0	0	0	0	0	0	0	0	+1
6	0	0	+1	0	0	0	0	0	+1
7	0	0	0	-1	-1	0	0	0	0
8	0	-1	0	-1	-1	0	0	0	0
9	0	0	0	0	0	0	0	+1	0
10	0	0	0	0	0	0	0	0	-1
11	0	0	0	0	0	0	+1	+1	0
0	0	0	+1	+1	0	0	0	+1	0
Actual Closure Error (Feet)	11N	2N	55N	47N	14N	3N	14N	88N	21S

N = North, S = South

TABLE 5-3

LOCAL TEST COURSE ZOSS LONGITUDE ERRORS

Checkpoint \ Test Run	Arc Seconds								
	(#29) 11/10/75	(#30) 11/10/75	(ZOSS #11) 2/25/76	(ZOSS #12) 3/12/76	(ZOSS #13) 3/25/76	(ZOSS #14) 4/1/76	4/26/76	(ZOSS #15 4/28/76	12/15/76
0	0	0	0	0	0	0	0	0	0
1	+1	+1	0	0	0	0	0	0	0
2	-1	-1	0	+1	0	0	0	0	0
3	+1	+1	-1	+1	0	0	0	0	0
4	+2	+2	0	+1	0	0	+1	0	+1
5	+2	+2	-1	+1	0	0	0	0	+1
6	+1	+1	-1	0	0	0	0	-1	+1
7	+1	+1	-1	0	-1	0	0	-1	+1
8	+2	+1	-1	+1	0	+1	0	0	+2
9	+2	+1	-1	0	0	0	+1	0	+2
10	+2	+1	-1	+1	+1	0	+1	0	+2
11	+1	+1	-1	+1	+1	0	+1	0	+1
0	+1	-1	-1	+1	+1	0	+1	0	0
Actual Closure Errors (Feet)	39W	40E	64E	44W	48W	1W	66W	13E	7W
	W = West, E = East								

The first four runs of Table 5-4 are representative of the altitude error data obtained on the local test course after the offset angle had been determined. By now a routine had been added to the software package that caused the current latitude, longitude, and altitude to be saved and printed on the line printer at the next opportunity using a sense switch on the RAC-251 computer. This allowed us to more accurately record the indicated checkpoint position on the fly.

In April of 1976, we further modified the vertical channel by implementing a full fledged vertical filter using the ZEUS option (see Section 2). The altitude data shown in the last three runs of Table 5-4 were taken in this configuration. Spherical closure errors under 25 feet were not uncommon in this configuration for local dynamic runs.

TABLE 5-4

LOCAL TEST COURSE ZOSS ALTITUDE ERRORS

Checkpoint \ Test Run	Feet							Estimated Altitude (Feet)
	*(ZOSS #11) 2/25/76	*(ZOSS #12) 3/12/76	*(ZOSS #13) 3/25/76	*(ZOSS #14) 4/1/76	** 4/26/76	**(ZOSS #15) 4/28/76	** 12/15/76	
0	0	0	0	0	0	+7	+1	160
1	-2	-2	-6	-6	+5	+7	+1	158
2	-9	-11	-19	-20	-1	-2	+1	196
3	-5	-10	-22	-27	+4	+4	+1	240
4	-11	-18	-42	-48	-5	0	0	270
5	-10	-19	-59	-68	-2	+1	-1	263
6	-11	-21	-71	-73	-2	+1	0	283
7			-94	-104	0	0	+2	278
8			-100	-112	0	-1	+1	241
9	-9	-20	-88	-100	+4	-1	+3	202
10	-11	-23	-87	-102	+4	0	+4	183
11	-11		-68	-83	+12	0	+1	218
0	-5	-18	-23	-38	+15	+2	+11	160

*Without ZEUS
**With ZEUS

SECTION 6

EXTENDED NAVIGATION TESTS

The performance of the system operated in the zero side-slip (ZOSS) mode was consistently accurate for the local dynamic tests, as indicated in the previous section. The local run system error appears to be bounded by 100 feet radial error for all runs and by 100 feet spherical error in the final ZOSS with zero up-slip (ZEUS) filter configuration. For all practical purposes, the CDU quantization error (1 arc second) and map error are the dominating error sources.

Since the ZOSS mode makes use of the lateral constraint of the vehicle and the local test course was a relatively short, winding closed path (17 miles long with a 6-mile maximum radial departure) the hypothesis had been advanced in the original ZOSS test with the Ring Laser Gyro Strapdown Inertial System (Reference [3]) that the good performance was due in part to path geometry. So a relatively straight course had been set up using the Massachusetts Turnpike for the base. It was the best available course to examine the filter performance for relatively poorly conditioned geometry. This test course, which is shown in Reference [3], is 117 miles one way with a maximum separation of 100 miles at the end point. It is basically an east-west traverse which runs from the Raytheon, Sudbury, facility in eastern Massachusetts to a point just over the New York state border and back over the same route. Table 6-1 lists the coordinates of the checkpoints and their road distance from the starting point. One easily identifiable checkpoint such as a river, underpass, or overpass was chosen for each 7.5 minute Geological Survey quadrangle traversed, with additional points in the beginning and far point quadrangles.

As discussed earlier, the same basic Raytheon software/hardware package was used in testing with the CSDL SIMU as with the Ring Laser Gyro IMU. The exceptions of course were in the software interface area, instrument compensation routine, and filter parameters. Although both inertial measurement units tested were strapdown configurations, there were radical differences in their construction, error models, and error characteristics (see Section 2 and 3 herein and in Reference [3]). The Kalman filter parameters were selected to suit the particular system being tested. Table 6-2 compares the filter parameters ordinarily used with each system. It is readily seen that the gyro and accelerometer error parameters are about an order of

TABLE 6-1

MASSACHUSETTS TURNPIKE TEST COURSE
CHECKPOINT DESCRIPTION

Checkpoint Number	Checkout Description	Latitude	Longitude	Statute Road Miles from Checkpoint 0
0	Boresight, Sudbury	42°21'50"	71°26'01"	0
1	Edmunds R. + Edgell Rd. Framingham	42°19'43"	71°26'10"	3
2	Edgell Rd. + Rt. 9 Framingham	42°18'01"	71°26'06"	5
3	Mass. Pike Toll Gate Entrance, Framingham	42°17'38"	71°28'46"	8
4	Mass. Pike + I495 Ramp	42°15'52"	71°34'13"	13
5	Ruggles St. + Mass. Pike Upton	42°13'44"	71°37'19"	16
6	Power Line + Mass. Pike Millbury	42°13'23"	71°44'05"	23
7	Mass. Pike + I290 Auburn	42°11'34"	71°51'14"	29
8	Mass. Pike + New Spencer Rd.	42°09'10"	71°59'10"	36
9	Mass. Pike + Exit 9 Sturbridge	42°07'47"	72°03'48"	40
10	Mass. Pike + Marsh Hill Rd., Warren	42°10'22"	72°11'30"	48
11	Mass. Pike + Quaboag River	42°10'18"	72°15'44"	51
12	Mass. Pike + Chicopee River, Wilbraham	42°09'26"	72°24'36"	59
13	Mass. Pike + Interchange 5 (Rte. 33)	42°10'12"	72°34'54"	68
14	Mass. Pike + New Haven R.R., W. Springfield	42°08'25"	72°41'14"	74
15	Mass. Pike + Rte. 20 Russell	42°09'24"	72°48'57"	81
16	Mass. Pike + Chester Rd. Blandford	42°11'54"	72°56'16"	88
17	Mass. Pike + Algerie Rd. Otis	42°14'01"	73°02'18"	94
18	Mass. Pike + Appalachian Trail, Becket	42°17'20"	73°09'28"	102
19	Mass. Pike, Rte. 102 Stockbridge	42°18'25"	73°21'08"	111
20	Mass. Pike Toll Booth	42°19'36"	73°21'52"	113
21	N.Y.S. Thruway + Rte. 22 Canaan	42°21'29"	73°25'41"	117

TABLE 6-2

FILTER PARAMETERS

	RLG SIMU Tests	CSDL SIMU Tests
Gyro Initial Bias	6 meru	0.2 meru
Gyro Wide-Band Noise	$(20\ \mu sec)^2/sec$	0
Gyro Random Walk	$(1\ meru)^2/hr$	$(0.1\ meru)^2/hr$
Accelerometer Initial Bias	100 mgals	20 mgals
Accelerometer Random Walk	$(100\ mgals)^2/hr$	$(5\ mgals)^2/hr$
Initial Azimuth	0 (optical)	0.5 mrads
Level Angle Offset	0.1 mrads	0.02 mrads
Velocity Measurement CAL Mode	0.01 ft/sec	0.01 ft/sec
Velocity Measurement ZOSS	0.5 ft/sec	ZOSS Prefilter

magnitude apart with the exception that the CSDL gyros do not exhibit any wide-band noise (random walk in output angular error - see Reference [5]. These values were derived from our laboratory and field calibration tests with both systems and verified by the free navigation performance. Section 3 contains a detailed description of the final Kalman filter formulation used here, and Sections 2 and 5 of Reference [3] do the same for the Ring Laser Gyro Tests.

The extended ZOSS tests on the Massachusetts Turnpike test course were begun after the system and software were completely checked out by local free navigation and ZOSS tests as discussed in Section 5. The first five extended ZOSS tests performed in October and November of 1975 were with the same Kalman filter formulation as used with the Ring Laser Gyro tests. The start procedure was the same as with the local ZOSS tests: start in the A/E mode for ten minutes, transferring to calibration mode for three to five minutes, then switching to ZOSS and departing. All checkpoints were taken on the fly with no stopping except for the toll booths getting onto and off the Massachusetts Turnpike and lunch at the far end. A typical run took 2-1/2 hours to get to the far point where we put the system in the calibration mode for about an hour while we ate lunch. After lunch we transferred to the ZOSS mode and returned. Our ground speed varied from about 20 to 30 MPH on the steep hills to 50 MPH on the level and faster downhill.

In the figures which follow, each of the symbols on the curves represents an error value at a checkpoint. The data points are connected by straight line segments on the graphs for visual purposes only. The numbers above the curve represent the checkpoint number whose coordinates can be found in Table 6-1. Figure 6-1 shows the RMS longitude errors versus distance travelled for these first five runs along with the RMS longitude data from the original extended ZOSS tests using the Sperry ring laser gyros. Although there was some improvement, it was nowhere near the performance level we expected or had observed in the local runs. During these first five runs some minor modifications were made, mainly to the Kalman filter, adding the zero side-slip smoothing prefilter (run #2); second order covariance integration and better synchronization of the direction cosine matrix for side-slip velocity resolution (run #3); IMU-to-van boresight error replacing the y accelerometer error in the state formulation (run #4); and a thermal shroud with temperature controller placed over the CSDL SIMU (run #5). None of these modifications made any significant difference in the results. The local test runs were still excellent and the extended runs about the same.

Looking at the RMS longitude and latitude data from these first five runs (x curve Figures 6-1 and 6-2), one sees an obvious error growth as the far point is approached (checkpoint #21) and a corresponding decrease in error as the system returns. This correlation between distance from the starting point and error magnitude was traced to the ground speed calculation in the Kalman filter. A simple spherical earth model had been used in calculating ground speed for output purposes and the Kalman filter ZOSS interface. This caused small errors in the ground speed due to earth flattening effects which get larger the farther one travels away from the starting point.

This error was corrected in the beginning of December 1975 by changing the ground speed determination routine to use the earth radii based on the ellipticity and the current latitude from the navigation routine. The next long ZOSS run (#6 performed on December 2, 1975) was significantly improved. The maximum longitude error indicated was 9 arc seconds (675 feet) while the maximum latitude error indicated was 8 arc seconds (800 feet). This appeared to solve the major offset distance problem.

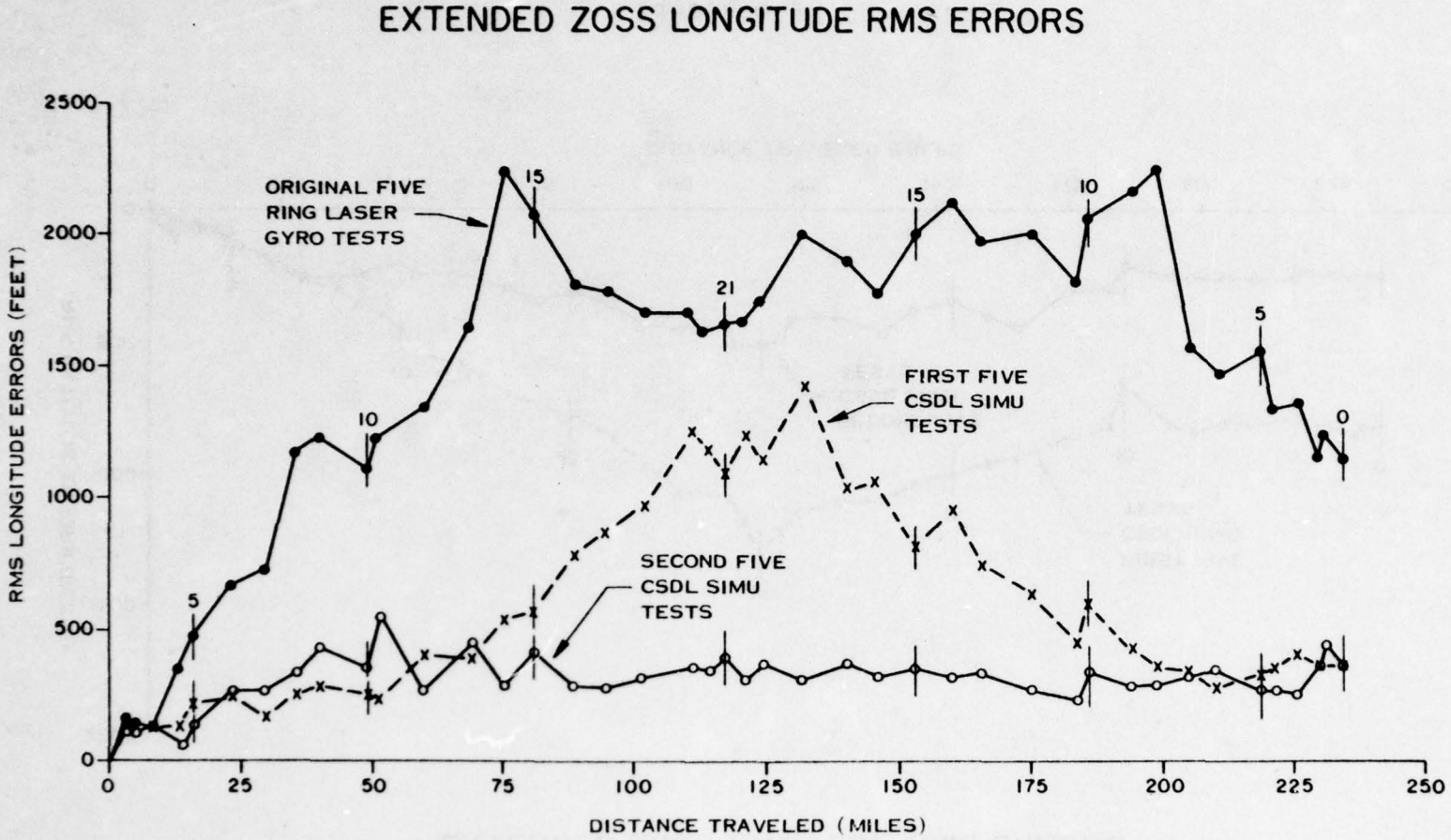

EXTENDED ZOSS LONGITUDE RMS ERRORS
RMS LONGITUDE ERRORS (FEET)
2500
2000
1500
1000
500
0
0
25
50
75
100
125
150
175
200
225
250
DISTANCE TRAVELED (MILES)
ORIGINAL FIVE
RING LASER
GYRO TESTS
FIRST FIVE
CSDL SIMU
TESTS
SECOND FIVE
CSDL SIMU
TESTS
5
10
15
21
15
10
5
0

Figure 6-1

EXTENDED ZOSS LATITUDE RMS ERRORS

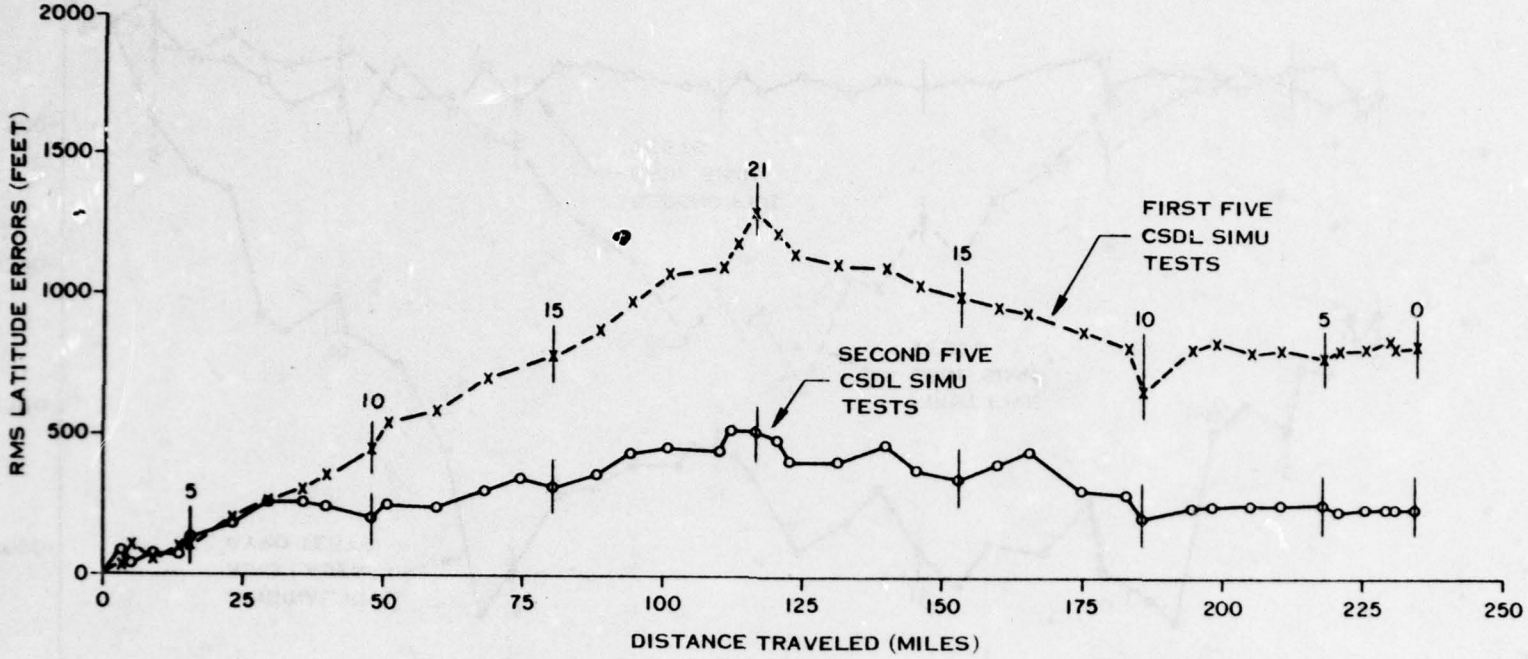


Figure 6-2

The residual horizontal errors were now small enough to motivate us to re-examine the software for other small error sources which might not have been visible in prior tests with less accurate instruments. The clamped vertical channel was a prime suspect, since altitude-dependent terms which in fact feed into the horizontal channels were not being computed. Accordingly, we developed a quick-and-dirty altitude estimation routine, based on resolving forward speed through the pitch angle of the SIMU augmented by a pitch offset between the SIMU and the van.

The horizontal channel data obtained with the modified software was much improved. The open circle data points in Figures 6-1 and 6-2 represent the RMS longitude and latitude errors for the second five Massachusetts Turnpike runs to New York. The first of these, run #6 of December 2, 1975, contained only the corrected ground speed routine. It was included with the others which had the altitude rate and altitude estimator mechanized as well, because of the similarity in results.

Although the altitude estimator did not improve horizontal navigation as hoped, it worked surprisingly well in the altitude channel itself. The altitude estimator was variable in performance varying between 40-foot and 1200-foot closure errors (corresponding to misalignment angles of the pitch offset of about 30 microradians and 1 milliradian respectively). Although we attempted to calibrate the misalignment angle through local runs and using data from previous long runs, the actual angle the "average" van velocity vector made with the vertical appeared to be dependent on loading, speed, amount of gas in the tanks, and things over which we had no control: wind, temperature (stiffness of the springs), etc. In light of this, some remarkable performance was observed. We had crossed our low point at the Connecticut river (110 feet above sea level) and high point (1740 feet high) within 25 feet.

Comparing this later data with the first set of data obtained, one sees almost half an order of magnitude improvement in performance. We can hypothesize that the same level of improvement could be obtained with the Ring Laser Gyro system if these tests were repeated with the improved software.

Analyzing the filter data from the second five runs, we noticed that the level gyro biases and side-slip misalignment angle as estimated by the Kalman filter were changing during the run in a somewhat repeatable way. We at first suspected insufficient pre-run calibration, and tried changing our start-up procedures. We would start in the A/E mode for ten minutes as usual, transfer to calibration mode for three to five minutes, and then to ZOSS as before, but then we would make a one-hour circuit of the local test course in the ZOSS mode (allowing the filter to settle), returning to the starting point. The system would be briefly put in the calibration mode to fine trim any velocity errors. We also reset the latitude, longitude, and altitude errors, then proceeded to New York and back as before. On one of these runs we experienced mechanical difficulties (could not get into high gear), but we kept going anyway. The on-the-road time was extended from five to seven hours with the same type of results. The Kalman filter error tended to track in position, not time. After several runs, varying gains and filter parameters with basically the same results, we began asking the question - can we do any better, or are we limited by unmodeled error forces, e.g., gravity anomalies and deflections of the vertical. A preliminary analysis indicated that our horizontal error magnitudes were consistent with global RMS deflections of the vertical, and a subsequently obtained anomaly contour map (Figure 6-3) derived from Reference [6] further suggests that the deflection on our test course would be primarily in the east-west direction.

Lacking the gravity anomaly survey information of Reference [6] at that time, we decided to see if the navigation system itself could estimate gravity anomalies en route. To do this, we constructed the zero-up-slip (ZEUS) filter, as described in Section 3. Following checkout of the ZEUS filter in local navigation tests, in which it showed outstanding ability to track altitude (see Table 5-4), its first extended test was in New York ZOSS Run #15 of April 28, 1976. This was the best run to date. Our spherical closure error was less than 180 feet. The longitude errors were bounded by 525 feet and the latitude errors by 300 feet. The horizontal error results are shown in Figure 6-4. It is interesting to note that on the return trip the mobile test van is typically 100 feet south of where it was on the outgoing trip due to the width of the divided highway. This is evident in the latitude data shown in Figure 6-4. One significant error source affecting the data could have been the uncertainty of location of the checkpoints.

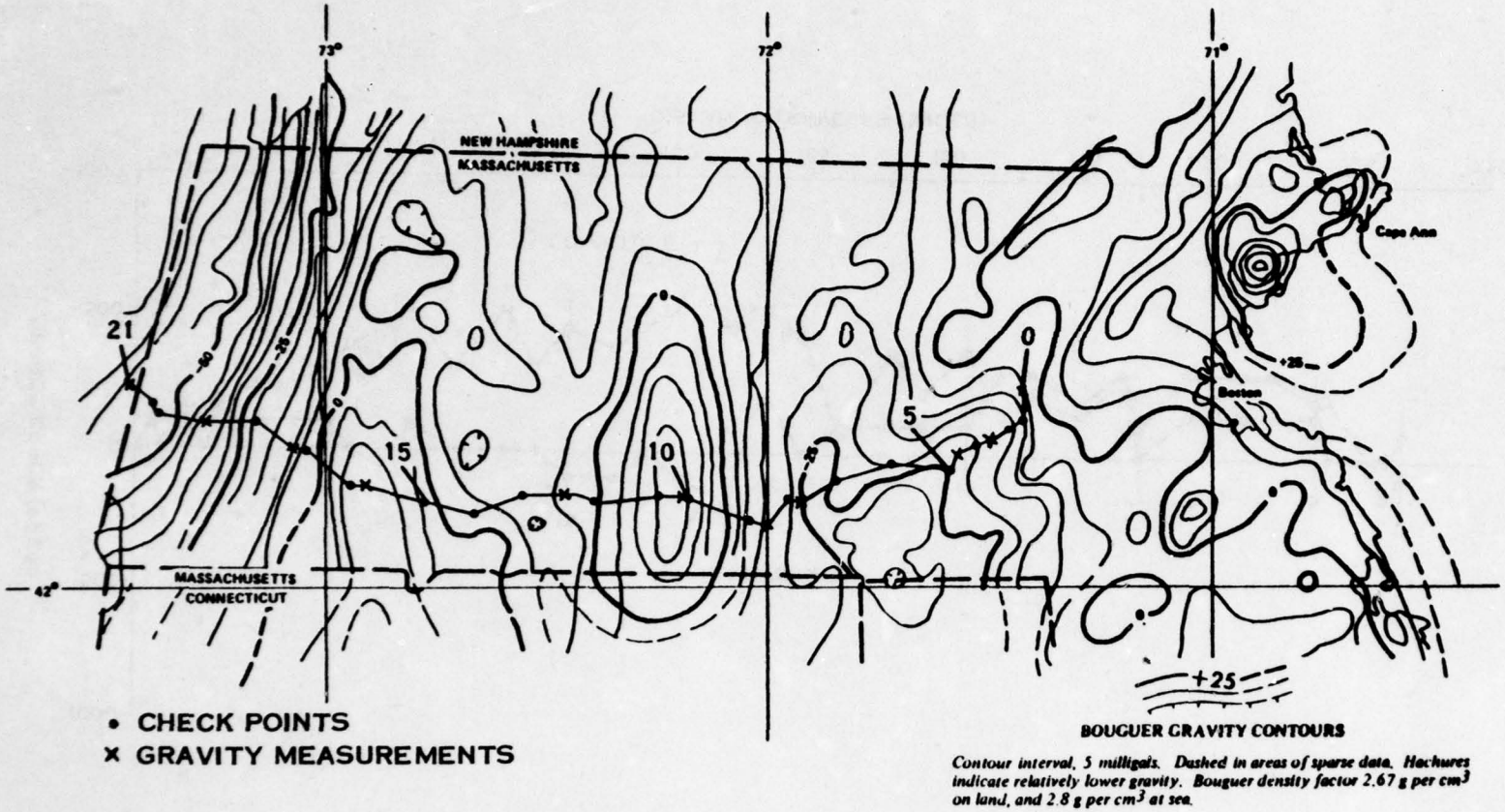


Figure 6-3 Massachusetts Gravity Anomaly Contour Map

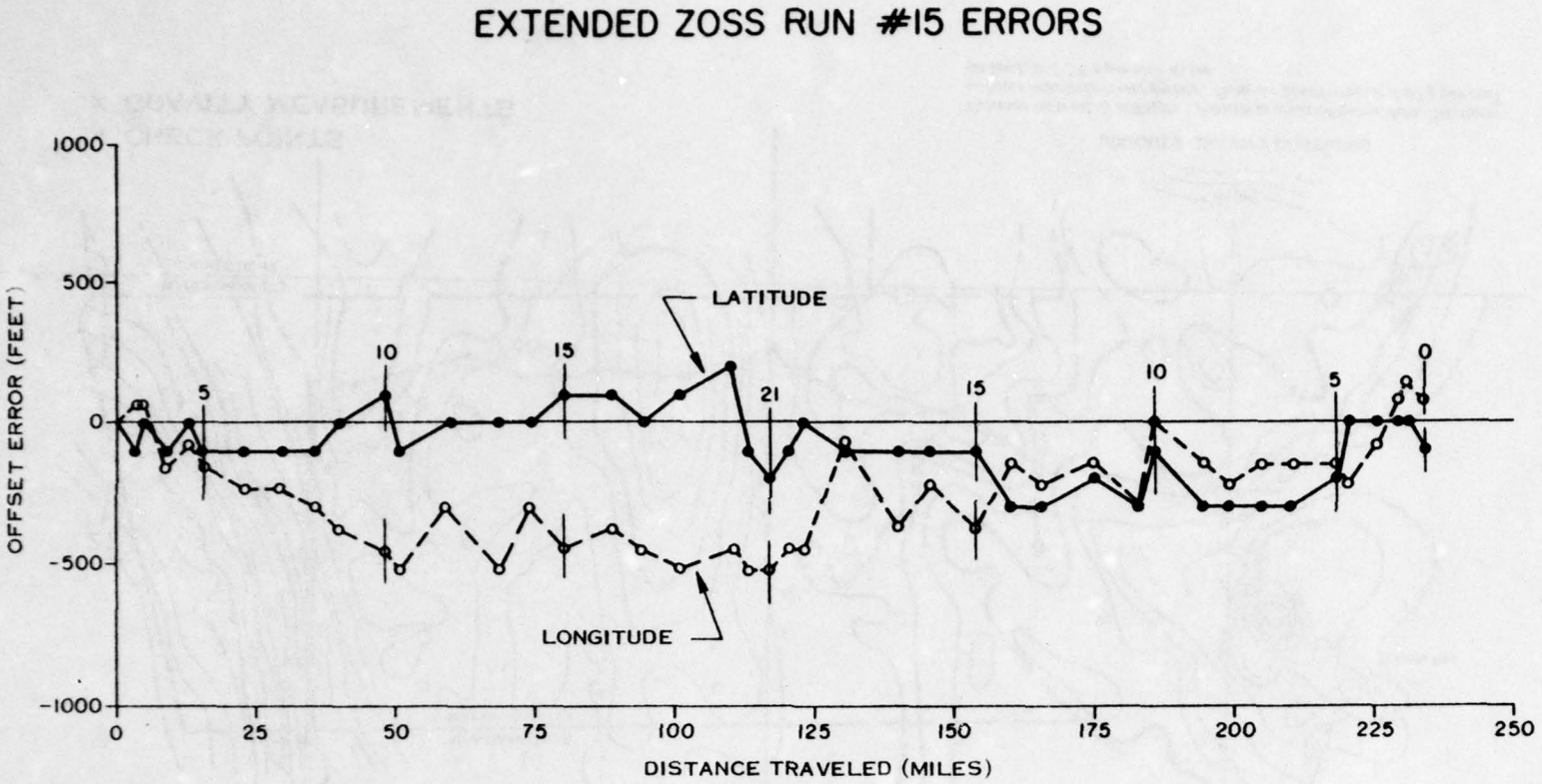

EXTENDED ZOSS RUN #15 ERRORS
OFFSET ERROR (FEET)
1000
500
0
-500
-1000
LATITUDE
LONGITUDE
5
10
15
21
15
10
5
0
0
25
50
75
100
125
150
175
200
225
250
DISTANCE TRAVELED (MILES)

Figure 6-4

In addition to the good latitude and longitude data, we obtained some very interesting altitude and gravity anomaly data. Figure 6-5 contains a plot of the gravity anomaly data estimated in the navigation computer, versus longitude for the outbound and inbound portions of this run. Below it on the same graph, is a plot of the indicated altitude profile. It is seen that the indicated anomalies correlate visually with the altitude profile, and are consistent with the frequently-encountered phenomenon of density anomalies beneath mountain ridges. It is also noteworthy that the anomaly estimates are phase-shifted between the eastbound and westbound legs of the trip, showing a time lag which is probably indicative of unrealistic parameter selection in the ZEUS filter. We planned to take more runs and investigate further but we developed problems with our support equipment: generators and air conditioning. And while they were being repaired, other commitments were made for the equipment and personnel.

Finally, in December of 1976, we briefly returned to testing to get some data on the gravity anomaly problem. With the aid of John Mastroelli of CSDL gravity readings were made at selected points on the Massachusetts Turnpike test course using a LaCoste and Romberg model G gravimeter. These were at intermediate points other than the checkpoints (rest areas where we could stop and take data). Figure 6-6 shows the gravity anomaly readings reduced from the gravimeter measurements, compared with the computer-estimated anomaly taken on the final run. Clearly, the ZEUS filter is indeed estimating the anomalies. The reduced phase shift between eastbound and westbound anomaly estimates is probably due to the frequent pauses (about 15 minutes each) to take gravimeter data, during which the ZEUS filter had time to catch up.

To summarize the vertical navigation results, we may infer even from limited tests that the vertical (ZEUS) filter is a promising method of providing useful estimates of both altitude and gravity anomaly information. Furthermore, the large anomaly changes on our particular test course are strongly suggestive of the hypothesis that unmodeled deflections of the vertical are responsible for much of the residual error in horizontal navigation, particularly in the longitude channel.

Figures 6-7 and 6-8 summarize the horizontal error results for the eight complete extended ZOSS runs since the software repair of run #6. The plotted data are the ± 1 sigma errors about the

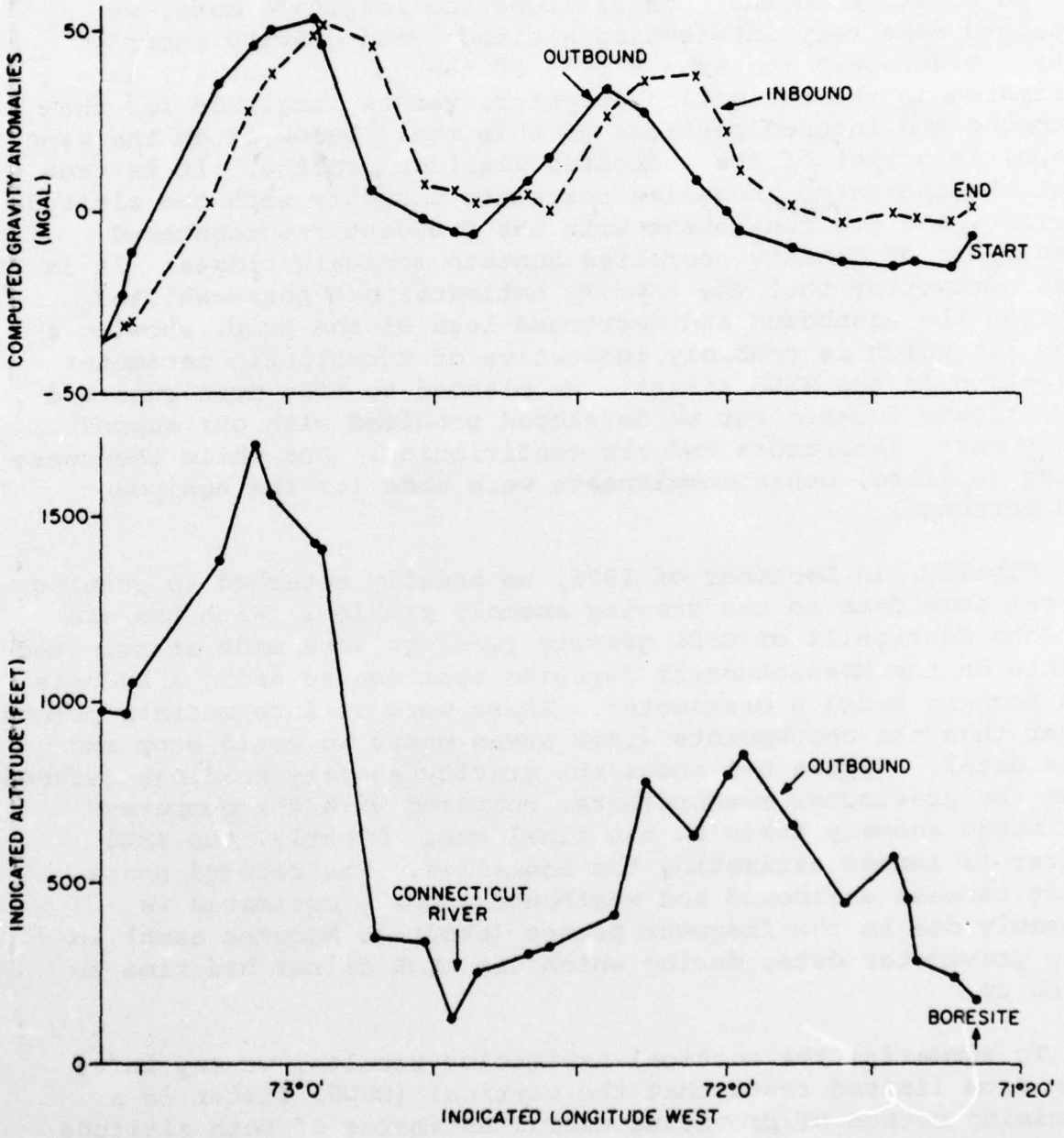


Figure 6-5 Indicated Altitude and Gravity Anomaly, ZOSS Run #15

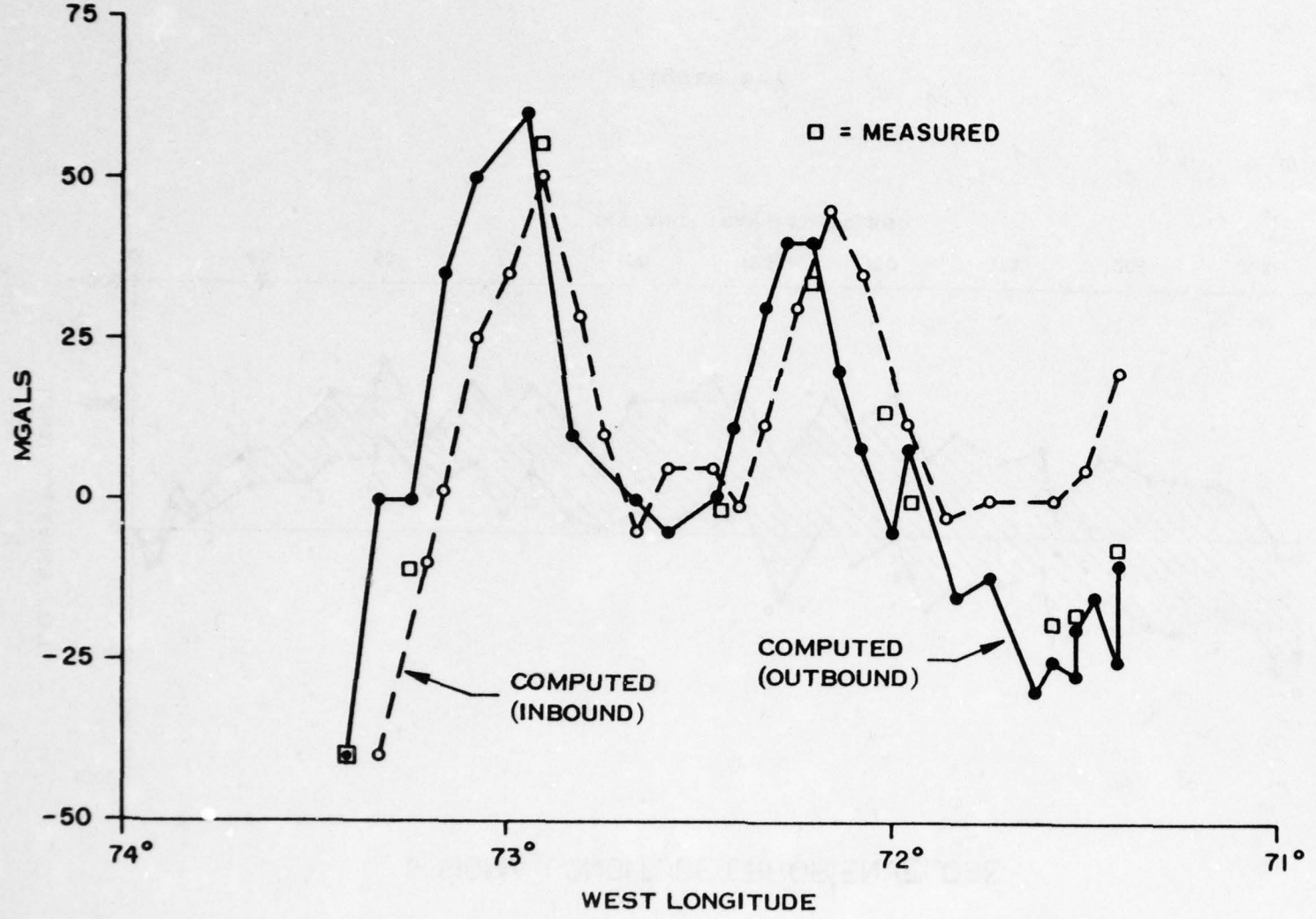
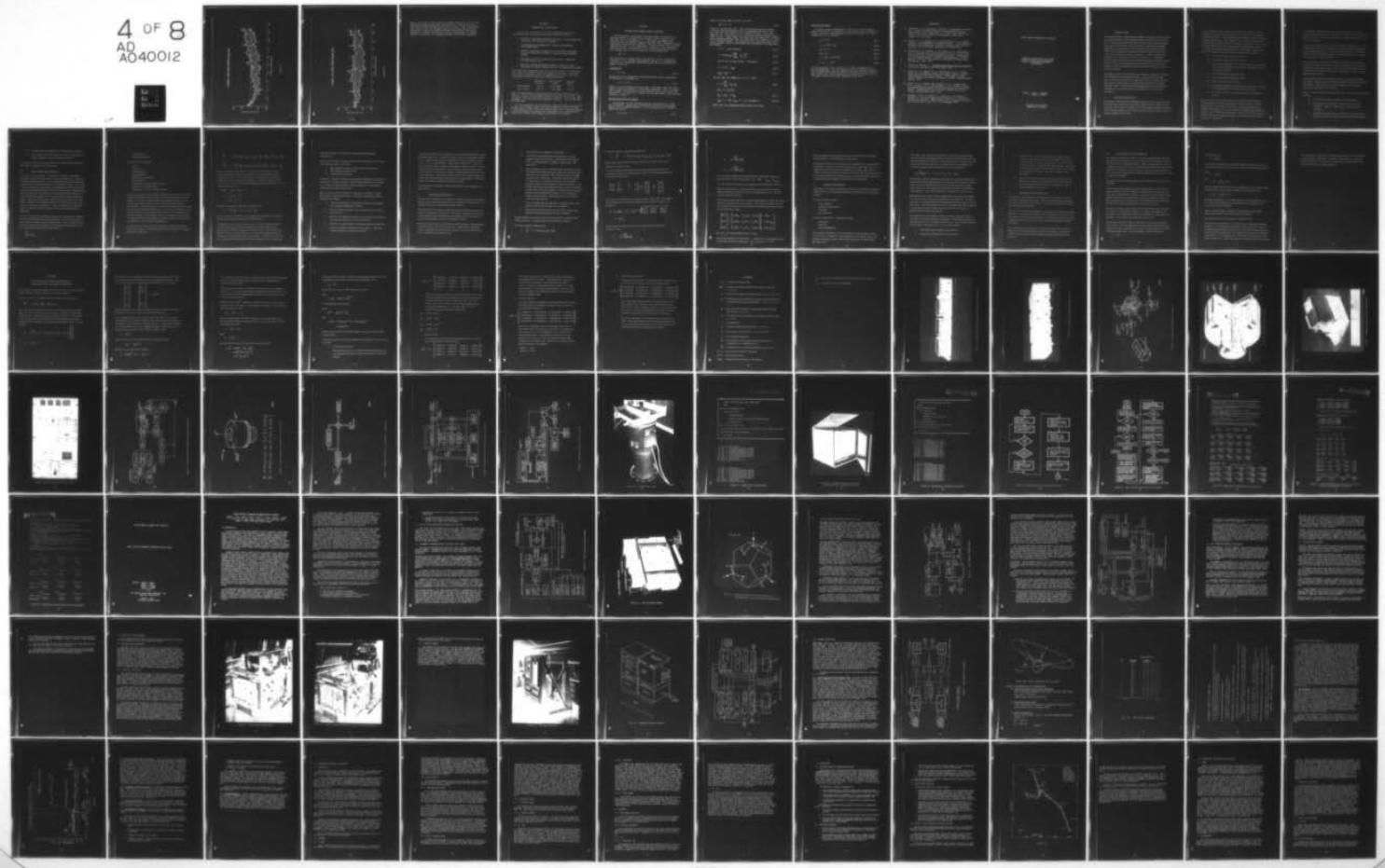


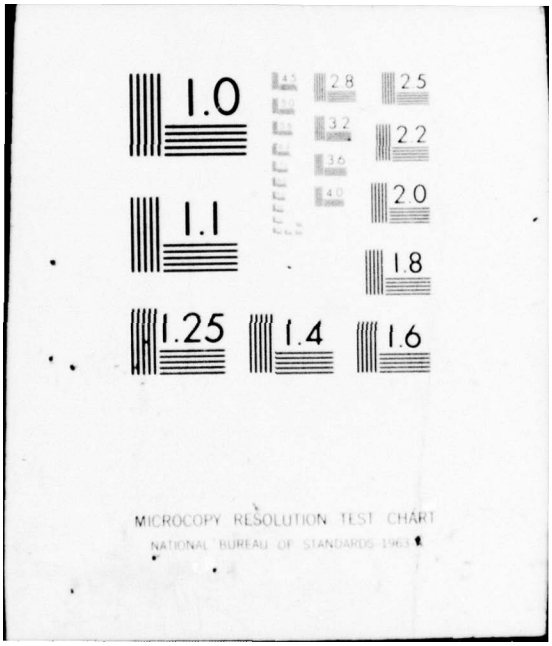
Figure 6-6 Measured and Indicated Gravity Anomalies, ZOSS Run #17

AD-A040 012 ARMAMENT DEVELOPMENT AND TEST CENTER EGLIN AFB FLA F/G 17/7
PROCEEDINGS OF THE BIENNIAL GUIDANCE TEST SYMPOSIUM (8TH) HELD --ETC(U)
MAY 77

UNCLASSIFIED ADTC-TR-77-3-VOL-1 NL

4 OF 8
AD
A040012




1.0
1.1
1.25
1.4
1.6
1.8
2.0
2.2
2.5
2.8
3.2
3.6
4.0
MICROCOPY RESOLUTION TEST CHART
NATIONAL BUREAU OF STANDARDS 1963

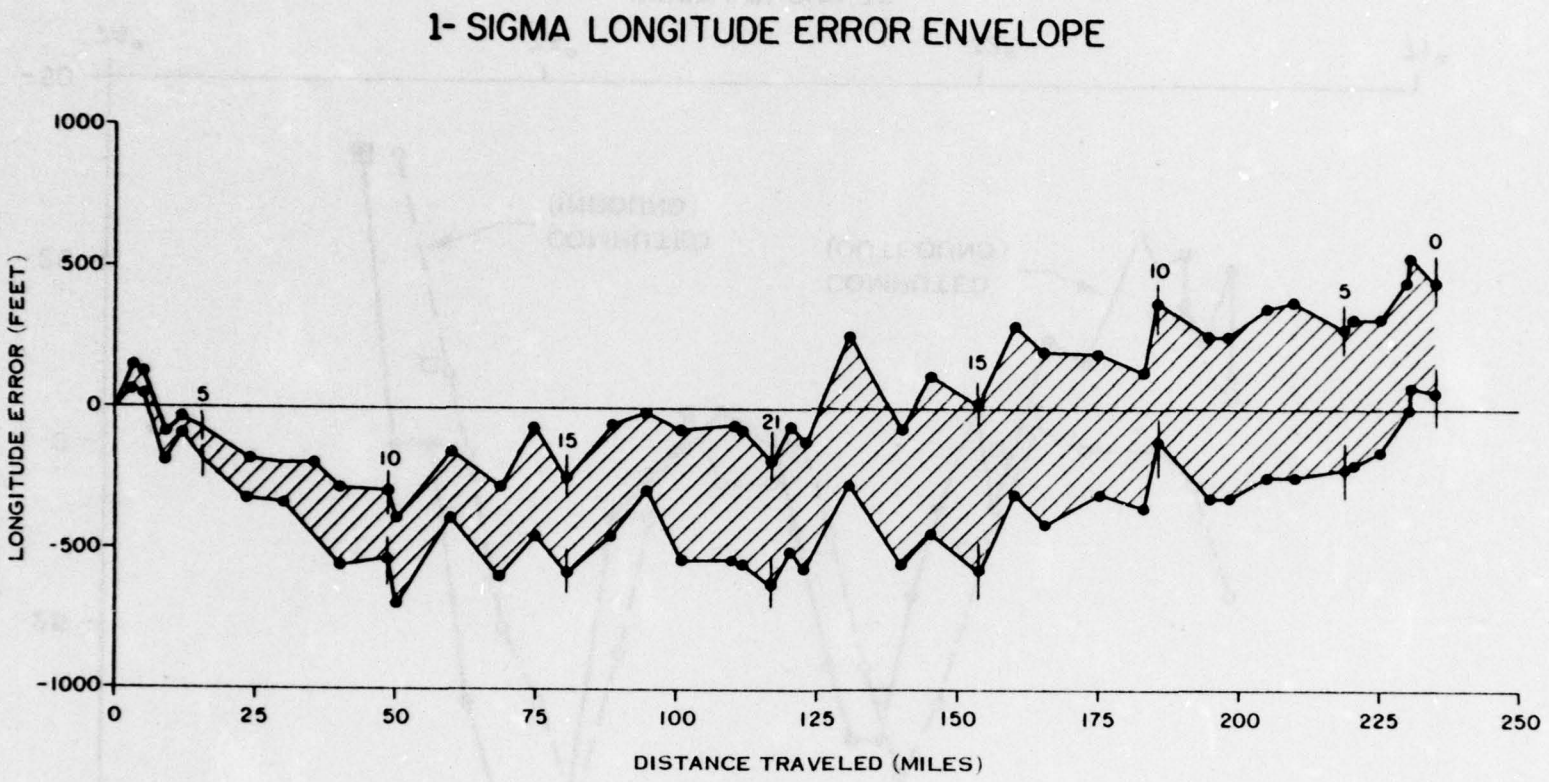

1- SIGMA LONGITUDE ERROR ENVELOPE
LONGITUDE ERROR (FEET)
1000
500
0
-500
-1000
0
25
50
75
100
125
150
175
200
225
250
DISTANCE TRAVELED (MILES)
5
10
15
21
15
10
5
0

Figure 6-7

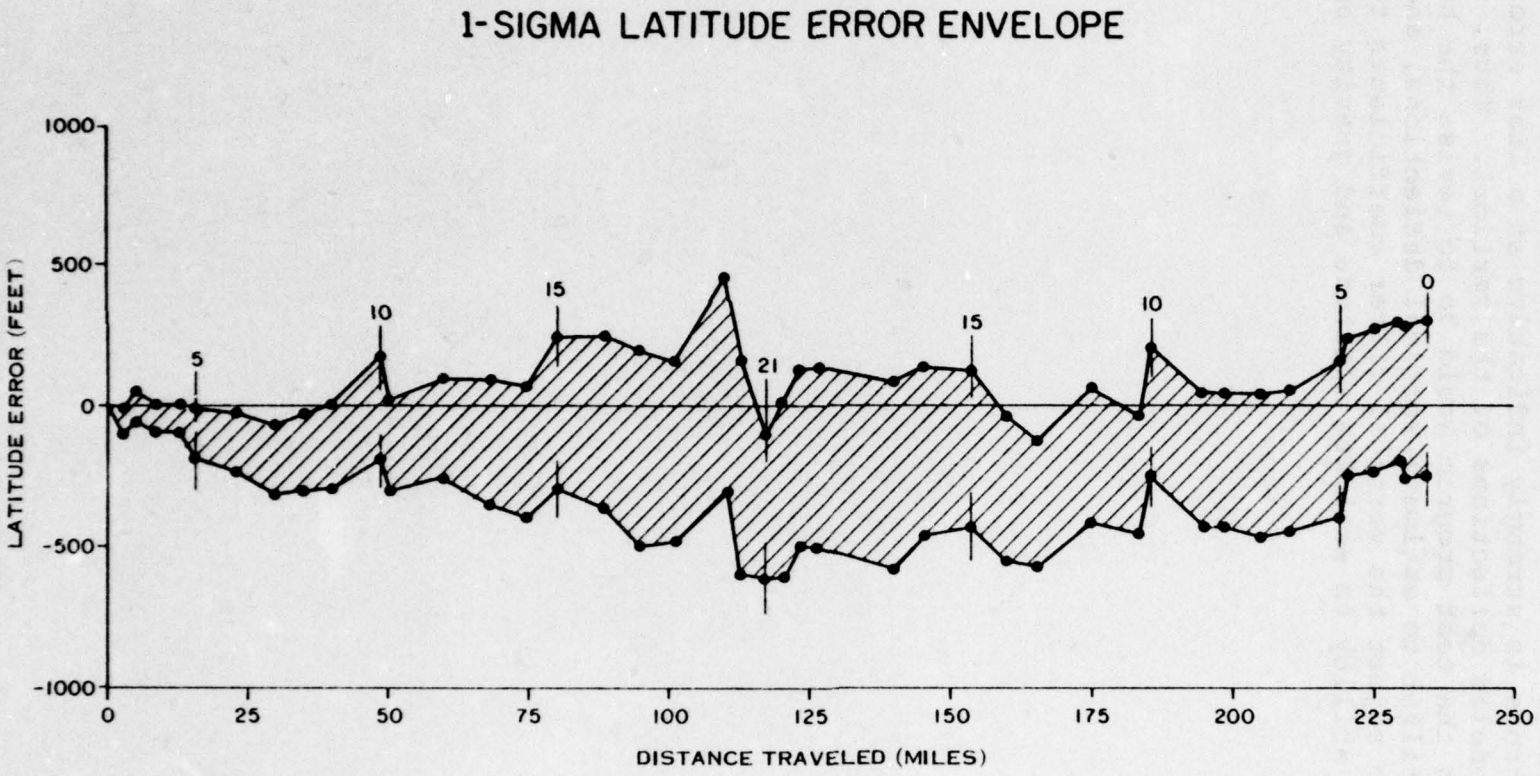

1-SIGMA LATITUDE ERROR ENVELOPE
LATITUDE ERROR (FEET)
1000
500
0
-500
-1000
0
25
50
75
100
125
150
175
200
225
250
DISTANCE TRAVELED (MILES)
5
10
15
21
15
10
5
0

Figure 6-8

mean. The large ratio of mean to standard deviation in the early longitude errors is strongly indicative of a bias error source such as unmodeled deflections of the vertical. Thus, the logical next step in the test program would be to revise the horizontal navigation filter to estimate vertical deflections, and simultaneously to adjust the vertical filter coefficients to further improve its ability to estimate altitude and gravity anomalies.

SECTION 7

SUMMARY AND CONCLUSIONS

A series of terrestrial inertial navigation tests were conducted, with the following salient characteristics:

1. Raytheon computation hardware/software, as developed over many years of navigation testing.

2. A high-quality strapped down inertial measurement unit (CSDL SIMU).

3. Careful laboratory calibration of the SIMU, followed by field calibration checks of gyro and accelerometer biases.

4. No external aids from optical references, landmarks, or fifth wheel, etc.

5. Special Raytheon-developed software filters to take advantage of motion constraints in a strapped down system.

The tests were conducted over both a short course (17 miles, one hour) and an extended course (234 miles, six hours). For runs following corrections of known computational errors, the root-mean-square terminal errors are summarized below:

	Horizontal Error	Error Growth Rate	Vertical Error
Short Course	58 ft	1/105 NMPH	11 ft
Long Course	403 ft	1/90 NMPH	178 ft

The root-mean-square vertical errors cited above were for runs using a vertical filter implemented late in the test series. The vertical filter also estimated gravity anomalies with fairly good accuracy. For our best run a spherical closure error of 180 feet was observed.

At the conclusion of the currently reported tests, our opinion is that the residual errors are due primarily to irregularities in the gravity field, and that further tests with the computational filters adjusted to estimate and compensate these irregularities would show further improvement in navigational accuracy.

APPENDIX

SQUARE-ROOT KALMAN FILTER ALGORITHM

The horizontal navigation filter described in Section 3.2 was programmed in a square-root algebra, drawn directly from Kaminski, et al, (Reference [7]). We highly recommend this algorithm for its greatly improved dynamic range (compared to the covariance Kalman filter algebra). We also believe that it saved computation time in our application, although at the expense of program storage. The basis for the filter is a matrix S which is a square root of the covariance P in the sense that

$$SS^T = P$$

The algorithm is divided into three parts: First, noise-free integration of S between measurements; second, a triangulation algorithm to incorporate integrated noise in S; and third, the update algorithm.

Integration

$$\dot{S} = MS \qquad \text{(I-1)}$$

where matrix M incorporates the deterministic static equations as described in Section 3.2.

$$S = S + \dot{S}\,\Delta t \qquad \text{(I-2)}$$

where Δt is the integration time step. The equal sign here (and below) always represents a replacement operation. For a strapped down system, the elements of M may change drastically during the integration, so there is no useful way to cheat with a pre-computed transition matrix.

Triangularization Algorithm

The purpose of the triangularization algorithm is to "add" the integrated square-root noise matrix (q) to the integrated square-root covariance matrix. If q is adjoined to S to form a (N by 2N) matrix

$$A = (S\ q) \qquad \text{(T-1)}$$

then it is seen that if $q\,q^T = Q$, then

$$AA^T = P + Q \qquad \text{(T-2)}$$

which is the desired form. The triangularization algorithm in effect post-multiplies A by an orthogonal matrix in such a way that the right half of A is reduced to zero. Note that equation T-2 is preserved if A is post-multiplied by any orthogonal matrix. Thus, after the algorithm, the noise has in effect been incorporated back into the left half of A (namely, S), which is the desired result. The algorithm does not explicitly find the orthogonal matrix, but proceeds by elementary row operations as follows.

$K = 1$ (row counter) (T-3)

$$\sigma = \text{sign}(A_{KK}) \left(\sum_{J=K}^{2N} A_{KJ}^2 \right)^{\frac{1}{2}} \qquad \text{(T-4)}$$

If $K = N$, to step (T-10). Otherwise (T-5)

$$\beta = 1/\sigma(\sigma + A_{KK}) \qquad \text{(T-6)}$$

$$A_{KK} = A_{KK} + \sigma \qquad \text{(T-7)}$$

Do the next two steps for $L = K + 1:1:N$

$$Y = \beta \sum_{J=K}^{2N} A_{KJ}\, A_{LJ} \qquad \text{(T-8)}$$

For $J = K:1:2N$

$$A_{LJ} = A_{LJ} - Y\, A_{KJ} \qquad \text{(T-9)}$$

$$A_{KK} = -\sigma \quad \text{and} \quad A_{KJ} = 0 \quad \text{if J exceeds K} \qquad \text{(T-10)}$$

Done if $K = N$, otherwise step K and go to (T-4)

Measurement Update

For each scalar measurement Z, there is a corresponding measurement matrix C (actually, a row vector) and a measurement noise variance R, with details as noted in Section 3.2. The computation is as follows.

$$F = S^T C^T \tag{M-1}$$

$$a = 1/(F^T F + R) \tag{M-2}$$

$$K = S F a \tag{M-3}$$

$$\Delta X = K z \tag{M-4}$$

$$\gamma = 1/\left(1 + (R a)^{\frac{1}{2}}\right) \tag{M-5}$$

$$S = S - \gamma K F^T \tag{M-6}$$

In the foregoing, the F vector is a useful intermediate to save computation; a is the reciprocal of the expected variance of the measurement from the state prediction; K is the Kalman gain vector; ΔX is the correction to the state vector; and γ is the magic factor which makes equation (M-6) work.

REFERENCES

[1] Matthews, J. B. and Taylor, George R., "Development Program for a General Purpose Computer and Strapdown Inertial Measurement Unit", AIAA Paper No. 69-850, AIAA Guidance, Control and Flight Mechanics Conference, New Jersey, August 18 - 20, 1969.

[2] Taylor, G. R., Donaghy, J. F., and Putnam, B. G., "Field Tests of a Developmental Strapdown System". Fifth Biennial Guidance Test Symposium, Inertial Guidance Test Facility, Holloman Air Force Base, New Mexico, October 1970.

[3] Matthews, J. B., Gneses, M. I., Pasik, D. J., and Taylor, G. R., "Results of the Developmental Testing of the First Ring Laser Gyro Inertial Navigation System." Proceedings of the Seventh Biennial Guidance Test Symposium, Central Inertial Guidance Test Facility, Holloman Air Force Base, New Mexico. May, 1975.

[4] Britting, Kenneth, R., Inertial Navigation Systems Analysis, John Wiley and Sons, Inc., New York, 1971.

[5] Pasik, D. J., Gneses, M. I., and Taylor, G. R. "A Ring Laser Gyro Strapdown Inertial Navigation System: Performance Analysis and Test Results." AIAA Paper 75-1095, AIAA Guidance and Control Conference, Boston, Massachusetts. August, 1975.

[6] Kane, M. F., Simmons, Gene, Diment, W. H., Fitzpatrick, M. M., Joyner, W. B., and Bromery, R. W., "Bouguer Gravity and Generalized Geologic Map of New England and Adjoining Areas." Department of the Interior, United States Geological Survey Map GP-839, 1972.

[7] Kaminski, Paul G., Bryson Jr., Arthur E., and Schmidt, Stanley F., "Discrete Square Root Filtering: A Survey of Current Techniques", IEEE Transactions on Automatic Control," Vol. AC-16, No. 6, pp. 727 - 736, December 1971.

EIGHTH BIENNIAL GUIDANCE TEST SYMPOSIUM

LABORATORY CALIBRATION OF A PRECISION STRAPDOWN INERTIAL NAVIGATION SYSTEM HAVING A NON-ORTHOGONAL INSTRUMENT CONFIGURATION

AUTHORS: PATRICK J. DONOGHUE
LELAND B. COTTER

TELEDYNE SYSTEMS COMPANY
NORTHRIDGE, CALIFORNIA

I INTRODUCTION

The implementation of inertial grade strapdown navigation systems requires a precise knowledge of vehicle angular motion as well as linear accelerations. These are provided respectively by high accuracy rate gyroscopes and linear accelerometers. Recent advances in instrument technology, especially in dry tuned gyros, have provided sensors which have the potential of very accurate determination of angular rates and accelerations over a broad spectrum of dynamic conditions. In order to realize this potential, it is necessary to be able to account for i.e., compensate, several instrument and system effects that would otherwise obscure vehicle motions. This in turn requires a precise laboratory measurement and isolation of the necessary parameters at the instrument level via system level calibrations.

This paper presents the development of a method of calibrating a skewed-axis strapdown inertial navigation system. The particular strapdown system considered uses two two-degree-of-freedom dry tuned gyros and three linear accelerometers as a single thread element in a quadruply redundant system. Both the theory and implementation of the calibration techniques are described and data are presented after a brief system description.

II SYSTEM DESCRIPTION

A quadruply redundant digital strapdown navigation system has recently been developed for the Messerschmitt-Bölkow-Blohm Aircraft Company of West Germany. This system, designated as RIICS (Redundant Inertial Information and Computation System) is the major sensor and computational element in a control configured test vehicle.

Four independent digital computer/converter units, together with four strapdown inertial measurement units and a single control display unit constitute the system. This configuration provides for a Fail-Op/Fail Op/ Fail Safe flight system. The computer units, as shown in figure 1 are Teledyne System Company TDY-43 computers. Each unit is a 16K x 16 bit machine (expandable to 32K with plug-in and 64K potential). It has a 3.36 MHz clock yielding a typical thru-put of 320K ops. It has special features for flight control data and IMU interface which include:

(1) 128 dc analog input channels ($\pm$ 10 vdc).

(2) 8 dc analog output channels ($\pm$ 10 vdc).

(3) High speed independent inter-box DMA channels, which allow up to a 1K block of data to be automatically transferred to the 3 recipient computers.

(4) 8 x 16 BIT Parallel input logic words.

(5) 8 x 16 BIT Parallel output logic words.

(6) Programmable real time counter.

(7) IMU and CDU interfaces using a serial channel I/O, converted to IC RAM DMA which eliminates program control.

(8) 2K IC RAM which allows faster processing of selected sub-routines.

The four system inertial units (IMU's) are Teledyne TDS-3D systems. A photograph of the 4 IMU's per system is shown in figure 2. These systems utilize three linear accelerometers and two two-degree-of-freedom dry tuned gyros in a non-orthogonal configuration as depicted in figure 3. The two gyros are skewed with respect to the vehicle roll axis by 30°, while the three accelerometers are arranged in a conventional orthogonal configuration.

The strapdown inertial sensor is the primary sensor for all aircraft attitude control and guidance. A single IMU contains all of the instruments, caging electronics, conversion electronics and computer interface for one of the four channels.

A key element in the system is the Teledyne SDG-5 strapdown gyro. The strapdown gyro has been designed specifically for high-grade strapdown inertial navigation systems. The gyro is dry and features an elastically supported rotor with a dynamically tuned suspension system. A cutaway view of the gyro is shown in figure 4.

The accelerometer utilized in the RIICS system is the Systron-Donner model 4841 linear accelerometer, which has performance characteristics consistent with the requirements of an inertial grade strapdown system and which has been used in other similar applications. Figure 5 shows a photograph of the device.

The final major element of the RIICS system is the control and display unit (CDU). This unit provides the interface between the operator and the quad system. This system has internal redundancy features and is separately connected to each computer.

Figure 6 shows the front panel of the RIICS CDU. It possesses the following features;

(1) An integral navigation and flight control display unit.

(2) Simultaneous and independent communication to all four computers. Inputs for display from a switch selected computer.

(3) Quadruply redundant feature for flight critical elements e.g., flight control selection switches and system failure displays.

(4) Protection against single failure/multiple effect conditions.

(5) Total software control of display functions is augmented by display CUEING to assist in operator interface.

Formulation of the calibration problem for the skewed axis system just described is developed in the next section.

III THE CALIBRATION PROBLEM

The basic navigation problem, whether for strapdown or gimballed systems, requires the integration of vehicle accelerations in a reference navigational coordinate frame. For a gimballed system this is provided directly by the compensated platform accelerometer outputs. For a strapdown system these are provided by a transformation of the body mounted accelerometer outputs through the body to reference frame transformation. This transformation is provided by a measurement and subsequent integration of body axis angular rates as indicated by the body mounted rate gyros. This latter mathematical operation is performed entirely in the system computer and completely replaces the complex mechanical and electrical structure of a platform. A flow of computations is depicted in figure 7, wherein the vehicle attitude is shown to be represented by a quaternion.

As may be noted from the figure, both gyro and accelerometer compensation is required before the attitude integration, acceleration resolution and navigation computations may be performed. This is required so that the various non-ideal mechanisms of the sensors may be removed. For the accelerometers this includes the effects of:

bias

scale factor

axis alignment

temperature effects

For the gyros this includes:

bias

scale factor

axis alignments

mass unbalance

quadrature g-sensitivity

anisoelasticity

temperature variation of scale factor

temperature variation of bias

temperature variation of mass unbalance

As seen in the previous section (figure 3) the gyros are mounted in a non-orthogonal fashion both with respect to the body principal axes and with respect to each other. This presents a particularly unique set of constraints under which calibration of the system parameters may be accomplished. In particular it may be noted that standard instrument type tests of the gyro within the system e.g., a four point vertical test, would require cumbersome test fixtures and procedures. As developed in this discussion however, the particular system level approach taken results in a straightforward and simple set of procedures for the calibration that is independent of the instrument configuration.

As a basis for the mathematical developments to follow, consider the equations for the static torques measured by the two degree-of-freedom gyro (refer to figure 8).

$$\frac{M_x}{H} = (1 + DSF_x)\left\{\omega_y + \zeta_{yx}\omega_x + \zeta_{yz}\omega_z - \frac{P}{H}a_y + \frac{Q}{H}a_x - \frac{A}{H}a_y a_z + B_x\right\}$$

$$-\frac{M_y}{H} = (1 + DSF_y)\left\{\omega_x + \zeta_{xy}\omega_y + \zeta_{xz}\omega_z - \frac{P}{H}a_x - \frac{Q}{H}a_y - \frac{A}{H}a_x a_z + B_y\right\}$$

The nomenclature of the equations is defined in the glossary of terms. Fundamentally these equations show the gyro torque measurements as consisting of the cross axis rate plus bias, g and g^2 effects, and rates coupled through small angle misalignments. In addition, implicit in the above relation is a linear temperature dependence of the scale factor, mass unbalance and bias, viz.

$$DSF = DSF_0 + DSF_T * T$$

$$P = P_0 + P_T * T$$

$$B = B_0 + B_T * T$$

For the accelerometer, the basic measurement is:

$$A_i = SFA_i\left\{a_i + \zeta_{ij}a_j + \zeta_{ik}a_k + b_i\right\}$$

Here, the input acceleration a_i is corrupted by misalignments ζ and bias while being measured through the scale factor SFA_i.

The gyro and accelerometer equations as given above represent both the models for the error producing mechanisms as well as the basis for implementing software compensation of these errors. The software compensation utilizes values for the sensor coefficients as determined from calibration procedures described in detail below. The specifics of the software compensation follow directly from the equations and are graphically

depicted in figures 9 and 10 for the accelerometers and gyros respectively.

There are three basic procedures utilized in the calibration of the strap-down system sensors. These are:

1. Static System Calibration (Gyros and Accelerometers)
2. Rate Calibration (gyros only)
3. Temperature Calibration

In general, each of the calibration procedures is designed to automate the acquisition, annotation, transfer, and processing of data for the calibration. Figure 11 shows the basic system configuration and interfaces employed during system calibration.

Each of the three basic procedures is organized according to a single general basic calibration procedure. The basic calibration procedure consists of five steps:

a. Creation of data tapes - acquisition of measured calibration data on punched paper tape via TTY1.

b. Creation of data tape files - data is stored on off-line disk file via TTY2.

c. Execution of calibration equations - processing and creation of constants tape disk files on off-line processor.

d. Creation of constants tapes - punch paper tape from disk files.

e. Entering calibration constants into the system - read octal constant values into operational program.

The System Calibration procedures are a very important part of the system development process. In addition to being a means of calculating a specific set of constants, they are also a sophisticated means of testing for system errors, e.g., model validation, repeatability, stability etc. They are also extremely useful in software compensation checkout in that a "closure" calibration may be performed. This consists in using previously determined calibration constants and software compensated data as the basis for a new calibration. Under ideal conditions, the newly calculated data will reveal unit scale factors and zeroes for all other parameters. Otherwise, either a hardware or software inconsistency exists.

The development of the three calibration procedures is developed in the next section.

IV THE RATE CALIBRATION

The rate test is performed to measure the system level gyro scale factors, the body to gyro direction cosine elements, and the gyro axis angular misalignments from the nominal cluster design values.

The scale factors are used in both the static data problem and the system software compensation calculations. The angular misalignments are used in the system software compensation calculations, while the direction cosines are applied within the static calibration problem.

The test is performed on a precision rate table (see figure 12) and consists of a three position, two direction each test. Although two independent solution algorithms are used the raw input data is common and obtained from a simplified four step procedure.

1. The system level constants are initialized.

2. A data file is initialized with a titling header containing pertinent system and test data. This data file may take the form of a punched paper or magnetic cassette tape. (See figure 13.)

3. The instrument cluster is mounted on the rate table in one of the test positions allowing the rate input vector and the cluster body axis to be coincident. The rate table is driven through exactly 360° at a fixed rate. During the rotation the system is command via a computer discrete from the rate table encoder to gather and average gyro torquer information. The discrete also starts and stops a precision clock that allows the average table rate to be computed. At the end of each rotation the test position identification number, the averaged gyro torquer equivalent rates, and the precision clock times are recorded on the data file.

   This is repeated for three positions, two directions for each position until the raw rate data set is complete.

4. The raw data set is then stored on an off line computer disc where the desired parameters are later extracted.

The two equations assumed for the rate test solutions are shown for the X body rate case. The superscript also denotes this condition.

For static calibration applications:

a) $$M_x^X = (1 + DSF_x)\,[C_{11}\omega_X + \Sigma\epsilon_x]$$

For system software compensation application:

$$b) \quad M_x^X = (1 + DSF_x)\left[\tilde{C}_{11}\,\omega_X + \tilde{C}_{21}\,\zeta_{yx}\,\omega_X + \tilde{C}_{31}\,\zeta_{yz}\,\omega_X + \Sigma\epsilon_x\right]$$

Where $\Sigma\epsilon_x \equiv$ the sum of all non rate related error torques; bias, mass unbalance, quadrature, etc.

It is obvious that the two equations must be equivalent and therefore the relationship between the true direction cosines of (a) and the Misalignments of (b) may be expressed as:

$$\begin{bmatrix}\omega_x\\ \omega_y\end{bmatrix} = \begin{bmatrix}1 & \zeta_{xy} & \zeta_{xz}\\ \zeta_{yx} & 1 & \zeta_{yz}\end{bmatrix} \tilde{C}_B^{Gi} \begin{bmatrix}\omega_X\\ \omega_Y\\ \omega_Z\end{bmatrix} = C_B^{Gi} \begin{bmatrix}\omega_X\\ \omega_Y\\ \omega_Z\end{bmatrix}$$

The solution for scale factors and true direction cosines C_B^{Gi} is a straightforward application of the sum of squares law for direction cosines. In particular,

$$\left(1 + DSF_x\right)\left(C_{11}^2 + C_{12}^2 + C_{13}^2\right)^{1/2} = \sqrt{\left(\frac{\Delta M_x^X}{\Delta\omega_X}\right)^2 + \left(\frac{\Delta M_x^Y}{\Delta\omega_Y}\right)^2 + \left(\frac{\Delta M_x^Z}{\Delta\omega_Y}\right)^2}$$

$$= \left(1 + DSF_x\right)$$

Substituting the scale factor back into each position test yields each direction cosine:

$$C_{11} = \frac{\Delta M_x^X}{(1 + DSF_x)\Delta\omega_X}$$

$$C_{12} = \frac{\Delta M_x^Y}{(1 + DSF_x)\Delta\omega_Y}$$

$$C_{13} = \frac{\Delta M_x^Z}{(1 + DSF_x)\Delta\omega_Z}$$

Here we let the mathematical prefix Δ signify the algebraic difference between CW and CCW torques/rates. (e.g. $\Delta\omega_X = \omega_{X_{CW}} - \omega_{X_{CCW}}$)

It is also clear that the $\Sigma\epsilon_x$ term disappears when differences are taken.

Since we need direction cosines for the spin axis also but are unable to measure torques we perform a vector cross product of x x y. Thus all necessary axes are located.

The solution for the scale factors and misalignments is an application of the small angle estimate and linear algebra. The reference equation (b) may be re-written in matrix form including the test information from the other two test positions. Thus;

$$\begin{bmatrix} \Delta M_x^X \\ \Delta M_x^Y \\ \Delta M_x^Z \end{bmatrix} = \begin{bmatrix} \tilde{C}_{11}\Delta\omega_X + \tilde{C}_{21}\Delta\omega_X + \tilde{C}_{31}\Delta\omega_X \\ \tilde{C}_{12}\Delta\omega_Y + \tilde{C}_{22}\Delta\omega_Y + \tilde{C}_{32}\Delta\omega_Y \\ \tilde{C}_{13}\Delta\omega_Z + \tilde{C}_{23}\Delta\omega_Z + \tilde{C}_{33}\Delta\omega_Z \end{bmatrix} \begin{bmatrix} (1 + DSF_x) \\ (1 + DSF_x)\zeta_{yx} \\ (1 + DSF_x)\zeta_{yz} \end{bmatrix}$$

where $\tilde{C}_{ij} \equiv$ nominal design direction cosine.

This matrix equation is of the form $B = A\mu$ where v is the unknown vector of scale factors and misalignments. The solution is $\mu = A^{-1} B$

The misalignments are separated from the scale factors by dividing by the scale factor - the first element of the vector.

In both algorithms the most serious error contributors are uncompensated temperature variations and non-orthogonalities of body input rates. It is imperative that both of these be thoroughly monitored. Other less contributory factors include wow and flutter in the rate table and timing errors. It is also important that the absolute values of the total inertial input rates be somewhat equal although 1% variations may be tolerated.

V STATIC CALIBRATION

The purpose of the static calibration procedure is to determine coefficient values for the error producing mechanisms in both the gyros and accelerometers.

For the gyro these include:

- mass unbalance
- quadrature g-sensitivity
- fixed bias
- anisoelasticity

For the accelerometer, mechanisms include:

- scale factor
- fixed bias
- axis misalignments

The procedure followed is to accurately position the instrument cluster into a series of orientations so that both the inertial angular input vector and the local gravity vector to the cluster body axes are well defined. (See figure 14.)

The angular input and linear acceleration vectors excite the instrument error parameters through the body to instrument transformation matrices determined during the rate tests. Since the scale factor is known from the rate test and the rate input vector is well defined for each position, the x-axis static equation for any given position may be written as:

$$\frac{M_x}{H\,(1 + DSF_x)} - \omega_y = -P_x a_y + Q_x a_x + B_x - A_x a_y a_z$$

With N data positions taken we may load up a N x 4 coefficient matrix and solve for the unknown parameters. Since the rank of the matrix is 4 but its order may be greater than 4 the solution becomes more than a simple matrix inversion. The mathematical basis for the solution is developed in the appendix. The solution algorithm is repeated for each gyro axis.

Although the same routine could be applied to the accelerometer problem it is not since they are nominally orthogonal to the body axes. We therefore apply a straightforward and standard approach using simple sums and differences. The accelerometer solution is carried further than necessary to yield integrity checks of the test platform positioning accuracy or possible cluster mount torsional sag.

The ideal set, and best subsets of positions used is determined from a covariance analysis described in the appendix. The minimum number of required positions for a complete solution is six. The procedure followed during a static calibration cycle is a four step procedure.

1. The system level constants are initialized.
2. A data file is initialized as in the rate test.

3. The instrument cluster is then placed in a numbered test position. The system is commanded to gather and average instrument data over a specified interval. At the end of the interval the system outputs the data along with the corresponding test position number to the data file. This step is repeated for selected positions until a data set is complete. (See figure 15.)

4. The data file is then stored on an off line computer disc file where this raw data is combined with the previously solved rate test data and the static solution is completed. This is discussed further in section VII.

VI TEMPERATURE CALIBRATION

The purpose of the temperature calibration test is to determine certain temperature dependent parameters. These include gyro mass unbalance, gyro and accelerometer scale factors, and gyro and accelerometer fixed bias temperature coefficients.

The test is performed in a straightforward manner by enclosing the subject hardware in a thermally controlled chamber and performing the static and rate tests at desired temperature points. An alternate and simpler method of heating that may be used involves the use of heavy insulation to force self heating.

The resulting data from the tests is reduced as usual in their respective program and the outputs of these programs are read by a temperature coefficient program (TC) which computes the desired temperature sensitivities.

VII DATA REDUCTION AND RESULTS

The calibration problem is solved in an off line computer where the raw data files have been stored on a disc. There are four programs used, two of which must be considered essential. These compute the static and rate compensation parameters and are titled STALSF and RATTST respectively. The other two programs may be termed accessory and compute temperature coefficients and system level constants updates in octal formats. They are titled TC and CON.

The mainline flow of the data reduction algorithms may be seen in figure 16 and 17.

Some of the special features of the static data program in particular include the ability to use any arbitrary but numbered set of test positions, input editing when desired, automatic computer file log maintenance, and a quality check option. Both the static and rate programs read the raw data title information and record it in the output title along with the date and time of computer execution and any operator comments.

The static calibration solution algorithm is described briefly in Section V and in detail in the appendix. However, an option of the program is to accept gyro level determined values for anisoelasticity rather than compute them. The solution matrix then becomes an N x 3.

A particularly attractive feature of the static processing is the quality check routine. Once the unknown vectors for both the gyros and accelerometers have been computed they are used to predict what the measured inputs should have been. As in the appendix, the data observed is

$$Y = [\alpha^T]\,\chi$$

and the solution is

$$\hat{X} = [\alpha^T]^\dagger Y$$

By looking at the differences of predicted and actual measured data an indication of the test noise level and or possible bad data points emerges.

Thus

$$\hat{Y} = [\alpha^T] \hat{X}$$

and

$$Y - \hat{Y} = [\alpha^T] (X - \hat{X})$$

These residual differences can also be substituted into the solution routine and the solution re-processed, yielding a theoretical closure viz

$$(X - \hat{X}) = [\alpha^T]^\dagger (Y - \hat{Y})$$

Since the differences $(Y - \hat{Y})$ reflect test noise, the new solution vector $(X - \hat{X})$ represents parameter uncertainty as well as another model verification and test validation.

Figures 18 and 19 depict a sample of both computed values and the reprocessed results for the static calibration problem.

A discussion of the rate calibration is considered next.

The rate test data reduction is comprised of two completely independent solutions. One computes the scale factors and true direction cosines to be applied during the static data reduction. The other computes the scale factors and axis misalignments to be applied to the system level software compensation. The techniques used to extract the parameters were discussed in Section IV. Some of the options available include limited editing

of the input data, temperature normalization of the raw data, and automatic computer filelog maintenance. The output of this program is written on both the terminal and on a disc file for later use. A sample output of the rate test calibration is shown in figure 20.

APPENDIX

SOLUTION AND COVARIANCE ANALYSIS OF THE STATIC GYRO CALIBRATION PROBLEM

This appendix shows the development of the gyro static calibration problem and the method of solution including a covariance analysis.

As seen in section V, a single x-axis gyro torque may be written as

$$\frac{M_x}{H} = \omega_y - \frac{P}{H} a_y + \frac{Q}{H} a_x - \frac{A}{H} a_y a_z + B_x$$

Here, both the gyro/system scale factors and the gyro/system misalignments have been removed via pre-processing or software compensation based upon rate calibration measurements (see section IV). The equation for the y axis torque is similar and will not be developed. Re-writing, modifying notation slightly, and incorporating indexing to indicate position numbers

$$y(i) = \frac{M_x(i)}{H} - \omega_y(i) = \begin{bmatrix} -a_y(i) & a_x(i) & -a_y(i) \cdot a_z(i) & 1 \end{bmatrix} \begin{bmatrix} P' \\ Q' \\ A' \\ B \end{bmatrix}$$

or

$$y(i) = \alpha^T_{(i)} \cdot X$$

The indexed position numbers represent the different positions into which the system may be placed during the static calibration procedures. Over a set of N positions, the composite measurement vector Y is given by

$$Y = \begin{bmatrix} y(1) \\ y(2) \\ . \\ . \\ . \\ y(N) \end{bmatrix} = \begin{bmatrix} \alpha^T(1) \\ \alpha^T(2) \\ . \\ . \\ . \\ \alpha^T(N) \end{bmatrix} \quad X = [\alpha^T] X$$

With this notation, the calibration problem is seen to be one of solving for the unknown four-vector X given the N measurements in Y.

For an orthogonal gyro set, the entries in α^T are either 1's or zeroes. Thus solutions for X are quite simple in this case and in fact the general formulation of the problem is not usually written. For the specific application considered here with a non-orthogonal gyro set, solutions for X are obtained using a general inverse of $[\alpha^T]$, viz $[\alpha^T]^\dagger$. Thus

$$X = [\alpha^T]^\dagger Y$$

A specific solution may be obtained by pre-multiplying by $[\alpha]$

$$[\alpha] Y = [\alpha][\alpha^T] X$$

and then inverting the product $[\alpha][\alpha^T]$.

$$\hat{X} = ([\alpha][\alpha^T])^{-1} [\alpha] Y = [\alpha^T]^\dagger Y$$

This solution $\hat{\chi}$ is the least squares solution using a Moore-Penrose pseudo-inverse. It exists whenever there are four linearly independent row vectors $\alpha^T(i)$ within $[\alpha^T]$.

This solution is the basis for the static calibration calculations shown in section VII. It is not mandatory that this solution be utilized however, and in fact any four linearly independent rows $\alpha^T(i)$ may be used as the basis for a 4 by 4 inverse solution.

Whatever inverse $[\alpha^T]^\dagger$ is utilized, a statistical covariance of the solution χ may be found, as follows. Let ξ_i represent the additive noise corrupting each measurement. Then

$$y(i) = \alpha^T(i) \cdot \chi + \xi_i$$

Here ξ_i represents the total effect of the gyro noise and the electronic conversion noise which are assumed to have a zero mean value. For the total measurement set

$$Y = [\alpha^T] \cdot \chi + \bar{\xi}$$

with

$$\hat{\chi} = [\alpha^T]^\dagger \cdot Y$$

then the expected value of $\hat{\chi}$ is χ and the covariance of $\hat{\chi}$ is

$$\begin{aligned} \text{cov}(\hat{\chi}) &= E(\hat{\chi}\,\hat{\chi}^T) - E(\hat{\chi}) \cdot E(\hat{\chi}^T) \\ &= E\left\{[\alpha^T]^\dagger \xi\xi^T ([\alpha^T]^\dagger)^T\right\} \\ &= [\alpha^T]^\dagger P_\xi ([\alpha^T]^\dagger)^T \end{aligned}$$

For the calibration problem at hand, a reasonable assumption is that the individual measurements are statistically independent. Thus

$$P_{\xi} = \sigma^2 I$$

where σ^2 is the variance of the measurement noise.

Then

$$\text{cov}(\hat{\chi}) = \sigma^2 [\alpha^T]^{\dagger} ([\alpha^T]^{\dagger})^T$$

for independent measurements.

When

$$[\alpha^T]^{\dagger} = ([\alpha][\alpha^T])^{-1}[\alpha] \quad .$$

then

$$\text{cov}(\hat{\chi}) = \sigma^2 ([\alpha][\alpha^T])^{-1}[\alpha] \cdot [\alpha^T]([\alpha][\alpha^T])^{-1}$$

$$= \sigma^2 ([\alpha][\alpha^T])^{-1}$$

which is the covariance of the least squares estimate with independent measurements.

As specific cases for study, the following four examples of covariance are presented:

1. Twenty four point test:

   When all 24 positions are utilized and the least squares solution employed, all four gyro axes have the same covariance, namely.

$$\text{cov}(\hat{X}) = \sigma^2 \begin{bmatrix} .1250D+00 & -.1155D-09 & -.8095D-17 & -.3238D-16 \\ -.1155D-09 & .1250D+00 & .1590D-16 & .4626D-17 \\ -.8095D-17 & .1590D-16 & .4167D-01 & .6141D-10 \\ -.3238D-16 & .4626D-17 & .6141D-10 & .6667D+00 \\ P & Q & B & A \end{bmatrix}$$

(The other axes are identical.) This result shows that the cross correlations between gyro elements are zero and that the basic measurement noise level σ^2 is reduced in each case by the values .125, .125, .667 and .042 for the gyro parameters P Q A and B respectively. For example, with $(.01^{o}/hr)^2$ measurement noise, the results indicate that

$\sigma_P = 0.0035\ ^{o}/hr/g$

$\sigma_Q = 0.0035\ ^{o}/hr/g$

$\sigma_A = 0.0082\ ^{o}/hr/g^2$

$\sigma_B = 0.0020\ ^{o}/hr$

2. Six Point Test

A six point test utilizing each principal body axis in a vertical and inverted position gives the result

$$\text{cov}(\hat{X}) = \sigma^2 \begin{bmatrix} .5000D+00 & -.4620D-09 & -.5551D-16 & -.1480D-15 \\ -.4620D-09 & .5000D+00 & .5089D-16 & -.3701D-16 \\ -.5551D-16 & .5089D-16 & .1667D+00 & .2456D-09 \\ -.1480D-15 & -.3701D-16 & .2456D-09 & .2667D-01 \end{bmatrix}$$

This result can be seen to be the same as case 1 except that it is scaled by the ratio of 24/6. Thus under ideal conditions the 24 point test is only better to the extent that more data is taken. Conversely, longer data averages reduce the variance proportionately. The 24 point test is superior however in that test cube integrity (orthogonality/flatness) can be ascertained from the redundant data.

3. A Four Point Test

As initial methods of calibration, some specific four point tests were performed and evaluated. For gyro 1 axis 1, one set of measurements resulted in:

$$\mathrm{cov}(\hat{\underline{X}}) = \sigma^2 \begin{bmatrix} 0.132180D+01 & 0.821797D+00 & -0.517638D+00 & -0.905989D+00 \\ 0.821797D+00 & 0.132180D+01 & -0.517638D+00 & -0.905989D+00 \\ -0.517638D+00 & -0.517638D+00 & 0.500000D+00 & 0.437559D+00 \\ -0.905989D+00 & -0.905989D+00 & 0.437559D+00 & 0.609917D+01 \end{bmatrix}$$

which gives reasonable values for the diagonal elements considering that just four positions are utilized. For example the bias variance of 0.5 can be adjusted to 0.333 just due to the fewer positions used. However this is still a factor of two difference in variance or 0.707 in standard deviation, when compared to the six point test. There is also a high correlation between elements. For example

$$\rho(P,Q) = 0.62$$
$$\rho(P,A) = -0.79$$

4. Another Four Point Test

Using positions that were intuitively intended to calibrate gyro 1, the covariance for gyro 2 axis 1 is calculated to be:

$$\mathrm{cov}(\hat{\chi}) = \sigma^2 \begin{bmatrix} 0.151782D+02 & 0.146782D+02 & 0.193185D+01 & 0.470940D+02 \\ 0.146782D+02 & 0.151782D+02 & 0.193185D+01 & 0.470940D+02 \\ 0.193185D+01 & 0.193185D+01 & 0.500000D+00 & 0.609441D+01 \\ 0.470940D+02 & 0.470940D+02 & 0.609441D+01 & 0.153901D+03 \end{bmatrix}$$

This result shows that while these four positions give reasonable results for the other gyro, the values for this case are much worse. In fact it tends to magnify errors in some cases. For example, while bias uncertainty is the same, the mass unbalance is magnified from 0.01^{o}/hr/g to 0.04^{o}/hr/g.

From these examples it is concluded that the six point test, under certain assumptions is the most efficient effective test. It is also seen that using four point tests and ordinary inverse solutions can lead to very unsatisfactory results.

GLOSSARY

M_i = Torque about ith gyro axis

DSF_i = Torquer scale factor difference from unity of ith axis. (i = x or y)

ω_i = Total inertial input rate about ith axis (i = x, y, z, X, Y, Z)

ζ_{ij} = Misalignment error allowing rate inputs to gyro ith axis due to rate inputs about nominal jth axis (i = x or y, j = x, y, z, $i \neq j$)

P_i = Spin axis mass unbalance or pendulousity apparent about the ith axis. (i = x or y)

Q_i = G-sensitive bias or quadrature term apparent about ith axis (i = x or y)

A = Anisoelasticity

B_i = Fixed bias apparent about ith axis. (i = x or y)

a_i = Acceleration along ith axis (i = x, y, z, X, Y, Z)

H = Gyro Angular Momentum

C_a^b = True direction cosine transformation matrix from 'a' coordinates to 'b' coordinates (3 x 3)

$\tilde{C}_a^b$ = Nominal direction cosine transformation from 'a' to 'b'

x, y, z = Gyro reference axes (z = spin axis)

X Y Z = Body reference axis

DSF_T = Sensitivity of scale factor to temperature

P_T = Sensitivity of pendulosity or mass unbalance to temperature

B_T = Sensitivity of bias to temperature

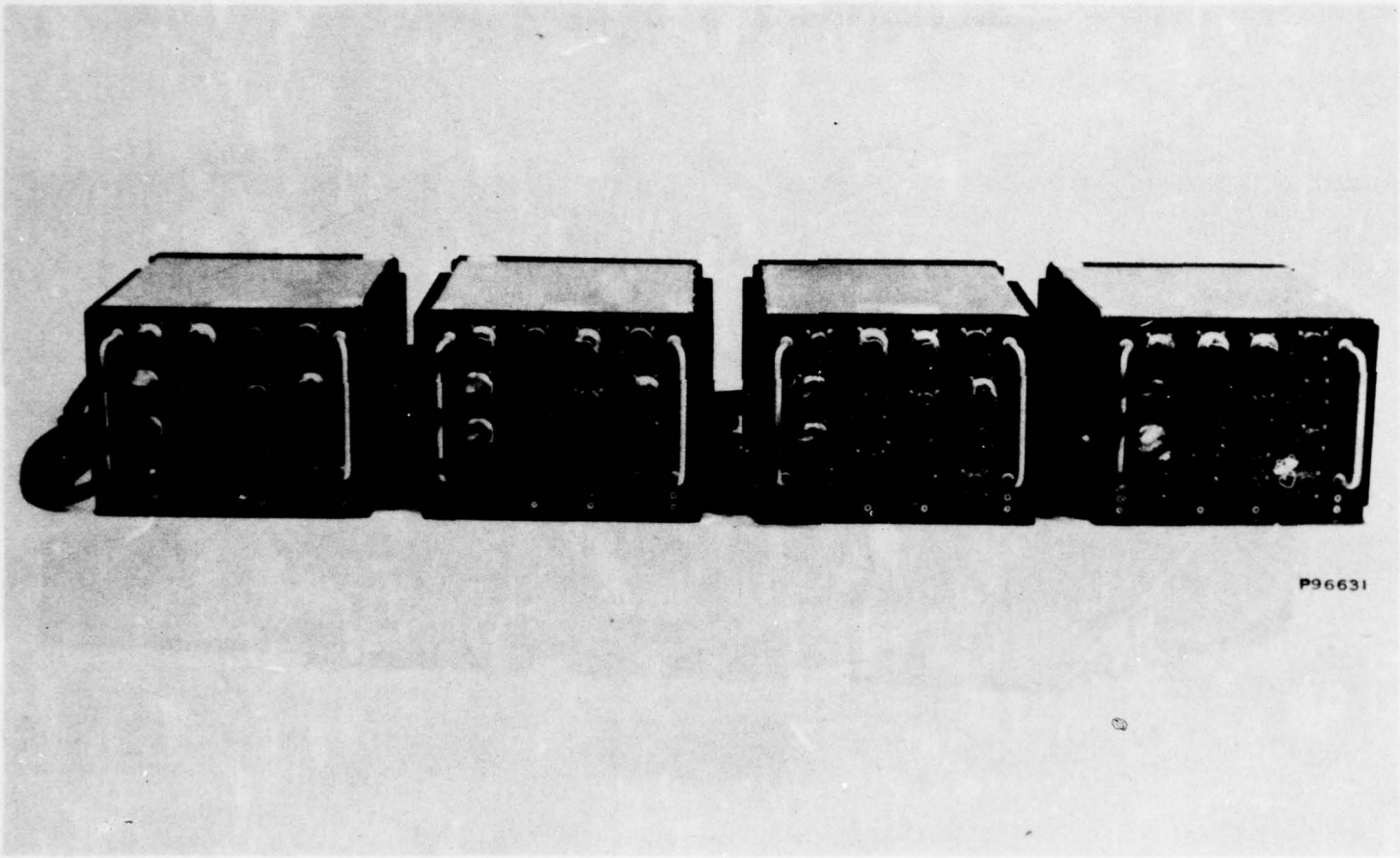


Figure 1. Teledyne RIICS Quad Redundant Computer/Converter Units

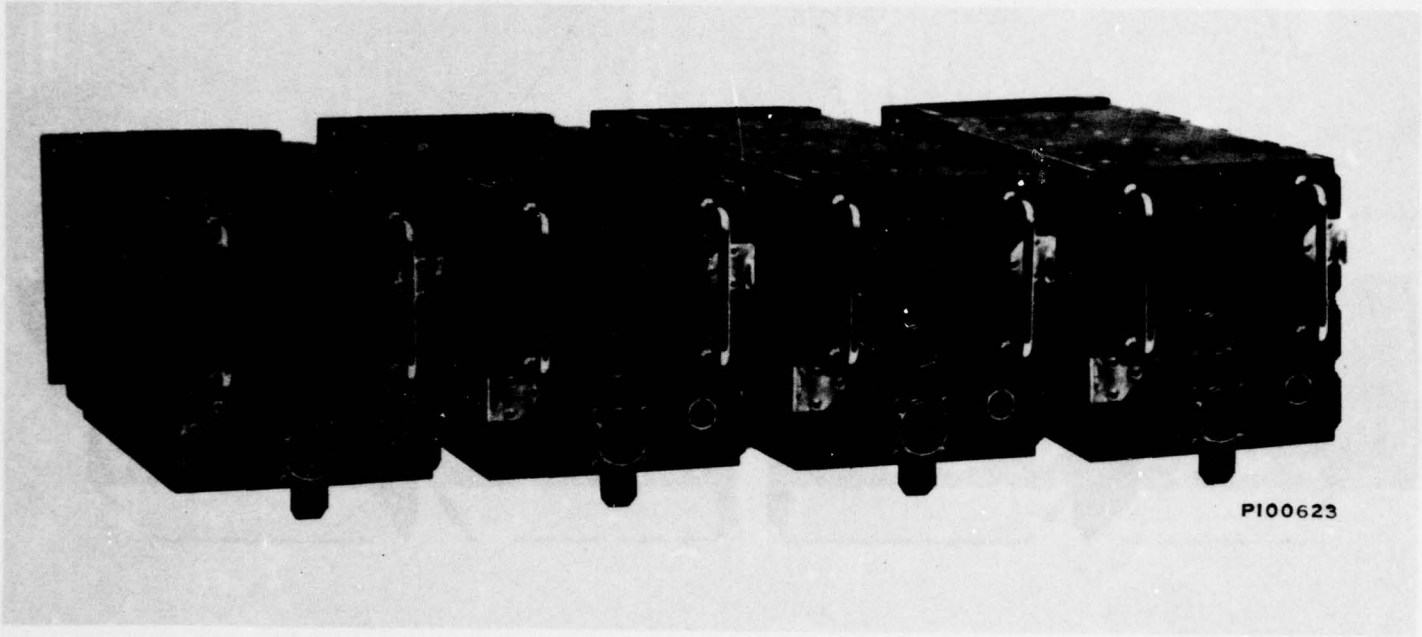


Figure 2. Teledyne Quad Redundant Strapdown IMU's

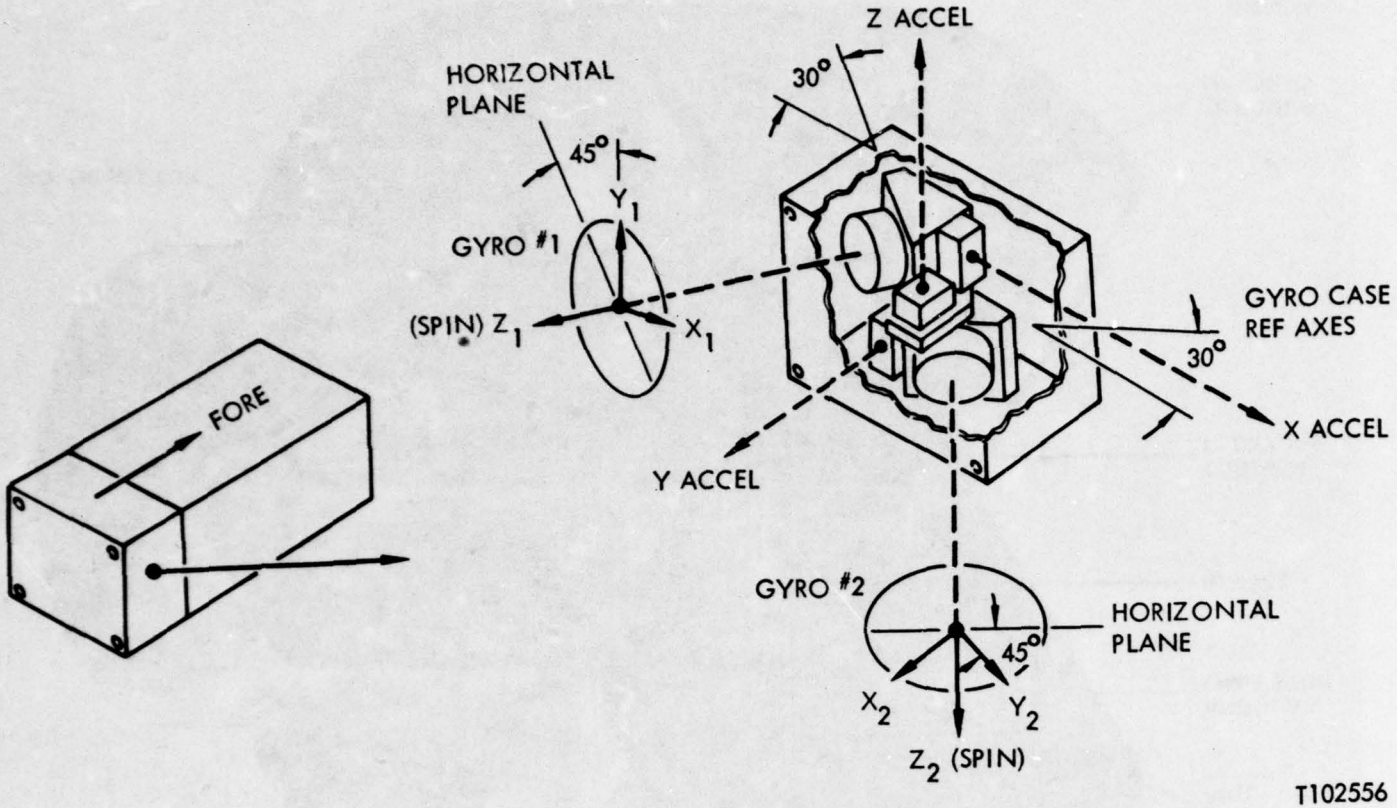


Figure 3. Instrument Assembly Axis Orientation

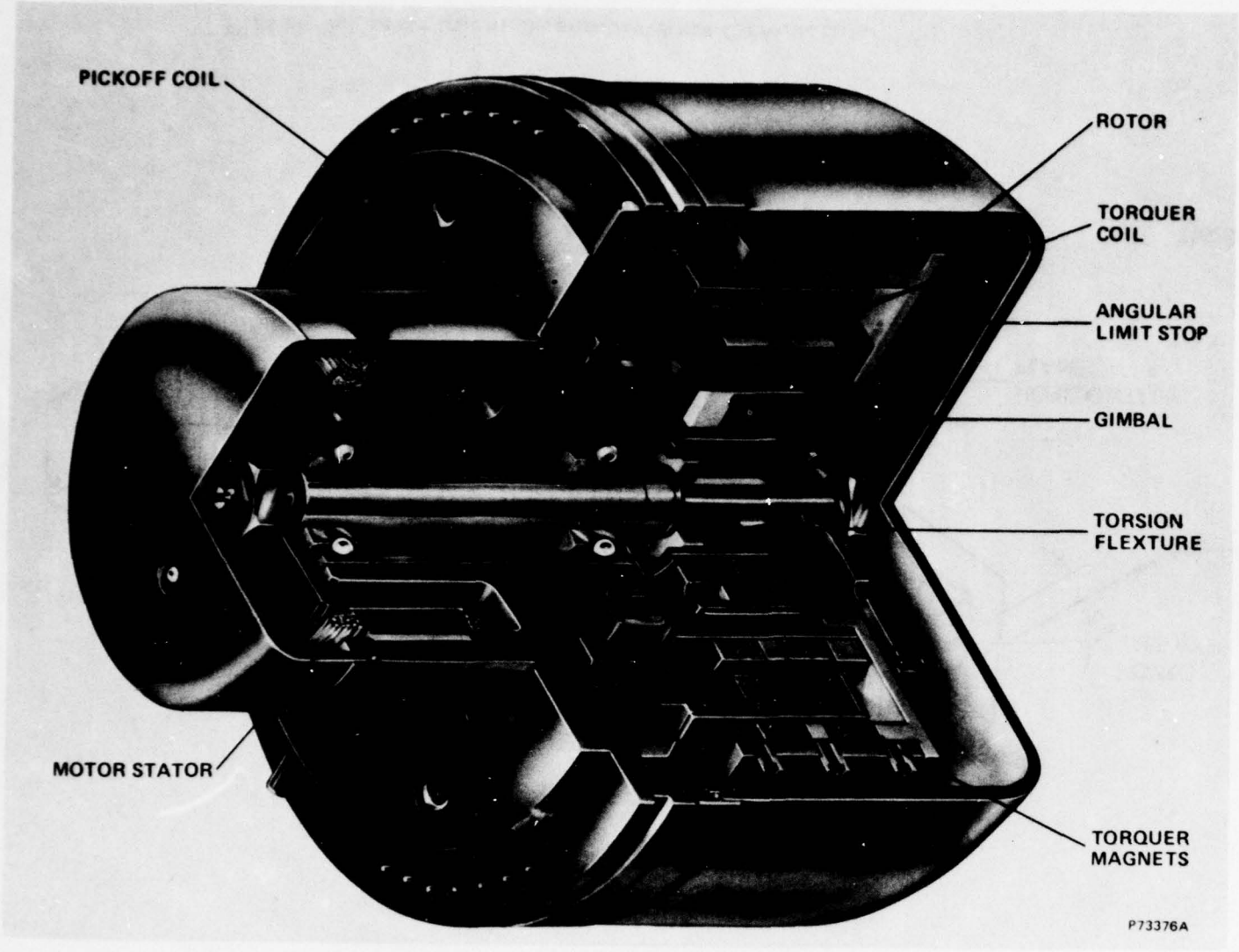


Figure 4. Teledyne Inertial Rate Sensor

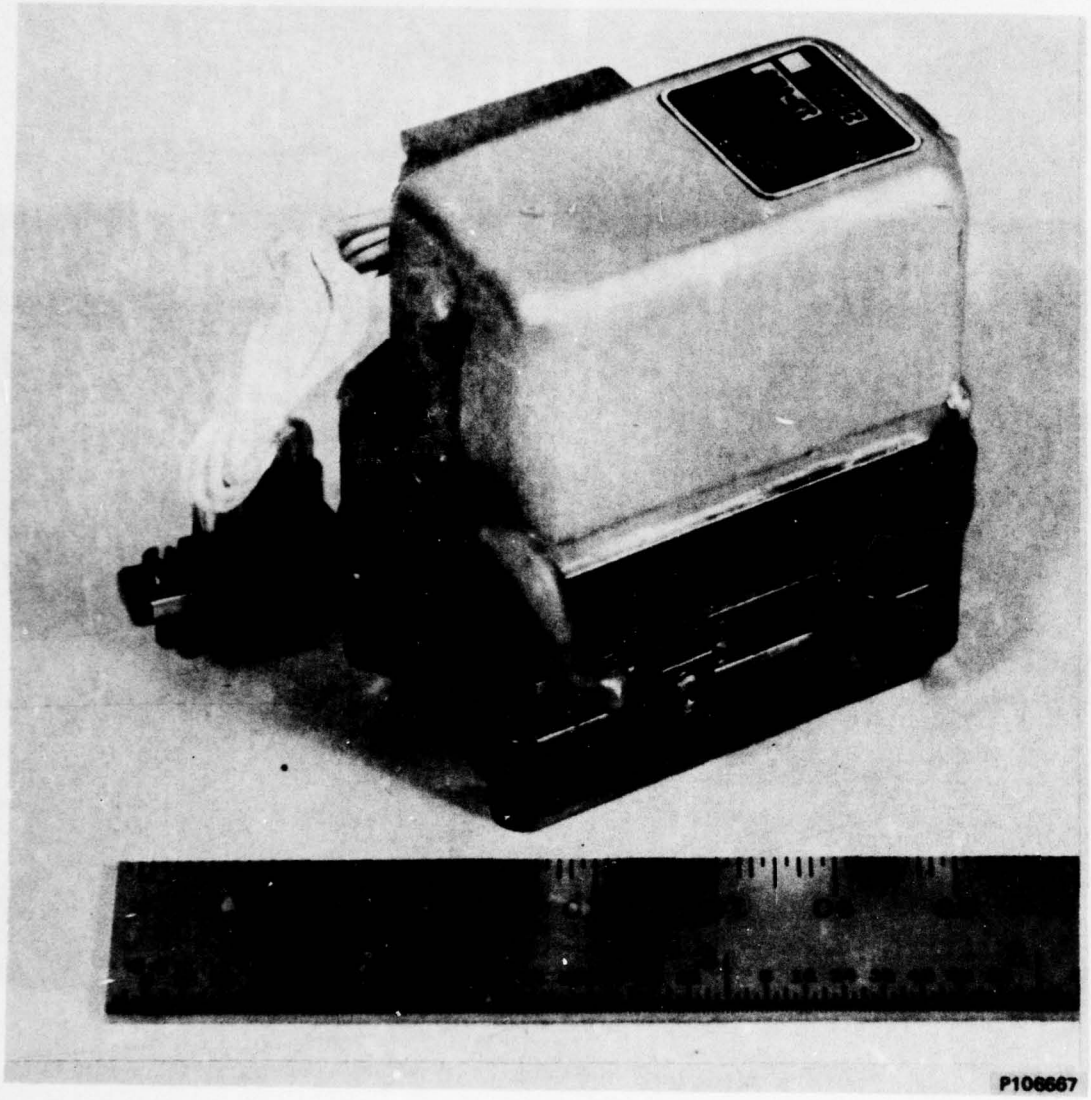


Figure 5. Photograph of the Model 4841 Accelerometer

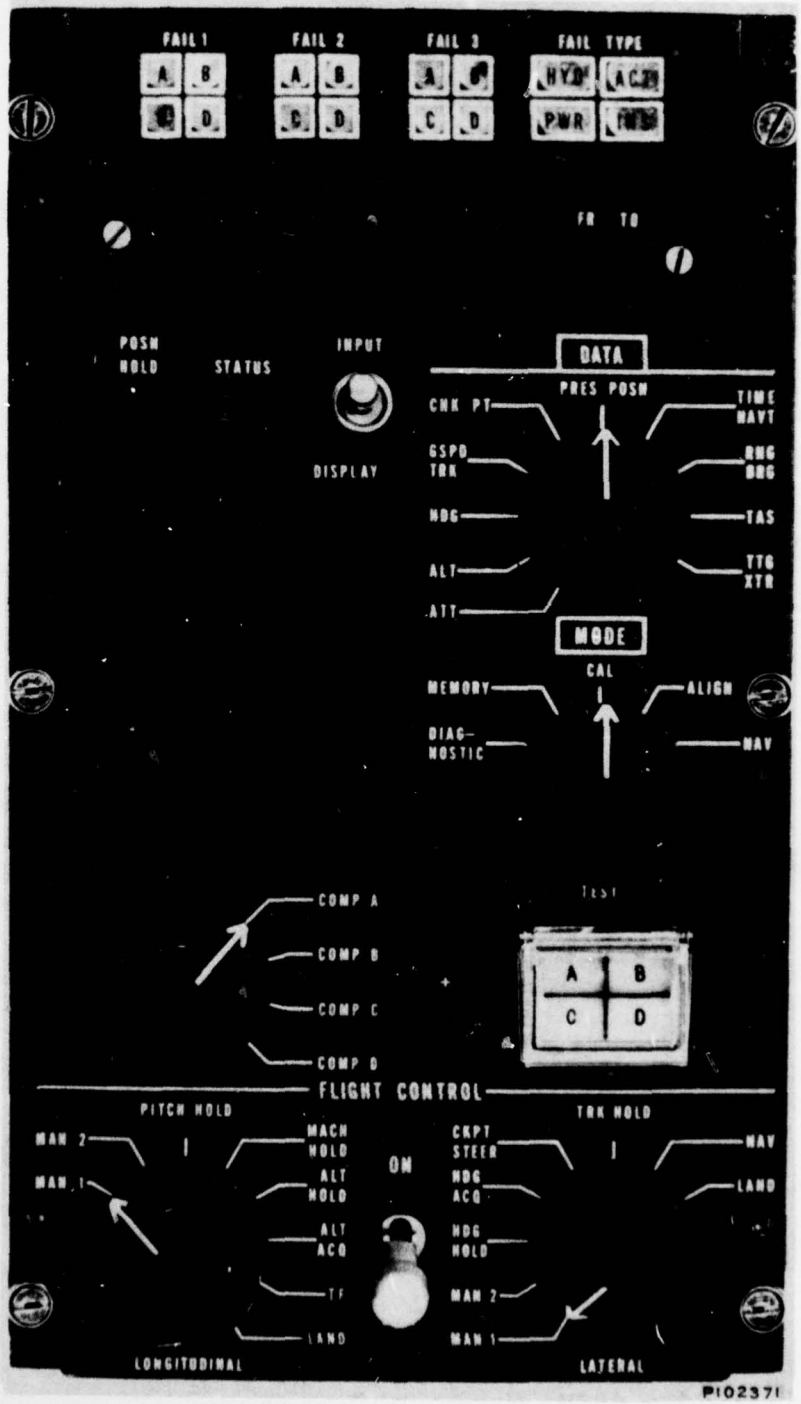


Figure 6. Teledyne RICCS CDU Front Panel

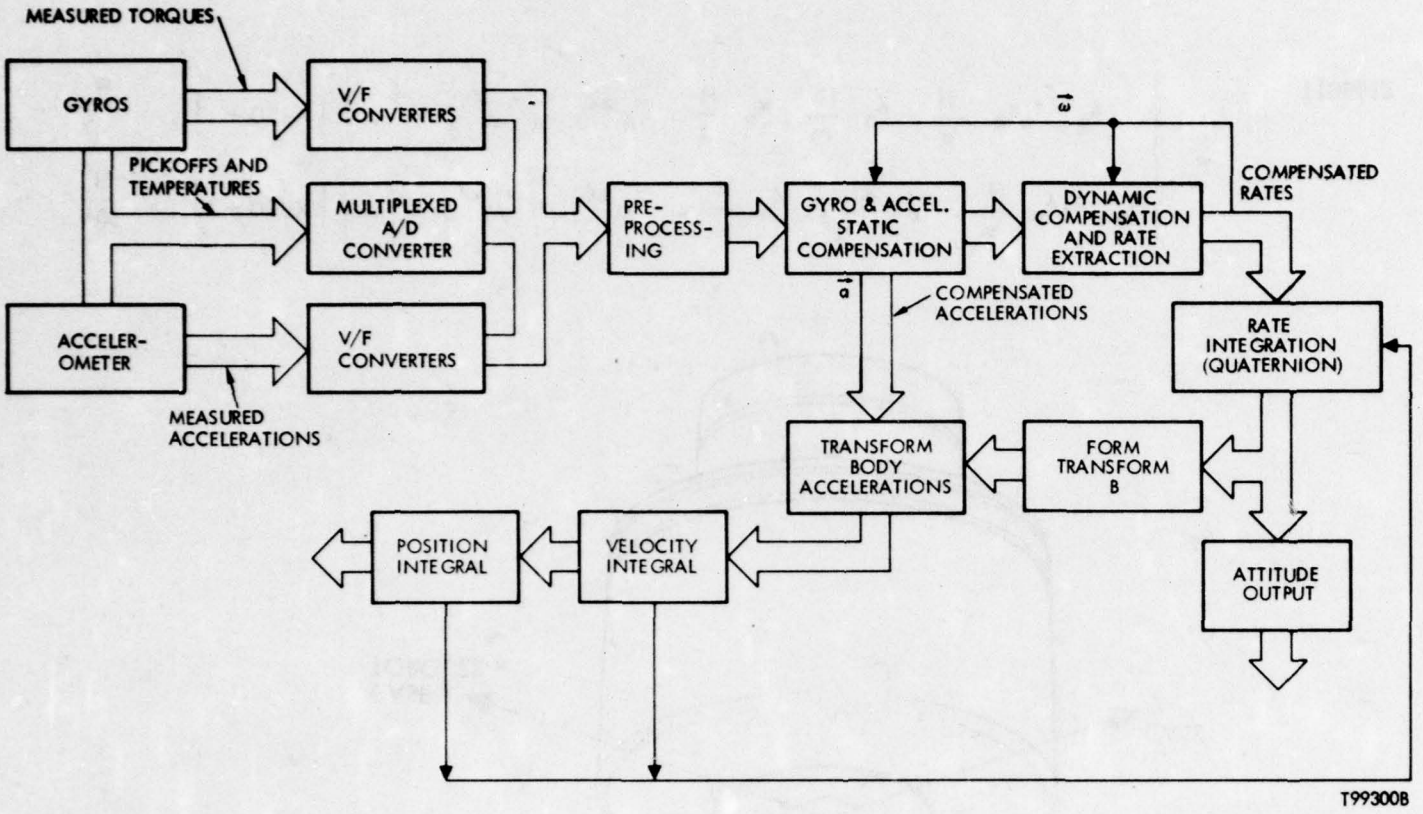
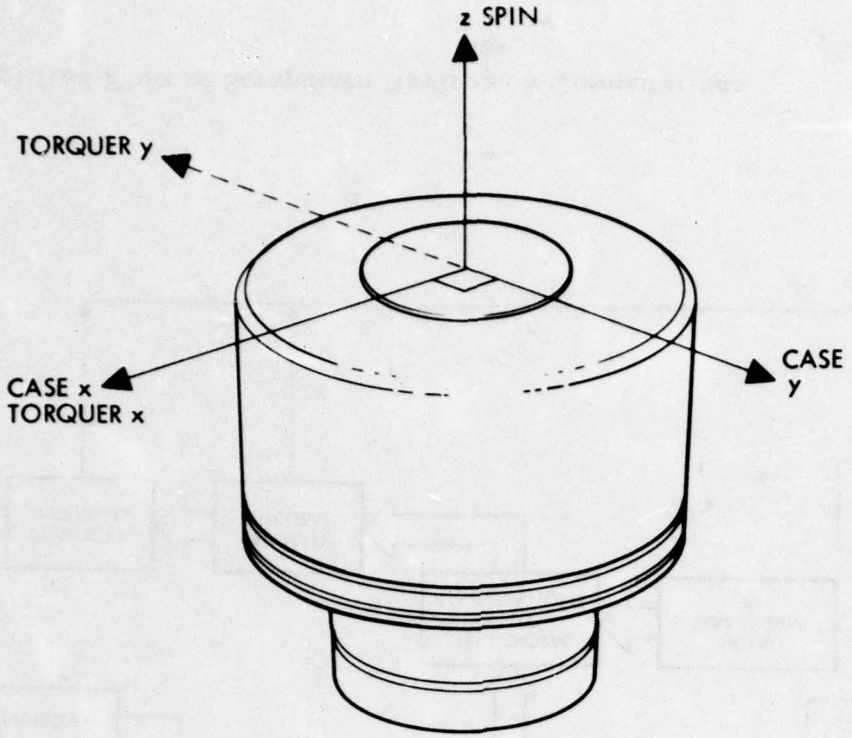


Figure 7. Simplified Flow of Strapdown Navigation Computations



$$\frac{MX}{H} = \left[1 + DSFX\right]\left\{ W_y + \zeta_{yx}W_x + \zeta_{yz}W_z - \frac{P}{H}\,a_y + \frac{Q}{H}\,a_x - \frac{A}{H}\,a_y a_z + B_x \right\}$$

$$-\frac{MY}{H} = \left[1 + DSFY\right]\left\{ W_x + \zeta_{xy}W_y + \zeta_{xz}W_z - \frac{P}{H}\,a_x - \frac{Q}{H}\,a_y - \frac{A}{H}\,a_x a_z + B_y \right\}$$

T106612

Figure 8. Static Torque for Two Degree-of-Freedom Gyro

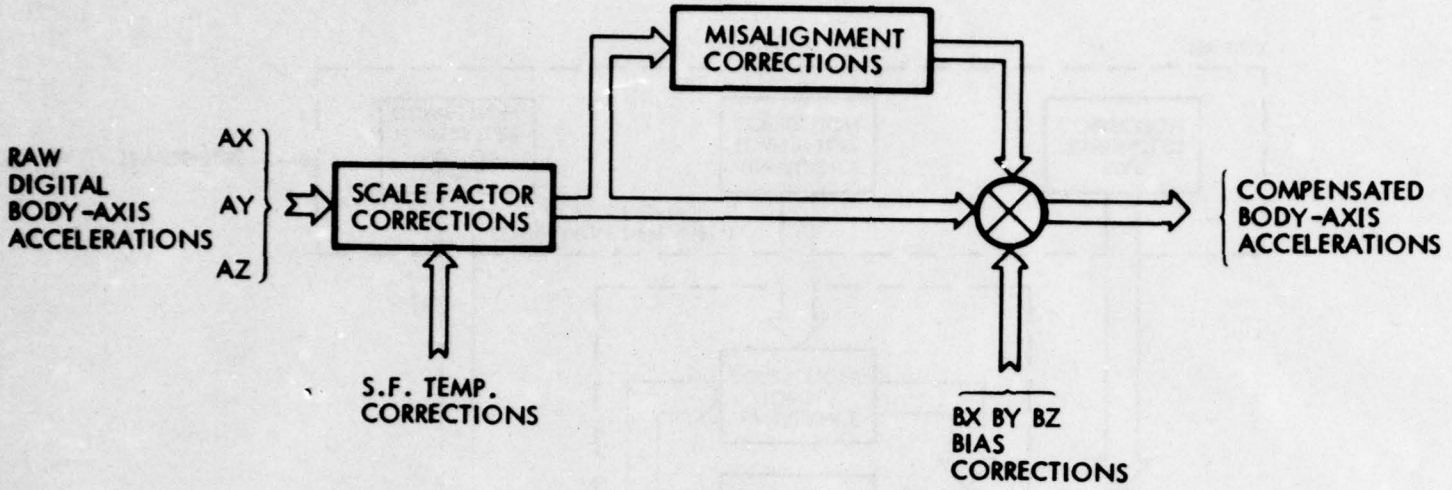


Figure 9. Computational Flow for Accelerometer Compensation

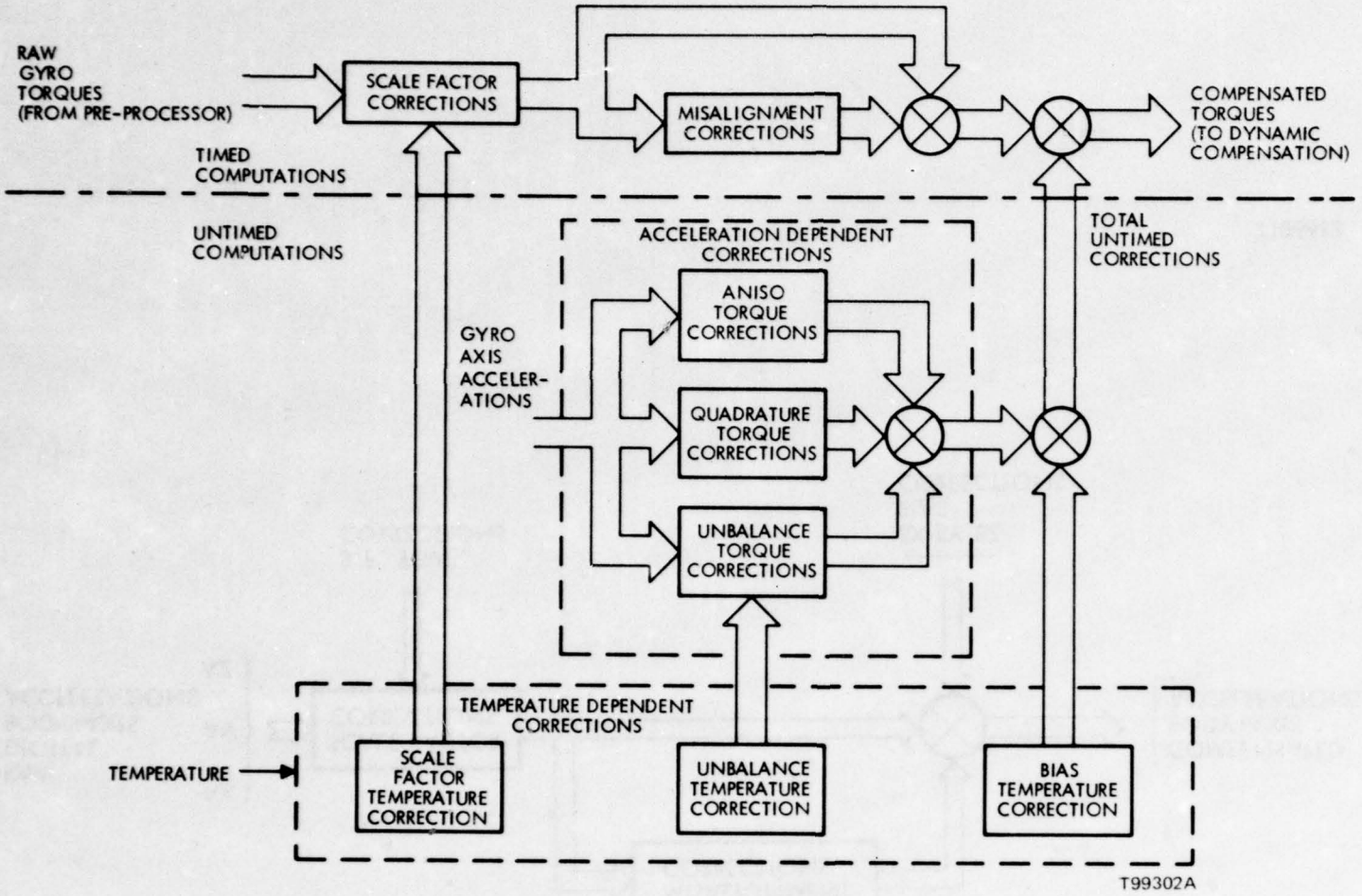


Figure 10. Computational Flow for Static Gyro Compensation

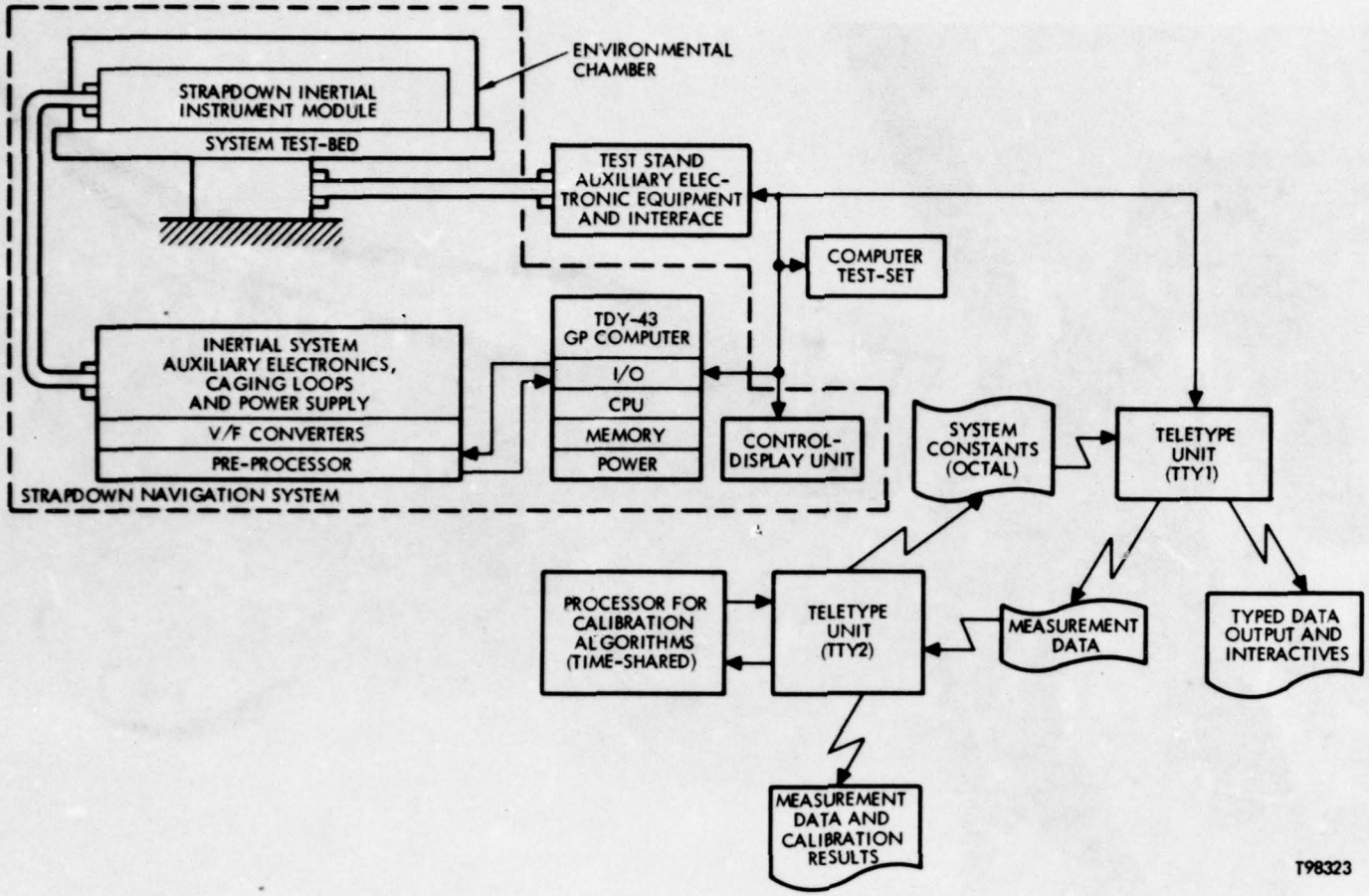


Figure 11. Strapdown System Calibration Network

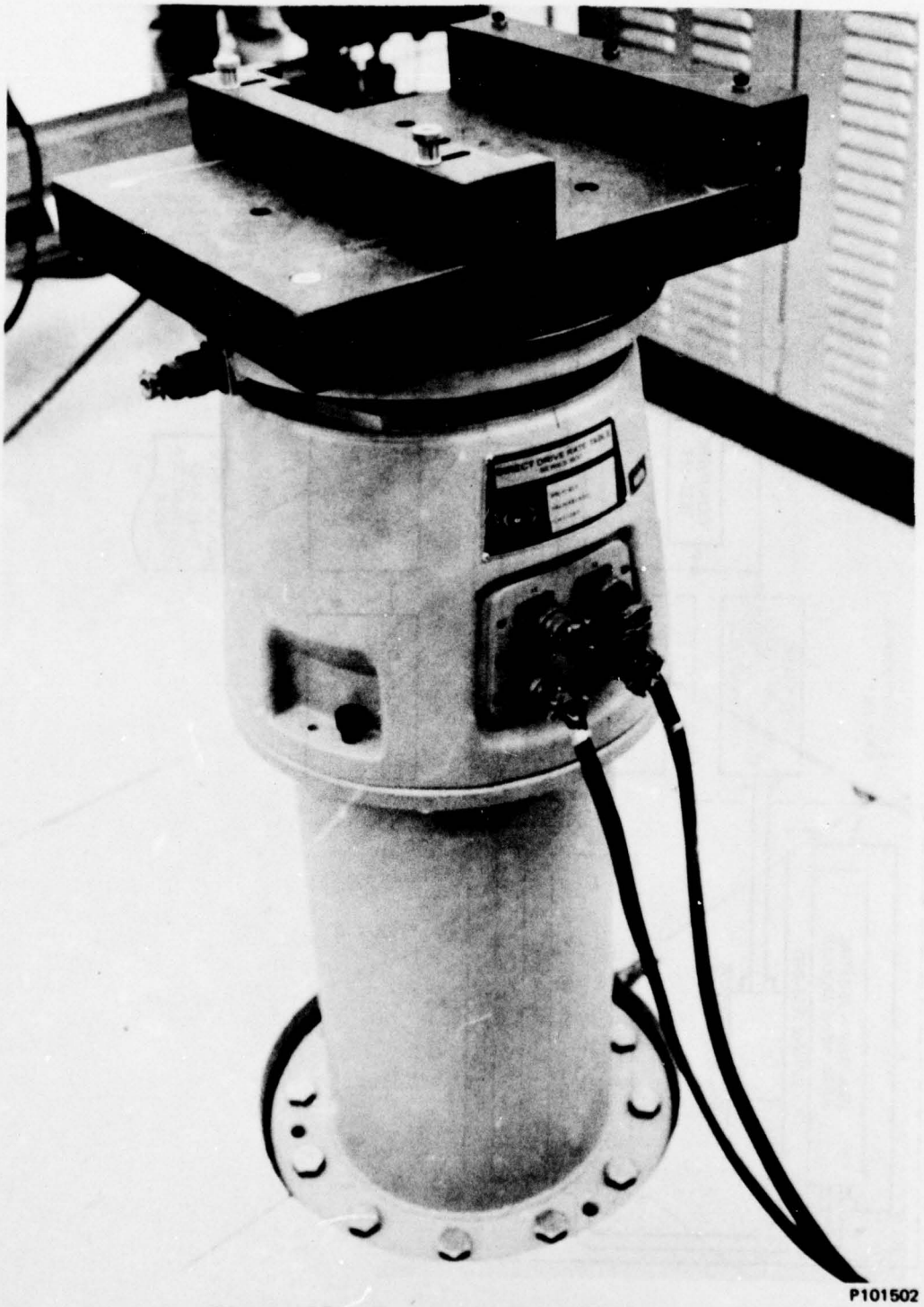


Figure 12. Precision Rate Table

BEST AVAILABLE COPY

```
*************************************************************************
*
*      ***** MRB-RIICS RATE DATA TAPE *****
*
*      DEMO
*
*  *** TEST INFORMATION ***
*
*      IMU ID NO: E113
*
*           DATE:6 DEC 1976
*
*           TEST:SIMULATED RAW DATA FOR DEMO PURPOSES
*
*          START:1630 HRS
*
*  *** TEST DESCRIPTION ***
*
*    C7 RATE TEST DATA DUMPS FOR SCALE FACTORS AND DIRECTION COSINES
*
*   *** REFERENCE TEMPERATURE ***
*
*      TO=  95.0
*
*************************************************************************
```

```
 1. TEST =  1001.0D+00
 2. WY1  =  0.154890371093D+05 DEG/HR
 3. WX1  =  0.155086367187D+05 DEG/HR
 4. WY2  = -0.154822382812D+05 DEG/HR
 5. WX2  = -0.154887324218D+05 DEG/HR
 9. TG1  =  0.927771325100D+02 DEG F.
10. TG2  =  0.932009649200D+02 DEG F.
14. NREVS=  0001.0D+00
15. DELT = 59.202158D+00 SEC
```

```
 1. TEST =  1003.0D+00
 2. WY1  = -0.154915351562D+05 DEG/HR
 3. WX1  = -0.155108378906D+05 DEG/HR
 4. WY2  =  0.154839101562D+05 DEG/HR
 5. WX2  =  0.154899472656D+05 DEG/HR
 9. TG1  =  0.929029822300D+02 DEG F.
10. TG2  =  0.933373422600D+02 DEG F.
14. NREVS=  0001.0D+00
15. DELT = 59.149515D+00 SEC
```

Figure 13. Sample Rate Test Data (Raw)

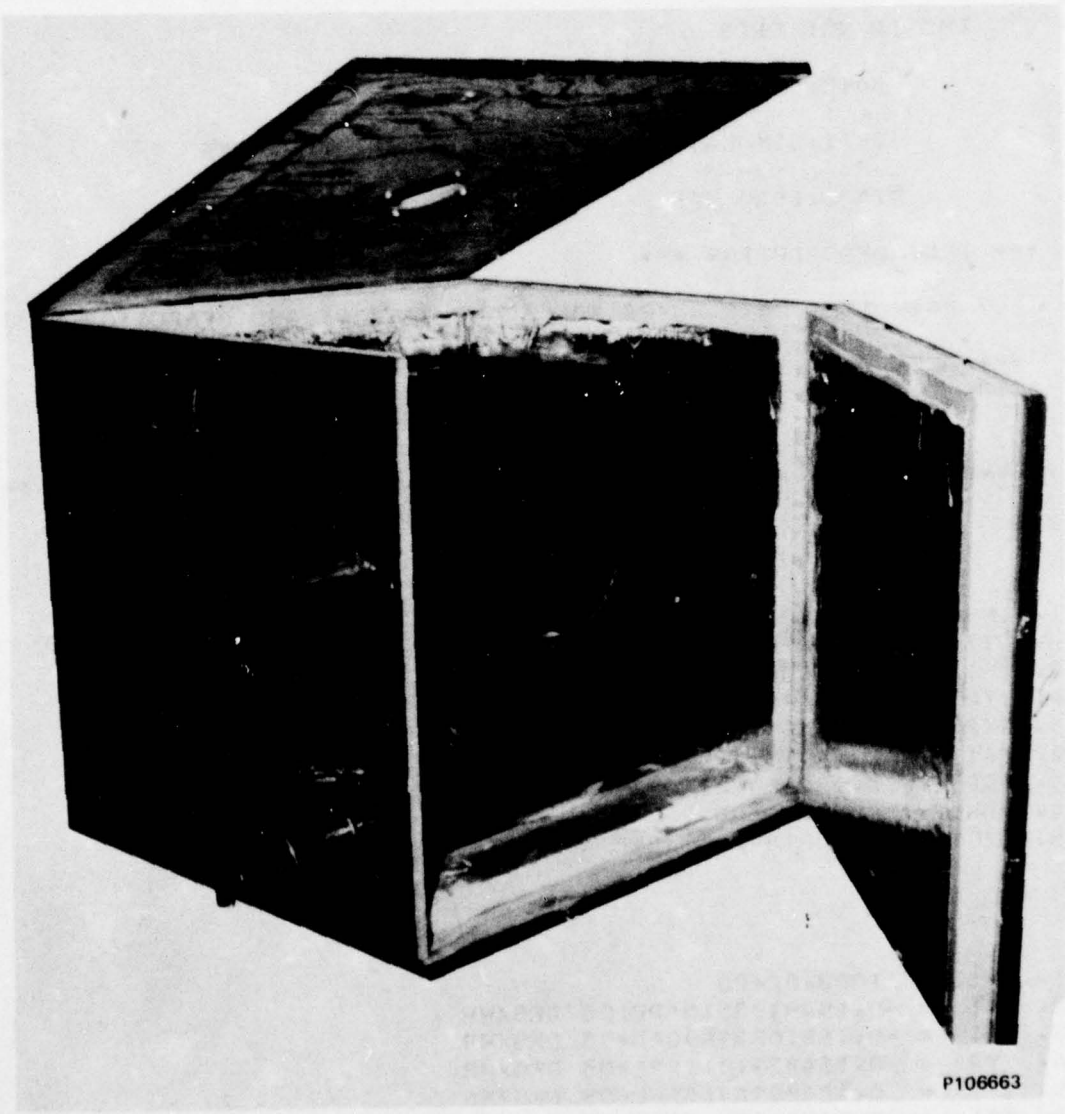


Figure 14. Strapdown Instrument Assembly
in Reference Cube on Static Test Fixture

BEST AVAILABLE COPY

```
**********************************************************************
*
*     ***** MBB-RIICS STATIC DATA TAPE *****
*
*   13SC1
*
* *** TEST INFORMATION ***
*
*     IMU ID NO: E113
*
*          DATE:7 DEC 1976
*
*          TEST:DEMO OF RAW STATIC DATA
*
*         START:0920
*
* *** TEST DESCRIPTION ***
*
*   C5 STATIC DATA DUMPS FOR 24 POSITION TEST
*
*  *** REFERENCE TEMPERATURE ***
*
*     T0=  95.0
*
**********************************************************************


 1. TEST =  1021.0D+00
 2. WY1  =  0.933203125000D+01 DEG/HR
 3. WX1  = -0.935742187000D+01 DEG/HR
 4. WY2  = -0.703125000000D+00 DEG/HR
 5. WX2  =  0.751953120000D+00 DEG/HR
 6. A1C  = -0.100007916000D+01 GEES
 7. A2C  =  0.547392000000D-02 GEES
 8. A3C  = -0.293400000000D-04 GEES
 9. TG1  =  0.895482985900D+02 DEG F.
10. TG2  =  0.898050389200D+02 DEG F.
11. TA1  =  0.872851324000D+02 DEG F.
12. TA2  =  0.885161435600D+02 DEG F.
13. TAF  =  0.132394194600D+03 DEG F.


 1. TEST =  1017.0D+00
 2. WY1  = -0.701171870000D+00 DEG/HR
 3. WX1  =  0.460937500000D+00 DEG/HR
 4. WY2  =  0.969335937000D+01 DEG/HR
 5. WX2  = -0.967382812000D+01 DEG/HR
 6. A1C  =  0.100014573000D+01 GEES
 7. A2C  =  0.570726000000D-02 GEES
 8. A3C  = -0.442200000000D-04 GEES
 9. TG1  =  0.897242364800D+02 DEG F.
10. TG2  =  0.900250957000D+02 DEG F.
11. TA1  =  0.874978258600D+02 DEG F.
12. TA2  =  0.887172403300D+02 DEG F.
13. TAF  =  0.132461871620D+03 DEG F.
```

Figure 15. Sample Static Calibration Data (Raw)

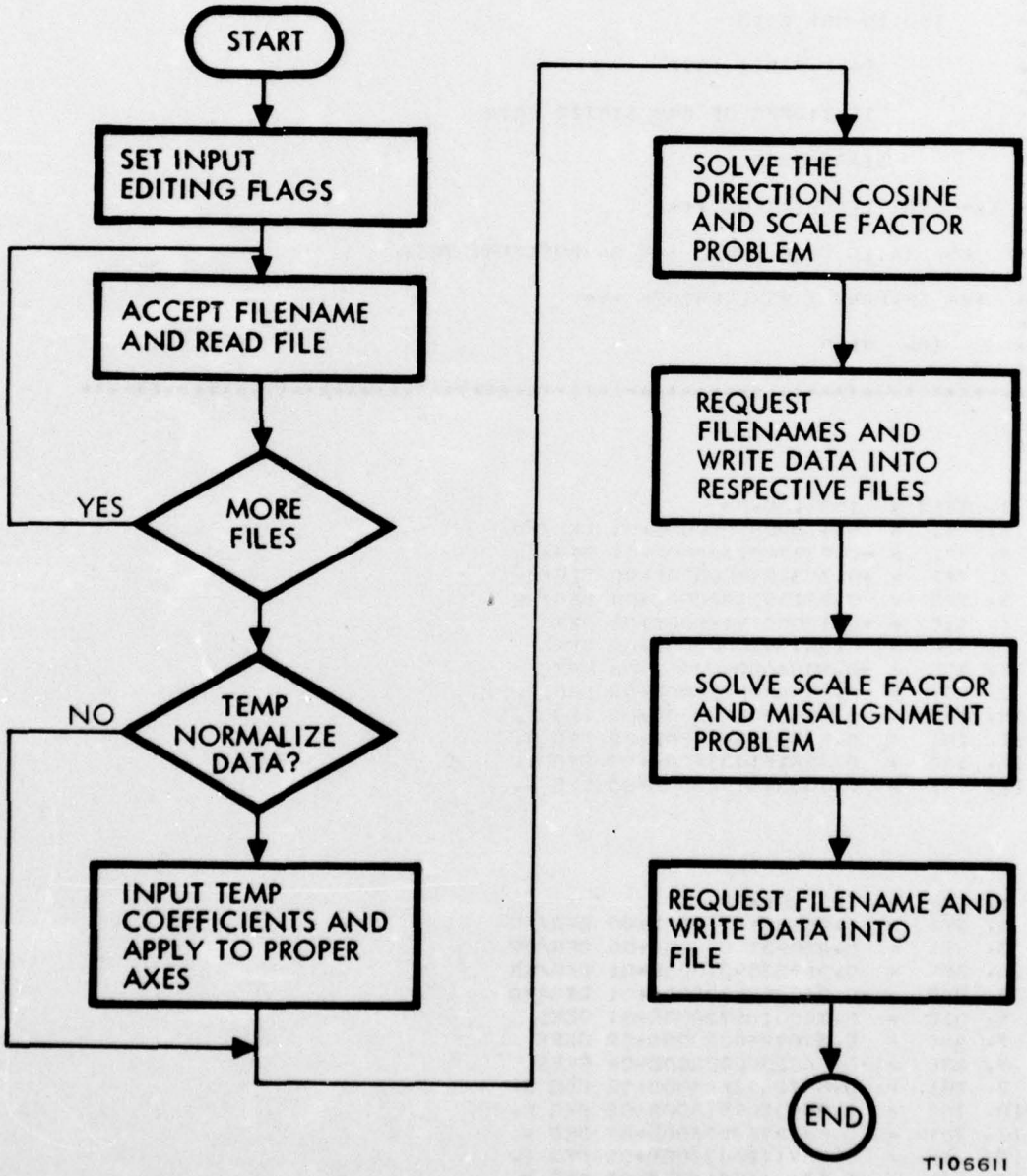


Figure 16. Rate Test Data Processing Flow Diagram

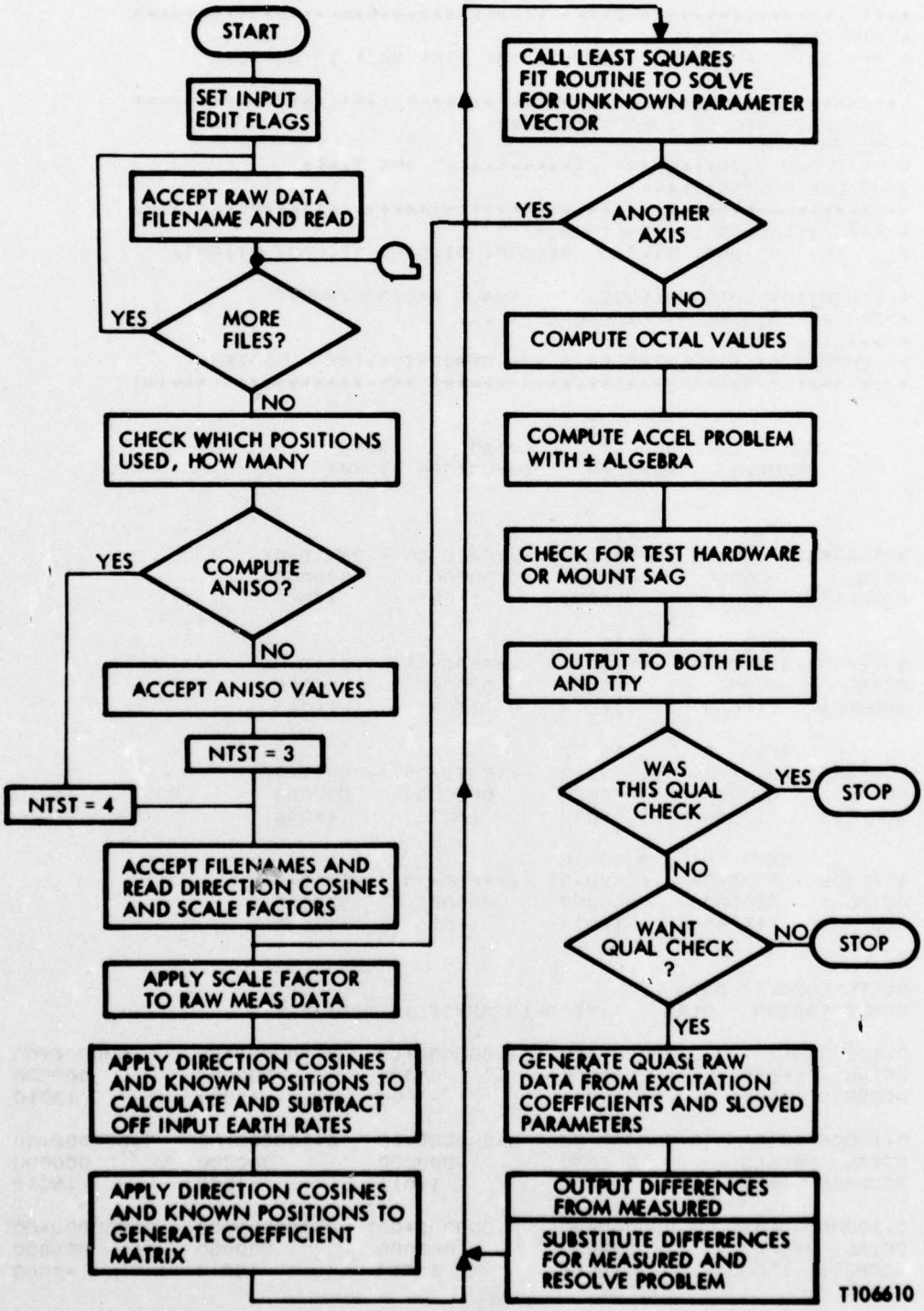


Figure 17. Static Test Data Processing Flow Diagram

BEST AVAILABLE COPY

```
*****************************************************************
* FILENAME = DEMO
* *** DATE OF DATA:  5-JAN-77 THE TIME WAS: 13:46 50.3
*
*****************************************************************
* RAW DATA HEADER INFORMATION **
* SYSTEM NO:
* DATE RAW DATA:********************  THE TIME:
* HEADER COMMENTS:***
*****************************************************************
* *** REFERENCE TEMPERATURE ***
*     IO=  95.000, 91.000, 91.000, 91.000, 91.000, 91.000,
*
* DIRECTION COSINES:FUNDC      SCALE FACTORS:FUNSF
* RAW FILES USED HERE:FJDLPC     ,,,
* ,,,,,,,
*  COMMENTS: SIMULATED DATA FOR DEMONSTRATION PURPOSES
*****************************************************************/

        MU            Q             ANISO        BIAS
        DG/HR/G       DG/HR/G       DG/HR/G/G    DG/HR

          GYRO  1     AXIS  1
AVERAGE .2660D-05   .1691D-05  -.1847D-05  -.7541D-06
OCTAL     000000      000000      000000      000000
ADDRESS    16062       16071       16075       16042

          GYRO  1     AXIS  2
AVERAGE .2361D-04  -.2264D-04  -.6886D-04   .2811D-04
OCTAL     000000      000000      000000      000000
ADDRESS    16063       16072       16075       16043

          GYRO  2     AXIS  1
AVERAGE .1374D-04   .1277D-04  -.1847D-05  -.7541D-06
OCTAL     000000      000000      000000      000000
ADDRESS    16064       16073       16076       16044

          GYRO  2     AXIS  2
AVERAGE .1523D-04   .6082D-05  -.6886D-04   .2811D-04
OCTAL     000000      000000      000000      000000
ADDRESS    16065       16074       16076       16045


ACCELEROMETER DATA
SCALE FACTOR    BIAS      MISALIGNMENTS TO BODY X,Y,Z

0.1000000D+01   0.00000D+00   0.00000D+00   0.00000D+00   0.00000D+00
OCTAL  066663       000000        000000        000000        000000
ADDRESS  15001       15004         -1000         15007         15010

0.1000000D+01   0.00000D+00   0.00000D+00   0.00000D+00   0.00000D+00
OCTAL  066663       000000        000000        000000        000000
ADDRESS  15002       15005         15011         -1000         15012

0.1000000D+01   0.00000D+00   0.00000D+00   0.00000D+00   0.00000D+00
OCTAL  066663       000000        000000        000000        000000
ADDRESS  15003       15006         15013         15014         -1000
```

Figure 18. Sample Static Calibration Processing Output

BEST AVAILABLE COPY

```
*** QUALITY OF GYRO DATA ***
  DIFFERENCES OF REAL AND ESTIMATED SYSTEM OUTPUTS(DG./HR)
POS       X1             Y1             X2             Y2

  1 -.377036D-06  .140552D-04 -.377036D-06  .140552D-04
  5 -.377036D-06  .140552D-04 -.377036D-06  .140552D-04
  9  .196335D-05  .632890D-05  .778253D-05 -.371212D-05
 13 -.159631D-05 -.203781D-04 -.740549D-05 -.103430D-04
 17  .121322D-05  .680325D-06 -.419589D-05 -.894177D-05
 21 -.836180D-06 -.147355D-04  .457292D-05 -.511340D-05


-------------------------------------------------------------------------
     .121288D-05  .133413D-04  .506969D-05  .101813D-04  GYRO SIGMAS


***QUALITY OF ACCEL. DATA ***
  DIFFERENCES OF REAL AND ESTIMATED SYSTEM OUTPUTS(GEES)
POS

  1  .000000D+00  .000000D+00  .282045D-15
  5  .000000D+00  .000000D+00  .000000D+00
  9  .000000D+00  .282045D-15  .000000D+00
 13  .000000D+00  .000000D+00  .000000D+00
 17  .282045D-15  .000000D+00  .000000D+00
 21  .000000D+00  .000000D+00  .000000D+00


-------------------------------------------------------------------------
     .906493D-16  .906493D-16  .906493D-16  ACCEL. SIGMAS


THEORETICAL CLOSURE VALUES

        MU          G          ANISO       BIAS
        DG/HR/G     DG/HR/G    DG/HR/G/G   DG/HR


          GYRO  1    AXIS  1
AVERAGE .5622D-06 -.5622D-06  .2054D-15  .1394D-06
OCTAL     000000     000000     000000     000000
ADDRESS    16062      16071      16075      16042

          GYRO  1    AXIS  2
AVERAGE-.4729D-05 -.4729D-05 -.3620D-14  .2456D-05
OCTAL     000000     000000     000000     000000
ADDRESS    16063      16072      16075      16043

          GYRO  2    AXIS  1
AVERAGE .1350D-05 -.1350D-05 -.1123D-14 -.7622D-06
OCTAL     000000     000000     000000     000000
ADDRESS    16064      16073      16076      16044

          GYRO  2    AXIS  2
AVERAGE .8131D-05  .8131D-05 -.1256D-14  .8522D-06
OCTAL     000000     000000     000000     000000
ADDRESS    16065      16074      16077      16045


ACCELEROMETER DATA
SCALE FACTOR   BIAS     MISALIGNMENTS TO BODY X,Y,Z

0.1000000D+01  0.00000D+00  0.00000D+00  0.00000D+00  0.00000D+00  0.00000D+00
OCTAL  066663       000000       000000       000000       000000       000000
ADDRESS 15001        15004        -1000        15007        15010

0.1000000D+01  0.00000D+00  0.00000D+00  0.00000D+00  0.00000D+00  0.00000D+00
OCTAL  066663       000000       000000       000000       000000       000000
ADDRESS 15002        15005        15011        -1000        15012

0.1000000D+01  0.00000D+00  0.00000D+00  0.00000D+00  0.00000D+00  0.00000D+00
OCTAL  066663       000000       000000       000000       000000       000000
ADDRESS 15003        15006        15013        15014        -1000


ACCELEROMETER HORIZONTAL POSITION BIASES
          ACCEL. X              ACCEL. Y              ACCEL. Z
             (G)                   (G)                   (G)
BIAS  .0000E+00  .0000E+00  .0000E+00  .0000E+00  .0000E+00  .0000E+00
AVG. BIAS          0.000000E+00          0.000000E+00          0.000000E+00
   OCTAL               000000                000000                000000
 ADDRESS               -1000                 -1000                 -1000
EXIT
```

Figure 19. Residual Differences and Theoretical Closure Values for Sample Static Calibration

BEST AVAILABLE COPY

```
**********************************************************************
*
* FILENAME = DEVO DAT
* DESCRIPTION: TORQUER SCALE FACTORS,MISALIGNMENT
*     TERM. SEN. SCALE FACTORS
* DATE OF DATA:  6-DEC-76 THE TIME WAS: 17:24 50.1
**********************************************************************
* DAS DATA HEADER INFORMATION **
* SYSTEM NO: FIT3
* DATA DAS DATA:6 DEC 1976                THE TIME:1710
* HEADER CONTENTS:DEVONSTRATION OUTPUT
**********************************************************************
* REFERENCE AND AVERAGE INSTRUMENT TERM VALUES
*  95.000, 94.950, 95.040,  0.000,  0.000,  0.000,
* DAS FILES USED WERE:13DC1      ,,,
* ,,,,,,,
*  COMMENTS:SAMPLE OUTPUT WITH SIMULATED DATA
**********************************************************************


          SFX1              MIXY              MIXZ
            0.999975          0.000003          0.000014
OCTAL VALUES
            000003            177756            177744
ADDRESSES     16022             16034             16035


          SFY1              MIYY              MIYZ
            0.999997          0.000010          0.000001
OCTAL VALUES
            000000            177747            177775
ADDRESSES     16023             16039             16033


          SFZ2              MZXY              MZXZ
            1.000027          0.000013          -0.000018
OCTAL VALUES                                      !
            177775            177746            000046
ADDRESSES     16024             16040             16041


          SFY2              MZXY              MZXZ
            1.000025          0.000039          -0.000006
OCTAL VALUES
            177775            177656            000014
ADDRESSES     16025             16036             16037
```

Figure 20. Sample Rate Test Calibration Processing Output

EIGHTH BIENNIAL GUIDANCE TEST SYMPOSIUM

FLIGHT TESTING A REDUNDANT STRAPDOWN INERTIAL SYSTEM

AUTHORS: THOMAS L. SHUCK
ROBERT A. BOOTH
JEROLD P. GILMORE
THOMAS P. SCHAMP
T. T. CHIEN

THE CHARLES STARK DRAPER LABORATORY, INC.
CAMBRIDGE, MASSACHUSETTS

RONALD J. HRUBY
NASA AMES RESEARCH CENTER

Flight Testing a Redundant Strapdown Inertial System

THOMAS L. SHUCK, ROBERT A. BOOTH, JEROLD P. GILMORE, THOMAS P. SCHAMP,
T.T. CHIEN, Charles Stark Draper Laboratory, Inc., Cambridge, Mass.
RONALD J. HRUBY, NASA Ames Research Center

1.0 INTRODUCTION

In recent years military and commercial aircraft operations have become more and more dependent upon sophisticated avionic systems for routine operational mission success. The need for a dependable avionic capability especially in navigation, guidance and control has stimulated development of a compatible fault tolerant inertial system and associated computational processor. The anticipated even higher density aircraft operations of the future coupled with the anticipated introduction of STOL and VTOL aircraft to the transportation field has emphasized the need for control, guidance and navigation systems with "Fail Operational" redundancy provisions to assure successful safe operation during critical phases such as approach, landing and take-off flight path maneuvers.

Current aircraft avionic systems utilize a proliferation of sensors, sensor systems and display devices for various flight modes. These systems often overlap in function and provide a measure of control and navigational backup. Redundancy when implemented is most often achieved in this backup sense. For example, several Radio NAV. functions, an Inertial System and basic attitude and heading sensors are usually available. In transoceanic commercial aircraft where INS reliability is considered necessary for operational success, redundancy has been implemented and triplicate systems are flown. In general, when implemented, redundancy is achieved by either additional similar hardware or alternate functional elements added on a subsystem by subsystem basis. An integrated implementation of functions and hardware to achieve a real-time fault tolerant navigation, guidance and control avionic capability is almost totally lacking in current aircraft avionic implementations. The responsibility for making even the simplest decisions regarding the use of this profileration of equipment, when a fault appears, or for that matter determining which subsystem is faulty is essentially part of the pilot's work-load. Such requirements in time-critical flight phases significantly stress pilot-reaction time, especially in high density operations with limited stability vehicles. Excessive pilot work-loads are already a limiting factor in safe vehicle operations.

An integrated redundent avionic implementation with self-contained fault identification and adaptation capabilities is clearly needed for future aircraft operations. The integration of functions to eliminate unnecessary backup configurations is also an obvious goal. The logistic and maintenance aspects of the ever increasing avionic equipment complement presents increasing operational availability problems with attendent increasing cost factors.

The concepts embodied in the C. S. Draper Lab Strapdown Redundant Inertial System (SIRU) make it uniquely suited for initial evaluation and aircraft flight demonstrations of fault-tolerant navigation, guidance and control. The SIRU system features redundant sensors and electronics with a complementary dual processor configuration. The processing includes self-contained fault detection, isolation and recertification software algorithms. SIRU was flight tested by the NASA/Ames Research Center with technical and test engineering support from the Charles Stark Draper Laboratory.

The SIRU redundant inertial configuration is an appropriate core element for integrated fault-tolerant GN&C demonstrations in that it provides basic wide range vehicle rate sensing, an all attitude display and navigational outputs all with a fault-tolerant - "Fail Operational" capability. Thus, SIRU embodies all time critical navigation and control sensing and processing functions in a redundant implementation and subsequent incorporation of radio navigation and control functions may then be implemented in the context of this core capability. SIRU would then provide a highly reliable, transient free, continuous, wide bandwidth control and memory function while Radio NAV. updates would provide low frequency, long duration, static accuracy. In the event of a radio aid failure or drop out, time permits use of an alternate aid or most probably successful mission completion on the inertial memory function.

SIRU also incorporates modular construction features. The modularity, coupled with the extensive self-contained fault identification and localization software/hardware diagnostics should provide significant operational logistic and maintainability advantages.

Laboratory test evaluations of the SIRU system in both static and dynamic environments with various inertial component failure configurations have been conducted and results of this testing are documented in detail in several publications.

The flight test results presented in this paper are based on 34 flight tests flown between May 20, 1975 and September 25, 1975 in NASA's CV340 aircraft. These flights originated from NAS Moffett and were mostly conducted in the vicinity of NALF Crow's Landing but also included longer flights to Sacramento and Bakersfield, California to evaluate navigation performance. A total of 28 hours of flight time was utilized conducting these tests.

The flight test program demonstrated the above listed features and in the course of its completion, fulfilled the following objectives:

1. Mature operational concepts of;

   a. fault tolerant redundancy management
   b. pilot/system interaction and supervision
   c. ground based experience in diagnostics and maintenance
   d. preflight calibration, alignment and checkout

2. Established a baseline for integrated strapdown inertial system performance

   a. projected performance requirements for aircraft application
   b. defined fault detection thresholds for navigation and flight control in an operational environment.

2.0 FLIGHT SYSTEM MECHANIZATION HARDWARE DESCRIPTION

The flight test configuration that was used in the flight evaluations of SIRU may be divided into four blocks or equipment, the dual computer assembly, the displays and tape transport and the reference system (Figure 2.1). The system is experimental in nature and is not configured to be representative of production flight hardware. Rather, the system has been configured to perform in real time as a finished system while maintaining flexibility and the necessary features to permit a complete evaluation of its performance in the flight environment.

2.1 REDUNDANT STRAPDOWN INERTIAL REFERENCE UNIT (SIRU)

The inertial reference unit consists of the instrument package, power supply assembly, instrument package heat exchangers, electronics assembly, and multiplexer. Redundancy concepts have been implemented in all of these assemblies.

Redundant Instrument Package: The redundant instrument package (Figure 2.2) is an assembly of six single-degree-of-freedom gyroscope modules and six linear accelerometer modules mounted on an alignment structure (π-frame). Each module is prealigned, normalized and includes the instrument, its pulse torque-to-balance electronics, temperature controller, and other associated electronics such as pre-amplifier and inertial instrument normalizing components.

The module outputs are in the form of an increment of angular motion $\Delta\theta$ and velocity ΔV for the gyro and accelerometer module, respectively. These outputs are processed through the computational structure to attain inertial attitude and velocity and body angular rate and acceleration.

Geometric redundancy is achieved by using a nonorthogonal mounting configuration in which the instrument input axes are oriented to correspond to the array of normals to the faces of a dodecahedron (Figure 2.3). This concept for redundancy and descriptions of its implementation in the SIRU system are well documented in the literature and will not be pursued in this paper.

Power Supply Assembly: The power supply assembly is configured to run off aircraft 400 Hz and provide redundant power to the instrument package, electronics assembly and multiplexer. The power supply provides over voltage, under voltage, transient spike and temporary loss of aircraft power protection for the system. The NiCad battery pack provides the system with uninterrupted power when switching from ground to aircraft power, during loss-of-power transients and, for a short period of time (approximately 15 minutes), can provide continued redundant capability if either the A or B

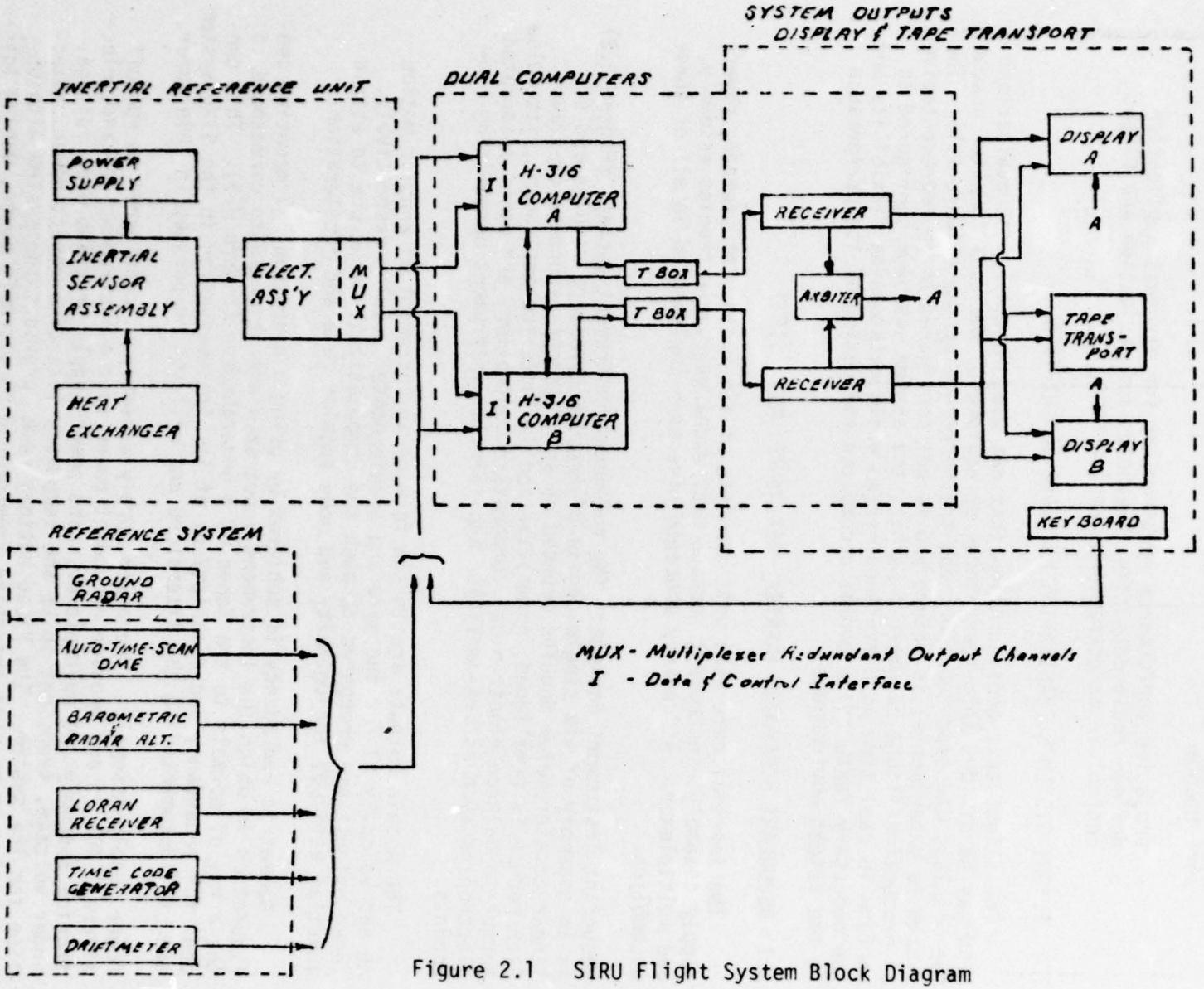


Figure 2.1 SIRU Flight System Block Diagram

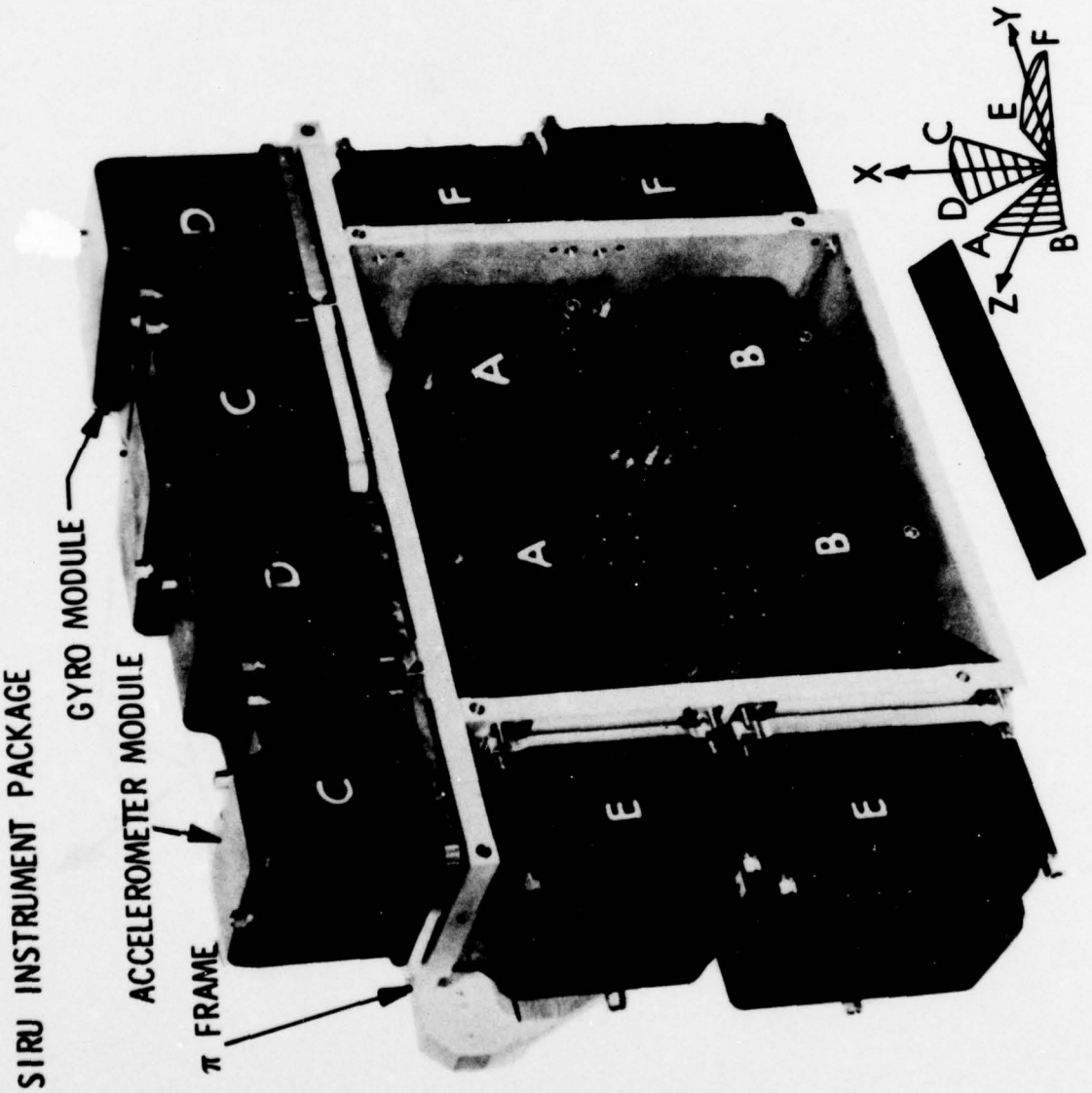


Figure 2.2 SIRU Instrument Package

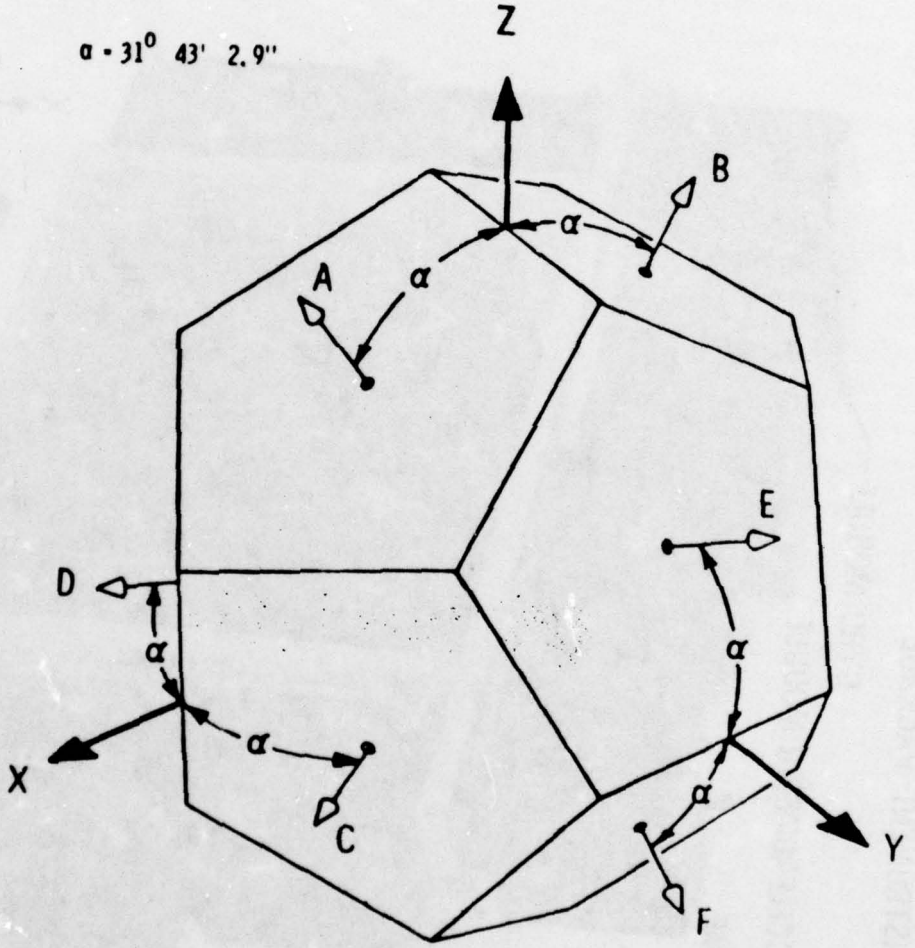


Fig. 2.3. Instrument Input Axes Orientation Relative to The Instrument Frame Triad and the Dodecahedron

supplies becomes inoperative during a flight test.

Instrument Package Heat Exchanger: Design of the heat exchanger for the instrument mounting structure (π-frame) presented an interesting challenge since the SIRU hardware had originally been designed to operate with a spacecraft type low temperature liquid coolant interface. Thus, a low cost heat exchanger concept was required to be compatible with the NASA aircraft environment (cabin temperature as high as 94°F and limited heat sink capability) and consistent with the redundant provisions of the SIRU hardware. As a result a finned liquid to air heat exchanger using forced cabin air flow was configured. Two separate exchangers, pumps and fans are used. Each alone is capable of providing an adequate coolant capability for the instrument package.

Electronics Mechanization: Redendant techniques are employed in the electronic mechanization to provide a system output data flow that is free from any single point failure mechanisms. Figure 2.4 illustrates the basics of the mechanization. Functional axes have been defined that correspond to each dodecahedron measurement axis. Each axis consists of a gyro and an accelerometer module supported by common power supplies. These power sources include: a 2 phase 800 Hz gyro wheel power supply; a 9600 Hz supply for suspension and signal generator excitation and a dc axis supply. The dc axis supply provides the modules' torque electronics with the required logic (5v) and amplifier (+10v) voltage levels and a separate floating excitation (15v) for each precision voltage reference (PVR). This per-axis implementation enables the isolation of any failure to a specific instrument axis or, at most, to a functional axis. The functional axis concept was implemented for ac and floating dc power.

The mechanization allows for the incremental $\Delta\theta$ and ΔV outputs of each instrument module to be stored redundantly in an interface multiplexer. The multiplexer transmits data to the computer assembly on dual buses. A serial data transmission format is used. The multiplexer includes provisions for digitized analog data (voltages, etc.) for automatic monitoring to enable more extensive fault localization, e.g. to replaceable modules.

Redundant dc power distribution to the functional axes is achieved by the use of dual dc power supplies. These supplies are designed so that each can independently support the total load of all functional axes. They are isolated from each other by diode networks to provide fail-safe operation.

The timing control pulses for the torque electronics and synchronization functions for the various power supplies are redundantly implemented. The oscillators are mechanized in a triple-redundant configuration with output frequency comparisons by individual failure detectors.

Dual redundancy is employed in the scaler implementation, and high/low frequency detectors test both the 115.2 kpps and 200 pps outputs. The control pulses to the torquing electronics are also tested for their presence and proper sequence. The selection logic gates only one scaler at a time to the system functional axes and power supplies, but both scalers are con-

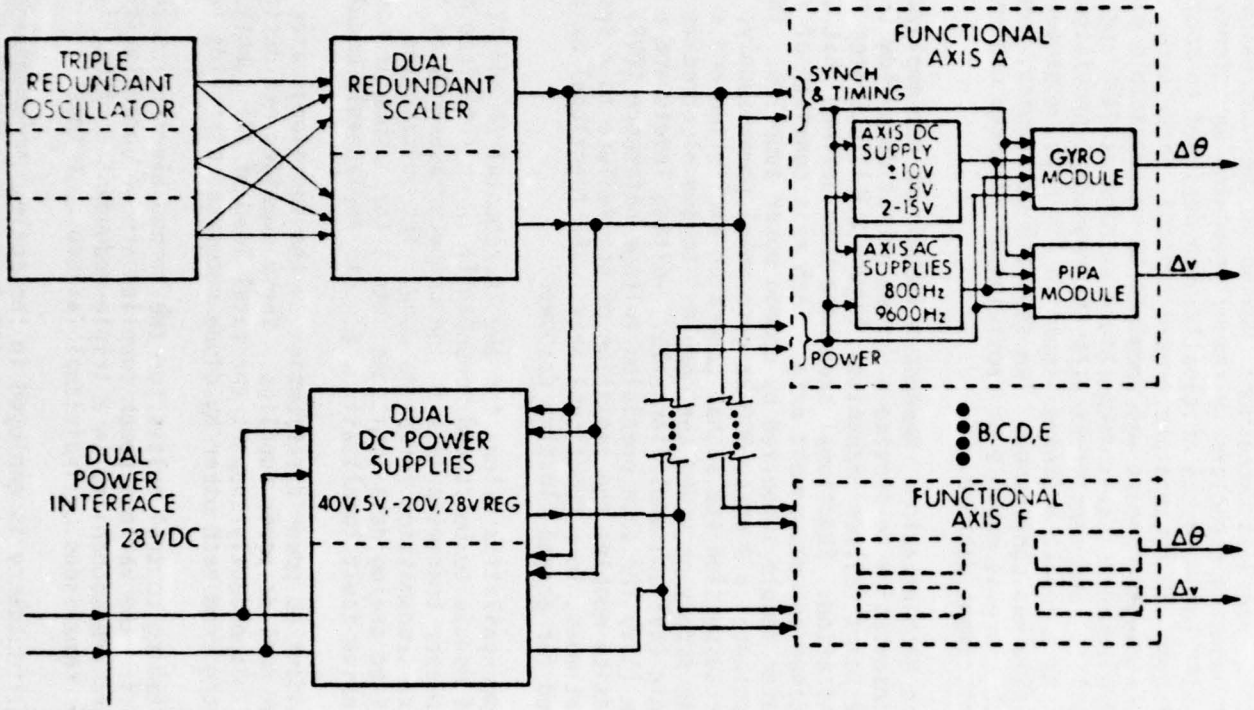


Fig. 2.4. Block Diagram of SIRU System

tinuously operated and monitored by their detectors. In both the scaler and oscillator implementation, provisions for test sequencing of all the combinations are included.

It is important that with respect to the dc power supply and the scaler, the electronic system configuration was mechanized to provide only fail-safe isolation characteristics because the relative reliability of the particular functional elements was used to determine the redundancy level to be implemented. For example, the estimated failure rate of a 40v power supply is less than 10 failures per million hours whereas a gyro module failure rate estimate might range between 100 and 200 failures per million hours, determined principally by the inertial instrument and the torque electronics. Thus, dual redundancy is sufficient for the dc power supply; it does not compromise the end-to-end system reliability index and still provides fail-safe operation. Similar considerations were applicable to the dual implementation of scalers. Inclusion of a third scaler and dc power supply would represent a relatively simple design modification.

Each gyro and accelerometer module includes its own temperature controller, preamplifier, torque control loop, etc. Scale factor stability and linearity performance on the order of 2 and 20 ppm respectively has been achieved with the present instrument control loop with a 1 rad/sec design range. The gyro and accelerometer modules both use a standard pulse on demand ternary torque-to-balance control loop. The electronic mechanization has been described in detail in the referenced documents; the multiplexer is described below for completeness.

Multiplexer: The multiplexer (Figure 2.5) is a redundant assembly which provides for buffering and transfer of the six axes of velocity and angle measurement data and includes special fault detection and test monitoring hardware.

The special hardware in the multiplexer is provided to augment and enhance the fault localization capabilities of the primary real-time monitoring provided in the basic SIRU software. The multiplexer hardware provisions include:

1) Warning status logic and appropriate software servicing signals to the operator (pilot) should any of the system dual or triple redundant axes fail. This covers those limited functions which are not mechanized six times over such as the dual scaler and 40/5 volt power supply, and the triplex clock. This feature also assures that status of all electronics can be verified in preflight checkout.

2) Provide, in the event a fault exists, the ability to isolate it to a replaceable functional module for repair. The multiplexer incorporates a limit-test sequencer that scans approximately one hundred thirty six points and continually updates a display indicating the in-spec or out-of-spec status of each point. Should any point, such as a dc axis power supply, exceed specification, the multiplexer flags the offending component or subassembly.

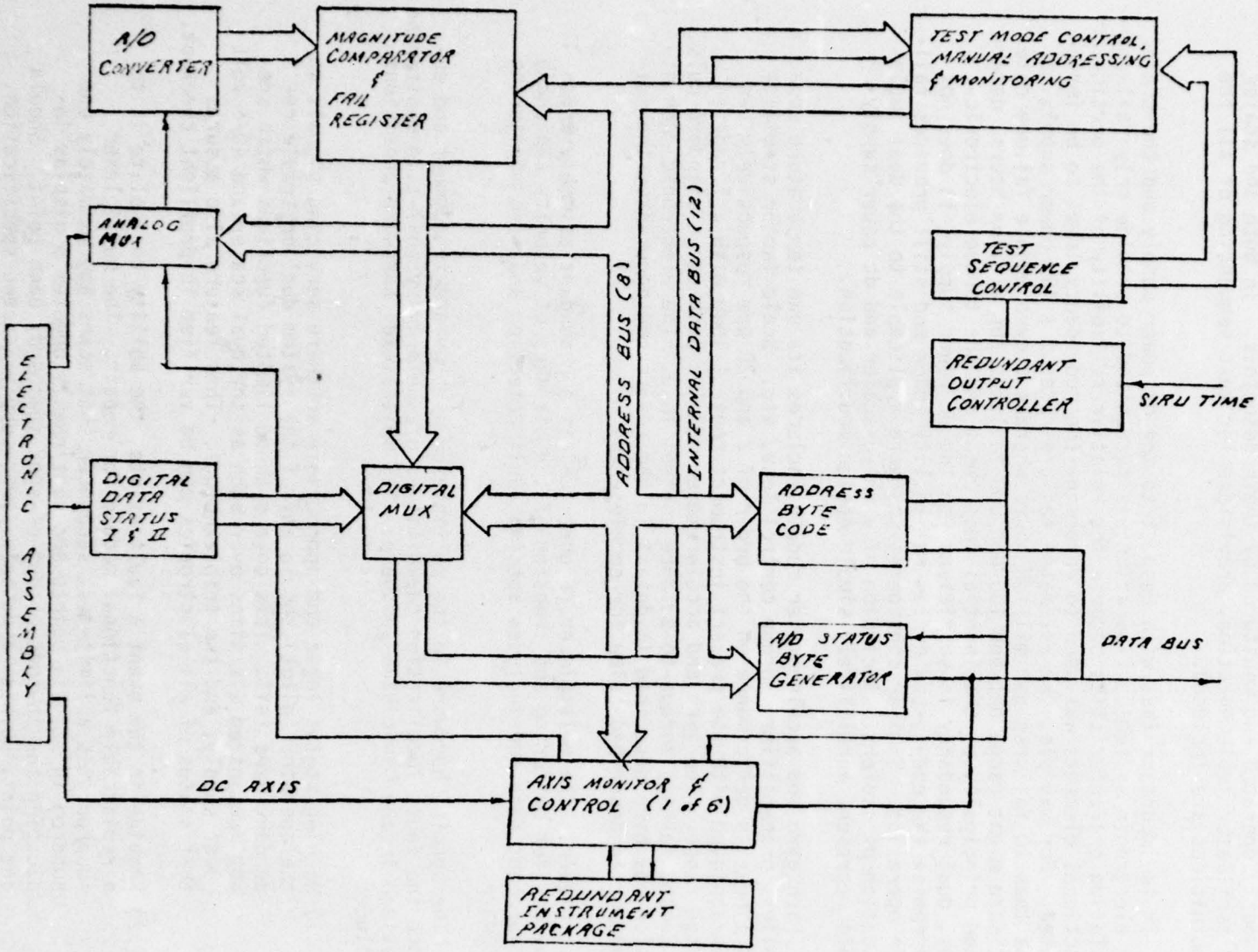


Figure 2.5 SIRU Multiplexer Schematic

Concurrently, the parameter magnitude is stored in reserve memory in the computer for post flight diagnostics.

3) Provide a high rate analog/digital diagnostic readout for detailed troubleshooting and performance monitoring. The multiplexer hardware incorporates an A/D that can be moded to monitor individual supplies, etc. at a high rate (40/sec) with fine resolution. This function enables a total-troubleshooting capability during pre or post-flight operations but is not intended to be operational during flight on-line operations. The multiplexer does have a third mode of operation that permits continual monitoring of any one parameter without interrupting the continuous scan. This feature allows the test engineer to track the operation of key parameters without interfering with the flight test in process.

2.2 DUAL COMPUTERS/REDUNDANCY MECHANIZATION

Dual H-316 Computers: The dual computer configuration was selected for the flight test program to provide redundancy compatible with the redundant SIRU hardware and software configurations. The ruggedized Honeywell H-316 computer in particular was selected to provide this capability at a minimum cost to the program. The H-316 computer was software compatible with all existing SIRU software negating the need for recoding and the design approach used in the ruggedized H-316 parallels the requirements of the "MIL Spec" airborne computer.

The computers are mechanized to run in a "prime-backup" mode. The prime data is used as the valid system output unless the prime channel shows a failure or the test engineer (pilot) forces a switchover. Each computer runs an identical software program and the two computers are loosely synchronized by software checkpoints where comparisons are made and go-ahead signals issued.

Data is acquired by the computers from the multiplexer and airborne reference system, processed, and output to the redundancy management hardware. Self-test programs are run in the background and the results transmitted along with the data for determination of the prime computer status.

Redundancy management of the two computers is handled by dual transfer boxes (T boxes), dual receivers, and an arbiter (Figure 2.1).

T Box: This box is the heart of the redundancy mechanization. It includes the computer self-test feature "night watchman" and I/O wraparound to insure that data received by the T box is identical to the data sent by the computer. It provides the capability for the two computers to compare data and to exchange data in an attempt to recover from transient failures. The T box initiates a serial transfer of data to the receiver when the computer self and cross opinion is output. Parity is generated on this serial word and an echo check is performed on the transmission.

Receiver: The receiver consists of the shift register to accept the incoming data from the T box. It checks parity of the transmission, returns the data for echo check and records the result of the echo test. It also detects the "word watch" which is a code word output by the computers at specified intervals. If the code word does not appear on schedule, a failure is indicated. The destination address is decoded in the receiver and parallel data directed to the display, arbiter, or tape transport.

Arbiter: The arbiter receives all of the redundancy and self-check information from the two receivers, buffers this information and makes the choice of remaining with the prime computer or switching to the backup computer. In addition to determining "prime-backup" computers, the arbiter controls a panel of lights indicating the nature of any computer failure including disagreement of the two computers. Manual override of the arbiter's choice is also provided.

2.3 DISPLAY/FLIGHT RECORDER

Displays: The two displays provide a continuous real-time monitoring capability of all data output by the dual computers. Navigation and aircraft body information will normally be displayed, however, any information output by the computers can be displayed by operator intervention.

Each panel can be manually switched to display the output of either computer A or B or the output of the designated prime. In addition to the self-scan panel, there is a LED display of gyro and accelerometer fail status, computer self and cross opinion, identification of prime and electronics fail. Electronics fail is a warning that one of the dual or triple redundant modules in the electronics assembly has failed and the operator can call up the proper page on the self-scan panel and determine exactly which module has failed.

The display and receiver have been designed to be representative of an applied system in which the display might be remotely located with respect to the system (pilots display vs. test engineers display) and it is anticipated that as the flight test program matures a pilots display could easily be added when desired.

Flight Recorder and Keyboard: A digital flight recorder serves the dual purposes of loading the computer operating programs and during tests, recording all computer outputs for post flight analysis. The tape produced is compatible with industry standards and thus simplifies the data retrieval and reduction.

A simple keyboard is provided to allow the convenient loading of programs from the tape transport and to permit the test engineer, by altering instrument compensation loads, to introduce gyro and accelerometer failures of varying magnitudes at opportune times during flight testing.

Reference System: The reference system (Figure 2.1) consists of two radars at the NASA Crow's Landing test field for use during approach area evaluation.

The reference system airborne complement consists of an auto-time-scan DME receiver, barometric and radar altimeters, a Loran C receiver, a time code generator and a driftmeter.

The time code generator was used to synchronize the radar data tapes with the flight recorder tapes for post flight analysis.

The remaining equipment, including visual sightings from the driftmeter, was used during the flight test program to establish reference flight paths against which the SIRU's navigation performance was evaluated.

3.0 FLIGHT TEST SYSTEM HARDWARE

This section contains technical and design descriptions of the construction and installation of the SIRU flight test system.

3.1 CONFIGURATION AND MOUNTING

The SIRU Flight Test System is assembled into two separate structures designated as the inertial system pallet and the computer console. The two-structure approach was dictated by the advantages inherent in the capability to install and remove the equipment from the CV340 as a minimum number of complete assemblies. Both structures were designed to mount on the port side of the CV340 aircraft. The computer console, mounted on its support structure, is 59 inches long and is centered approximately at aircraft station 480. The inertial system pallet is 40 inches long and is centered approximately at aircraft station 394. This positioning creates a 37-inch wide access to the emergency exit centered approximately at aircraft station 424. The open emergency exit provides line-of-sight exposure to the porro prism mounted on the inertial package fixture to permit external system alignment calibration.

3.1.1 INERTIAL SYSTEM PALLET

The inertial system pallet (Figures 3.1 and 3.2) contains all those assemblies directly associated with the support of the redundant instrument package. These consist of the instrument package, its mounting and test fixture, the electronics assembly, the multiplexer, the heat exchanger assembly, the dual power supplies (A and B), the power distribution box, the NiCd battery and the basic pallet. The complete assembly weighs 608 pounds and requires approximately 1500 VA of 3-phase 400 Hz power.

The power supplies, distribution box, battery, and heat exchanger are hard mounted to a single plate which is shock-mounted to the base of the pallet. With this mounting, the load of these heavy assemblies is, thus, transferred directly to the mounting deck inducing a minimum influence on the upright members which support the inertial package. The electronics assembly and multiplexer, which are mounted as one integral unit, are shock-mounted to the forward vertical face of the pallet. This assembly is hinged on the inboard edge to provide easy access to the electronics assembly for maintenance and repair.

The inertial package, attached to its mounting fixture, is bolted to the top surface of the pallet. The mounting fixture has a built-in repositioning capability to permit multiple-position testing of the strapdown system eliminating the need for a special test table to be installed at the Ames Research Center. Mounted on the test fixture is the porro prism which is used to accurately determine the location, in aximuth, of the system's X axis with respect to the true north. The porro prism is located at an angle of 35° 36' 2.75" from the system's Y axis and at a height above the deck which permits optical sighting to it from a ground based theodolite. The porro prism angular position has been calibrated with respect to the precision optical cube

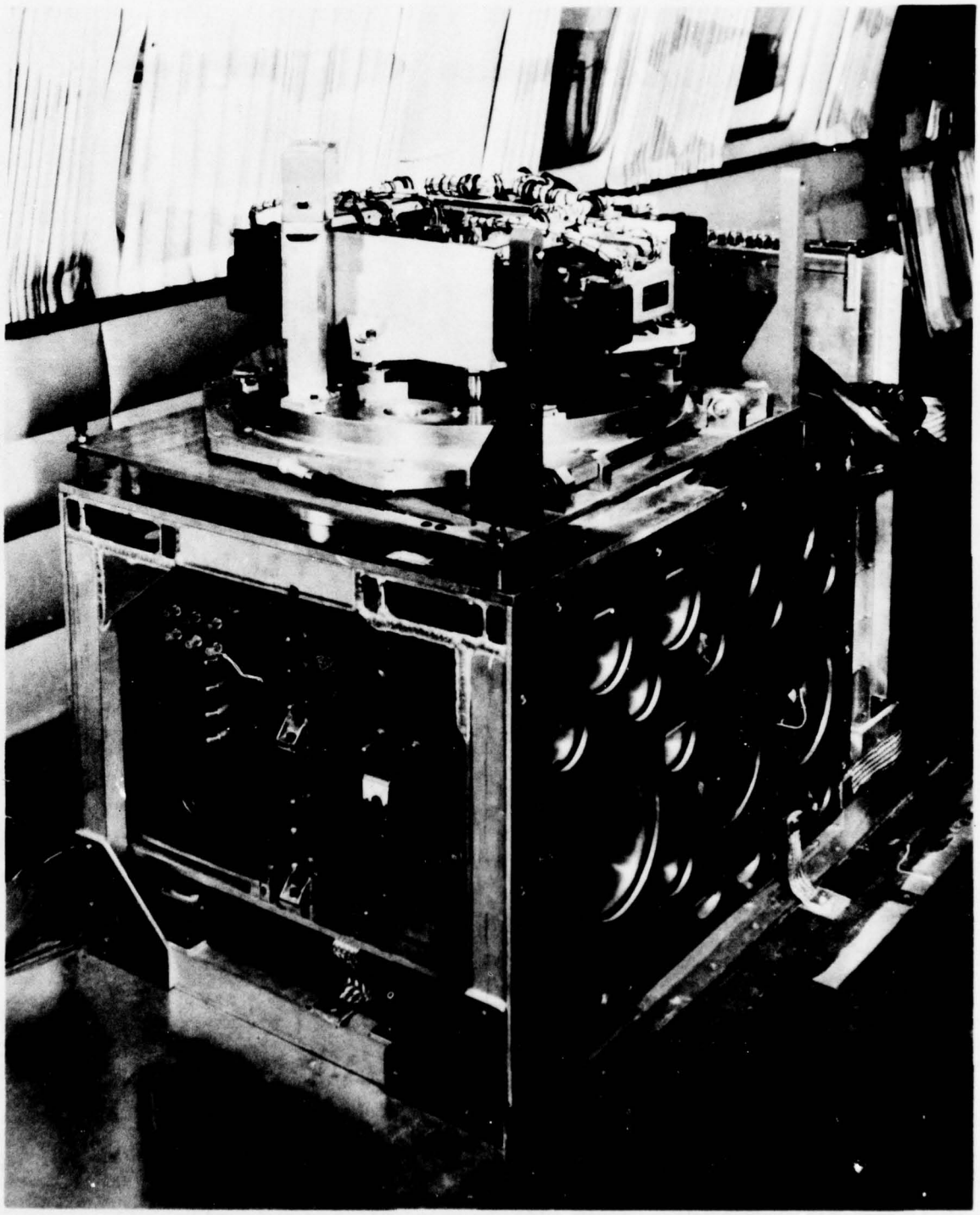


Figure 3.1 SIRU Inertial System Pallet

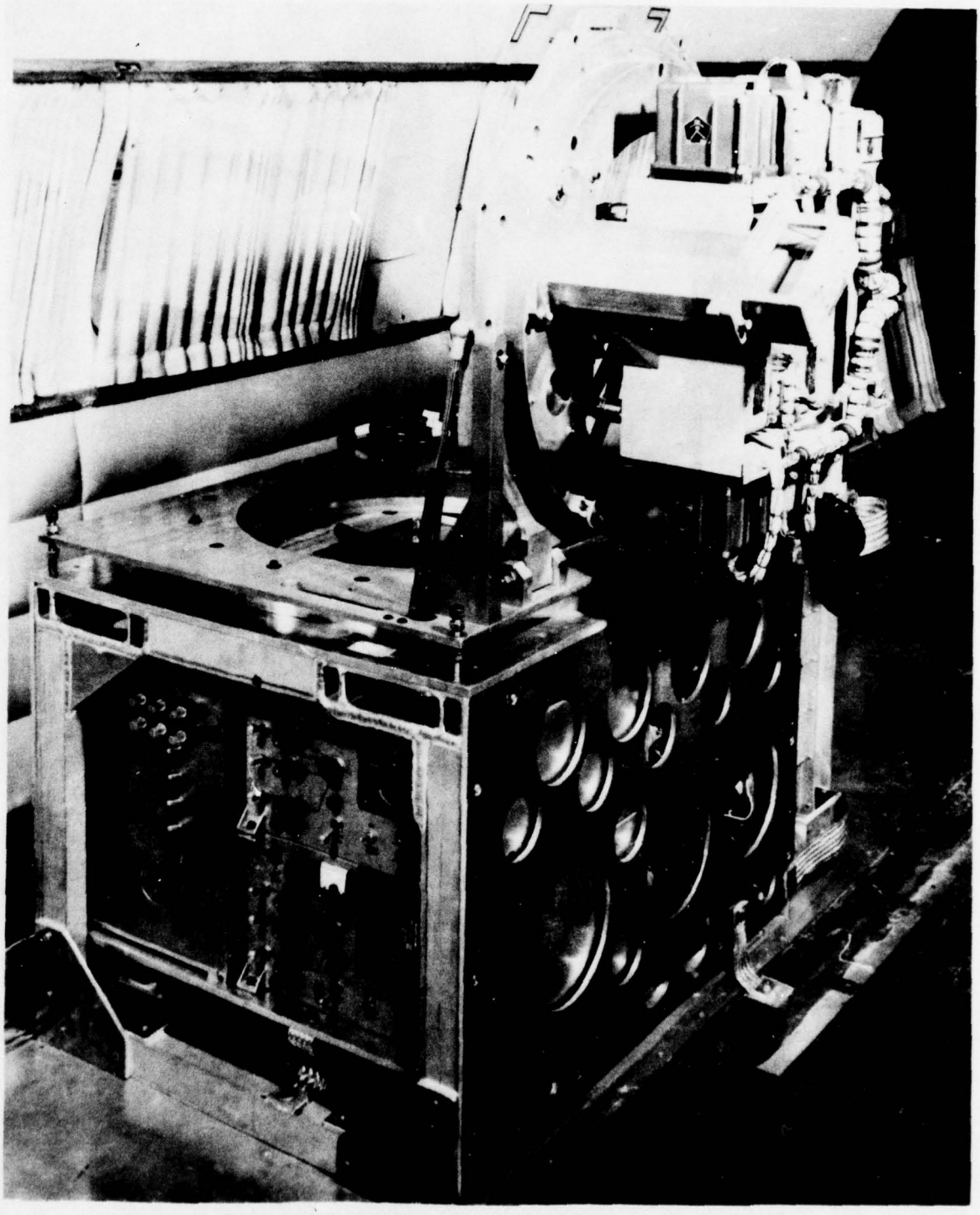


Figure 3.2 Inertial System Pallet Multiple Position Test Configuration

which is mounted on the underside of the inertial package and provides the reference coordinates for the system.

3.1.2 COMPUTER CONSOLE

The computer console (Figure 3.3) contains the equipment associated with the processing of the inertial data. The individual elements are assembled into an especially rugged cabinet constructed from aluminum extrusions. The cabinet is shock-mounted to its support structure and the support is bolted to the deck of the CV340. The complete assembly, including the support structure, weighs 659 pounds and requires approximately 2400 VA of single phase, 400 Hz power. The two H316 computers, the heaviest equipment items, are mounted side-by-side in the bottom of the cabinet to keep the center of gravity of the assembly as low as possible. Figure 3.4 identifies the remaining drawers in the cabinet. Figure 3.5 is a diagram showing the computer console power and signal cabling.

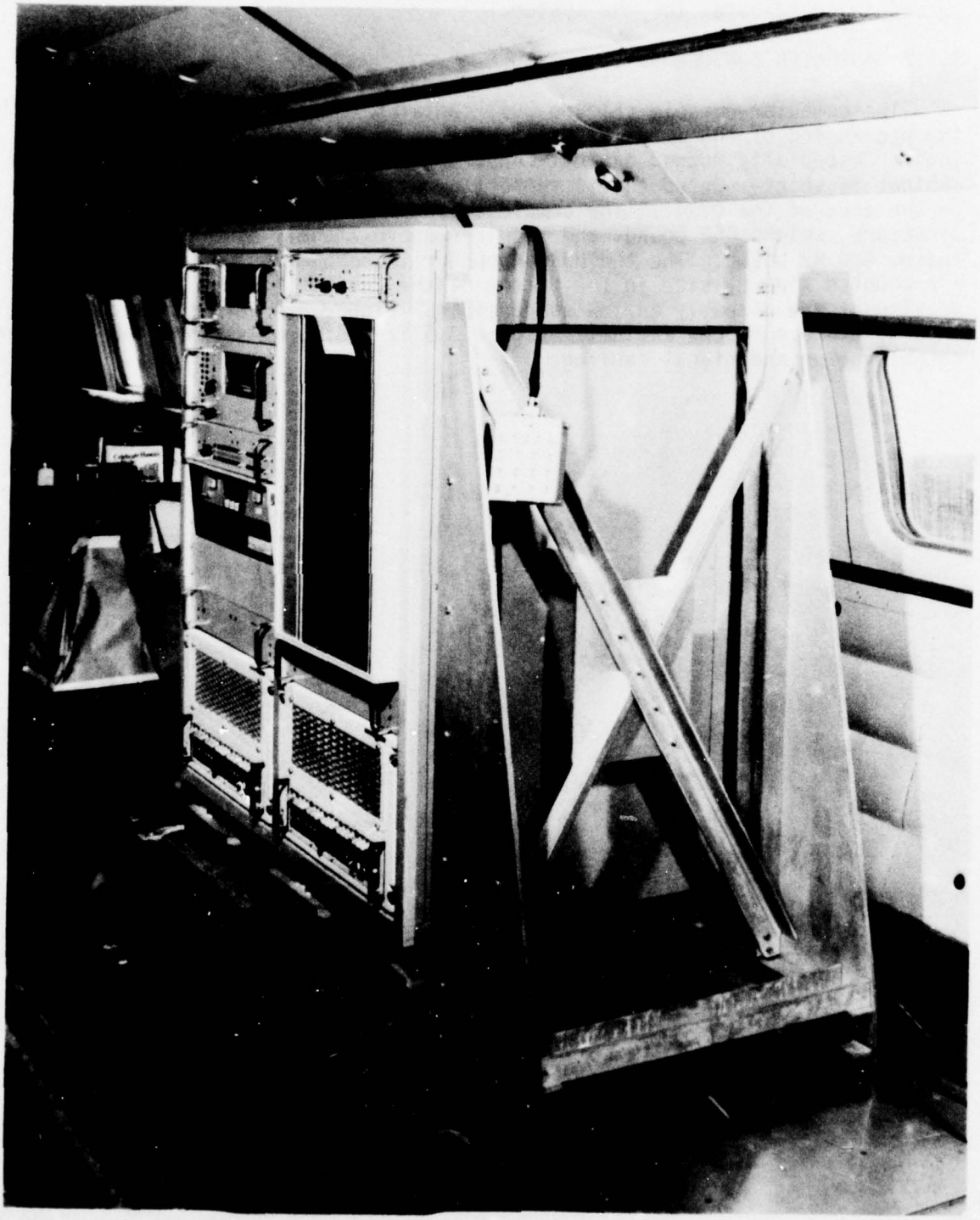


Figure 3.3 SIRU Computer Console

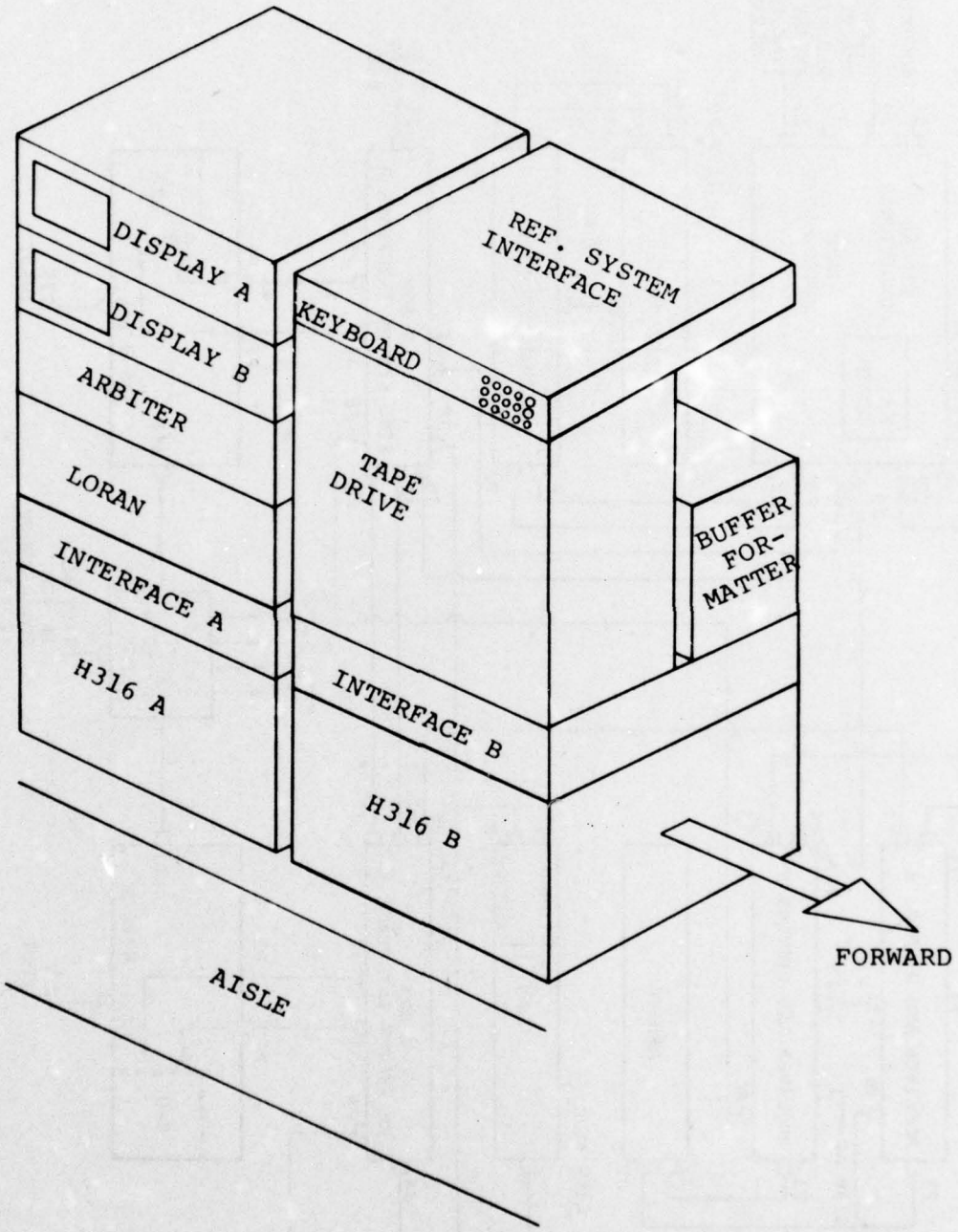


Fig 3.4 Computer Control Console

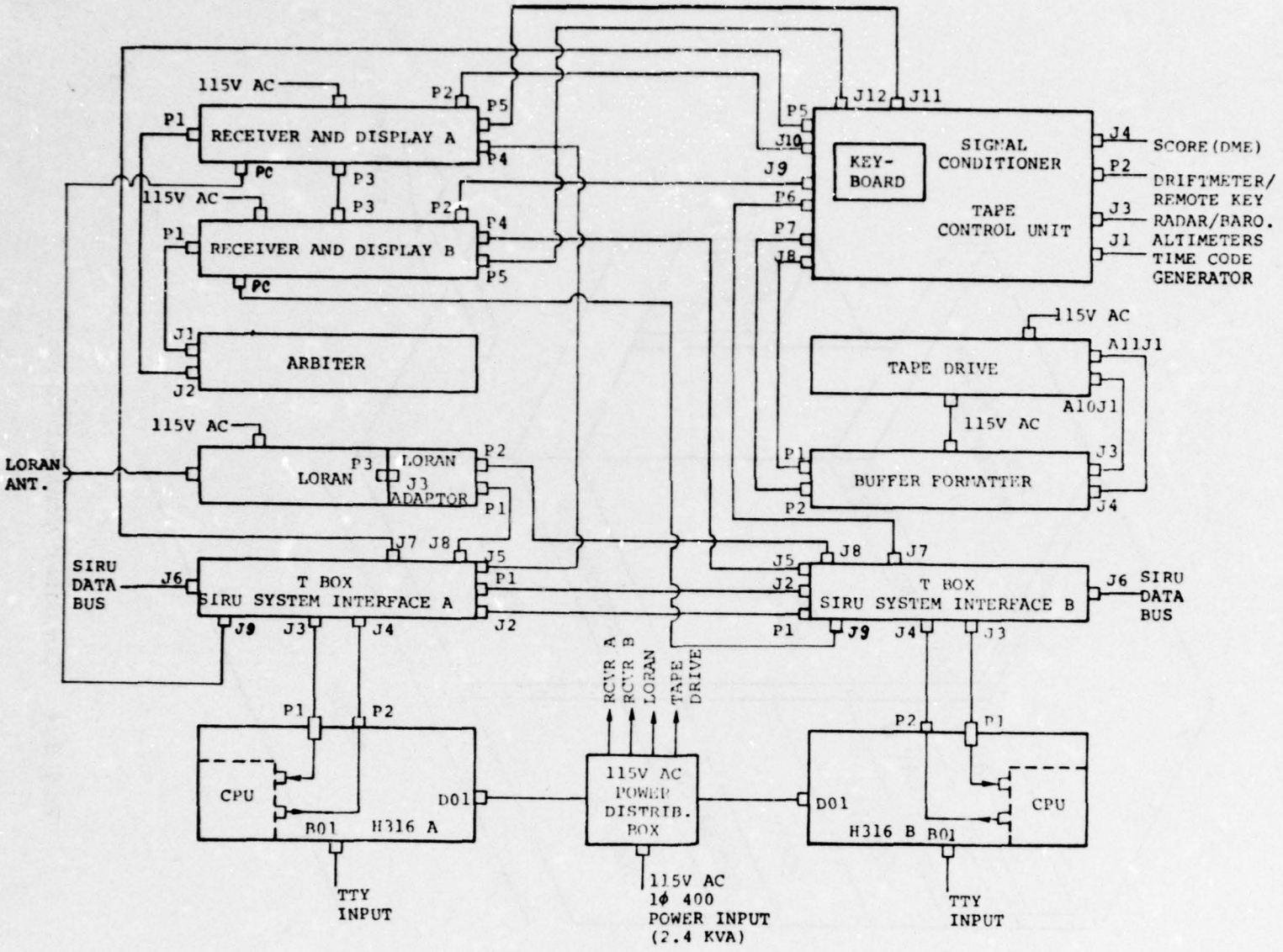


Figure 3.5 Computer Console Cabling

4.0 SOFTWARE DESCRIPTION

Basic SIRU: The basic sofware flow developed to operate the redundant instrument assemblage is shown in Figure 4.1 and has been described in detail in previous papers. Briefly, the raw instrument data is received and compensation applied for the static and dynamic instrument-loop errors. The corrected incremental body motion and velocity information is then processed by the failure isolation equations and, if no failure is detected, it is then processed by the appropriate least-square matrix which outputs the reference-triad solution. If a failure is detected and isolated, the failure state is entered into the adaptive matrix generator which reorganizes the matrix processor. Failure detection and isolation of up to two out of six of both instrument types can be effected without significant errors and a third failure of either instrument type is detected. Isolation of third failures for many types of faults is also effected (e.g. if the third fault degradation is larger than a prior identified failure). The matrix processor therefore uses no known bad data and the outputted triad body incremental maneuver solution is then processed to yield the inertial attitude and velocity solution.

A quaternion form,3rd order attitude algorithm has been implemented in the software.

4.1 Failure Detection and Isolation (FDIA): Two types of FDIA algorithms have been implemented in the software. One technique, referred to as the Total Squared Error Algorithm (Fig. 4.2) operates on the compensated instrument data to estimate the difference ($\hat{E}_A$) between what one instrument axis actually reads (A) and what that measurement is estimated to be ($\hat{A}$) on the basis of the other instrument axis measurements. The dodecahedron array shown in the figure yields a symmetrical conical array that allows simple scalar comparisons of data to achieve this solution. A fault is known to exist (detected) when the sum of the squares of all the individual errors (TSE) exceeds a preselected threshold. The fault is isolated (localized to a specific measurement axis) by effecting a fault isolation ratio test (R). The thresholds used for TSE and R are primarily based upon the quantization level of the raw data and the system environment noise.

The second type of FDI used in based on a statistical technique using sequential, probability ratio, testing. The statistical technique operates at a lower iteration rate than the TSE algorithm. It uses the output of a set of 15 "parity" (scalar) equations (Figure 4.3) that equal zero if no fault exists. It tests these outputs against a statistically normal model, using a specified confidence, to ascertain if a performance degradation exists and to classify the type of degradation observed (e.g. a constant bias shift, a ramping bias). For stable performance changes, the algorithm estimates the performance change and recompensates the measurement axis data. The algorithm self-tests the recompensation estimate and when it certifies that a correct compensation coefficient has been implemented, the adaptive matrix is modified to put this data axis back on line.

The redundancy management structure using the TSE algorithm is summarized in Figure 4.4. The statistical FDI algorithm has been integrated into this structure to implement the recalibration loop and its more sensitive

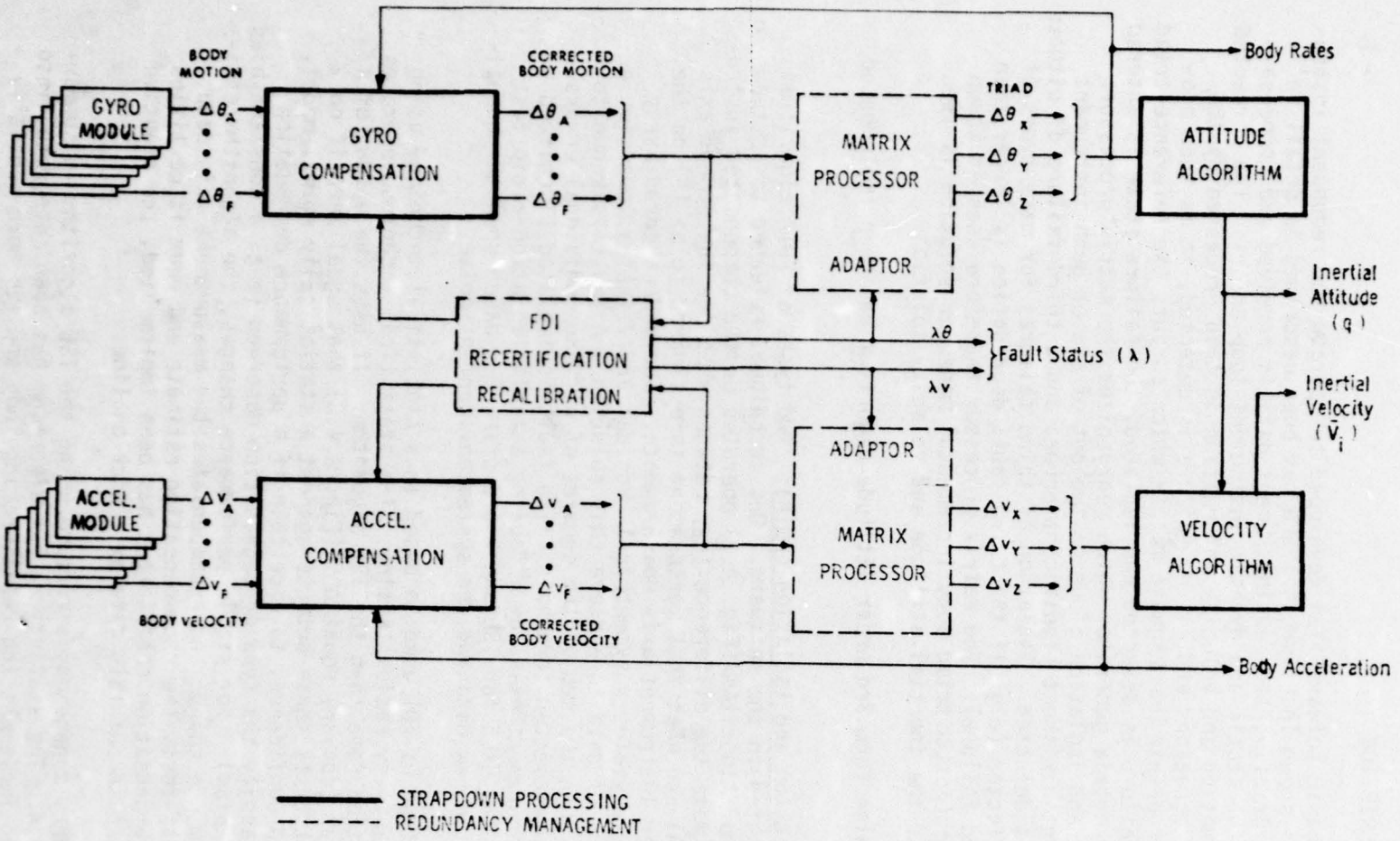
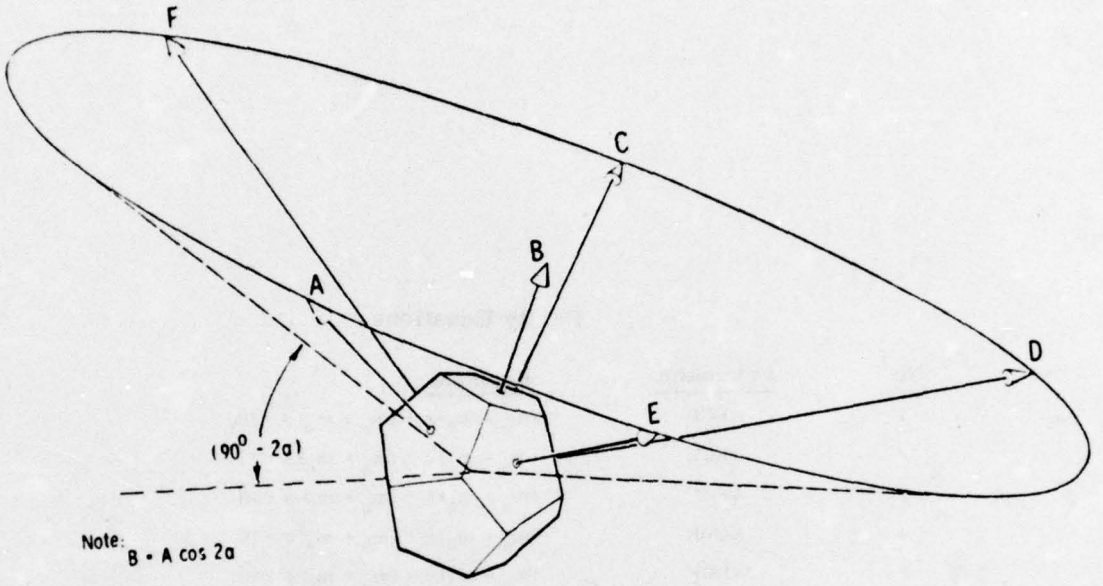


Figure 4.1 Basic Software Flow Diagram



Basic TSE - Fault Detection and Isolation

CONICAL REPRESENTATION OF DODECAHEDRON

- Individual Meas. Axis Error Estimates
  ($\hat{E}j$) difference between actual meas. and what other meas. say actual should be.
  (Body-Frame- Data Accumulation)

- Fault Detection (TSE)
  Total Square Error exceeds an acceptable threshold sum of each estimated error squared $(\hat{E}j)^2$

- Fault Isolation- R
  Ratio of individual $(\hat{E}j)^2$ to the TSE exceeds preselected level- (δ)
  R_0 > 1st Fail
  R_1 > 2nd Fail

Figure 4.2

Parity Equations

No.	Instruments	Equations
1	ABCD	$(m_a - m_b)c + (m_c + m_d)s = \|\epsilon\|$
2	ABCE	$(m_b - m_c)c - (m_a + m_e)s = \|\epsilon\|$
3	ABCF	$-(m_a + m_c)c + (m_b + m_f)s = \|\epsilon\|$
4	ABDE	$-(m_a + m_d)c + (m_b + m_e)s = \|\epsilon\|$
5	ABDF	$(m_b - m_d)c - (m_a + m_f)s = \|\epsilon\|$
6	ABEF	$(m_e + m_f)c - (m_a + m_b)s = \|\epsilon\|$
7	ACDE	$(m_d - m_e)c + (m_a - m_c)s = \|\epsilon\|$
8	ACDF	$(m_c - m_f)c + (m_a - m_d)s = \|\epsilon\|$
9	ACEF	$(m_a - m_f)c + (m_c - m_e)s = \|\epsilon\|$
10	ADEF	$(m_a - m_e)c + (m_d - m_f)s = \|\epsilon\|$
11	BCDE	$(m_c + m_e)c - (m_b + m_d)s = \|\epsilon\|$
12	BCDF	$-(m_d + m_f)c + (m_b + m_c)s = \|\epsilon\|$
13	BCEF	$(m_b - m_e)c - (m_c + m_f)s = \|\epsilon\|$
14	BDEF	$(m_b - m_f)c - (m_d + m_e)s = \|\epsilon\|$
15	CDEF	$(m_c - m_d)c + (m_e - m_f)s = \|\epsilon\|$

Note: m_a = measurement of axis A accelerometer or gyro $s = \sin(\alpha)$
$c = \cos(\alpha)$ ϵ = Threshold Level

Fig. 4.3 SIRU Parity Equations

- ♦ ACCUMULATE "LATEST"DATA T* MINUTES DEEP
  - $\Delta\theta$ & ΔV registers accumulate T minutes of data, discard old data T/n min. segments
  - new increment prior to each algorithm iteration Δt
    (*T/n selected on basis of desired FDI resolution)
- ♦ FDI TEST PRIOR TO EACH ALGORITHM ITERATION
  - Accumulation - Max Resolution of "Soft" Fails
  - Test at Δt - Limits Max error propagation
- ♦ FIRST FAIL ISOLATE → 2nd FAIL SEARCH & CONTINUE 1st FAIL TEST
  - 2nd Fail Search does not use already faulted meas. axis; 1st Fail continues using all data
    - If 2nd Fail is original, 1st fail order changes - "Worst" Fail always 1st Fail
    - RECERTIFICATION for "Healed" Fails, transients (latch repitative transients)
- ♦ 2nd FAIL ISOLATED → 3rd FAIL SEARCH
  - 3rd Fail Alarm → Remember 2nd Fail - (reset its accumulator)
  - Do 2nd Fail TSE, if 3rd Fail > orig. 2nd Fail it will isolate as new 2nd fail
  - If can't isolate, continue alarm (accept. BITE for reorganization)
- ♦ MATRIX PROCESSOR REORGANIZED TO STOP PROCESSING "FAULT ISOLATED AXES" PRIOR TO Δt
  - "PASS NO KNOWN BAD DATA" transient free output - multiple "Hard and Soft" Fails
  - Minimum Geometric Performance Degradation as Fault Axes are Removed

Figure 4.4 Basic TSE - Redundancy Management Summary

detection and isolation capabilities.

An example of fault detection, isolation, compensation, and recertification (FDICR) is illustrated by figure 4.5. This data was taken while the CV340 was on the ground at Crow's Landing and the SIRU system was in alignment mode prior to going into the navigation mode. At about 850 seconds the system developed excessive error as indicated by the magnitude of the TSE plot. The FDICR algorithm detected this error, isolated the source to the E axis axis gyro (first fail isolate) which had developed excessive bias errors due to high component temperature caused by aircraft cabin temperatures in excess of the SIRU cooling system design limits. The E axis gyro data was taken off line and the system continued to operate with data from the other five instruments. No appreciable decrease in the TSE could be seen at this time because the F axis gyro was experiencing the same temperature problem. At about 1450 seconds, the second error source was isolated to the F axis gyro and its data was taken off line (2nd fail search and isolate). An appreciable reduction in TSE can be seen at this time. Meanwhile, a new bias compensation was being calculated for the E axis gyro. At about 3250 seconds, a steady state value of -7 meru had been determined (compensation) and the data from this instrument was put back into the system (recertification). Evidence that the new bias compensation was valid is demonstrated by no discernible change in the TSE plot. The F axis gyro data had also been going through a recompensation calculation and appears to be approaching a steady state value. However, the fine alignment program was terminated ($\simeq$ 3600 sec.) and the subsequent flight test was flown with only five instruments on line, since the recertification feature was not available in the navigation mode.

4.2 Self-Alignment: The self-alignment algorithm computationally initializes the system reference orientation in the preflight phase. The algorithm uses sensor data to establish a reference frame corresponding to the local vertical attitude and a North earth rotational axis. The system mechanical reference axes (body orientation) are then displayed with respect to the inertial coordinate reference frame. The self-alignment algorithm operates in two sequences. In the initial phase, coarse alignment, level orientation is established using the indicated accelerometer data, and the horizontal earth rate vector is roughly determined by computing the change in the gravity vector in an inertial coordinate frame. The coarse alignment mode for a azimuth range of $\pm 90^{0}$ achieves an accuracy of better than 1^{0} in about 5 minutes. The fine mode computationally implements conventional gyrocompassing concepts. In this mode, azimuth is precisely determined to better than 1 milliradian in about 15 minutes.

Several other software routines have been implemented in the SIRU flight configuration. They include: a flight line, single position, self-calibration sequence, a self-alignment algorithm, and a local vertical, navigation algorithm. These routines and their operational theory are briefly reviewed below.

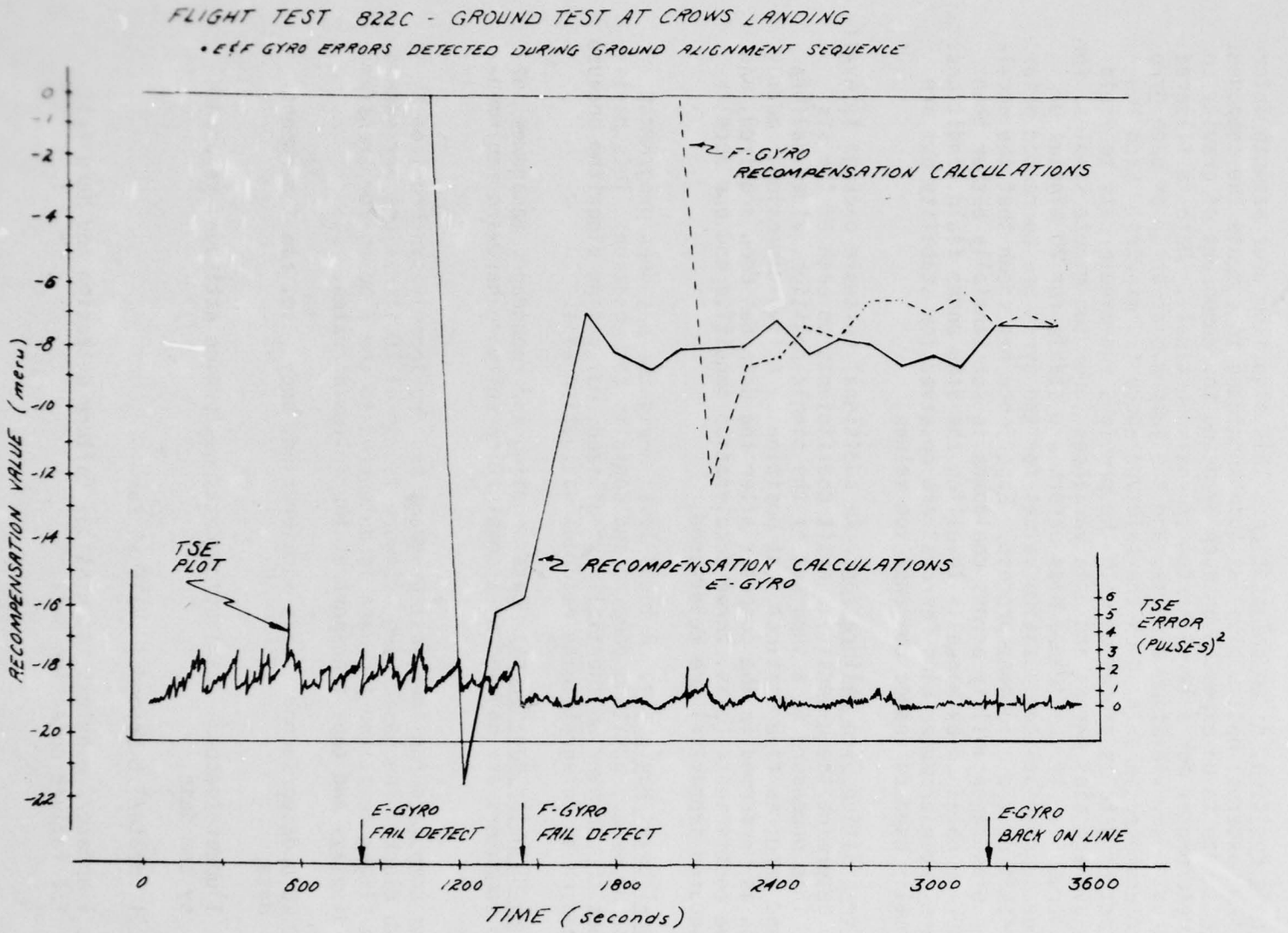

FLIGHT TEST 822C - GROUND TEST AT CROWS LANDING
• E & F GYRO ERRORS DETECTED DURING GROUND ALIGNMENT SEQUENCE
F-GYRO RECOMPENSATION CALCULATIONS
TSE PLOT
RECOMPENSATION CALCULATIONS E-GYRO
RECOMPENSATION VALUE (mew)
0
-2
-4
-6
-8
-10
-12
-14
-16
-18
-20
-22
TSE ERROR (PULSES)²
6
5
4
3
2
1
0
E-GYRO FAIL DETECT
F-GYRO FAIL DETECT
E-GYRO BACK ON LINE
0
600
1200
1800
2400
3000
3600
TIME (seconds)
SM-12/75

Figure 4.5

4.3 Single Position, Aided Calibration: This algorithm uses azimuth information from external optics plus latitude knowledge to compute the component of earth's rate to be expected on each gyro and the component of gravity on each accelerometer for a level system (Z_b-axis vertical). Data is filtered to attenuate any vibration effects, and the lumped bias error of each gyro and accelerometer is printed on the teletype every two minutes. Each two-minute set of data is processed with the previous two-minute sets to yield running average bias errors and data variances (over two-minute samples) for each instrument. If the lumped bias errors are stable for 20 minutes or more, the appropriate compensation values for the gyros are corrected prior to the start of the alignment process. Experience has shown that the accelerometer bias repeatability across cooldowns is substantially better than the accuracy obtained by manually levelling the SIRU under field conditions. Therefore, accelerometer bias "errors" are observed for stability but are not normally used to change compensation values.

4.4 Five-Position Gyro Calibration: An additional software package is available to determine the g-sensitive drift coefficients on each of the six gyros. This procedure is a superset of the single-position, aided calibration, and requires five distinct test positions. A five-dimensional matrix solution is performed in the computer after the data has been acquired, and the five coefficients (bias, three acceleration sensitive and one acceleration squared sensitive) are determined.

4.5 Local Level Navigator: A local level navigator has been programmed with the necessary attitude damping and Coriolis compensation. This navigator was chosen over an inertially stabilized, navigation algorithm because it is easier to integrate with external navigation aids.

4.6 Dual Computer Management: Data handling and redundancy management of the two computers are handled by a combination software-hardware implementation.

The computers run identical programs and are loosely synchronized by the SIRU clock. The basic SIRU software is run at 20 iterations per second for the flight test, and the data is outputted to the T boxes for transfer to the displays and tape transport at the following rates.

1. 20 updates/second: body acceleration, body rate, raw instrument data.

2. 1 update/second: navigation data, quaternion attitude, reference system data.

3. 1 update/3.8 seconds: BITE status.

4. 1 update/2 minutes: statistical failure detection and hard fail TSE failure detection data.

5. Keyboard inputs are rerouted for display and recording whenever keyboard inputs are received.

6. Contents of the electronic maximum/minimum value memory is available on command.

Each computer, in addition to the system data, outputs status information on its own health and an opinion of the other computer's health at a rate of 20 times per second. Self-opinion is based on internal CPU tests and memory check-sum tests. Cross opinion is based on a comparison with the other computer's output. The computer also performs a wraparound test on its output to the T box and is required to reset a flag in the T box within a specified time ("night watchman") or the T box will report the computer bad.

Failure checks on the computers and transmission electronics, totally implemented in hardware, are a parity check, an echo check, a wordwatch and a time test.

4.7 Ground Diagnostics: Digital representations of over 100 analog functions are delivered sequentially to the computer during system operation. The computer performs a check on each parameter to determine if the magnitude of the latest data falls outside of a range determined by the maximum and minimum values of all previous data. If this range is exceeded, the new value is stored in reserved memory. This stored data can be read out on command, normally during pre- or post-flight ground testing. As noted in the hardware discussion of the multiplexer, the capability exists to monitor and record any of these functions continuously for use in diagnosing problems.

5.0 HARDWARE AND SOFTWARE LIMITATIONS

5.1 PERSPECTIVE

Before discussing the limitations of the SIRU software and hardware with respect to flight testing in a Corvair 340 aircraft, it is necessary to be aware of the system's original purpose and design missions.

SIRU was originally designed as a redundant strapdown replacement for the Apollo spacecraft gimballed IMU. This meant that it had to meet the operational, electrical, mechanical, environmental, and mission interface requirements of the spacecraft. These requirements have significant ramifications when one wants to install and operate this system in a propellor driven conventional aircraft.

Operationally, the system was designed to operate for long periods of time without cooldown or powerdown. Preflight calibration was a one-time thing with adequate time in a quiet environment. This is not the case in an aircraft operational environment. The system had to be turned off at the end of each day. This required a preflight calibration before each flight test under sometime hurried conditions and not always in a quiet environment.

The dynamics of a spacecraft are considerably different that those of a conventional aircraft. In the case of the CV340, the dynamics were, for all practical purposes, unknown. This made the dynamic compensation of the inertial components difficult at best.

Mission time for the CV340 was typically one hour, whereas for the Apollo spacecraft it was measured in days. The gyro quantization level used was less than adequate for an aircraft, but represented no problem in the spacecraft mission.

Thermally, the system was designed to operate with a temperature controlled ethylene glycol coolant circulated through the Π frame and electronic assembly heat exchangers to a space radiator. In the CV340, it was necessary to use aircraft cabin ambient air as the cooling medium via a liquid to air to a liquid to solid heat exchanger on the Π frame, and a solid to air heat exchanger on the electronic assembly. This system was adequate for a $40^{\circ}F$ to $88^{\circ}F$ cabin air temperature range.

All of the above factors represented significant limitations which will be referenced in the following paragraphs.

5.2 HARDWARE

5.2.1 GYROS

The 18 IRIG Mod D was designed for continuous operation in a spacecraft environment. The orientation of the output axes were optimized for a space

mission and therefore not optimum for an aircraft environment. Because of the operational safety requirement to turn the system off when unattended, gyro parameter shifts were encountered across cooldown and powerdown which necessitated frequent calibrations. The quantization level of 44 arc seconds was adequate for long term space missions with periodic updates, but not for the short term high dynamic environment of the CV340. The rate limitation of 1 radian per second, again, is no problem in a spacecraft, but does represent a limitation in an aircraft. A two-hour warmup requirement is also no problem in the long countdown of a spacecraft but is definitely a limitation for an operational aircraft.

5.2.2 ACCELEROMETER

The 16 PM PIP accelerometer and its torque loop were originally designed for the Poseidon missile. Its performance was more than adequate in all respects in the aircraft environment.

5.2.3 SIRU MOUNTING FIXTURE

This fixture was designed to permit calibration of the IMU in tne aircraft. It provides positioning of the inertial package to four cardinal points (90° rotations) about the system Z axis and one 90° rotation to put the Z axis in the vertical or horizontal plane. This permits putting ±X, ±Y, and +Z axis down for multiple position calibration. Physical complexity did not permit a design which would have allowed a -Z axis down orientation. This missing sixth position would have improved the calibration accuracy.

A pair of wedge rings were provided to permit levelling the system prior to the aided single or multiple position test. It was quickly discovered that the aircraft was off level more than these rings could adjust for. It was therefore necessary to jack up the nose of the aircraft by about 3° to put the level within range of the wedge rings. This was not only time consuming but required the assistance of the aircraft crew chief and his assistants.

To determine the degree of level, a 10 second bubble was mounted on the fixture in a recessed well so that it could be rotated 360°. The mounting surface had been precision machined with respect to the system reference cube. With time and repeated operations, this soft aluminum surface became worn and the repeatability and uncertainty reached the point where the known repeatability of the accelerometer biases was felt to be better than the bubble uncertainty. Although the bubble continued to be used in levelling the system, accelerometer biases were not changed as a result of the aided calibration.

5.2.4 PALLET COOLING SYSTEM

As discussed in paragraph 5.1, this system was limited to a cabin air temperature of $+40^{o}F$ to $+88^{o}F$. Outside of this range, the inertial component temperature controllers would not control the gyro and accelerometer

temperatures resulting in parameter shifts which would be detected by the FDI software. On many occasions, the aircraft cabin ambient air temperature exceeded +88°F and went as high as +100°F. The aircraft air conditioning system in the early part of the flight test program was not functioning properly. Even after repair, when it was performing according to its specifications, it was not adequate when the aircraft was sitting on the ground in the sun where the outside air temperature was +100°F. One flight test was conducted at night to avoid this problem. Operation of the air conditioning required that the engines be running which restricted operation of the system for test and calibration purposes while sitting on the apron at Ames. No adequate ground cooling air supply was available. It is estimated that high cabin air temperature accounted for inertial component "soft" failures on approximately half of the flight tests. Paradoxically, this problem caused over cooling of some inertial components when the cabin temperature was in normal operating range of the SIRU system. It was discovered that the outlets of the aircraft air conditioning were exhausting cold air directly onto certain inertial components causing them to get too cold and thereby indicating a soft failure to the FDI. This problem was solved by redirecting the flow of the air.

5.2.5 REFERENCE SYSTEM

5.2.5.1 BARO-ALTIMETER

No provision was available to adjust this device for local barometric pressure. Therefore it would sometimes indicate a maximum altitude of 9372.6 ft, even though the aircraft actually flew below that altitude.

5.2.5.2 RADAR ALTIMETER

This device was limited to 5,000 ft. The majority of the navigation flights were flown above this altitude. Also since a radar altimeter gives height above the terrain, the height of the terrain must be known to correlate the altitude above sea level.

5.2.5.3 DME

Because of its design mechanization, its time generator had to be reset each time a way point was marked in order to provide good correlation with the waypoint. This required in turn that the DME reset be synchronized with the driftmeter mark to the computer. The driftmeter camera circuit was finally mechanized so that it reset the DME and provided a mark to the computer when the camera shutter was tripped. However, if the computer mark was initiated from the keyboard, no reset was provided for the DME. This was the case when the driftmeter camera computer mark malfunctioned at times and had to be backed up by the keyboard.

5.2.5.4 DRIFTMETER

A driftmeter was incorporated into the flight test system to permit generating a mark to the computer when the aircraft passed over a waypoint. Mounted to the eyepiece of the driftmeter was a single lens reflex 35 mm camera to record the position of the waypoint with respect to the driftmeter reticule. The flash synch switch of the camera was wired to provide a mark to the computer when the shutter was tripped. The operator would look through the eyepiece of the camera when alerted by the pilot and take a picture when the waypoint passed through the center of his reticule. The driftmeter gyro failed after the first few flights. No replacement was available so that the line-of-sight was no longer vertically stabilized resulting in errors when the aircraft was not level. The camera synch connector proved to be unreliable resulting in the loss of an accurate computer mark during early flights. This problem was cured by hardwiring the synch cable into the camera. The circuitry to provide a mark to the computer and reset the DME time simultaneously did not function properly initially due to unknown excessive camera contact bounce. This was solved by incorporating "anti-bounce" circuitry.

5.2.5.5 RADAR BEACON

A radar beacon was installed in the CV340 to permit more accurate and more continuous tracking by the Crow's Landing NASA radar facility. An attenuator had to be inserted into the antenna system when flying close to Crow's Landing and removed when flying at a distance. This required close coordination with the radar operators and was another possible problem in flight operations.

5.3 SOFTWARE

5.3.1 BASE MOTION ISOLATION

Post flight analyses indicates that the base motion isolation mechanization did not perform as well as expected and was the cause of excessive errors in estimates of north and level about east during fine alignment. See paragraph 8.2.1 for further details.

5.3.2 INTERVAL INTEGRATION

Using computed body velocity at the end of each one-second navigation update to approximate the average velocity over the update causes acceleration induced position errors. Paragraph 8.2.2 discusses this error in detail.

5.3.3 FDI

5.3.3.1 STATISTICAL FDI

The statistical FDI threshold limits were specified to be 1.5 times the standard deviation of the gyro error derived from the laboratory test environment. Flight test experience showed that the gyro errors were greatly increased as compared to the laboratory dynamic test data. The original

were .06°/HR for static condition and a maximum dynamic increase of .12°/HR to give a maximum threshold of 0.18°/HR. These were changed to .48°/HR static and .96°/HR maximum dynamic increase to give a maximum threshold of 1.54°/HR. These increases were derived more intuitively than analytically and proved to be inadequate as evidenced by the large number of "false" failures. The software was then modified to remove the statistical FDI in the navigation mode and therefore in the flight mode (after SFT 717). FDI was then totally dependent upon TSE which had thresholds of 1.14°/HR MASE and 1.48°/HR maximum dynamic increase to give a maximum threshold of 2.62°/HR. Later analysis (see paragraph 8.3.3) shows that the statistical limits should be .75°/HR static with a maximum dynamic increase of 1.75°/HR to give a maximum threshold of 2.50°/HR. These limits should permit utilization of the statistical FDI during the navigation of flight mode.

5.3.3.2 TSE

The TSE failure detection thresholds were initially determined on the basis of laboratory tests. No information on aircraft dynamics was available. As discussed in 8.3.1, this threshold is both mission and environment sensitive. The initial gyro TSE MASE (Maximum Allowable Squared Error) was .76°/HR with a maximum dynamic increase of .81°/HR resulting in a maximum threshold of 1.57°/HR. After the experience of several flight tests which indicated that gyro "failures" were being indicated as a result of aircraft turn maneuvers, these limits were raised to 1.14°/HR for TSE MASE and 1.98°/HR for TSE maximum dynamic increase giving a maximum threshold of 3.12°/HR. The accelerometers initially were set at .14 cm/sec^2 for first fail MASE and .13 cm/sec^2 for second fail MASE. These were changed to .28 and .26 cm/sec^2 respectively. No further failures during aircraft maneuvers occurred after the above limits were incorporated. The limits were determined by studying flight test data (TSEs) during aircraft maneuvers.

6.0 FLIGHT TESTS

6.1 ARC-CV340 FLIGHT TEST EVALUATION FOR SIRU

The purpose of this flight test program was to provide NASA-ARC with an independent evaluation of the CSDL SIRU as a fault-tolerant instrument package and navigation system for short haul aircraft. The SIRU navigation system was installed in the CV-340 CTOL aircraft for flight testing to begin at ARC in May 1975. Data from SIRU and from various navaids (6 DME channels, drift meter, radar and barometric altimeters) was recorded in flight on magnetic tape to enable the evaluation. In addition, magnetic tape recordings of the data from the two Nike radars at Crow's Landing was available when the aircraft was in the radar range.

The evaluation included an assessment of:

a. SIRU's performance as a reliable free-inertial navigation system for aircraft, as evidenced by the flight tests navigational accuracy

b. SIRU's potential (and limitations) as a reliable redundant inertial reference unit for an aircraft control system (autopilot), and

c. The potential performance of an aided-inertial navigation system based on SIRU.

The flight test evaluation was divided into three major computational tasks. These are:

1. Post-flight analysis and evaluation of system position measurement accuracy.

2. On-site support and data processing for SIRU flight tests (planning).

3. Analysis of the flight test data and diagnostic recorded data to evaluate SIRU's redundancy management performance and radio aided potential for accuracy update.

6.2 EVALUATION PROCEDURES

1. Process external (radar, DME) measurement data to obtain precision position and velocity information as a reference for evaluating SIRU's recorded navigation data

2. Simulate SIRU's in-flight software system on a computer to enable post-flight navigation in the laboratory, using flight-recorded sensor data. The simulation shall include capabilities for data compensation and for failure detection and isolation.

3. Analyze the nature of SIRU's output signals as to their appropriateness as input signals to an aircraft control system.

4. Evaluate the flight test data for aided-inertial navigation performance having SIRU as the basic reference unit. This includes a provision for combining recorded external measurement data with recorded SIRU sensor data to effect an aided-inertial navigation estimate.

Analytical Mechanics Associates provided technical support to ARC to carry out this evaluation program.

6.3 ANALYSIS AND EVALUATION

The ARC-CSDL flight test analysis program:

a. Analyzed and evaluated SIRU's performance as a free-inertial navigation system as shown by the flight tests. Performance criteria established which were compatible with both the CV-340's and V/STOL flight characteristics and SIRU's design characteristics. SIRU's navigational accuracy was assessed for a variety of flight patterns and ranges and for both failure-free and simulated-failure operation;

b. Investigated and evaluated the SIRU concept mechanization as the reference unit for an aircraft control system sensing using actual flight test data in the investigation. Transients at failure, quantization and noise in signals investigated to assess their effects in autopilot use. Gyro and accelerometer specifications (i.e., full-scale measurements, quantization levels, ect.) will be determined for a V/STOL aircraft's-autopilot use;

c. Evaluated SIRU's potential as the reference unit of an aided-inertial aircraft navigation system. Data weights and processing procedures will be determined to optimize both the navigation accuracy and the dependability of the aided system.

6.4 AIRCRAFT FLIGHT PROCEDURES FOR ISRU EVALUATION

The test program progressed from ground checkout of the self-calibration and self-alignment program through flight tests under varying environmental conditions and flight profiles.

Two types of flight paths were flown in this program. One to evaluate navigation performance and the other to evaluate system performance in a STOL environment. An example of a navigation run is shown in figure 6.4.1. This flight was four hours in duration. Other navigation runs were typically one to four hours in duration.

There were over 30 VOR-DME, VORTAC, TACAN stations located in the flight test area that were available to the six channel DME of the reference system.

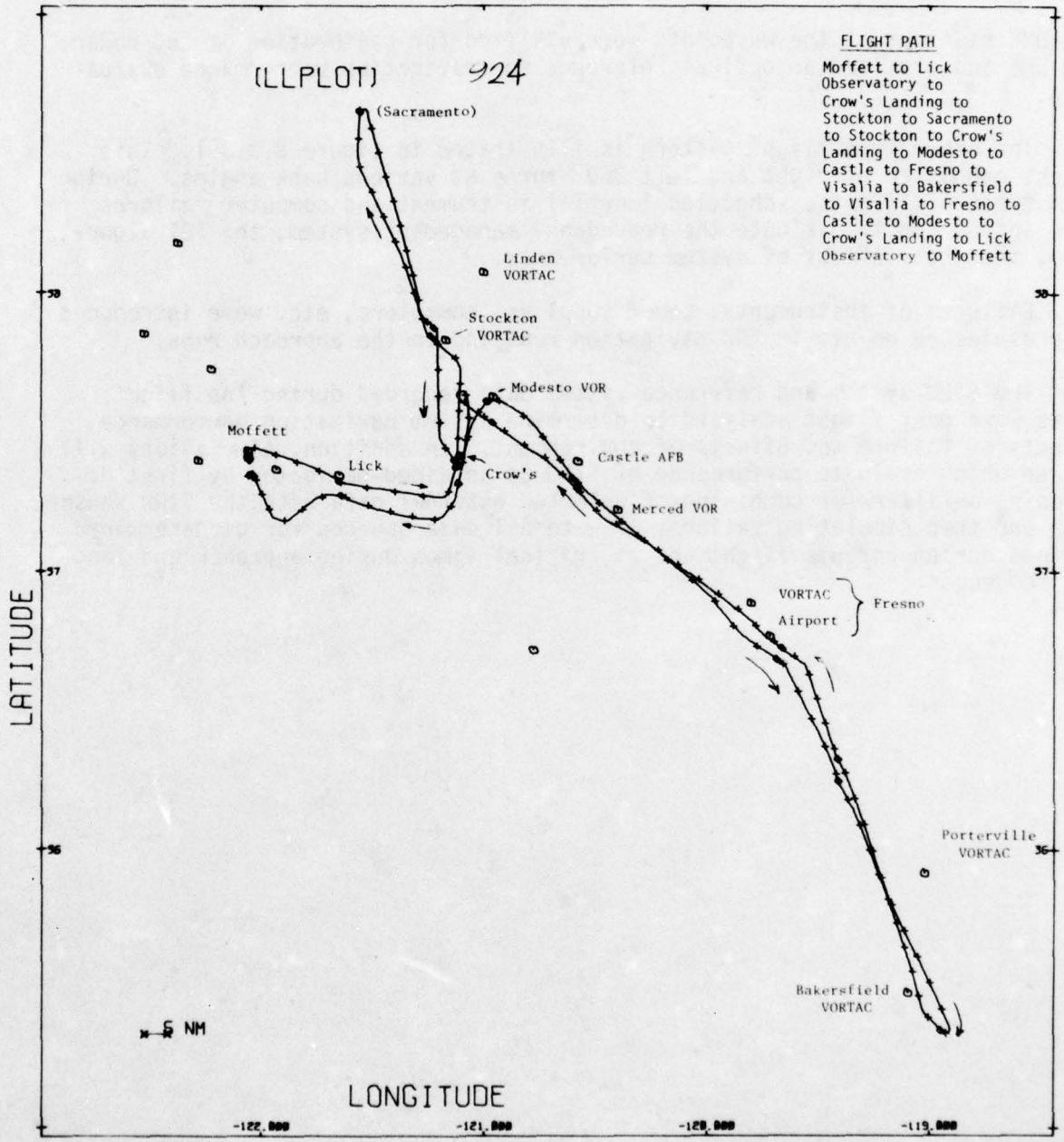

(LLPLOT) 924
FLIGHT PATH
Moffett to Lick Observatory to Crow's Landing to Stockton to Sacramento to Stockton to Crow's Landing to Modesto to Castle to Fresno to Visalia to Bakersfield to Visalia to Fresno to Castle to Modesto to Crow's Landing to Lick Observatory to Moffett
(Sacramento)
Linden VORTAC
Stockton VORTAC
Modesto VOR
Moffett
Lick
Crow's
Castle AFB
Merced VOR
VORTAC
Airport
Fresno
Porterville VORTAC
Bakersfield VORTAC
5 NM
LATITUDE
LONGITUDE
-122.000
-121.000
-120.000
-119.000

Figure 6.4.1

The DME stations at the waypoints were utilized for calibration of the radar, and DME and provided an optical reference for navigation performance evaluation.

The other type flight pattern is illustrated in figure 8.3.3.1. This flight consisted of right and left 360° turns at various bank angles. During both types of flights, scheduled inertial instrument and computer failures were introduced to evaluate the redundancy management system, the FDI algorithm, and their effect of system performance.

Failures of instruments, power supplies, computers, etc. were introduced at preselected points in the navigation runs and in the approach runs.

The SIRU system and reference system data recorded during the flight tests were post flight analyzed to determine system navigation performance, effects of failure and effects of environment. In addition, simulations will be run which evaluate performance of SIRU as an aided-navigator by first developing a filter for combining of selected external data with the SIRU sensor data and then simulating failures of external data sources for predetermined periods during enroute flight and at critical times during approach and landing sequences.

7.0 OPERATIONAL RESTRAINTS AND DIFFICULTIES

7.1 POWER

Because of aircraft and hangar safety requirements and the lack of personnel to continously monitor the system, system power had to be turned off each night. This meant that there were, on the average, a minimum of five cooldown and powerdowns a week resulting in the requirement for frequent calibrations. (Reference 5.1, System Cooldown and Powerdown Sensitivity.)

During the major portion of the flight test program, when moving the aircraft from the hangar to the apron, it was necessary to disconnect ground power in the hangar and reconnect it out on the apron or energize the aircraft APU on the apron. The aircraft APU could not be operated in the hangar because of safety requirements. This meant that if an aided calibration were run in the hangar the morning of a flight test, it was necessary to shut down. This introduced the possibility of errors in the calibration parameters determined in the hangar. The problem was circumvented, towards the end of the program, by connecting long ground power cables to the aircraft. This allowed the aircraft to be connected to ground power until it cleared the hangar, at which time the aircraft APU could be used. Because of its limited capability (15 minutes), the SIRU battery was not used during this transition.

Numerous power outages were experienced in the hangar and on the apron. In the hangar, power was furnished by 28VDC rectifiers operating from 208V 3Ø 60Hz power. Frequently, these units failed, were unable to sustain the load, or did not regulate properly. Problems were encountered with faulty power cables, faulty power junction boxes and improperly fused hangar power outlets. Considering the main purpose for being in the hangar was to run preflight calibration, power interruptions meant either delay in commencing the calibration or requiring a repeat of the test after allowing time for the IMU to thermally restabilize. A multiple position calibration required five hours. To lose power at the end of the fourth hour meant the loss of a calibration, a day's work, and the possible delay of a flight test.

On the apron, ground power was provided by mobile gasoline powered APU's. Difficulties with these units included running out of gasoline, failure during operation, inability to sustain load, and inability to regulate voltage. Again, these units were being used to provide power during tests and calibrations. Outages usually were costly in terms of time and schedule. In addition to the powerdown and cooldown problems of the IMU, the computer would usually dump across powerdowns and require reloading and restarting the programs. Even without dumping, one cannot restart a navigation program in the middle of a run.

7.2 ENVIRONMENTAL

The apron or taxiway at Ames was the normal parking place for the CV340 because of restricted availability of hangar space. Frequently, it was too windy to permit IMU calibrations. When the wind was not present, there was always the possibility of disturbance by prop wash or jet blast from taxiing

aircraft. Ambient temperature problems were consistently encountered. Aircraft air conditioning depended upon the engines running, which was not practical most of the time. There were no adequate auxiliary sources of cooling air available. Thus, on a sunny day, only very limited time for system operating was possible due to the high cabin air temperature (the SIRU temperature in the test configuration was 88°F). This often resulted in moving into the hangar after working hours and conducting tests late into the night. Even this operation was restricted at times by the nonavailability of aircraft maintenance personnel required to meet safety standards. The net effect of these restrictions, considering the available manpower, was to hamper problem solving and detract from operational readiness for flight testing.

7.3 PREFLIGHT CALIBRATION

In addition to the power and environmental difficulties, several other additional operational problems were encountered that degraded preflight calibration. When environmental conditions were suitable on the apron for preflight calibrations, the proper parking space was not always available. Aided calibration required that the aircraft be near a position and azimuth reference. There were two locations on the apron that met these requirements. However, the CV340 was occasionally pre-empted by a larger or higher priority aircraft, or another aircraft would be parked so that it blocked the line-of-sight to the azimuth references. In the hangar, there were limited areas where the CV340 was in view of the azimuth references. Other aircraft were usually parked in the preferred area or parked so that they blocked the line-of-sight to the azimuth references. To compound the situation, it was difficult to physically position the aircraft in the hangar within view of the azimuth reference. The final problem was keeping people off of the aircarft during calibration. In spite of warning signs, ropes across the aircraft ladder, etc., some curious or careless individual would manage to come aboard or disturb the aircraft during a "quiet" calibration run.

7.4 FLIGHT TEST SCHEDULING

7.4.1 General

Many factors determined the time scheduling of flight tests. Among these were frequency or number of tests required in given time period, pilot availability, aircraft availability, Crow's Landing availability, availability of radar coverage and weather. Because of the limited time allotted to the total flight test program, anything that delayed a flight test or caused it to be moved ahead usually meant a compression of the scheduled time between flights.

7.4.2 Flight Frequency

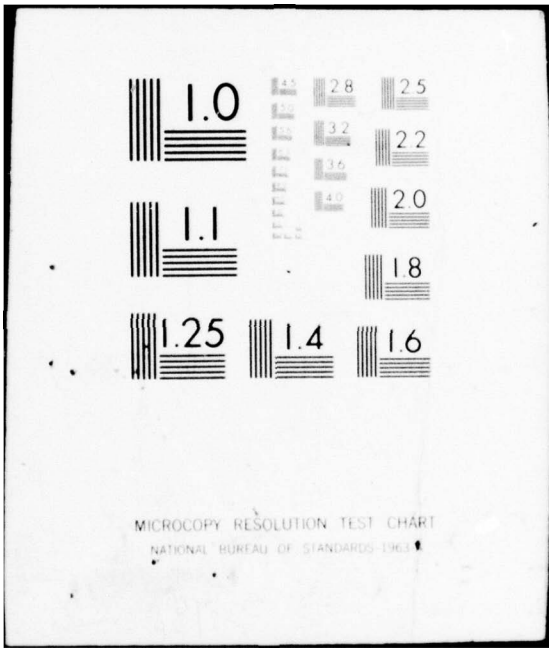
During the periods that the aircraft was available, the average time between flights was 3 1/2 working days. During this time period, post-flight analysis, trouble shooting, preflight calibration, flight plan generation,

AD-A040 012 ARMAMENT DEVELOPMENT AND TEST CENTER EGLIN AFB FLA F/G 17/7
PROCEEDINGS OF THE BIENNIAL GUIDANCE TEST SYMPOSIUM (8TH) HELD --ETC(U)
MAY 77

UNCLASSIFIED ADTC-TR-77-3-VOL-1 NL

5 OF 8
AD
A040012




1.0
1.1
1.25
1.4
1.6
2.8
2.5
3.2
2.2
3.6
2.0
4.0
1.8
MICROCOPY RESOLUTION TEST CHART
NATIONAL BUREAU OF STANDARDS-1963

any repair work, equipment modification, and software modifications all had to be accomplished. With the limited time availability, it was impossible to effect adequate post-flight analysis between flights. This resulted in conducting flight tests with unknown system or procedural problems which should have been identified and resolved before conducting further tests.

For most flight tests, due primarily to the time lost in mailing of the tapes from Ames to CSDL, even the first cut at data reduction and review at CSDL from one flight could not occur until after the succeeding flight had been conducted. Often a second test would have been flown before a more detailed analysis of the data could be completed. An increased analysis capability at Ames could have reduced the turn around-time and alleviated this problem somewhat.

To illustrate, flights 530 through 618, a total of three flights and 5 flight tests, were conducted over approximately a two week period. A significant gyro compensation load error was entered in the flight tape on flight test 530 and was not identified until after test 618. Thus, as a result of the tight schedule combined with the flight operations learning curve problem at the beginning of the program, five flight tests were essentially invalid due to a bad compensation load.

The initial flight test plan called for two weeks between flights. This would have allowed for more time for data analyses at ARC, AMA, and CSDL and provided more meaningful planning for subsequent tests. It would have permitted time to phase in corrections and software modifications based upon the test data analysis. For example, CSDL evolved a "quick-calibration" technique to replace the existing single-position calibration. The technique estimated north axis drift by least squares fitting and derived from this the lumped X and Y body axis drifts which could then be corrected more rapidly and accurately. Had more time been available during the flight test program, this calibration procedure could have been phased in. However, insufficient time was available to permit its verification in the field. The procedure more closely corresponded to an "operational usage" concept.

7.5 FLIGHT TEST OPERATIONS

7.5.1 Tape Recording Time

Flight test data acquisition objectives were to both demonstrate real-time performance and to permit AMES postflight test reconstruction and simulation. Thus, not only performance data, but all raw sensor data was recorded. As a result the flight test data magnetic tape recorder operated at maximum rate, limited to 40 minutes with a 2400 ft. reel and 50 minutes with a 3600 ft. reel. This limitation caused some flight tests to be cut short so that the plane could land, rewind the tape and reinitialize the flight program. To run out of tape in flight would cause loss of continuity in recorded data and make data reduction difficult. Slowing the data rate to extend tape time was preferable to running out, but prohibited the use of the Ames/AMA post-flight reconstruction programs.

8.0 TEST RESULTS

8.1 INTRODUCTION

The test results presented in this section do not represent the total test results from the SIRU Flight Test Program. They are the results of analysis performed at the Charles Stark Draper Laboratory but do not include the extensive analysis performed by the NASA Ames Research Center in conjunction with Analytic Mechanics Associates, Inc. Their analyses include an evaluation of navigation performance which compares the inertial navigation data with the reference system data (radar, DME, optical sightings) and an evaluation of the potential of the SIRU system concepts for aided navigation, integrated avionics, aided redundancy management, redundant flight control, etc. The CSDL analysis is limited to an evaluation of software/dynamic error sources and a selective assessment of the FDI implementation.

8.2 SOFTWARE/DYNAMIC ERROR SOURCES

8.2.1 Fine Alignment Errors due to Angular Motion

Navigation accuracy is limited by the accuracy of the computational coordinate frame alignment relative to the physical coordinate frame at the instant that navigation mode begins. The SIRU fine alignment algorithm (variable gain gyrocompassing) was performance-verified in the laboratory under static conditions and also in the presence of small oscillations about the vertical system axis. Alignment performance in the presence of angular motion about horizontal axes (causing accelerometer outputs to vary) was not investigated prior to flight testing.

The extent of fine alignment error is impossible to determine from recorded flight test data because - a) raw data (for reconstruction purposes) was not recorded during alignments, and b) algorithm command signals were not recorded. At times, the quaternion was observed (as well as recorded) during alignment. Because the quaternion tracks base motion while responding to commanded rotation signals, it alone cannot be used as a measure of alignment performance.

The fine-alignment algorithm generates commanded rotation rates about Down, East, and South to bring the quaternion into proper alignment and hold it there. Earth rate compensation is included in the commanded rates. Base motion isolation is implemented with the usual gyro information. A simple block diagram is shown in Figure 8.2.1.1.

A single special test was designed to observe alignment performance in the aircraft. The operating program was modified to record the commanded rotation rates, which are shown in Figures 8.2.1.2 through 8.2.1.6.

East and South commanded rates control the level loops, with each loop having two first-order time constants of 10 and 21 seconds to attentuate environmental noise. These commands converge to zero and the south component of Earth rate, respectively, after the initial large commands. The Down

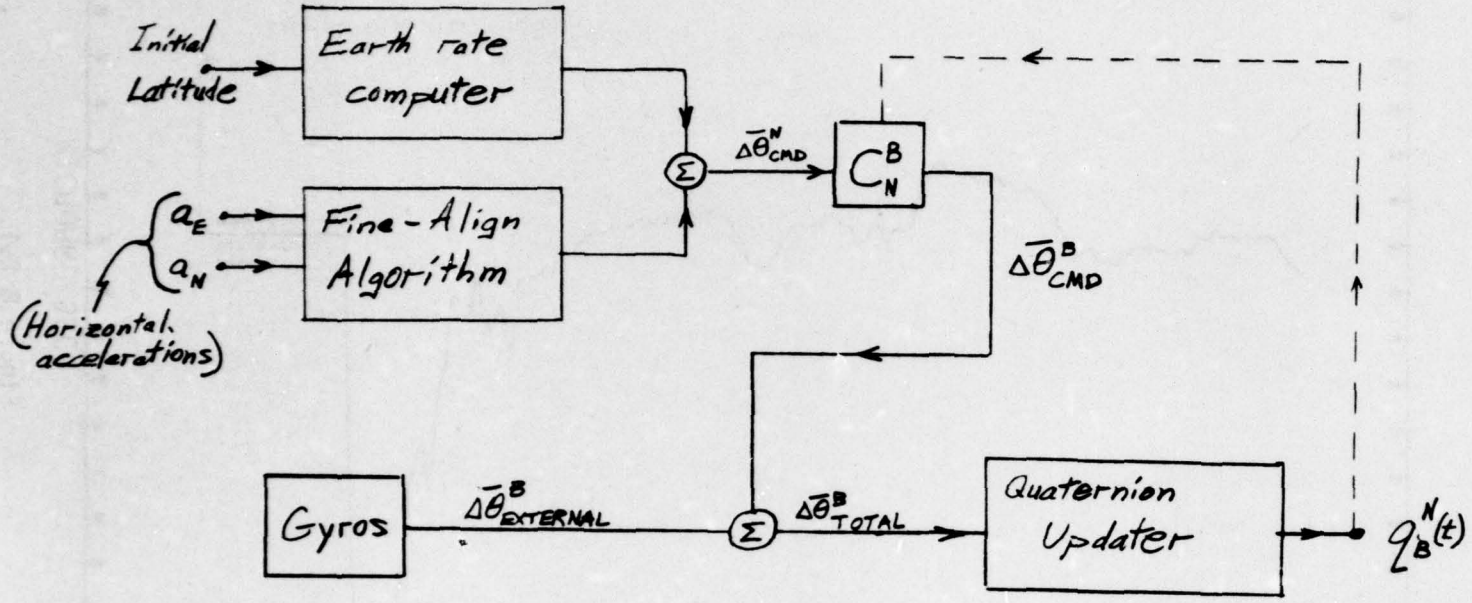


Figure 8.2.1.1 Fine Alignment Block Diagram

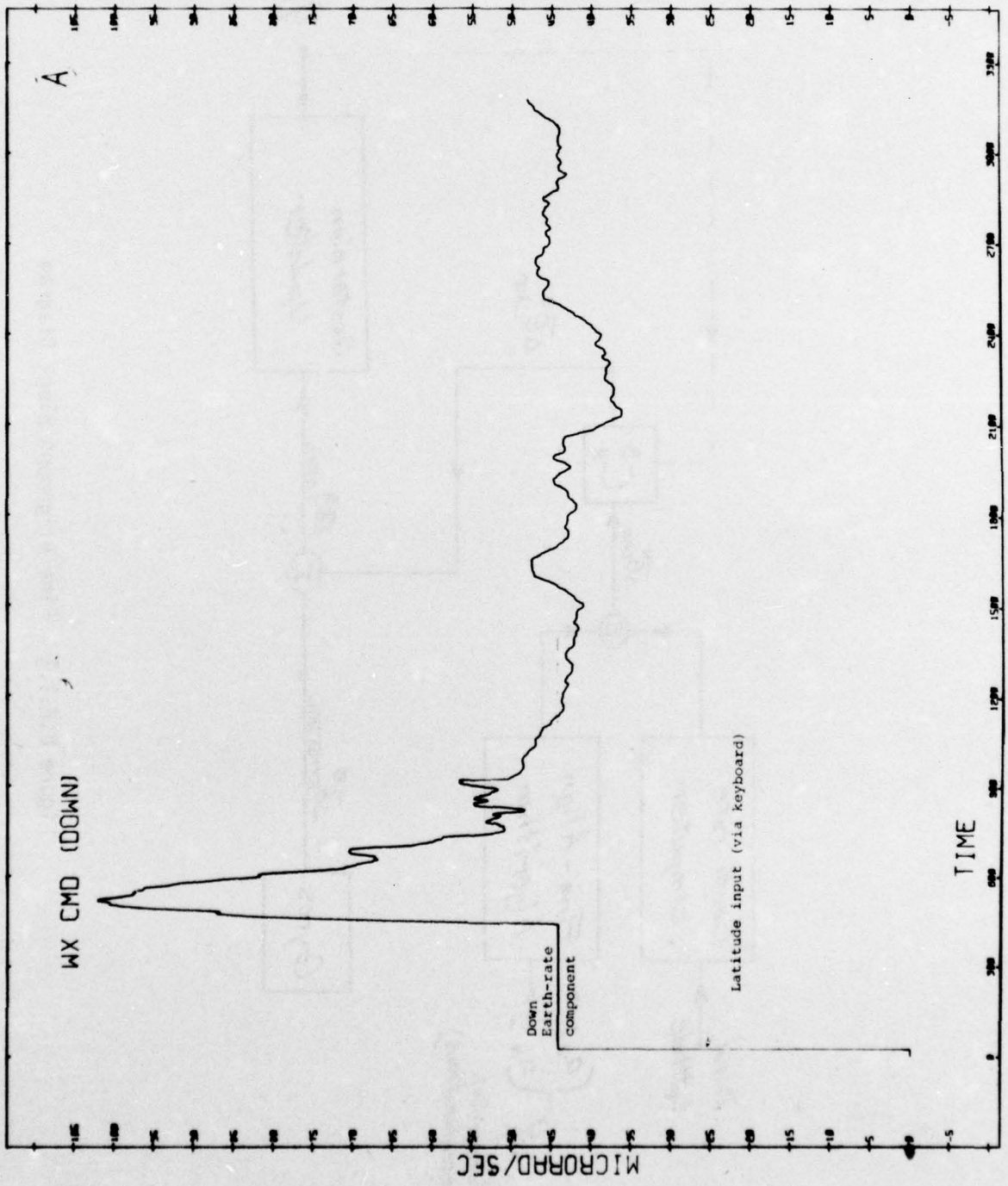

A
WX CMD (DOWN)
Down
Earth-rate
component
Latitude input (via keyboard)
TIME
MICRORAD/SEC

Figure 8.2.1.2

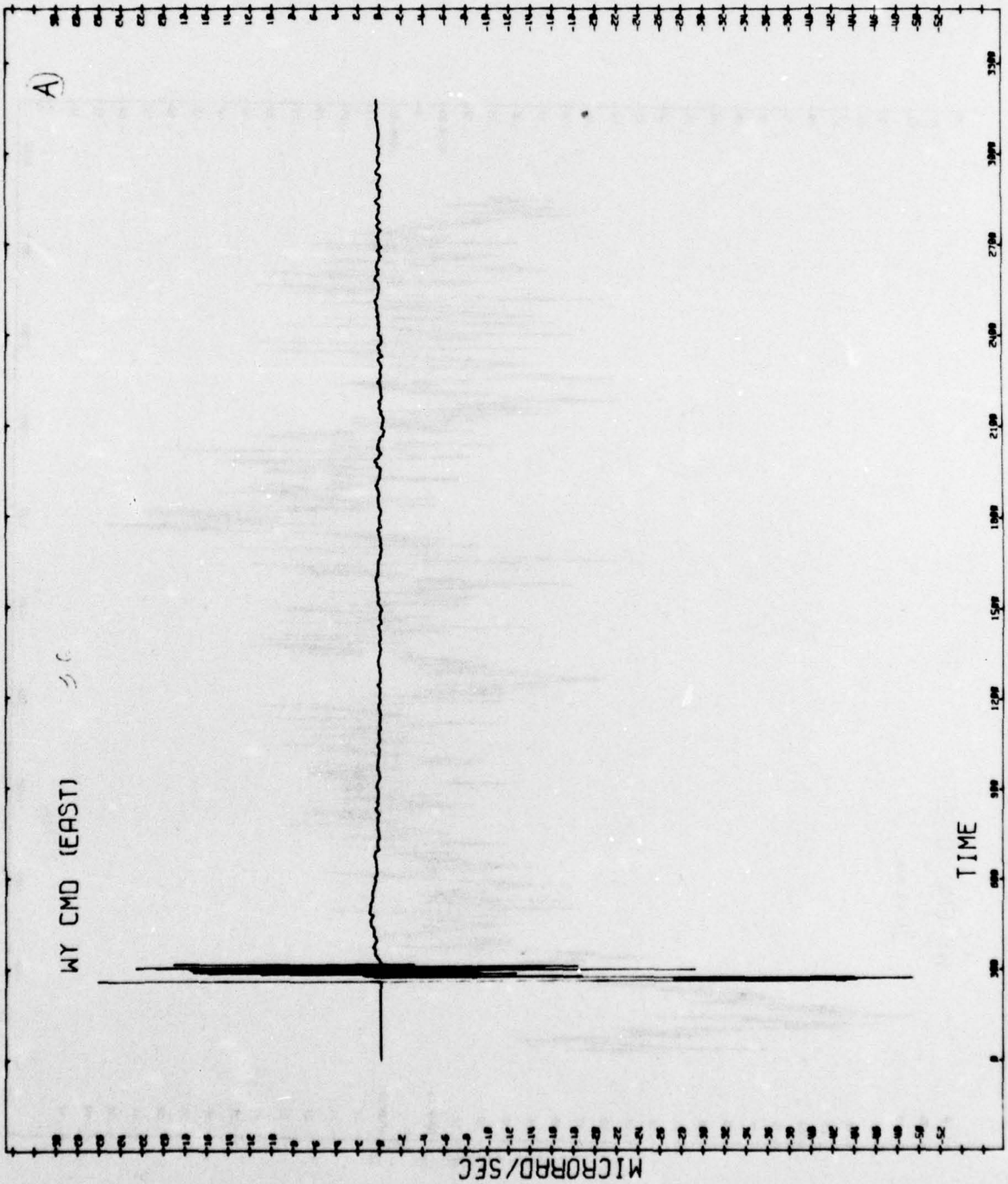


Figure 8.2.1.3

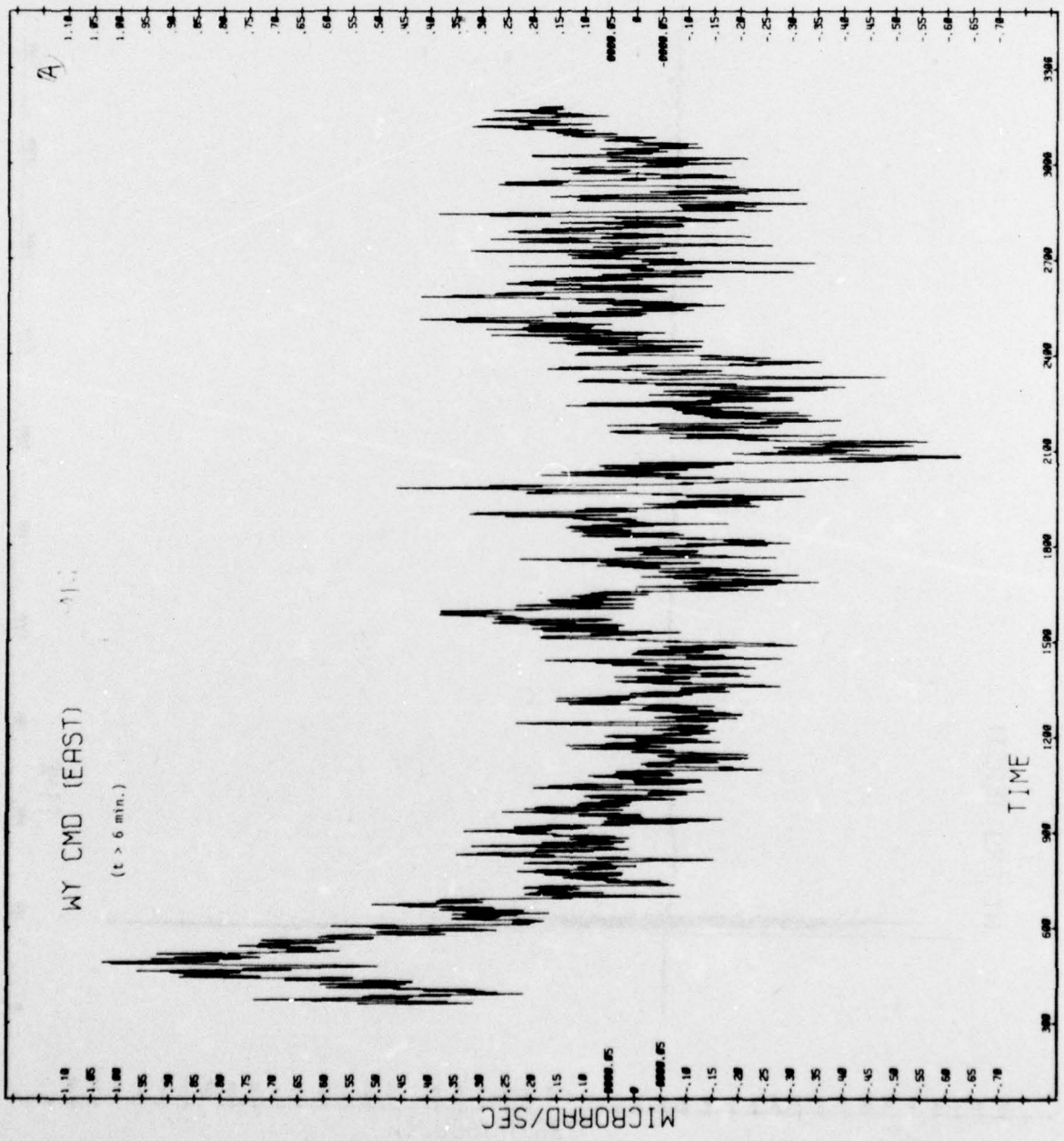


Figure 8.2.1.4

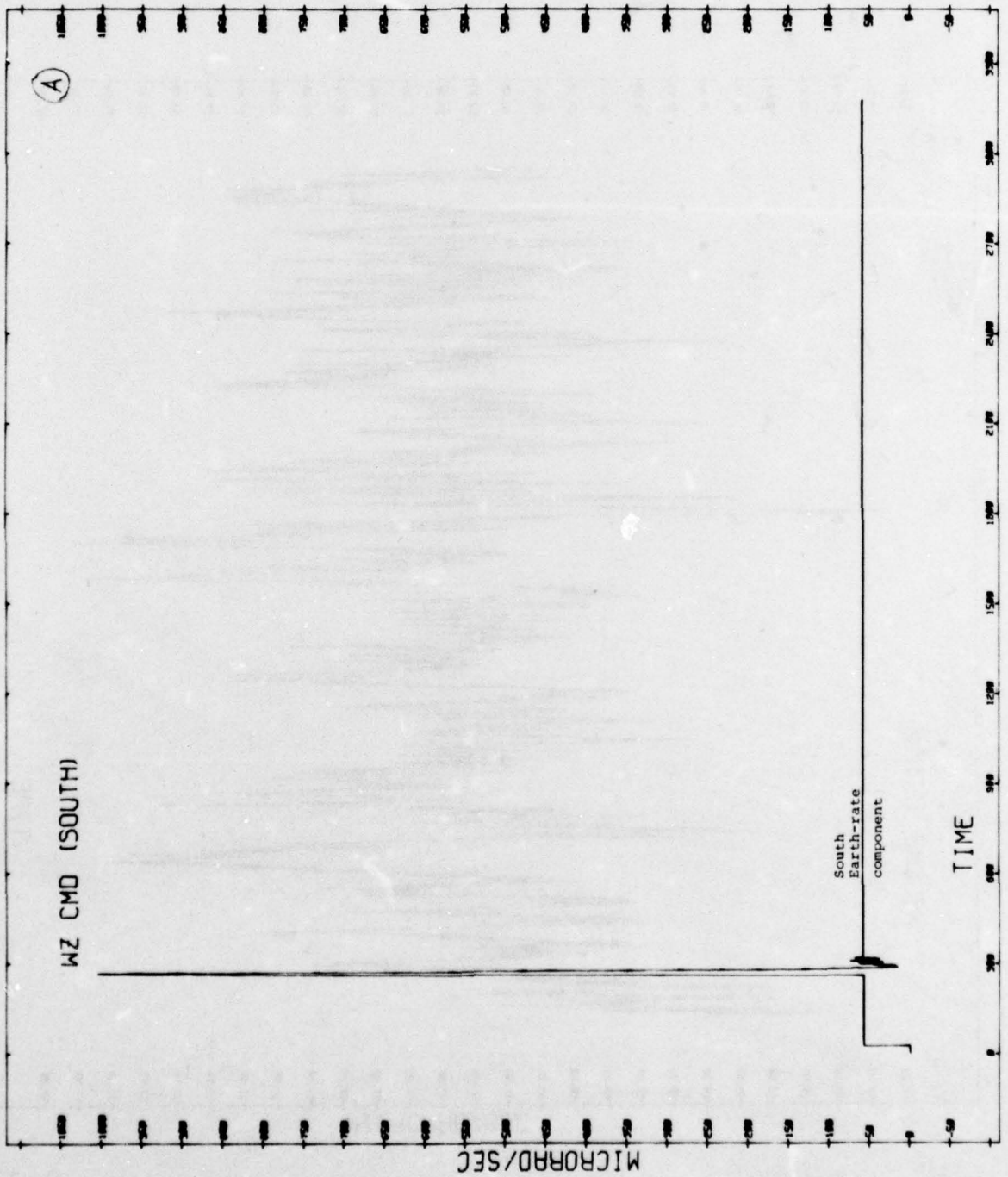


Figure 8.2.1.5

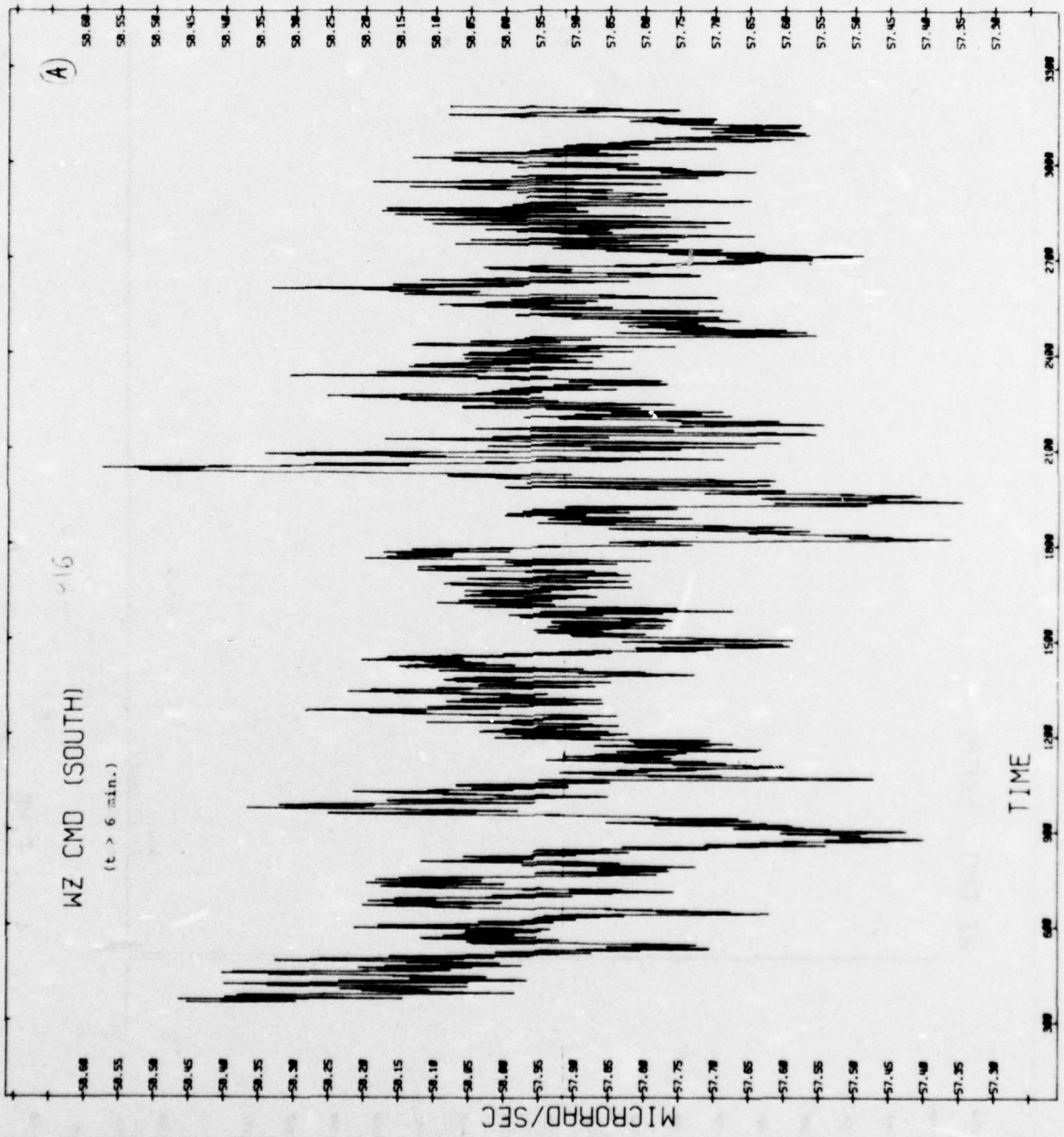


Figure 8.2.1.6

commanded rate is not so convergent on the Down component of Earth rate as it should be. The negative excursion at t = 2100 seconds was found to have caused a 3 mrad. change in the algorithms estimate of true North and 70 μrad. change in the level estimate about East. These control loops should be in steady-state for t > 1500 seconds.

This evidence, together with FDI data showing that all gyros and accelerometers were on-line and reasonably stable throughout the test, indicates that base-motion isolation was not performing well enough. Base motion did not exceed .5 deg. about any axis during this special test, yet the alignment was undesirably distrubed. One reason is that the slightly miscompensated accelerometer data is "second-guessing" the gyro data when g-sensitive attitude changes occur. For instance, a small step attitude change about the aircraft's pitch axis is immediately sensed (somewhat imperfectly) by the gyros and the quaternion is updated accordingly. The accelerometer data is now accumulated in this slightly different orientation. Unless the average East and South velocities continue to hover around zero (as they ideally would) the alignment algorithm will begin generating an attitude correction signal. This will drive the system toward a new steady-state "level-definition" while forcing transient errors in the "North-definition".

Alignment data of the types described in this section were not available for any of the other recorded tests. The magnitude of navigation errors resulting from alignment algorithm problems is, therefore, unknown. Extrapolation of navigation accuracy from this single special test is unwise because compensation values and environmental conditions varied among flight tests.

8.2.2 Velocity Algorithm Errors - interval integration

A small amount of bounded position error is present in all navigation test data due to using the computed body velocity at the end of each one-second navigation update to approximate the average velocity over that update. By itself, this algorithmic defect causes acceleration-induced position errors only; vehicle velocity is correctly updated over each interval. Therefore, position error propagation in the absence of significant vehicle acceleration is negligible (for position errors of 100 to 300 feet).

In a simplified form, the navigation algorithm which was used is:

$$\bar{V}^N(nT) = \bar{V}^N((n-1)T) + \Delta\bar{V}^N(nT)$$

$$\bar{S}^N(nT) = \bar{S}^N((n-1)T) + \bar{V}^N(nT)\cdot T$$

where $\bar{V}^N$ and $\bar{S}^N$ are velocity and position vectors in the pseudo-inertial N-frame (local-level coordinates corrected for earth-rotation). The navigation algorithm update period, T, is one second in this case. It will also be noted at this point that most of this algorithmic error can be eliminated by making a first-order correction to the position update:

$$\bar{S}^N(nT) = \bar{S}^N((n-1)T) + \left[\bar{V}^N((n-1)T) + \frac{\Delta\bar{V}^N(nT)}{2}\right] \cdot T$$

For the case of straight-line vehicle acceleration up to a cruise velocity, V, with uniform acceleration over each T-second interval, the position error is:

$$\bar{\varepsilon}(nT) \equiv \hat{\bar{S}}(nT) - \bar{S}(nT) = 1/2\ \bar{V}(nT) \cdot T$$

Straight-line acceleration in the CV340 up to V = 200 knots produces an indicated position ($\hat{\bar{S}}$) 170 feet ahead of actual position. Deceleration (straight-line) to $\bar{V}$ = 0 causes this position error to return uniformly to zero.

Vehicle acceleration of constant magnitude perpendicular to its velocity vector produces circular motion. When perpendicular acceleration is removed, straight-line motion resumes with an acceleration-caused position offset. This position error is conveniently expressed in local-level vehicle coordinates with $\bar{i}_z$ down and with $\bar{i}_x$ and $\bar{i}_y$ defined, respectively, by the projections of the vehicle's nose and right wing into the level plane. It is assumed that navigation updates occur fast enough (every T seconds), compared to the maximum sustained angular velocity about $\bar{i}_z(\omega)$, that sin (ωT) can be approximated as (ωT). For the simple case of a constant rate turn starting as t = 0, the resulting position error is approximately:

$$\varepsilon(t) \equiv \varepsilon(\omega t) = \bar{i}_x \left[c_x \sin(\omega t) + c_y(1 - \cos(\omega t))\right] + \bar{i}_y \left[c_y \sin(\omega t) + c_x(\cos(\omega t) - 1)\right]$$

where $c_x = V\omega T^2/2$

$c_y = VT/2$

For a typical 3°/sec CV340 turn (ω = .05, V = 200 ft/sec) we have

c_x = 7.5 feet

c_y = 150 feet

The position error vector for various amounts of turn is then:

$$\bar{\varepsilon}(45^\circ) = \bar{i}_x \cdot 49.2' + \bar{i}_y \cdot 108.3'$$

$$\bar{\varepsilon}(90^\circ) = \bar{i}_x \cdot 157.5' + \bar{i}_y \cdot 142.5'$$

$$\bar{\varepsilon}(180^\circ) = \bar{i}_x \cdot 300' + \bar{i}_y \cdot (-15')$$

$$\bar{\varepsilon}(360^\circ) = \bar{i}_x \cdot 0 + \bar{i}_y \cdot 0$$

It is seen that this error approaches its maximum value for turns in the vicinity of 180° and returns to zero magnitude for complete circles.

8.2.3 Dynamic Gyro Errors

Gyro scale factor and misalignment compensation values cannot be readily determined when the strapdown system is mounted in the aircraft. This presents fundamental problems when installing a replacement gyro, for instance. Laboratory compensation data must be transferred to the operating environment with an uncertain level of confidence.

Errors from these terms (particularly misalignments) show up most noticeably when the aircraft makes large changes in heading. Navigation accuracy may be impaired by the typically large (180°) turns which occur on the taxiway prior to takeoff and in the air shortly afterwards.

The parity equation residuals (from the deterministic failure detection subroutine) have proven to be of some help in gauging the magnitude of these dynamic gyro errors. In one specific case, a badly miscompensated gyro was greatly improved by observing squared gyro-error magnitudes and adjusting a particular misalignment value to substantially decrease this error magnitude over a 180° turn. Specifically, it was found that abnormally high total squared errors (TSE) were present during large turns of flight tests in June and the first half of July, 1975. Turns of 180° produced TSE's of from 70 to 90 pulses squared (44 $\widetilde{\text{sec}}$ per pulse) which corresponds to an acquired system attitude error in the vicinity of 400 $\widetilde{\text{sec}}$ or about 600 ppm. Ground experiments led to a 250 μrad correction to the C gyro (nominally horizontal input axis) misalignment term in the direction of the nominal vertical axis. Subsequent flight tests (July 24 to termination) had uniformly lower TSE's of from 20 to 30 pulses squared for 180° turns. This corresponds to an acquired system attitude error or about 200 $\widetilde{\text{sec}}$, or 300 ppm. The improvement is approximately what would be expected from the change in misalignment compensation which was made.

Further trial and error improvement to dynamic compensation terms was not attempted. The redundant nature of SIRU should permit a self-correcting misalignment calibrator to be implemented which would yield much smaller attitude errors during typical flight test maneuvers.

A simple example will show the effect of misalignment errors on navigation accuracy. An aircraft with a perfectly initialized alignment of the SIRU system makes a 180° turn on the runway prior to takeoff. Assume all 6 gyros are perfectly compensated except one nominally horizontal gyro (C-gyro) which is misaligned toward the vertical by a small amount, δ radians. The 180° turn has zero component along the C-axis, but a total rotation ($\delta \cdot 180^{\circ}$) is erroneously registered. This translates into a body-axis computational misalignment of ($180^{\circ} \cdot \delta/2$), which can be viewed as an initial level error. This starts a position error propagating with an 84 minute (Schuler) period and with an angular magnitude (relative to Earth's center) equal to the magnitude of the system's level-error. The position error magnitude, in nautical miles, is approximately:

$$|\bar{\varepsilon}(t)| = \frac{60 \text{ n. mi.}}{\text{deg.}} \; (180^{o} \; \delta/2) \left[1 - \cos\left(\frac{2\pi t}{84 \text{ min.}}\right)\right]$$

Peak position error magnitude (at t = 42 min) is

$$|\varepsilon_{peak}| = \frac{60 \text{ n. mi.}}{\text{deg.}} \; (180^{o} \cdot \delta)$$

A misalignment error of δ = 250 μrad in this example would then yield a peak position error 2.7 nautical miles.

8.2.4 Vibration Spectrum Data Presentation

Inertial instrument data has been analyzed for vibration content as an aid to investigating potential error sources. Gyro data has been spectral-analyzed for angular vibration content while accelerometer data has been analyzed for linear vibration content. Raw data from individual instruments has been examined, but more meaningful information can be obtained from the compensated body-axis angular rate and accelerations. These are discussed here. It is recalled that the X, Y, and Z strapdown system axes are in close alignment with the aircraft's roll, pitch, and yaw axes, respectively.

Two typical regimes were analyzed from data recorded on the flight test of September 18, 1975 (tape SF918B from test in vicinity of Crow's Landing). The first was a preflight period in which the aircraft was on the ground, static, but with both engines operating. The second section analyzed was a level flight segment in which aircraft heading was relatively constant. Data was recorded at full rate (20 inertial updates per second) during this flight test, so that the maximum frequency which may be reconstructed is 10 Hz.

Angular vibration data for the static section is shown in Figures 8.2.4.1 through 8.2.4.6, which present the input data and its power spectral density magnitude for each axis. Structural vibration resonances are evident for each axis. Motion about the aircraft's roll axis has a sharp resonance at 7 1/2 Hz, while motion about the pitch axis has a dominant resonance of similar magnitude just above 1 Hz. Aircraft oscillations about the vertical are also dominant at just over 1 Hz.

Linear vibration data for the static section is shown in Figures 8.2.4.7 through 8.2.4.12. If the x-y body plane is approximately level (as in the SIRU flight tests), then small angular vibrations about the X-axis will cause linear acceleration vibrations along the Y-axis. A sinusoidal oscillation of amplitude b yields:

$$\theta_x(t) = \theta_{xo} + b \sin(\omega t)$$

$$\dot{\theta}_x(t) \equiv \omega_x(t) = b\omega \cos(\omega t)$$

The deviation in acceleration along the Y-axis is:

$$\delta a_y(t) = -g \cdot \sin(b \sin(\omega t)) \cdot \cos(\theta_{x0})$$
$$\simeq -g \cdot b \sin(\omega t)$$

and the velocity deviation:

$$\delta V_y(t) = \int_0^t \delta a_y(\tau)\, d\tau$$
$$= \frac{gb}{\omega} \cos(\omega t)$$

The body acceleration data (actually delta-velocity data) from SIRU tests is integrated to obtain velocity before doing spectral analysis. The ratio of the velocity deviation to the applied angular velocity (in the example above is:

$$\frac{\delta v_y(t)}{\omega_x(t)} = \frac{g}{\omega^2}$$

With this background, the ΔVX and ΔVY data are seen to have many of the same natural frequencies as the corresponding angular data.

A static aircrafts's vibratory characteristics are of primary importance with respect to alignment algorithm performance and primary interest is with the angular (gyro) data.

In-flight vibratory data (from level cruise) differs from ground data primarily in having much larger amplitudes at much lower frequencies (<1 Hz). Angular data is presented in Figures 8.2.4.13 through 8.2.4.18. All three axes have angular excursions with typical periods of from 2 to 10 seconds. High frequency engine vibrations do not lie within the detection bandwidth of the sampling rate. Linear vibration data (Figures 8.2.4.19 through 8.2.4.24) has very low frequency velocity excursions, as would be expected in flight.

The data presented here is a spectral analysis of the inertial system's output. There are two limitations to using pulse-rebalanced instruments for this purpose - low bandwidth (due to low sampling rate) and low-amplitude distortion (due to pulse quantization). A comprehensive analysis of vibratory effects on a strapdown system would require better knowledge of the real spectral content (input to the strapdown system). Analog instruments and a continuous tape recorder could be used to obtain vibratory data for

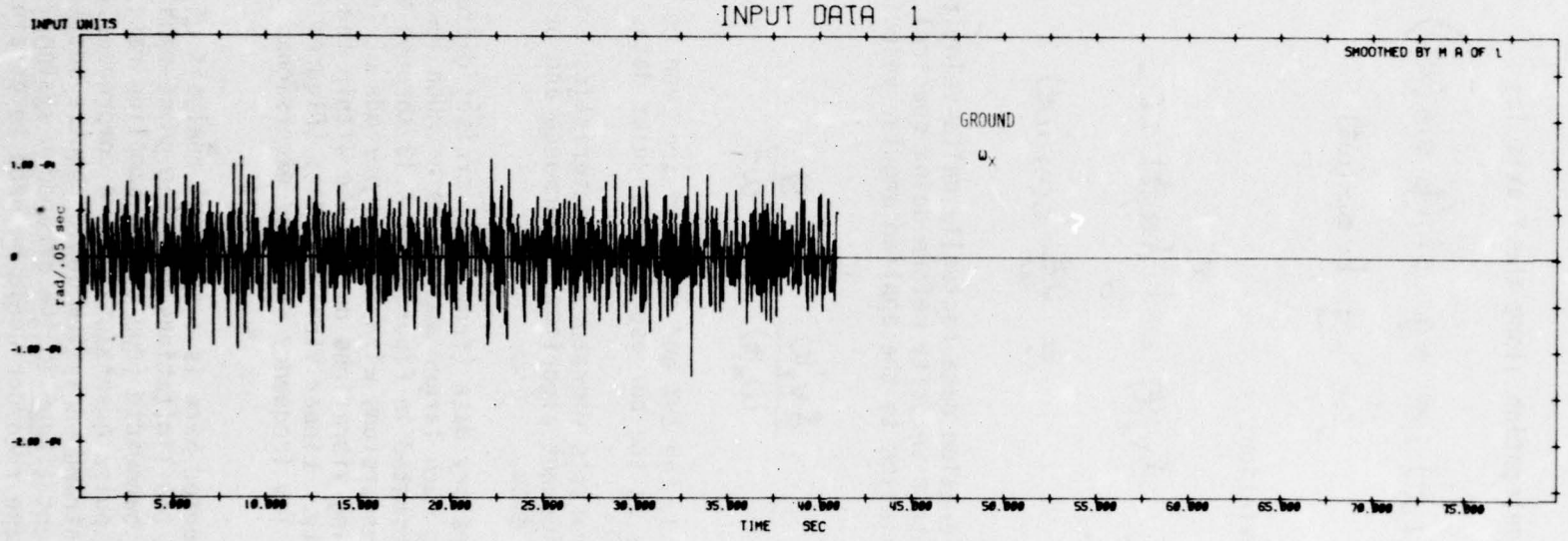

INPUT DATA 1
INPUT UNITS
SMOOTHED BY M A OF 1
GROUND
ω_x
rad/.05 sec
5.000
10.000
15.000
20.000
25.000
30.000
35.000
40.000
45.000
50.000
55.000
60.000
65.000
70.000
75.000
TIME SEC

Figure 8.2.4.1

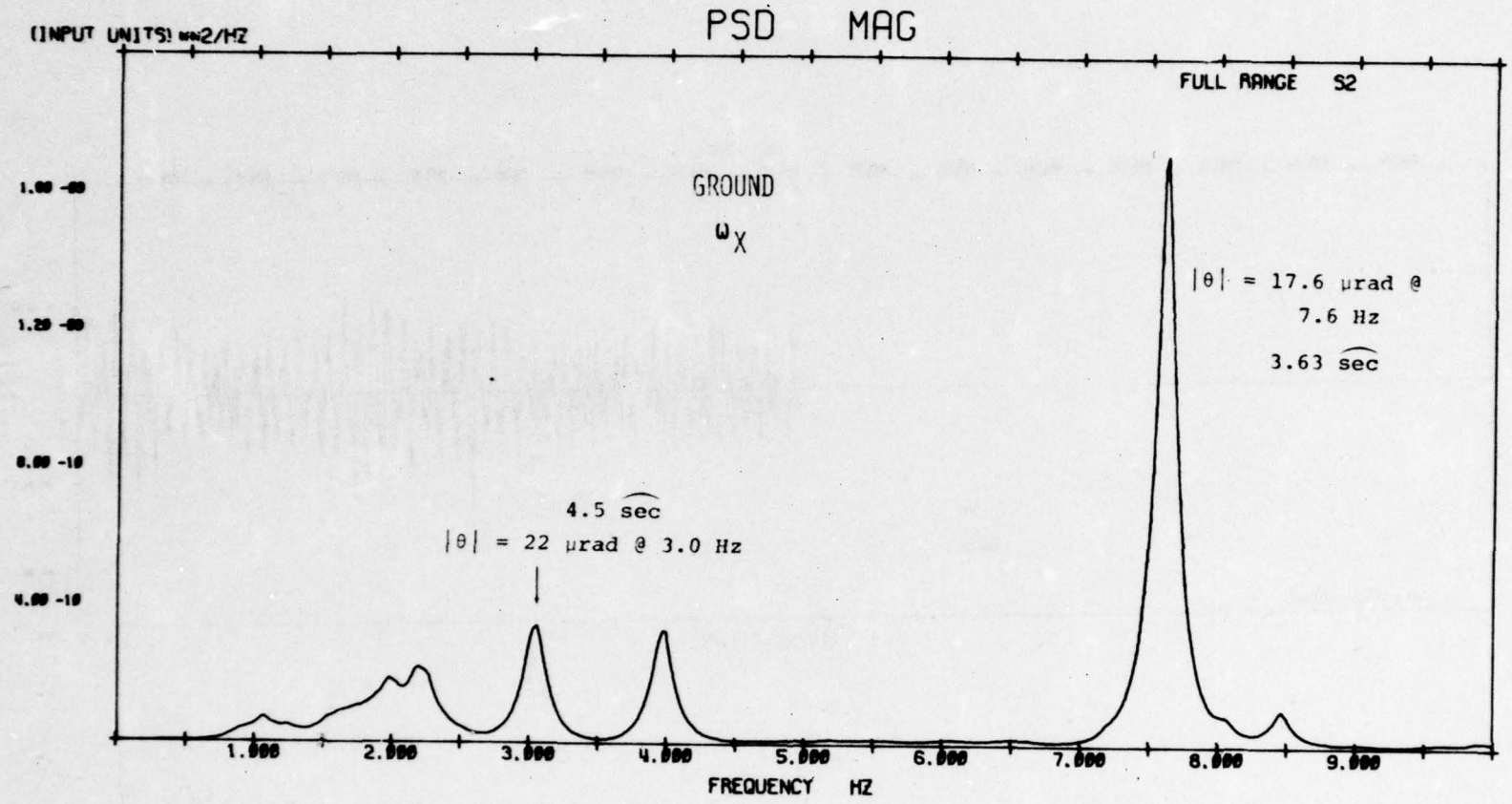

PSD MAG
(INPUT UNITS) **2/HZ
FULL RANGE S2
GROUND
ω_X
|θ| = 17.6 μrad @
7.6 Hz
3.63 sec
4.5 sec
|θ| = 22 μrad @ 3.0 Hz
1.000
2.000
3.000
4.000
5.000
6.000
7.000
8.000
9.000
FREQUENCY HZ

Figure 8.2.4.2

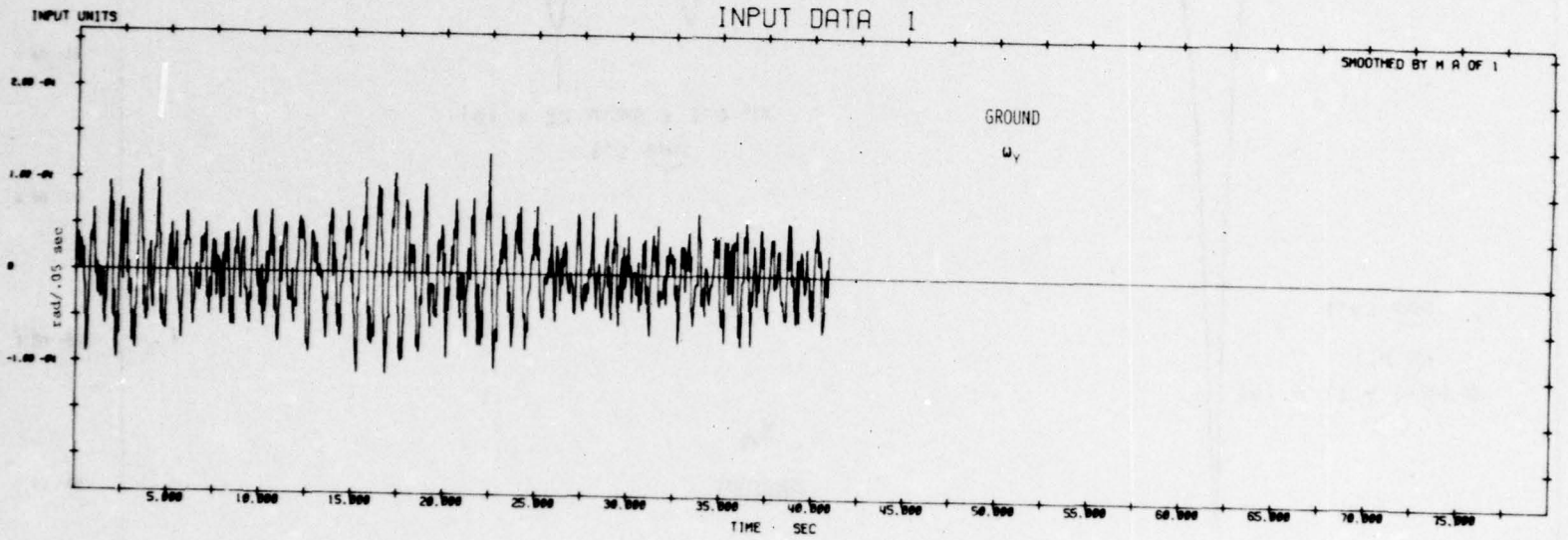

INPUT UNITS
INPUT DATA 1
SMOOTHED BY M A OF 1
GROUND
ω_y
rad/.05 sec
5.000
10.000
15.000
20.000
25.000
30.000
35.000
40.000
45.000
50.000
55.000
60.000
65.000
70.000
75.000
TIME - SEC

Figure 8.2.4.3

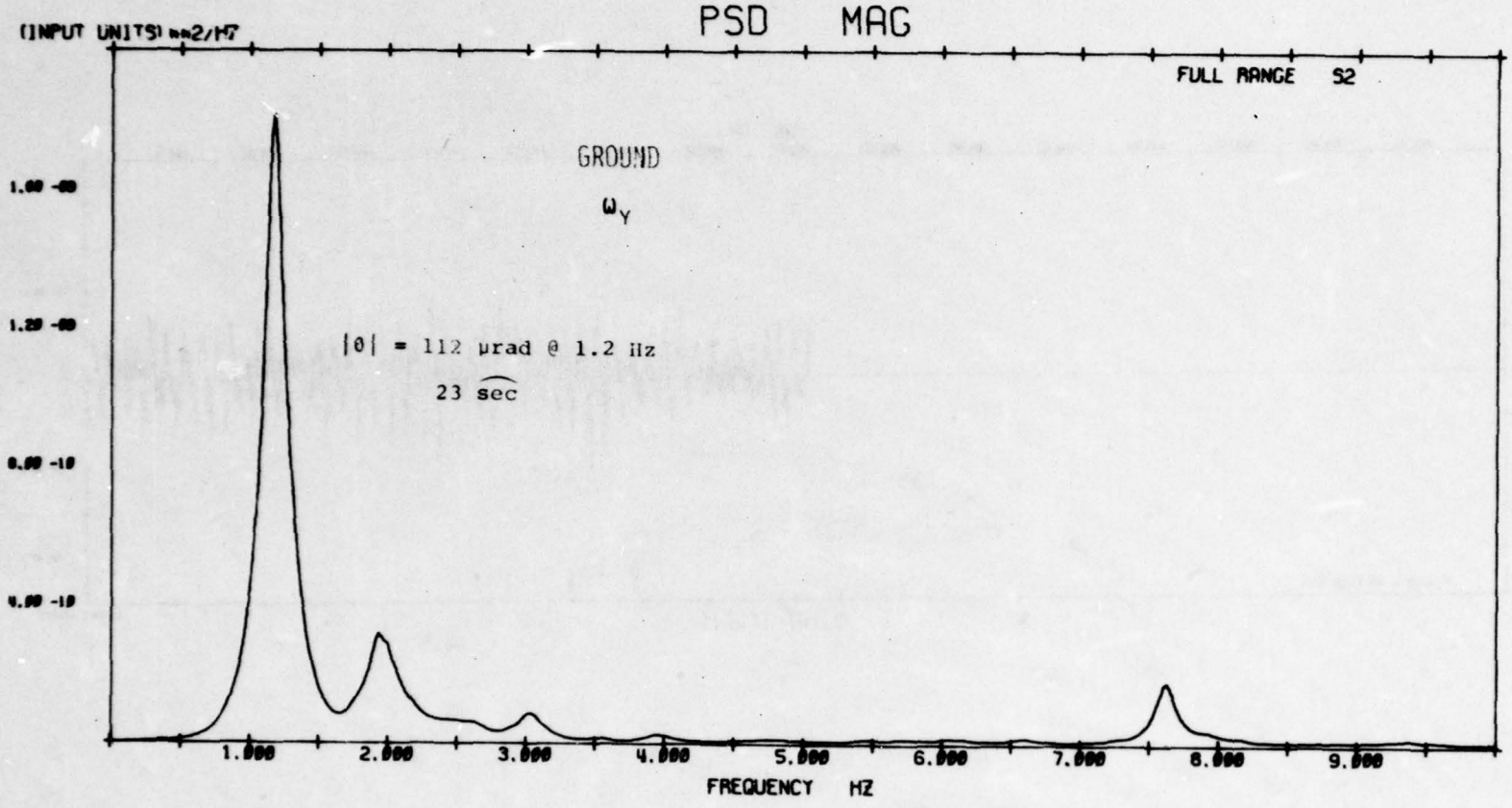

PSD MAG
(INPUT UNITS) mm2/HZ
FULL RANGE S2
GROUND
ω_Y
|θ| = 112 μrad @ 1.2 Hz
23 sec
1.000
2.000
3.000
4.000
5.000
6.000
7.000
8.000
9.000
FREQUENCY HZ

Figure 8.2.4.4

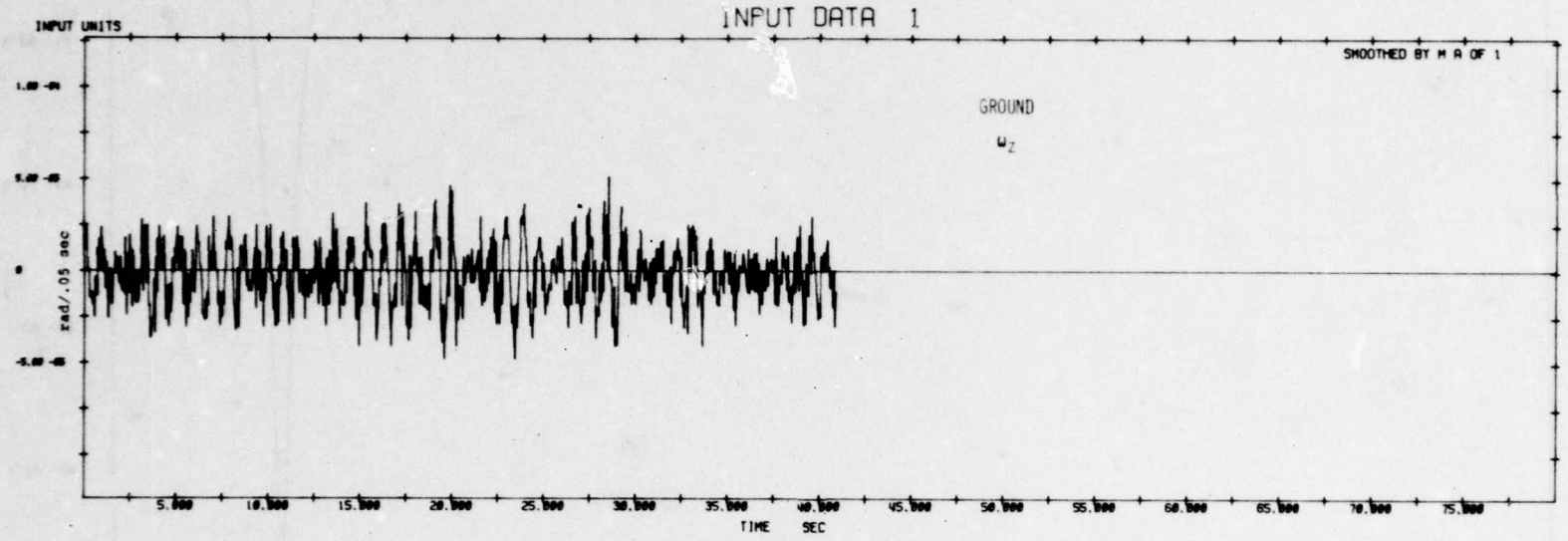

INPUT DATA 1
INPUT UNITS
SMOOTHED BY M A OF 1
GROUND
ω_z
rad/.05 sec
5.000
10.000
15.000
20.000
25.000
30.000
35.000
40.000
45.000
50.000
55.000
60.000
65.000
70.000
75.000
TIME SEC

Figure 8.2.4.5

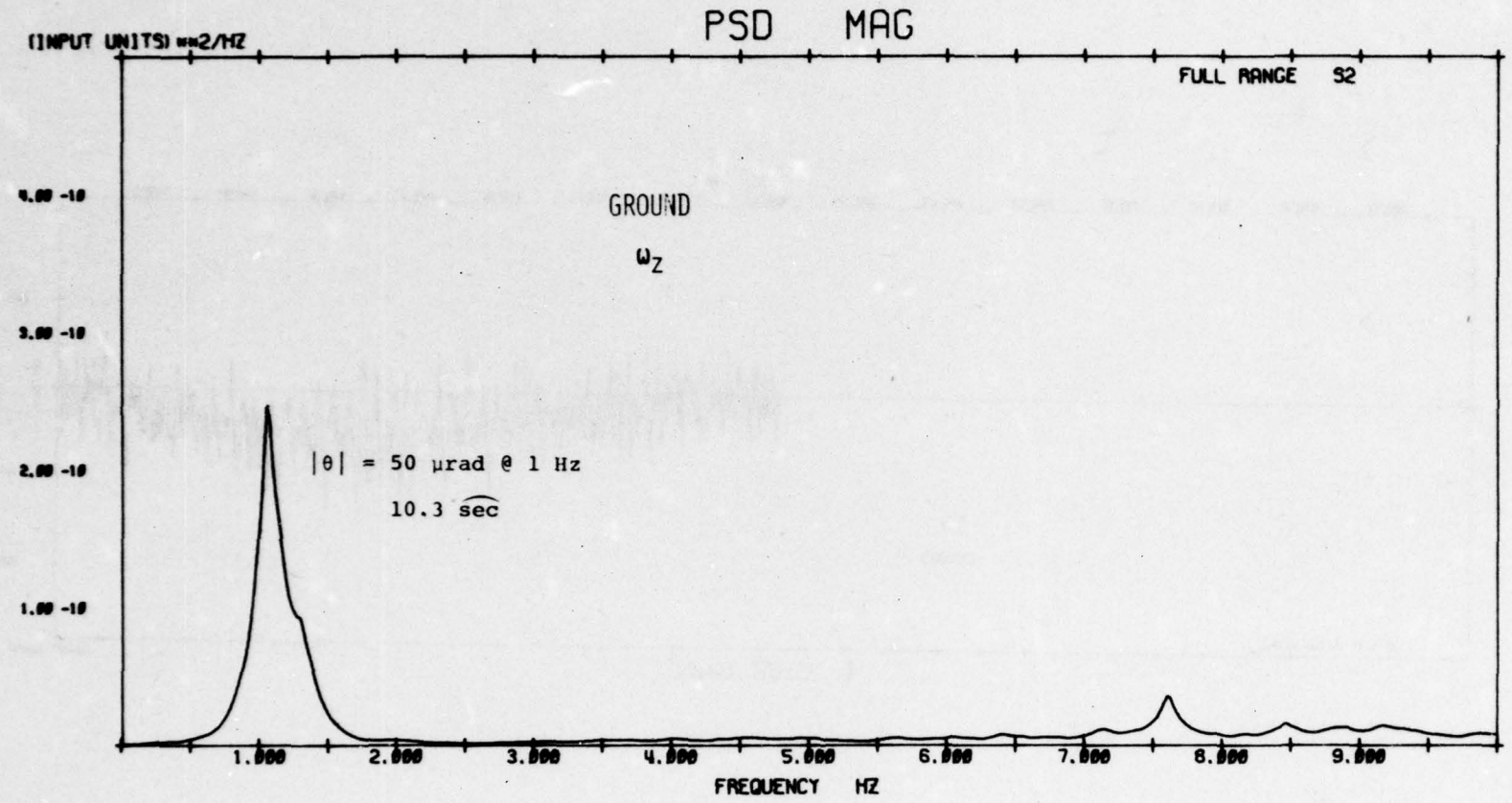

PSD MAG
(INPUT UNITS) **2/HZ
FULL RANGE S2
GROUND
ω_Z
|θ| = 50 μrad @ 1 Hz
10.3 sec
1.000
2.000
3.000
4.000
5.000
6.000
7.000
8.000
9.000
FREQUENCY HZ

Figure 8.2.4.6

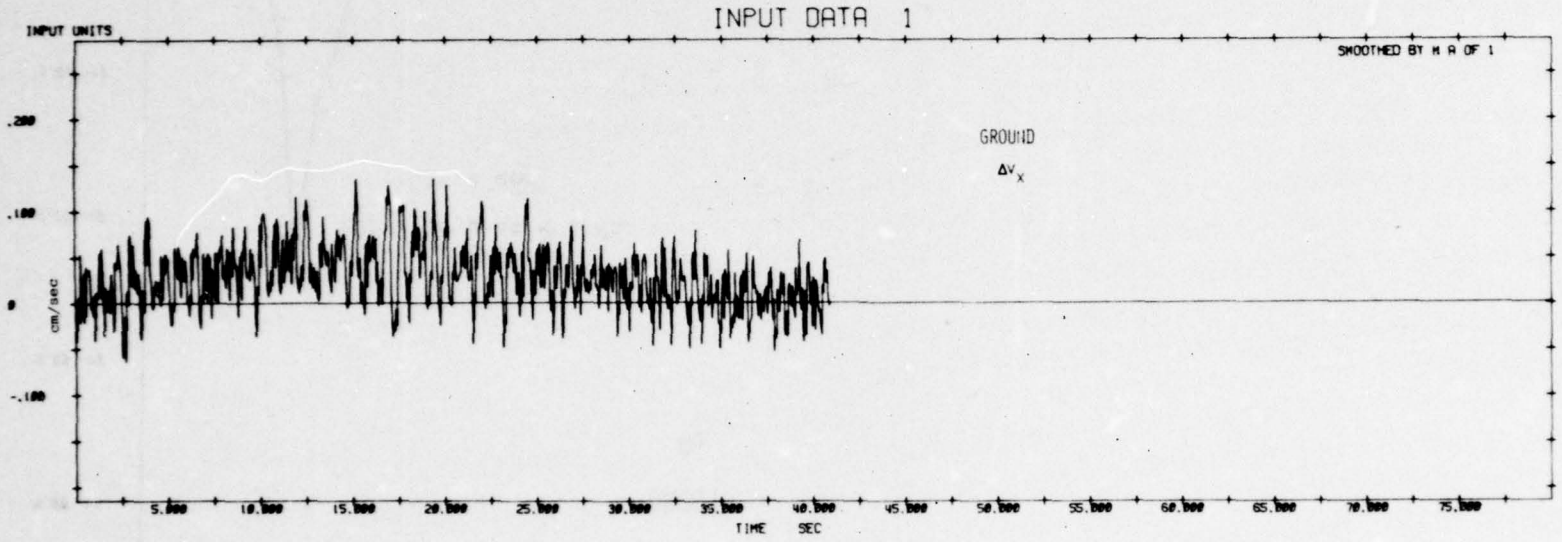

INPUT DATA 1
INPUT UNITS
SMOOTHED BY H A OF 1
GROUND
ΔV_x
.200
.100
0
-.100
cm/sec
5.000
10.000
15.000
20.000
25.000
30.000
35.000
40.000
45.000
50.000
55.000
60.000
65.000
70.000
75.000
TIME SEC

Figure 8.2.4.7

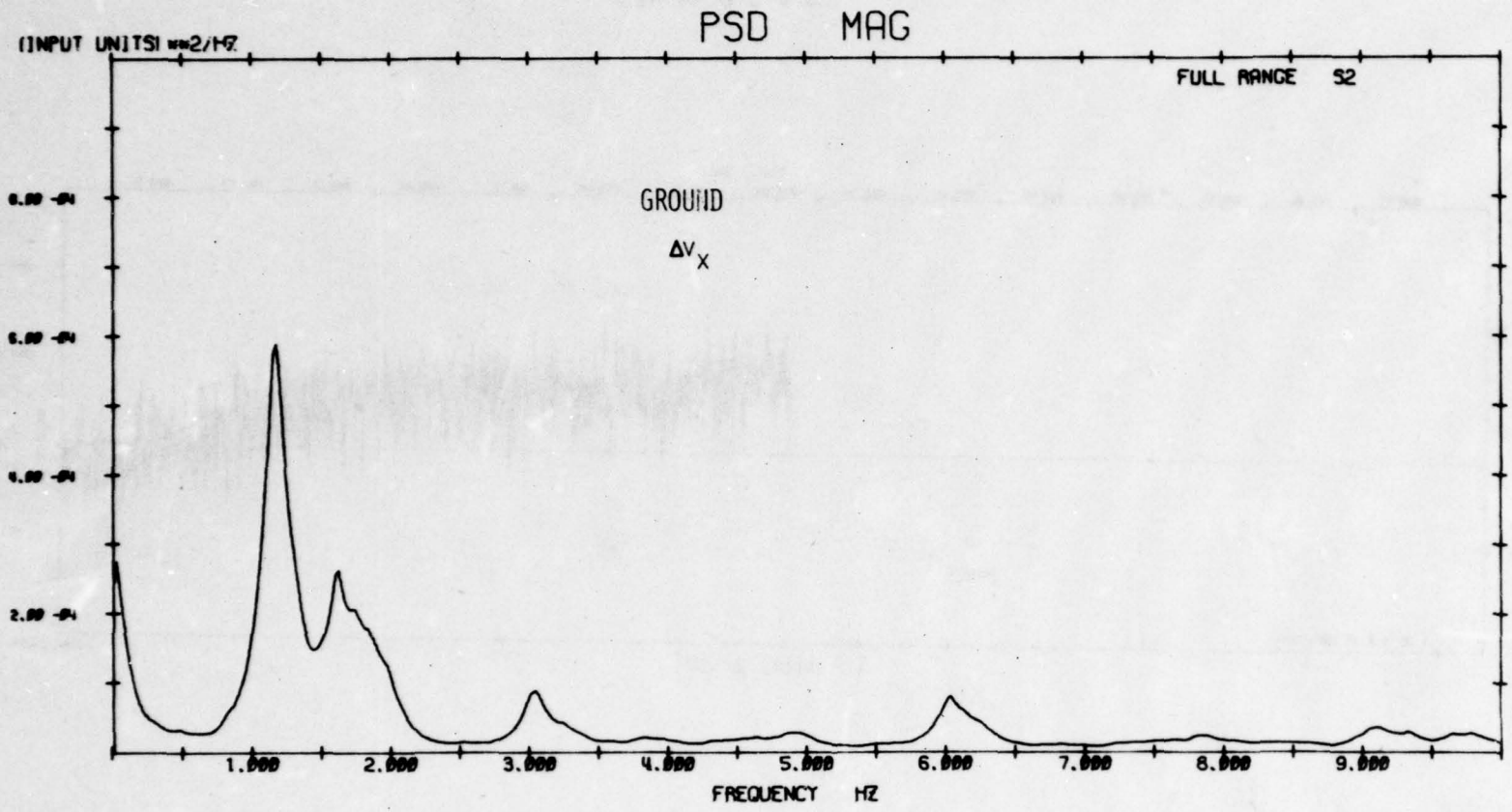

PSD MAG
(1)NPUT UNITS) m=2/HZ
FULL RANGE S2
GROUND
ΔV_X
1.000
2.000
3.000
4.000
5.000
6.000
7.000
8.000
9.000
FREQUENCY HZ

Figure 8.2.4.8

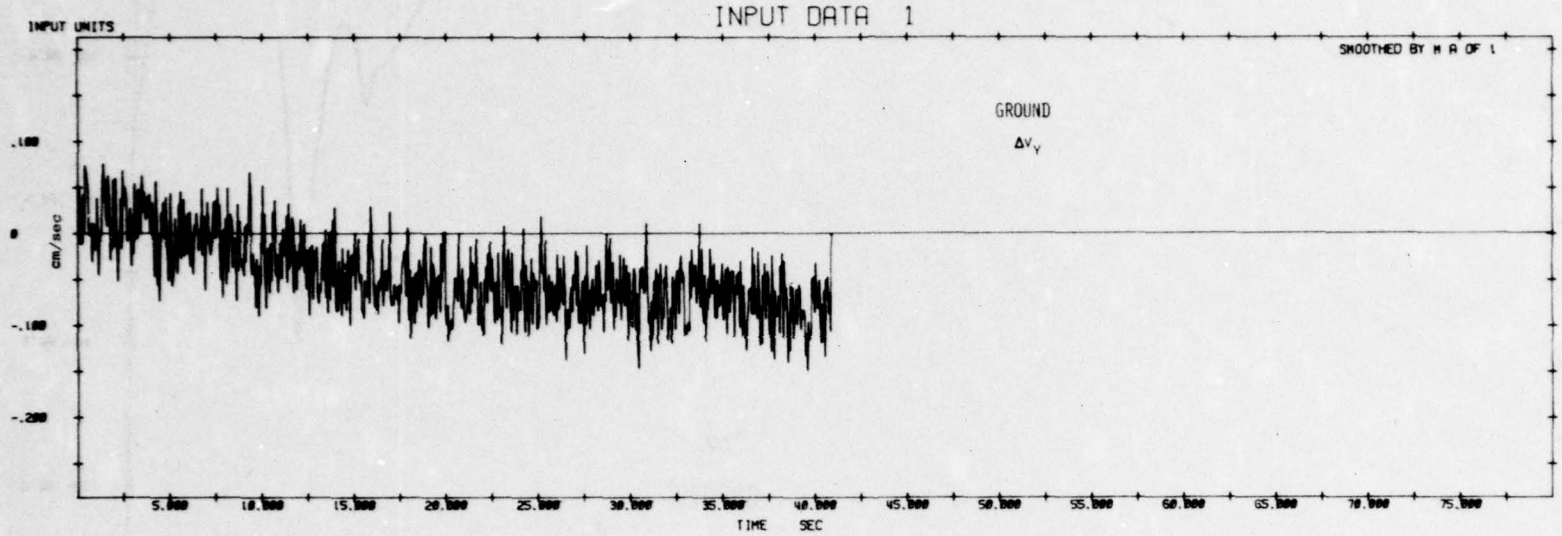

INPUT DATA 1
INPUT UNITS
SMOOTHED BY M A OF 1
GROUND
ΔV_Y
.100
0
-.100
-.200
cm/sec
5.000
10.000
15.000
20.000
25.000
30.000
35.000
40.000
45.000
50.000
55.000
60.000
65.000
70.000
75.000
TIME SEC

Figure 8.2.4.9

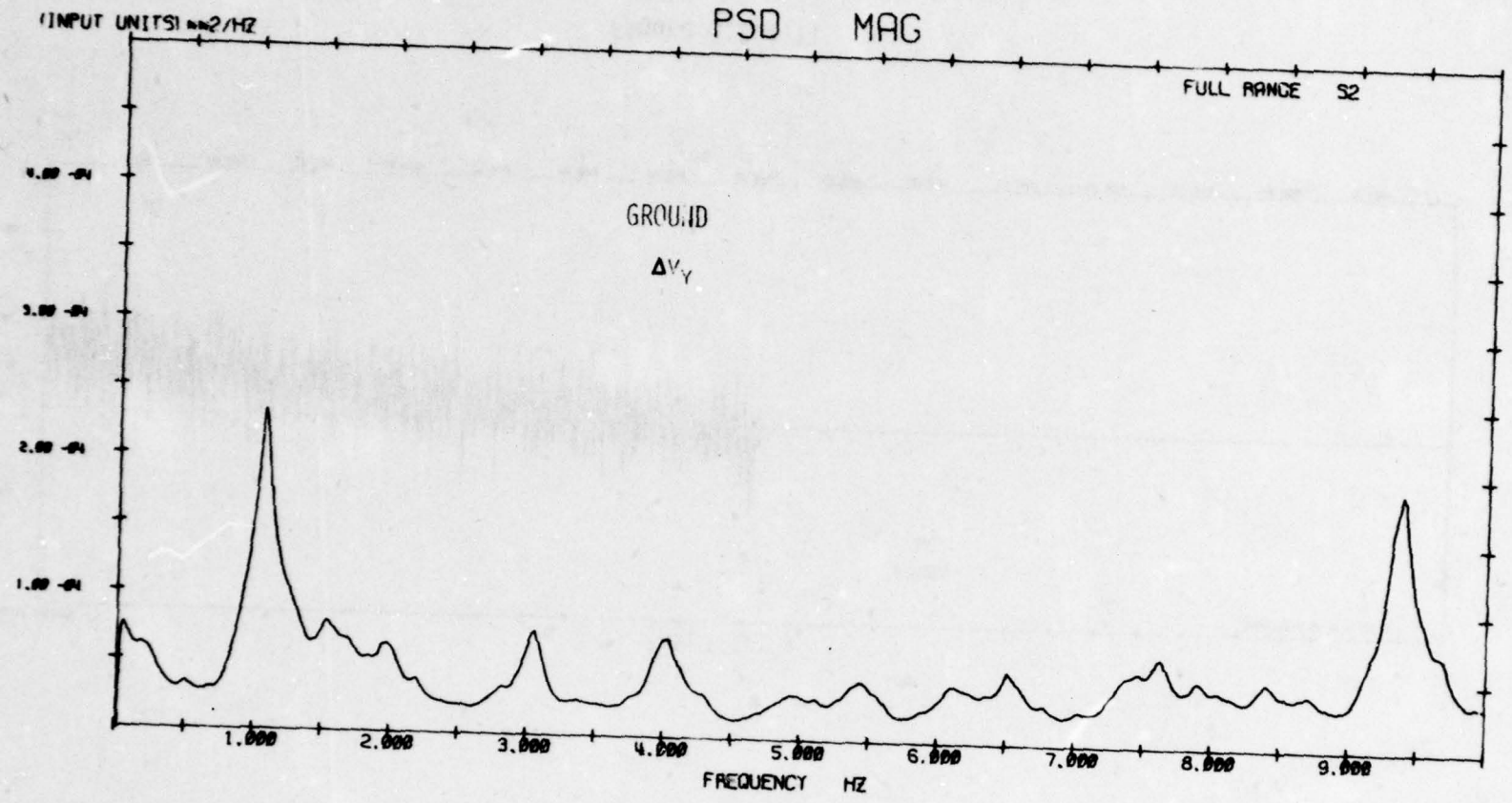


Figure 8.2.4.10

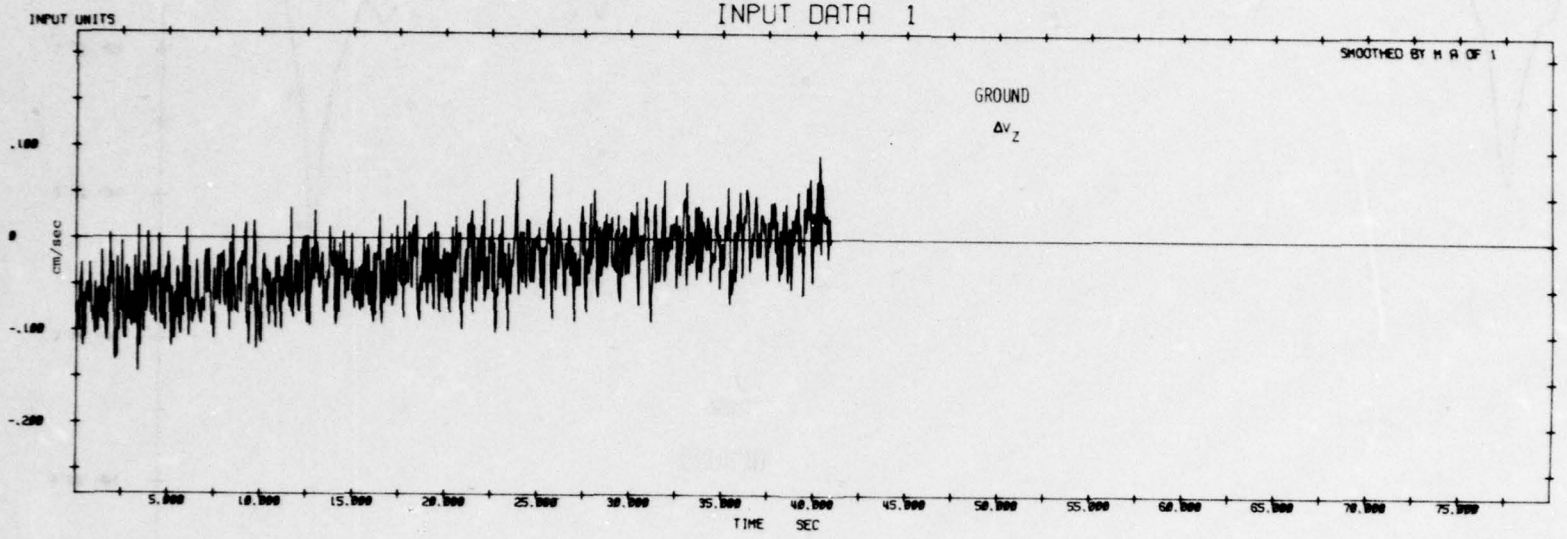


Figure 8.2.4.11

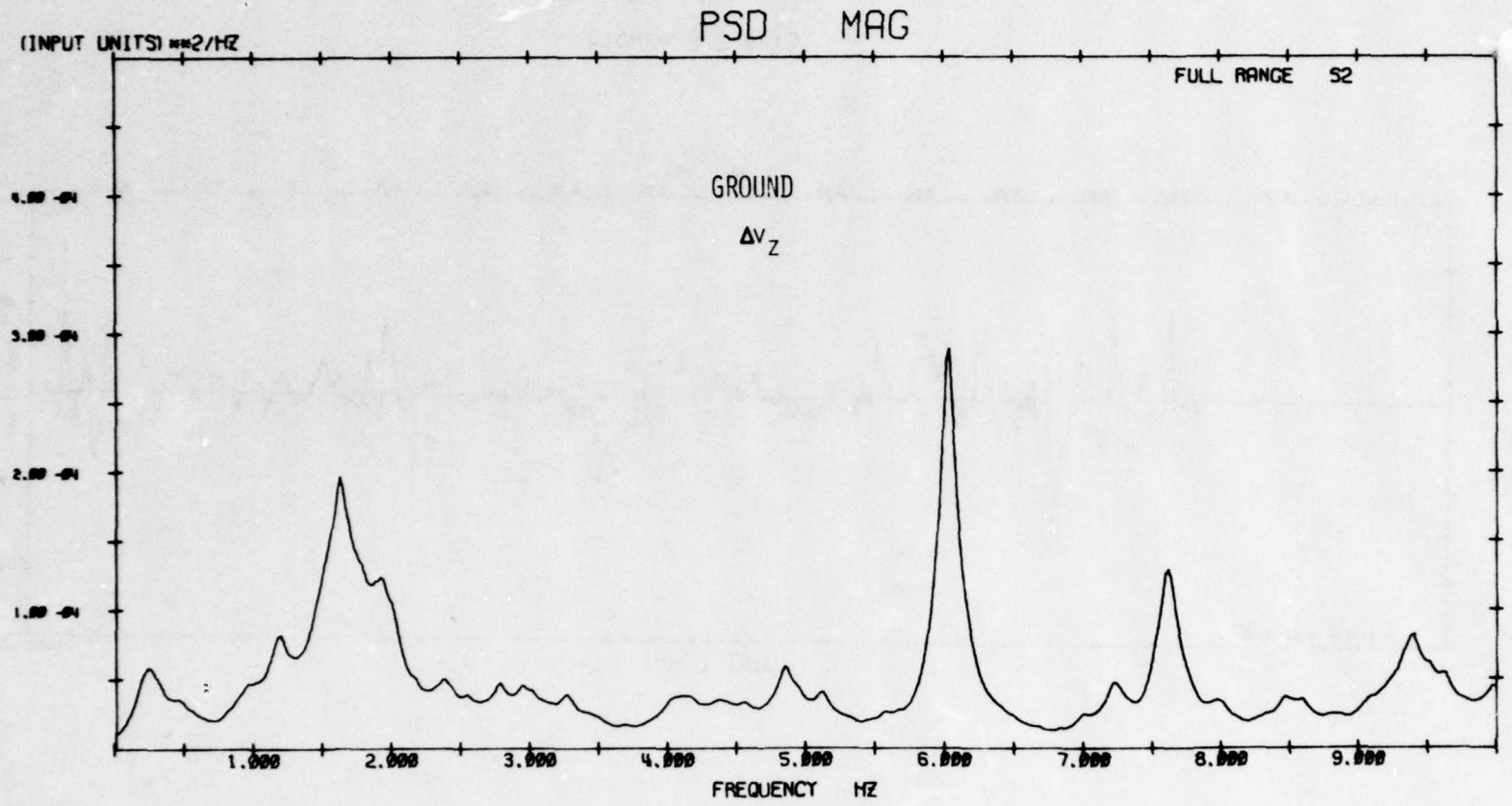


Figure 8.2.4.12

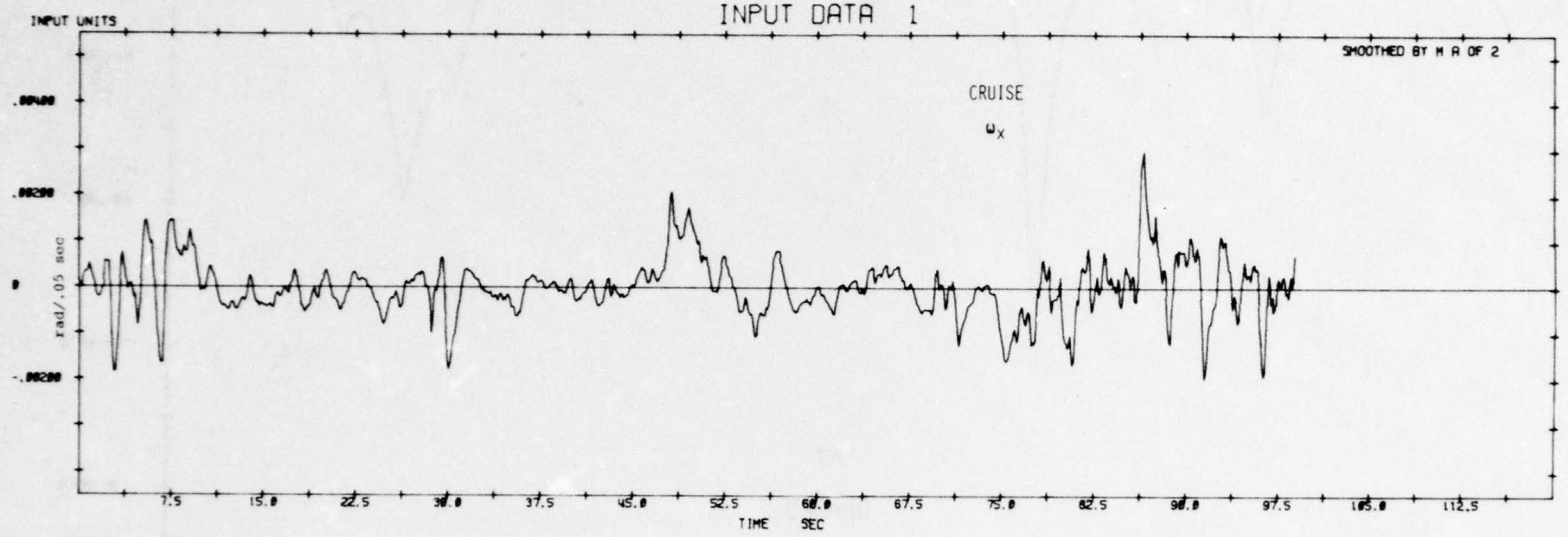


Figure 8.2.4.13

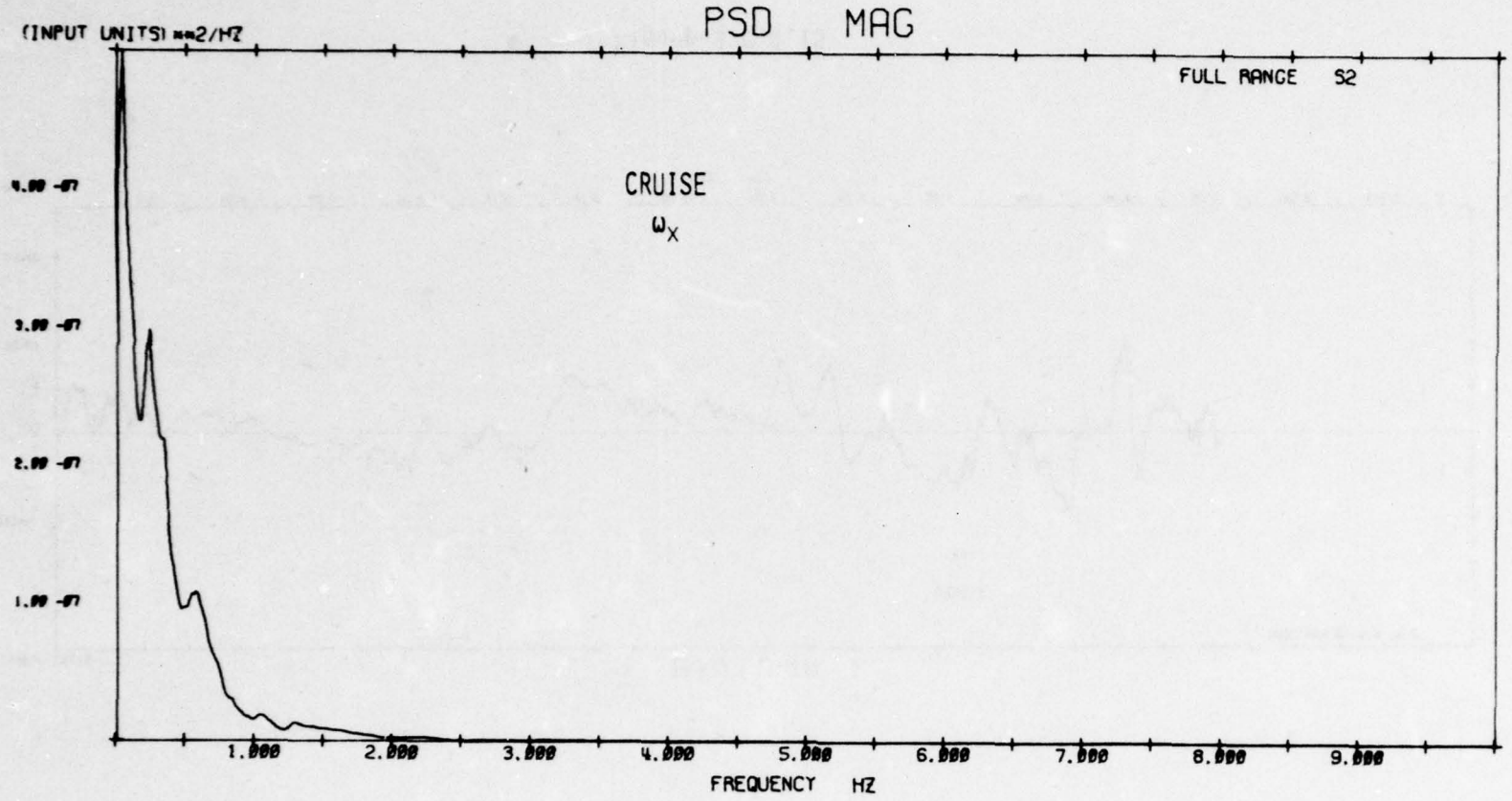


Figure 8.2.4.14

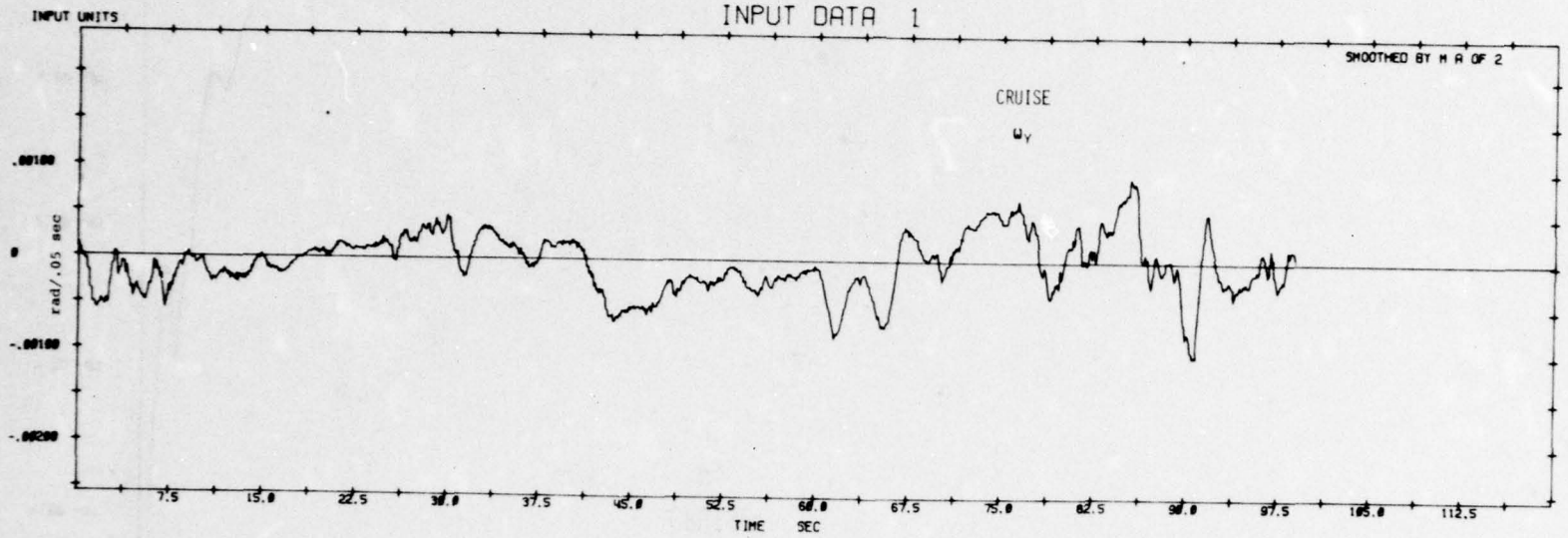


Figure 8.2.4.15

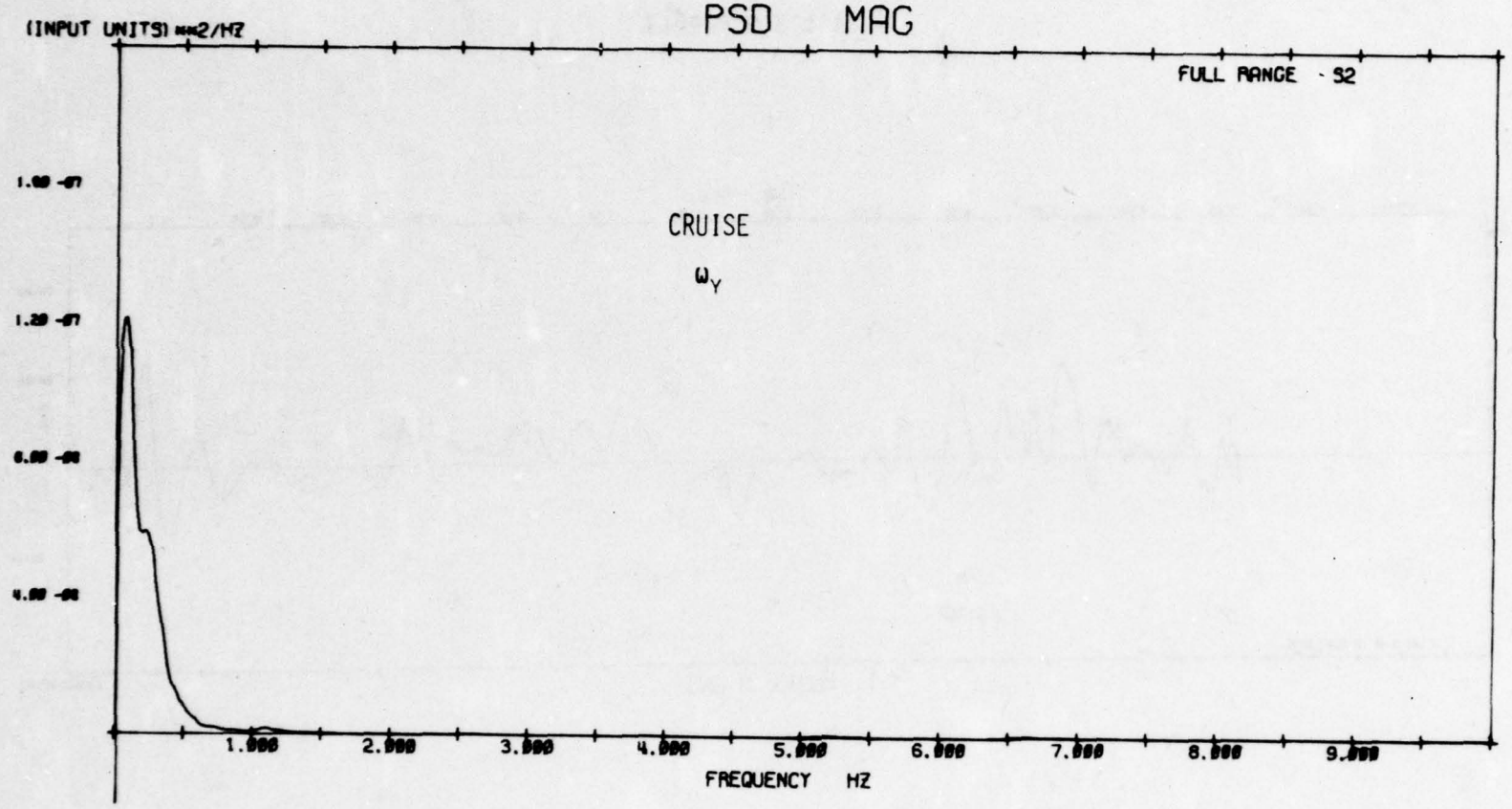


Figure 8.2.4.16

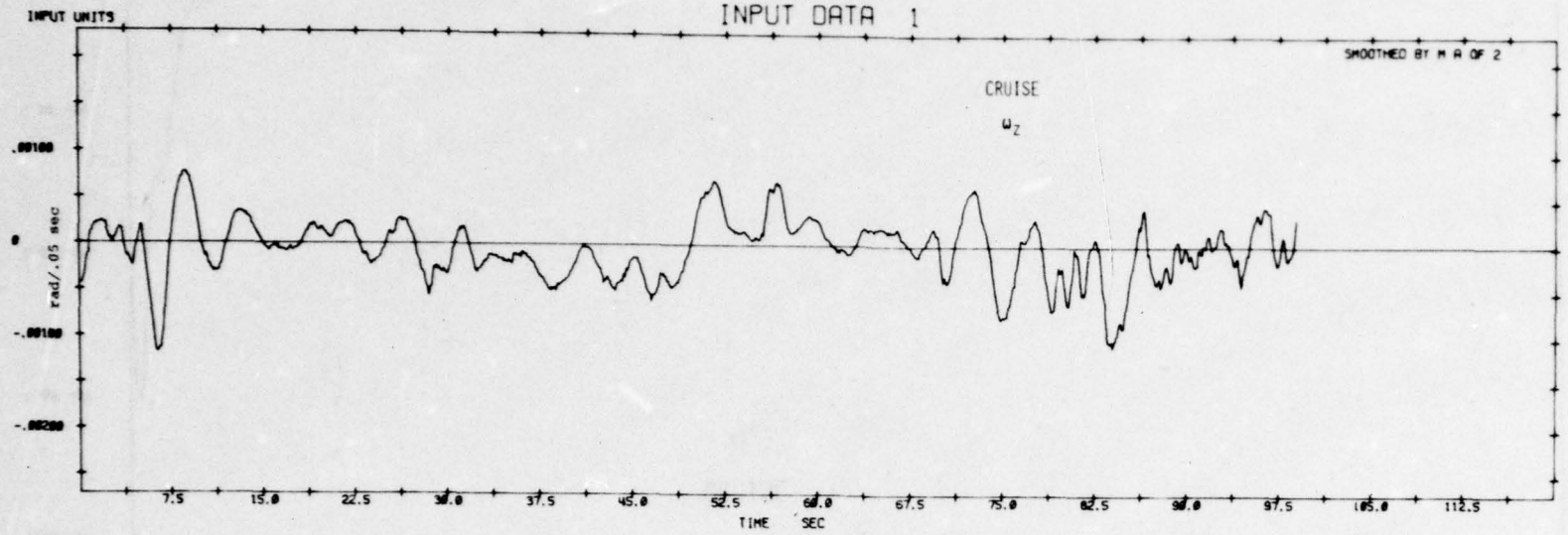


Figure 8.2.4.17

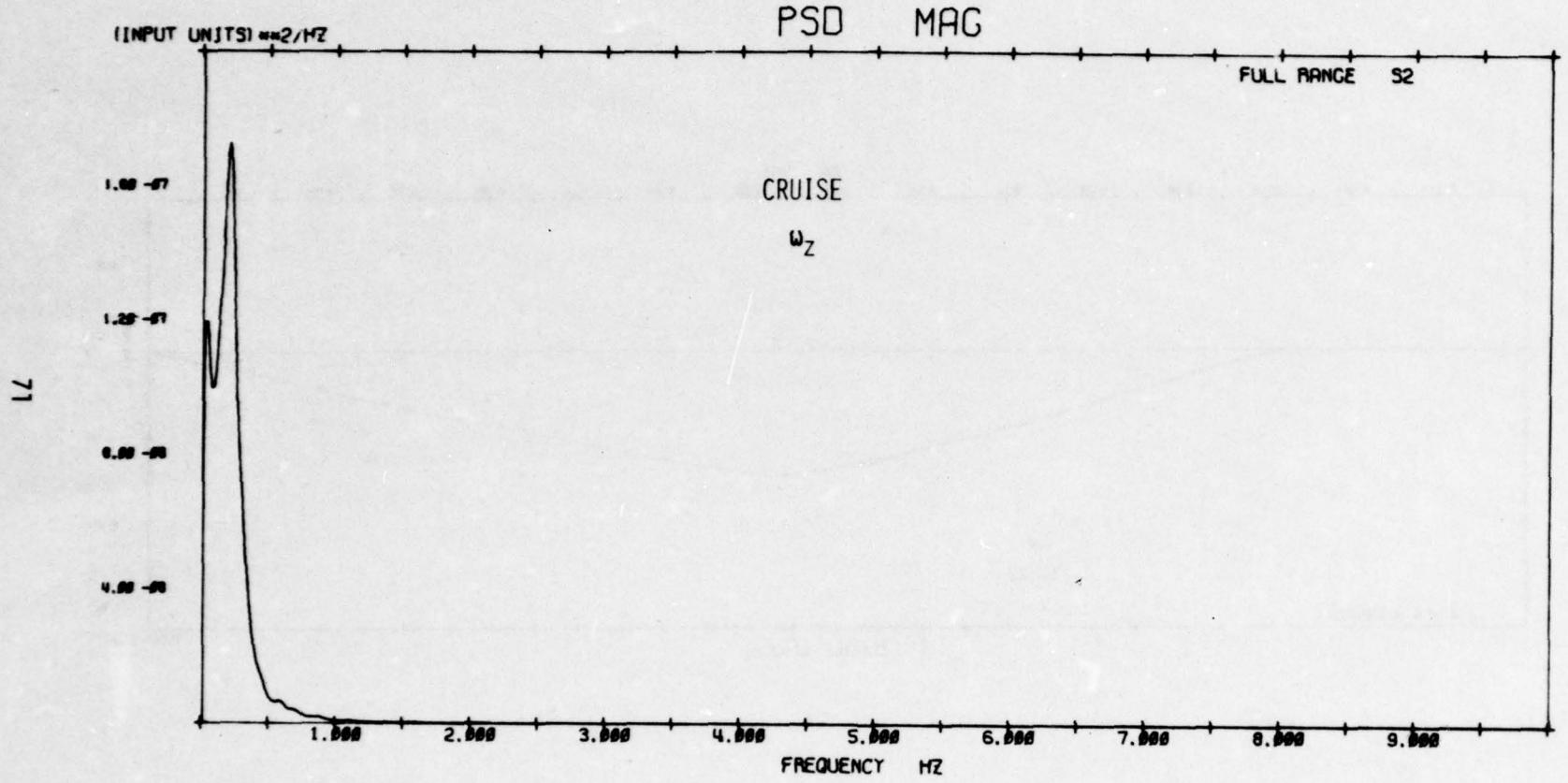


Figure 8.2.4.18

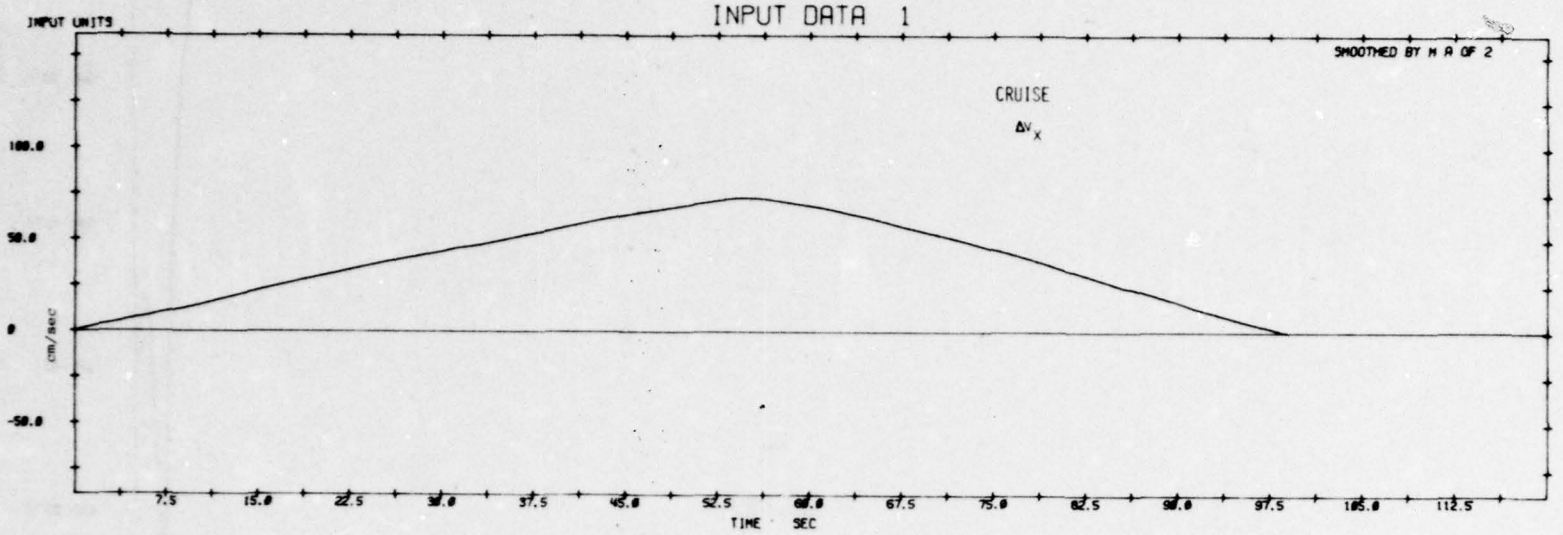


Figure 8.2.4.19

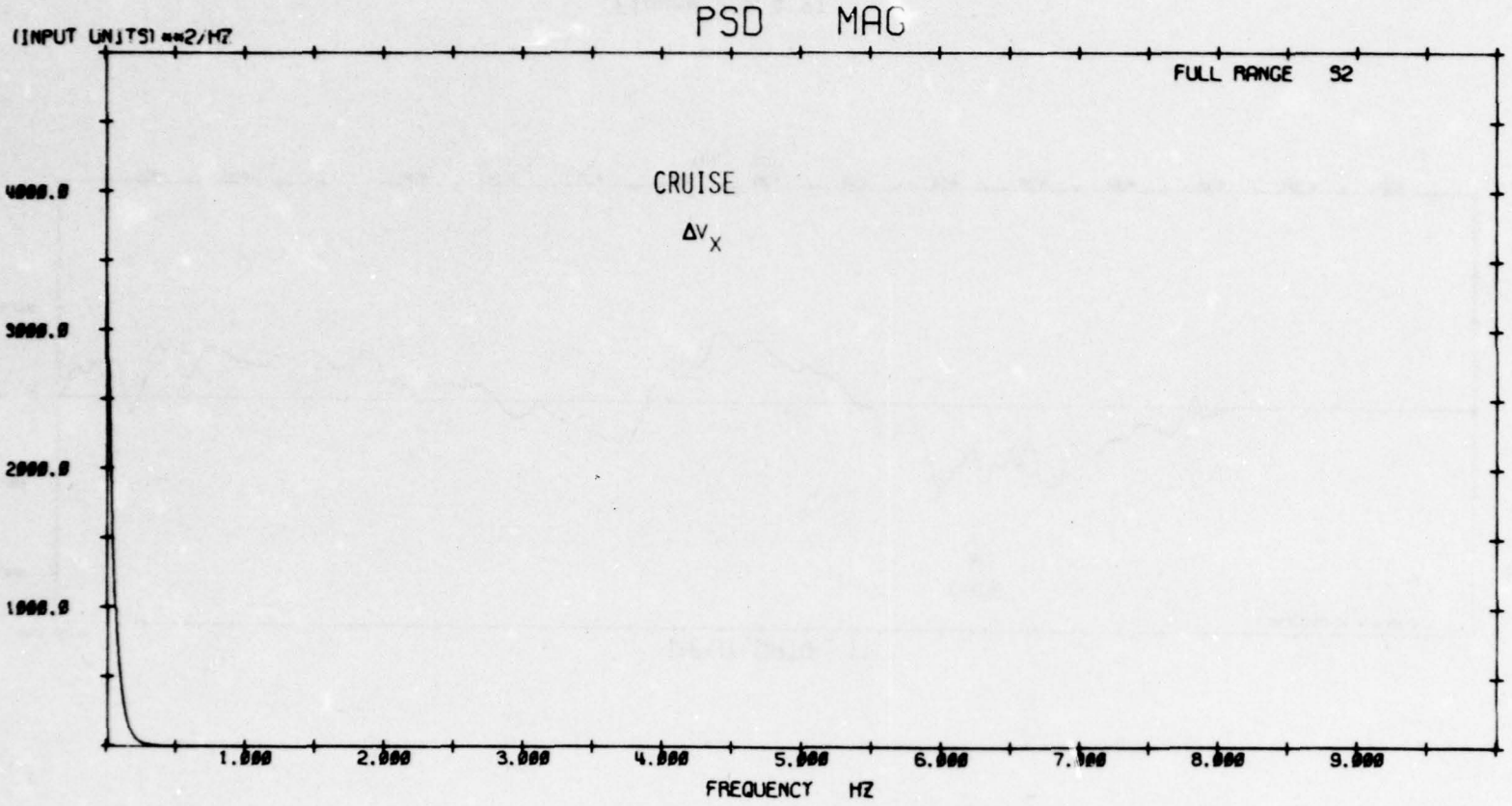


Figure 8.2.4.20

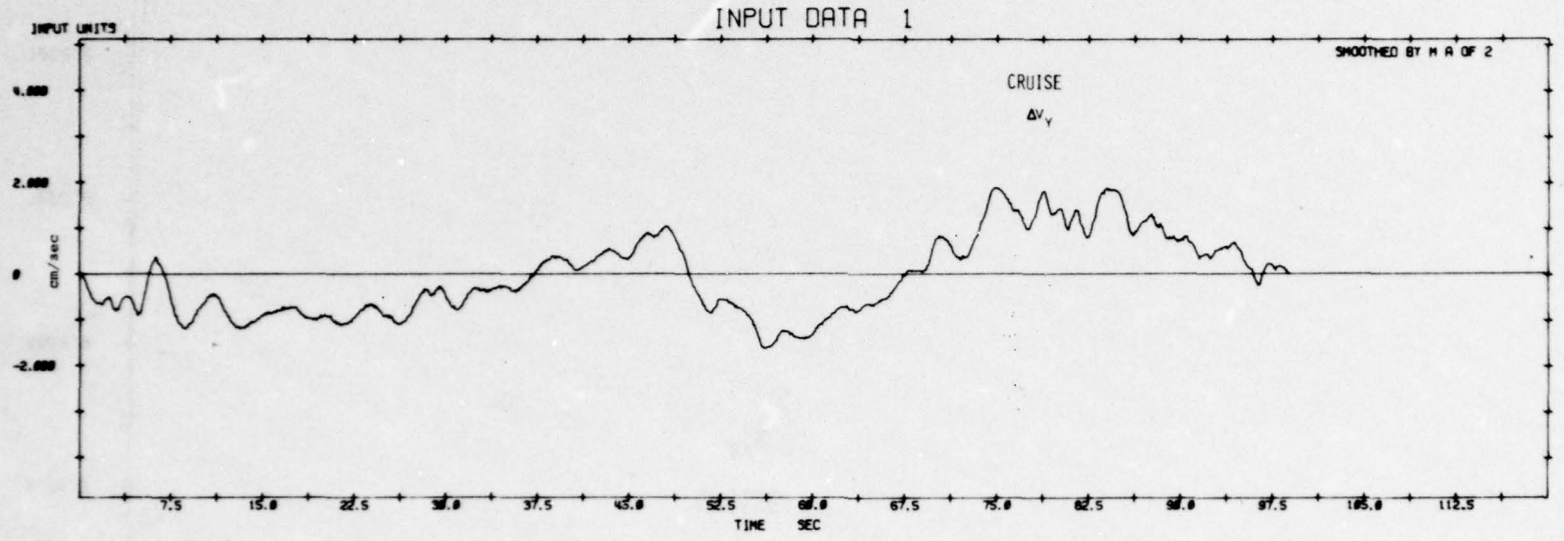


Figure 8.2.4.21

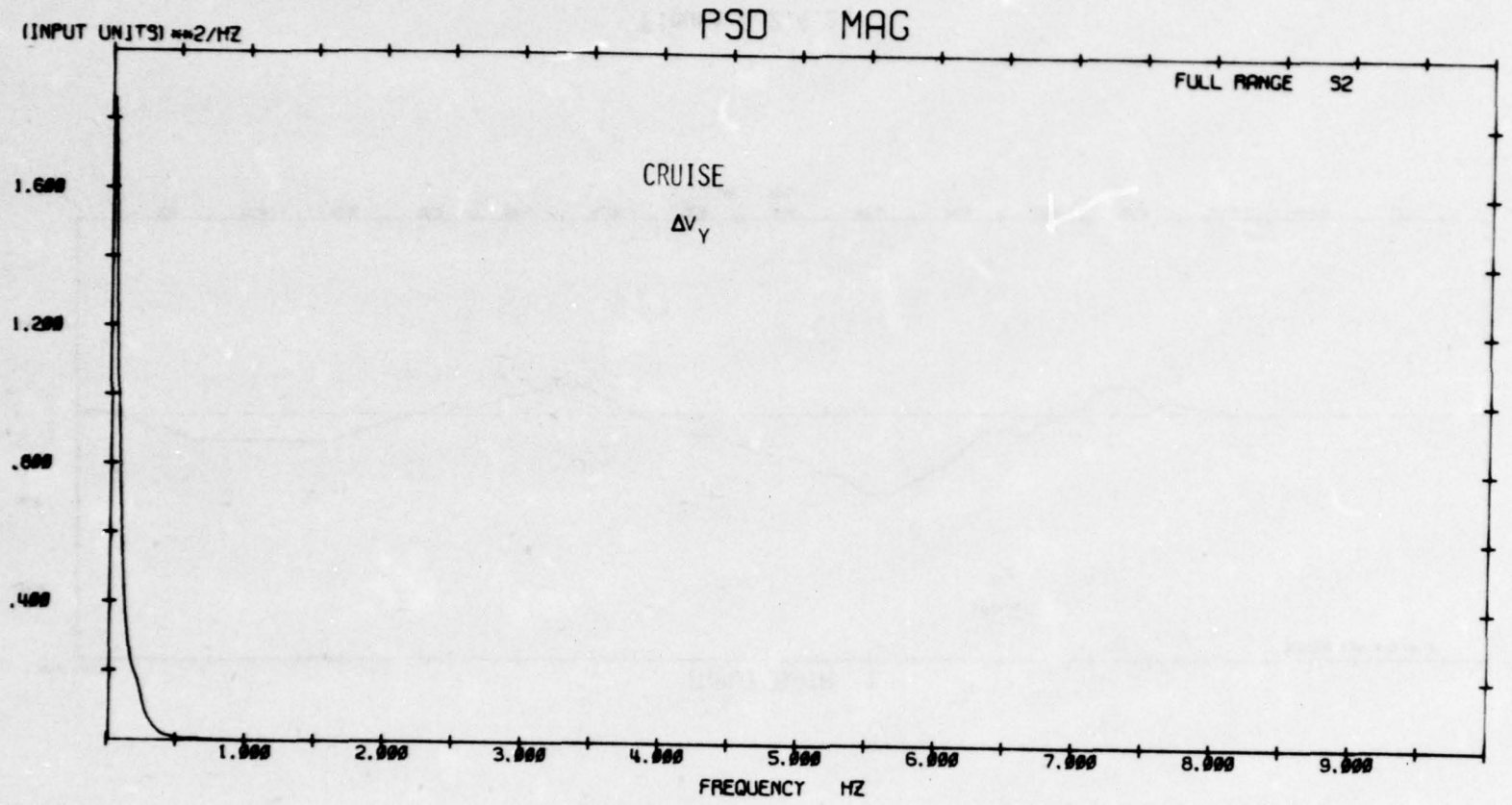


Figure 8.2.4.22

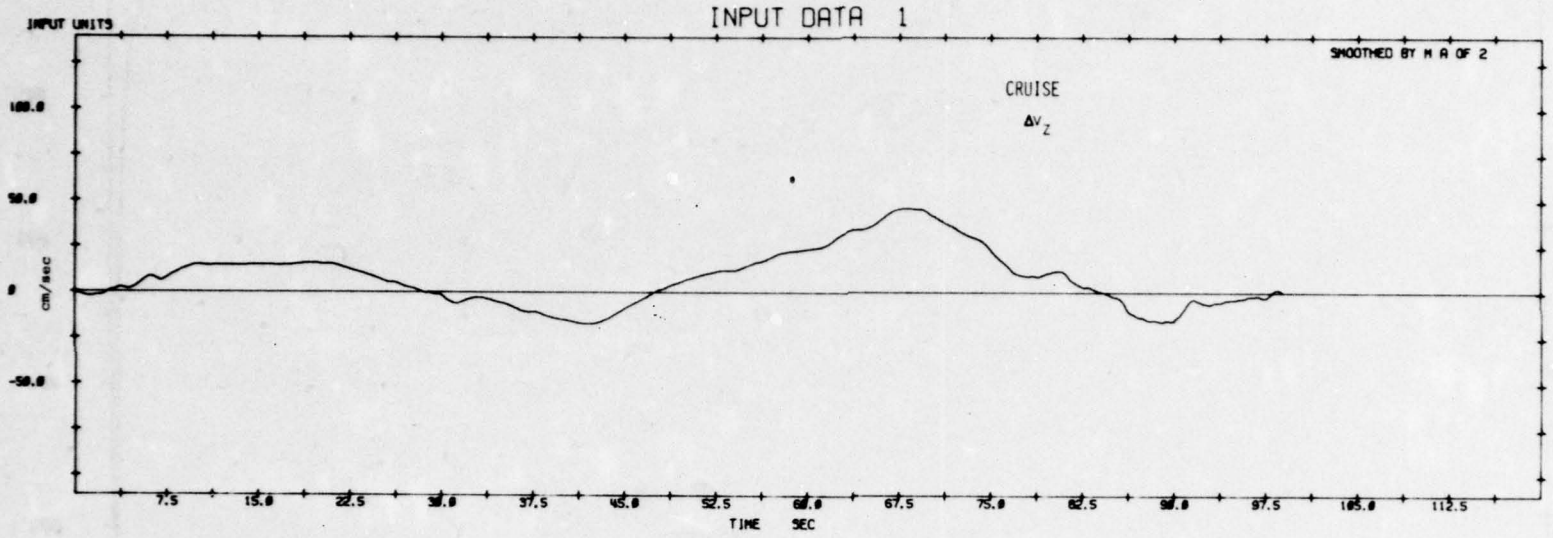


Figure 8.2.4.23

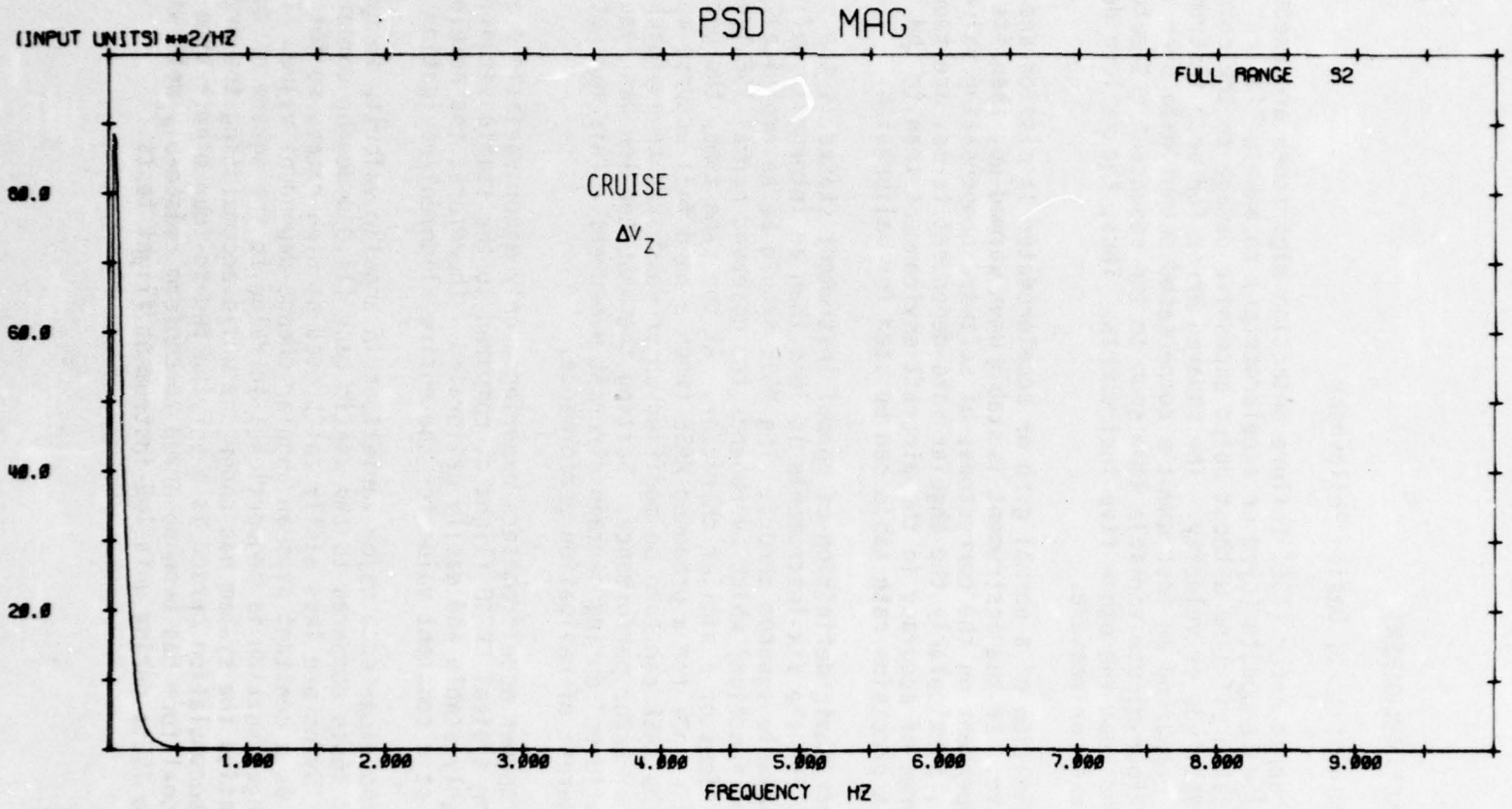


Figure 8.2.4.24

this purpose.

8.3 REDUNDANCY MANAGEMENT

8.3.1 Deterministic FDI Design Philosophy

Total squared error (TSE) failure detection algorithms are executed at each inertial data update (gyro or accelerometer) to enable "failed" instruments to be taken off-line without doing excessive damage to the computational body attitude or velocity. The squared error for each instrument is formed by comparing an instrument's compensated output data over the previous two to four-minute variable time span to the redundant estimate of its output created from the other five instruments. Thus, the failure definition is a relative-error measure.

The definition of a normal gyro or accelerometer is mission-and environment-sensitive. If the instrument is stable when warmed-up, then its accuracy is mainly dependent on the correctness of software compensation values. These values, particularly the angular rate-dependent terms, are known with a lesser degree of accuracy in the aircraft environment than in the laboratory, where a precision rate table can be used for calibration.

The algorithmic definition of normal instrument status is the state such that the TSE for the six instruments is less than an internally defined MASE (maximum allowable squared error). The MASE should be an empirically extracted value (or function) which overbounds the observed normal TSE levels from previous missions of a similar character. At the same time, the potential navigational errors for a proposed MASE (when a hard fail occurs) must be examined. The MASE can then be modified up or downwards to approach a desired level of error performance. Setting the MASE too low can lead to predictable "failures" during certain aircraft maneuvers. This may not be in the best interest of navigation performance.

The strapdown accelerometers experience only minor variations in specific force for typical CV340 flight as compared to the static situation. They are also highly stable and easily calibrated. Therefore, the accelerometer MASE is set at a constant value for the entire alignment/navigation duration.

The gyros experience major variations in angular velocity in typical CV340 flight tests compared to the static case (11,000 deg/hr compared to 15 deg/hr). Gyros are less easily calibrated at high rates, so the gyro MASE is set as a constant plus an angular change-dependent value. This angular change function is proportional in value to the square of the net angular rotation the system has undergone while accumulating the present TSE. (The accumulation period is a varying two-to-four minute time span.) This functional form has been observed to conform reasonably well with the typical gyro TSE's during unfailed-instrument flight tests.

8.3.2 FDI's Effect on Navigation Accuracy

Two aspects of navigation accuracy can be investigated concerning FDI actions. One concerns the deterioration of accuracy caused by a slightly bad gyro or accelerometer whose error magnitude is just under the detection level of the relevant FDI algorithm. The second aspect concerns the magnitude of navigation errors which occur when an instrument has a "hard fail" and (typically) is detected and put off-line within a few seconds after failure.

A keyboard modification midway through the SIRU flight tests made it possible to add software bias errors to instruments in the B computer while continuing normal (baseline) operations in the A computer. This allows comparison of navigation performance with and without the hard fail occurrence.

An accelerometer hard fail causes a velocity increment to be added to the system's navigation velocity. (For simplicity, the system is assumed initially to have all instruments on-line with low TSE's up to the point of the single instrument degradation.) This accelerometer failure has a minor, second-order effect on the attitude of the failed system since the accelerometer outputs couple into the gyro data by way of g-sensitive compensation.

The magnitude of the velocity error increment which corrupts the navigation performance depends on both the MASE value and the orientation of the accelerometer which is failing. Only the horizontal velocity error affects navigation because the vertical channel is tied down. The latter months of flight testing had a first-fail search MASE of 288 pulses^2 (4 cm/sec was the design pulse value). Assume all accelerometers are error-free except for one horizontal instrument with bias error b_ϵ cm/sec^2. If this bias error is begun at t = 0, then the accumulated instrument velocity is

$$V_\epsilon(t) = b_\epsilon t$$

and the TSE IS

$$TSE(t) = (b_\epsilon t)^2 + 5\ (.2(b_\epsilon t)^2) = 2\ (b_\epsilon t)^2$$

The bad accelerometer is taken off-line at the point when TSE(t) $\geq$ MASE. Define V_ϵ^* as the value of $V_\epsilon(t)$ just prior to that point. The worse case V_ϵ^* is then found:

$$2(V_\epsilon^*)^2 = MASE = 288\ pulse^2$$

$$V_\epsilon^* = 12\ pulses = 48\ cm/sec$$

This total instrument velocity error is reduced by a factor of two in the transformation to body coordinates so that the worse case maximum velocity error increment is

$$\frac{\sqrt{MASE/2}}{2} = 24 \frac{cm}{sec} = .79 \frac{Ft}{sec} = .47 \text{ knot}$$

This maximum value of velocity error occurs only if the aircraft maintained a constant heading during the instrument degradation period. If the aircraft was turning, the velocity error magnitude and direction will be modulated accordingly. In either case, a consistant velocity error in the navigation frame results. Unfortunately, none of the four flight tests which had scheduled accelerometer failures yielded a clear example of comparative (A:B) navigation performance for a single accelerometer failure. (This was due to operating both computers identically on some flights and to scheduling multiple instrument failures on others.)

The other performance aspect of FDI operation concerns a low level instrument degradation which escapes detection, thereby degrading navigation for the duration of a flight. The maximum TSE accumulation period is four minutes, so the maximum undetected accleerometer bias error (b^*_ϵ is found from:

$$\left(b^*_\epsilon \cdot 4 \text{ min.}\right) \equiv V^*_\epsilon = \sqrt{(MASE/2)}$$

For MASE = 288 pulse^2, this reduces to:

$$b^*_{\epsilon.} = \frac{48 \text{ cm/sec}}{240 \text{ sec}} = .2 \frac{cm}{sec^2}$$

Again, this instrument bias error is attenuated by a factor of 2 in conversion to body coordinates. This constant bias error of $(b^*_\epsilon/2)$ can produce a maximum position error (for horizontal degraded accelerometer / straight - line flight):

$$\epsilon^*(t) = \tfrac{1}{2}\left(b^*_\epsilon/2\right) t^2 = .05 \frac{cm}{sec^2} t^2$$

This theoretical maximum, which is unlikely to be approached in practice, results in a 21,260 foot position error one hour after the bias error begins. Note that this bias error b^*_ϵ is actually a <u>change</u> in instrument bias after navigation has begun. Alignment level loops cancel effects of initial biases.

A hard gyro fail causes an angular error increment (misalignment) to become present in the inertial system's attitude reference. This misalignment causes navigation errors the same as any other misalignment. Also, the strapdown system is then subject to further alignment degradation when large angular motions of the aircraft occur.

The gyro MASE was set to a base level of 40 pulse^2 (44 $\widehat{sec}$ per gyro pulse) for flight tests from July, 1975 onwards. A dynamic increase in the MASE of up to 120 pulse^2 was designed. This increase was calibrated to hit its upper limit for changes in body attitude of 180 degrees (or more) during any TSE accumulation period.

If all but one of the gyros are well-compensated, then the gyro-failure-caused attitude error may be derived analogously to the accelerometer derivation. Gyro errors appear both from bias and from misalignment errors, so the error is modeled simply as an angular error $\theta_\varepsilon(t)$ (from one bad gyro). The maximum gyro error θ^*_ε is again found from

$$\theta^*_\varepsilon = \sqrt{\left(\frac{MASE}{2}\right)}$$

For a nonrotating system, MASE = 40 pulse^2 and

$$\theta^*_\varepsilon = \sqrt{20} \cdot 44\,\widehat{sec} = 197\,\widehat{sec} = .95 \text{ mrad}$$

The maximum body attitude error is one-half that of the failed gyro: .475 mrad. (Note also that when large angular motion occurs, MASE is 4 times its static value, so that the body attitude error from a single misaligned gyro could be as much as twice that from a static error detection.)

Navigation errors from a failed gyro are most significant over the first few hours for a gyro with horizontal input axis. The resulting Schuler-period position error (for .475 mrad. level error) reaches a first peak magnitude (at t = 43 minutes) of 3.28 nautical miles (19,950 feet). However, this value is observed only for a static navigation test or (approximately) for a low speed flight at constant heading. Changes in heading are misinterpreted by the misaligned strapdown system with the potential effect of worsening the misalignment.

A comprehensive example from a flight test on September 5, 1975 will demonstrate gyro FDI performance as it relates to navigation accuracy. This flight (SF905C) was a long loop flight out of Crow's Landing with a navigation mode duration of 39 minutes. Both A and B computers were initialized and aligned together. F gyro had an unplanned failure during alignment and was kept off line in both computers for the remainder of the test. A 6 deg/hr bias error was inserted into the E gyro compensation after the flight was underway. This error insertion was done in the B computer only, so that A computer remained as a reference. E and F gyros

are in the body y-z plane (wing - vertical) so the preliminary F gyro failure makes the system's navigation performance more sensitive to an E gyro degradation than would otherwise be the case.

Figure 8.3.2.1 shows the reference computer's heading (modulo 360°) for the period of navigation. The MASE forcing function in Figure 8.3.2.2 is calculated on the basis of angular motion observed over the TSE accumulation period. Note the effect of azimuth angle changes on this function. The TSE plots in Figures 8.3.2.3 and .4 (for computers A and B) show how this forcing function is used to increase the MASE up to the maximum of 160 $pulses^2$ squared.

The A computer is seen to have increased TSE during the turns, but not enough to incur a failure. The E gyro bias error was inserted in B computer shortly after 2700 seconds and E gyro was taken off-line about 50 seconds later. The TSE at removal was between 40 and 160 $pulses^2$ (as seen in Figure 8.3.2.4) because the gyro was "caught" when the MASE snapped back toward its static value at the end of a two minute accumulation period. Resultant gyro fail status changed to both E and F off-line (Figure 8.3.2.5). (Later in the flight, E gyro's bias error was removed and it went on-line again at around 3500 seconds.)

The resulting attitude change of the B computational body frame compared to the A body frame is shown in Figures 8.3.2.6, .7, .8. These figures are complicated somewhat by the fact that the aircraft made a 90 degree turn while E gyro was degraded but before it was taken off-line (refer back to Figure 8.3.2.1). The beginning of the degradation caused "Δ tilt about y" and "Δ azimuth" to become non zero and vertically reach the maximums of 2.2 min and 1.4 min, respectively. The concurrent body attitude change coupled with the growing misalignment about y to produce a misalignment about x, "Δ tilt about x", as well. The 180° azimuth change at 2850 seconds adds further changes to the comparative alignment deviations.

Because of the several large azimuth turns and the short duration of navigation following gyro degradation, it cannot be expected that navigation position error will fit a simple form. Figures 8.3.2.9, .10, .11 show deviations between the two computer's computations of speed, latitude, and longitude.

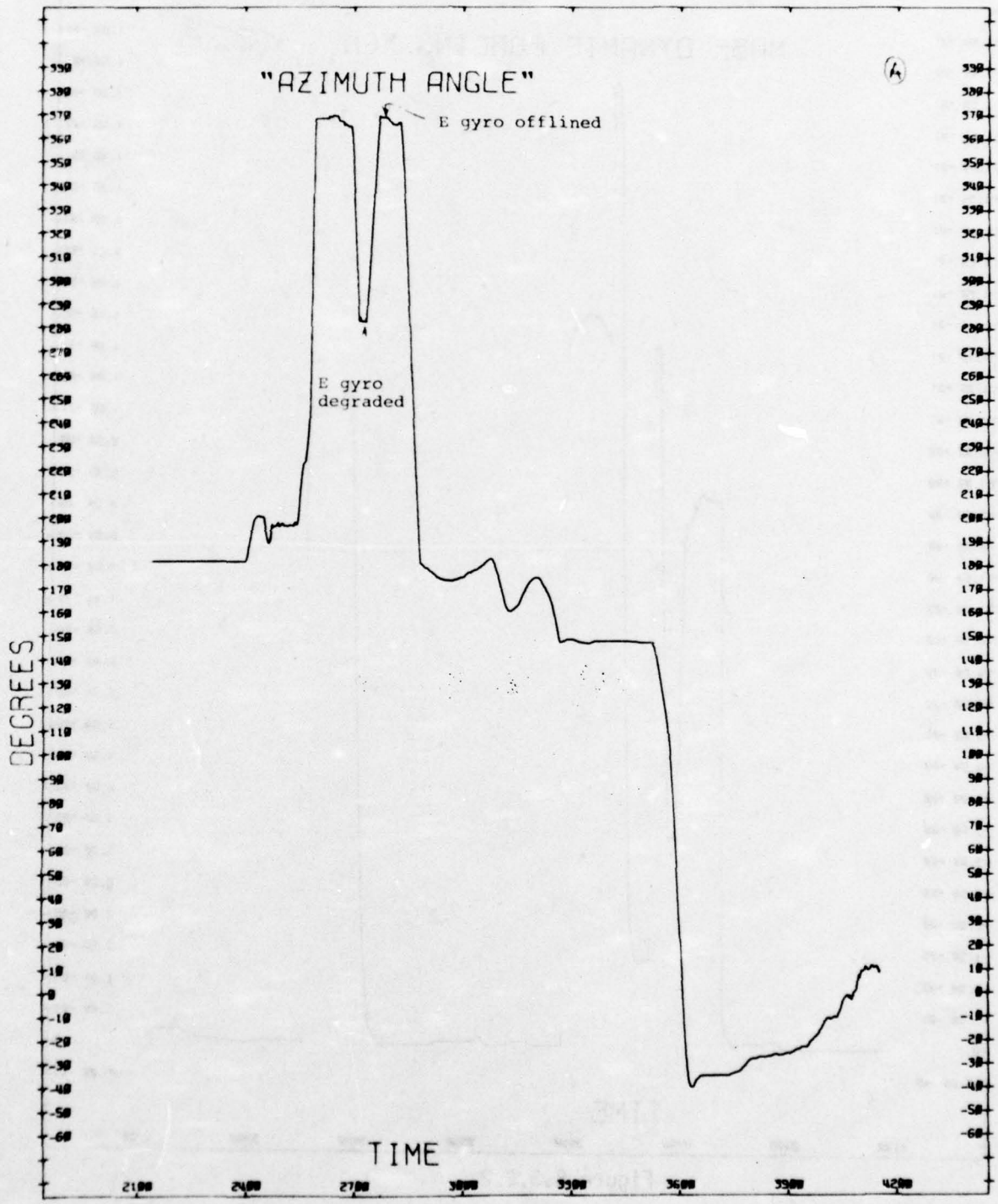


Figure 8.3.2.1.

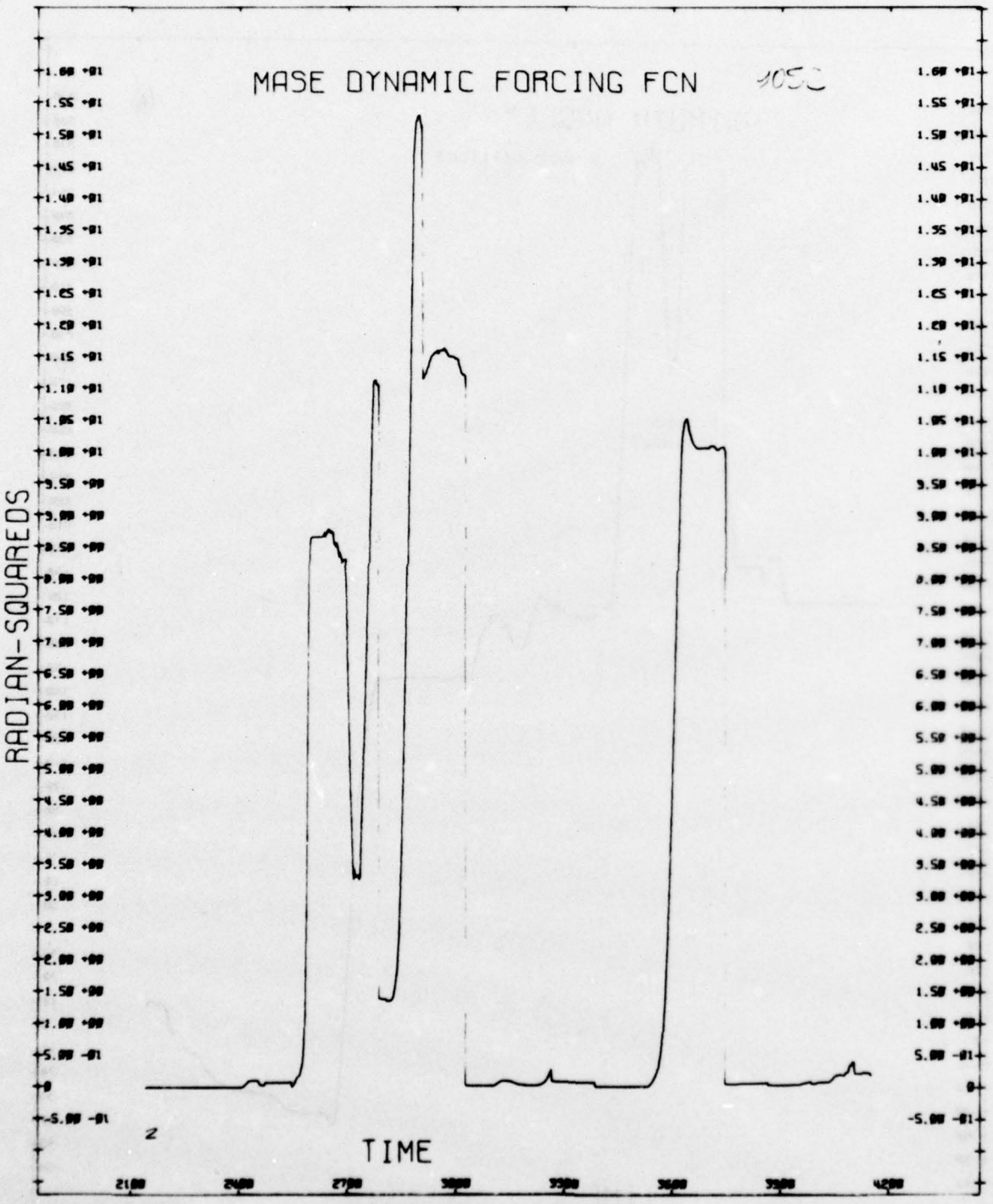


Figure 8.3.2.2

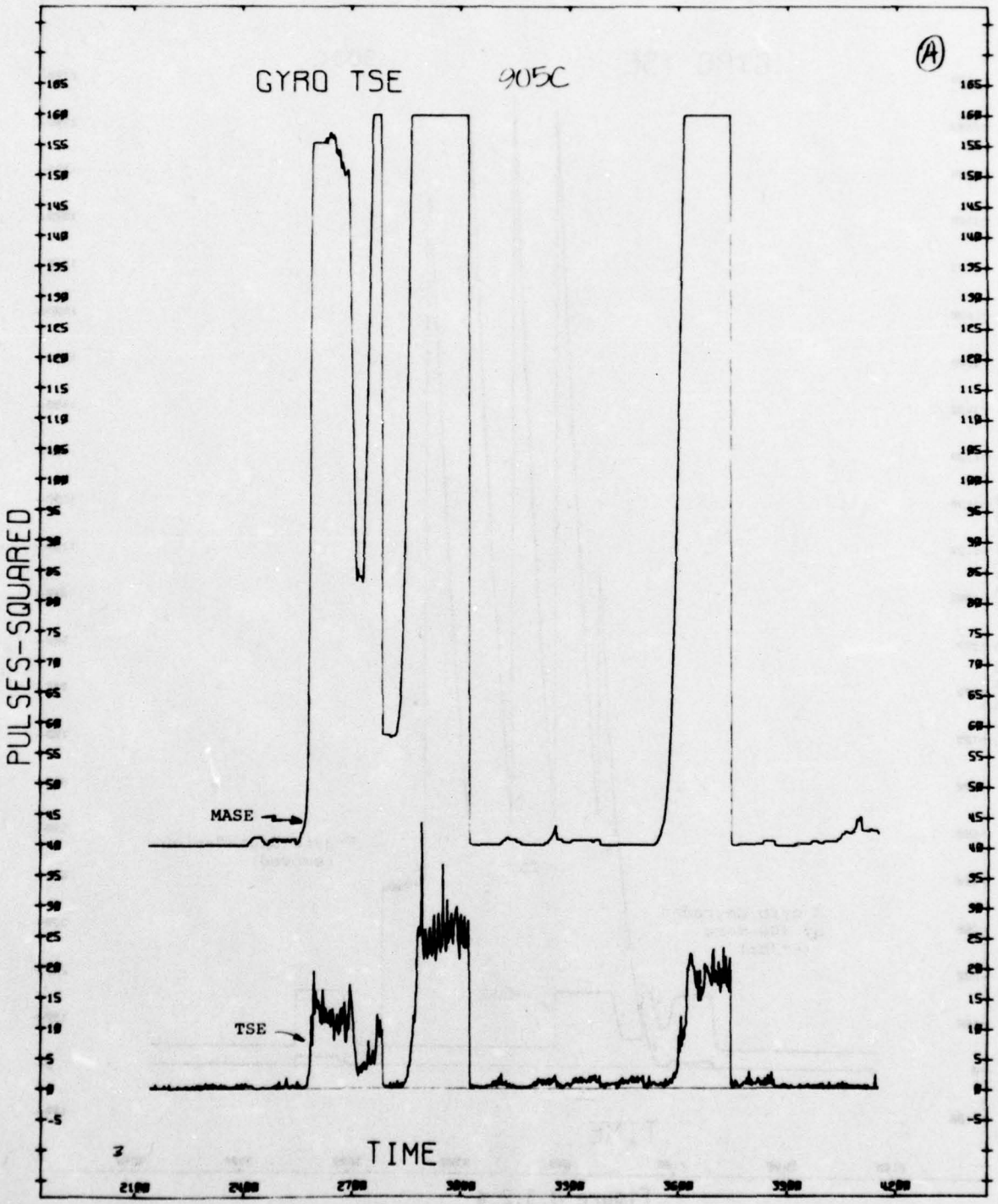


Figure 8.3.2.3

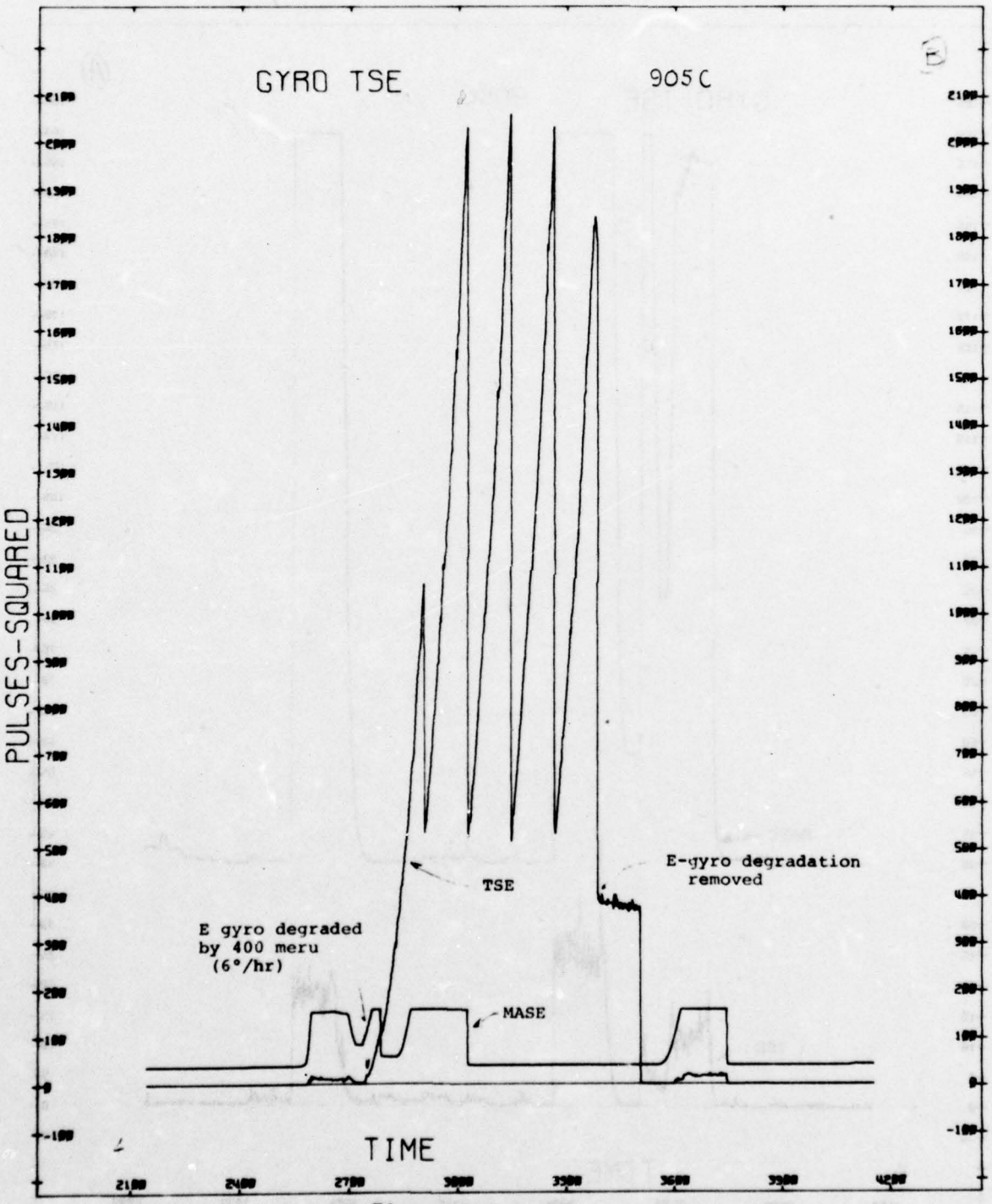

GYRO TSE
905C
PULSES-SQUARED
TIME
TSE
E-gyro degradation removed
E gyro degraded by 400 meru (6°/hr)
MASE

Figure 8.3.2.4

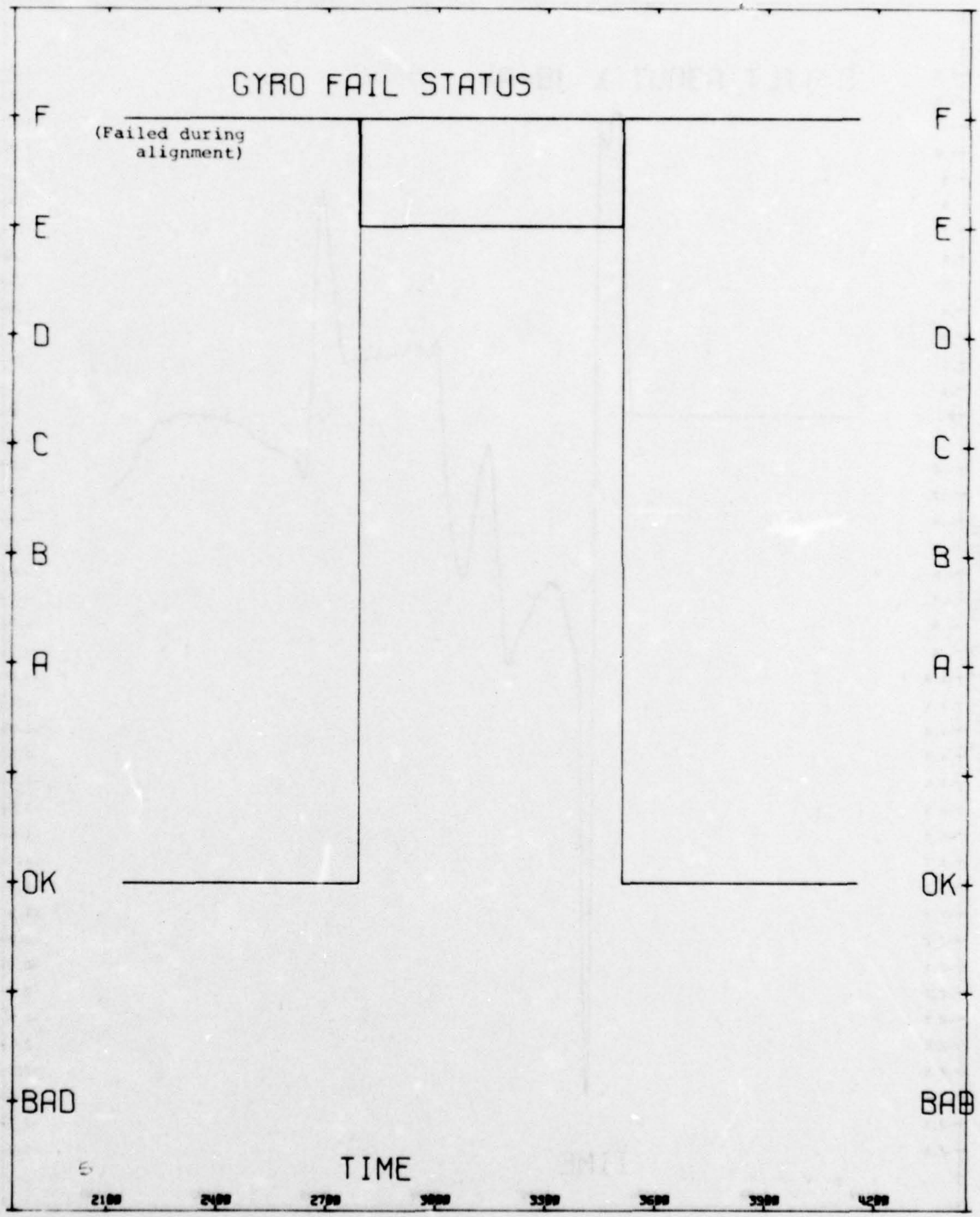

GYRO FAIL STATUS
F
(Failed during alignment)
E
D
C
B
A
OK
BAD
TIME
2100
2400
2700
3000
3300
3600
3900
4200

Figure 8.3.2.5

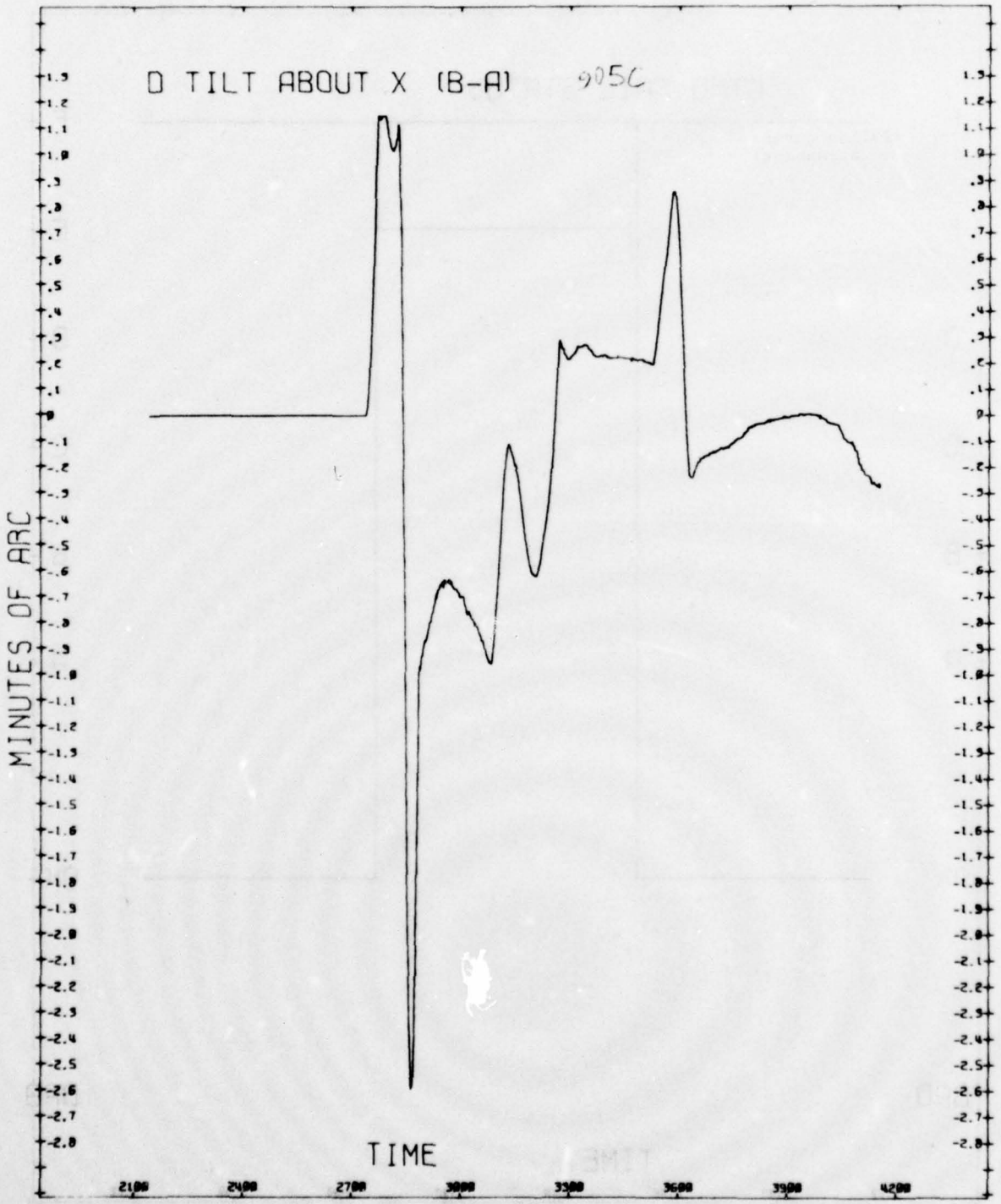

D TILT ABOUT X (B-A) 905C
MINUTES OF ARC
TIME
2100
2400
2700
3000
3300
3600
3900
4200

Figure 8.3.2.6

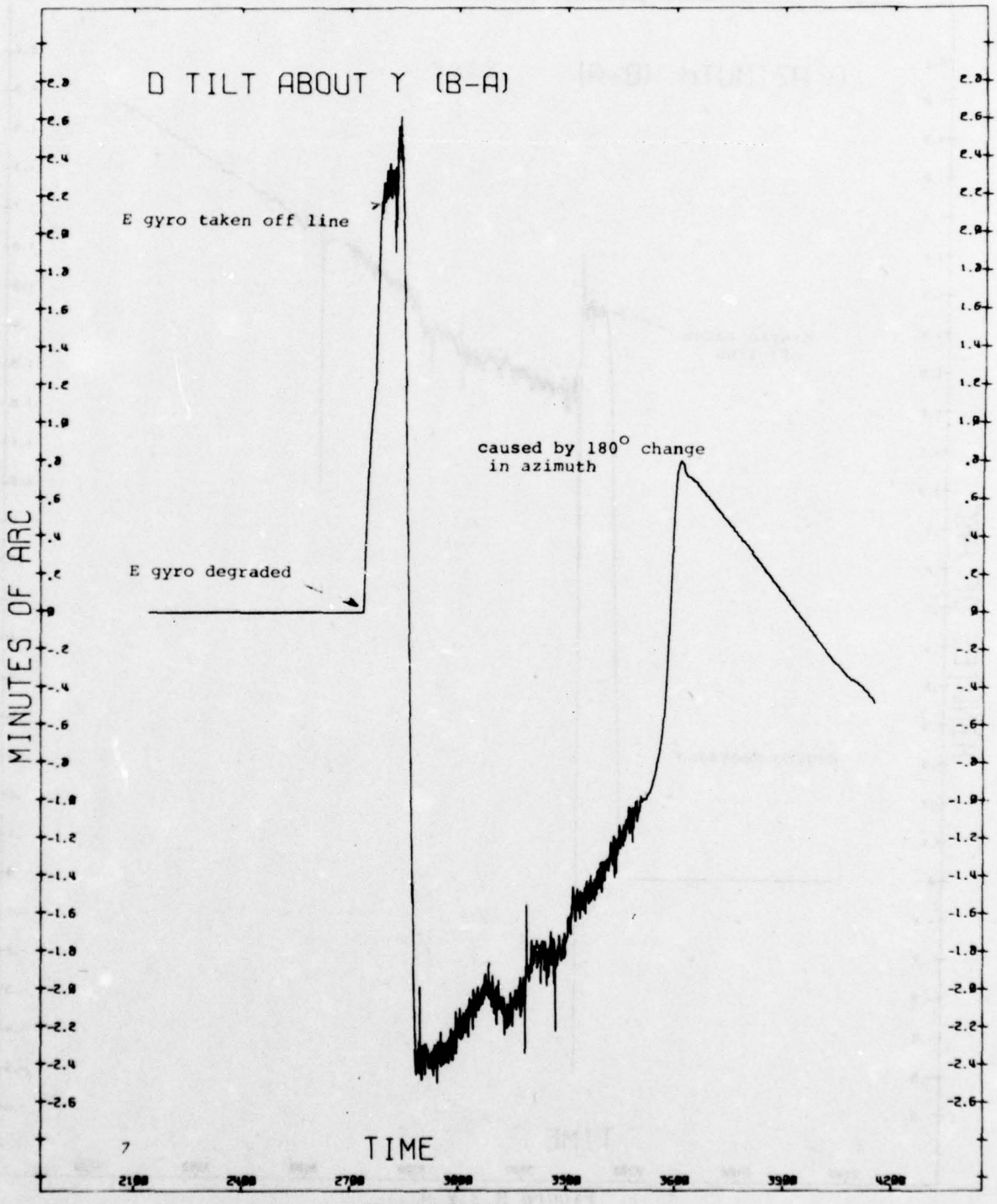

D TILT ABOUT Y (B-A)
E gyro taken off line
caused by 180° change in azimuth
E gyro degraded
MINUTES OF ARC
TIME

Figure 8.3.2.7

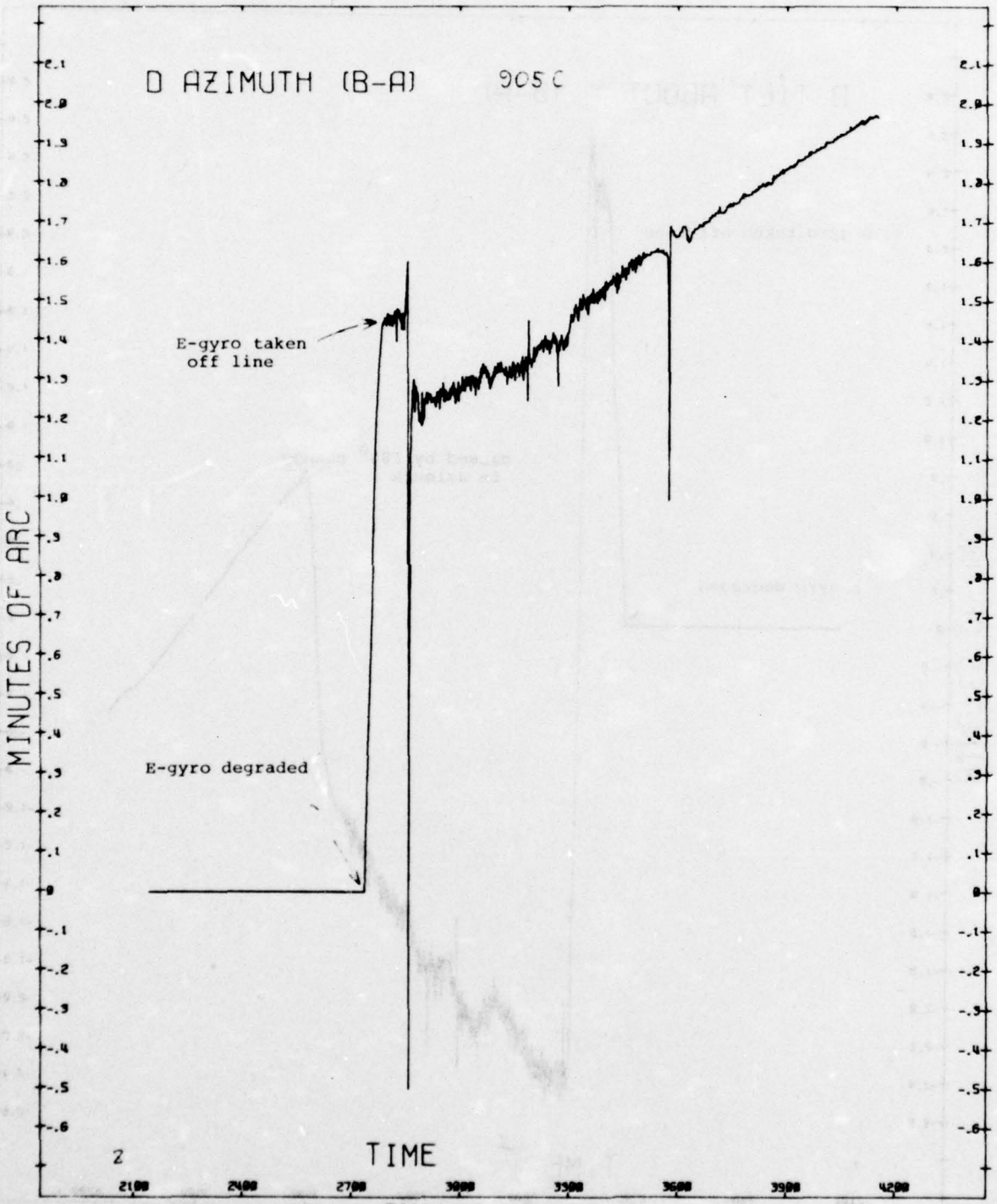

D AZIMUTH (B-A) 905 C
E-gyro taken off line
E-gyro degraded
MINUTES OF ARC
TIME
2100
2400
2700
3000
3300
3600
3900
4200

Figure 8.3.2.8

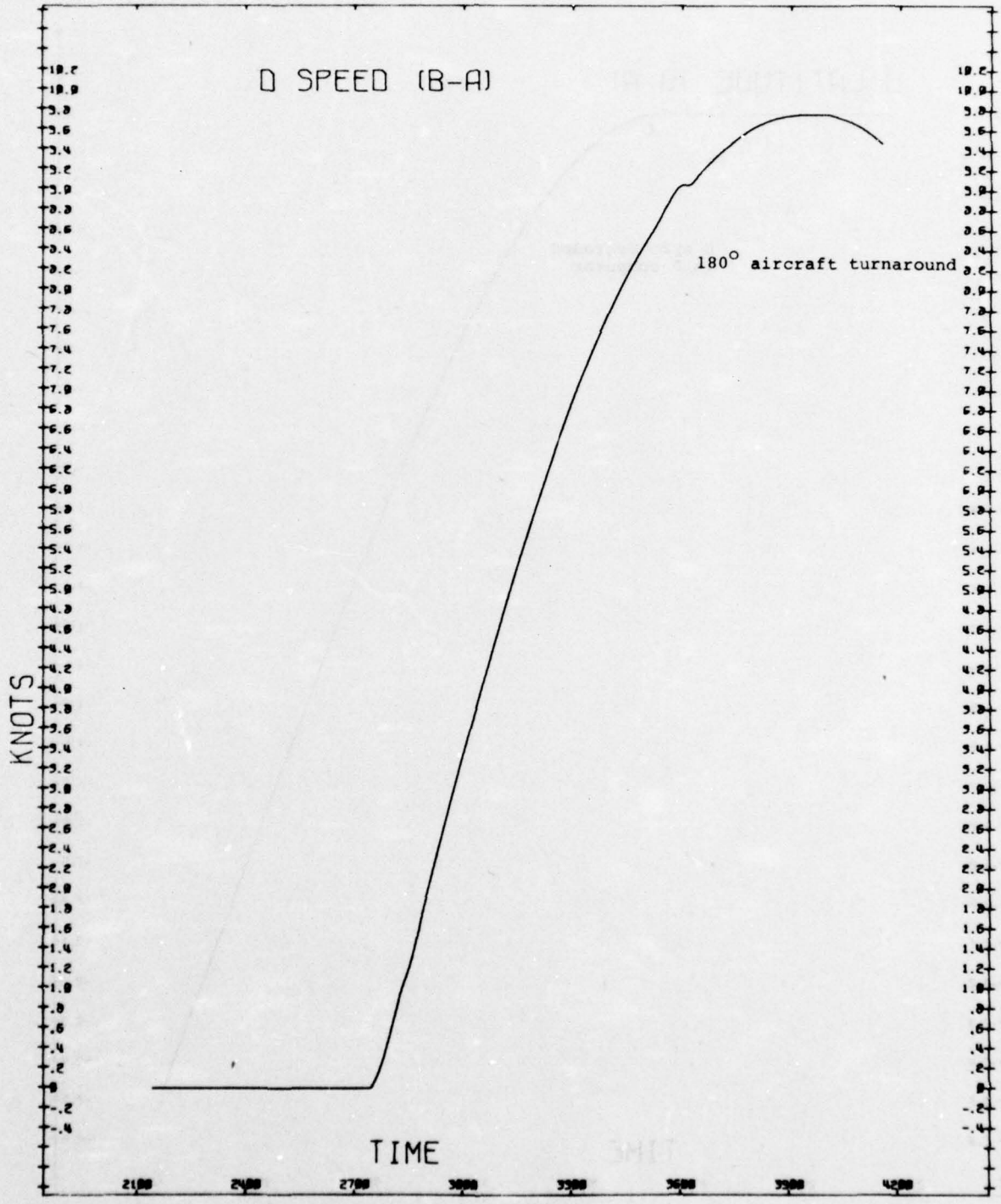


Figure 8.3.2.9

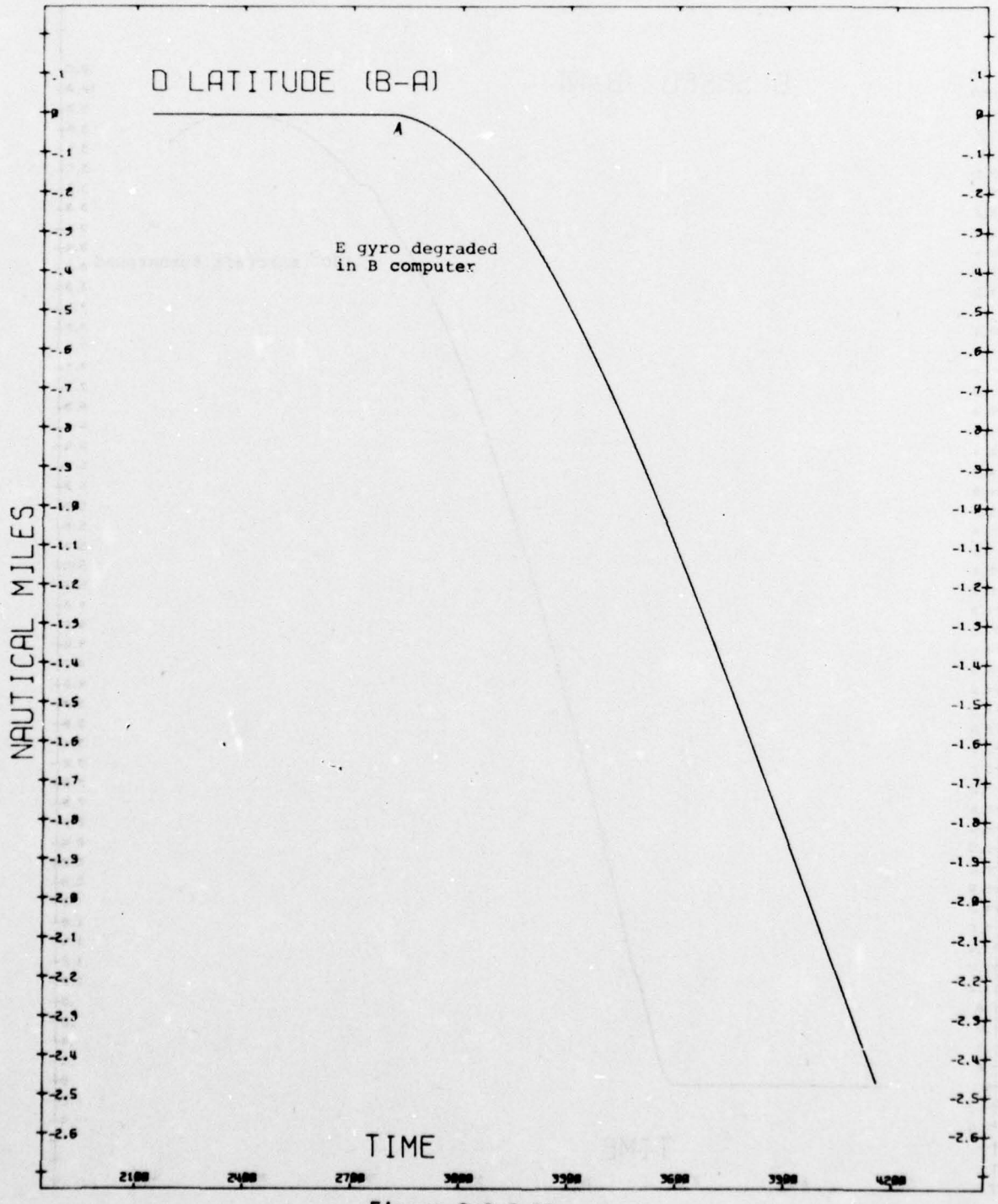


Figure 8.3.2.10

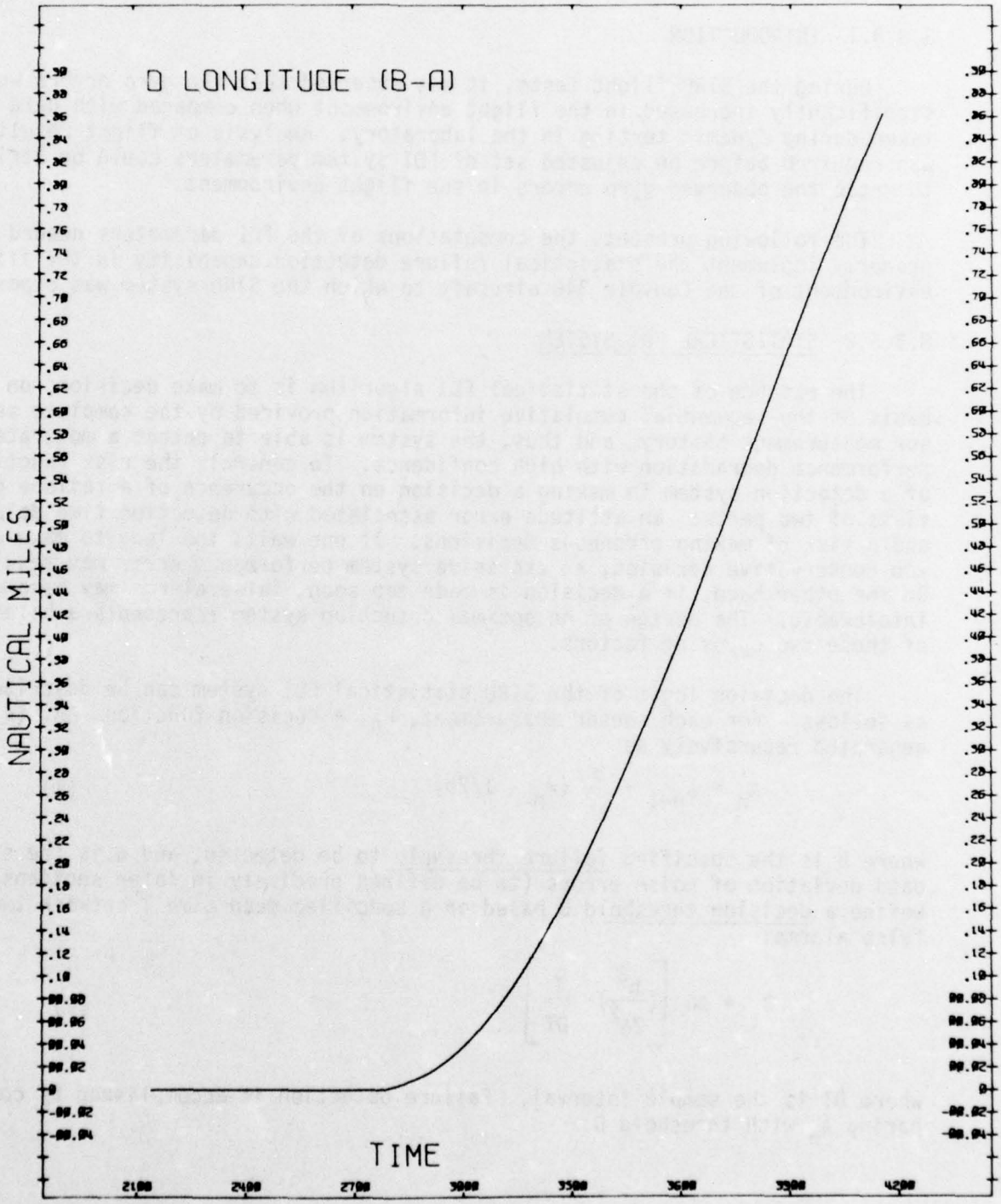


Figure 8.3.2.11

8.3.3 DETERMINATION OF STATISTICAL FDI FAILURE THRESHOLDS FOR THE FLIGHT TEST ENVIRONMENT

8.3.3.1 INTRODUCTION

During the SIRU flight tests, it was observed that the gyro errors were significantly increased in the flight environment when compared with data taken during dynamic testing in the laboratory. Analysis of flight results was required before an adjusted set of FDI system parameters could be derived to match the observed gyro errors in the flight environment.

The following presents the computations of the FDI parameters needed to properly implement the statistical failure detection capability in the flight environment of the Convair 340 aircraft to which the SIRU system was exposed.

8.3.3.2 STATISTICAL FDI SYSTEM

The essence of the statistical FDI algorithm is to make decisions on the basis of the sequential cumulative information provided by the complete sensor measurement history, and thus, the system is able to detect a moderate performance degradation with high confidence. In general, the risk function of a detection system in making a decision on the occurence of a failure consists of two parts: an attitude error associated with detection time delay and a risk of making erroneous decisions. If one waits too long to make a too conservative decision, an excessive system performance error may result. On the other hand, if a decision is made too soon, false alarms may become intolerable. The design of an optimal detection system represents a balance of these two opposing factors.

The decision logic of the SIRU statistical FDI system can be described as follows. For each sensor measurement, r_n, a decision function, Λn, is generated recursively as

$$\Lambda_n = \Lambda_{n-1} + \frac{b}{\delta^2}\,(r_n - 1/2b) \qquad (1)$$

where b is the specified failure threshold to be detected, and δ is the standatd deviation of noise errors (to be defined precisely in later sections). Define a decision threshold B based on a specified mean time T between two false alarms:

$$B = \ln\left[\left(\frac{b^2}{2\delta^2}\right)\cdot\frac{T}{DT}\right] \qquad (2)$$

where DT is the sample interval. Failure detection is accomplished by comparing Λ_n with threshold B:

$\Lambda_n \geq B$: declare failure

$0 \leq \Lambda_n < B$: take more data (3)

$\Lambda_n < 0$: reset $\Lambda_n = 0$ and continue taking data

For the specified T, the mean detection time $\tau(T)$ is given approximately by the expression

$$\tau(T) = \left[\frac{2\delta^2}{b^2} \cdot (B - 1.5)\right] \cdot DT \tag{4}$$

The failure threshold b and the decision threshold B are the two basic parameters to be specified for proper function of the statistical FDI system. Before defining their specifications, the dynamic data taken from the flight tests will be compared to the dynamic data taken from laboratory tests.

8.3.3.3 SIRU FLIGHT TEST DATA

In general, there are two approaches to specify the failure threshold. The first is to specify the failure threshold derived from mission requirements. An example is the IMU failure threshold in the shuttle mission to satisfy a required terminal footprint. The SIRU system, on the other hand, specifies failure threshold through the sensor quality. Through the laboratory experiments, the implemented threshold was specified to be 1.5 times the standard deviation of the gyro error derived from the laboratory test environment. During SIRU flight tests, it was observed that the gyro errors were greatly increased in the flight environment as compared with the laboratory dynamic test data. Therefore the implemented failure threshold must be updated to match the flight dynamic data.

Figure 8.3.3.1 illustrates a SIRU flight profile tested in Central Valley, California on September 18, 1975. The standard deviations of the six parity equation residuals are presented in Table 1. The parity residuals are sampled at 30 second intervals. Because of the limited duration of this flight, only 14 data are available to be used in computation for the 3°/sec (CCW) turn, 16 data for the 3°/sec (CW) turn, and only 6 data are used in computation for the level flights. If the maximum values are taken to be the standard deviations used for failure threshold specification, then we find for the turns

$$\delta_p = 2.88\ ^o/hr \tag{5}$$

and for level flights,

$$\delta_p = 1.01\ ^o/hr \tag{6}$$

For a comparison, two data sets from dynamic tests conducted in the laboratory environments are presented. For the oscillatory tests, with 0.5^o

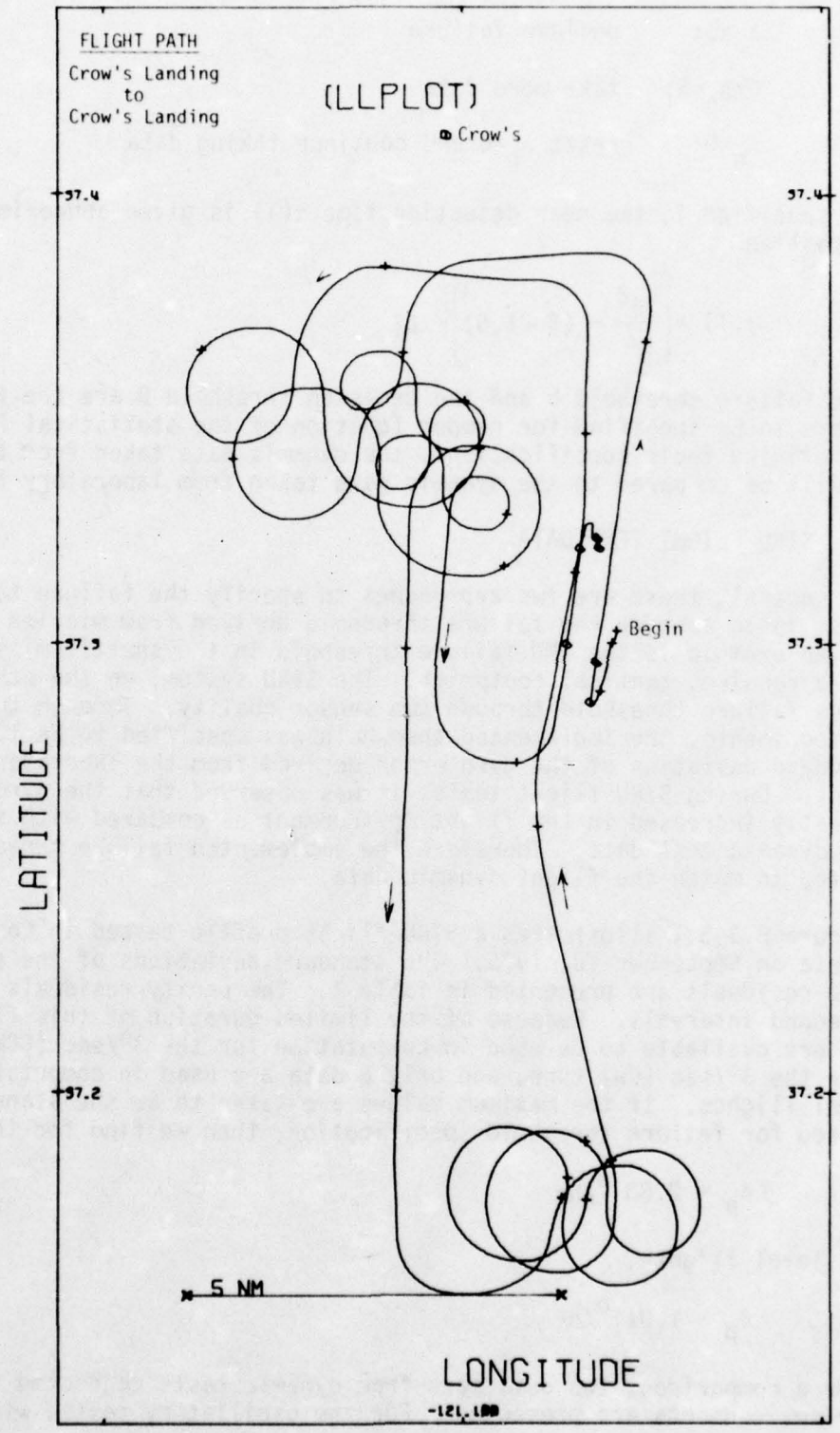


Figure 8.3.3.1
SIRU FLIGHT TEST PROFILE

peak to peak magnitude at 0.5 Hz, the parity residual standard deviation was found to be

$$\delta_p = 0.1\ ^{o}/hr \tag{7}$$

while the parity residual standard deviation for slew (turn) tests with 5°/sec was computed to be

$$\delta_p = 0.24^{o}/hr \tag{8}$$

Notice that the laboratory test data are sampled at two minute intervals. If we assume that the flight test data are uncorrelated at 30 second intervals, then the standard deviations corresponding to 30 second sample intervals for the laboratory test data can be shown to be

$$\tilde{\delta}_p = 0.1^{o}/n \cdot \sqrt{\frac{2}{0.5}} \tag{9}$$

$$= 0.2^{o}/n$$

for the oscillatory test data, and

$$\tilde{\delta}_p = 0.24^{o}/n \cdot \sqrt{\frac{2}{0.5}} \tag{10}$$

$$= 0.48^{o}/n$$

for the slew test data.

A comparison of the flight data for turning in Equation (5) and the slew test data in Equation (10) shows an increase of the standard deviation in flight test data by a factor of 6. If we compare the data in Equation (6) for the level flight under vibration environment with the laboratory oscillatory test data in Equation (9), a factor of 5 in the standard deviation of the flight test data is observed.

With this comparison as background, it is easy to see why the statistical FDI system parameters used in the laboratory are unsuitable for the flight environment. The failure threshold for laboratory testing is set at 1.5 times the standard deviation of the laboratory test data. The statistical FDI system therefore identifies errors with magnitudes greater than this threshold as indicating a "failure" in the system. In the flight environment, however, errors of this magnitude are to be interpreted as "normal." It is necessary, therefore, to increase the failure threshold to be compatible with system behavior in the flight environment.

8.3.3.4 SUGGESTED FDI IMPLEMENTATION

In this section, the proper parameters of both failure threshold b and decision threshold B will be defined for the flight environment, and the expected detection performances derived. On the basis of laboratory and flight test experiences, three parameter sets corresponding to ground operations, level flight, and turn flight phases should be implemented.

8.3.3.4.1 GROUND PHASE

Using the parameters derived from laboratory test data, the statistical FDI system functioned properly, and no updates of either failure or decision thresholds is required.

8.3.3.4.2 LEVEL FLIGHT PHASE

The following parameters are used to specify the failure threshold b and decision threshold B. The parity residual standard deviation is computed to be the RMS of the six parity residual errors shown in Table 1.

$$\begin{aligned} \delta_p &= 0.67^{\circ}/hr \\ T &= \text{Mean Time between False Alarms} \\ &= 24 \text{ hours} \\ DT &= \text{sample time} \\ &= 30 \text{ seconds} \end{aligned} \tag{11}$$

From the laboratory tests, a failure threshold b of 1.5 times the gyro standard deviation δ_g is specified

$$b = 1.5\ \delta_g \tag{12}$$

where

$$\delta_g = \frac{1}{\sqrt{2}} \cdot \delta_p \tag{13}$$

therefore the system can detect an error

$$\begin{aligned} b_L &= 1.5 \cdot \frac{1}{\sqrt{2}} \cdot 0.67 \\ &= 0.71^{\circ}/hr. \end{aligned} \tag{14}$$

Based on evaluation of the flight data, the failure threshold b_L for the level flight phase will be specified to be 0.75°/hr.

FLIGHT MODE	PARITY RESIDUALS STANDARD DEVIATION (°/hr)					
	δ_{p1}	δ_{p2}	δ_{p3}	δ_{p4}	δ_{p5}	δ_{p6}
3°/sec (CCW)	1.04	2.28	0.96	0.70	2.56	2.88
3°/sec (CW)	1.24	1.99	0.88	0.76	1.96	2.10
Level Flight	0.36	0.69	1.01	0.68	0.33	0.72

Table 1

SIRU Flight Test Data

Rewrite Equation (2) to be consistent with the nomenclatures:

$$B_L = \ln \left[\left(\frac{b_{L,p}^2}{2\delta_{L,p}^2} \right) \cdot \frac{T}{DT} \right] \tag{15}$$

where $B_{L,p}$ and $b_{L,p}$ are the standard deviation and the failure magnitude at the parity residual outputs:

$$\begin{aligned} \delta_{L,p} &= 0.67^o/hr \\ b_{L,p} &= \cos(31^o43') \cdot b_L \\ &= 0.64^o/hr \end{aligned} \tag{16}$$

Then B_L is computed to be

$$B_L = \ln \left[\left(\frac{0.64^2}{2 \cdot 0.67^2} \right) \cdot \frac{(24 \cdot 60)}{0.5} \right] \tag{17}$$

$$= 7.17$$

The mean detection time $\tau_L(T)$ can be computed from Equation (4)

$$\tau_L(T) = \left[\frac{2\delta_{L,p}^2}{b_{L,p}^2} \cdot (B_L - 1.5) \right] \cdot DT \tag{18}$$

$$= \left[\frac{2 \cdot 0.67^2}{0.64^2} \cdot (7.17 - 1.5) \right] \cdot 30$$

$$= 373 \text{ seconds}$$

The resulting attitude error due to the detection time can be calculated to be

$$\begin{aligned} \psi &= \frac{1}{\sqrt{2}} \cdot b_L \cdot \tau_L(T) \\ &= \frac{1}{\sqrt{2}} \cdot 0.75 \cdot 373 \\ &= 198 \widehat{sec} \end{aligned} \tag{19}$$

In summary, the statistical FDI system for the level flight phase can detect a gyro error magnitude of $0.75^o/hr$ with a resultant attitude error of 198 $\widehat{sec}$ for a specified confidence of 24 hours between false alarms.

8.3.3.4.3 TURN FLIGHT PHASE

The parity residual standard deviation is computed to be the RMS of the six values listed for 3°/sec (CCW) in Table 1:

$$\delta_{T,p} = 1.94^{o}/hr \tag{20}$$

In general, there is only a relatively short duration of turning flight in any overall flight profile. If we assume that the turn flight duration is 10% of the total flight time, then a balanced specification of mean time between false alarms should be

$$T_T = 10\% \times 24 \text{ hrs} = 2.4 \text{ hrs} \tag{21}$$

Using the same approach as in Section 8.3.3.4.2, specify the failure threshold b_T to be

$$b_T = 1.5 \cdot \frac{1}{\sqrt{2}} \cdot 1.94 \tag{22}$$

$$= 2.06^{o}/hr$$

Specify b_T to be 2.5^{o}/hr. The decision threshold B_T can now be computed

$$B_T = \ell n \left(\frac{b_{T,p}^2}{2\delta_{T,p}^2}\right) \cdot \frac{T_T}{DT} \tag{23}$$

where

$$b_{T,p} = \cos(31^{o}43') \cdot 2.5$$

$$= 2.13^{o}/hr \tag{24}$$

$$\delta_{T,p} = 1.94^{o}/hr$$

Therefore

$$B_T = \ell n \left[\left(\frac{2.13^2}{2 \cdot 1.94^2}\right) \cdot \frac{(24 \cdot 60)}{0.5}\right] \tag{25}$$

$$= 5.16$$

Similarly the mean detection time is

$$\tau_T(T) = \left[\frac{2\delta_{T,p}^2}{b_{T,p}^2}\ (B_T - 1.5)\right] \cdot DT \qquad (26)$$

$$= \left[\frac{2 \cdot 1.94^2}{2.13^2}\ \cdot (5.16 - 1.5)\right] \cdot 30$$

$$= 182 \text{ seconds}$$

The resulting attitude error due to the detection time can be shown to be

$$\psi = \frac{1}{\sqrt{2}} \cdot b_T \cdot \tau_T(T) \qquad (27)$$

$$= \frac{1}{\sqrt{2}} \cdot 2.5 \cdot 182$$

$$= 322 \ \widehat{\text{sec}}$$

Thus, the statistical FDI system for the turn-flight phase can detect a gyro failure magnitude of 2.5°/hr and results in an attitude error of 322 $\widehat{\text{sec}}$ for a specified confidence of 24 hours between false alarms over the entire flight duration.

To check the reasonableness of the implemented values of the failure and decision threshold, consider the decision function magnitude generated by a maximum error of 2.88°/hr (Table 1).

Assume that the error occurred after reset of the preceeding sample. Then utilizing Equation (1):

$$\Lambda_n = \Lambda_{n-1} + \frac{b_{T,p}}{\delta_{T,p}^2}\ \cdot \left(r_n - \frac{1}{2} b_{T,p}\right) \qquad (28)$$

$$= 0 + \frac{2.13}{1.94^2}\ \cdot \left(2.88 - \frac{1}{2}\ \cdot 2.13\right)$$

$$= 1.03$$

A comparison of Λ_n with the decision threshold B_T of 5.16 indicates that B_T presents a safety factor of 5 preventing the error (2.88°/hr) from generating a false alarm.

8.3.3.5 CONCLUSION

The preceeding analyzes the SIRU statistical FDI system for the flight test environments observed in recent flight tests of the SIRU system. The flight test data was processed and compared with the laboratory test data. It was shown that an increase of a factor of five in the sensor errors has been observed in the flight test environment. As a result, it was concluded that for the statistical FDI system to function properly in the observed flight test environments, the FDI parameters must be modified to match the sensor error data in the real flight environments. The parameters of the failure threshold are then specified to be 0.75^{o}/hr and 2.5^{o}/hr for the level and turn-flight phases, respectively. The decision thresholds, during both level and turn-flight phases, are also suggested. The resulting attitude errors from the detection delay in the level flight and the turn flight phase are shown to be 198 $\widehat{\text{sec}}$ and 322 $\widehat{\text{sec}}$ respectively.

No consideration is given to corrective action which might be taken to reduce the errors observed in the flight environment. A significant portion of these larger errors are known to be related to the instrument scale factor compensation routine implemented, to an uncertainty in the instrument misalignments, and to the rigid mounting fixture used in flight. Corrective action can be taken to alleviate these contributions to the observed errors, thus making it possible to implement the statistical FDI system with thresholds not significantly higher than those used in the laboratory environment. This would reduce the projected attitude errors presented by a factor of approximately 5.

EIGHTH BIENNIAL GUIDANCE TEST SYMPOSIUM

MICRON CONFIGURED TO MEET STANDARD MEDIUM ACCURACY NAVIGATOR SPECIFICATION

AUTHOR: J. C. PINSON

ROCKWELL INTERNATIONAL
AUTONETICS GROUP
ANAHEIM, CALIFORNIA

MICRON Configured to Meet Standard Medium

Accuracy Navigator Specification

1. Introduction

MICRON is a low cost, strapdown inertial navigation system being developed by Rockwell International Corporation under contract from the U. S. Air Force Avionics Laboratory at Wright-Patterson Air Force Base. MICRON is being developed as the standard medium accuracy navigation system (0.8 nautical mile per hour (1.5 km/hr) CEP rate) for future aircraft/missiles requiring medium accuracy.(1)

The micro-electrostatic gyro (MESG) is the heart of the MICRON system. The MESG consists of a one centimeter diameter spherical rotor suspended electrostatically by eight (spherical triangle shaped) capacitor plates. The rotor is untorqued, so its rotor spin axis is inertially fixed. The gyro is used in a strapdown mechanization and uses a unique mass-unbalance modulation technique for obtaining a whole angle reading of the gyro case attitude with respect to the rotor spin axis.(2)

Two N57A brassboard MICRON systems have been built and tested. The test results show better performance than the 0.8 nautical mile per hour (1.5 km/hr) performance goal under van test and flight test environments.

The contract effort now underway is to design, fabricate and test a MICRON Engineering Prototype Model (EPM). A design improvement, inertial instrument assembly rotation, has been incorporated in EPM to reduce navigation errors observed in the N57A brassboard MICRON tests, particularly velocity errors. The MICRON EPM system is configured to fully meet the standard medium accuracy navigator specification, and will be tested at the Holloman Air Force Base Central Inertial Guidance Test Facility early in 1977. The system (including inertial instruments, instrument electronics, computer, analog I/O, dual redundant digital I/O, and power supply) characteristics are:

(1) Jerry A. Schwarz, "Micro-Navigator (MICRON)", Presented to AGARD at the XXXth Technical Meeting of the Avionics Panel on Medium Accuracy Low Cost Navigation 8-12 Sept. 1975, Sandefjord, Norway, 18 July 1975

(2) Robert R. Duncan, "A Strapdown Inertial Navigator Using Miniature Electrostatic Gyros" Autonetics Group of Rockwell International, Anaheim, California, 1 March 1973

Acquisition Price	$ 50,000
10-year Life Cycle Cost	$100,000
MTBF	1200 hrs in tactical aircraft environment
Accuracy	0.8 n mi/hr CEP rate 2.5 ft/sec/axis velocity error
Size	960 in^3 (15,700 cm^3)
Weight	39 lbs (18 kg)
Power	270 watts

In the material that follows, section 2 shows that accelerometer and gyro angle readout errors cause much larger system velocity and position errors in a strapdown system than they do in a stabilized platform system. Section 3 shows that incorporation of inertial instrument assembly rotation is a cost-effective solution to this problem in a strapdown system and has other benefits as well. Section 4 summarizes the results of a series of laboratory navigation runs that validate the above conclusions.

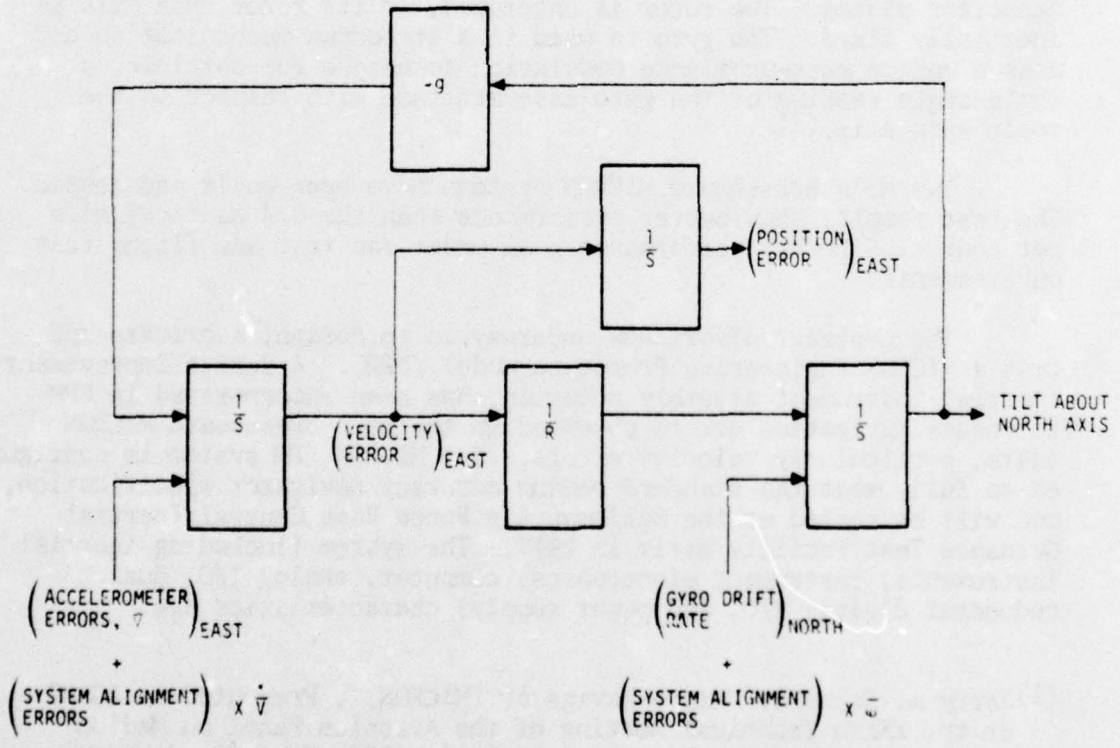


Fig. 1 Inertial Navigator East Channel Error Block Diagram

2. Error Propagations in a Strapdown System

Figure 1 shows a block diagram representation of the simplified single-channel error equation for an inertial navigator. The east channel is shown. The north channel diagram is similar and can be obtained by substituting, in Fig. 1, north for east and minus east for north. The interpretation of the quantities labeled on the block diagram is obvious when the navigator being analyzed has a locally level gyro stabilized platform. The block diagram is, however, equally applicable in analyzing the errors in any inertial navigator, including a strapdown system.[3] To use the block diagram of Fig. 1 to analyze the errors in a strapdown system, it is necessary to form error vectors of accelerometer and gyro errors. Form the accelerometer error vector by putting the three accelerometer errors each along their respective sensitive axes; form the gyro error vector similarly. The level-and-east component of this accelerometer error vector is used to drive the east channel error block diagram of Fig. 1, as is the level-and-north component of the gyro drift rate error vector. Using these inputs, the east position error and east velocity error for the strapdown system are obtained just as shown on the block diagram; the block diagram tilt output gives the error (as a rotation about north) in the vertical computed by the strapdown navigator. It is significant to notice that constant accelerometer errors in a strapdown system lead to a time varying driving function input to the error block diagram when the aircraft attitude changes, in particular, when aircraft heading changes.

The error block diagram of Fig. 1 can also be used to determine the steady-state tilt error at the end of stationary self-alinement. When operated in a self-alinement mode, the navigator has additional loops mechanized to effect error damping. When the oscillatory errors are damped during stationary alinement, it is seen from Fig. 1 that

$$\begin{pmatrix} \text{Tilt} \\ \text{About} \\ \text{North} \\ \text{Axis} \end{pmatrix} \cdot g - \begin{pmatrix} \text{Accelerometer} \\ \text{Errors} \end{pmatrix}_{\text{East}} = 0 \qquad (1)$$

Because of the correlated tilt established during alinement, the accelerometer errors cause no velocity or position errors when the system is switched out of the alinement mode and into the navigate mode. And for

[3] Cornelius T. Leondes, "Guidance and Control of Aerospace Vehicles," University of California Engineering and Sciences Extension Series, McGraw-Hill Book Company, Inc., New York, 1963

a stabilized platform system, where the accelerometer error vector remains nearly fixed with respect to north and east regardless of aircraft maneuvers, little velocity or position error is caused by aircraft attitude (heading) changes during flight.

In a strapdown system, however, significant velocity and position errors are caused by constant accelerometer errors. An analytical example in which strapdown system velocity and position errors are driven by a constant accelerometer bias error is shown in Fig. 2. The only error source present for this example is a constant accelerometer bias error of 100 ug's along the roll axis of the aircraft. The aircraft is headed east during alinement wherein the 100 ug accelerometer bias error produces a 20 sec-of-arc tilt about a north axis. When the navigator is switched into the navigate mode at t = -10 min, no velocity or position errors begin. But when the aircraft in the example takes off and flies south at t = 0, the tilt error (still about north) and the accelerometer error (now south) cause equal position and velocity errors in the east and north channels, as shown in Fig. 2. The aircraft in the example turns and flies east at t = 42 min, and south at t = 84 min, continuing to pump the velocity and position errors, with the result shown in Fig. 2. The east and north velocity errors each peak at 2.5 ft/sec at 21 minutes, 5 ft/sec at 63 minutes, and 7.5 ft/sec at 105 minutes. Radial position error peaks at 5650 ft at 42 and 84 minutes and 11,300 ft at 126 minutes. It can be computed from the velocity and position error curves of Fig. 2 that the peak time-rms velocity error in either east or north in the time interval between 0 and 120 minutes is 3.9 ft/sec (equal, as it happens, in east and north) and that the least squares fitted straight line to radial position error between times zero and 60 minutes has a slope of 0.98 n mi/hr.

The Fig. 2 example can be generalized somewhat by considering an ensemble of aircraft flights, each with the same flight profile, and each with a constant accelerometer bias error along the aircraft roll axis which varies from flight to flight and is distributed normally with zero mean and 100 ug rms value. The ensemble and time-rms velocity error is 3.9 ft/sec per channel, as before. The ensemble CEP rate is the radial error rate associated with the median magnitude bias error, 68 ug. The CEP rate is 0.98 n mi/hr (68/100) = 0.67 n mi/hr.

The example worked out here shows the system errors resulting from a single accelerometer error source for one flight profile. It illustrates, however, a number of points worthy of note.

a. Accelerometer errors, and gyro angle readout errors (which propagate similarly) are sources of significant system errors in a strap-

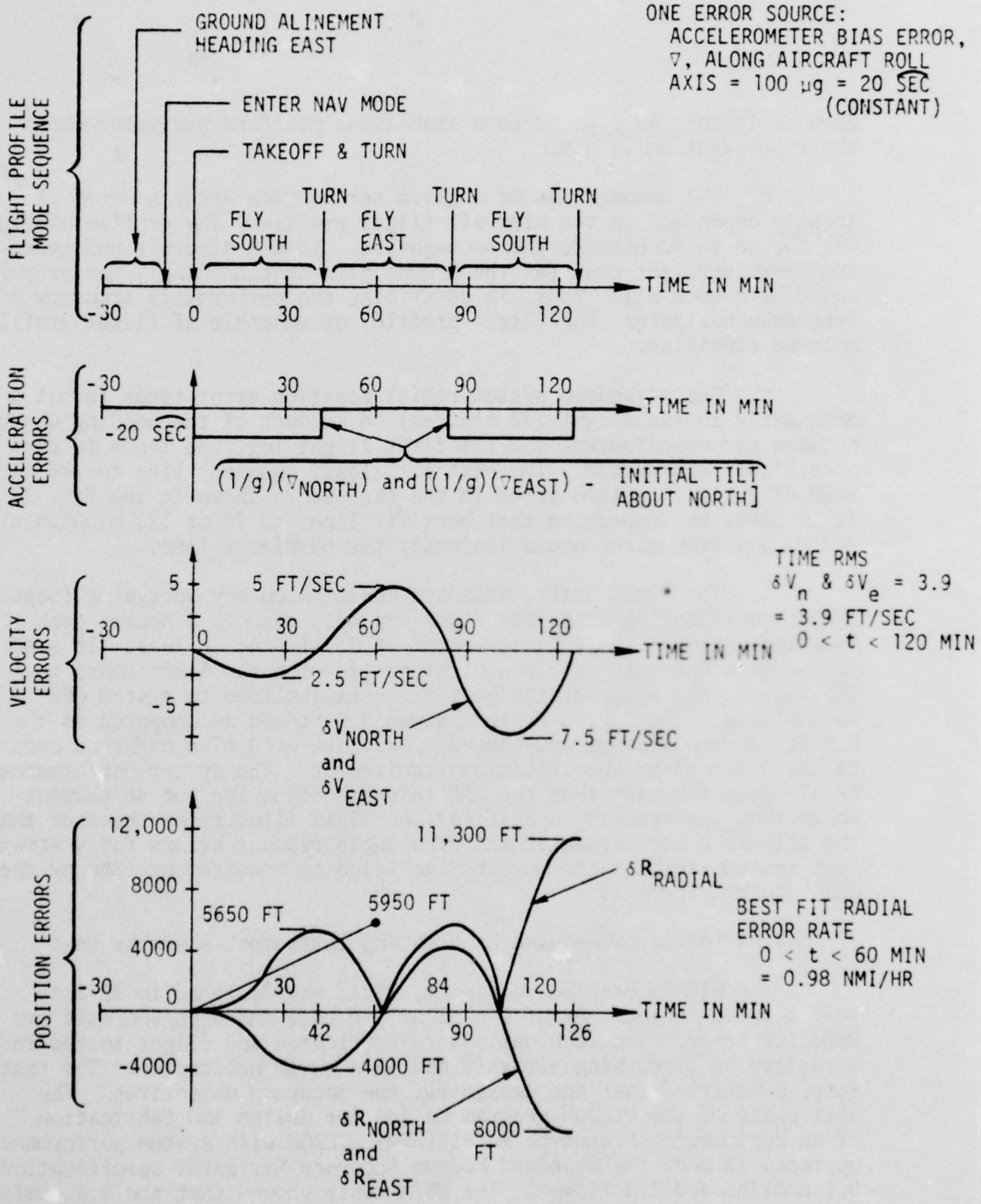


Fig. 2 Errors Caused by a Constant Accelerometer Bias Error in a Strapdown System

down navigator, as opposed to a stabilized platform navigator where their propagation is nil.

b. The propagation of a given set of such error sources is greatly dependent on the aircraft flight profile. The profile of Fig. 2 was chosen to accentuate the propagation. If the aircraft had taken off and flown straight east (at the ground alinement heading), the propagation would have been nil. Thus, in describing the performance accuracy of a strapdown navigator, the flight profile, or ensemble of flight profiles, must be specified.

c. The strapdown system radial position error tends to hit a peak early in the flight (42 minutes) on account of the heading change between ground alinement and the first flight leg, and tends to grow more slowly thereafter. The best fit (least squares) line to the first hour of radial position error in the example is shown in the Fig. 2. It is clear by inspection that best fit lines to 90 or 120 minutes of radial position error would lie under the 60-minute line.

d. The Final Draft, Standard Medium Accuracy Navigator (Sept. 1976) specification calls for a per channel, zero to 2 hours, peak time-and-ensemble rms velocity error of 2.5 ft/sec or less. It also calls for a CEP rate of 0.8 n mi/hr or less for the first hour; the CEP rate is the slope of the best fit straight line to system CEP versus time. The Fig. 2 system showed 3.9 ft/sec as compared to the 2.5 ft/sec requirement and showed a CEP rate of 0.67 n mi/hr as compared to the 0.8 n mi/hr specification requirement. The system performance is 17 percent better than the CEP rate specification but 56 percent worse than the velocity specification. This illustrates the fact that the allowable accelerometer and gyro angle readout errors for a strapdown system are dictated more by the velocity requirement than by the CEP rate requirement.

3. Navigation Error Reduced by Rotating Instrument Assembly Unit

The MICRON brassboard system, N57A, was designed in 1972 to meet accuracy objectives of 1 n mi/hr CEP rate and 5 ft/sec/axis rms velocity error. Two such units were fabricated and flight tested in a variety of fixed wing aircraft and in a UH-1H helicopter. The test results verified that the design met the accuracy objectives. The next phase of the MICRON program called for design and fabrication of an Engineering Prototype Model (EPM) MICRON with system performance upgraded to meet the Standard Medium Accuracy Navigator specification - 0.8 n mi/hr and 2.5 ft/sec. The N57A tests showed that the 0.8 n mi/hr requirement could be met with the N57A design but that substantial changes would have to be made to meet the 2.5 ft/sec requirement.

N57A uses accelerometers whose bias stability is about 50 ug rms. The MESG wide-angle pickoff mechanization in N57A gives the gyro case attitude with respect to the gyro rotor spin axis to an rms accuracy of about 0.1 milliradian. This angle readout error is roughly equivalent to 100 ug rms of accelerometer error in terms of system error propagation. It is clear from the example of the previous section that the accelerometer and gyro angle readout accuracies require improvement to meet the Standard Nav Spec velocity requirement with the N57A mechanization. The accelerometers would have to be replaced with more accurate and, necessarily, more expensive ones. The 0.1 mr gyro angle readout error is the rms residual that remains after a rather complex error model has been used to compensate the raw gyro output in the MICRON computer. Reducing this 0.1 mr error would mean development of additional error model terms to characterize this residual error, implementation of additional calibration procedures to determine the parameter values in the model for each gyro and mechanization in system computer of the additional model terms to effect the compensation.

An alternative approach is more cost-effective in reducing system error than the approach of reducing instrument errors described in the previous paragraph. This alternative approach can be introduced as follows. Notice that the system errors in the Fig. 2 example were initiated by the step changes in acceleration error that were caused by the changes in system heading. If the system could be operated in such a way that heading changed continuously through 360° many times per 84 minutes, these acceleration errors would be averaged out, largely. To accomplish this a single axis of rotation is added to the strapdown system. The strapdown instrument set, the instrument assembly unit (IAU), is rotated back and forth through 360° about aircraft yaw (mostly near vertical). The IAU is rotated continuously in both the alinement and navigation modes. During alinement, the effect of the horizontal component of accelerometer error is averaged out and no leveling error occurs. This error continues to be averaged out in the navigation mode, so no navigation error results.

A motor is used to turn the IAU at a uniform rate in yaw relative to the aircraft through 360° in one minute. Having rotated 360°, the motor reverses direction and the IAU is rotated back through 360° in the other direction at the same rate... and so forth. No sliprings are required. During this rotation procedure, MICRON continues to operate as a strapdown navigator, continuously computing latitude, longitude, altitude, north, east, and vertical velocities, and IAU attitude. In order to obtain aircraft attitude, a resolver is added to the IAU rotation axis to allow conversion of IAU attitude to aircraft attitude. Thus, the rotation has little impact on the

basic operation of MICRON as a strapdown navigator but rather is added to average out some error sources and improve accuracy. Rotation axis alinement, bearing runout, rotation rate and angle--none of these need to be rightly specified. The accuracy of the resolver needed on the rotation axis is determined only by the accuracy required in the determination of aircraft yaw attitude. If a failure occurs which stops IAU rotation, the system will continue to operate but with the somewhat larger errors associated with a non-rotated system.

In addition to averaging out the accelerometer errors, IAU rotation also reduces errors occurring in the MICRON micro-electrostatic gyros (MESGs). Figure 3 shows a projected representation of the MESG. The gyro electrodes are shown, each an octant of a sphere. The IAU rotation axis is parallel to $\bar{I}_R$, a vector from the center of the sphere pointing straight up out of the paper through one of the electrode centers. The spherical gyro rotor (not shown) is supported electrostatically within the electrodes, and its spin axis is shown as $\bar{I}_S$, a vector perpendicular to the surface of the sphere. The location of the spin axis on the sphere is represented by two Euler angles, a longitude angle ϕ relative to an electrode-fixed reference and a co-latitude angle θ, both with $\bar{I}_R$ taken as the pole of the coordinate system. In this strapdown system, the spin axis can, at one time or another, assume every orientation relative to the electrode pattern. That is, ϕ, θ can take on their full range of values ($0 < \phi < 360^\circ$, $0 < \theta < 180^\circ$). The rotor spin-axis orientation is nearly fixed relative to inertial space; therefore, the useful output of the gyro consists of determining ϕ and θ by means of a wide-angle pickoff.*

Two sorts of errors exist in the MESG operation: (1) pickoff errors, i.e., errors in determining ϕ, θ, and (2) drift-rate errors, i.e., motion of the spin axis in inertial space. Each of these errors can be represented as an error vector tangent to the surface of the sphere at the emergence point of $\bar{I}_S$. Each of these error vectors can be represented as north and east components (relative to $\bar{I}_R$ as the pole) along $\bar{I}_N$ and $\bar{I}_E$ shown in Figure 3. In the MICRON mechanization, the angle errors are modeled as a function of ϕ, θ, the model coefficient values calibrated and used to compensate the angle errors in the MICRON computer to an accuracy of 0.1 mr rms over the sphere. Drift-rate errors are modeled as a function of ϕ, θ and g and compensated to an accuracy of 0.01 deg/hr rms. These 0.1 mr angle and 0.01 deg/hr drift rate residual errors have been found to be repeatable unmodeled effects, mostly, as opposed to time variable errors.

* Things are mechanized in terms of direction cosines in the actual MICRON system, not in terms of ϕ, θ, but the difference is immaterial to the present discussion.

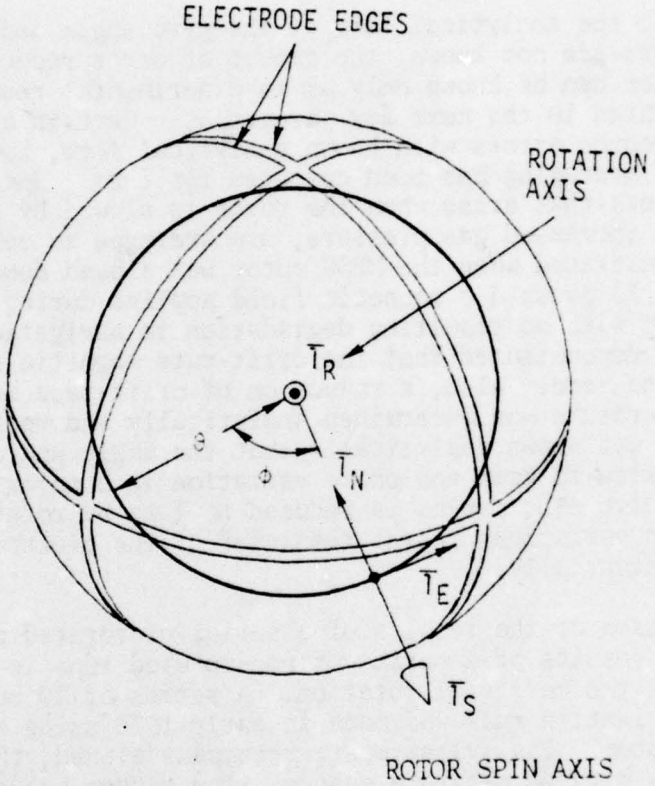


Fig. 3 Electrostatic Gyro

Rotating the MICRON IAU reduces these residual angle and drift-rate errors by averaging them. To consider the effects of rotation, imagine that the vectors $\bar{I}_R$, $\bar{I}_S$, $\bar{I}_E$ and $\bar{I}_N$ remain fixed and that the electrode pattern rotates through 360° about $\bar{I}_R$. θ remains constant as Ø is exercised through its full range of values. $\bar{I}_E$, $\bar{I}_N$, and $\bar{I}_S$ constitute an inertially fixed coordinate frame, or nearly so during the short period of one IAU rotation. The gyro errors that propagate into navigation errors are then the average north and average east components of the MICRON residual gyro errors, averaged over a full 360° in Ø. This average greatly reduces the magnitude of the propagating gyro errors.

4. System Test Results

Because the analytical form of the gyro angle and drift-rate residual errors are not known, the amount of error reduction achieved by the rotation can be known only as an experimental result, which will be presented in the next few paragraphs. Certain environmental effects do produce errors with known analytical form, however, and the effect of averaging has been computed for them. Specifically, the major errors that arise when the rotor is slowed by increased drag, as from increased gas pressure, are averaged to zero by rotation. This was demonstrated when the MESG rotor was slowed down 8 Hz (from 2460 Hz) by a 10-gauss d-c magnetic field applied during a rotated navigation run with no resulting degradation in navigation accuracy. This run also demonstrated that the drift-rate magnetic sensitivity was averaged to zero. Also, a reduction of drift-rate sensitivity to rotor temperature was determined analytically and verified experimentally. It was shown analytically that the angle and drift-rate error sensitivity to gain and phase variation in a major portion of the support servo electronics is reduced to zero by rotation. The sensitivity to variations in the remainder of the electronics is decreased substantially.

Comparison of the results of a series of rotated navigation runs with the results of a series of non-rotated runs is the best way to exhibit the merits of rotation. A series of 20 non-rotated laboratory navigation runs was made in early 1976 using an N57A MICRON brassboard system. The system was gyrocompass alined, then navigated for 40 minutes with no attitude change. The system heading was changed +90 deg-of-arc at t = 40 and 80 minutes. The duration of the navigation run was 120 minutes. The north and east velocity errors and the radial position error for a typical one of these runs are shown in Figure 4. The ensemble characteristics of the 20 runs will be discussed later.

A series of 10 rotated laboratory navigation runs was made in mid-1976. The same N57A MICRON brassboard system was used for these runs as for the non-rotated runs. Having been constructed as a non-rotated system, the N57A was mounted on a Goerz automatic three-axis table to allow rotation of the whole system for these runs. The inside axis of the Goerz table (the one nearest N57A) was used to achieve the back-and-forth 360° rotation. The outer two axes were used to put the inside axis, the rotation axis, at any desired orientation with respect to the lab. A simulated fighter mission of 260-min duration was defined that made use of this all-attitude capability. It simulated the aircraft attitudes that would be assumed during a fighter mission, including takeoff, cruise, combat, return cruise, and landing. During the combat phase, the Goerz table was used to

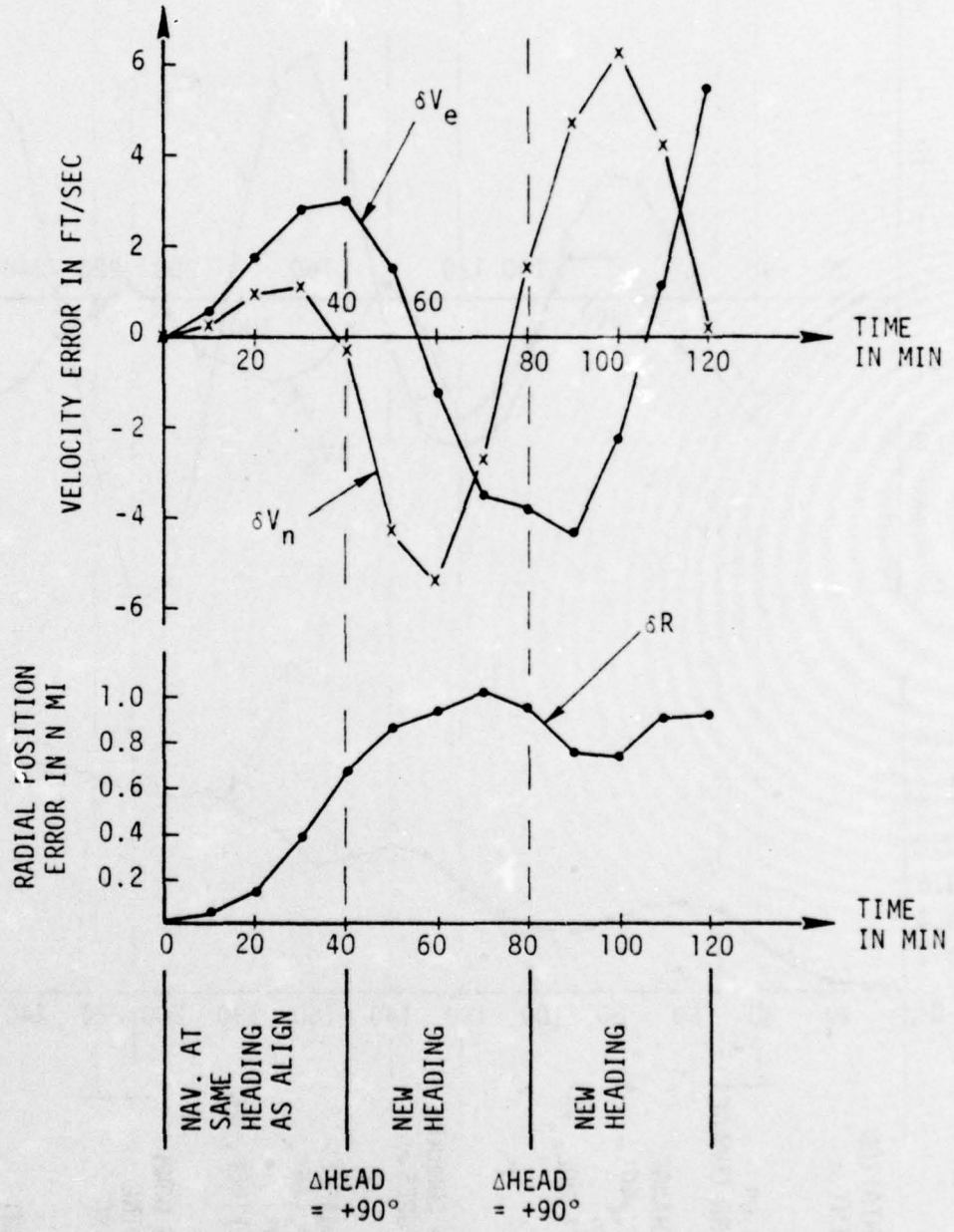


Fig. 4 Navigation Run (Non-rotated) # 0429761050

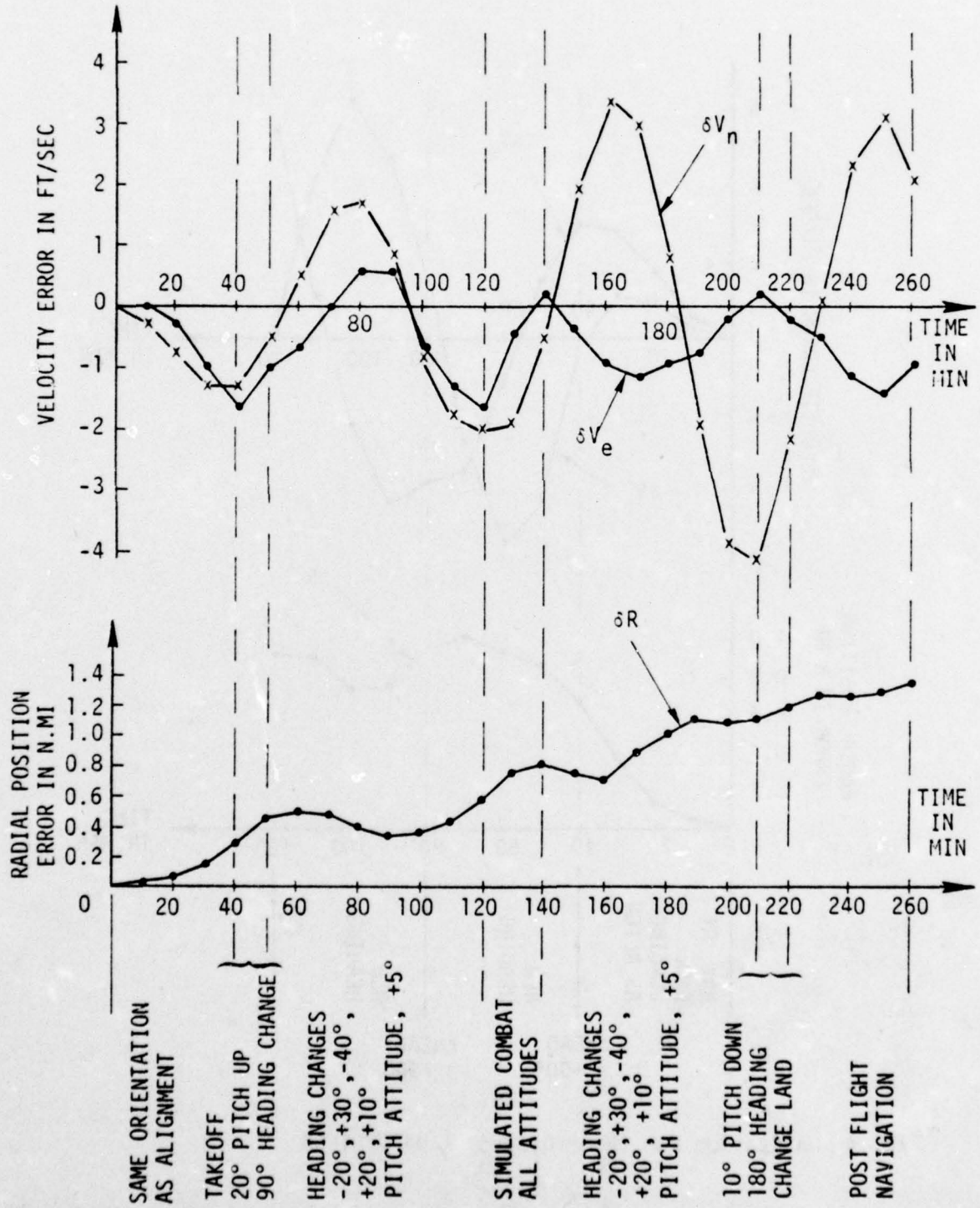


Fig. 5 Rotated Nav Run #0527761040 With Attitude Profile of Fighter Mission

rapidly put the N57A through the sorts of attitudes that would be seen in an aircraft during air-to-air combat. The north and east velocity errors and the radial position error for a typical one of those runs are shown in Fig. 5.

Ensemble navigation error characteristics for the 20 non-rotated runs and 10 rotated runs are plotted together in Figs 6 and 7 for easy comparison. Figure 6 shows the ensemble rms of the time rms velocity error versus time; north error or east error is plotted, whichever is larger. The values at two hours, 3.34 ft/sec and 1.19 ft/sec, for the non-rotated and rotated ensembles, are to be compared with the 2.5 ft/sec velocity error required by the Standard Nav Spec. Figure 7 plots CEP (estimated by sample median) versus time for the two ensembles. The slopes of the least-squares fitted straight lines to the first hour's data, 0.681 n mi/hr and 0.358 n mi/hr, for the non-rotated and rotated ensembles are to be compared with the 0.8 n mi/hr CEP rate required by the Standard Nav Spec. It can be concluded from studying Figs 6 and 7 that rotation reduces velocity errors by approximately a factor of 3 and CEP rate by approximately a factor of 2. The non-rotated system meets the Standard Nav Spec CEP rate requirement, and the rotated system beats the requirement by a factor of 2. The non-rotated system does not meet the Standard Nav Spec velocity requirement. The rotated system beats the requirement by a factor of 2. Thus, it is seen that the use of a single axis of non-precision rotation allows use of the N57A instrument set, without expensive improvements, in a strapdown system that easily meets the Standard Nav Spec accuracy requirements.

In the future, MICRON will also find use in those applications that require more accurate navigation than what is called for in Standard Medium Accuracy Navigator specification. In many lab runs where the N57A rotation axis was kept always vertical, unlike the simulated fighter mission profile, CEP rates of 0.1 n mi/hr and better were achieved. With further error model development, modeling average angle readout and drift-rate errors as a function of θ (see Fig. 3), this better performance will be possible with the rotation axis moving as it would on a realistic flight profile. This development will result in a high-accuracy MICRON version that is identical to the Standard Nav version in hardware configuration but has added software error compensation.

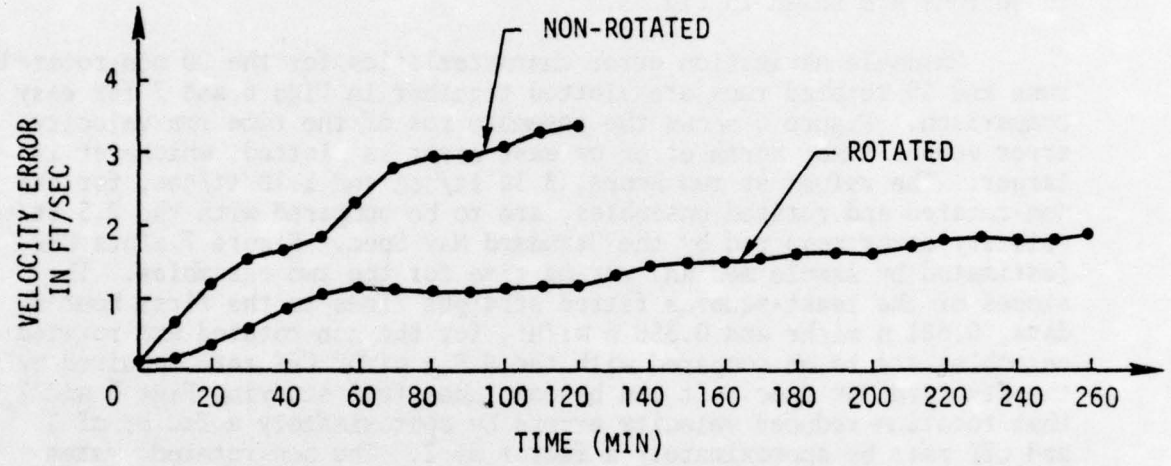


Fig. 6 Time and Ensemble rms Velocity Error (north or east, whichever is larger) for 20 Non-rotated Nav Runs and 10 Rotated Nav Runs

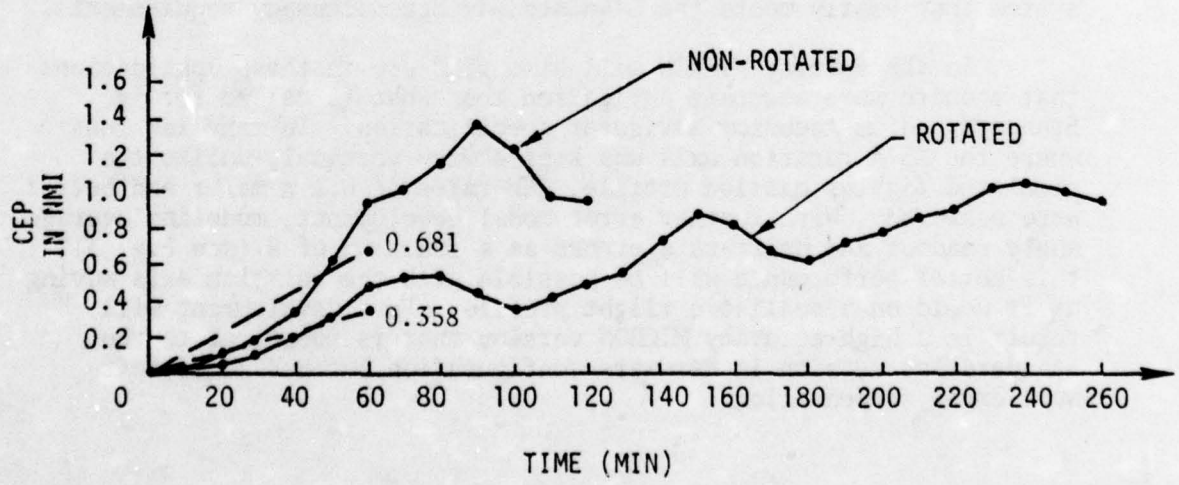


Fig. 7 CEP Estimated from 20 Non-rotated Nav Runs and 10 Rotated Nav Runs

EIGHTH BIENNIAL GUIDANCE TEST SYMPOSIUM

THEORETICAL AND EXPERIMENTAL DETERMINATION OF THE g^2 AND g^4 ERROR TORQUES OF A FREE-ROTOR GYROSCOPE

AUTHORS: S. L. ZEDEKAR
ROCKWELL INTERNATIONAL CORP.
AUTONETICS GROUP
ANAHEIM, CALIFORNIA

CAPT J. E. JUSTIN
SAMSO
LOS ANGELES, CALIFORNIA

ABSTRACT

Theoretical studies show that the so-called g^2 coefficients of a free-rotor gyroscope are functions of the applied acceleration. Although too small to be measured in a 1-g situation, under high g conditions the higher order nonlinearities cause significant error torques. This paper briefly reviews the theoretical derivation of the higher-order g coefficients. The paper includes the experimental effort which confirmed that the nonlinearities could be adequately represented for missile guidance compensation by g^4 coefficients. Specifically, each of the nonlinear coefficients is represented by a curvilinear surface which is a function of two g^2 coefficients.

The experimental phase of this study consisted of testing a number of gyros under high accelerations, using a specially designed linear vibrator. The paper describes the performance of the linear vibrator and the methods used to achieve precision acceleration calibration at low frequencies.

The paper gives the general derivation of the appropriate equations, presents the experimental results, compares these results to the theoretical values, and evaluates possible and known test errors.

CONTENTS

		Page
Abstract		ii
I.	Introduction	1
II.	Theory	2
	A. Description of the Gyro	2
	B. Source of Acceleration Sensitivity Nonlinearities	4
	C. Reynolds Equation	4
	D. Torque Equations	6
	E. The Effect of Viscous and Pressure Gradient Torques	7
	F. Calculation of g^n Coefficients	12
III.	Experimental Testing	20
	A. Description of Test Equipment	20
	B. Performance Characteristics	25
	C. Test Method	27
	D. Exposure Conditions	27
	E. Test Data	28
IV.	Experimental Results	31
V.	Conclusions	38
References		39

ILLUSTRATIONS

Figure		Page
1.	A Gas-Film Supported Free-Rotor Gyro	3
2.	Coefficient Flow Chart	13
3.	Load and Torque Relationship in Radial Plane	17
4.	Linear Vibration Test Station	21
5.	Ling Table Assembly	22
6.	Close-Up of Vibration Table	23
7.	Close-Up Rear-View of Table	24
8.	New Linear Vibrator Operating Range	26
9.	Gyro Orientation	27
10.	Gyro Test Results, B Coefficient	32
11.	Gyro Test Results, E Coefficient	33
12.	Gyro Test Results, J Coefficient	34
13.	Gyro Test Results, P Coefficient	35
14.	Gyro Test Results, R Coefficient	36
15.	Gyro Test Results, N Coefficient	37

TABLES

Table		Page
1.	Coefficients for Theoretical Algorithm	19
2.	Engineering Test Conditions	28
3.	Comparison of Theoretical and Experimental Planar Algorithms	31

I. INTRODUCTION

The purpose of this paper is to describe a 2-year gyro accuracy improvement program which included theoretical and experimental studies of the higher-order g effects in a free-rotor gyro. This paper reviews the theoretical derivation of these higher-order g coefficients. It confirms that the nonlinearities in the so called g^2 coefficients could be adequately represented for missile guidance compensation by g^4 coefficients appropriately related to the individual g^2 coefficients. In addition, testing methods using a precision linear vibrator were developed and representative test results on one gyro are included.

The paper is divided into four sections: the theory, experimental testing, experimental results, and conclusions. The fundamental forms of the g^4 coefficients were shown experimentally and agree with the theoretical predictions within the expected accuracy. It was further shown that acceptable estimates for the significant g^4 coefficients can be made from the labeled value of the g^2 coefficients. These coefficients are currently measured during gyro functional acceptance testing.

II. THEORY

A. DESCRIPTION OF THE GYRO

The gyro used to stabilize the guidance platform is a free-rotor, two-degree-of-freedom gyro in which angular displacements of the platform containing the gyros are sensed relative to the inertially stable gyro rotors. Capacitor pickoff displacement signals, applied to gimbal servos, cause the platform to maintain alignment with the inertial plane of the gyro rotor. The rotor is caused to precess at desired rates, such as earth rate, about two axes by torques applied to the rotor through a precision electromagnetic torquer. As shown in Fig 1, the nonmagnetic, beryllium rotor is supported on a spherical autolubricated gas bearing which allows unlimited freedom about the spin axis and limited freedom about any axis normal to spin, with no additional output-axis bearings required.

The gyro motor is an induction type, having a copper eddy current cylindrical sleeve attached to one side of the rotor. The sleeve operates in a rotating magnetic flux produced in an annular gap. An outer laminated stator having a three-phase winding is separated by the annular gap from an inner laminated stator which serves as a flux-return path.

The torquer also operates on the principle of eddy-current induction forces produced in a cylindrical manganin sleeve. The torquer sleeve is attached to the side of the rotor opposite the motor. By varying the magnetic fields produced by a four-pole mumetal structure having a separate coil on each pole, torques may be applied in any direction normal to the rotor spin axis.

The displacement pickoff consists of a four-segment annular ring mounted on a ceramic insulator adjacent to one side face of the rotor rim. As the rotor is tilted with respect to an axis of the pickoff plane, the capacitance between the rotor and the approaching segment of the ring is increased, while the capacitance of the opposite receding segment is decreased. The rotor-to-pickoff-segment capacitances are connected to the ends of a transformer winding having a 4.8 kHz excitation applied between the winding center tap and the rotor. The transformer secondary produces a phase-sensitive output proportional to the rotor tilt relative to the pickoff plane. The two pairs of plates and two transformers provide pickoff signals about two orthogonal axes.

A beryllium housing supports the spinning beryllium rotor through the stationary beryllium-ball portion of the spherical gas bearing. One half of the housing contains the motor and pickoffs; the other half contains the torquer. A welded mumetal enclosure surrounding the berryllium housings provides a leak-free container for the hydrogen gas, shielding from magnetic fields, thermal isolation, and protection for the electrical printed circuits.

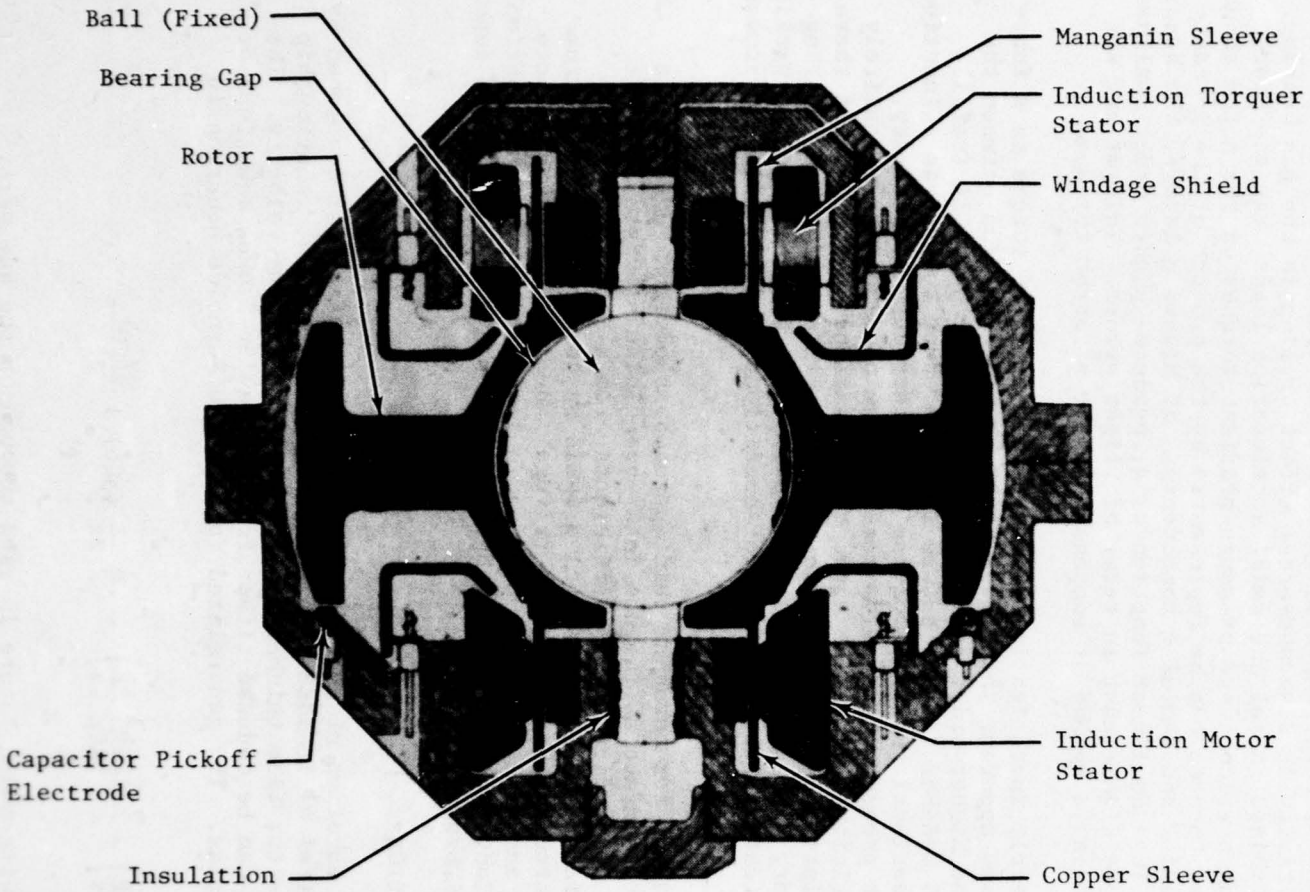


Fig 1. A Gas-Film Supported Free-Rotor Gyro

B. SOURCE OF ACCELERATION SENSITIVITY NONLINEARITIES

In the free-rotor gyro employing an autolubricated spherical gas bearing as the means of rotor support, the principal nonlinearity in the acceleration sensitivity is a second-order effect arising in the gas bearing. Under low level combined radial and axial acceleration loads, the gas bearing deflection causes viscous and pressure gradient torques on the rotor about radial axes. These torques can be represented by the product of the g^2 coefficients and the axial and radial g components. At higher g levels, the bearing deflection, which is a nonlinear function of g, produces higher order nonlinear torques which become significant in terms of flight errors. This effort was concerned with finding a method of compensating the g^4 error torques.

From the early investigation of the nonlinearity of torque as a function of g, it became apparent that there might be a correlation between the g^2-coefficients and higher-order terms. The analyses of Castelli (ref 1), Tipei (ref 2), and Zedekar (ref 3) showed that the error torque was a function of various nondimensional groups involving parameters such as geometry, viscosity, ambient pressure, and polar moment. The nonlinearity is entirely due to the eccentricity ratio. The above considerations indicated that there would be some variation due to elongation of the cavities and thrust bearing deviations; however, a reasonably smooth function should result for the various nonlinear coefficients. Over the range of conditions studied, this has proven to be the case.

The motivation for pursuing this approach is obvious in that if a sufficiently smooth surface of the nonlinear coefficients exists, then it would be possible to predict these coefficients from a knowledge of the measured g^2-coefficients. The alternative would be to directly measure the g^4-coefficients through vibration or centrifuge. Besides being vastly more expensive, direct measurement would postpone implementation of a compensation scheme until the individual fielded gyroscopes were recycled through the depot or factory and calibrated.

C. REYNOLDS EQUATION

The basic equation of hydrodynamic lubrication was first developed by Osborne Reynolds (ref 4) in 1886. This equation expresses the relationship between the viscosity, film thickness, pressure, and sliding velocity. The Reynolds equation can be deduced either from the Navier-Stokes equations or from basic principles. The generalized form of the Reynolds equation is

$$\frac{\partial}{\partial x}\left(\frac{\rho h^3}{12\mu}\frac{\partial p}{\partial x}\right) + \frac{\partial}{\partial z}\left(\frac{\rho h^3}{12\mu}\frac{\partial p}{\partial z}\right) = \frac{1}{2}\frac{\partial}{\partial x}(\rho U h) + \frac{\partial(\rho h)}{\partial t} \qquad (1)$$

The following nomenclature is used throughout the analysis.

a, b = coefficients

A_s = applied axial acceleration in units of g

A_r = applied radial acceleration in units of g

C = radial clearance

C_d = coefficient

E, B = g^2 coefficients

e = bearing eccentricity

h = clearance

J,N,P,R = g^4 coefficients

ln = natural logrithm

p = pressure

P_a = ambient pressure

R = gas constant; radius

T = torque

t = time

U = velocity

$W_\perp$ = bearing load normal to eccentricity

$W_{||}$ = parallel component of bearing load

W_a = axial load

W_r = radial load

Y = load parameter

Δ = depth of thrust pad

ε = eccentricity ratio = $\frac{e}{C}$

$\Lambda = \frac{6\mu\ \omega R^2}{P_a C^2}$

λ = mean free path of gas

μ = absolute viscosity

ρ = density

τ = shear stress

ω = angular velocity

Using C, P_a, and $1/\omega$ to normalize various quantities and assuming isothermal conditions:

$H = \frac{h}{C}$

C = radial clearance when $\varepsilon = 0$

$P = p/p_a$

$\tau = \omega t$

$\rho = \frac{P}{RT}$

Equation (1) is transformed into the following:

$$\frac{\partial}{\partial X}\left(PH^3 \frac{\partial P}{\partial X}\right) + \frac{\partial}{\partial Y}\left(PH^3 \frac{\partial P}{\partial Y}\right) = \Lambda \left(\frac{\partial}{\partial Y} + 2 \frac{\partial}{\partial \tau}\right)(HP) \qquad (2)$$

In spherical coordinates, Reynolds equation becomes:

$$\sin \phi \frac{\partial}{\partial \phi}\left[\sin \phi \, (H)^3 P \frac{\partial P}{\partial \phi}\right] + \frac{\partial}{\partial \theta}\left[(H)^3 P \frac{\partial P}{\partial \theta}\right] = \Lambda (\sin \phi)^2 \left(\frac{\partial}{\partial \theta} + 2 \frac{\partial}{\partial \tau}\right)(HP) \qquad (3)$$

where $\Lambda = \dfrac{6\mu \omega R^2}{P_a C^2}$ is the usual compressibility number.

The above forms of the Reynolds equation apply to full film lubrication for both compressible and incompressible fluids. The solution of the Reynolds equation for a particular bearing configuration results in an expression for the pressure throughout the film as a function of viscosity, film shape, and velocity. Integration of the pressure over the film area yields the load supported by the film. In addition to the load capacity, an expression for the torque exerted on the bearing can also be developed.

D. TORQUE EQUATIONS

The velocity distribution in the direction of motion can be used to evaluate the shear stress in the X direction

$$\tau_x = \mu \frac{\partial U}{\partial y} = -\frac{\mu U}{h} - \left(\frac{h}{2} - y\right) \frac{\partial p}{\partial x} \qquad (4)$$

At the moving surface (Y = 0), this becomes

$$\tau_x = -\frac{\mu U}{h} - \frac{h}{2} \frac{\partial p}{\partial x} \qquad (5)$$

At the stationary surface (Y = h),

$$\tau_x = -\frac{\mu U}{h} + \frac{h}{2} \frac{\partial p}{\partial x} \qquad (6)$$

Integrating over the bearing surface, the friction force becomes

$$F = \iint \tau_x \, dx \, dz = - \iint \frac{\mu U}{h} \, dx \, dz \pm \iint \frac{h}{2} \frac{\partial p}{\partial x} \, dx \, dz \tag{7}$$

The upper sign in the last term is for the stationary surface, and the lower sign is for the moving surface.

Integrating the second term of Eq (7) by parts:

$$\int_x \frac{h}{2} \frac{\partial p}{\partial x} \, dx = \frac{1}{2} \left\{ h \, (p-p_a) \Big|_{x_1}^{x_2} - \int \frac{\partial h}{\partial x} \, (p-p_a) \, dx \right\} \tag{8}$$

and noting the $p = p_a$ at both edges of the film, the first term of Eq (8) vanishes. Then Eq (7) becomes:

$$F = - \iint \frac{\mu U}{h} \, dx \, dz \pm \frac{1}{2} \iint (p-p_a) \frac{\partial h}{\partial x} \, dx \, dz \tag{9}$$

Examination of Eq (9) shows that the friction forces on the moving and stationary surfaces are not equal. The first term on the right is due to the viscous drag and is dependent on the viscosity and the velocity gradient. The second term is due to the pressure forces and for this to be other than zero, there must exist both a pressure gradient and a varying film thickness.

In spherical coordinates, the torque equation is

$$\vec{T} = \mu \int_{\phi_1}^{\phi_2} \oint \frac{\bar{R} \times (\bar{\omega} \times \bar{R})}{h} R^2 \sin \phi \, d\phi \, d\theta$$

$$\pm \int_{\phi_1}^{\phi_2} \oint \bar{R} \times \left(\frac{h}{2} \bar{\nabla} P \right) R^2 \sin \phi \, d\phi \, d\theta \tag{10}$$

Again the first term is due to the velocity gradient, and the second is due to the pressure gradient. The upper sign refers to the stator and the lower to the rotor.

E. THE EFFECT OF VISCOUS AND PRESSURE GRADIENT TORQUES

In 1955, Cogan (ref 5) developed the first successful gas-lubricated spherical bearing, and later predicted the effect of bearing design on the performance of a free-rotor gyroscope. Specifically, he derived expressions for the g^2-coefficients by solving the first term of Eq (10) and assuming that the pressure gradient effects were small.

In 1968, Zedekar (ref 3) extended the above analysis to the generalized case including the pressure gradient effects. He determined expressions for the torque along the direction of the applied radial load and the torque normal to the direction of the applied radial load.

The first term of Eq (10), the term due to velocity gradient, becomes

$$T_{\perp} = 3C_d\omega \left[\sum_{n=0}^{\infty} \frac{n\varepsilon^{2n}}{(2n+3)(2n+1)} \right] \sin\alpha \cos\alpha \sin\gamma \tag{11}$$

$$T_{\parallel} = 3C_d\omega \left[\sum_{n=0}^{\infty} \frac{n\varepsilon^{2n}}{(2n+3)(2n+1)} \right] \sin\alpha \cos\alpha \cos\gamma \tag{12}$$

The second term of Eq (10), the term due to pressure gradient, becomes

$$T_{\perp} = \frac{h_o}{2} (\varepsilon_a W_r - \varepsilon_{\parallel} W_a) \tag{13}$$

$$T_{\parallel} = \frac{h_o}{2} \varepsilon_{\perp} W_a \tag{14}$$

where

$T_{\perp}$ = torque normal to direction of radial load

$T_{\parallel}$ = torque parallel to direction of radial load

h_o = gas bearing radial clearance

$\varepsilon_{\parallel}$ = bearing radial eccentricity ratio parallel to direction of radial load

$\varepsilon_{\perp}$ = bearing radial eccentricity ratio normal to direction of radial load

ε_a = axial bearing eccentricity ratio

W_a = axial force

W_r = radial force

C_d = bearing drag coefficient, for a perfect sphere $C_d = \frac{8\pi\mu R^4}{3\ h_o}$

R = radius of sphere

μ = absolute viscosity

ω = angular velocity

n = integer

ε = eccentricity ratio $\frac{e}{h_o}$

e = bearing eccentricity

α = angle between $\bar{\omega}$ and $\bar{\varepsilon}$

γ = angle between radial load and radial eccentricity

Expand Eq (11) and (12) and note that (see Fig 3 in part F below):

$$\varepsilon_r = \varepsilon \sin \alpha$$

$$\varepsilon_{||} = \varepsilon \sin \alpha \cos \gamma$$

$$\varepsilon_{\perp} = \varepsilon \sin \alpha \sin \gamma$$

$$\varepsilon_a = \varepsilon \cos \alpha$$

$$T_{\perp} = \frac{h_o}{2} (\varepsilon_a W_r - \varepsilon_{||} W_a) + \frac{C_d \omega}{5} \varepsilon_{\perp} \varepsilon_a \left[1 + \frac{6}{7} \varepsilon^2 + \frac{5}{7} \varepsilon^4 + \ldots\right] \quad (15)$$

$$T_{||} = \frac{h_o}{2} \varepsilon_{\perp} W_a + \frac{C_d \omega}{5} \varepsilon_{||} \varepsilon_a \left[1 + \frac{6}{7} \varepsilon^2 + \frac{5}{7} \varepsilon^4 + \ldots\right] \quad (16)$$

Although there is little theoretical work to determine the function form of ε_a, it can be inferred that it is of the form:

$$\varepsilon_a = Y + K_1 Y^3 + K_2 Y^5 + \ldots \quad (17)$$

where

$$Y = \frac{3C^2 W}{8\pi\mu R^4}$$

W = applied load

By noting Eq (13) and (17) the torque components become:

$$T_{\perp} = a_{00} A_a A_r + a_{20} A_a^3 A_r + a_{02} A_a A_r^3 + a_{40} A_a^5 A_r + a_{22} A_a^3 A_r^3 + a_{04} A_a A_r^5 + \ldots \quad (18)$$

$$T_{||} = b_{00} A_a A_r + b_{20} A_a^3 A_r + b_{02} A_a A_r^3 + b_{40} A_a^5 A_r + b_{22} A_a^3 A_r^3 + b_{04} A_a A_r^5 + \ldots \quad (19)$$

where

$$\left.\begin{matrix} a_{i,j} \\ b_{i,j} \end{matrix}\right\} \text{ coefficients}$$

A_s = applied axial acceleration in units of g

A_r = applied radial acceleration in units of g

By converting the above torques to drift rates, and resolving these components into torques along the conventional free-rotor gyro control axes (see Fig 6, ref 3), the following is obtained:

$$\frac{T_1}{I\omega} = E\,A_1A_s + P\,A_1A_s^3 + R\,A_1^3\,A_s - B\,A_2A_s - J\,A_2A_s^3 - N\,A_2^3A_s + \ldots \quad (20)$$

$$\frac{T_2}{I\omega} = E\,A_2A_s + P\,A_2A_s^3 + R\,A_2^3A_s + B\,A_1A_s + J\,A_1A_s^3 + N\,A_1^3A_s + \ldots \quad (21)$$

where

E,B = g^2 coefficients

J,N,P,R = g^4 coefficients

A computer program for the numerical solution of Eq (17) was developed for this effort by V. Castelli (ref 1) which follows, in time, the transients of pressure and flow at each bearing point as well as the integration of the equations of motion.

Integration of the transient forces gives both the average and the fluctuations of all forces and torques of interest.

When steady-state forces and torques are desired, the rotor center is maintained at a fixed eccentric location. When the dynamic response is desired, the integration of the equations of motion is performed.

The solution is obtained by time integration of Reynolds equation with the inclusion of the effects of molecular mean free path.

The major features of the computer algorithm are

(1) No special equations are needed at steps in the clearance such as at the sides of pockets.

(2) Good speed of computation since only tridiagonal matrices are inverted.

(3) Good numerical stability since a linearized stability analysis shows that the method is unconditionally stable.

(4) Good accuracy since, if it were not for the nonlinearity given by the P divisors, the approximation over two time steps is of the order $(\Delta T)^2$.

For static runs, the computation is started from ambient pressure initial conditions, and the algorithm is applied until cyclicity is attained in the solution. Since the pocket pattern on the rotor is cyclic, the cyclicity of the solution is tested at points fixed on the stator and at intervals of time equal to the rotation of one geometry cycle. When cyclicity has been achieved, the pressure field and the shear forces are integrated to produce the desired forces and torques.

Some additional features of the numerical analysis program are:

(1) Clearance deviations: A grid of values of dimensionless clearance deviations can be read in which is added to the clearance as computed from mean clearance, elongations, and eccentricities. The clearance deviations are dimensionless with respect to the mean equatorial clearance of the top hemisphere. In entering the deviations, it should be remembered that clearance is associated with grid intervals and not with grid points.

(2) Ambient pressure variations: The ambient pressure can be varied as a function of time. The variation can be specified as connected, piecewise linear functions of time.

(3) Torque averaging: The torques acting on the rotor can be averaged over a number of specified intervals of time and the results are additional outputs.

(4) Polynomial fitting: Least square fitting of polynomials can be requested for the following functions:

   (a) Rotor torques vs ambient pressure

   (b) Rotor torques vs axial g-excitation

   (c) Rotor torques vs parallel g-excitation

   The degree of the fitted polynomial can be specified (up to fifth) as well as the time interval over which the fitting is performed.

(5) Variable Punchout: Upon proper input specification, the program will punch out on cards the successive values of any of the following variables: Time; axial, parallel, and normal eccentricities; axial, parallel, and normal total torque; ambient pressure; axial and parallel g-excitation. These can be used for off-line data analysis.

F. CALCULATION OF g^n COEFFICIENTS

The computer program is used to solve the appropriate form of the Reynolds equation for a given set of nondimensional input parameters. Figure 2 is a flow diagram which indicates the computational setup involved in obtaining the required coefficients.

(1) The following group of nondimensional groups are calculated for each run:

$$\text{PLAM} = \frac{6\mu\ \omega R^2}{PaC^2\gamma}$$

$$\text{PDEP}_i = \frac{\Delta i}{C}$$

$$\eta_T,\ \eta_B = \frac{\lambda}{C}$$

$$\text{CBOCT} = \frac{\text{bearing clearance of bottom hemisphere}}{\text{bearing clearance of top hemisphere}}$$

$$\text{FREE} = \frac{\lambda}{C}$$

HDEV = M × N array which gives any deviation of geometry

$$\text{COVR} = \frac{C}{R}$$

In addition to the above, a number of inputs is required to show the angular extent of the bearings, the size of the polar orifices, check points for determination of cyclicity of pressure, degree of convergence, and output format.

Nomenclature:

Λ = bearing compressibility number

μ = absolute viscosity of gas

ω = angular velocity of rotor

R = radius of ball

Pa = ambient pressure

C = radial clearance of the bearing measured at the equator when the bearing is centered

γ = ratio of specific heats (indicates how much the bearing deviates from isothermal)

Δ_i = array of individual thrust pad depths

ℓ = elongation of a rotor half from a hemispherical surface

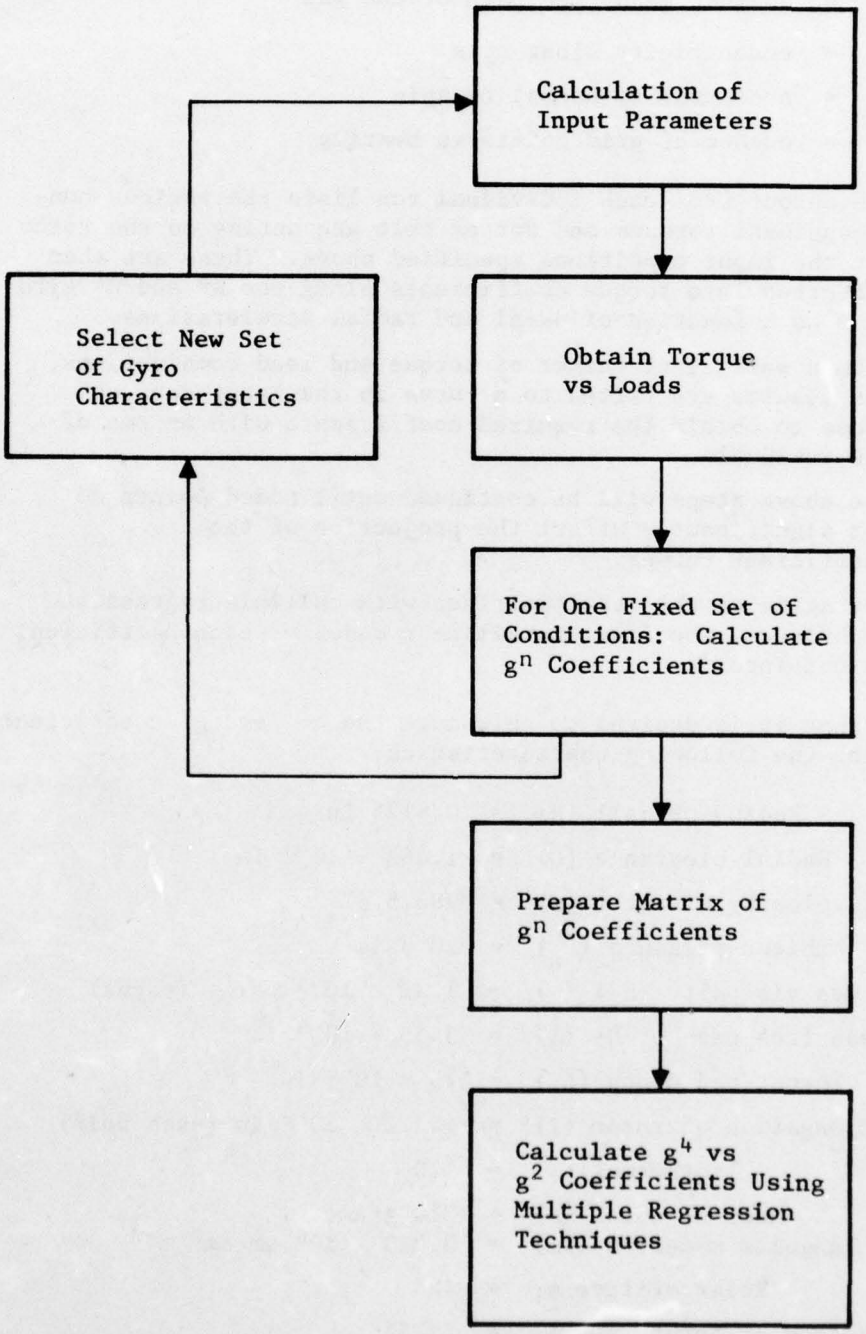


Fig 2. Coefficient Flow Chart

λ = ambient mean free path of the gas

e_a = eccentricity along spin

e_r = eccentricity normal to spin

M,N = number of grid points in bearing

(2) The output from each individual run lists the various non-dimensional torques and forces that are acting on the rotor for the input conditions specified above. These are then converted into torque coefficients along the A* and B* gyro axes as a function of axial and radial accelerations.

(3) From a sufficient number of torque and load combinations, the results are fitted to a curve in the least-squares sense to obtain the required coefficients with an rms of the residuals.

(4) The above steps will be continued until added points do not significantly affect the projection of the coefficient curves.

(5) Operating on the above matrices with multiple regression techniques, the final curvilinear model of each coefficient is obtained.

Assume that it is desired to calculate the g^2 and g^4 coefficients for a gyro having the following characteristics:

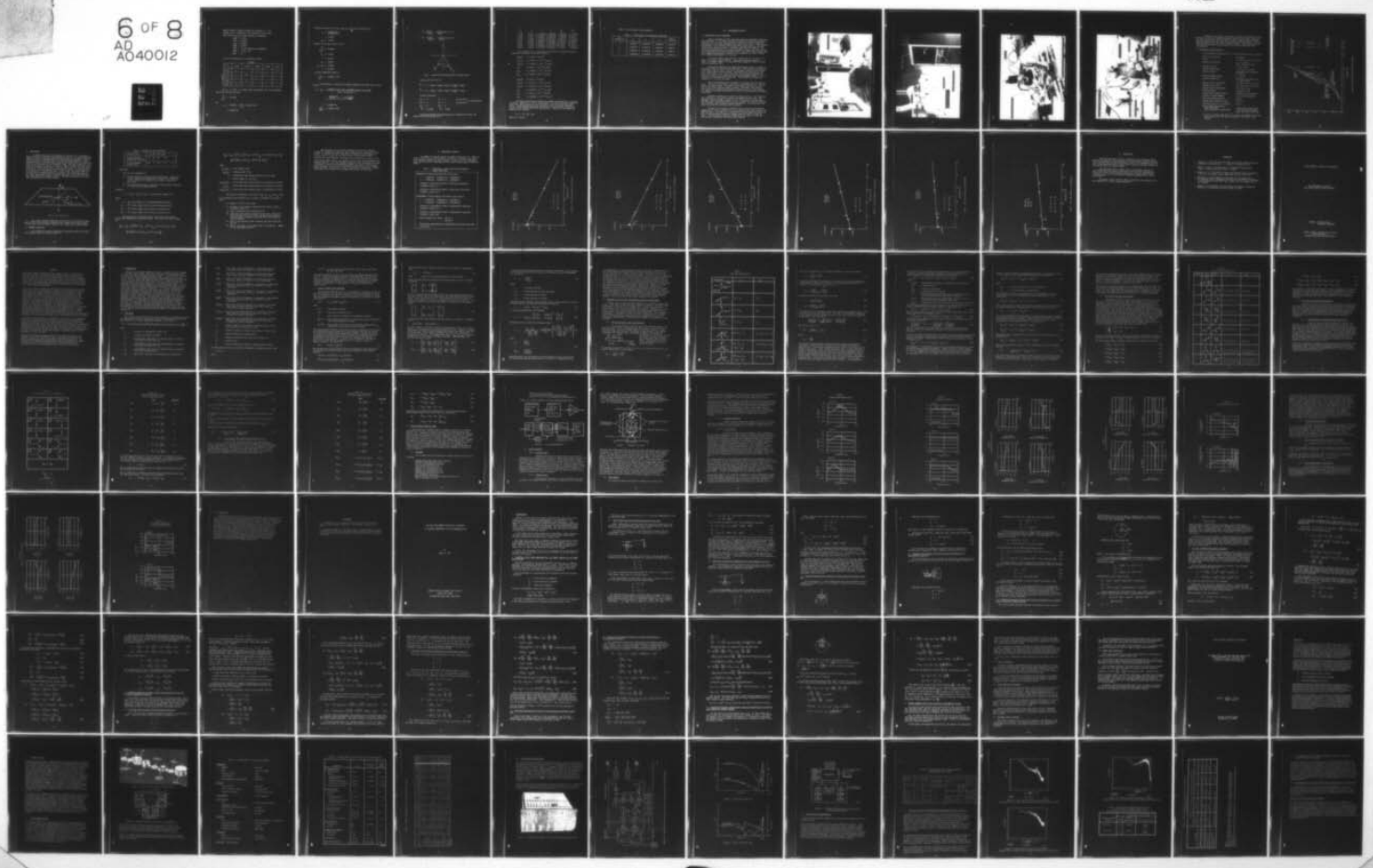
Radius of ball (R)	=	0.8125 in
Radial clearance (C)	=	1.445×10^{-4} in
Angular velocity of rotor (ω)	=	986.5 s^{-1}
Ambient pressure (P_a)	=	20 psia
Gas viscosity (H_2) (μ)	=	1.31×10^{-9} psi s (reyns)
Mean free path of H_2 (λ)	=	3.55×10^{-6} in
Thrust pad depth (Δ_i)	=	75×10^{-6} in
Elongation of rotor (l)	=	$+41.2 \times 10^{-6}$ in (each half)
Isothermal (γ)	=	1.0
Mass of rotor (m)	=	310 grams
Angular momentum ($I\omega$)	=	3.829×10^6 gm-cm^2 s^{-1}
Polar orifice ϕ_1	=	18°
Bottom of thrust pad ϕ_2	=	23.5°
Top of pad ϕ_3	=	60.3°

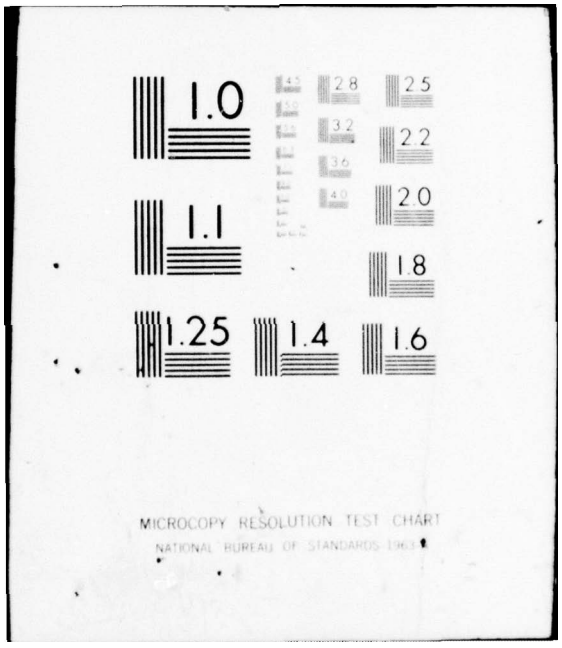
*These axis are defined later in Fig 9.

AD-A040 012 ARMAMENT DEVELOPMENT AND TEST CENTER EGLIN AFB FLA F/G 17/7
PROCEEDINGS OF THE BIENNIAL GUIDANCE TEST SYMPOSIUM (8TH) HELD --ETC(U)
MAY 77

UNCLASSIFIED ADTC-TR-77-3-VOL-1 NL

6 OF 8
AD
A040012




1.0
1.1
1.25
1.4
1.6
2.8
2.5
3.2
2.2
3.6
2.0
4.0
1.8
MICROCOPY RESOLUTION TEST CHART
NATIONAL BUREAU OF STANDARDS 1963

Angular extent of pads in direction of motion ϕ_1 = 50°

Bottom rotor is rotated 60° with respect to the top rotor

Both cavities and all thrust pockets are identical

PLAM = 12.257

PDEP = 0.51903

η_T, η_B = 0.28512

FREE = 0.02457

HDEV = 0.0 (no deviation of geometry)

COVR = 1.7785×10^4

CBOCT = 1.0

Use the following sets of eccentricity ratios:

Radial →

+ Axial ↓ ε_a \ ε_r	0.0244	0.0488	0.0732	0.0976	0.122
0.139	X		X		X
0.278		X		X	
0.417	X		X		
0.566		X			
0.659	X				

For ε_a = 0.139, ε_r = 0.0244 (from the computer run) the normalized load along the spin axis was

$$\frac{W_a}{P_a R^2} = 0.072190$$

and

$$W_a = 0.072190 \times 20 \frac{\text{lb}}{\text{in}^2} \times (0.8125 \text{ in})^2$$

$$= 0.953134 \text{ lb}$$

Dividing the load by the rotor mass, the spin axis acceleration is

$$g_a = \frac{0.953134 \text{ lb}}{0.682819 \text{ lb/g}}$$

$$= 1.39588$$

$$g_a^2 = 1.94848$$

Likewise in the axis normal to spin

$$\frac{W_r}{P_a R^2} = 0.072600$$

$$g_r = 1.40381$$

$$\Gamma = 29.107°$$

$$g_r^2 = 1.97069$$

$$g_a \times g_r = 1.959548$$

$$\Upsilon = 19.39632$$

and the normalized torque is

$$\frac{T}{P_a R^3} = 1.555639 \times 10^{-6}$$

By dividing the torque by the angular momentum, the drift rate is (see Fig 3):

$$\dot{\phi} = \frac{T}{I\omega} = \frac{1.555639 \times 10^{-6} \times 20 \times (0.8125)^3 \text{ lb in} \times 1.13 \times 10^6}{3.829 \times 10^6 \text{ gm-cm}^2 \cdot \text{s}^{-1}}$$

$$\times \frac{\frac{\text{gm-cm}^2 \text{ s}^{-2}}{\text{lb in}} \times 2 \times 10^5 \left(\frac{°/h}{\text{rad/s}}\right)}{1}$$

$$\dot{\phi} = 0.98408 \text{ °/h}$$

$$\frac{\dot{\phi}}{g_a g_r} = 0.50266 \text{ °/h/g}^2$$

$$\tilde{\tilde{B}} \equiv \left(\frac{\dot{\phi}}{g_a g_r}\right)_{\perp} = \left(\frac{\dot{\phi}}{g_a g_r}\right) \sin(\gamma + \Gamma)$$

$$\tilde{\tilde{E}} \equiv \left(\frac{\dot{\phi}}{g_a g_r}\right)_{\parallel} = \left(\frac{\dot{\phi}}{g_a g_r}\right) \cos(\gamma + \Gamma)$$

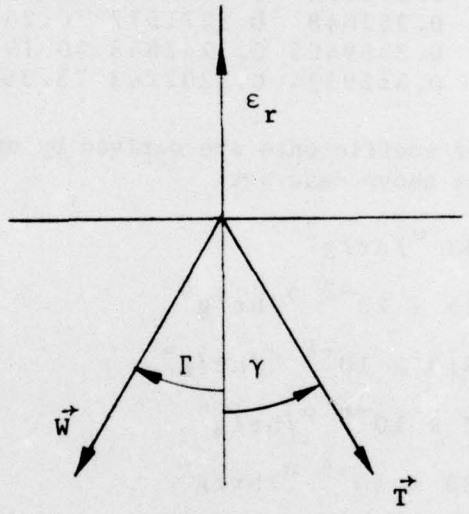


Fig 3. Load and Torque Relationship in Radial Plane

From Eq (18) and (19) or

$$\tilde{\tilde{B}} = B_{00} + B_{20}g_a^2 + B_{02}g_r^2 + B_{40}g_a^4 + B_{22}g_a^2g_r^2 + B_{04}g_r^4 + \ldots$$

$$\tilde{\tilde{E}} = E_{00} + E_{20}g_a^2 + E_{02}g_r^2 + E_{40}g_a^4 + E_{22}g_a^2g_r^2 + E_{04}g_r^4 + \ldots$$

In prior notations:

$B_{00} = B$		$E_{00} = E$		B_{40}, B_{22}, B_{04}	g^6 coefficients
$B_{20} = J$		$E_{20} = P$		E_{40}, E_{22}, E_{04}	
$B_{02} = N$		$E_{02} = R$			
$\tilde{\tilde{B}} = 0.37648$		$\tilde{\tilde{E}} = 0.3304$			

Continuing through the remaining sets of eccentricity ratios, one obtains the following tabulation:

ε_a	ε_r	B	E	g_a^2	g_r^2
0.139	0.0244	0.3764886	0.3330496	1.948467	1.970692
0.139	0.0732	0.3729403	0.3307690	1.980664	17.82405
0.139	0.122	0.365885	0.3264778	2.046403	50.01633
0.278	0.0488	0.3677395	0.3313711	8.208421	8.057260
0.278	0.0976	0.3628055	0.3287198	8.411310	32.48082
0.417	0.0244	0.356011	0.3293084	19.93192	20.81745
0.417	0.0732	0.352648	0.3271577	20.25957	18.83452
0.556	0.0488	0.3369405	0.3242843	40.19226	8.784237
0.695	0.0244	0.3159574	0.3202243	73.36148	2.354818

The following set of coefficients are derived by applying multiple regression techniques to the above data set:

$B_{00}(B) = 0.379853\ ^{o}/hr/g^2$

$B_{20}(J) = -1.37835 \times 10^{-3}\ ^{o}/hr/g^4$

$B_{02}(N) = -2.864513 \times 10^{-4}\ ^{o}/hr/g^4$

$B_{40} = 6.65662 \times 10^{-6}\ ^{o}/hr/g^6$

$B_{22} = 1.196583 \times 10^{-5}\ ^{o}/hr/g^6$

$B_{04} = 7.11528 \times 10^{-7}\ ^{o}/hr/g^6$

$E_{00}(E) = 0.334411\ ^{o}/hr/g^2$

$E_{20}(P) = -4.12344 \times 10^{-4}\ ^{o}/hr/g^4$

$E_{02}(R) = -1.62838 \times 10^{-4}\ ^{o}/hr/g^4$

$E_{40} = 2.701691 \times 10^{-6}\ ^{o}/hr/g^6$

$E_{22} = 1.06545 \times 10^{-5}\ ^{o}/hr/g^6$

$E_{04} = -1.804697 \times 10^{-8}\ ^{o}/hr/g^6$

The above technique was followed to analyze 55 combinations of geometry to obtain a family of g^2 and g^4 coefficients. The radial clearance, depth of thrust pad, and elongation of the rotor halves were the primary parameters varied. Using multiple regression techniques, an algorithm was obtained for each of the g^4 coefficients of Eq (20) and (21). The form of the regression equation is as follows:

$$K_i = a_0 + a_1 B + a_2 E$$

where K_i = J,N,P,R

Table 1 is the result of this analysis.

Table 1. Coefficients for Theoretical Algorithm

g^4 Coefficient	a_0	a_1	a_2	rms of Residuals
J	0.0009174	-0.0039157	-0.0009266	0.0001048
N	0.0001273	-0.0003517	-0.0005841	0.0000277
P	0.0002328	-0.0007841	-0.0002806	0.0000321
R	0.00009325	-0.00008856	-0.0005638	0.0001107

III. EXPERIMENTAL TESTING

A. DESCRIPTION OF TEST EQUIPMENT

The g^4 calibration of the free-rotor gyros was performed in the gyro test laboratory. A new linear vibration system was procured by Autonetics Group for this test from Ling Electronics, Division of Altec Corporation. Photographs of the system equipments are shown in Fig 4 and 5. This vibrator incorporates a dual thruster and hydrostatic bearing assembly to provide linear motion vibration within a frequency range from 5 to 1000 Hz. The hydrostatic bearing table is specially designed to utilize the driving force of two Ling Model 370 thrusters powered from a Ling Model 8004-2 solid-state power amplifier exhibiting a combined force capability of a 500 lb vector and a maximum displacement of 3.5 in p-p.

The linear vibrator was bolted to a granite block 3 ft wide × 6 ft long × 3 ft high, weighing 9000 lb. The granite block was cemeted to three 6 in diameter pads, 4 in tall, which were cemented to the 4 ft thick concrete laboratory floor.

The gyro was mounted in an adjustable mounting bracket as shown in the close-up view of the vibration table Fig 6. This bracket is mounted on a base plate with two pins. The one at the center allows the gyro bracket to be rotated about a vertical axis. The other pin is shown in the rear view of the table, Fig 7. This latter pin is an indexing alignment pin. Holes are located in the base plate which allow alignment angles, θ, to be varied in 15° increments from 0 to $\pm$ 90°. In this test, the gyros were oriented at $\theta = 0 \pm 30, \pm 45, \pm 60°$.

Three accelerometers were attached to the moving table as shown in Fig 7. The servo accelerometer, a precision electromagnetic unit, was the primary calibration unit. The Endevco accelerometer was used as a feedback in the table amplifier control circuit. The Endevco peak reading unit provides the calibrated acceleration signal directly to the computer as a monitor of maximum acceleration, to meet the non-detrimental g-exposure requirement.

Auxiliary equipment was required as shown in Fig 4. Gyro Universal Test Station No. 1 was used to control and operate the test gyro. The auxiliary console provided housings for the oscilloscope, the Ling model TEC-100-4 table equalizing control circuit, a counter, a precision differential voltmeter, and an Anadex Frequency Synthesizer. The latter unit provided the adjustable precision table frequency.

Cooling to the system is provided from two sources; lab airconditioning air at 55°F is provided to cool the gyro and the table thruster, as shown in Fig 4. Not shown is a 1 hp exhaust fan which pumps the warmed air from the two thrusters through the exhaust manifold, which is shown in Fig 7. The SSPA console requires cooling water, not shown, to cool the 4000 VA driver amplifiers and system power supplies.

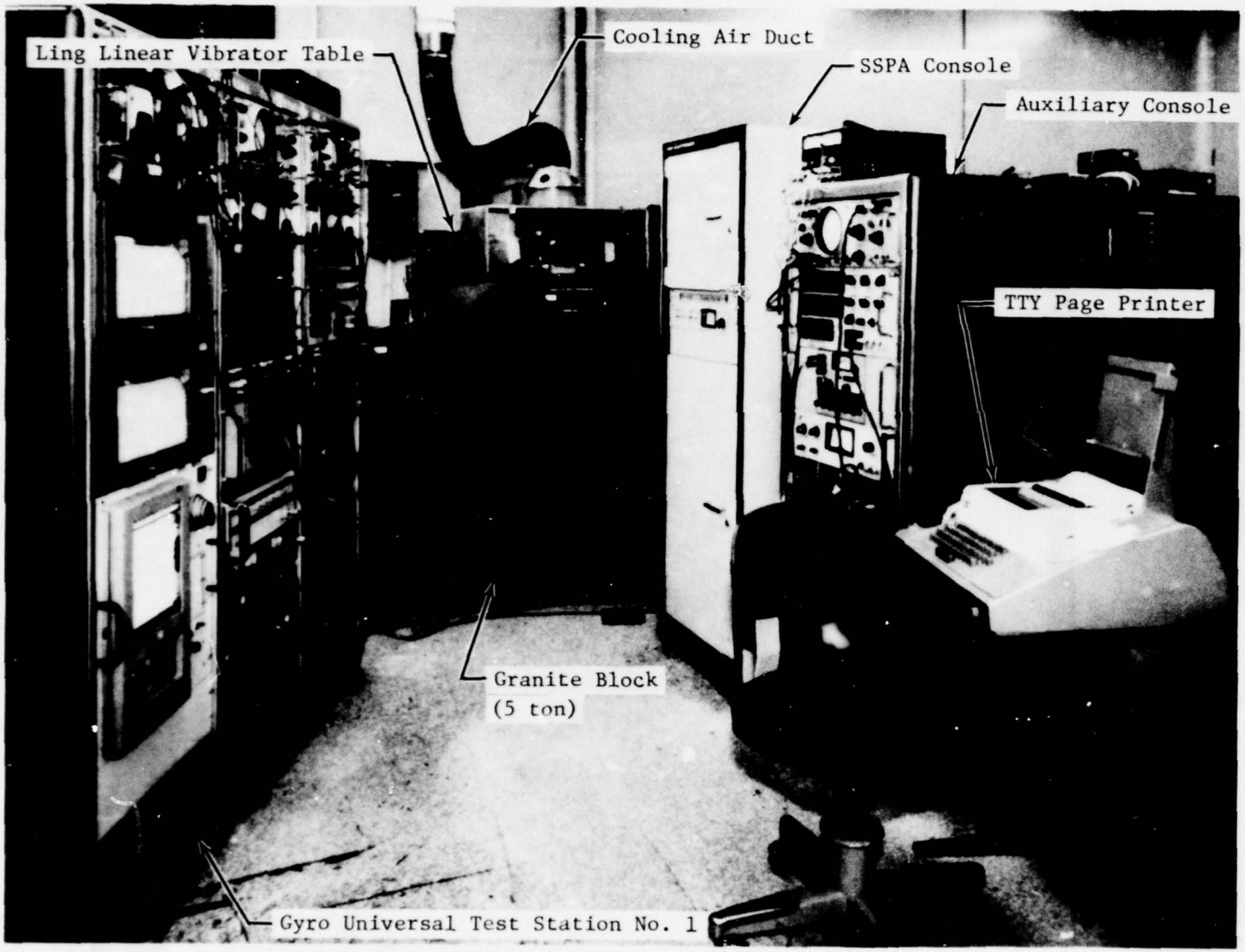


Fig 4. Linear Vibration Test Station

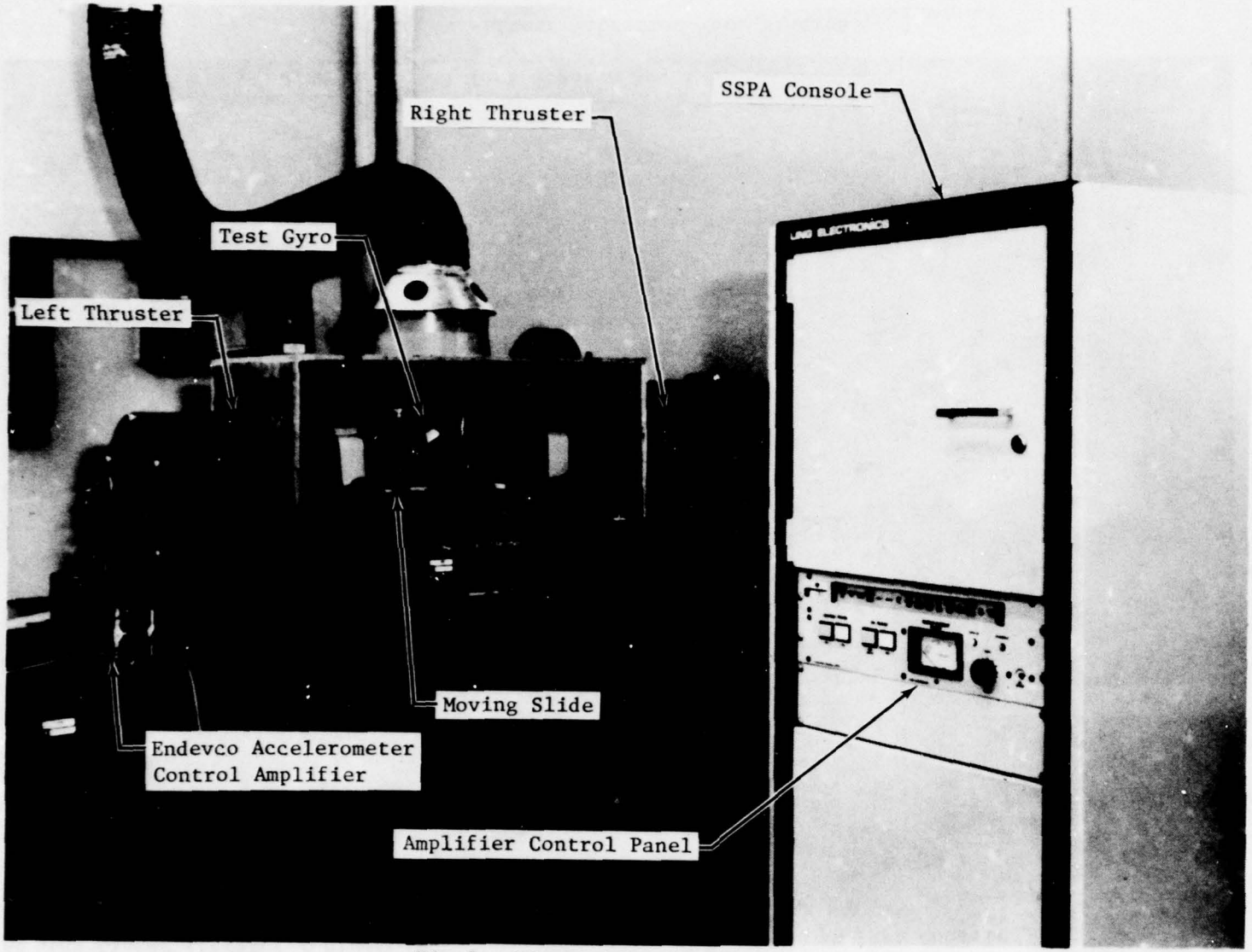


Fig 5. Ling Table Assembly

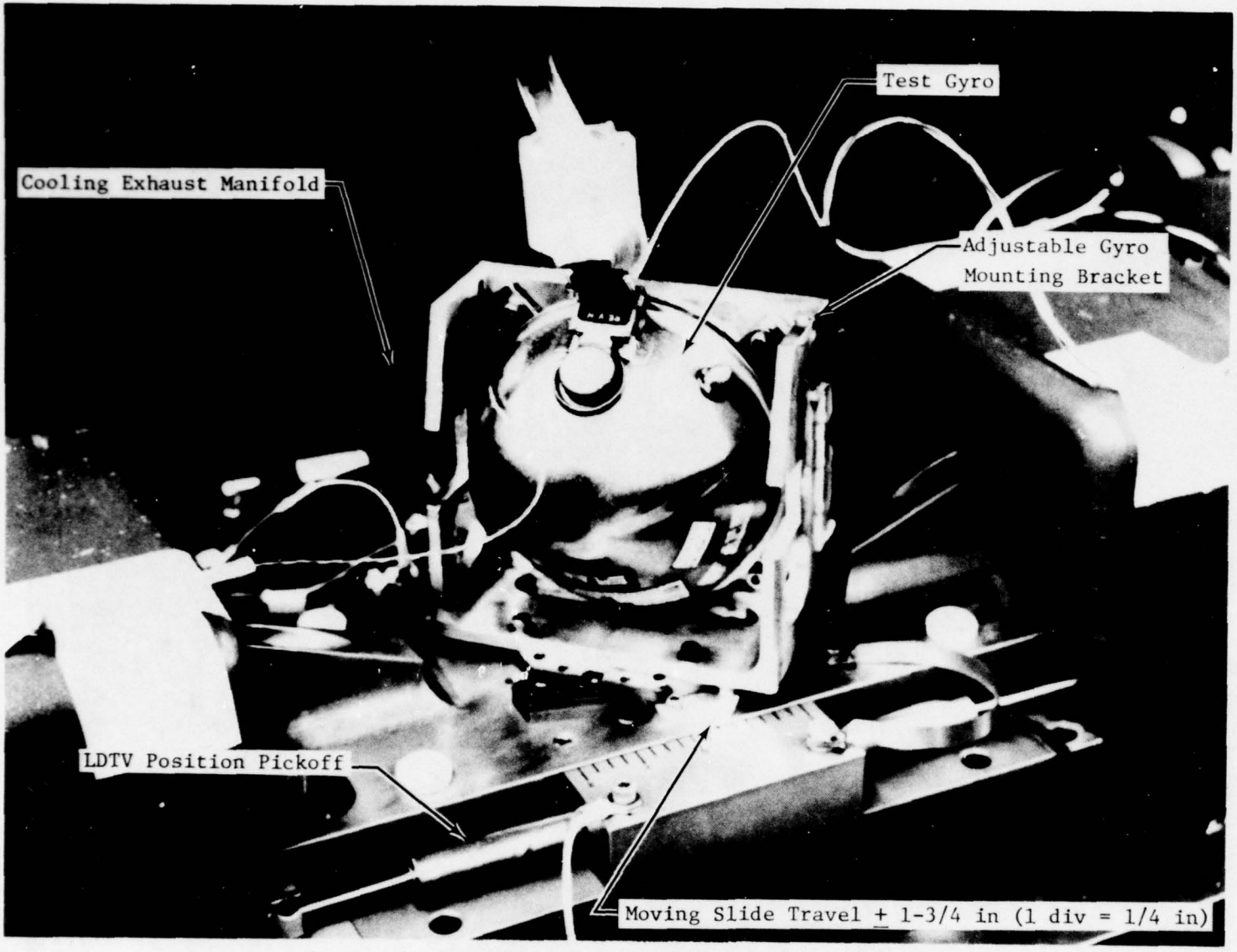


Fig 6. Close-Up of Vibration Table

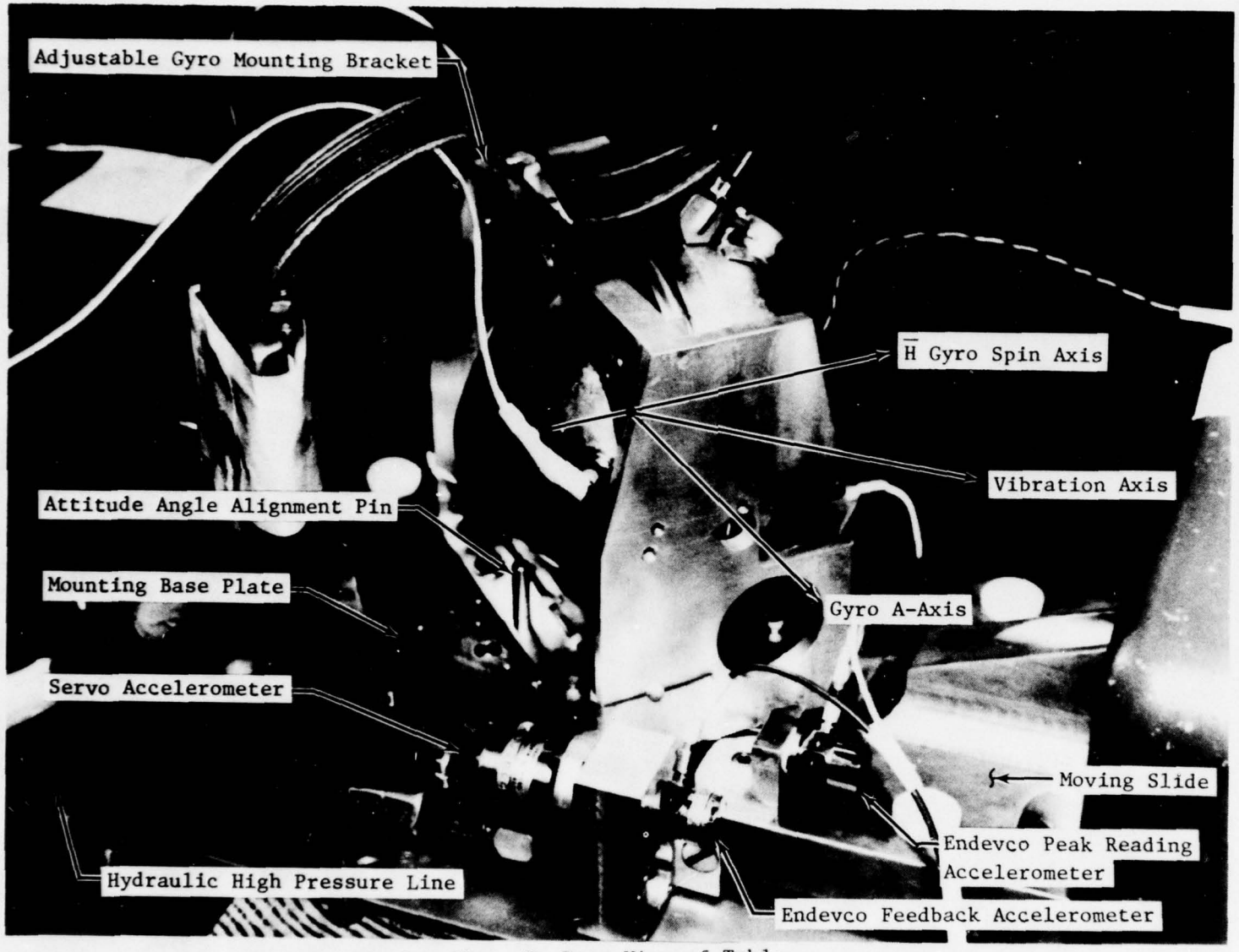


Fig 7. Close-Up Rear-View of Table

A hydraulic power supply is provided to supply the hydrostatic slide bearing. It provides a 3000 psi hydraulic control source with a safety cut-out system which shuts off the electrical power to the thrusters any time that the hydraulic pressure falls below a safe operating pressure. The high pressure supply line to the table is shown on Fig 7. The pressure control valve and cutoff switch are not shown but are located below the servo accelerometer.

B. PERFORMANCE CHARACTERISTICS

The performance characteristics of the Linear Vibrator are as follows:

Plane of acceleration	Horizontal
Force	0 - 500 lb force vector (min)
Maximum acceleration	15 g - no load 12 g - with 10 lb load
Maximum velocity	75 in/s vector
Maximum displacement	2 in vector (4 in p-p)
Physical stops	Cushioned stops (clearance $\pm$ 1.75 in)
Usable frequency range	5 - 1000 Hz
Harmonic distortion	Less than 4 pct THD in the 5 - 100 Hz range
Maximum roll or yaw angle*	Less than 10 arc sec vector
Maximum pitch angle*	Less than 30 arc sec vector
Maximum cross acceleration*	Less than 1.0 pct
Position signal	Provided by LVDT
Acceleration feedback signal	Provided by accelerometer
Weight of moving assembly	30 lb, without payload
Gyro and mounting bracket	8.6 lb
Minimum power amplifier output	4.0 k VA
Operating range (g vs frequency)	Fig 8
Utility Power Requirements	
Electrical power	20 kVA, 460 V, 3-ph, 60 Hz
Water cooling (for power ampl)	3 gpm flow @ 95°F maximum inlet temp with 20 psi drop

* In the 5 to 50 Hz range with a 7.5 lb mass load added to the slide mass, mounted with its center of gravity 3.25 in above table surface.

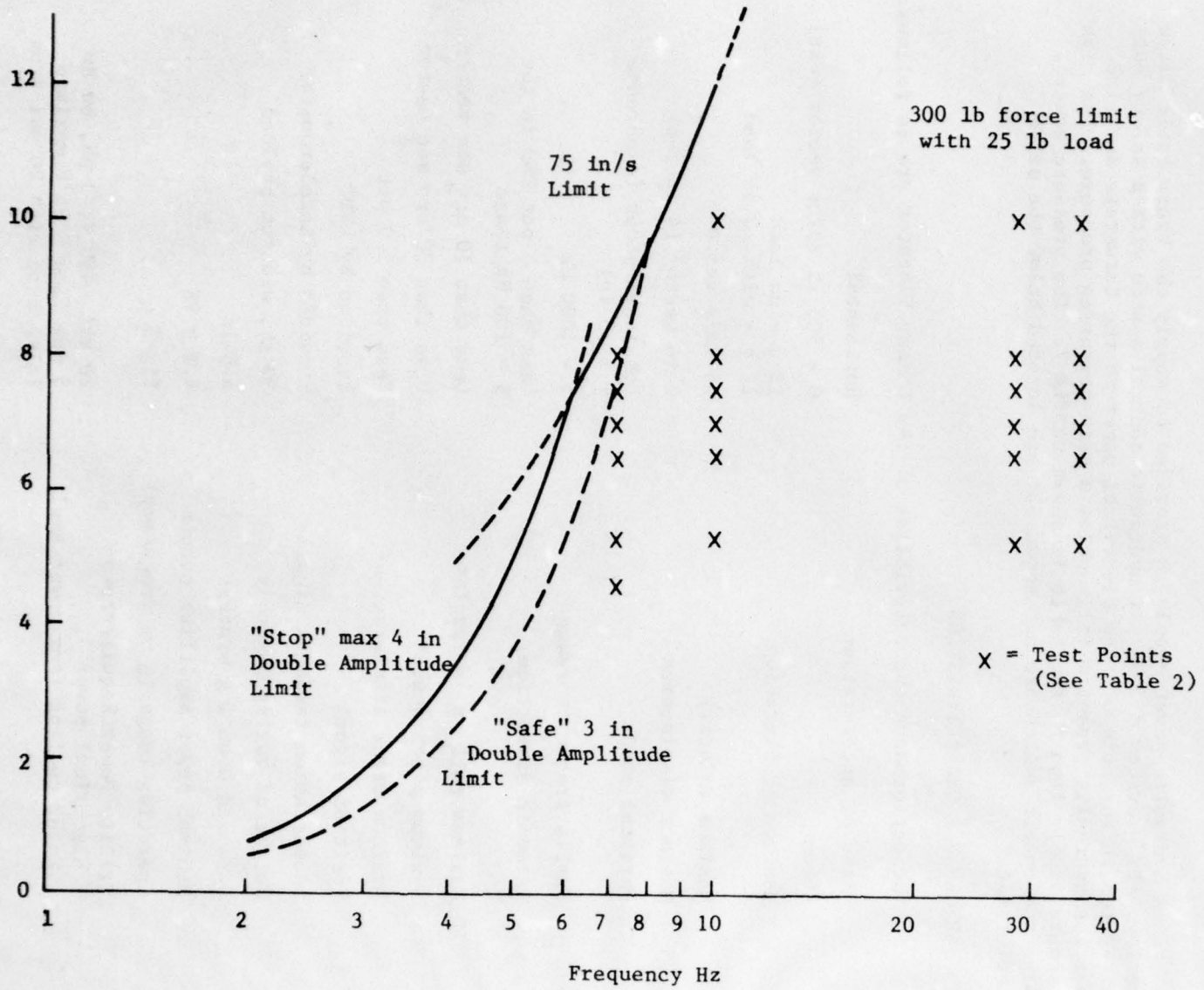


Fig 8 New Linear Vibrator Operating Range

C. TEST METHOD

To measure the four g^4-coefficients of the gyro, it is necessary to expose the gyro to sinusoidal accelerations of from 5 to 10 g peak amplitude. Vibration vector is applied along a horizontal axis and the gyro is mounted with its spin axis horizontal and its B axis vertically downward. A gyro mounting bracket is provided which allows the gyro spin axis to be positioned about the vertical axis in the horizontal plane. The angle between the spin axis and the vibration vector, is called θ. When θ is zero, the spin axis is along the vibration vector; when $\theta = 90°$, the gyro A-axis is along the vibration vector. The even harmonic coefficients, g^2 and g^4, are most sensitive to acceleration in orientations when $\theta = \pm 30$ to $\pm 60°$, and these angles are the ones used for measuring the g^4-coefficients. The frequencies used are the lowest ones possible within the operating range of the vibration table. The values selected are shown in Table 1. The gyro orientation on the test table vibrating slide is shown in Fig 9.

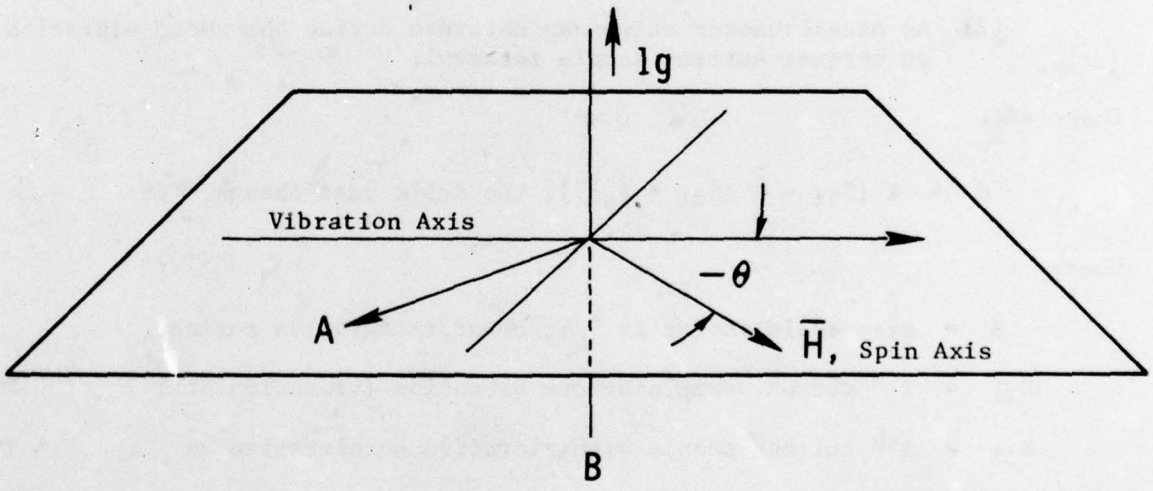


Fig 9. Gyro Orientation

The linear vibration system was used with the Gyro Universal Torque Test Station which provides the required gyro running power, caging loops for each axis, and the digital readout of the caging loop torquing signals.

D. EXPOSURE CONDITIONS

The acceleration levels, frequencies, orientation angles, and vibration duration times are listed in Table 2.

Table 2. Engineering Test Conditions

Positions Used	$0 \pm 30°, \pm 45°, \pm 60°$				
At Each Position, Frequencies Used (Hz)	35	28	10	7.25	
At Each Frequency, g-Levels Used	10	8	7.65	7.5	5.3

E. TEST DATA

The test data consisted of:

(1) A 3-min sample of torquer current for both axes. Three such samples sequentially obtained from vibration off, vibration on, and vibration off conditions were used to obtain one data point.

(2) An accelerometer value was obtained during the above vibration on torquer-current sample interval.

Computed:

$$\Delta = K \left[S_{2i} - \frac{1}{2} (S_{1i} + S_{3i})\right], \text{ the drift rate change, °/h}$$

where

K = gyro scale factor in °/hr/count/integration period

S_{1i} = i^{th} current sample before vibration (vibration off)

S_{2i} = i^{th} current sample with vibration acceleration on

S_{3i} = i^{th} current sample after vibration (vibration off)

The equations for the vibration test are derived from the gyro fourth-order acceleration sensitivity model. The A-axis and B-axis torques are

$$K_A I_A = K_{BO} - \frac{1}{2} G^2 \left[\cos^2 \theta \, F_B - \sin^2 \theta \, C_{3_B} + \cos \theta \sin \theta \, (E_B + R_B)\right]$$

$$- \frac{3}{8} G^4 \left[\sin \theta \cos^3 \theta \, P_B + \sin^3 \theta \cos \theta \, R_B\right]$$

$$K_B I_B = K_{AO} - \frac{1}{2} G^2 \left[- \cos^2 \theta F_A - \sin^2 \theta D_{3_A} + \cos \theta \sin \theta (B_A + N_A) \right]$$

$$- \frac{3}{8} G^4 \left[\sin \theta \cos^3 \theta J_A + \sin^3 \theta \cos \theta N_A \right]$$

where

$K_A I_A, K_B I_B$ = total torque (°/hr)

K_{BO}, K_{AO} = constant drift (°/hr)

G = acceleration input along vibration axis (g, peak)

θ = fixture angle (°), see Fig 9

F_A, F_B, E_B, B_A = second-order drift sensitivities to acceleration (°/hr/g^2)

C_{3_B}, D_{3_A} = third-order drift sensitivities to acceleration (°/hr/g^3)

P_B, R_B, J_A, N_A = fourth-order drift sensitivities to acceleration (°/hr/g^4)

The apparent discrepancy in the order of R_B, N_A, C_{3_B}, and D_{3_A} noted in the equations above results from a constant 1-g applied to the gyro B axis.

The sequence of test is as follows:

(1) By means of the precision adjustable test fixture, select a particular value of θ.

(2) Chose a vibration input frequency value.

(3) Apply discrete levels of vibration to the gyro. Before and after each vibration level input, average the gyro torquer current values. Average the currents while each vibration level is applied.

(4) Select a new vibration input frequency and repeat steps (2) and (3).

(5) Select a new angle θ and repeat steps (2) through (3). Repeat for all specified values of θ.

The following test data were tabulated for each test condition: θ, g-level, frequency, A-axis drift rate change, and the B-axis drift rate change. A computer then used these data to compute the coefficients F_B, C_{3_B}, E_B, R_B, P_B, F_A D_{3_A}, B_A, J_A, and N_A from the acceleration model equations for each frequency. Each of the g^2-coefficients, E_B and B_A, and the g^4-coefficients, J_A, B_A, N_A, and R_B at each of the test frequencies were computer analyzed. The four frequency values for each coefficient were used to determine a best-fit least-squares straight line curve. The zero-frequency intercept value for each coefficient was determined by the computer. These intercepts are for the g^2 and g^4 coefficients, respectively. The g^2 coefficients were compared to the tumble test results for each gyro.

IV. EXPERIMENTAL RESULTS

An example of the test results are shown in Fig 10 to 15. These are plots of the g^2 and g^4 coefficients as a function of frequency with their least squares intercept for zero frequency. Using all of the experimental data, the experimental algorithms for the various coefficients are shown in Table 3.

Table 3. Comparison of Theoretical and Experimental Planar Algorithms

THEORETICAL (Using Theoretical B&E Coefficients)

$J = 0.00091738 - 0.00391575\ \underline{B} - 0.00092656\ \underline{E}$

$P = 0.00023276 - 0.00078413\ \underline{B} - 0.00028064\ E$

Residuals of Theoretial Points to Theoretical Algorithm = $0.0001048\ °/hr/g^4$ for J

Residuals of Theoretical Points to Theoretical Algorithm = $0.0000321\ °/hr/g^4$ for P

EXPERIMENTAL (Using Vibration Test B&E g^2 Coefficients)

$J = 0.00087033 - 0.00346644\ \underline{B} - 0.00159355\ \underline{E}$

$P = 0.00034152 - 0.00002698\ \underline{B} - 0.00190728\ \underline{E}$

Residuals of Experimental Points to Experimental Algorithm = $0.0000759\ °/hr/g^4$ for J

Residuals of Experimental Points to Experimental Algorithm = $0.0000447\ °/hr/g^4$ for P

Above residuals are within: 10% for J
20% for P

Experimental Algorithm Can Be Transformed for Use With Test B&E Coefficients

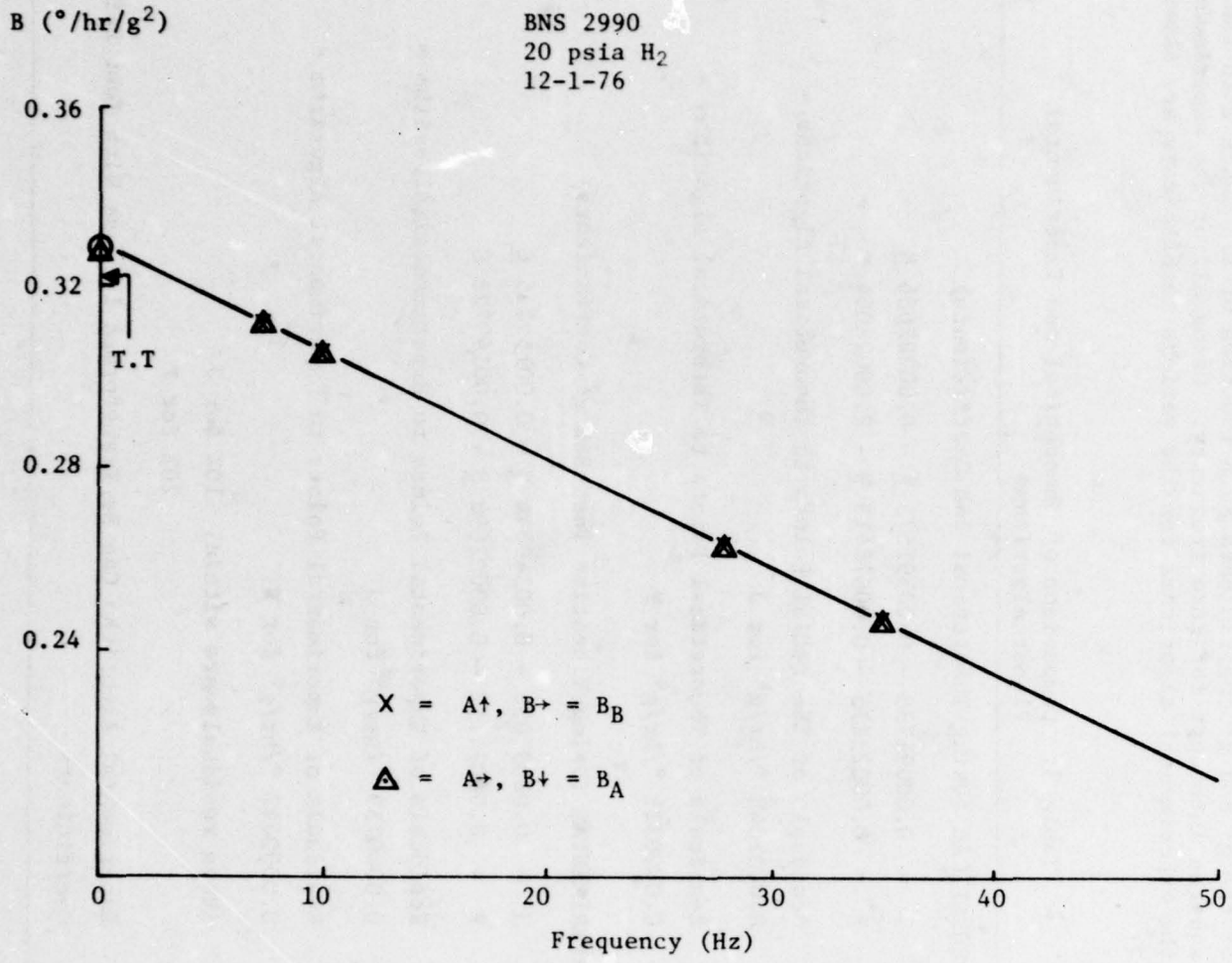


Fig 10. Gyro Test Results, B Coefficient

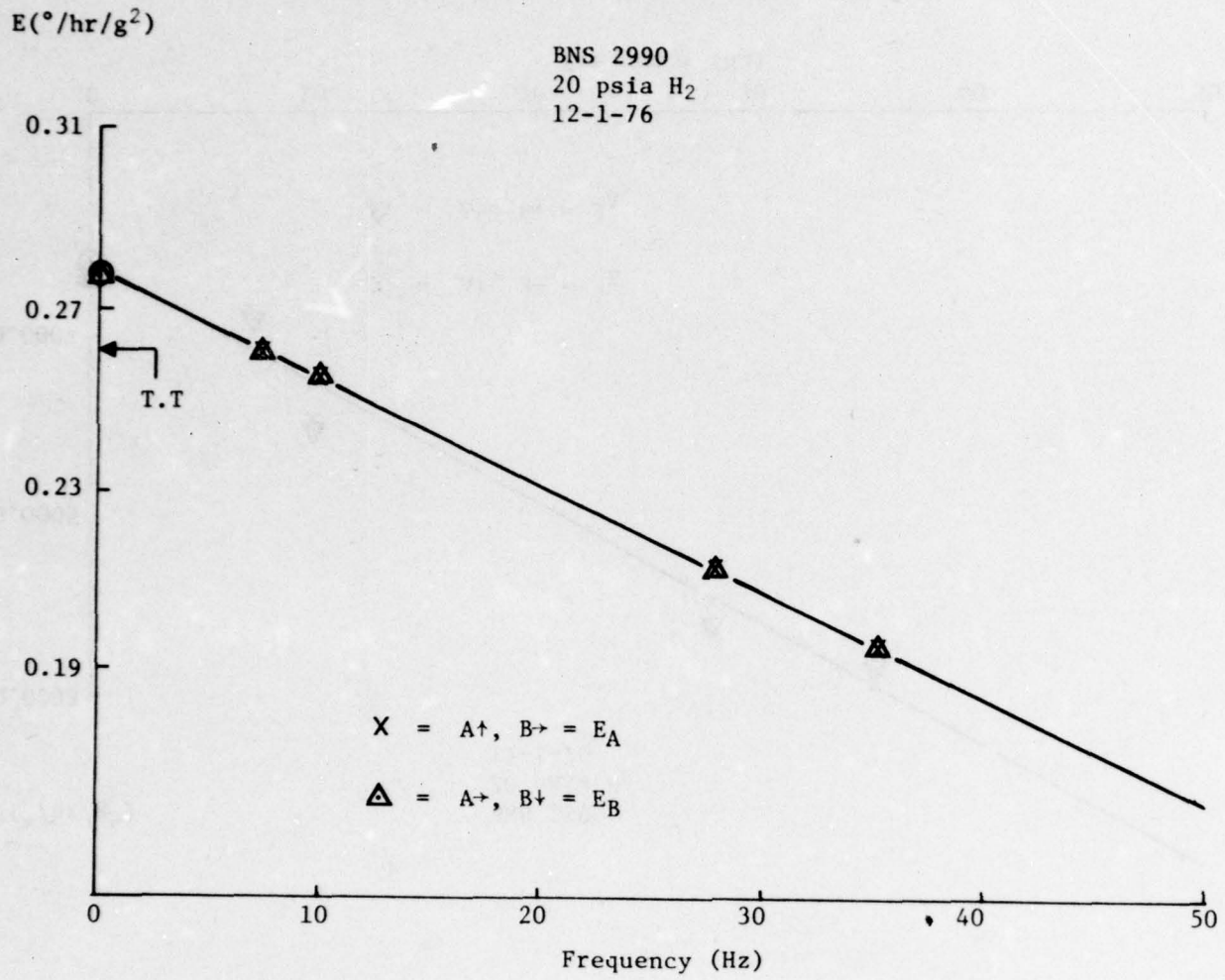


Fig 11. Gyro Test Results, E Coefficient

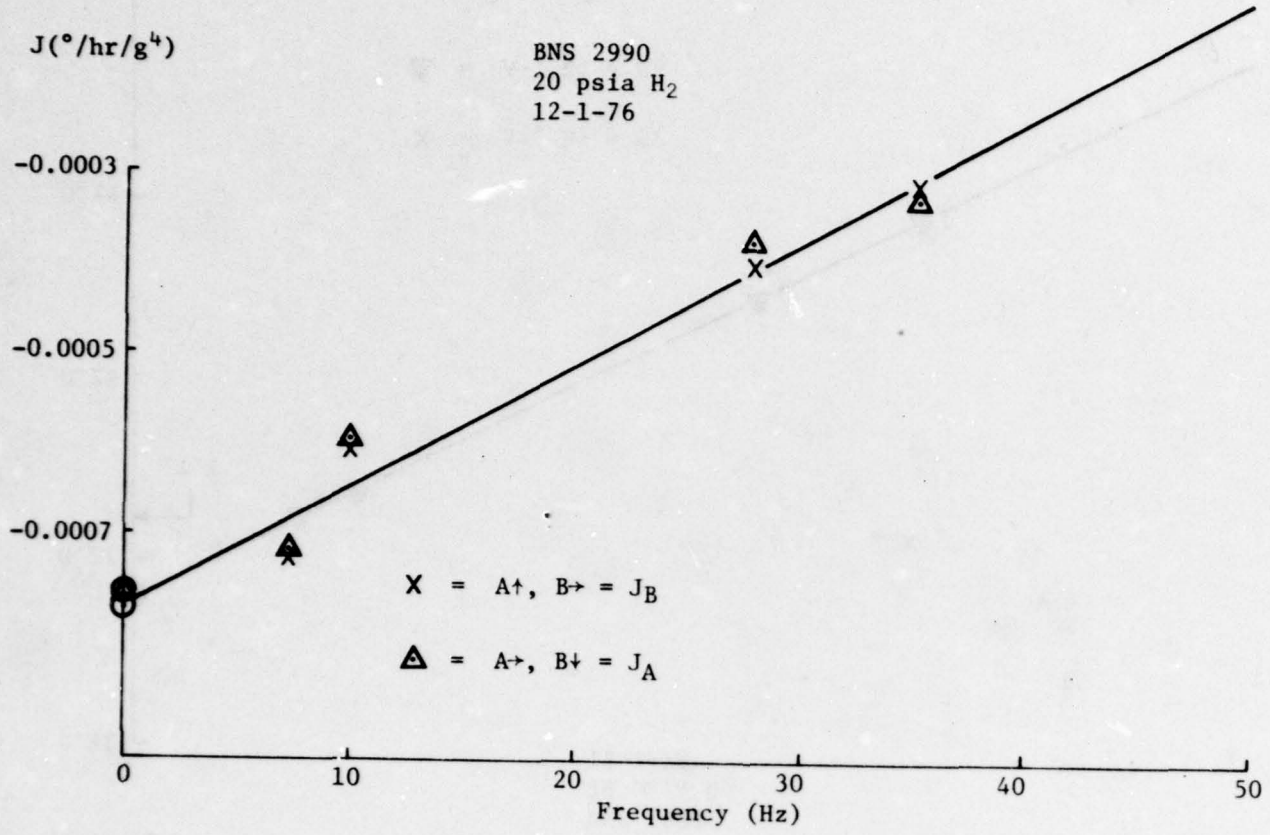


Fig 12. Gyro Test Results, J Coefficient

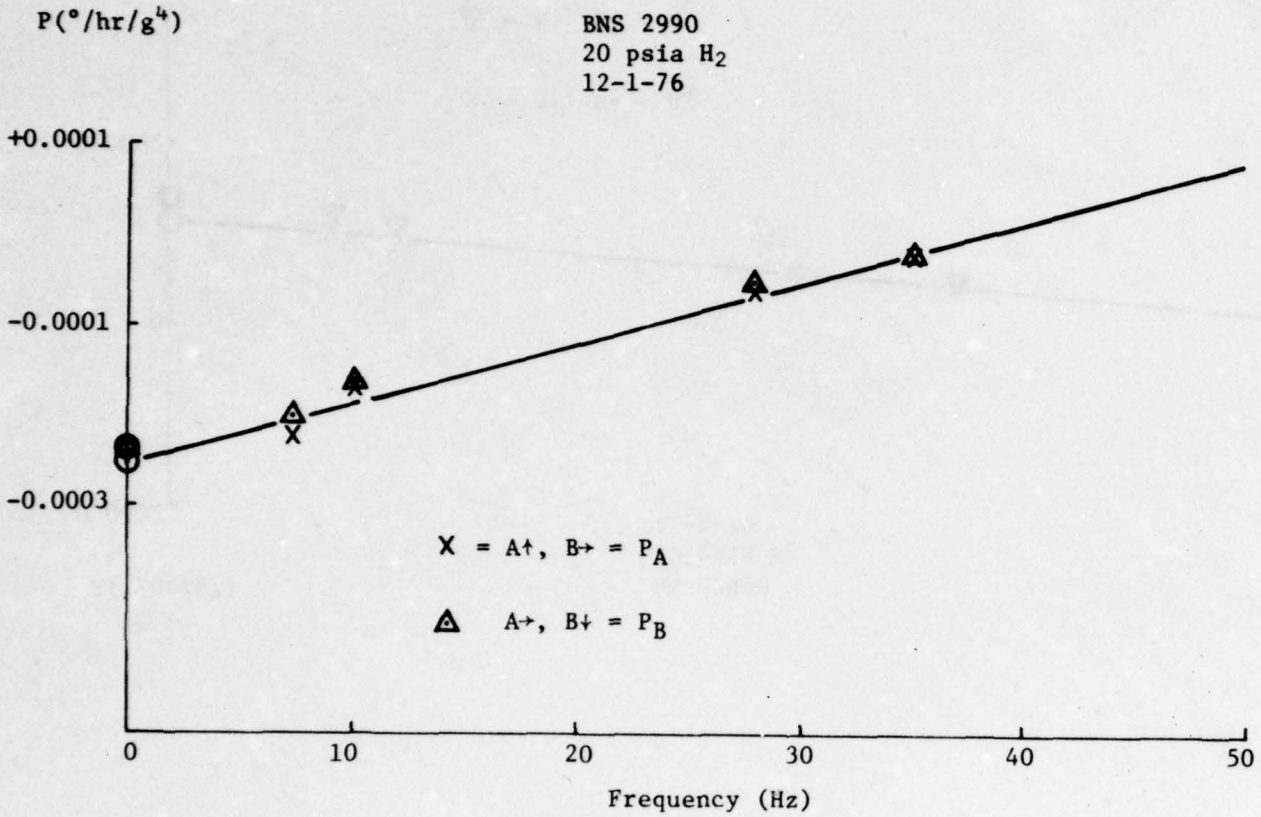


Fig 13. Gyro Test Results, P Coefficient

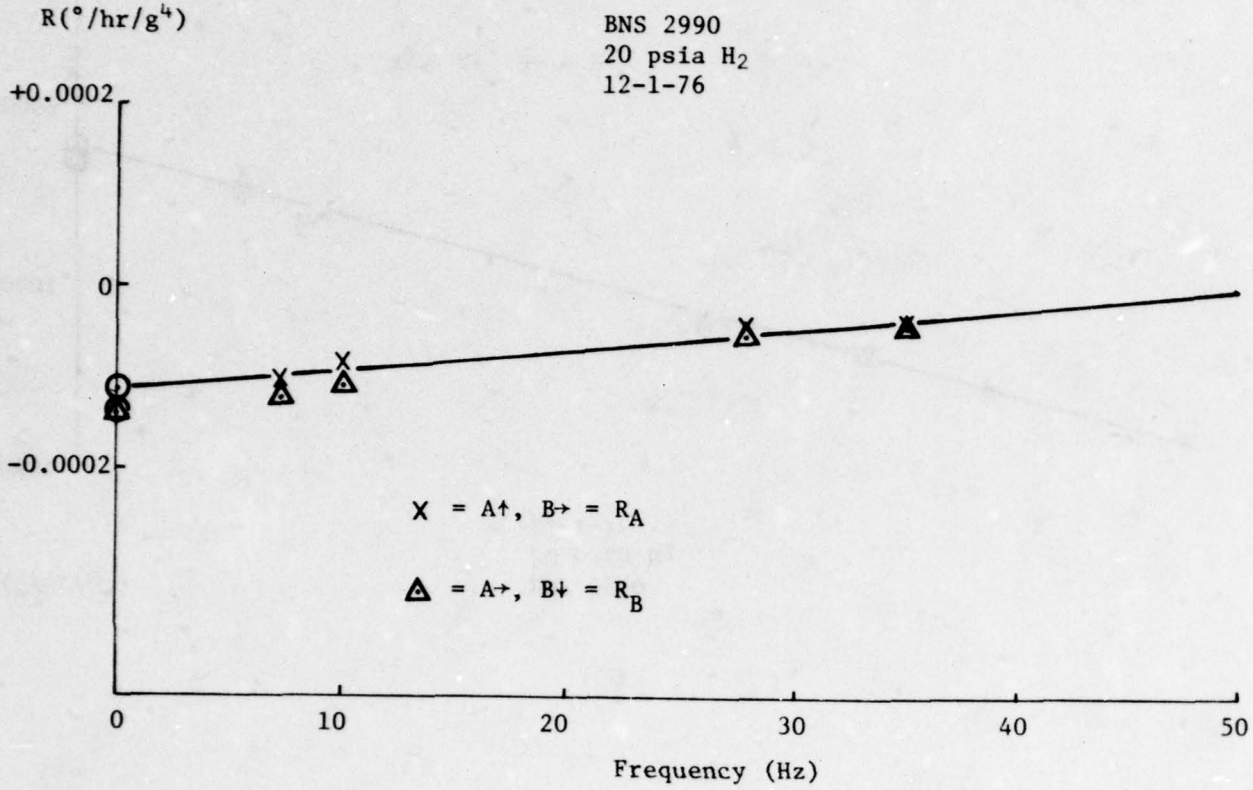


Fig 14. Gyro Test Results, R Coefficient

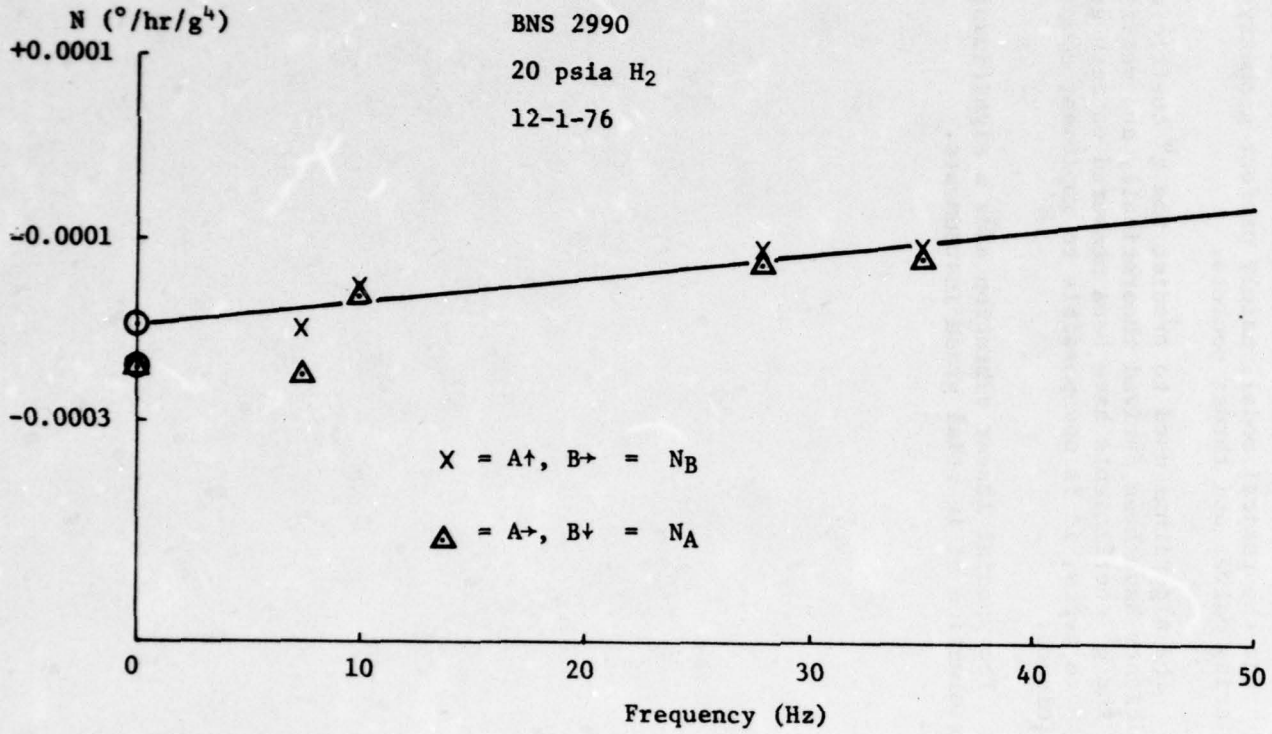


Fig 15. Gyro Test Results, N Coefficient

V. CONCLUSIONS

The functional form of the g^4 coefficients have been shown experimentally and agree with the theoretical predictions within expected accuracy. It is concluded that the main deviations are due to the assumption that were made in the theoretical model, mainly perfect geometry and axial symmetry of the bearing halves and thrust pockets.

The algorithms used to predict the g^4 coefficients from the g^2 coefficients have been derived theoretically and verified experimentally. Since the g^2 coefficients have been measured on each gyro during factory acceptance tests, it is now possible to implement compensation of the g^4 coefficients.

The special linear vibration adds a significant test capability for the examination of inertial grade instruments.

REFERENCES

1. Castelli, V., "The Calculation of Loads and Pressure Gradient Torques in a Spherical Gas Bearing at $\Lambda \to \infty$," Report to Autonetics, 1975.

2. Tipei, N., and V. N. Constantinescu, "Lubrification suprafetelor sferice," Communicarile Acad. R.P.R., 6, 1956.

3. Zedekar, S. L., "The Effect of Viscous and Pressure Gradient Torques on a Free Rotor Gyroscope," Trans. ASME Journal of Lub Tech. 1969.

4. Reynolds, O., "On the Theory of Lubrication and its Application to Mr. Beauchamp Tower's Experiments Including an Experimental Determination of the Viscosity of Olive Oil," Phil. Trans. Roy. Soc. London, Ser. A, 177, 157-234.

5. Cogan, S. W., "Free-Rotor Gyro Acceleration Sensitivity," Autonetics Division of North American Aviation, August 13, 1958.

EIGHTH BIENNIAL GUIDANCE TEST SYMPOSIUM

GYRO PERFORMANCE EVALUATION FROM LINEAR RANDOM VIBRATION TESTING

AUTHORS: MR ROBERT THEDE
1LT MICHAEL DELORENZO

CENTRAL INERTIAL GUIDANCE TEST FACILITY
6585TH TEST GROUP
HOLLOMAN AIR FORCE BASE, NEW MEXICO

ABSTRACT

In the past, linear vibration testing of gyros has been accomplished at discrete frequencies and discrete acceleration levels. Analysis of the test data has been restricted to determination of acceleration squared sensitivities from rectification effects found in data that were averaged over a long time period. The development of more precise linear vibration systems and more sophisticated data acquisition and data processing equipment is now making it possible to more fully evaluate a gyro's performance in a linear vibration environment.

This paper presents a method for obtaining gyro performance model coefficients from linear random vibration testing. Both acceleration sensitive and acceleration squared sensitive coefficients are obtainable. These coefficients are obtained from combinations of average auto and cross power spectra of the gyro's output, the applied acceleration, and the acceleration squared. A mini-computer with a Fourier Analyzer is used to collect the gyro and acceleration data through an analog to digital converter. The required power spectra are then formed and combined to yield the sensitivities of the gyro to acceleration and to acceleration squared as a function of frequency. The sensitivities obtained will contain rate inputs to the gyro which are also proportional to acceleration and acceleration squared. These rates can be separated from the gyro's acceleration sensitivities by accurately measuring the rates, by using multiple orientations of the gyro and assuming that the rates will be repeatable with the gyro reorientation or by testing two gyros simultaneously Procedures for rate separation using each of these methods are also presented

The results of a series of tests conducted on an Inertial Rate Integrating Gyro (IRIG) using these test and analysis procedures is also presented. These tests subjected the gyro to random vibrations along its spin axis. Multiple orientations of the gyro were used to separate the gyro's acceleration sensitivity from rate inputs. The results show a D_S coefficient (i.e., an error coefficient that results from a mass unbalance along the input axis of the gyro) which agrees very well with tumble test results at low frequencies, but which decreases with increasing frequency. Possible causes for this phenomena are also discussed.

The overall testing technique presented in this paper demonstrates the powerful and efficient contribution that random vibration coupled with spectral analysis can make to gyro dynamic performance evaluation. The technique when completely perfected and properly instrumented will enable extremely rapid and accurate evaluations of inertial gyroscopes in environments that closely approximate their operational environment.

1.0 INTRODUCTION

The goal of any dynamic modeling effort is to subject the test specimen to a precisely known dynamic input and to determine its performance characteristics from the corresponding specimen output. A test bed which has been in use for some time for dynamic modeling of gyroscopes is the precision linear vibrator. These past modeling efforts have concentrated on subjecting the gyro to a discrete sinusoidal acceleration at a single frequency and then determining the gyro's sensitivity to the square of acceleration by looking at the rectification produced in the gyro's average output. In 1973 Major Dino Lorenzini proposed subjecting the instrument to random accelerations over a band of frequencies (Reference 1). All gyro acceleration and acceleration squared sensitive coefficients could then be determined as functions of frequency from auto and cross power spectra of the gyro's output and the applied acceleration. The purpose of this paper is to formulate a simple random vibration gyro test based upon the procedures suggested by Major Lorenzini. Also presented in this paper will be several methods to separate rate inputs to the gyro from the gyro's acceleration sensitivities. A limited amount of testing using the methods suggested in this paper has been conducted on an IRIG-16 gyro, and results of these tests are also presented. The work presented in this paper is an effort of the SHIP/Tech C Follow-On Program being conducted by the Guidance Test Division 6585th Test Group, Holloman AFB, New Mexico under the sponsorship of the Space and Missile Systems Organization (SAMSO), Los Angeles Air Force Station, CA.

2.0 GYRO MODEL

The classical model which has been widely accepted for explaining unbalance and compliance torques in a gyroscope, and which is currently being used for gyro evaluation in a random vibration environment is as follows:

$$S_T i = D_F + D_I a_I + D_O a_O + D_S a_S + D_{II} a_I^2 + D_{OO} a_O^2 + D_{SS} a_S^2 + D_{IO} a_I a_O + D_{IS} a_I a_S + D_{OS} a_O a_S + \omega_I - \frac{I_O \dot{\omega}_O}{H} \quad (1)$$

where

i = current flow through the torquer (ma)

S_T = torquer scale factor (°/hr/ma)

a_I = acceleration, with respect to inertial space of the gyro case along the input axis (g)

a_O = acceleration, with respect to inertial space, of the gyro case along the output axis (g)

a_S = acceleration, with respect to inertial space, of the gyro case along the spin axis (g)

D_F = gyro drift (°/hr) which is insensitive to acceleration

$D_I a_I$ = gyro drift (°/hr) attributable to acceleration along the input axis, where D_I (°/hr/g) is a drift coefficient

$D_O a_O$ = gyro drift (°/hr) attributable to acceleration along the output axis, where D_O (°/hr/g) is a drift coefficient

$D_S a_S$ = gyro drift (°/hr) attributable to acceleration along the spin axis, where D_S (°/hr/g) is a drift coefficient

$D_{II} a_I^2$ = gyro drift (°/hr) attributable to the square of acceleration along the input axis, where D_{II} (°/hr/g^2) is a drift coefficient

$D_{OO} a_O^2$ = gyro drift (°/hr) attributable to the square of acceleration along the output axis, where D_{OO} (°/hr/g^2) is a drift coefficient

$D_{SS} a_S^2$ = gyro drift (°/hr) attributable to the square of acceleration along the spin axis, where D_{SS} (°/hr/g^2) is a drift coefficient

$D_{IO} a_I a_O$ = gyro drift (°/hr) attributable to the product of accelerations along the input axis and output axis, where D_{IO} (°/hr/g^2) is a drift coefficient

$D_{IS} a_I a_S$ = gyro drift (°/hr) attributable to the product of accelerations along the input axis and spin axis, where D_{IS} (°/hr/g^2) is a drift coefficient

$D_{OS} a_O a_S$ = gyro drift (°/hr) attributable to the product of accelerations along the output axis and spin axis, where D_{OS} (°/hr/g^2) is a drift coefficient

ω_I = angular velocity, with respect to inertial space, of the gyro case about the input axis (°/hr)

I_O = moment of inertia of the gyro float about its output axis

H = angular momentum of the gyro wheel

$\dot{\omega}_O$ = angular acceleration about the gyro's output axis

hr = sidereal hour

g = local acceleration of gravity, defined positive upward

The three gyro axes form a right hand, orthogonal coordinate frame such that

$$\bar{I} \times \bar{O} = \bar{S}$$

where

$\bar{I}$, $\bar{O}$, $\bar{S}$ are unit vectors along the gyro's input (IA), output (OA), and spin (SA) axes.

It should be pointed out that this is a steady state gyroscope model which does not include the frequency response of the instrument. Therefore, in order to accurately determine the gyro's acceleration sensitivities when applying sinusoidal accelerations it is important that the gyro's frequency response be determined and that the gyro output be compensated for this frequency response prior to determination of the gyro's acceleration sensitivities.

3.0 RANDOM VIBRATION TEST PROCEDURE

The proposed random vibration test is conducted by orienting the gyro on the linear vibrator with one axis vertical and either another axis along the line of vibration or two axes at 45 degrees to the line of vibration. Under any such orientation the gyro's output can be given by a quadratic in applied acceleration:

$$\phi(t) = D_o + D_x A(t) + D_{xx} A^2(t) \tag{2}$$

where

$\phi(t)$ = gyro output (deg/hr)

$A(t)$ = vibration acceleration (g)

D_o = gyro output not sensitive to acceleration (deg/hr)

$D_x A(t)$ = gyro output proportional to acceleration where D_x (deg/hr/g) is the proportionality constant

$D_{xx} A^2(t)$ = gyro output proportional to acceleration squared where D_{xx} (deg/hr/g^2) is the proportionality constant

The proportionality constants in the above equation contain gyro acceleration and acceleration squared sensitivities plus constants relating rate inputs to the gyro to acceleration and acceleration squared. The next section of this paper will discuss several possible methods for separating the gyro's acceleration sensitivities from rate inputs to the gyro that are also proportional to acceleration. D_x and D_{xx} are determined by removing the mean from the data and then converting it to the frequency domain by a Fourier transform. The result is

$$\phi(f) = D_x A(f) + D_{xx} A^2(f) \tag{3}$$

Two new equations are now formed by first multiplying the above equation by the conjugate of acceleration and then by the conjugate of acceleration squared.

$$A^*(f)\phi(f) = D_x A^*(f)A(f) + D_{xx} A^*(f)A^2(f) \tag{4}$$

$$A^{2*}(f)\phi(f) = D_x A^{2*}(f)A(f) + D_{xx} A^{2*}(f)A^2(f) \tag{5}$$

These equations can be rewritten in terms of power spectra by recognizing that:

$$G_{YZ} = Y^*(f)Z(f) \tag{6}$$

where G_{YZ} is the cross power spectrum of Y(f) and Z(f).

Using this power spectrum notation and writing equations 4 and 5 in matrix form gives:

$$\begin{bmatrix} G_{A\phi} \\ G_{A^2\phi} \end{bmatrix} = \begin{bmatrix} G_{AA} & G_{AA^2} \\ G_{A^2A} & G_{A^2A^2} \end{bmatrix} \begin{bmatrix} D_x \\ D_{xx} \end{bmatrix} \tag{7}$$

This is a transfer function equation for a two input, single output system. The vector on the left of the equal sign is the cross-spectrum vector of the output ϕ with the inputs A and A^2. The 2x2 matrix is the cross-spectrum matrix of the inputs. The frequency response functions are D_x and D_{xx}. The frequency response functions are determined by inverting the cross-spectra matrix.

$$\begin{bmatrix} D_x \\ D_{xx} \end{bmatrix} = \begin{bmatrix} G_{AA} & G_{AA^2} \\ G_{A^2A} & G_{A^2A^2} \end{bmatrix}^{-1} \begin{bmatrix} G_{A\phi} \\ G_{A^2\phi} \end{bmatrix} \tag{8}$$

A first inspection might indicate that the matrix to be inverted is singular. That is

$$(A^*A)(A^{2*}A^2) - (A^{2*}A)(A^*A^2) = 0$$

This will indeed be the case if only one determination is made of the power spectra or if a repeatable acceleration spectrum is used. However, if random acceleration levels are used and average power spectra are obtained this will not be the case. Under random acceleration A(f) and $A^2(f)$ at any given frequency are unrelated. The average cross powers, G_{A^2A} and G_{AA^2}, therefore approach zero as the number of averages increases. From equation 8 the solution for D_x and D_{xx} are:

$$D_x = \left(\frac{G_{A\phi}}{G_{AA}} - \frac{G_{A^2\phi}}{G_{A^2A^2}} \frac{G_{AA^2}}{G_{AA}} \right) \left(1 - \frac{G_{A^2A}}{G_{A^2A^2}} \frac{G_{AA^2}}{G_{AA}} \right)^{-1} \tag{9}$$

$$D_{xx} = \left(\frac{G_{A^2\phi}}{G_{A^2A^2}} - \frac{G_{A\phi}}{G_{AA}} \frac{G_{A^2A}}{G_{A^2A^2}} \right) \left(1 - \frac{G_{AA^2}}{G_{AA}} \frac{G_{A^2A}}{G_{A^2A^2}} \right)^{-1} \tag{10}$$

A coherency function representing the correlation between the input variables and the output variables as a function of frequency can also be determined. It is given by:

$$\gamma^2 = \frac{|G_{yz}|^2}{G_{yy}G_{zz}} \tag{11}$$

where

γ^2 = coherency function

G_{yz} = cross spectrum of input and output

G_{yy} = cross spectrum of inputs

G_{zz} = cross spectrum of outputs

Theoretically the coherency function should have a value between zero and one. In matrix notation the coherency function is written as:

$$\gamma^2 = [G_{yz}]^T \quad [G_{yy}G_{zz}]^{-1} [G_{yz}] \tag{12}$$

In the case presented here this becomes

$$\gamma^2 = \begin{bmatrix} G_{A\phi} & G_{A^2\phi} \end{bmatrix} \begin{bmatrix} G_{\phi\phi}G_{AA} & G_{\phi\phi}G_{AA^2} \\ G_{\phi\phi}G_{A^2A} & G_{\phi\phi}G_{A^2A^2} \end{bmatrix}^{-1} \begin{bmatrix} G_{A\phi} \\ G_{A^2\phi} \end{bmatrix} \tag{13}$$

Multiplying this out gives the following result:

$$\gamma^2 = \frac{\gamma^2_{A\phi} + \gamma^2_{A^2\phi}}{1 - \frac{G_{A^2A}}{G_{A^2A^2}}\frac{G_{AA^2}}{G_{AA}}} - \frac{|G_{A\phi}||G_{A^2\phi}|}{G_{\phi\phi}} \left[\frac{\frac{1}{G_{AA}}\frac{G_{A^2A}}{G_{A^2A^2}} + \frac{1}{G_{A^2A^2}}\frac{G_{AA^2}}{G_{AA}}}{1 - \frac{G_{A^2A}}{G_{A^2A^2}}\frac{G_{AA^2}}{G_{AA}}} \right] \tag{14}$$

where

$$\gamma^2_{A\phi} = \frac{|G_{A\phi}|^2}{G_{AA}G_{\phi\phi}}$$

$$\gamma^2_{A^2\phi} = \frac{|G_{A^2\phi}|^2}{G_{A^2A^2}G_{\phi\phi}} \tag{15}$$

Expressions have now been given for the determination of gyro acceleration and acceleration squared sensitivities as a function of frequency and for

the determination of the coherency function for any given orientation of the gyro during random vibration testing. Complete modeling of the gyro will require testing it in a number of orientations. One possible set of test orientations and the gyro coefficients contained in the D_x and D_{xx} coefficients is given in Table I. It can be seen that by combining the results from the six orientations presented, all of the gyro acceleration squared sensitive coefficients can be obtained. The acceleration sensitive coefficients are not completely separable from the acceleration squared sensitive coefficients. The acceleration sensitive coefficients, however, are usually much larger than the acceleration squared sensitive coefficients, therefore good estimates of the acceleration sensitive coefficients can still be obtained. If complete separation were required additional test orientations could be used. Determination of the gyro coefficients from the orientations presented in Table I requires that methods be available for removing any rate inputs to the gyro which are also proportional to acceleration and acceleration squared. The next section of this paper discusses this problem.

4.0 SEPARATION OF RATES FROM ACCELERATION SENSITIVE COEFFICIENTS

A linear vibration system usually consists of a vibration exciter which drives a slip table on which the test specimen is mounted. This slip table is designed to only move in a straight line. If this slip table were perfect there would be no rates present on the table. Imperfections in the table, however, will usually result in rates being present which will be proportional to the applied acceleration and possibly also to the square of acceleration. Therefore, in order to conduct a meaningful test, methods must be developed whereby these rates can be separated from the gyro's acceleration sensitivities. Three different methods for doing this are now presented.

4.1 Rate Measurements with Accelerometers

Any rocking motion of the slip table will introduce rates to the test item on the table. This motion will also result in accelerations on the slip table. It will be assumed that the slip table rocks as a rigid body about some point and that the rocking is proportional to the applied acceleration driving the table. Referring to Figure 1, the amount of acceleration at two points, P_1 and P_2, on the slip table caused by this rocking will now be determined. The rocking will result in displacements, d_1 and d_2 at points P_1 and P_2.

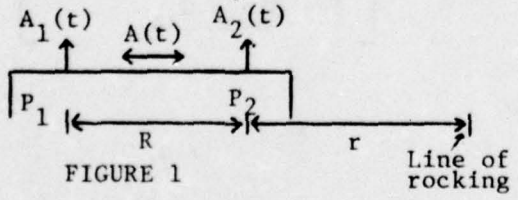


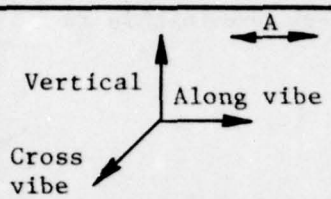
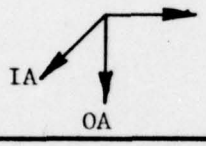
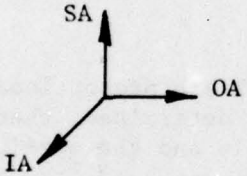
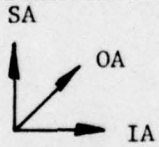
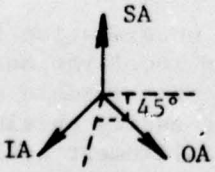
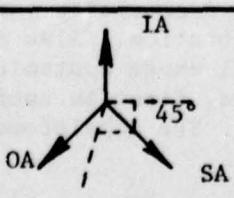
FIGURE 1

The angular acceleration at points P_1 and P_2 is the second derivative of the angular displacement at these points.

$$\ddot{\theta}(t) = \frac{A_1(t)}{R + r} = \frac{A_2(t)}{r} \tag{16}$$

TABLE I

GYRO TEST ORIENTATIONS

ORIENTATION	D_X	D_{XX}
		
	$D_S - D_{OS}$	D_{SS}
	$D_O + D_{OS}$	D_{OO}
	$D_I + D_{IS}$	D_{II}
	$\sqrt{2}/2\ (D_S - D_I)$	$1/2\ (D_{SS} + D_{II} - D_{IS})$
	$\sqrt{2}/2\ (D_O - D_I + D_{OS} - D_{IS})$	$1/2\ (D_{II} + D_{OO} - D_{IO})$
	$\sqrt{2}/2\ (D_S - D_O + D_{IS} - D_{IO})$	$1/2\ (D_{SS} + D_{OO} - D_{OS})$

This can be transferred to the frequency domain by a Fourier transform.

$$\ddot{\theta}(f) = \frac{A_1(f)}{R + r} \simeq \frac{A_2(f)}{r} \tag{17}$$

This gives the angular acceleration on the table. The rate is determined by integrating the angular acceleration. In the frequency domain this is achieved by multiplying by $\frac{j}{2\pi f}$ where $j^2 = -1$.

$$\dot{\theta}(f) = \frac{jA_1(f)}{2\pi f[R + r]} = \frac{jA_2(f)}{2\pi fr} \tag{18}$$

Equation 18 can now be solved for r and $\dot{\theta}(f)$

$$r = \frac{R}{A_1(f) - A_2(f)} \tag{19}$$

$$\dot{\theta}(f) = \frac{j\left[A_1(f) - A_2(f)\right]}{2\pi fR} \tag{20}$$

The rates which are of primary concern are those which are proportional to the acceleration of the slip table, A(t). The item to be determined, therefore, is the transfer function between the rates on the table and the acceleration of the table. This is given by

$$\frac{A^*(f)\dot{\theta}(f)}{A^*(f)A(f)} = \frac{j}{2\pi fR}\left[\frac{A^*(f)A_1(f)}{A^*(f)A(f)} - \frac{A^*(f)A_2(f)}{A^*(f)A(f)}\right] \tag{21}$$

This can be written as

$$H_{A\dot{\theta}} = \frac{j}{2\pi fR}[H_{AA_1} - H_{AA_2}] \tag{22}$$

where

$$H_{XY} = \frac{X^*Y}{X^*X} \tag{23}$$

The transfer function between the rates and the applied acceleration is determined by determining the transfer functions between accelerations perpendicular to the applied acceleration at two points on the table and the applied acceleration. These transfer functions could be easily obtained if perfect accelerometers could be obtained and if perfect alignment could be achieved. Any accelerometer will have some cross axis sensitivity and will not be aligned exactly perpendicular to the line of vibration. Also some purely lateral motion of the table may exist which will cause contaminating accelerations. A calibration procedure must, therefore, first be used before the desired transfer functions can be obtained. The accelerometer

which will be used to determine the acceleration at P_2 is first mounted at position P_1 in exactly the same orientation it will be mounted at P_2. Random vibration is applied and its output can be given by

$$A_{21}(t) = K_{02} + K_{21}A(t) + \delta_2 A(t) + A_{B1}(t) + A_{R1}(t) \quad (24)$$

where

$A_{21}(t)$ = acceleration indicated by accelerometer 2 at position 1

K_{02} = constant output

K_{21} = cross axis sensitivity

$A(t)$ = acceleration of the vibrator

δ_2 = input axis misalignment from a line perpendicular to the line of vibration, along the line of vibration

$A_{B1}(t)$ = acceleration caused by translational motion of the slip table along the accelerometers input axes

$A_{R1}(t)$ = acceleration caused by rocking of the Team table at position 1

The indicated acceleration is now converted to the frequency domain via a Fourier transform and the DC level is removed. The result is:

$$A_{21}(f) = K_{21}A(f) + \delta_2 A(f) + A_{B1}(f) + A_{R1}(f) \quad (25)$$

Auto and cross power spectra are then formed by multiplying both sides of the above equation by the conjugate of A(f).

$$A^*(f)A_{21}(f) = (K_{21} + \delta_2)A^*(f)A(f) + A^*(f)A_{B1}(f) + A^*(f)A_{R1}(f) \quad (26)$$

Both sides of this equation are now divided by the auto power spectrum of the vibration acceleration

$$\frac{A^*(f)A_{21}(f)}{A^*(f)A(f)} = K_{21} + \delta_2 + \frac{A^*(f)A_{B1}(f)}{A^*(f)A(f)} + \frac{A^*(f)A_{R1}(f)}{A^*(f)A(f)} \quad (27)$$

The term on the left of the equal sign in this equation is the transfer function between the indicated acceleration and the acceleration of the vibrator.

The last two terms in this equation are transfer functions between accelerations caused by translational motion and rocking motion of the slip table and the applied acceleration. Using transfer function notation this equation can now be rewritten as:

$$H_{AA_{21}}(f) = K_{21} + \delta_2 + H_{AA_{B1}}(f) + H_{AA_{R1}}(f) \quad (28)$$

Accelerometer 1 is now mounted in position P_1 and aligned precisely as it will be aligned during rocking determination. Random vibration is again applied and the same computational procedures are used as were used for accelerometer 2. If it is assumed that the translational and rocking transfer functions are repeatable from one run to another at any given point on the table the

transfer function between the acceleration indicated by accelerometer 1 when it is at position 1 and the applied acceleration will be given by:

$$H_{AA_{11}}(f) = K_{11} + \delta_1 + H_{AA_{B1}}(f) + H_{AA_{R1}}(f) \tag{29}$$

where

K_{11} = cross axis sensitivity of accelerometer 1

δ_1 = IA misalignment of accelerometer 1

The difference in cross axis sensitivity and IA misalignment of the two accelerometers can now be determined by subtracting equation 28 from equation 29.

$$H_{AA_{11}}(f) - H_{AA_{21}}(f) = K_{11} + \delta_1 - K_{12} - \delta_2 \tag{30}$$

This is the correction factor which will be required for rate determination. For simplification this correction factor will be referred to as C_{12}.

$$C_{12} = H_{AA_{11}}(f) - H_{AA_{21}}(f) \tag{31}$$

For rate determination the accelerometers are now mounted as shown in Figure 1 and random vibration is applied. Transfer functions between the indicated and applied accelerations are again formed exactly as was done during determination of the correction factor. The results are

$$H_{AA_{11}}(f) = K_{11} + \delta_1 + H_{AA_{B1}}(f) + H_{AA_1}(f) \tag{32}$$

$$H_{AA_{22}}(f) = K_{12} + \delta_2 + H_{AA_{B1}}(f) + H_{AA_2}(f) \tag{33}$$

These equations are subtracted and the correction factor (equation 31) is substituted in:

$$H_{AA_{11}}(f) - H_{AA_{22}}(f) - C_{12} = H_{AA_1}(f) - H_{AA_2}(f) \tag{34}$$

This is substituted into equation 22 for determination of the rate transfer function:

$$H_{A\dot{\theta}} = \frac{j}{2\pi fR}\left[H_{AA_{11}}(f) - H_{AA_{22}}(f) - C_{12}\right] \tag{35}$$

The rates proportional to acceleration about any axis on the slip table can, therefore, be determined with a pair of accelerometers, and the gyro output can be corrected accordingly. Since gyros are also sensitive to angular

accelerations about their output axes, this rate determination can be differentiated to give angular acceleration and the gyro output can also be compensated for this if the angular acceleration sensitivity is known. The procedure presented assumes that the rates are only proportional to acceleration. If rates proportional to acceleration squared are also present the procedures could be expanded to determine these also.

The drawbacks of using accelerometers to determine rates are that rigid body motion must be assumed and highly accurate accelerometers must be used. For g sensitive coefficient determination accuracy of 0.1 deg/hr/g the accelerometers cross axis sensitivity and misalignment must be repeatable to about 2 micro g/g from correction factor determination to rocking determination.

4.2 Rate Removal By Dual Gyro Testing

Separation of some of the gyro coefficients from rate inputs can be achieved by testing two similar gyros simultaneously. Since gyros are sensitive to angular accelerations about their output axes as well as to rates about their input axes a separation of all the coefficients from the two instruments cannot be achieved. Table II shows eight possible test orientations which can be used to completely separate five coefficients from each instrument. The outputs from the two instruments are added or subtracted to remove similar rates or angular accelerations from the data. This requires that both instruments have the same sensitivity to angular accelerations about their output axes. Table II shows the contents of the D_x and D_{xx} coefficients after the adding or subtracting has been accomplished. This summed or differenced data can then be processed as shown in Section 3.0 to determine the acceleration and acceleration squared sensitivities. Results from various orientations are then combined in order to separate the coefficients. The only g sensitive coefficient that can be separated is D_S.

$$1/2(D_{X5} + D_{X6}) = D_{S1} - D_{OS1} + D_{OS2} \tag{36}$$

$$1/2(D_{X6} - D_{X5}) = D_{S2} \tag{37}$$

D_{S1} is not separable from D_{OS1} and D_{OS2} using these orientations, however, D_S is usually much larger than D_{OS} and a good estimate of D_{S1} will be obtained.

The acceleration squared sensitive coefficients are separated as follows:

$$1/2(D_{XX1} + D_{XX2}) = D_{001} \tag{38}$$

$$1/2(D_{XX2} - D_{XX1}) = D_{002} \tag{39}$$

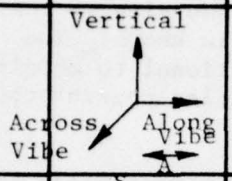
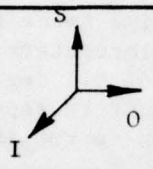
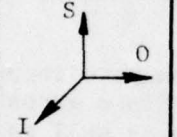
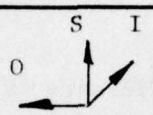
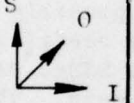
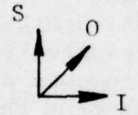
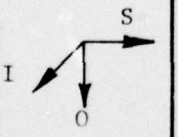
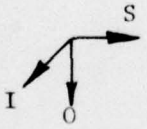
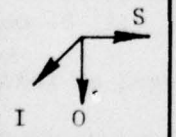
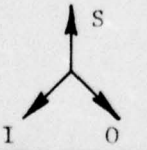
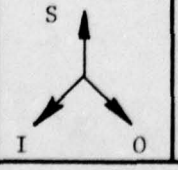
$$1/2(D_{XX3} + D_{XX4}) = D_{II1} \tag{40}$$

$$1/2(D_{XX4} - D_{XX3}) = D_{II2} \tag{41}$$

$$1/2(D_{XX5} + D_{XX6}) = D_{SS1} \tag{42}$$

TABLE II

DUAL GYRO TEST ORIENTATIONS

ORIENT	GYRO 1	GYRO 2	D_X	D_{XX}
				
1			$D_{01} - D_{02} + D_{OS1} - D_{OS2}$	$D_{001} - D_{002}$
2			$D_{01} - D_{02} + D_{OS1} - D_{OS2}$	$D_{001} + D_{002}$
3			$D_{I1} - D_{I2} + D_{IS1} - D_{IS2}$	$D_{II1} - D_{II2}$
4			$D_{I1} - D_{I2} + D_{IS1} - D_{IS2}$	$D_{II1} + D_{II2}$
5			$D_{S1} - D_{S2} - D_{OS1} + D_{OS2}$	$D_{SS1} - D_{SS2}$
6			$D_{S1} + D_{S2} - D_{OS1} + D_{OS2}$	$D_{SS1} + D_{SS2}$
7			$\sqrt{2}/2(D_{01} - D_{02} - D_{I1} + D_{I2} + D_{OS1} - D_{OS2} - D_{IS1} + D_{IS2})$	$1/2(D_{III} + D_{001} - D_{IO1} - D_{II2} - D_{002} + D_{IO2})$
8			$\sqrt{2}/2(D_{01} - D_{02} - D_{I1} + D_{I2} + D_{OS1} - D_{OS2} - D_{IS1} + D_{IS2})$	$1/2(D_{III} + D_{001} - D_{IO1} + D_{II2} + D_{002} - D_{IO2})$

$$1/2(D_{XX6} - D_{XX5}) = D_{SS2} \tag{43}$$

$$1/2(D_{XX1} + D_{XX2} + D_{XX3} + D_{XX4}) - D_{XX7} - D_{XX8} = D_{I01} \tag{44}$$

$$1/2(D_{XX2} - D_{XX1} + D_{XX4} - D_{XX3}) + D_{XX7} - D_{XX8} = D_{I02} \tag{45}$$

The advantage of testing in this manner is that no assumptions are required concerning slip table rigid body motion or rate repeatabilities. The disadvantage is that not all gyro coefficients can be obtained. If the gyros' sensitivity to angular accelerations is not significant, several more orientations can be used which will allow separation of all coefficients except D_I.

4.3 Rate Removal By Multiple Orientations

Separation of rates from acceleration sensitivities during random vibration testing of gyros can be achieved by using multiple orientations of the gyro if it is assumed that the rate inputs to the gyro are repeatable with gyro reorientation. Twelve suggested test orientations are shown in Figure 2. Several of these orientations give redundant information and could be omitted if such redundancy is not required. Other orientations could also be used which would give similar and perhaps additional information.

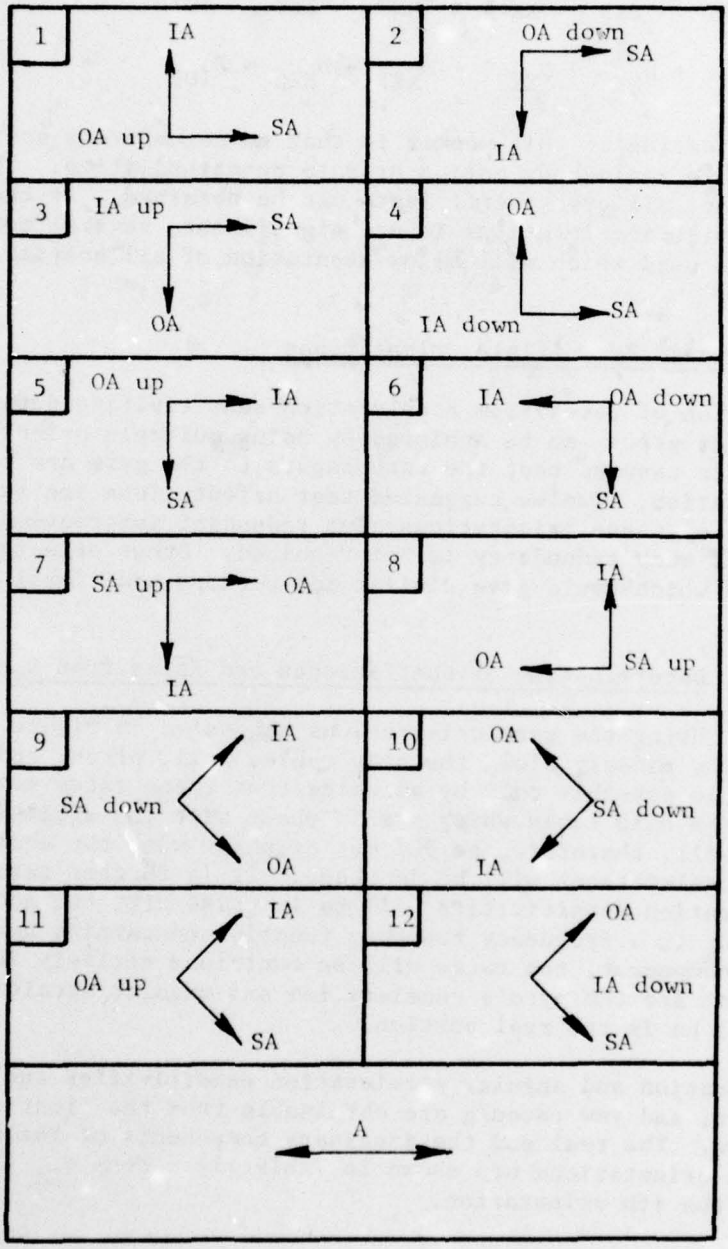
4.3.1 Determination of Coefficients and Rates from D_X

Using the gyro orientations suggested in Figure 2 the determination of the rates/g along the slip tables roll, pitch, and yaw axes (ω_R, ω_P, ω_Y) is possible only by assuming that these rates are caused by displacements of the slip table which are in phase with the applied acceleration. The rates will, therefore, be 90° out of phase with the acceleration and the angular accelerations will be in phase. It is further assumed that the gyro's acceleration sensitivities will be in phase with the acceleration. Remembering that D_X is a frequency response function containing both a real and an imaginary component, the rates will be contained entirely in the imaginary component and the gyro's acceleration and angular acceleration sensitivities will be in the real portion.

The gyro's acceleration and angular acceleration sensitivities and the slip tables roll, pitch, and yaw rates/g are obtainable from the first eight orientations shown. The real and the imaginary components of the D_X coefficient for these orientations are shown in Table III. Here D_{Xi} is the D_X coefficient from the ith orientation.

FIGURE 2

TEST ORIENTATIONS FOR RATE SEPARATION



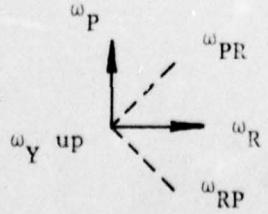


TABLE III
CONTENTS OF D_X COEFFICIENTS

	Real	Imaginary
D_{X1}	$D_S + D_{OS} - \frac{I_O\dot{\omega}_Y}{H}$	ω_R
D_{X2}	$D_S - D_{OS} + \frac{I_O\dot{\omega}_Y}{H}$	$-\omega_R$
D_{X3}	$D_S + D_{IS} + \frac{I_O\dot{\omega}_Y}{H}$	ω_Y
D_{X4}	$D_S - D_{IS} - \frac{I_O\dot{\omega}_R}{H}$	$-\omega_Y$
D_{X5}	$D_I + D_{IO} - \frac{I_O\dot{\omega}_Y}{H}$	ω_R
D_{X6}	$-D_I + D_{IO} + \frac{I_O\dot{\omega}_Y}{H}$	$-\omega_R$
D_{X7}	$D_O + D_{OS} - \frac{I_O\dot{\omega}_R}{H}$	$-\omega_P$
D_{X8}	$-D_O - D_{OS} + \frac{I_O\dot{\omega}_R}{H}$	ω_P

It can be seen from Table III that the rates are all obtainable directly from the imaginary portion of the D_X coefficient. The angular accelerations are then obtained by differentiating the rates. This is accomplished in the frequency domain by multiplying by $-j2\pi f$ where $j^2 = -1$.

$$\dot{\omega}_i = -j2\pi f\,\omega_i \tag{46}$$

The j in this equation indicates that the angular acceleration and the rate are 90 degrees out of phase.

The D_X coefficient is obtainable without making any assumptions about rate and coefficient phases. Two solutions are possible,

$$D_S = 1/2(D_{X1} + D_{X2}) = 1/2(D_{X3} + D_{X4}) \tag{47}$$

D_I is obtainable from orientations 5 and 6 and using the average ω_Y obtained from orientations 3 and 4 and assuming that $\frac{I_O}{H}$ is known from physical properties of the gyro.

$$D_I = 1/2\mathrm{Re}(D_{X5} - D_{X6}) - \frac{I_O}{H} 2\pi f\omega_Y \tag{48}$$

D_O is not separable from D_{OS} from orientations 7 and 8.

$$D_O + D_{OS} = 1/2\mathrm{Re}(D_{X7} - D_{X8}) - \frac{I_O}{H} 2\pi f\omega_R \tag{49}$$

If separation of D_O and D_{OS} were required additional test orientations could be used.

If $\frac{I_{O\omega}}{H}$ is large compared to the acceleration squared sensitive term excited by vibration and gravitational acceleration a good estimate of $\frac{I_O}{H}$ can be obtained from several orientations.

$$\frac{I_O}{H} \approx \frac{\mathrm{Re}(D_{X1} - D_{X2})}{4\pi f\omega_Y} \approx \frac{\mathrm{Re}(D_{X4} - D_{X3})}{4\pi f\omega_R} \tag{50}$$

4.3.2 Determination of Coefficients and Rates from D_{XX}

Using the same assumptions made during determination of the D_X coefficients the contents of the real and the imaginary components of the D_{XX} coefficients are given in Table IV for all of the suggested orientations. In this table the double subscripts on the rates indicate that they are rates per acceleration squared. It can be seen that these rates/g^2 are obtainable directly from the imaginary portion of the D_{XX} coefficient. D_{SS}, D_{II}, D_{OO}, and D_{IO} are all obtainable without making any phase assumptions.

TABLE IV
CONTENTS OF D_{XX} COEFFICIENTS

	Real	Imaginary
D_{XX1}	$D_{SS} - \frac{I_O}{H}\dot{\omega}_{YY}$	ω_{PP}
D_{XX2}	$D_{SS} + \frac{I_O}{H}\dot{\omega}_{YY}$	$-\omega_{PP}$
D_{XX3}	$D_{SS} + \frac{I_O}{H}\dot{\omega}_{PP}$	ω_{YY}
D_{XX4}	$D_{SS} - \frac{I_O}{H}\dot{\omega}_{PP}$	$-\omega_{YY}$
D_{XX5}	$D_{II} - \frac{I_O}{H}\dot{\omega}_{YY}$	ω_{RR}
D_{XX6}	$D_{II} + \frac{I_O}{H}\dot{\omega}_{YY}$	$-\omega_{RR}$
D_{XX7}	$D_{OO} - \frac{I_O}{H}\dot{\omega}_{RR}$	$-\omega_{PP}$
D_{XX8}	$D_{OO} + \frac{I_O}{H}\dot{\omega}_{RR}$	ω_{PP}
D_{XX9}	$1/2(D_{II}+D_{OO}+D_{IO}-\frac{I_O}{H}\dot{\omega}_{PP})$	$1/2\,\omega_{PR}$
D_{XX10}	$1/2(D_{II}+D_{OO}+D_{IO}+\frac{I_O}{H}\dot{\omega}_{RP})$	$-1/2\,\omega_{PR}$
D_{XX11}	$1/2(D_{II}+D_{SS}+D_{IS}-\frac{I_O}{H}\dot{\omega}_{YY})$	$1/2\,\omega_{PR}$
D_{XX12}	$1/2(D_{OO}+D_{SS}+D_{OS}-\frac{I_O}{H}\dot{\omega}_{PR})$	$-1/2\,\omega_{YY}$

$$D_{SS} = 1/2(D_{XX1} + D_{XX2}) = 1/2(D_{XX3} + D_{XX4}) \quad (51)$$

$$D_{II} = 1/2(D_{XX5} + D_{XX6}) \quad (52)$$

$$D_{OO} = 1/2(D_{XX7} + D_{XX8}) \quad (53)$$

$$D_{IO} = D_{XX9} + D_{XX10} - D_{II} - D_{OO} \quad (54)$$

D_{IS} and D_{OS} are obtained from orientations 11 and 12 and using angular accelerations computed from rates from other orientations.

$$D_{IS} = 2D_{XX11} - D_{II} - D_{SS} - \frac{I_O}{H} 2\pi f \omega_{YY} \quad (55)$$

$$D_{OS} = 2D_{XX12} - D_{OO} - D_{OS} - \frac{I_O}{H} 2\pi f \omega_{PR} \quad (56)$$

5.0 IRIG-16 RANDOM VIBRATION TESTS

A limited amount of random vibration testing using some of the methods suggested in this paper was conducted on an IRIG-16 gyroscope during June and July 1976. Separation of gyro coefficients from rate inputs was achieved using the multiple orientation procedures suggested in section 4.3. Attempts were also made to measure the rate inputs using the linear accelerometer method outlined in section 4.1. However, only marginal results were obtained due primarily to the poor quality of the linear accelerometers used. Results of these accelerometer measurements, therefore, are not included in this paper. This section presents a brief description of the equipment and procedure used in the random vibration testing and a summary of the results. A more detailed presentation of the equipment, test procedure, and results is given in Reference 2.

5.1 Equipment

The equipment used in performing the random vibration test was the following:

GENERAL RADIO 1381 Random Noise Generator
KROH-HITE 330AR Band Pass Filter
100 KVA LING ELECTRONICS Amplifier
LING Linear Vibration System
WILCOXIN 202 Accelerometers (4)
ENDEVCO 2272 Accelerometers (1)
ENDEVCO 2735 Charge Amplifier (5)
ROCKLAND 816 Low Pass Filter (6)
DATA TECHNOLOGY Multiplexer
HEWLETT-PACKARD 5451B Fourier Analyzer w/12 Bit ADC
IRIG-16 Gyroscope S/N J108

IRIG-16 Console Electronics
6" Precision Vibration Cube w/Fixture Heater
1-1/2" x 1-1/2" x 1" Accelerometer Attaching Plate (2)

Figure 3 is a block diagram of the test instrumentation setup.

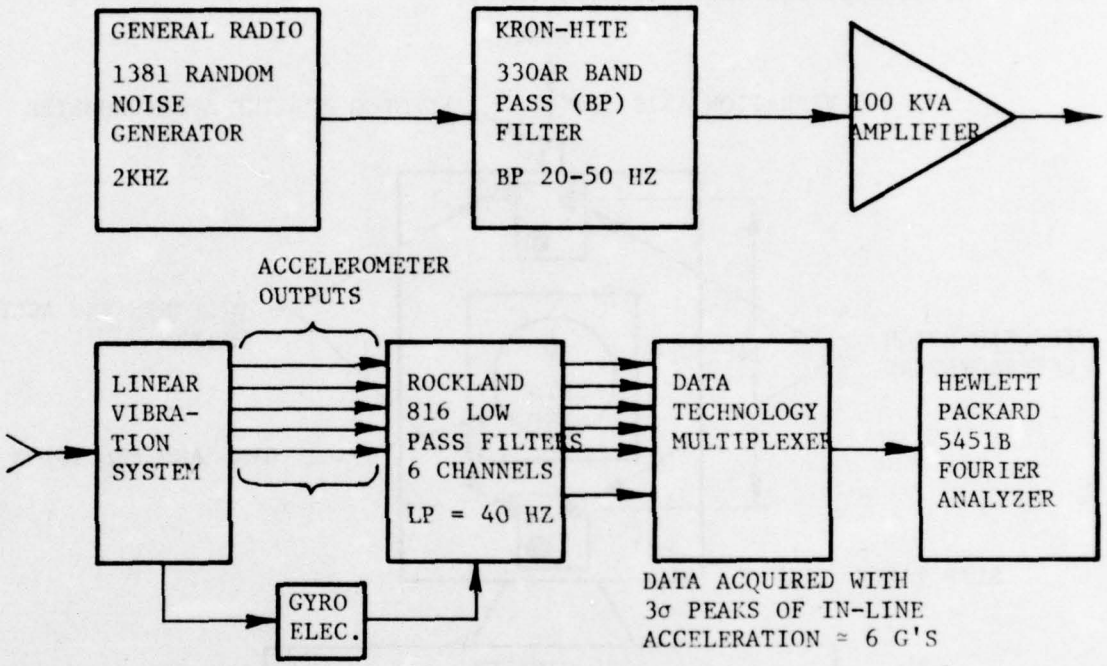


FIGURE 3. TEST INSTRUMENTATION

5.2 Test Procedures

5.2.1 Baseline Tests

Baseline tests were run before and after the series of vibration tests to insure that the gyro was functioning properly and that its performance was not affected by vibration. These tests included command rate scale factor tests, standard torque to balance tests, and a closed loop transfer function determination of the gyro in its torque to balance servo loop. Transfer functions were also determined for the Rockland 816 filters which were used to filter the gyro and in-line accelerometer signals. These measured transfer functions were used in compensating the recorded data. Comparison of the baseline results from before and after vibration testing showed no degradation of gyro performance.

5.2.2 Vibration Test

During actual vibration of J108, the signals which were recorded by the HEWLETT-PACKARD 5451B Fourier Analyzer were the following:

gyro torquer current, the output of the 4 WILCOXIN accelerometers, and the output of the ENDEVCO in-line accelerometer. The gyro signal generator secondary signal and the gyro heater duty cycle were monitored continuously on an oscilloscope, while the gyro cube temperature was monitored continuously on a strip chart recorder. Figure 4 is a schematic of the vibrator slip table as it appeared under dynamic test.

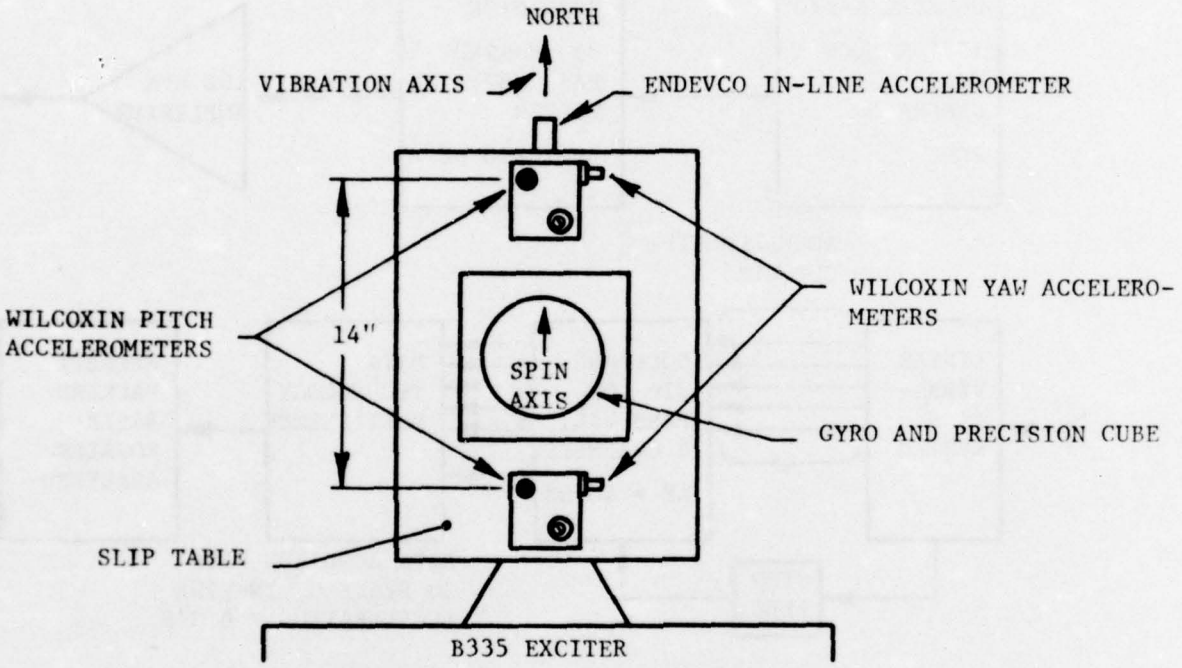


FIGURE 4. VIBRATOR SLIP TABLE

Vibration data analysis was performed using the gyro performance model presented in section 2.0. Data taken were recorded and scaled and then transfer function compensation was applied to both the gyro output and the in-line accelerometer output. An acceleration squared function was also formed by multiplying the measured in-line acceleration by itself in the time domain. All data were Hanned and then transformed to the frequency domain. The required power spectra as given in section 3.0 were then formed. The above steps were repeated a number of times on sequential data samples so that average power spectra were formed. These power spectra were then combined to give the gyro output proportional to acceleration, the gyro output proportional to acceleration squared, and the coherency functions. As stated in section 3.0 the acceleration sensitivities determined from the test will contain the gyro acceleration sensitivities plus any rate inputs to the gyro which are also proportional to acceleration. Separation of gyro coefficients from rate inputs was achieved using the multiple orientation procedures suggested in section 4.3.

5.3 Test Results

The vibration testing was limited to using only the first four

orientations shown in Figure 2. Three tests were run so that the repeatability of the results could be determined. Tests 1 and 2 used the first four orientations shown in Figure 2. Test 3 used only orientations 1 and 2.

The three tests conducted differed in the number of averages used in obtaining the power spectrums. Twenty averages were used on test 1, one hundred on test 2 and fifty on test 3. The frequency range examined and the applied acceleration spectrum was also varied from test to test. Typical power spectral densities of the vibration acceleration for each of the three tests are shown in Figure 5. The spectral densities differed from test to test because changes were made in the cut off frequencies of the band pass filter which was used to filter the random noise which was being used to drive the vibrator.

5.3.1 Coherence Functions

Typical coherence functions obtained from each of the tests are shown in Figure 6. It can be seen that the coherence is near one in all cases, and that the coherence improved as the number of averages increased.

5.3.2 D_S Coefficient

The real (in phase with acceleration) and the imaginary (out of phase) components of the D_S coefficient obtained from each orientation pair are shown in Figures 7, 8, and 9. The D_S coefficient obtained from one g tumble tests conducted before and after vibration averaged 50.2 deg/hr/g. In all cases the in phase component of D_S obtained from vibration tests at low frequencies agreed well with this. The coefficient, however, decreased with frequency. Also the imaginary component of this coefficient was significantly different from zero ranging from -5 to -10 deg/hr/g. Results of discrete frequency vibration tests conducted earlier showed a similar coefficient decrease with frequency and also an out of phase component. The cause of these anomalies has not yet been definitely determined. Several possible areas have been explored including in-line accelerometer phase shift, gyro input axis misalignment, and gyro float motion with respect to its case.

The charge amplifier of the in-line accelerometer or a misalignment of the gyros' input axis in the vibration cube could be causing the phase shift of the D_S coefficients. Checks on the charge amplifier revealed no phase shift over the frequency band of interest (i.e. 0-50 Hz). An IA alignment check of the gyro in the vibration cube showed a misalignment of less than 1 arc minute. A misalignment of more than 5 degrees would be required to produce the phase shift shown. The above results eliminated the two most likely sources of the phase shift. A search is continuing for other possible sources.

One possible cause for the frequency dependency of the D_S coefficient is float motion with respect to the case. In an effort to verify this theory, random noise excitation was introduced into the +IA and +SA magnetic suspension legs on both the torque generator and signal generator end of the gyro case. A transfer function was then run between the random noise input and the gyro

FIGURE 5

APPLIED ACCELERATION PSD'S

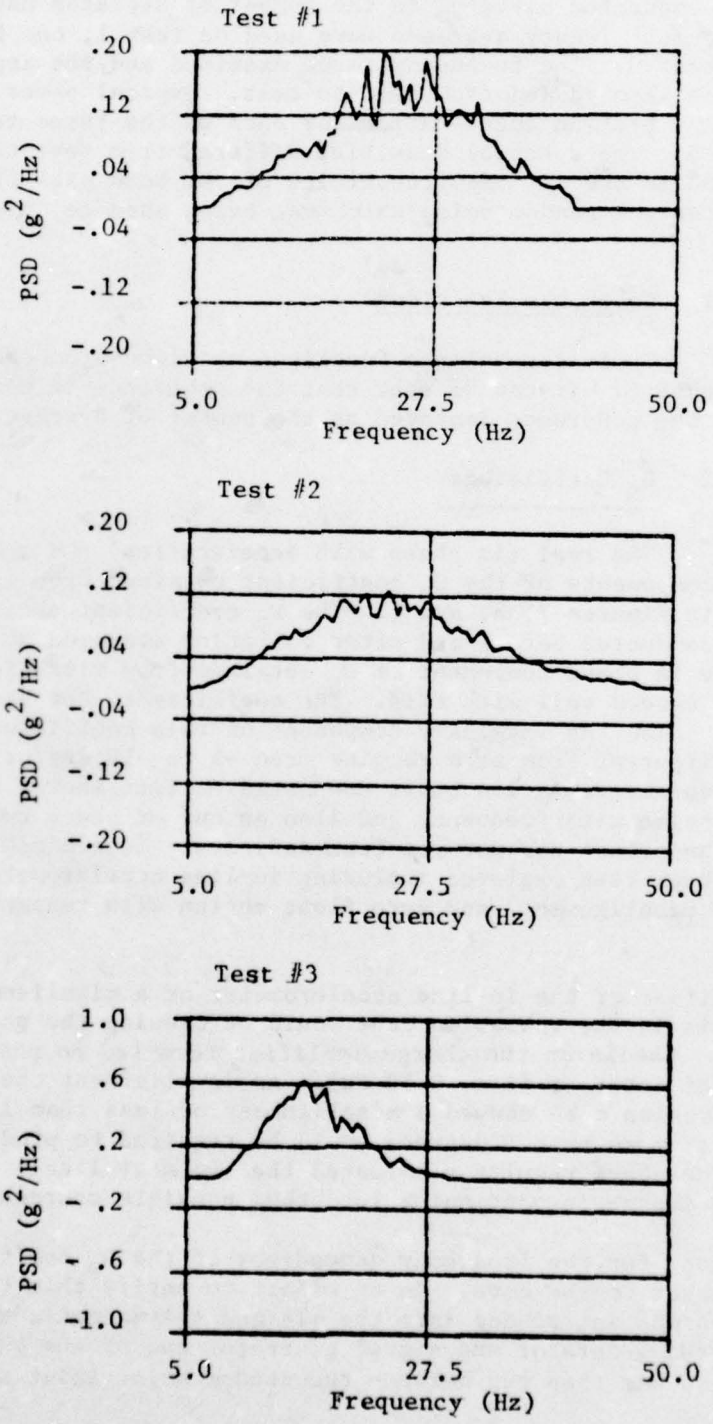
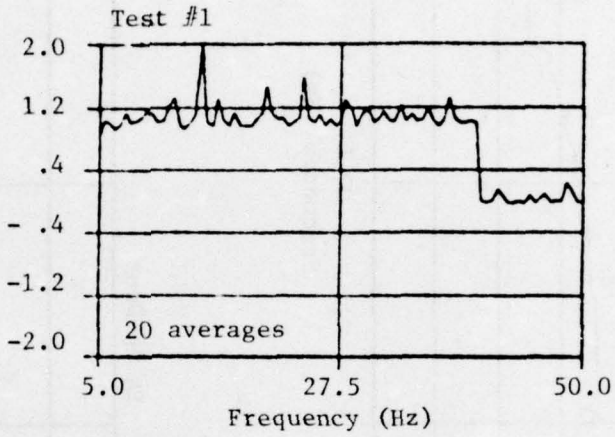
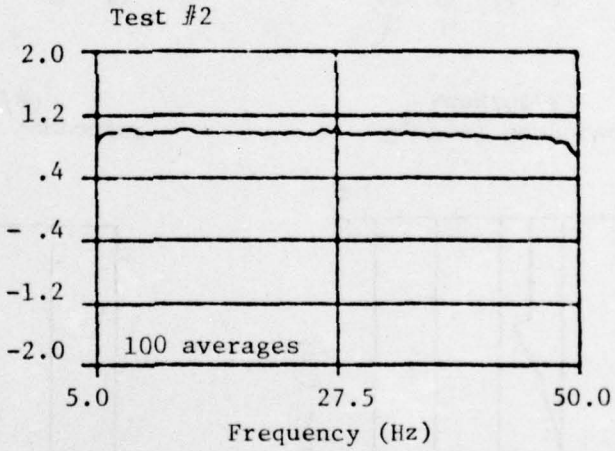


FIGURE 6

COHERENCE FUNCTIONS





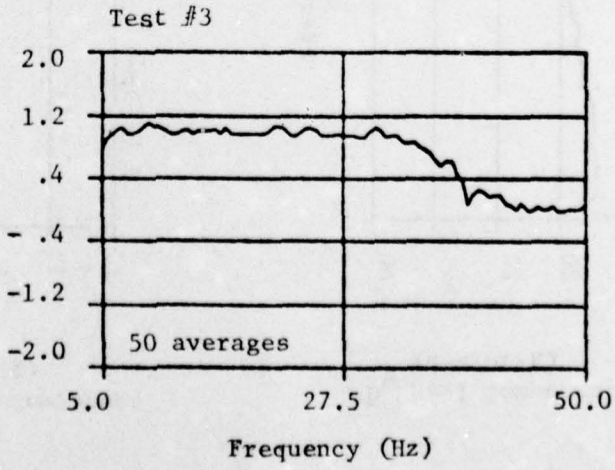


FIGURE 7

D_S COEFFICIENT FROM TEST #1

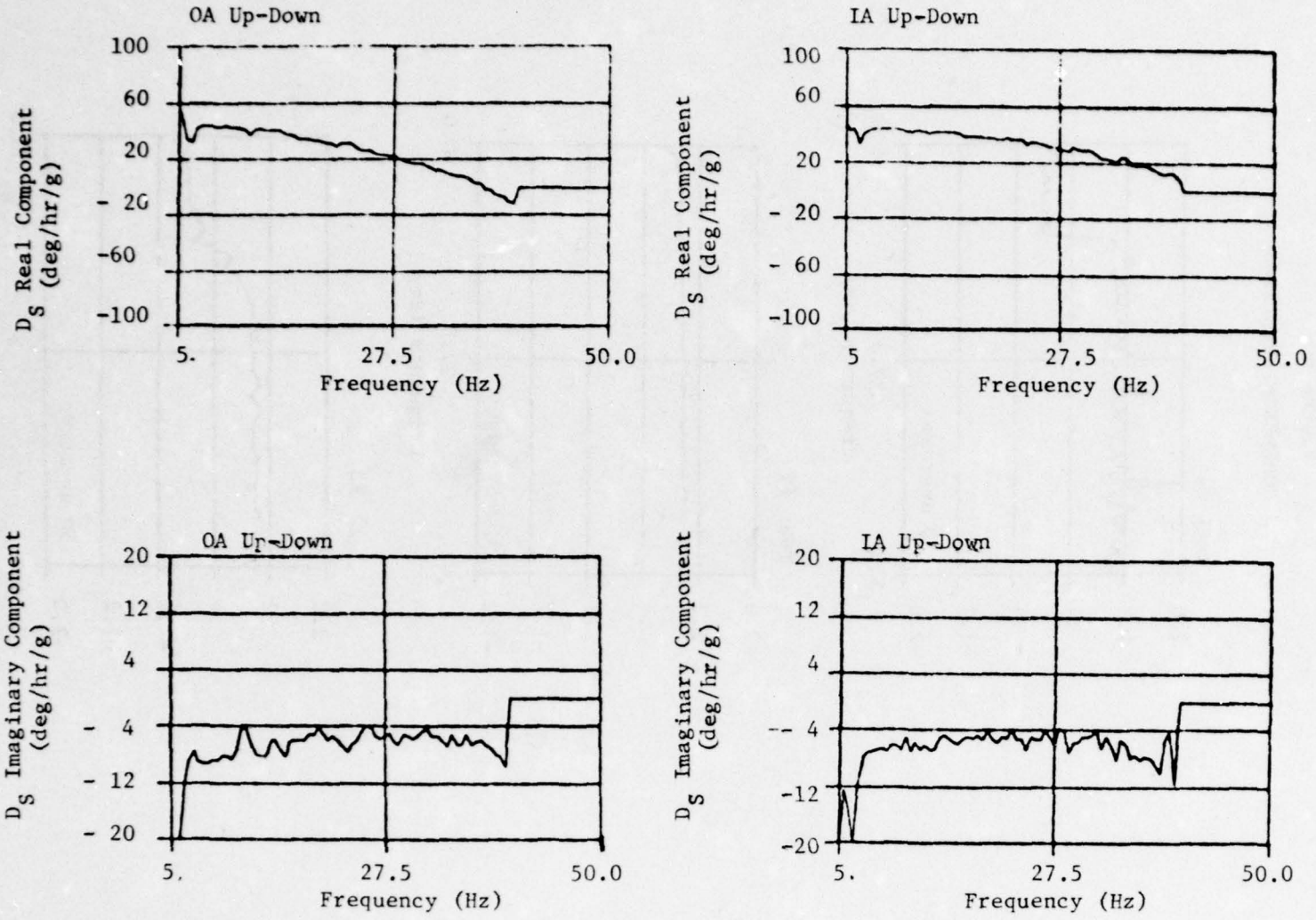


FIGURE 8

D_S COEFFICIENT FROM TEST #2

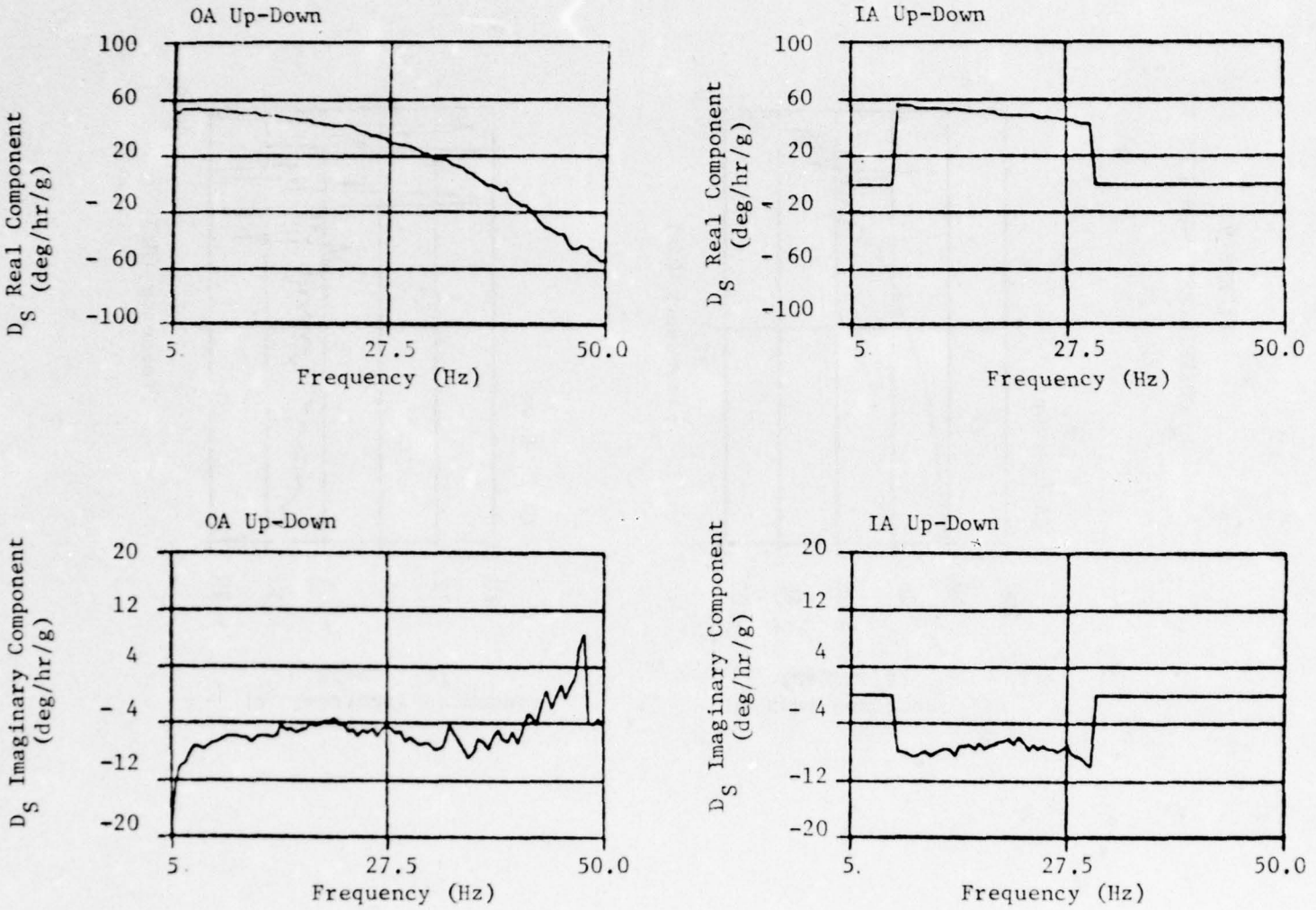
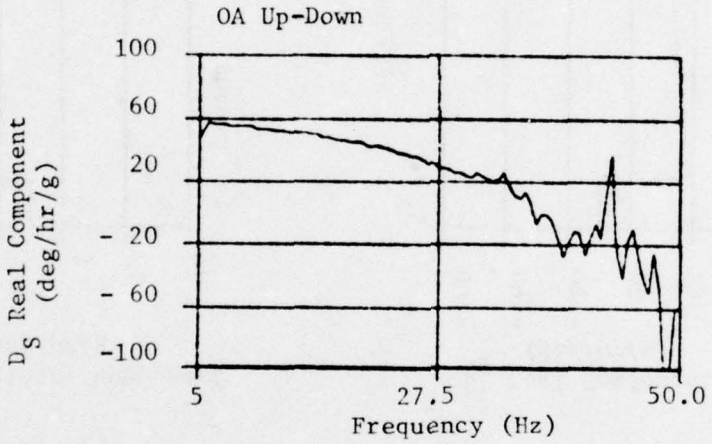
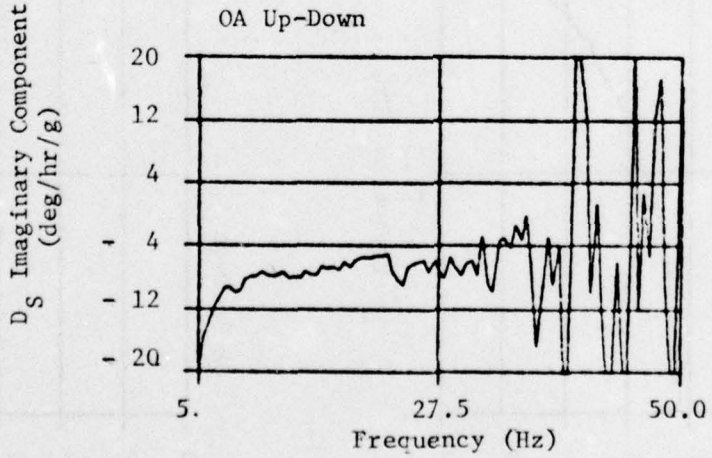


FIGURE 9

D_S COEFFICIENT FROM TEST #3





torquer current. The results indicated that at low frequencies (i.e. 0-20 Hz) there was no coherence between the gyro output and the random noise input. However, at the higher frequencies (i.e. 20-50 Hz) the torquer current and random noise input were coherent (i.e. $\gamma^2 \approx .8$). These results seem to support the D_S frequency dependency discovered in the vibration data. The incoherence of the torquer current and random noise at low frequencies indicates that the magnetic suspension is able to keep the float tracking the case, and this is a possible explanation for why the D_S coefficient at these frequencies agrees with the D_S coefficient obtained from 1g tests. The coherency of the two signals at the higher frequencies indicates that the magnetic suspension is not keeping the float tracking the case. This result is a possible reason for the D_S coefficient rolling off at the higher frequencies. Further research into this theory and others is continuing in an effort to correctly explain the D_S frequency dependency.

5.3.3 Slip Table Rocking Motion

The pitch and yaw rates per g on the slip table as indicated by the gyro for tests 1 and 2 and determined by the methods presented in section 4.3 are shown in Figure 10. The pitch rates are fairly large (40 deg/hr/g) and increase in magnitude with frequency. Integrating these rates reveals that they are caused by a linear displacement of .4 arc sec/g which is independent of frequency. Static deflection tests on the gyro vibration cube have indicated that a significant portion of this displacement could have been caused by cube deflection.

5.3.4 Output Axis Sensitivity to Angular Acceleration

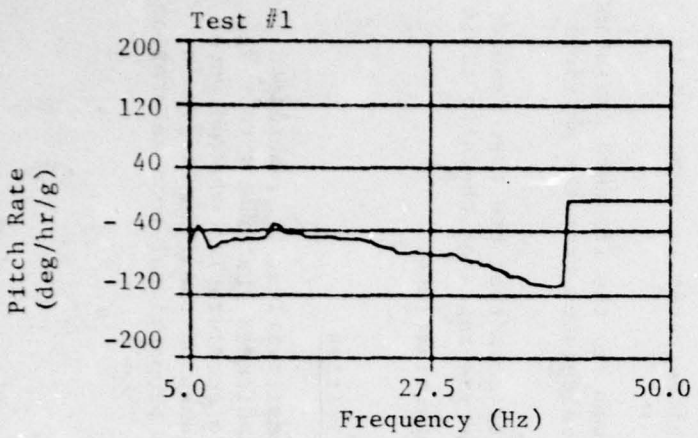
$\frac{I_O}{H}$ as determined from the pitch rates is presented in Figure 11. Also shown on these plots is the mean and the standard deviation of $\frac{I_O}{H}$ computed over all frequencies. $\frac{I_O}{H}$ as calculated from the physical properties of the gyro is .00875 sec. It can be seen that the test results agree very well with this predicted value. The yaw rates on the slip table were not large enough to permit accurate $\frac{I_O}{H}$ determinations.

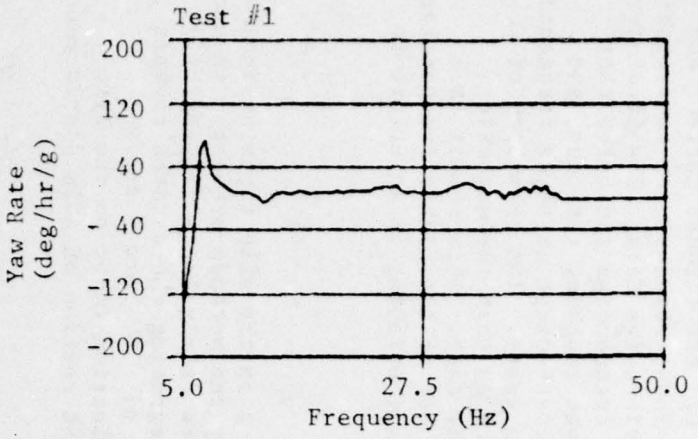
5.3.5 Acceleration Squared Sensitivities

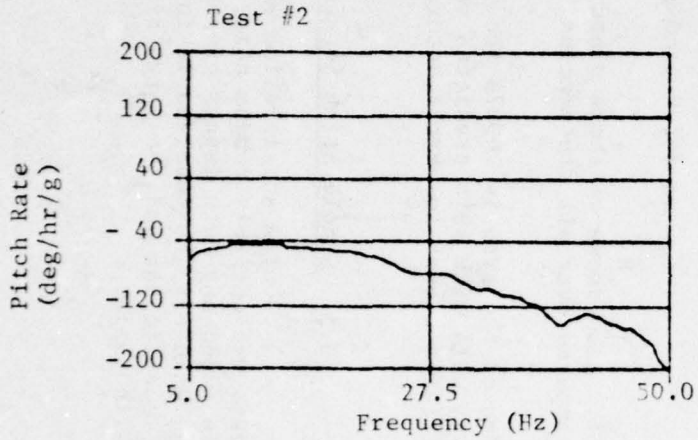
The acceleration squared sensitivities, D_{XX}, obtained from these tests was entirely random noise. This indicates that the gyro's D_{SS} coefficient and any rate inputs proportional to acceleration squared were not large enough to be resolveable in the presence of the IRIG-16 gyro's large D_S coefficient and the large pitch rates proportional to acceleration on the slip table.

FIGURE 10

RATES ON THE LINEAR VIBRATOR







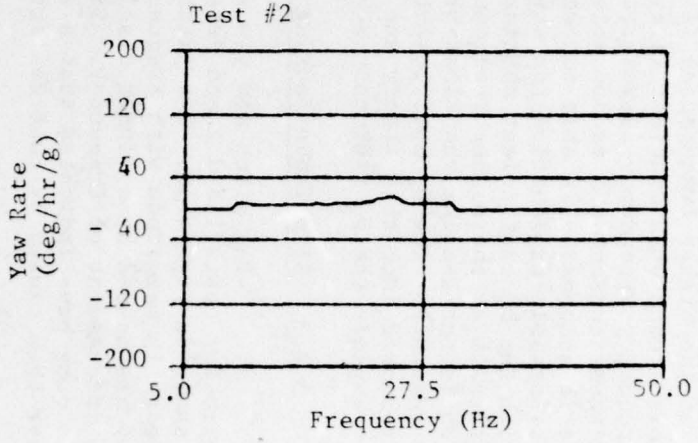
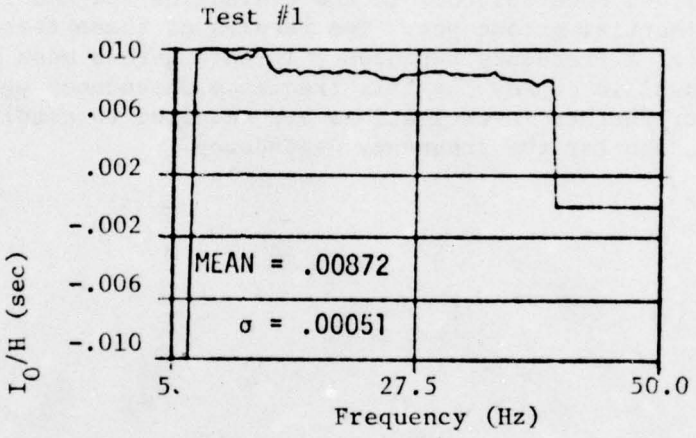
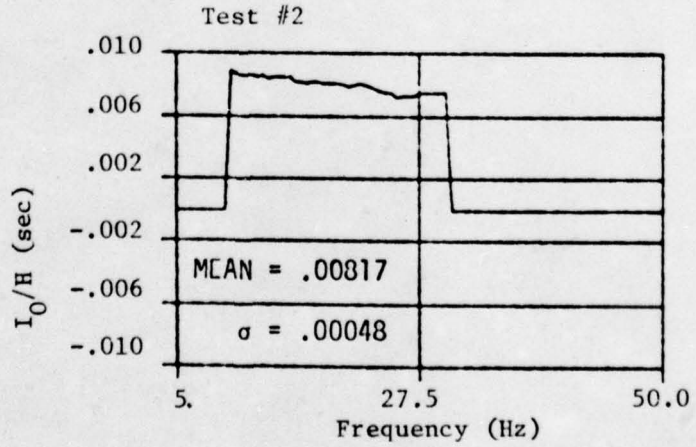


Figure 11

OUTPUT AXIS SENSITIVITY
TO ANGULAR ACCELERATION





6.0 CONCLUSIONS

A method whereby gyro acceleration and acceleration squared sensitivities can be obtained as a function of frequency from linear random vibration testing has been presented. Three methods have also been presented for separating the gyro's acceleration sensitivities from rate inputs to the gyro. These methods include measuring the rates with precision linear accelerometers, rate separation by dual gyro testing, and rate separation by multiple orientation testing. Results of tests conducted on an IRIG-16 gyro are also presented which verify that the use of linear random vibration can be a very useful and powerful tool in the evaluation and modeling of the performance of inertial gyroscopes. The results of these tests indicate the possibility of a frequency dependency in this gyro's mass unbalance coefficient. Possible causes for this frequency dependency were also presented however further investigations are required to conclusively determine the reason for the frequency dependency.

REFERENCES

1. Lorenzini, Dino A., "Testing of Precision Inertial Gyroscopes", Frank J. Seiler Research Laboratory, USAF Academy, Colorado, April 1973.

2. DeLorenzo, Michael L., and Thede, Robert, "Random Vibration Testing of IRIG-16 S/N J108", GDLC Test Event Report, Central Inertial Guidance Test Facility, Headquarters 6585th Test Group, Holloman AFB, New Mexico, 3 Sep 1976.

MULTIPLE ACCELEROMETER TESTING AS A TECHNIQUE TO ELIMINATE UNDESIRABLE TEST BED CHARACTERISTICS

by

Robert H. Fall

CENTRAL INERTIAL GUIDANCE TEST FACILITY
6585TH TEST GROUP
HOLLOMAN AIR FORCE BASE, NEW MEXICO

1. INTRODUCTION

Recovery of first order scale factor nonlinearities (sensitivity to the squares of input or cross-axis accelerations) is an important part of accelerometer testing that is often hampered by test bed errors. This paper will show that measurements formed from dual accelerometers mounted together can reduce the effect of test bed errors on the accelerometer coefficient recovery process by orders of magnitude. This can allow low tolerance test bed usage or enhancement of high precision test bed results to provide straightforward cost effective testing.

A brief summary of how error mechanisms on centrifuges, linear vibrators, and tumble test tables can affect first order scale factor nonlinearity estimates through rectification effects is given first.

The larger part of the paper is devoted to showing the derivation of dual accelerometer measurement equations and the resulting estimate errors (in a purely deterministic sense) when the measurements are made on imperfect test beds. The final error equations are based on present day instrumentation capabilities in order to make them both tractable and relevant.

Finally, the requirements on the a' priori knowledge of the instruments and the upper bounds on the test bed errors are reiterated and possible testing pitfalls are discussed.

2. CREATION OF FIRST ORDER NONLINEARITIES (g^2 TERMS) THROUGH TEST BED ERROR RECTIFICATION

Test bed accelerations into an accelerometer input axis are, in general, nonlinear even though the intended input is linear. The mechanism for this phenomenon will be shown here with only the essential errors. More complicated test bed models can be used to generate higher order nonlinearities, but for the most part, the errors described here predominate.

The accelerometer axis accelerations will be denoted using the following convention:

a_x = First cross-axis component

a_y = Second cross-axis component

a_z = Input axis component

A typical accelerometer output could be modeled as

$$K_0 + K_1 a_z + K_2 a_z^2 + K_3 a_x^2 + K_4 a_y^2 +$$

higher order terms

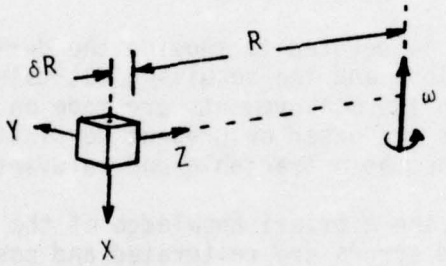
The ideal instrument will sense only a_z, so we can use only this component of the test bed acceleration to show where the nonlinearities arise.

Please note that these nonlinearities will be derived independently of any accelerometer model.

2.1 Centrifuge Accelerations Along Accelerometer Input Axis

This configuration is used to obtain the input axis scale factor nonlinearity. The accelerometer input axis is oriented nominally parallel to the centrifuge radius at a nominally fixed radius.

The predominant errors for a centrifuge are arm stretch (δR) and accelerometer tilt (α), about any axis perpendicular to the radius or acceleration vector.



With the accelerometer x-axis down, and the z-axis into the centrifuge acceleration the nominal accelerations at a constant centrifuge rate ω are:

$$a_x = -g$$

$$a_y = 0$$

$$a_z = A_c'$$

A_c' is used to denote the true acceleration $\omega^2 R'$ and $R' = R + \delta R$ where R is a fixed nominal radius and δR is the arm stretch.

If the accelerometer is misaligned a small angle α about the y-axis, then the true sensed accelerations for this example become:

$$a_x = -g - A_c'\alpha$$

$$a_y = 0$$

$$a_z = A_c' - g\alpha$$

The nonlinearities now appear if we model both arm stretch and tilt as linear functions of the nominal centrifuge acceleration ($\omega^2 R$). In light of known compliance effects, this is a reasonable thing to do. This allows us to write $\delta R = D'\omega^2 R$ and rescale $D' = DR$ so $\delta R = D\omega^2 R^2$. Then $A_c' = \omega^2(R+\delta R) = \omega^2 R(1+\omega^2 RD) = A_c + DA_c^2$. (D is in units of g's per g^2.) Also,

let $\alpha = \alpha_0 + CA_c'$ (A_c' will account for radius shift while tilting)

$= \alpha_0 + CA_c + CDA_c^2$

(C is in units of radians per g). The accelerations now become:

$$a_x = -g - \alpha_0 A_c - (C + \alpha_0 D)A_c^2 - 2CDA_c^3 - CD^2A_c^4 \quad (1a)$$

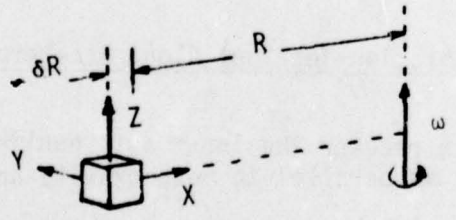
$$a_y = 0 \quad (1b)$$

$$a_z = -g\alpha_0 + (1 - gC)A_c + D(1 - gC)A_c^2 \quad (1c)$$

Examining the acceleration on the input axis (a_z), we see that a term (D(1-gC)) proportional to the square of the nominal centrifuge acceleration has been introduced which is independent of the accelerometer model. If an accelerometer model containing input axis g-squared terms is fit to a nominal centrifuge acceleration, this new term D(1-gC) due primarily to arm stretch will bias the accelerometer model g-squared coefficient estimate. The direct solution would appear to be the measurement of δR and α during testing so that $A_c = \omega^2(R + \delta R)$ would be used instead of $A_c = \omega R$. This solution is seen to be less than desirable if one is attempting to estimate input axis g-squared terms to less than $\pm.1$ part per million per g. The required radius measurement error is then ~.1 part per million per g or 10 micro-inches per g for a 100 inch centrifuge.

2.2 Centrifuge Accelerations Perpendicular to Accelerometer Input Axis

This configuration is used to determine the cross-axis scale factor non-linearity. The accelerometer input axis is oriented nominally parallel to the local gravity vector at a nominally fixed radius.



With the accelerometer x-axis into the centrifuge acceleration and the z-axis up, the nominal accelerations at a constant centrifuge rate ω are:

$$a_x = A_c'$$

$$a_y = 0$$

$$a_z = g$$

Again, rotating a small angle α about the y-axis, and substituting for δR and α as before:

$$a_x = A_c' - g\alpha$$

$$a_y = 0$$

$$a_z = g + A_c'\alpha$$

and

$$a_x = -g\alpha_0 + (1 - gC)A_c + D(1 - gC)A_c^2 \quad (2a)$$

$$a_y = 0 \quad (2b)$$

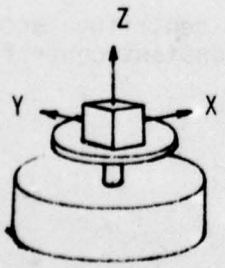
$$a_z = g + \alpha_0 A_c + (C + \alpha_0 D)A_c^2 + 2CDA_c^3 + CD^2A_c^4 \quad (2c)$$

For this case, the introduced g-squared coefficient on the z-axis is $C + \alpha_0 D$. Again, to remove this effect on the instrument model g-squared coefficient directly would require measuring α or C to fine levels. If the instrument coefficient is desired to $\pm$.1 part per million per g, then C must be known to ~.1 micro-radian per g or 0.02 arc-sec per g.

Assuming that both arm stretch and instrument tilt are truly linear, the accuracy requirements to calibrate g-squared terms to $\pm$.1 part per million per g for a 20 g centrifuge test on a 100 inch centrifuge are ~200 micro-inches of arm stretch and 0.4 arc-sec of instrument tilt. These can be improved somewhat by fitting techniques using multiple g levels, but still represent the order of magnitude of measurement capability. If the safe criteria of an order of magnitude of test bed accuracy more than instrument accuracy is desired the situation becomes completely intractable at today's measurement state-of-the-art.

2.3 Sinusoidal Accelerations (Vibration Testing) Along Accelerometer Input Axis

This configuration is used to recover the input axis nonlinearity and is commonly set up with a_z up, so it is parallel to both gravity and the shaker vibration axis.



Nominally, the accelerations are:

$$a_x = 0$$

$$a_y = 0$$

$$a_z = g + A_v \sin\omega t$$

where $A_v \sin\omega t$ is the commanded vibration acceleration at frequency $\frac{\omega}{2\pi}$

Introducing a small tilt α about the y-axis as was done in centrifuge testing, gives:

$$a_x = -\alpha(g + A_v \sin\omega t) \quad (3a)$$

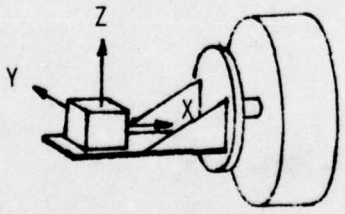
$$a_y = 0 \quad (3b)$$

$$a_z = g + A_v \sin\omega t \quad (3c)$$

This introduces no extraneous g-squared terms and, indeed, this configuration is essentially free of geometric rectification errors.

2.4 Sinusoidal Accelerations (Vibration Testing) Perpendicular to Accelerometer Input Axis

This configuration is used to recover the cross-axis nonlinearity and is set up with a_z up, parallel to gravity and a_x along the shaker vibration axis.



Nominally, the accelerations are:

$$a_x = A_v \sin\omega t$$

$$a_y = 0$$

$$a_z = g$$

Introducing the small tilt α about the y-axis as before gives:

$$a_x = A_v \sin\omega t - \alpha g$$

$$a_y = 0$$

$$a_z = g + \alpha A_v \sin\omega t$$

At this point, we will make α a linear function of the g level ($A_v \sin\omega t$), but to generalize we will further allow the compliance to be a function of ω and introduce a phase angle $\phi(\omega)$ also dependent on ω. With these generalizations,

$$\alpha = \alpha_0 + C(\omega)A_v \sin(\omega t + \phi(\omega)) \qquad \text{or}$$

$$\alpha = \alpha_0 + C(\omega)\cos\phi(\omega)A_v \sin\omega t + C(\omega)\sin\phi(\omega)A_v \cos\omega t$$

Substituting this into the sensed accelerations gives:

$$a_x = -\alpha_0 g + \{[1 - gC(\omega)\cos\phi(\omega)]\sin\omega t - gC(\omega)\sin\phi(\omega)\cos\omega t\}A_v \qquad (4a)$$

$$a_y = 0 \qquad (4b)$$

$$a_z = g + \alpha_0 \sin\omega t A_v + C(\omega)[\cos\phi(\omega)\sin^2\omega t + \sin\phi(\omega)\cos\omega t \sin\omega t]A_v^2 \qquad (4c)$$

Since most testing is done by observing the average output, we can take the time average acceleration to determine the magnitude of the new g-squared term.

$$\bar{a}_x = -\alpha_0 g \qquad (5a)$$

$$\bar{a}_y = 0 \qquad (5b)$$

$$\bar{a}_z = g + \frac{1}{2} C(\omega)\cos\phi(\omega)A_v^2 \qquad (5c)$$

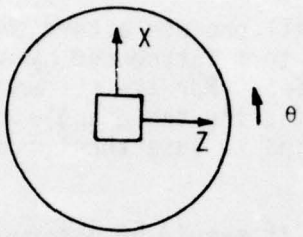
The bar here and elsewhere is used to denote the average as time approaches infinity.

Since the factor of $\frac{1}{2}$ in the g-squared term will be introduced by averaging any instrument g-squared effects too, it will be accounted for in the fitting process to recover the instrument g-squared coefficient. This means the extraneous g-squared term introduced by accelerometer tilt is $C(\omega)\cos\phi(\omega)$. This has the same units as in centrifuge testing (radians per g) and the same strict measurement requirements (.02 arc-sec per g), if it is to be removed by direct measurement.

2.5 Orthogonal Sinusoidal Accelerations Along and Perpendicular to Accelerometer Input Axis (Tumble Testing)

This testing cannot separate input-axis nonlinearities from cross-axis

nonlinearities, but is used to obtain a composite value. The orientation used is such that rotation occurs about a horizontal y-axis with the x-axis initially parallel with gravity.



Nominally the accelerations are:

$$a_x = g\cos\theta$$

$$a_y = 0$$

$$a_z = g\sin\theta$$

where θ is the angle of rotation about y.

If θ now becomes the indicated angle and a small misalignment with a one speed (once per revolution) component ($\gamma_0 + \gamma\sin(\theta+\delta)$) is introduced, the accelerations become:

$$a_x = g\cos[\theta + \gamma_0 + \gamma\sin(\theta + \delta)]$$

$$a_y = 0$$

$$a_z = g\sin[\theta + \gamma_0 + \gamma\sin(\theta +\delta)]$$

expanding with γ_0 and γ small, we get

$$a_x = g\cos\theta - g\gamma_0\sin\theta - g\gamma[\cos\delta\sin^2\theta + \sin\delta\cos\theta\sin\theta]$$

$$a_y = 0$$

$$a_z = g\sin\theta + g\gamma_0\cos\theta + g\gamma[\cos\delta\sin\theta\cos\theta + \sin\delta\cos^2\theta]$$

Further expanding this into terms of $\sin\theta$, $\cos\theta$, $\sin2\theta$, and $\cos2\theta$ (since most analysis would be done by Fourier or other harmonic techniques);

$$a_x = -(\tfrac{1}{2}\gamma\cos\delta)g + g\cos\theta - g\gamma_0\sin\theta + (\tfrac{1}{2}g\gamma\cos\delta)\cos2\theta - (\tfrac{1}{2}g\gamma\sin\delta)\sin2\theta \quad (6a)$$

$$a_y = 0 \quad (6b)$$

$$a_z = (\tfrac{1}{2}\gamma_s \sin\delta)g + g\sin\theta + g\gamma_0\cos\theta + (\tfrac{1}{2}g\gamma\cos\delta)\sin 2\theta$$

$$+ (\tfrac{1}{2}g\gamma\sin\delta)\cos 2\theta$$

Since instrument g-squared effects will produce a term proportional to $1/2g\cos 2\theta$, the erroneous "g-squared" term introduced by a one speed error in the tumble-test table resolver is $\gamma\sin\delta$. For the $\pm$.1 part per million per g accuracy in the instrument coefficient, the table angle resolver or position measurement device must constrain $\gamma\sin\delta$ to less than .1 micro radian or .02 arc-sec.

As a final note on this section, it should be observed that in Equations (1a), (2c), (6a), and (6c), nonlinearities were introduced which might not be present in the accelerometer model, and indeed could be raised to higher order nonlinearities by the model. This, in general, means the fitting process to recover instrument coefficients must be modified to account for the "new" nonlinearities.

3. THE DUAL INSTRUMENT MEASUREMENT EQUATIONS

This derivation is done using an accelerometer model similar to that of Pendulous Integrating Gyro Accelerometer (PIGA) type instruments, but can be done for any type of instrument. There is a primary requirement that the model "adequately" describes the instrument during testing. This implies that the dual instrument technique is not a good tool for establishing an instrument model, but should be used to establish coefficients in a known instrument model.

Let the instrument outputs be denoted by O_1 and O_2. The instrument models to be used for this paper are:

$$O_1 = (1/SF_1)[a_{z1} + K_{11}a_{z1}^2 + K_{21}a_{x1}^2 + K_{31}a_{y1}^2] + B_1 \qquad (7a)$$

$$O_2 = (1/SF_2)[a_{z2} + K_{12}a_{z2}^2 + K_{22}a_{x2}^2 + K_{32}a_{y2}^2] + B_2 \qquad (7b)$$

The K terms are those which are to be recovered.

Knowing that test bed errors contaminate primarily through the linear acceleration term and seeking to eliminate the errors, we will form two measurements, M_1 and M_2, using the nominal scale factors (SF_1', SF_2') and the nominal biases (B_1' and B_2') in the following manner:

When instruments 1 and 2 are parallel

$$M_1 = SF_1'(O_1 - B_1') - SF_2'(O_2 - B_2')$$

and when 1 and 2 are antiparallel

$$M_2 = SF_1'(O_1 - B_1') + SF_2'(O_2 - B_2')$$

This procedure eliminates the nominal input acceleration and its associated nonlinearities, but retains the difference (M_1) and sum (M_2) of the squared terms.

Letting $SF' = SF + \delta SF$, $B' = B + \delta B$, and $(1 + \frac{\delta SF}{SF}) = \beta$, we substitute the instrument model into M_1 and M_2 and get

$$\begin{aligned} M_1 = {} & a_{z1}\beta_1 - a_{z2}\beta_2 + (K_{11}\beta_1 a_{z1}^2 - K_{12}\beta_2 a_{z2}^2) \\ & + (K_{21}\beta_1 a_{x1}^2 - K_{22}\beta_2 a_{x2}^2) + K_{31}\beta_1 a_{y1}^2 - K_{32}\beta_2 a_{y2}^2) \\ & - \beta_1 \frac{\delta B_1}{SF_1} + \beta_2 \frac{\delta B_2}{SF_2} \end{aligned} \tag{8a}$$

$$\begin{aligned} M_2 = {} & a_{z1}\beta_1 + a_{z2}\beta_2 + (K_{11}\beta_1 a_{z1}^2 + K_{12}\beta_2 a_{z2}^2) \\ & + (K_{21}\beta_1 a_{x1}^2 + K_{22}\beta_2 a_{x2}^2) + (K_{31}\beta_1 a_{y1}^2 + K_{32}\beta_2 a_{y2}^2) \\ & - \beta_1 \frac{\delta B_1}{SF_1} - \beta_2 \frac{\delta B_2}{SF_2} \end{aligned} \tag{8b}$$

Equations (8a) and (8b) are true in the most general sense for the instrument model used. Now by considering the special case where both accelerometers are mounted in a common, perfectly rigid mount with a small single axis misalignment between their input axes, the desired dual instrument equations can be obtained.

When instruments 1 and 2 input axes are nominally parallel, but with a small misalignment α about the y axis and a linear relationship between a_{z1}, a_{z2} and a_{x1}, a_{x2} (as occurs on a centrifuge if the instruments are not at the same radius) we can write:

$$a_{x2} = \Delta_{1x} a_{x1} - \alpha_1 \Delta_{1z} a_{z1} \tag{9a}$$

$$a_{y2} = a_{y1} \tag{9b}$$

$$a_{z2} = \alpha_1 \Delta_{1x} a_{x1} + \Delta_{1z} a_{z1} \tag{9c}$$

$$a_{x2}^2 = \Delta_{1x}^2 a_{x1}^2 - 2\alpha_1\Delta_{1x}\Delta_{1z}a_{x1}a_{z1} + \alpha_1^2\Delta_{1z}^2 a_{z1}^2 \quad (10a)$$

$$a_{y2}^2 = a_{y1}^2 \quad (10b)$$

$$a_{z2}^2 = \alpha_1^2\Delta_{1x}^2 a_{x1}^2 + 2\alpha_1\Delta_{1x}\Delta_{1z}a_{x1}a_{z1} + \Delta 1_z^2 a_{z1}^2 \quad (10c)$$

Using the same constraints as above when the input axes are nominally anti-parallel, we obtain:

$$a_{x2} = -\Delta_{2x}a_{x1} + \alpha_2\Delta_{2z}a_{z1} \quad (11a)$$

$$a_{y2} = a_{y1} \quad (11b)$$

$$a_{z2} = -\alpha_2\Delta_{2x}a_{x1} - \Delta_{2z}a_{z1} \quad (11c)$$

$$a_{x2}^2 = \Delta_{2x}^2 a_{x1}^2 - 2\alpha_2\Delta_{2x}\Delta_{2z}a_{x1}a_{z1} + \alpha_2^2\Delta_{2z}^2 a_{z1}^2 \quad (12a)$$

$$a_{y2}^2 = a_{y1}^2 \quad (12b)$$

$$a_{z2}^2 = \alpha_2^2\Delta_{2x}^2 a_{x1}^2 + 2\alpha_2\Delta_{2x}\Delta_{2z}a_{x1}a_{z1} + \Delta_{2z}^2 a_{z1}^2 \quad (12c)$$

When these are substituted into (8a) and (8b), we get

$$\begin{aligned} M_1 = {} & a_{z1}(\beta_1 - \Delta_{1z}\beta_2) - \beta_2\alpha_1\Delta_{1x}a_{x1}[1 + 2\Delta_{1z}a_{z1}(K_{12} - K_{22})] \\ & + a_{z1}^2[K_{11}\beta_1 - \Delta_{1z}^2\beta_2(K_{12} + \alpha_1^2 K_{22})] \\ & + a_{x1}^2[K_{21}\beta_1 - \Delta_{1x}^2\beta_2(K_{22} + \alpha_1^2 K_{12})] \\ & + a_{y1}^2[K_{31}\beta_1 - K_{32}\beta_2] - \beta_1\frac{\delta B_1}{SF_1} + \beta_2\frac{\delta B_2}{SF_2} \end{aligned} \quad (13a)$$

$$\begin{aligned} M_2 = {} & a_{z1}(\beta_1 - \Delta_{2z}\beta_2) - \beta_2\alpha_2\Delta_{2x}a_{x1}[1 - 2\Delta_{2z}a_{z1}(K_{12} - K_{22})] \\ & + a_{z1}^2[K_{11}\beta_1 + \Delta_{2z}^2\beta_2(K_{12} + \alpha_2^2 K_{22})] \\ & + a_{x1}^2[K_{21}\beta_1 + \Delta_{2x}^2\beta_2(K_{22} + \alpha_2^2 K_{12})] \\ & + a_{y1}^2[K_{31}\beta_1 - K_{32}\beta_2] - \beta_1\frac{\delta B_1}{SF_1} - \beta_2\frac{\delta B_2}{SF_2} \end{aligned} \quad (13b)$$

These are the dual instrument model measurements obtained with the specified model in (7a), (7b), and the constraint that both instruments have a common, rigid mount. In the ideal case of perfect knowledge of the instrument scale factor and bias ($\beta = 1$, $\delta B = 0$) and no misalignments ($\Delta = 1$, $\alpha = 0$), the equations reduce to:

$$M_1 = a_{z1}^2(K_{11} - K_{12}) + a_{x1}^2(K_{21} - K_{22}) + a_{y1}^2(K_{31} - K_{32}) \qquad (14a)$$

$$M_2 = a_{z1}^2(K_{11} + K_{12}) + a_{x1}^2(K_{21} + K_{22}) + a_{y1}^2(K_{31} + K_{32}) \qquad (14b)$$

If these are rewritten as

$$M_1 = a_{z1}^2 C_{z1} + a_{x1}^2 C_{x1} + a_{y1}^2 C_{y1}$$

$$M_2 = a_{z1}^2 C_{z2} + a_{x1}^2 C_{x2} + a_{y1}^2 C_{y2}$$

It is obvious that if the C's are obtained by some estimation procedure when the a's are known then the K's can be solved for as follows:

$$K_{11} = \frac{C_{z1} + C_{z2}}{2}, \quad K_{12} = \frac{C_{z2} - C_{z1}}{2}$$

$$K_{21} = \frac{C_{x1} + C_{x2}}{2}, \quad K_{22} = \frac{C_{x2} - C_{x1}}{2}$$

$$K_{31} = \frac{C_{y1} + C_{y2}}{2}, \quad K_{32} = \frac{C_{y2} - C_{y1}}{2}$$

4. G-SQUARED COEFFICIENT ESTIMATE ERRORS FROM APPLICATION OF THE DUAL INSTRUMENT MEASUREMENT EQUATIONS

As was shown in the last part of Section 3, the g-squared model coefficients can be recovered with no contamination from the linear acceleration term in the ideal case. This section will apply state-of-the-art numerical constraints to the test bed errors and accelerometer model coefficient magnitudes to determine the potential deterministic errors in real life coefficient recovery situations using the dual measurement equations.

4.1 Centrifuge Accelerations Along Accelerometer Input Axis

Let us constrain the instrument measurement equations in the following manner. Since the nominal centrifuge frame accelerations are

$$a_x = -g$$

$$a_y = 0$$

$$a_z = A_c = \omega^2 R$$

only a_z can vary significantly from point to point, so $\Delta_{1x} = 1$, $\Delta_{2x} = 1$ and if instrument 2 is mounted a distance d greater radius than instrument 1, then $a_{z1} = \omega^2 R$ and $a_{z2} = \omega^2(R+d)$.

Letting $\frac{d}{R} = \varepsilon$, $a_{z2} = \omega^2 R(1+\varepsilon)$ and $\Delta_{1z} = (1+\varepsilon_1)$, $\Delta_{2z} = (1+\varepsilon_2)$. For any reasonable mount construction and alignment, $d \leq .1$ inch. This means for a 100 inch centrifuge $\varepsilon \leq .001$. Furthermore, parallelism of mounting surfaces can be maintained to ≤ 20 arc-seconds, so all α's can be considered to be $\leq 10^{-4}$ radians. Experience with PIGA type instruments has shown that short term scale factor stability is such that $\frac{\delta SF}{SF} \leq 10^{-5}$ is a reasonable assumption as is $\frac{\delta B}{SF} \leq 10^{-5}$g's. PIGA type instruments have typically small g-squared terms, so we will constrain these K's to be ≤ 10 parts per million/g.

Test bed errors can be constrained from experience on the Central Inertial Guidance Test Facility (CIGTF) 100 inch and 260 inch centrifuges to:

C (centrifuge mount compliance tilt) $\leq 3 \times 10^{-5}$ rad/g

D (radius arm linear g loading stretch) ≤ 10 parts per million/g

Finally, the centrifuge g level (A_c) is constrained to 20 g's maximum.

Since very fine resolution or strongly filtered data is difficult to obtain during dynamic testing, all terms in the measurement equation that are smaller than .1μg will be dropped.

With the above constraints Equations (13a) and (13b) become simplified to:

$$\begin{aligned} M_1 = {} & a_{z1}(\beta_1 - \beta_2 - \varepsilon_1) - \alpha_1 a_{x1} \\ & + a_{z1}^2[K_{11} - K_{12}(1 + 2\varepsilon_1)] \\ & + a_{x1}^2[K_{21} - K_{22}] \\ & + a_{y1}^2[K_{31} - K_{32}] - \frac{\delta B_1}{SF_1} + \frac{\delta B_2}{SF_2} \end{aligned} \qquad (15a)$$

$$\begin{aligned} M_2 = {} & a_{z1}(\beta_1 - \beta_2 - \varepsilon_2) - \alpha_2 a_{x1} \\ & + a_{z1}^2[K_{11} + K_{12}(1 + 2\varepsilon_2)] \\ & + a_{x1}^2[K_{21} + K_{22}] \end{aligned}$$

$$+ a_{y1}^2[K_{31} + K_{32}] - \frac{\delta B_1}{SF_1} - \frac{\delta B_2}{SF_2} \qquad (15b)$$

Now, substituting equations (1a), (1b), and (1c) for a_{x1}, a_{y1}, and a_{z1} into (15a) and (15b) and still keeping the earlier constraints, we get:

$$M_1 = [g\alpha_0\varepsilon_1 + g\alpha_1 + g^2(K_{21} - K_{22}) - \frac{\delta B_1}{SF_1} + \frac{\delta B_2}{SF_2}]$$

$$+ [\frac{\delta SF_1}{SF_1} - \frac{\delta SF_2}{SF_2} - \varepsilon_1(1 - gC) + \alpha_1\alpha_0]A_c$$

$$+ [K_{11} - K_{12}(1+2\varepsilon_1) - D\varepsilon_1 + C\alpha_1 - 2gC(K_{11} - K_{21} - K_{12} + K_{22})]A_c^2$$

$$+ [2D(K_{11} - K_{12})]A_c^3 \qquad (16a)$$

$$M_2 = [g\alpha_0\varepsilon_2 \quad g\alpha_2 + g^2(K_{21} + K_{22}) - \frac{\delta B_1}{SF_1} - \frac{\delta B_2}{SF_2}]$$

$$+ [\frac{\delta SF_1}{SF_1} - \frac{\delta SF_2}{SF_2} - \varepsilon_2(1 - gC) + \alpha_2\alpha_0]A_c$$

$$+ [K_{11} + K_{12}(1+2\varepsilon_2) - D\varepsilon_2 + C\alpha_2 - 2gC(K_{11} - K_{21} + K_{12} - K_{22})]A_c^2$$

$$+ [2D(K_{11} + K_{12})]A_c^3$$

Solving for K_{11} and K_{12} (which is what this centrifuge test is designed for) from the A_c^2 coefficients as in Section 3 using a $\hat{}$ to indicate an estimated quantity:

$$\hat{K}_{11} = K_{11} + K_{12}(\varepsilon_2 - \varepsilon_1) - D(\frac{\varepsilon_1 + \varepsilon_2}{2}) + C(\frac{\alpha_1 + \alpha_2}{2}) - 2gC(K_{11} - K_{21}) \qquad (17a)$$

$$\hat{K}_{12} = K_{12}(1 + \varepsilon_1 + \varepsilon_2) + D(\frac{\varepsilon_1 - \varepsilon_2}{2}) - C(\frac{\alpha_1 - \alpha_2}{2}) - 2gC(K_{12} - K_{22}) \qquad (17b)$$

From the previous constraints, the largest error contribution comes from the different radius locations of the accelerometers in the mount coupled with the radius stretch coefficient. This term is within $\pm$.01 part per million/g.

It should be noted that ε was assumed constant. If ε were a linear function of g level (if the instrument input axes were both in the vertical

plane, then the g induced α would also cause ε to change), then by substituting this g dependent ε into (16a) and (16b) one can see that this would cause the g coefficient of ε to propagate into the A_c^2 coefficient. This could easily be on the order of K_{11}, K_{12} and dual instrument testing will not reduce this error. For this reason the test geometry is critical for dual instrument input-axis g-squared coefficient recovery.

4.2 Centrifuge Accelerations Perpendicular to Accelerometer Input Axis

The nominal centrifuge frame accelerations for this configuration are:

$$a_x = A_c$$

$$a_y = 0$$

$$a_z = g$$

Here only a_x can vary significantly from point to point, so $\Delta_{1z} = 1$, $\Delta_{2z} = 1$ and $\Delta_{1x} = (1 + \varepsilon_1)$, $\Delta_{2x} = (1 + \varepsilon_2)$. If we continue to use the remaining constraints in 4.1, equations (13a) and (13b) can be simplified to

$$\begin{aligned} M_1 = {} & a_{z1}(\beta_1 - \beta_2) - \alpha_1(1 + \varepsilon_1)a_{x1} \\ & + a_{z1}^2[K_{11} - K_{12}] \\ & + a_{x1}^2[K_{21} - K_{22}(1 + 2\varepsilon_1)] \\ & + a_{y1}^2[K_{31} - K_{32}] - \frac{\delta B_1}{SF_1} + \frac{\delta B_2}{SF_2} \end{aligned} \tag{18a}$$

$$\begin{aligned} M_2 = {} & a_{z1}(\beta_1 - \beta_2) - \alpha_2(1 + \varepsilon_2)\, a_{x1} \\ & + a_{z1}^2[K_{11} + K_{12}] \\ & + a_{x1}^2[K_{21} + K_{22}(1 + 2\varepsilon_2)] \\ & + a_{y1}^2[K_{31} + K_{32}] - \frac{\delta B_1}{SF_1} - \frac{\delta B_2}{SF_2} \end{aligned} \tag{18b}$$

Now, substituting (2a), (2b), and (2c) for a_{x1}, a_{y1}, and a_{z1} into (18a) and (18b) still keeping constraints:

$$M_1 = [g(\frac{\delta SF_1}{SF_1} - \frac{\delta SF_2}{SF_2}) + g^2(K_{11} - K_{12}) - \frac{\delta B_1}{SF_1} + \frac{\delta B_2}{SF_2}]$$

$$- [\alpha_1(1 + \varepsilon_1)]A_c$$

$$+ [K_{21}-K_{22}(1+2\varepsilon_1) - D\alpha_1 + C(\frac{\delta SF_1}{SF_1} - \frac{\delta SF_2}{SF_2}) - 2gC(K_{21}+K_{12}-K_{11}-K_{22})]A_c^2$$

$$+ [2D(K_{21} - K_{22})]A_c^3 \qquad (19a)$$

$$M_2 = [g(\frac{\delta SF_1}{SF_1} - \frac{\delta SF_2}{SF_2}) + g^2(K_{11} + K_{12}) - \frac{\delta B_1}{SF_1} - \frac{\delta B_2}{SF_2}]$$

$$- [\alpha_2(1 + \varepsilon_2)]A_c$$

$$+ [K_{21}+K_{22}(1+2\varepsilon_2) - D\alpha_2 + C(\frac{\delta SF_1}{SF_1} - \frac{\delta SF_2}{SF_2}) - 2gC(K_{21}-K_{12}-K_{11}+K_{22})]A_c^2$$

$$+ [2D(K_{21} + K_{22})]A_c^3 \qquad (19b)$$

Solving for K_{21} and K_{22} as in Section 4.1, we get

$$\hat{K}_{21} = K_{21} + K_{22}(\varepsilon_2-\varepsilon_1) - D(\frac{\alpha_1+\alpha_2}{2}) + C(\frac{\delta SF_1}{SF_1} - \frac{\delta SF_2}{SF_2}) + 2gC(K_{11}-K_{21}) \qquad (20a)$$

$$\hat{K}_{22} = K_{22}(1 + \varepsilon_1 + \varepsilon_2) + D(\frac{\alpha_1 - \alpha_2}{2}) + 2gC(K_{12} - K_{22}) \qquad (20b)$$

Again, given the earlier constraints, the largest error contribution comes from the different radius locations of the accelerometer. The next most significant error source is the instrument misalignment in the mount coupled to radius stretch. These errors are within $\pm.01$ part per million/g and $\pm.001$ part per million/g respectively. Any g dependency of ε does not feed directly into the A_c^2 coefficient as it did in Section 4.1. The g coefficient of ε would be reduced by a factor $\alpha \simeq 10^{-4}$ and would be of the same magnitude as the other errors.

4.3 Sinusoidal Accelerations (Vibration Testing) Along Accelerometer Input Axis

Since it was shown in Section 2.3 that no geometric rectification occurred for this configuration, dual instrument testing does not significantly enhance coefficient recovery for this type of test.

4.4 Sinusoidal Accelerations (Vibration Testing) Perpendicular to Accelerometer Input Axis

This configuration allows some simplification of Equations (13a) and (13b) since all Δ's = 1, and only a mount compliance C affects the accelerations. Another simplification to be made is to make the measurements as time averages since this is a common procedure in vibration testing. The time averages of (13a) and (13b) with $\Delta = 1$ and previous constraints are:

$$\begin{aligned}\bar{M}_1 = {} & \bar{a}_{z1}(\beta_1 - \beta_2) - \beta_2\alpha_1[\bar{a}_{x1} + 2\overline{a_{x1}a_{z1}}(K_{12} - K_{22})] \\ & + \overline{a_{z1}^2}[K_{11} - K_{12}] \\ & + \overline{a_{x1}^2}[K_{21} - K_{22}] \\ & + \overline{a_{y1}^2}[K_{31} - K_{32}] - \frac{\delta B_1}{SF_1} + \frac{\delta B_2}{SF_2} \qquad (21a)\end{aligned}$$

$$\begin{aligned}\bar{M}_2 = {} & \bar{a}_{z1}(\beta_1 - \beta_2) - \beta_2\alpha_2[\bar{a}_{x1} - 2\overline{a_{x1}a_{z1}}(K_{12} - K_{22})] \\ & + \overline{a_{z1}^2}[K_{11} + K_{12}] \\ & + \overline{a_{x1}^2}[K_{21} + K_{22}] \\ & + \overline{a_{y1}^2}[K_{31} + K_{32}] - \frac{\delta B_1}{SF_1} - \frac{\delta B_2}{SF_2} \qquad (21b)\end{aligned}$$

Taking the time averages of a_{x1}, a_{y1}, a_{z1}, $a_{x1}a_{z1}$, a_{x1}^2, a_{y1}^2, and a_{z1}^2 from Equations (4a), (4b), and (4c), we obtain:

$$\bar{a}_{x1} = -\alpha_0 g$$

$$\bar{a}_{y1} = 0$$

$$\bar{a}_{z1} = g + \tfrac{1}{2}C(\omega)\cos\phi(\omega)A_v^2$$

$$\overline{a_{x1}a_{z1}} = -g\alpha_0[g + \tfrac{1}{2}C(\omega)\cos\phi(\omega)]A_v^2$$

$$\overline{a_{x1}^2} = g^2\alpha_0^2 + [\tfrac{1}{2} - gC(\omega)\cos\phi(\omega) + g^2C(\omega)]A_v^2$$

$$\overline{a_{y1}^2} = 0$$

$$\overline{a_{z1}^2} = g^2 + [\frac{\omega_0^2}{2} + gC(\omega)\cos\phi(\omega)]A_v^2 + C^2(\omega)[\frac{1}{8}\cos^2\phi(\omega) + \frac{1}{4}]A_v^4$$

Substituting these into Equations (21a) and (21b) gives

$$\overline{M}_1 = [g(\frac{\delta SF_1}{SF_1} - \frac{\delta SF_2}{SF_2}) + g^2(K_{11} - K_{12}) - \frac{\delta B_1}{SF_1} + \frac{\delta B_2}{SF_2}]$$
$$+ \frac{1}{2}[K_{21}-K_{22}+C(\omega)\cos\phi(\omega)(\frac{\delta SF_1}{SF_1} - \frac{\delta SF_2}{SF_2})-2gC(\omega)\cos\phi(\omega)(K_{21}+K_{12}-K_{11}-K_{22})]A_v^2$$
$$+ C(\omega)^2[(\frac{1}{8}\cos^2\phi(\omega) + \frac{1}{4})(K_{11} - K_{12})]A_v^4 \qquad (22a)$$

$$\overline{M}_2 = [g(\frac{\delta SF_1}{SF_1} - \frac{\delta SF_2}{SF_2}) + g^2(K_{11} + K_{12}) - \frac{\delta B_1}{SF_1} - \frac{\delta B_2}{SF_2}]$$
$$+ \frac{1}{2}[K_{21}+K_{22}+C(\omega)\cos\phi(\omega)(\frac{\delta SF_1}{SF_1} - \frac{\delta SF_2}{SF_2})-2gC(\omega)\cos\phi(\omega)(K_{21}-K_{12}-K_{11}+K_{22})]A_v^2$$
$$+ C(\omega)^2[\frac{1}{8}\cos^2\phi(\omega) + \frac{1}{4})(K_{11} + K_{12})]A_v^4 \qquad (22b)$$

Solving for K_{21} and K_{22} from the A_v^2 coefficients:

$$\hat{K}_{21} = K_{21} + C(\omega)\cos\phi(\omega)(\frac{\delta SF_1}{SF_1} - \frac{\delta SF_2}{SF_2}) - 2gC(\omega)\cos\phi(\omega)(K_{21} - K_{11}) \qquad (23a)$$

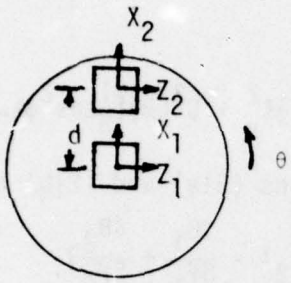
$$\hat{K}_{22} = K_{22} - 2gC(\omega)\cos\phi(\omega)(K_{22} - K_{12}) \qquad (23b)$$

With the dual instrument technique a large frequency dependent error is greatly reduced. This alleviates the difficulty of dynamically monitoring small angles at high frequencies.

For $C(\omega) \leq 3\times10^{-4}$ rad, all errors are less than .01 part per million/g.

4.5 Orthogonal Sinusoidal Accelerations Along and Perpendicular to Accelerometer Input Axis (Tumble Testing)

For this type of test the maximum input is 1g. For this reason, the cut-off level for contributing terms will be lowered to .001μg. To simplify the geometry, we will consider accelerometer 1 to be mounted at the center of rotation of the test table, and accelerometer 2 mounted a distance d from the center as shown.



Under these conditions, to account for the gravity gradient, $a_{x2} = (g - d(\frac{dg}{dh})\cos\theta)\cos\theta$, $a_{z2} = (g - d(\frac{dg}{dh})\cos\theta)\sin\theta$, so we can consider $\Delta_{1x} = \Delta_{2x} = \Delta_{1z} = \Delta_{2z} = 1 - \frac{d}{g}(\frac{dg}{dh})\cos\theta$ and by our earlier convention $\varepsilon = -\frac{d}{g}\frac{dg}{dh}\cos\theta$.

Let us also constrain the errors for the test table γ_0, γ so that $\gamma_0 \leq 10^{-4}$ radians and $\gamma \leq 10^{-5}$ radians.

We can now substitute Equations (6a), (6b), and (6c) into Equations (13a) and (13b) keeping only terms greater than .001μg. This procedure gives us

$$
\begin{aligned}
M_1 = {} & [\frac{g^2}{2}(K_{11} + K_{21} - K_{12} - K_{22}) + \frac{d}{2}(\frac{dg}{dh}) - \frac{\delta B_1}{SF_1} + \frac{\delta B_2}{SF_2}] \\
& + [(\frac{\delta SF_1}{SF_1} - \frac{\delta SF_2}{SF_2}) + \gamma_{01}\alpha_1)g\sin\theta \\
& + [\gamma_{01}(\frac{\delta SF_1}{SF_1} - \frac{\delta SF_2}{SF_2}) - \alpha_1\beta_2]g\cos\theta \\
& + [2\gamma_{01}(K_{11} - K_{12} - K_{21} + K_{22} - 2\alpha_1(K_{12} - K_{22})]\frac{g^2}{2}\sin 2\theta \\
& + [-K_{11} + K_{12} + K_{21} - K_{22} + \frac{d}{g^2}(\frac{dg}{dh})]\frac{g^2}{2}\cos 2\theta \qquad (24a)
\end{aligned}
$$

$$M_2 = [\frac{g^2}{2}(K_{11} + K_{21} + K_{12} + K_{22}) + \frac{d}{2}(\frac{dg}{dh}) - \frac{\delta B_1}{SF_1} - \frac{\delta B_2}{SF_2}]$$

$$+ [(\frac{\delta SF_1}{SF_1} - \frac{\delta SF_2}{SF_2}) + \gamma_{02}\alpha_2]g\sin\theta$$

$$+ [\gamma_{02}(\frac{\delta SF_1}{SF_1} - \frac{\delta SF_2}{SF_2}) - \alpha_2\beta_2]g\cos\theta$$

$$+ [2\gamma_{02}(K_{11} + K_{12} + K_{21} + K_{22}) + 2\alpha_2(K_{12} - K_{22})]\frac{g^2}{2}\sin 2\theta$$

$$+ [-K_{11} - K_{12} + K_{21} + K_{22} + \frac{d}{g^2}(\frac{dg}{dh})]\frac{g^2}{2}\cos 2\theta \qquad (24b)$$

Solving for the combined K's from the $\frac{g^2}{2}\cos 2\theta$ coefficients, we obtain:

$$\hat{K}_{21} - \hat{K}_{11} = K_{21} - K_{11} + \frac{d}{g^2}(\frac{dg}{dh}) \qquad (25a)$$

$$\hat{K}_{22} - \hat{K}_{12} = K_{22} - K_{12} \qquad (25b)$$

The primary error is due to the gravity gradient ($\frac{dg}{dh}$). Since the gradient is $\simeq .1\mu g/ft$ and d would be $< .5$ ft, the total error introduced into $\hat{K}_{21} - \hat{K}_{11}$ would be $\simeq .05$ part per million/g. This is a deterministic type of error since d is easily measured and $\frac{dg}{dh}$ is generally well known, so it can be removed by direct computations. Instrument swapping in the mount so that $\hat{K}_{21} - \hat{K}_{11}$ becomes $\hat{K}_{22} - \hat{K}_{12}$ on another test will allow both instruments to be calibrated without knowledge of d or $\frac{dg}{dh}$.

5. GENERAL COMMENTS ON THE USE OF MULTIPLE ACCELEROMETER TESTING

The results of the previous section were based on many assumptions about the instrument model, the test bed errors, and the test mechanization. For this reason use this paper as a guide to the method of analyzing errors in a dual accelerometer test, not as an exposition of the error sources.

Dual instrument testing offers the possibility of greatly enhancing instrument g-squared coefficient recovery not only through the reduction of test bed errors, but also through enhanced "signal" visibility and additional data error detection capability.

In the dynamic test modes where up to 20 g's are applied, the subtractive

measurement process employed reduces the total signal to usually less than .001 g. This makes the g-squared instrument effects a much more significant part of the signal and often improves the numerical computational accuracy of most coefficient estimation schemes.

Errors caused by instrument, test bed, and data collection hardware failure or degradation can usually be easily isolated if more than one instrument is being tested. For expensive tests, such as the centrifuge tests, the capability to detect errors and restart the tests before much time and money have been spent is enough justification alone for dual instrument testing.

At this point a reiteration of the limitations on the various tests is in order.

5.1 Model Limitations

The dual instrument measurement equations (13a) and (13b) were derived for a specific instrument model assuming incomplete knowledge of the instrument scale factors and biases. The instrument model must be well known. If this is the case, a similar derivation can be made for any specific instrument where g-squared terms can be recovered from test data.

It was also assumed that the instruments were misaligned in the mount about a single axis. This is not generally true and should be accounted for in specific cases. Usually the test geometry can be arranged so that misalignments about the other two axes are not critical.

5.2 Centrifuge Test Limitations

Input axis testing is most affected by radius differences in the instruments and centrifuge radius stretch. This is true despite the specific constraints employed in this paper. Dual instrument testing shifts the problem of measuring stretch to one of measuring g-dependent mount tilt (if it exists) and its related instrument radius shift. This may or may not be a significant gain, depending on the centrifuge instrumentation and geometry.

Cross axis testing is also affected by radius differences in the instruments, radius stretch, and, additionally, instrument misalignment in the mount. The radius difference error will predominate independently of the specific test bed unless extreme care is taken.

The most favorable aspect of cross axis testing is that g-dependent mount tilts do not significantly affect coefficient recovery. This makes dual instrument cross axis testing on a centrifuge an important error-free test procedure.

5.3 Vibration Test Limitations

The primary assumption that might cause trouble is the modeling of the acceleration as a sinusoid. One should be careful that the average and rms acceleration levels are well known before using them in the coefficient estimation.

The signal enhancement and error detection capabilities of dual instrument testing recommend it for both input and cross axis vibration testing, even though input axis testing does not suffer from test bed errors.

In general, dual instrument vibration testing is also an important error-free test procedure which does not require dynamic angle monitoring.

5.4 Tumble Test Limitations

The biggest problem with this test is the limitation of the inputs to 1g and the coupling of g-squared coefficients.

The low level inputs mean that the g-squared effects are $\simeq 10^{-5}$g's at best and relatively sophisticated estimation schemes are necessary to reduce measurement noise and other unmodelled environmental effects.

Dual instrument testing in this fashion does eliminate the requirement to account for lunar and solar effects on gravity since this effect is reduced by a factor $(\frac{\delta SF_1}{SF_1} - \frac{\delta SF_2}{SF_2})$ on the order of 10^{-5}. Except for the gravity gradient effect, virtually all test table errors that could propagate into a g-squared coefficient (if a valid instrument test table model is used) are eliminated. This makes dual instrument tumble testing a much more tractable low level input test if the coupled g-squared coefficient recovery is not objectionable.

In summary, centrifuge (instrument cross axis), vibration, and tumble testing for recovery of g-squared instrument coefficients can be greatly enhanced by the technique of multiple accelerometer testing.

EIGHTH BIENNIAL GUIDANCE TEST SYMPOSIUM

AN EXAMINATION OF LOW POWER SPECTRAL DENSITY (PSD) NOISE PERFORMANCE OF A DRY TUNED GIMBAL TWO-DEGREE-OF-FREEDOM GYROSCOPE, AND METHODS FOR FURTHER NOISE REDUCTION

AUTHORS: ROBERT B. IRVINE
JOHN W. RITTER

TELEDYNE SYSTEMS COMPANY
NORTHRIDGE, CALIFORNIA

ABSTRACT

Recent test and evaluation of dry, tuned gimbal, two-degree-of-freedom gyroscopes has revealed power spectral "noise" levels that compare favorably with floated gyro standards currently used in high accuracy pointing and attitude stabilization systems. Power spectral density test data on the Teledyne SDG-5 dry tuned gyroscope are presented and compared with published results for single-degree-of-freedom floated gyroscopes. The specific capabilities and limitations of the dry tuned gyro approach for high accuracy pointing applications are discussed.

Gyro noise in the strictest sense may be defined as that component of the angular rate output which does not represent the measurement of the true angular rate input to the gyroscopic sensor, but is a spurious output resulting from sensor imperfections, including the associated control and output interface electrical circuitry. The principal sources of the noise for either floated or dry-tuned gyros may be categorized as follows:

1. Suspension system induced torques.

2. Non-suspension system induced torques.

3. Electrical/Magnetic field noise.

The predominant source of low frequency angular rate noise present in inertial gyros results from angular motions or misalignments of the driven (spin reference) axis with respect to the case fixed (stationary) axes. These motions (which ideally do not exist), although small, result in suspension system induced torques acting upon the rotor, or "noise".

It is shown that it is possible to effect significant reductions in this dominant source of noise by the optimization of the basic design parameters of the dry-tuned gyroscope. In particular, it is shown that this noise reduction is most sensitive to the ratios of rotor inertias to gimbal inertias, as well as to the number of gimbals utilized in the design. Tradeoffs of noise reduction versus gyro maximum shock/acceleration capability are presented. In addition further refinements related to angle pickoff accuracy considerations are described.

I. INTRODUCTION

During calendar year 1976, Teledyne Systems Company initiated a program to accurately determine the spectral noise characteristic for the dry-tuned two-degrees-of-freedom SDG-5 Gyroscope. The demand for this data was quite sufficient from a number of potential users in such applications as high accuracy spacecraft stabilization (e.g. DRIRU II and Space Telescope), high energy laser (HEL) pointing, and a number of other important applications. Initial testing was conducted in-house early in the program where it was determined that more sophisticated data acquisition systems were desirable and, primarily that higher stability well instrumented test piers would be required. Teledyne then contacted the Martin-Marietta Corporation, Denver, Colorado and the Space and Missile Systems Organization (SAMSO), Los Angeles AFS, California where the SDG-5 was added to the list for test of candidates competing for the High Altitude Attitude Reference System (HAARS). Additional testing was accomplished at the Boeing Aerospace Company and at Lockheed Missiles and Space Company.

Sufficient data was obtained to show that the Teledyne SDG-5 gyroscope is an extremely attractive rate sensor for use in fine pointing control system applications where jitter is required in the milliarc-second region and that operate with bandwidths to 10 Hz. The instrument is particularly attractive in view of its high reliability, low relative cost to existing standards and capability of operation over a broad temperature range without the use of temperature control. No selection of instruments was made and units were tested on an "as available" basis. Standard laboratory analog rebalance loops were employed and no gyro heaters, precision temperature control or temperature compensation was used in the test series.

II. GYRO DESCRIPTION

The Teledyne SDG-5 is a dry gyro and features an elastically supported rotor with a dynamically tuned suspension system. The two-degree-of-freedom strapdown gyro consists of four major subassemblies: the case, torquer coils, pickoffs, and rotor containing its tuned three-gimbal suspension system. These subassemblies are shown in Figure 1 and a schematic cross section of the gyro is shown in Figure 2. The gyro case supports a set of ball bearings which in turn carry the shaft. Mounted on one end of the shaft is the motor hysteresis ring and on the other end is the rotor and suspension system. The torquer coils and pickoff subassembly are attached to the case. The end covers, when soldered in place, provide the hermetic seal for the gyro.

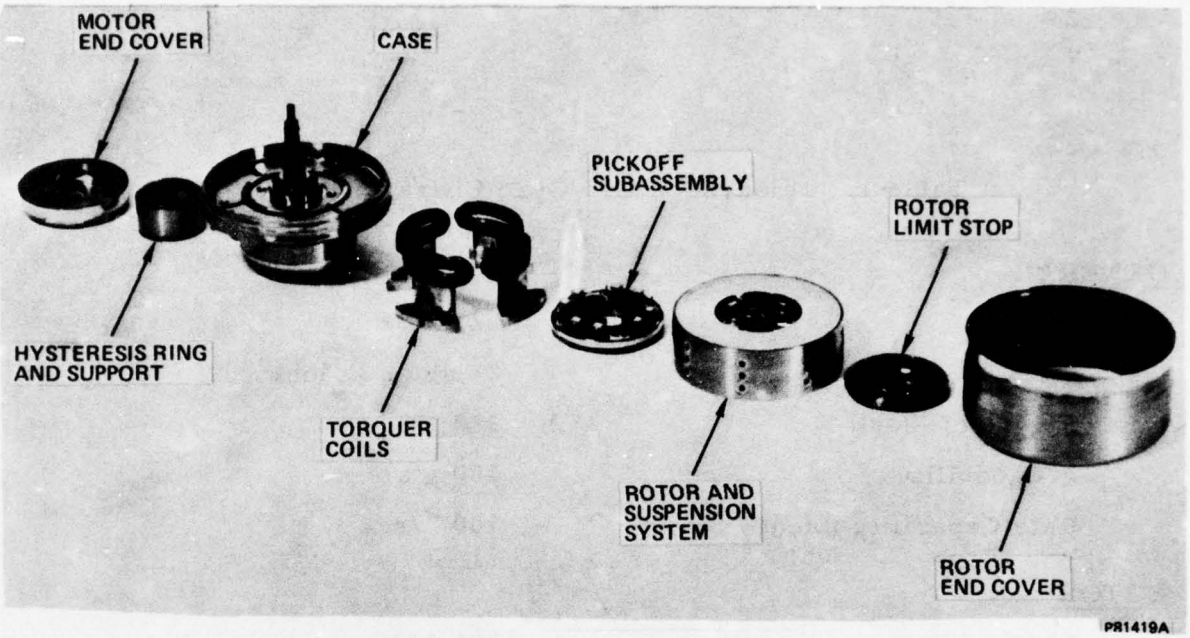


Figure 1. SDG-5 Strapdown Gyro Subassemblies

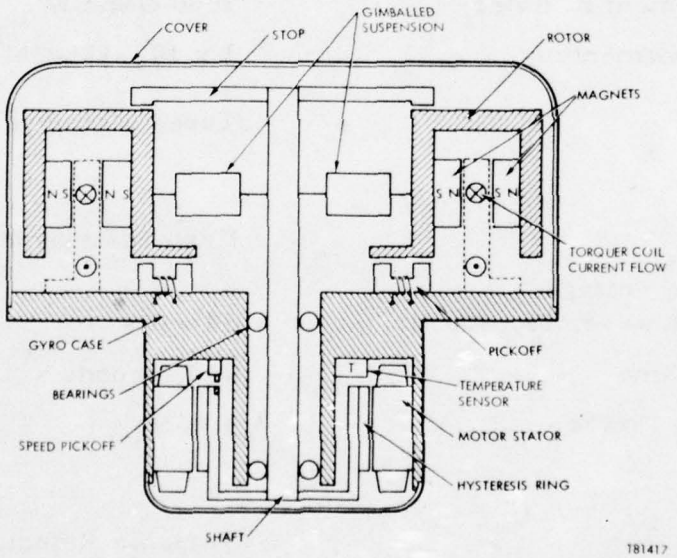


Figure 2. Schematic Cross-Section of the Strapdown Gyro

The Teledyne SDG-5 Gyro has an angular momentum of 1×10^6 CGS units while operating at 6,000 RPM on standard R-4 size ball bearings. A summary of physical characteristics is presented in Table 1 and a summary of key performance characteristics is shown in Table 2.

Table 3 presents a summary of instrument characteristics [4] for single-degree-of-freedom floated gyros and a comparison of the SDG-5 two-degree-of-freedom dry gyro.

Table 1. Teledyne SDG-5 Gyro Characteristics

GENERAL	
Weight	< 2.3 lbs
Size	3" dia x 3" long
Figure of Merit	320
g-Capability	150 g's
Rate Capability (Steady State)	100 °/sec
ROTOR	
Mass of Rotor	260 GMS
Polar Moment of Rotor	1600 GM-CM^2
Angular Momentum	1 x 10^6 GM-CM^2/sec
SUSPENSION	Tuned 3 gimbal
SPIN MOTOR	
Type	Hysteresis Synchronous
Excitation Voltage (RMS sine wave, 3ϕ, 400 Hz)	30 volts
Run-Up Time	<30 seconds
Operating Power	2 watts
PICKOFF	
Type	Variable Reluctance Transformer
Excitation Frequency	48K Hz sinewave
Excitation Voltage	7 VRMS
Nominal Scale Factor	100 V/RAD
TORQUER	
Type	Voice Coil
Nominal Scale Factor	160 °/Hr/ma
HEATER - None Required	

Table 2. Teledyne SDG-5 Gyro Performance Characteristics

Parameter	Units	Specification Value	Typical Value (mean)
G-Insensitive Bias			
Absolute Value	^{o}/Hr	0 ± 2.0	< 0.50
Stability			
Continuous Operation (Random Drift)	^{o}/Hr 1σ	.001 Max.	0.0005
Shutdown Repeatability	^{o}/Hr 1σ	.01 Max.	0.0016
Temperature Cycle Stability	^{o}/Hr 1σ	-	0.0033
Temperature Sensitivity	^{o}/Hr/^{o}F	$0 \pm .002$	0.00059
G-Sensitive Bias			
Absolute Value	^{o}/Hr/G	0 ± 1.0	< 1.0
Stability			
Continuous Operation (Random Drift)	^{o}/Hr/G 1σ	.002 Max.	0.0007
Shutdown and Temperature Cycle Repeatability	^{o}/Hr/G 1σ	-	0.008
Temperature Sensitivity	^{o}/Hr/G/^{o}F	$0 \pm .02$	0.0032
Torquer Scale Factor			
Absolute Value	^{o}/Hr/MA	150 Min.	160
Linearity	PPM Peak	100 Max.	25
Asymmetry	PPM Peak	-	3
Temperature Sensitivity	PPM/^{o}F	-230 ± 20	-229
Axis Alignment			
Absolute Value	$\widehat{\text{Sec}}$	60 Max.	30
Stability	$\widehat{\text{Sec}}$	-	10
Angular Rate Capability			
Steady State	^{o}/Sec	100	>100
Transient	^{o}/Sec	400	>500
Anisoelasticy	^{o}/Hr/g^2	$0 \pm .03$	.01
Gyro Time Constant	Seconds	100 Min.	200

T101556A

Table 3. Summary Comparison of Instrument Characteristics

Characteristic	Units	SDF Floated Gyro [4]									TDF Dry Gyro
		MIT/CSDL						Nortronics		Honeywell	Teledyne
		TGG V1	TGG Proto	TGG Pre-Proto	2 FBG+F-OAO	25 IRIG	18 IRIG	GIT-1B	K7	GG 334	SDG-5
Wheel	Type	No Wheel	Hemispherical Gas		Ball	Spool Gas	Spool Gas	Spool Gas	Spool Gas	Spool Gas	Ball
H	gm-cm^2/sec		0.5×10^6	0.7×10^6	1.7×10^6	0.54×10^6	0.15×10^6	1.8×10^6	0.18×10^6	0.2×10^6	1.0×10^6
Speed	RPM		32,000	24,000	12,000	24,000	24,000	24,000	72,000	24,000	6,000
Run Power	Watts		16.5	~12	3	9	5	6	0.5	3.5	2
Gain H/C		NA	1.2	0.87	1.0	0	0.2	1	9	0.4	NA**
Characteristic Time $(I/C)_{OA}$	Millisec	0.57	0.75	0.75	1	0.59	0.33	~1.0	4	0.5	NA**
Torque Generator	Type	EM (2 winding)	EM (2 winding)	EM (2 winding)	EM (2 winding)	EM	EM	PM	PM	PM	PM
Sensitivity	MERU	2.4/ma^2	5.2/ma^2	2.4/ma^2	0.165/ma^2	6/ma^2	120 eru/ma	*	7×10^3/ma	8×10^4/ma	11 eru/ma
Max Rate		100 eru	100 eru	< 100 eru	40 eru	360 eru	60°/sec	*	3°/sec	110°/sec	100°/sec
Signal Generator	Type	EM E	EM Bridge	EM E	EM	EM	EM	EM	EM	EM	EM
Sensitivity	MV/MRAD$_{OA}$	84	110 Tuned	84	34	32	20	-20	40	24	100
Suspension	Type	EM Tapered	EM Tapered	EM Tapered	EM Tapered	EM Tapered	EM Tapered	EM	Taut Wire	Dither Jewel	Tuned Gimbal
Radial TC		8 min	8 min	8 min	*	*	*	*	*	*	NA**
Axial TC		3.4 hrs	3.4 hrs	3.4 hrs	*	*	*	*	*	*	NA**
Operating Temp	°F	121	135	135	135	135	132	180	170	180	0 to 200°F
Mounting Configuration		End Stud	Tapered End Stud	End Stud	End Stud	End Stud	End Mounted	End Stud	Center Flange	Center Flange	Center Flange
Environment		NA	Missile Boost	Missile Boost	Satellite	Missile	Satellite	Gyro Compassing	Navigator Satellite	30g max.	150g max.
Life Expectancy	MTBF (hrs)	NA	100K	100K	20K	*	*	*	100K	NA	100K +

*Not Available
**Not Applicable

T107226

III. SUPPORT ELECTRONICS

The SDG Electronics/Control Unit [6] contains the necessary analog rebalance electronics to cage both axes of the SDG-5. A photograph of the 19 inch rack-mounted panel is shown in Figure 3. Controls, located on the front panel are used to control the caging process and provide a convenient means for selecting various torque output scaling functions. Generally, the unit contains the necessary regulated and precision DC voltages, the gyro 48 kHz pickoff excitation, caging electronics and precision analog scaling electronics for each gyro axis. Refer to Figure 4 for the functional block diagram and to Figures 5 and 6 for measured cross and direct-axis control loop frequency response curves.

The previously described electronics was interfaced with the data acquisition system and the gyro mounted on the test pier as available at the various facilities. The functional organization utilized was as shown in Figure 7.

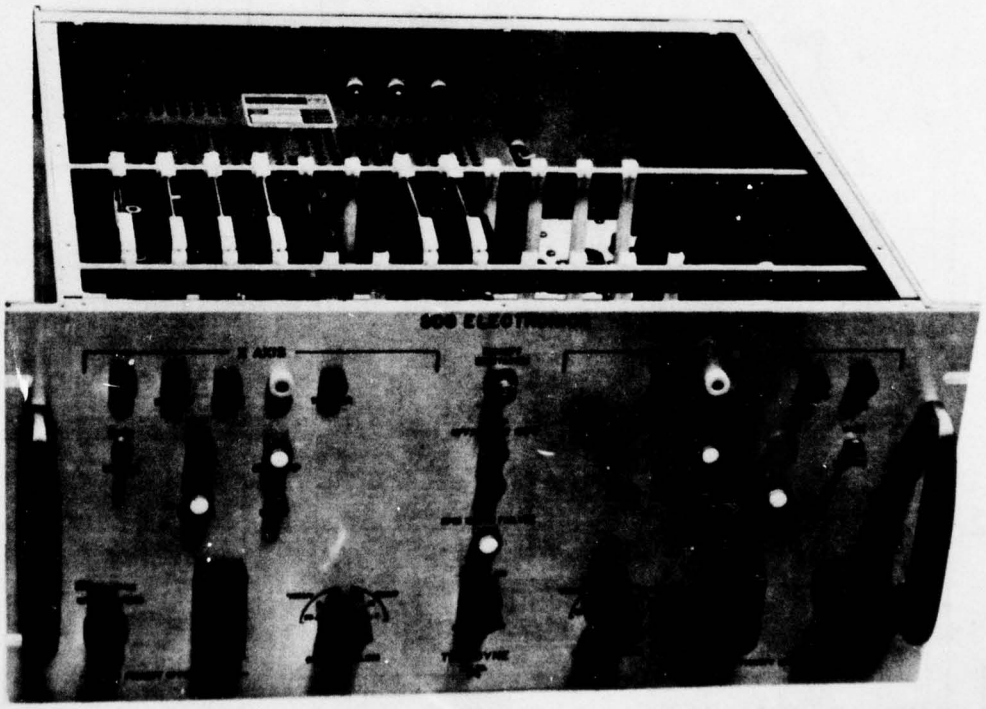


Figure 3. Teledyne Strapdown Gyro Laboratory Test Equipment [6]

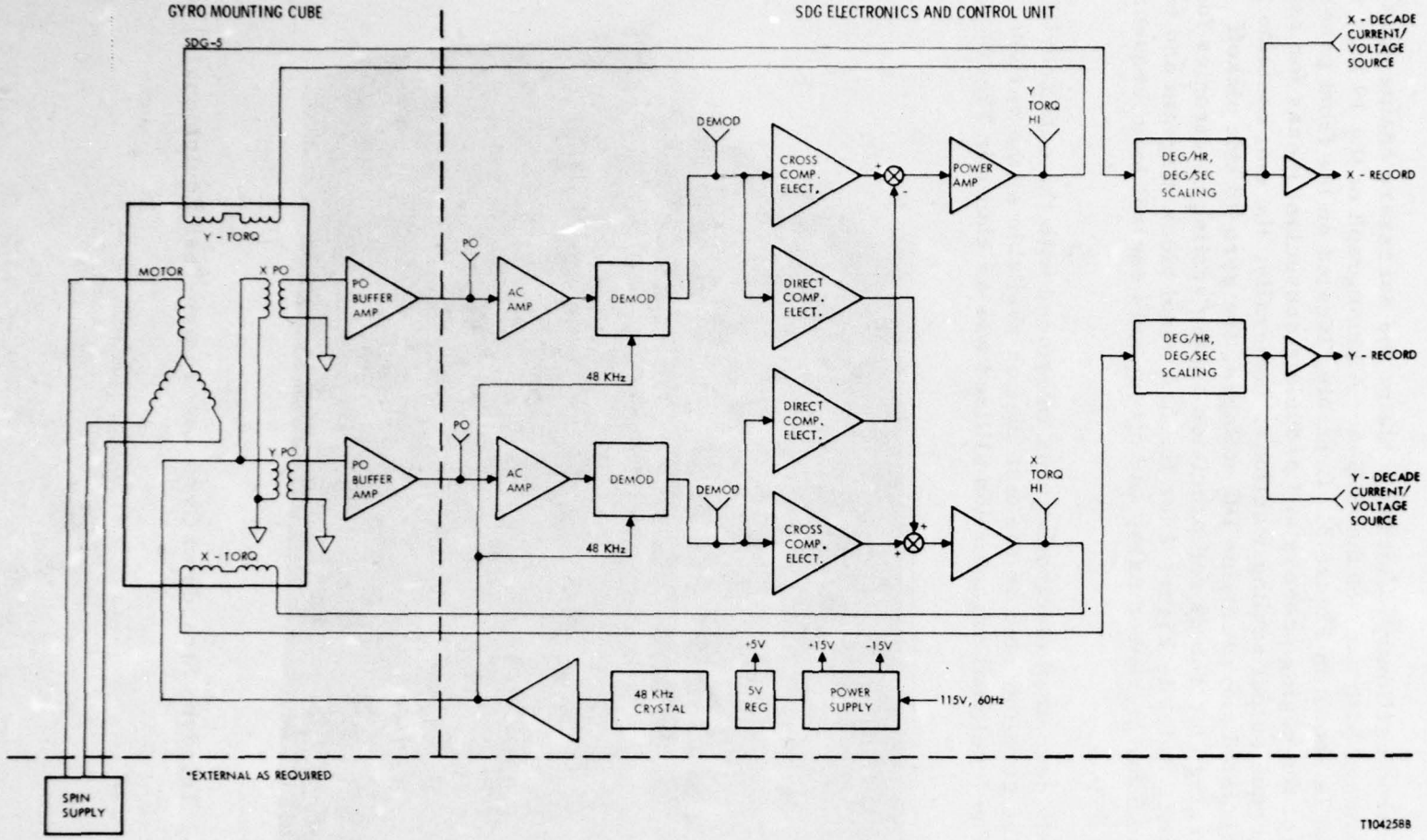


Figure 4. Functional Block Diagram of Teledyne Strapdown Gyro Test Mechanization

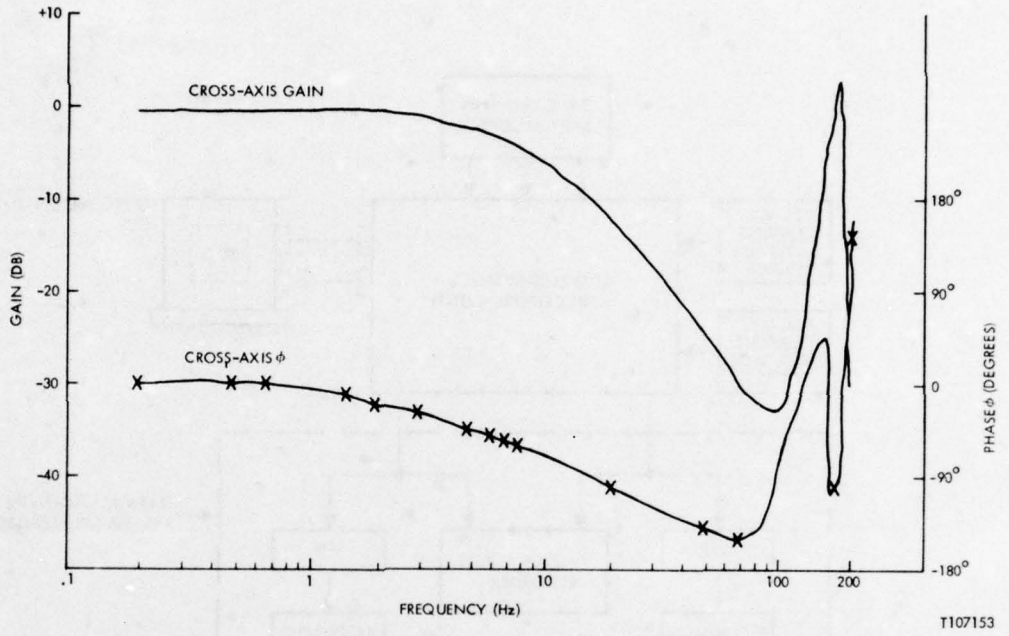


Figure 5. Cross Axis Bode Plot

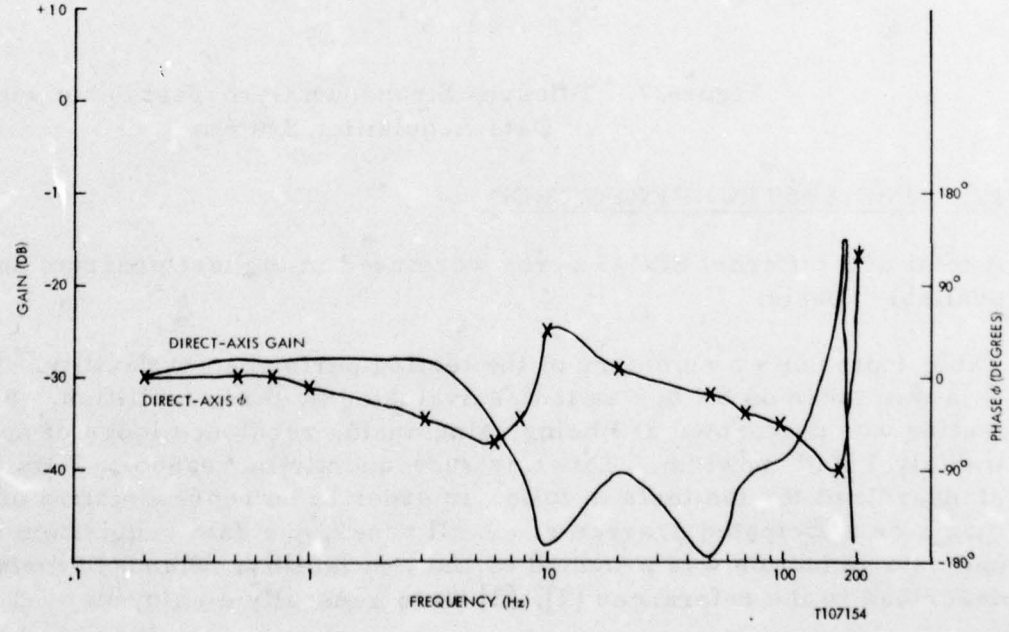


Figure 6. Direct Axis Bode Plot

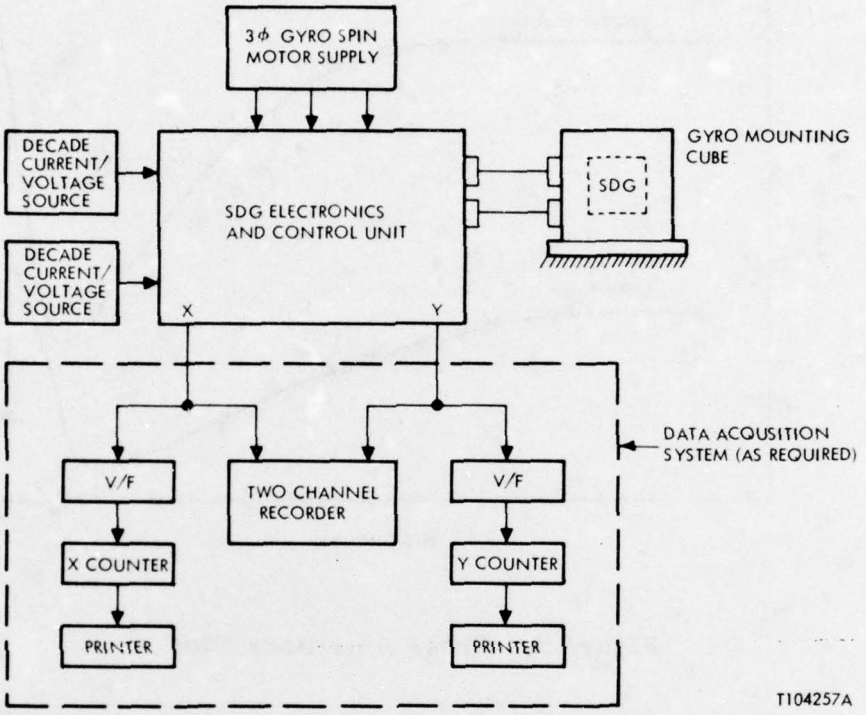


Figure 7. Teledyne Strapdown Gyro Test Setup with Data Acquisition System

IV. PSD TESTING PERFORMED

A total of 5 different SDG-5 gyros were used in the test program on an "as available" basis.

Table 4 presents a summary of the testing performed by facility. Most data was taken on SN 069 as it was evaluated by three facilities. Initial testing was performed at Boeing using analog rebalance loops of approximately 1 Hz bandwidth. This was subsequently increased to 7 Hz and standardized for the tests to follow in order to be representative of requirements on anticipated programs. In all cases, the data acquisition system and data reduction was provided by the test facility. Standard methods as described in the references [1], [2] were generally employed.

Table 4. Summary of PSD Testing Performed On Teledyne SDG-5 Gyro

Test Facility	No. Gyros Tested	Test Period	Gyro Test Equipment Used/ Caging Loop Bandwidth	Data Acquisition System	Test Pier	Test Report
Boeing Aerospace Co. (Seattle, Wash.)	4 (SN's 034, 035, 068, 069)	21 July 1976 to 20 July 1976	Teledyne Strapdown Gyro Laboratory Test Equipment [6] (Standard Configuration) Analog Loop Approx 1 Hz	Omniferous FFT Analyzer Nicolet Scientific Corp Model 400A	Seismic Pad	Raw Data Available - No formal report anticipated
Martin-Marietta Corp. (Denver, Colorado)	2 (SN's 068, 069)	2 August 1976 to 29 October 1976	Teledyne Strapdown Gyro Laboratory Test Equipment [6] (Standard Configuration) Analog Loop Approx 7 Hz	MMC-A/D Converter [5] PRIME Computer	MMC Granite Pier at south end of Fine Pointing Dimensionally Stable Simulator [5]	Spring 1977 [5] (Proprietary Report)
Holloman A.F.B. CIGTF (Alamogordo, N.M.)	1 (SN 069)	2 Sept. 1976 to 12 October 1976	As Above/7 Hz	Holloman-A/D Converter [1] HP 2100 Computer	CIGTF Tilt Meter Instrumented Test Pad [1]	The Teledyne SDG-5 Gyro Test, Report No. TBD February 1977 [8]
Boeing Aerospace Co. (Seattle, Wash.)	1 (SN 069)	15 Oct 1976	As Above/7 Hz	Omniferous FFT analyzer Nicolet Scientific Corp. Model 400A	Seismic Pad and Lab Floor	Raw Data Available - No formal report anticipated
Lockheed Missiles and Space Co. (Sunnyvale, Ca.)	1 (SN 036)	24 Dec 1976 to 5 Feb 1977	As Above/7 Hz	LMSC A/D and V/F Converter HP2100 or Intellec 8	LMSC Test Piers	LMSC Test report

T107225

V. SUMMARY AND COMPARISON OF TEST RESULTS BY FACILITY

Teledyne provided two SDG-5 gyros and associated test equipment to the Holloman AFB-CIGTF for evaluation as part of the HAARS testing program. Only S/N 069 was evaluated due to schedule constraints. The data acquisition system, filtering employed, test equipment and data reduction techniques are well described in [1] and are, therefore, not discussed herein. Figures 8, 9 and 10 present typical PSD gyro outputs in $(DEG/HR)^2$ /Hz for the gyro evaluated. These data provide a high confidence PSD signature for the unit evaluated over the frequency range .0001 Hz to approximately 2.5 Hz.

As equipment specifications for hardware (e.g. DRIRU II) sometimes specify the gyro output noise limits in ^{o}/HR RMS over a specific frequency range, the noise characteristic for the SDG-5 gyro was measured in appropriate units by the Martin-Marietta Corporation. Table 5 presents a comparison of of the measured SDG-5 output in ^{o}/HR RMS versus the DRIRU II specification.

Data as available from the other test facilities are presented in Table 6 for comparison purposes. The data from Holloman CIGTF and the Martin-Marietta Corporation is seen to correlate reasonably well in the frequency band of .001 Hz to 5 Hz.

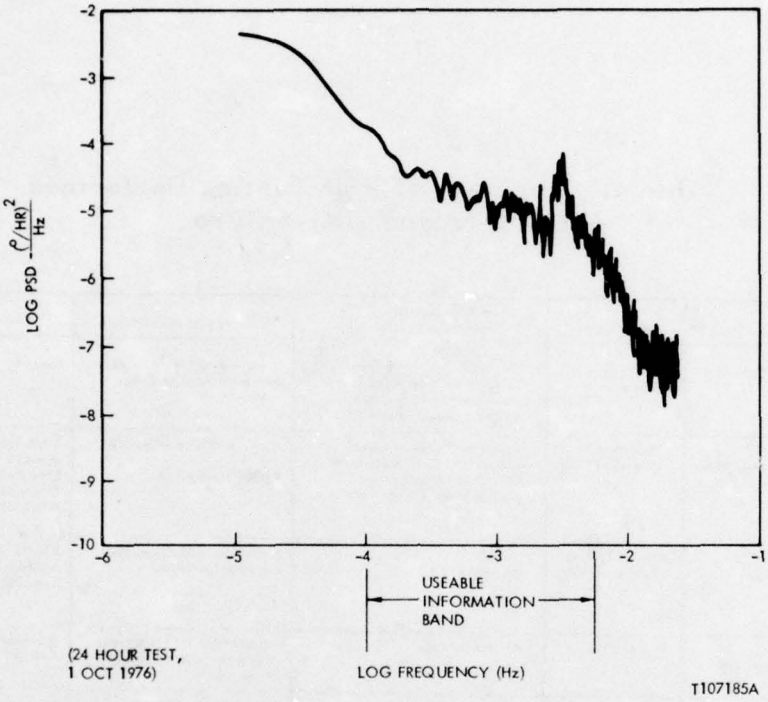


Figure 8. Power Spectral Density Gyro Output of Teledyne SDG-5 S/N 069 (Data Courtesy of Holloman AFB-CIGTF)[8]

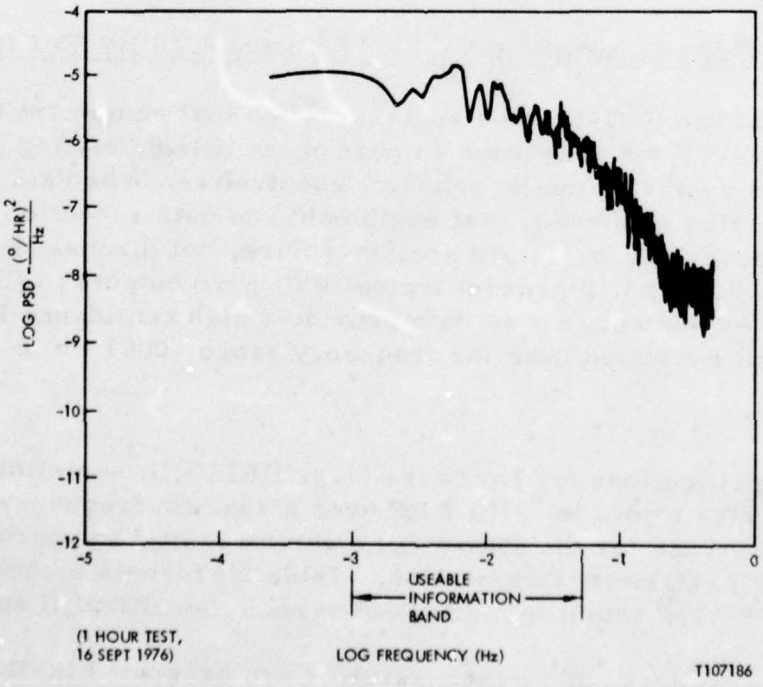


Figure 9. Power Spectral Density Gyro Output of Teledyne SDG-5 S/N 069 (Data Courtesy of Holloman AFB-CIGTF)[8]

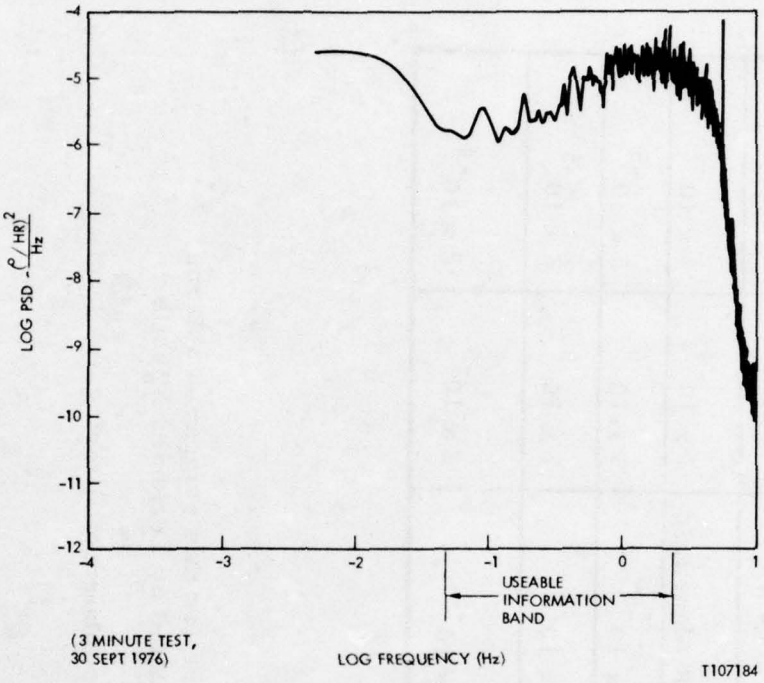


Figure 10. Power Spectral Density Gyro Output of Teledyne SDG-5 S/N 069 (Data Courtesy of Holloman AFB-CIGTF) [8]

Table 5. Comparison of Measured SDG-5 Output In (^{o}/Hr RMS) vs DRIRU II Specification (Data Courtesy of Martin-Marietta Corp - Denver, Co)

Frequency Range (Hertz)	Performance in ^{o}/Hr RMS		
	Axis	DRIRU II Specification	SDG-5 Performance
.01-1.0	X	.05 Max.	.004
	Y		.0032
.01-7.0	X	.5 Max.	.029
	Y		.028

Table 6. Inter Facility Comparison of PSD Test Results on Teledyne SDG-5 Gyro

Facility	Measured Gyro Noise Over Frequency (Hz) in $(^{\circ}/\mathrm{Hr})^2/\mathrm{Hz}$				
	.0001-.001	.001-.01	.01-.1	.1-1	1-5
Boeing Aerospace Co.	Not Measured	Not Measured	Not Measured	2×10^{-4}*	1×10^{-4}
Martin-Marietta Corp.	Not Measured	7×10^{-5}	2×10^{-5}	5×10^{-6}	5×10^{-5}
Holloman CIGTF	6×10^{-5}	1×10^{-5}	1×10^{-6}	7×10^{-6}	2×10^{-5}
Lockheed Missiles and Space Co.	Not Measured	Not Measured	3×10^{-5}	2×10^{-5}	2×10^{-4}

NOTE:
SDG-5 S/N 069, SAV, axis being tested east or west was used for this comparison at the first three facilities listed above. SDG-5 S/N 036 was evaluated by Lockheed Missiles and Space Co.
*Possible aliasing problem in data acquisition system due to incorrect filtering availability at time of test.

VI. COMPARISON OF PSD CHARACTERISTICS OF SDG-5 DRY TDF AND SDF FLOATED GYROS

A comparison of the noise characteristics between the Teledyne SDG-5 dry TDF gyro with data for floated SDF gyros as reported in [4] was made. For convenience in making this comparison, the units of $(\text{arc-sec})^2/\text{Hz}$ were used. A graphical presentation of this comparison is presented in Figure 11. The reader is cautioned that the sample size (one or two units) is small and that the data presented for dry TDF gyros is limited to the Teledyne SDG-5. Nonetheless, it appears that the dry-tuned ball bearing gyro performance compares quite favorably in the bandwidth of .01 Hz to approximately 5 Hz with currently used floated standards used in low jitter attitude stabilization and precision pointing systems.

VII. METHODS FOR FURTHER NOISE REDUCTION IN DRY TUNED GYROS

The dry tuned gyro has a number of characteristic features that provide for implementing several methods for noise reduction to even lower levels than determined in the previously described testing. These consist of basic optimization of physical design parameters as briefly outlined in the following discussion.

Physical Increase in Angular Momentum

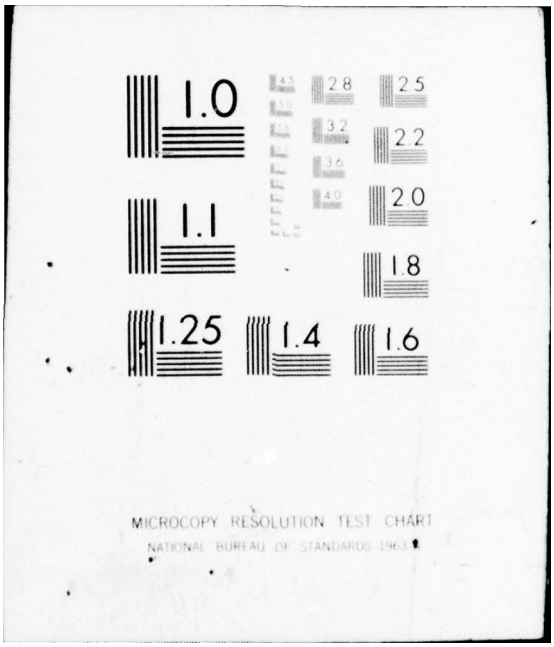
The angular momentum of the dry gyro can be increased by adding mass to the rotor while maintaining the same spin speed with the attendant decrease in torque generator scale factor. A factor of two increase in angular momentum is readily attainable in the SDG-5. The reduction in scale factor (160°/Hr/ma for SDG-5) to one-half (80°/Hr/ma) is quite acceptable for most pointing applications where maximum rate is limited to approximately $\pm 50^\circ$/sec. Teledyne has produced gyros (the SDG-3B) with 2×10^6 cgs units angular momentum in lieu of 1×10^6 cgs units for the SDG-5. Figures 12 and 13 make the comparison of key characteristics.

AD-A040 012 ARMAMENT DEVELOPMENT AND TEST CENTER EGLIN AFB FLA F/G 17/7
PROCEEDINGS OF THE BIENNIAL GUIDANCE TEST SYMPOSIUM (8TH) HELD --ETC(U)
MAY 77

UNCLASSIFIED ADTC-TR-77-3-VOL-1 NL

7 OF 8
AD
A040012




1.0
2.8
2.5
3.2
2.2
3.6
4.0
2.0
1.1
1.8
1.25
1.4
1.6
MICROCOPY RESOLUTION TEST CHART
NATIONAL BUREAU OF STANDARDS 1963

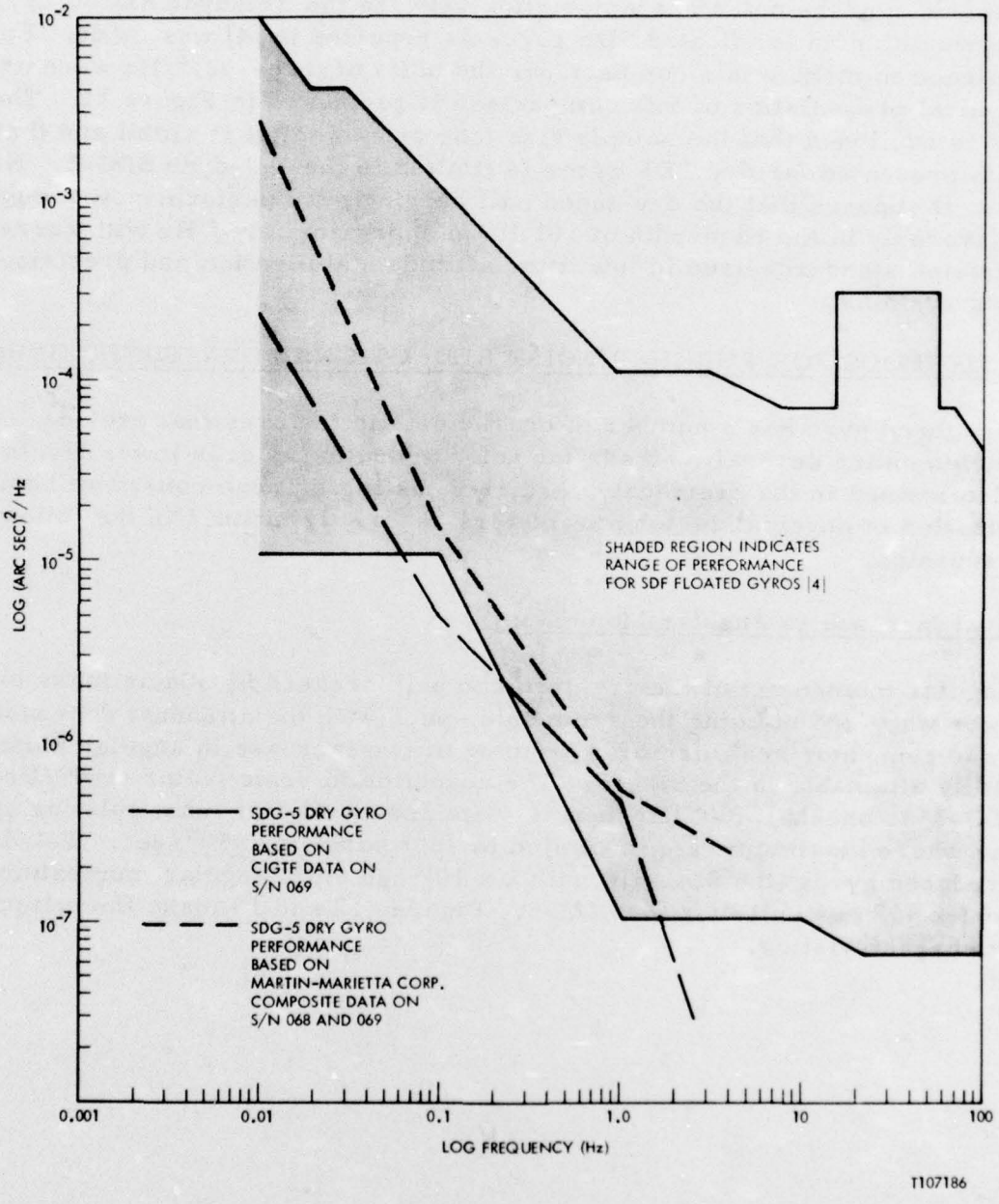
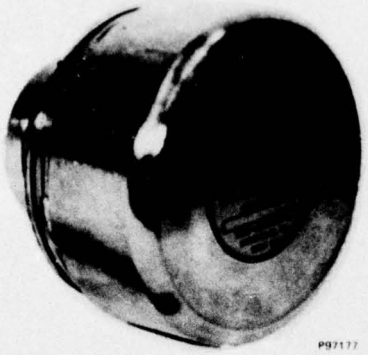
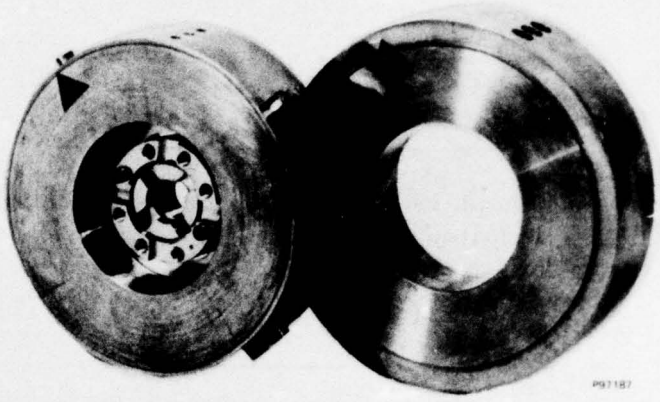


Figure 11. Graphical Comparison of Noise Characteristics in (arc sec)^2/Hz for Teledyne SDG-5 Dry TDF Gyro with Floated SDF Gyros [4]



SDG-3B



SDG-5 ROTOR AND SDG-3B ROTOR
(FOR COMPARISON)

Figure 12. Photograph of SDG-3B Gyroscope

APPLICATIONS

Shipboard Inertial Navigation

Spacecraft Guidance and Control, Fine Pointing

Requirements for very Low Drift Rates, Low Noise and with Moderate Rate Inputs

SPECIFICATIONS

	SDG-3B	SDG-5 (for comparison)
Size	3.25" dia x 3" long	3.0" dia x 3" long
Weight	2.9 lbs	2.3 lbs
Random drift (1σ) (Spec)	$<.0005^{o}$/hr	$<.001^{o}$/hr
Repeatability (day to day) 1σ - (Spec)	$<.005^{o}$/hr	$<.01^{o}$/hr
Angular momentum (H)	2×10^{6} CGS units	1×10^{6} CGS units
Spin speed	6000 RPM	6000 RPM

Figure 13. SDG 3B Gyro Characteristics

Increase In Gyro Figure-of-Merit (F_m)

If one considers a figure of merit for the elastically supported gyro as defined by [9] as follows

$$F_m = \frac{C + \sum_{1}^{n} A_n}{\sum_{1}^{n} (A_n + B_n - C_n)}$$

where:

C = principal moment of inertia of the rotor about the Z or spin axis

A_n, B_n, C_n = principal moments of inertia of the nth gimbal about the X_n, Y_n, Z_n axes respectively

n = number of gimbals

it can be shown that the F_m is approximately inversely proportional to the number of gimbals employed. This F_m for the standard SDG-5 three-gimbal gyro is 320 and can be increased to approximately 1000 by reducing the number of gimbals from 3 to 1. There is an attendant reduction in environmental "g-capability" by approximately 3 and some potential increase in 2N angular sensitivity. Teledyne has produced a small quantity of 1-gimbal units that have demonstrated extremely low random drift characteristics. No attempt to measure PSD for the 1-gimbal configuration has been made to date. This area is recommended for future investigation and evaluation for applications with relatively low environments requirements.

Mechanization of Gimbal Angle Pickoffs

The dry gyro lends itself to incorporation of an additional instrument angle pickoff which measures the angular motion of the gimbal with respect to the case. This mechanization has been shown by [3] to provide a signal which may be used to directly compensate for "noise". As a natural consequence, a highly accurate rotor angular nulling signal, independent of the usual pickoff mechanical instability or creep is automatically provided. To the extent that the undesired shaft-to-case motion is inducing the gyro output noise, the power spectral density of this noise may be reduced by compensation by a factor which is determined essentially by the total

mechanization scale factor error. If this error is assumed to be on the order of 1.5%, as is readily achieveable, then a reduction of the basic gyro output noise spectral noise by a factor of 0.015 could be realized. Teledyne is currently developing under contract from the USAF-AFAL/FDL an instrument called the Spin Coupled Accelerometer Gyro (SCAG) which is equipped with both rotor-to-case and gimbal-to-case angle pickoffs. The instrument has the necessary output information to effect the angular rate noise compensation as discussed by [3].

This same gimbal angle pickoff concept has been considered for incorporation in the SDG-5 and appears attractive.

VIII. SUMMARY AND CONCLUSIONS

The following conclusions are made based on the foregoing data and discussions:

1. The SDG-5 gyro output noise power spectral density characteristics have been determined to a high confidence level in the frequency band of .001 Hz to 5 Hz by the testing accomplished to date.

2. The SDG-5 is an excellent candidate gyro for fine pointing applications where low noise performance below 1 Hz are specified in milliarc-seconds and that operate with control system bandwidths in the region of 1 Hz.

3. The SDG-5 PSD performance compares quite favorable with currently used SDF floated gyros below 1 Hz and from 1 Hz to 10 Hz the SDG-5 performance compares midrange with other state-of-the-art precision gyroscopes.

4. A number of attractive methods for effecting a further decrease in the SDG-5 noise characteristics are readily available and should be pursued.

IX. ACKNOWLEDGEMENTS

The authors wish to express their gratitude to the following organizations for their cooperation in conducting the reported testing in a demanding schedule environment and on an as equipment/gyro availability basis:

The Martin-Marietta Corporation
Holloman AFB-CIGTF
The Boeing Aerospace Company
The Lockheed Missiles and Space Company

REFERENCES

[1] Price, Craig H., Gyro Noise Testing in the Low Frequency Range Using PSD Analysis. Paper presented at the AIAA Guidance and Control Conference, San Diego, California/August 16-18, 1976.

[2] Gates, R. L., Testing Technology for Fine Pointing Systems, Paper presented at the Seventh Biennial Guidance Test Symposium, Holloman AFB, New Mexico/ May 14-16, 1975.

[3] Erdley, H. F., Teledyne Low Noise Gyro. Teledyne Technical Report dated July 1976.

[4] Truncale, A, Koenigsberg, W. and Harris, R., Spectral Density Measurements of Gyro Noise. Charles Stark Draper Laboratory Report E-2641, February 1972.

[5] Gates, R. L., Evaluation of Noise Characteristics of the Teledyne SDG-5 Gyroscope for Fine Pointing Applications. Martin-Marietta Corporation Proprietary Report

[6] Teledyne Document 50317, Description and Operating Instructions for the Teledyne Strapdown Gyro Laboratory Test Equipment, September 1976.

[7] Strapdown Gyro - Description and Performance Data Summary. Teledyne Systems Company, January 1976.

[8] The Teledyne SDG-5 Gyro Test - Performed by the 6585th Test Group, Holloman Air Force Base - CIGTF, Report No. TBD, February 1977

[9] Craig, Robert J.G., Theory of Errors of a Multigimbal, Elastically Supported, Tuned Gyroscope. IEEE Transactions on Aerospace and Electronic Systems, Vol. AES, No. 3, May 1972.

EIGHTH BIENNIAL GUIDANCE TEST SYMPOSIUM

STELLAR UPDATE DEMONSTRATION FOR UPPER STAGE BOOSTERS

AUTHORS: G. R. QUASIUS
J. O. BOUTELLE
D. E. SANDERS
S. P. KAU

HONEYWELL, INC.
AVIONICS DIVISION
ST. PETERSBURG, FLORIDA

STELLAR UPDATE DEMONSTRATION FOR UPPER STAGE BOOSTERS

SUMMARY

This paper presents the results of a stellar update demonstration conducted in April 1976 by the Honeywell Avionics Division in St. Petersburg, Florida. The purpose of the test was to prove the technical feasibility of attitude update and gyro drift calibration of an inertial measurement unit for use in Interim Upper Stage and ELV booster applications. Use of stellar update in these applications improves mission accuracy, allows use of moderate performance gyros, and makes attitude performance independent of mission duration.

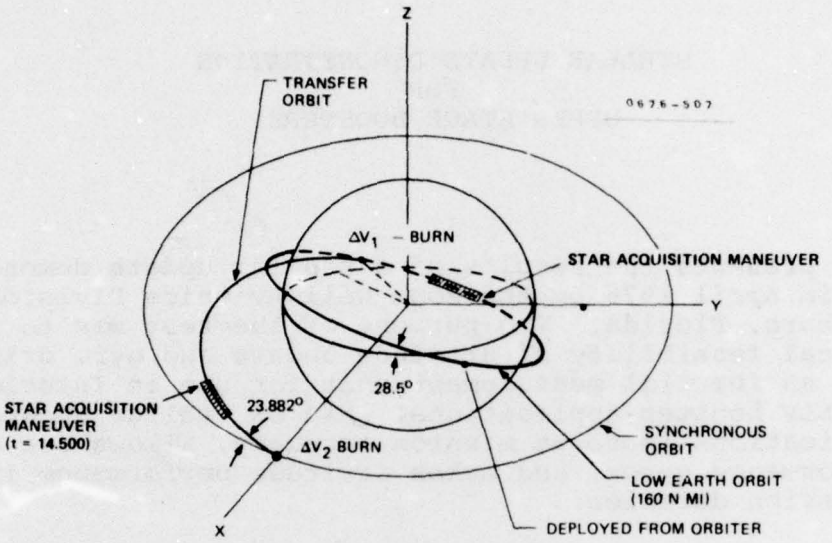
The test was conducted with an H-478 IMU and IUS prototype star scanner. During an update, information is gathered by maneuvering about the boost vehicle roll axis (laboratory rate table axis) to cause a star to transit the photosensitive slits of a strapdown star scanner. This star transit information from two stars is processed in a Kalman filter to update IMU attitude and calibrate IMU gyro drifts.

The paper first presents the analytic studies used to establish a test setup representative of the mission. In particular, the star field (separation, magnitude, and color), maneuvering profile, degree and type of update algorithm, and the accuracies to be demonstrated, were assessed. The baseline test setup, a description of the hardware, and the stellar update technique are then explained. Lastly, the test results are presented and evaluated. The tests demonstrated attitude update accuracies of less than 150 arc-seconds and a four-fold reduction of gyro bias drifts.

DEMONSTRATION REQUIREMENTS

Accuracies

The Space Shuttle will transport an "upper stage" (IUS or TUG) to low Earth orbits. From there the "upper stage" will carry payloads to higher altitude orbits such as the equatorial geosynchronous orbit shown in Figure 1. This mission includes a 4.5-hour wait in low Earth orbit before deployment from the shuttle, and a 5.25-hour coast to synchronous altitude after the transfer burn. This long mission duration implies stringent gyro



● PERFORM UPDATE OF ATTITUDE AND GYRO DRIFT PRIOR TO EACH MAIN BURN

FIGURE 1. REFERENCE TRAJECTORY (FOR EARTH ORBIT TO SYNCHRONOUS ORBIT)

drift performance for a pure inertial mechanization of the navigation system. A viable alternative employs a star scanner to update the inertial attitude before each major burn. Demonstration of the technical feasibility of this application of stellar update is the reason for the test reported in this paper.

The tolerances for attitude update and gyro drift are derived from analysis of the requirements for both the synchronous injection mission and the 12-hour highly eliptical mission. The highly eliptical mission requires the orbital inclination errors to be <0.06 degree (216 arc-seconds). The synchronous injection mission is driven by the velocity errors resulting from attitude error during the last major burn. Table 1 shows an error budget for the synchronous injection mission. It shows the attitude tolerance is less severe than for the 12-hour eliptical mission. For this reason, and to allow for additional attitude error build-up from the time of update until the actual burn, the tolerances in Table 2 were established for the stellar update demonstration.

Note that gyro bias drifts of 0.6 deg/hr and mass unbalance drifts of 3 deg/hr/g are acceptable if stellar update is used. In contrast, a 10-hour pure inertial mission would require an equivalent gyro bias drift of 0.007 3-sigma to match the performance of the stellar updated system.

TABLE 1. SYNCHRONOUS INJECTION
STELLAR UPDATE ERROR BUDGET

Error Sources		Velocity Errors		
Type	Value 3σ	Down Range	Cross Range	Radial
Inertial Attitude Error at Final Burn	285 sec	6.7 fps	8.3 fps	16.0 fps
Gyro Drift	0.6 deg/hr	<1.0	<1.0	<1.0
All other errors including upper bound initial conditions and 3 deg/hr/g gyro mass unbalance drift	---	13.4	8.2	37.6
Total RSS Error		15.0	11.7	40.9
Requirement		16.0	12.0	75.0

TABLE 2. DEMONSTRATION REQUIREMENTS FOR STELLAR UPDATE

Error Source	Allowable Mission Tolerance	Demonstration Requirement
Attitude	216 sec-eliptical 285 sec-synchronous	150 sec*
Gyro Drift	<0.6 deg/hr	<0.6 deg/hr*

* Also compatible with conventional expendable launch vehicles.

Update Timeline

The length of time allowed for stellar attitude update and drift calibration is found by examining the shortest interval available in any mission. The shortest interval occurs when the upper stage must be deployed as soon as possible after reaching low Earth orbit, but before the first orbital node (that is, the first transfer burn possibility). This time interval is at least 20 minutes long; however, other vehicle activity may further constrain the available time. For this reason, a 4-minute attitude update profile and an additional 11-minute gyro drift calibration profile were used.

During an update, information is gathered by maneuvering the vehicle roll axis to cause a star to transit photosensitive slits of a strapdown star scanner. The geometry of the star scanner field of view (FOV) with respect to the vehicle is shown in Figure 2. The FOV contains six slits, mechanized in redundant crows feet patterns as shown in Figure 3. The vehicle rotates to cause a star to transit each of the three slits. Two transits, separated in time, appear at the output of one channel of electronics while one output pulse is generated by the redundant channel. Any two transits are sufficient for update. The IMU inertial reference frame is noted at each transit time for use in calculating corrections with respect to the stellar inertial frame as observed by the star sensor. Additional transits on a second star separated from the first star by about 90 degrees are used for a three-axis update.

The flight update procedure is illustrated in Figure 4. It begins by orienting the vehicle roll axis normal to the plane containing the two target stars. A sequence of transits is then obtained from two stars by maneuvers about the vehicle roll axis. After the update sequence is complete, the vehicle is maneuvered to the burn attitude. The laboratory demonstration was done by simulating the vehicle roll maneuvers for the update through the use of a single axis precision air bearing table.

Star Selection

To ensure the proper star magnitudes and angular separations were used in the test, a star selection study was performed using the Smithsonian Astrophysical Observatory (SAO) Star Catalog. The locations and silicon magnitude of the 1812 brightest stars were analyzed for availability, interferences from other celestial bodies, and angular separation using typical low equatorial and polar orbits. The results of that study led to the selection of the seven-star catalog shown in Table 3. Use of these seven stars assures that:

1. Two stars are available for any mission orbit.

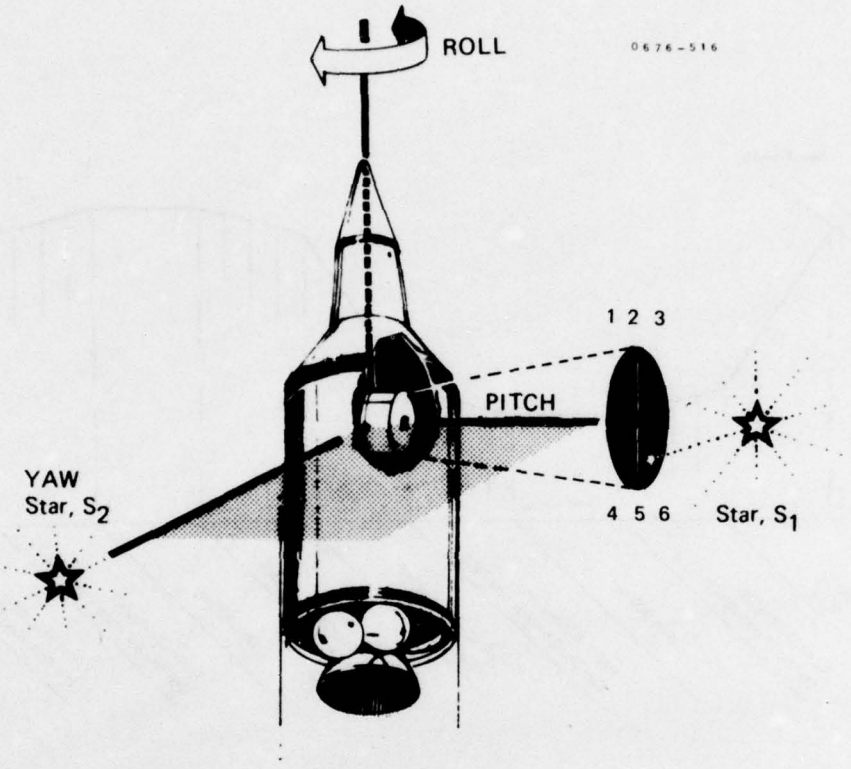


FIGURE 2. STELLAR UPDATE VIEWING

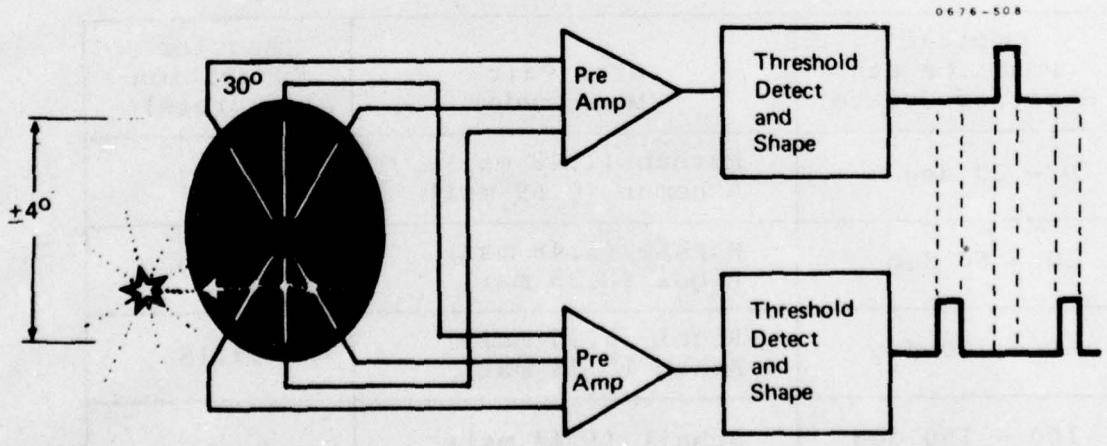


FIGURE 3. STAR SCANNER MECHANIZATION

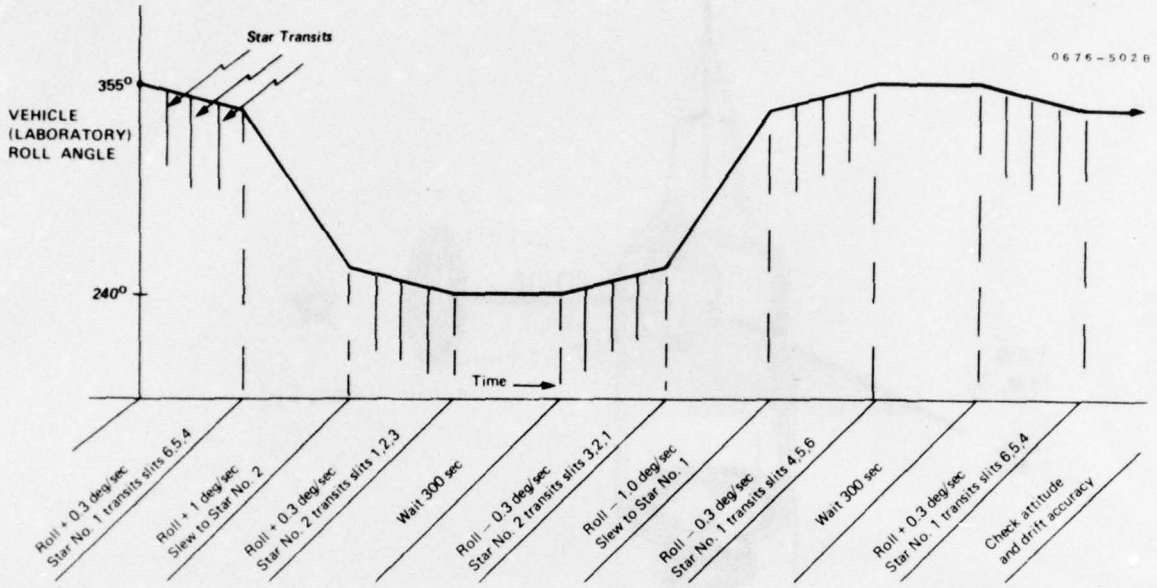


FIGURE 4. STELLAR UPDATE MANEUVER PROFILE

TABLE 3. THE SEVEN NAVIGATION STARS

Orbital Position at Start of Update	Star Pair (Magnitude)	Angular Separation (degrees)
0 - 30 deg	Marhab (1.48 msi) Achemar (0.69 msi)	88.73
30 - 60 deg	Marhab (1.48 msi) Rigel (0.35 msi)	83.79
60 - 100 deg	Rigel (0.35 msi) Kohab (1.44 msi)	69.15
100 - 150 deg	Suhail (1.44 msi) Arcturus (-0.33 msi)	85.92
150 - 260 deg	Arcturus (-0.33 msi) Atria (1.29 msi)	87.61
260 - 360 deg	Marhab (1.48 msi) Achemar (0.69 msi)	88.73

2. No selected star is within 30 degrees of the sun, moon, or planets.

3. All are brighter than +1.5 silicon magnitude.

4. There are no conflicting stars +2.5 magnitude or brighter within 6 degrees of the target star.

It should be noted that tests of a star scanner similar to that used in the demonstration showed no performance degradation after direct pointing at the sun for one hour.

The star selection study showed that one star pair was 21 degrees from the ideal separation of 90 degrees. Since star simulator piers were not available at that separation, a 108-degree angle (18 degrees greater than 90) was used for the separation of the two target stars.

Update Algorithm Development

The real time algorithms mechanized during the test resulted from analyses of several update techniques and subsequent refinement of the selected algorithm. The first step was to decide between a two or three star update, a six or nine state Kalman filter, and whether or not a deterministic technique could be used. The results of these analyses are given in Table 4. The mechanized algorithm used the profile shown in Figure 4 and sighting technique of Figure 3. A six state fixed gain Kalman filter containing three attitude and three drift states was used.

TABLE 4. PROCESSING TECHNIQUE ANALYSIS

Trade	Results
Two or three star update.	Two star update errors as good as three star update - use two star.
Six state filter (3 attitude and 3 drift) or nine state filter (include gyro scale factor).	Low sensitivity to scale factor - use six state.
Kalman filter or deterministic (least squares).	Kalman filter gives slightly better performance and requires less software when redundancy factors are considered.

Using the profile of Figure 4, it was verified that 15 star transits give complete observability of the six attitude and rate error states. Further, complete observability is preserved if the 2nd, 5th, 8th, 11th and 14th transits are deleted, corresponding to a failure in one scanner electronic channel.

In Figure 4 the dwelling or "wait 300 seconds" on a star allows attitude buildup due to gyro drift, and thus better observability of drift states. The purpose of slewing from star S_1 to star S_2 is to induce cross coupling between the pitch and yaw axes (see Figure 2). The pitch error is not directly observable by measurements on star S_1, as this is the optics line of sight. Rotation and subsequent measurements at star S_2 produces the coupling and complete observability.

Laboratory Setup

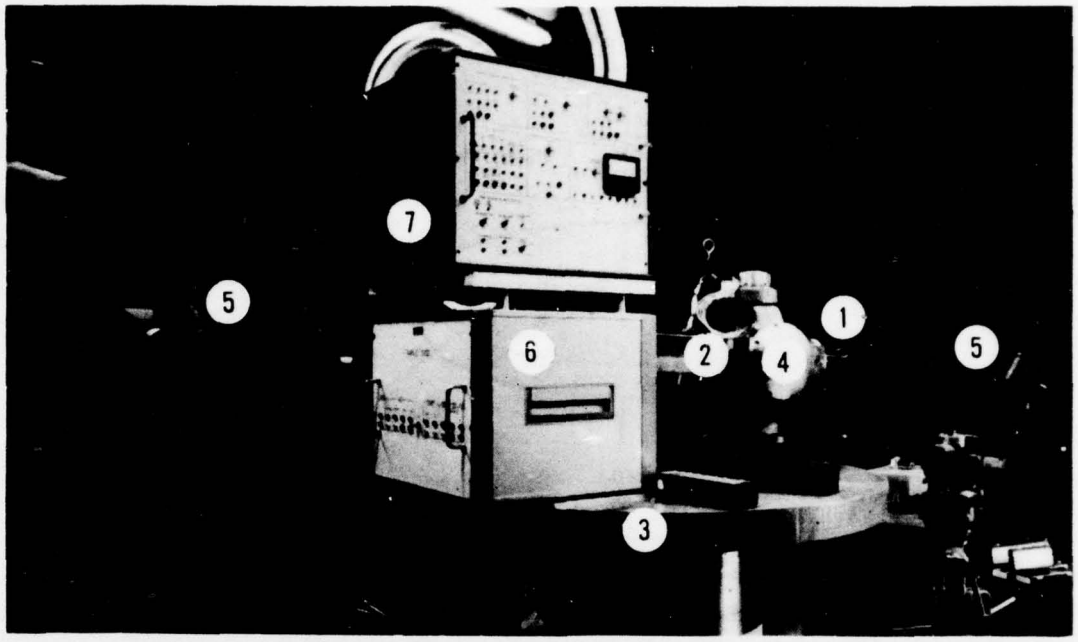
A photograph of the laboratory equipment used to demonstrate IUS stellar update is shown in Figure 5. A schematic view of the geometry of the setup is shown in Figure 6. The H-478 IMU and star scanner shown are mounted in a precision gimbal on top of an air bearing table. The precision gimbal is used in calibrating the star scanner and remains fixed during update testing. The star sources were set at a maximum of +1.0 silicon magnitude, type G0.

They are 108 degrees apart. Star 1 is 3.4 degrees below level, and Star 2 is 0.8 degree above level. The geometry allows all six slits to be used in the test. Note that while the rate table motion was single axis, all three gyro axes were evaluated as the result of misalignment with the table spin axis ($\approx$3.4 degrees) and need to accurately measure Earth's rate as a function of table position.

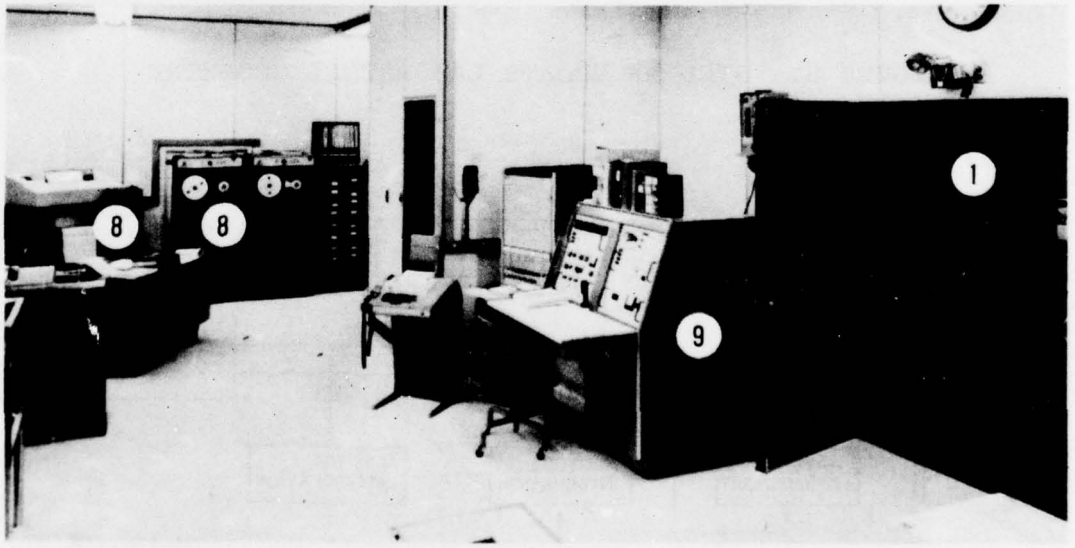
The strapdown algorithm is a second order direction cosine type. The dot product computation, which is key to the update process, is explained in the appendix. It is important to note that each star transit is processed separately. The strapdown algorithm and Kalman filter fully account for changes in attitude or rates between star transits.

The actual star transit pulse arrives at the computer a few tenths of a second after the star physically crosses the center of the slit. Determination of this delay for various rates is part of the star scanner calibration process. Knowing this time delay and the body rates at the time of transit (rate derivation block in Figure 7), the dot product attitude error can be accurately calculated. Note again that the time or rates between star transits are not directly used in the update processing algorithm.

A7606-014



A7606-013



EQUIPMENT

1 Star Scanner

2 IMU – H478

3 Precision Air Bearing Rate Table with 12 inch inductosyn readout

4 Gimbal set used in Star Scanner calibration

5 Star Simulators 5 inch beam, 5 arc-second collimation error, select filters for color and brightness

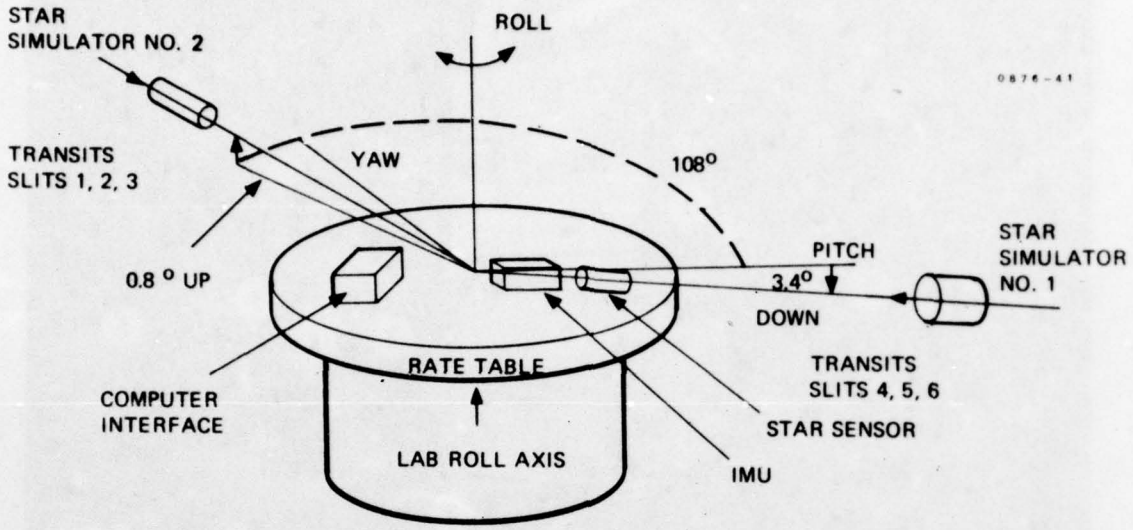
6 Gimbal Control Electronics

7 Time base (0.1 sec) and sensor computer interface electronics

8 Lab computer for real time data processing

9 Rate Table control system

FIGURE 5. TEST FACILITY



STAR 1 AND STAR 2 SEPARATED BY 108°
STAR 1 IS 3.4 DEGREES BELOW LEVEL FOR TRANSITS ON SLITS 4, 5, AND 6
STAR 2 IS 0.8 DEGREES ABOVE LEVEL FOR TRANSITS ON SLITS 1, 2, AND 3

FIGURE 6. STELLAR UPDATE LABORATORY GEOMETRY

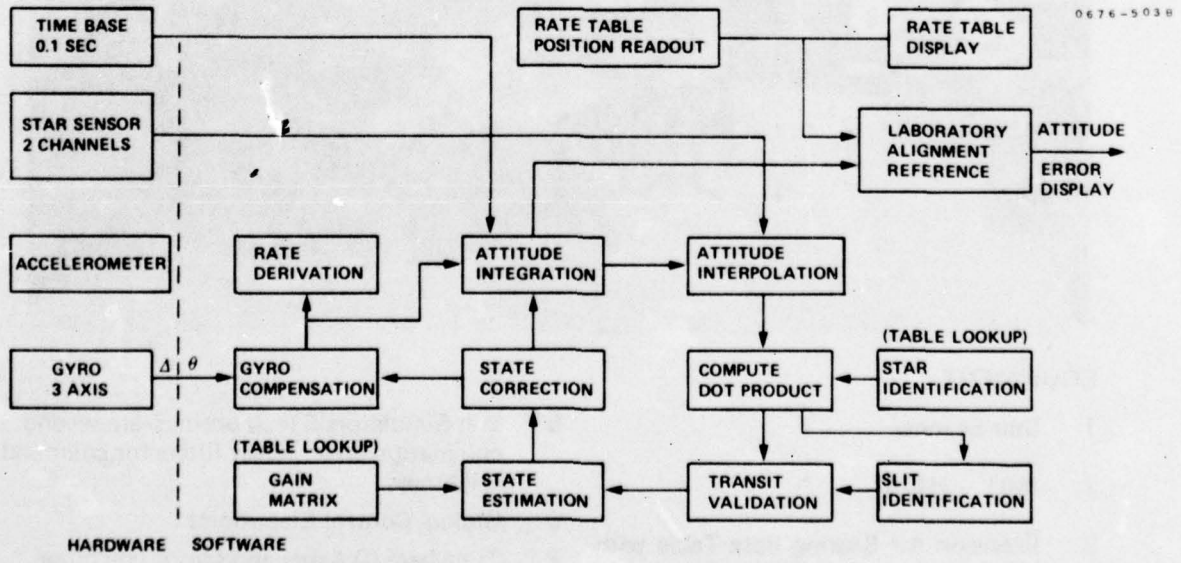


FIGURE 7. STELLAR UPDATE PROCESSING BLOCK DIAGRAM

Test Results

A series of 13 stellar update tests were conducted for a range of initial attitude and gyro drift conditions. The results, shown in Table 5 and summarized in Table 6, met required tolerances in all trials. The errors in Table 5 are the differences between the vehicle body axes, determined by the stellar updated IMU, and the rate table readouts. All error sources, such as strapdown algorithm processing, alignments, gyro drift, and star scanner bias and noise, are included. As such, they represent total in-flight error.

The gyro and star scanner measurements are transferred to a laboratory computer for real time processing at a rate of 10 times/second. The digital output from the gyros was scaled at 15 arc-seconds/pulse.

Calibration of the star sensor demonstrated a random error of less than 15 arc-seconds RMS on each of the six slits for scan rates of 0.1 to 0.3 degree per second. The star scanner field of view was ±4 degrees.

The algorithm for processing the gyro and star scanner data is outlined in Figure 7. Except for the sensor data collection, the algorithm was coded in FORTRAN and run in a DDP-516 using the floating point hardware option. Note that computational requirements have been minimized by using an off-line calculation of the Kalman gain. This off-line calculation of gain is done for the nominal star scan profile.

Initial attitude conditions of ±2 degrees were derived from anticipated structural transfer from the Shuttle IMU prior to deployment. Anticipated maximum 1 degree/hour gyro initial conditions were increased to 2 degrees/hour in pitch to fully exercise this axis. The star scanner optical axis is nominally aligned along the body pitch axis during this test series which makes it the most difficult axis to update.

The update software uses a precalculated fixed gain Kalman filter established for anticipated initial errors and maneuver rates. The variety of initial conditions proves the capability of the software to perform under flight conditions. In addition, tests 11 and 12 were conducted at scan and slew rates of 0.2 degree/second and 0.8 degree/second to test off nominal rate conditions.

A trace of test No. 12 is shown in Figure 8. This is a test with two degree initial attitude errors and approximately one degree/hour drift rates. In this test, the rate profile was changed from the nominal (0.3 degree/hour scan and 1 degree/second slew) profile to a slower profile (0.2 degree/hour scan and 0.8 degree/

TABLE 5. TEST RESULTS

0676-5058

Test No.	Initial Conditions						Post Update Conditions					
	Attitude Error-Deg			Rate Error-Deg/Hour			Attitude Error-Arc-Sec			Rate Error-Deg/Hour		
	Yaw	Roll	Pitch	Yaw	Roll	Pitch	Yaw	Roll	Pitch	Yaw	Roll	Pitch
1	0	0	0	0.06	-0.61	0.08	-25	-25	- 75	-0.26	-0.04	0.26
2	2	2	2	0.13	0.28	-0.54	75	25	62	0.08	0.25	-0.19
3	0	0	0	-0.89	-1.14	-1.78	25	0	100	-0.20	0.26	0.31
4	2	2	2	-0.63	-0.44	-1.39	37	25	-125	-0.04	0.42	-0.17
5	2	-2	2	-1.26	0.86	-1.20	112	0	150	0.25	0.54	0.04
6	2	-2	-2	-0.91	1.06	1.40	100	25	62	0.25	0.54	-0.42
7	-2	-2	-2	-0.86	-0.85	-1.00	100	-50	25	0.21	0.46	0.25
8	1	0	0	0.90	0.45	0.40	12	-50	125	0.10	0.21	-0.23
9	0	1	0	0.73	-0.45	-1.66	100	-25	125	0.21	-0.08	0.08
10	0	0	1	-0.22	-0.43	-0.68	25	-62	125	0.16	0.27	0.25
11**	0	0	0	-0.18	-0.20	2.02	25	12	100	0.00	0.17	0.29
12**	2	-2	-2	-0.83	1.46	0.83	50	-25	25	-0.04	0.29	-0.44
13	0	0	0	0.18	-1.2	-0.2	0	-25	- 25	0.06	0.19	0.13

** Test conducted at 0.2 deg/second for star transits and 0.8 deg/second slew rate between stars

TABLE 6. TEST SUMMARY

	Initial Condition Spread						Final Error Spread					
	Attitude-Deg			Rate-Deg/Hour			Attitude-Arc-Sec			Rate-Deg/Hour		
	Yaw	Roll	Pitch	Yaw	Roll	Pitch	Yaw	Roll	Pitch	Yaw	Roll	Pitch
Max Plus	+2	+2	+2	+0.73	+1.06	2.02	112	+25	+150	+0.25	+0.54	+0.31
Max Minus	-2	-2	-2	-1.26	-1.20	-1.78	-25	-62	-125	-0.26	-0.08	-0.44
Mean							48.92	-13.46	44.15	+0.06	0.268	0.012

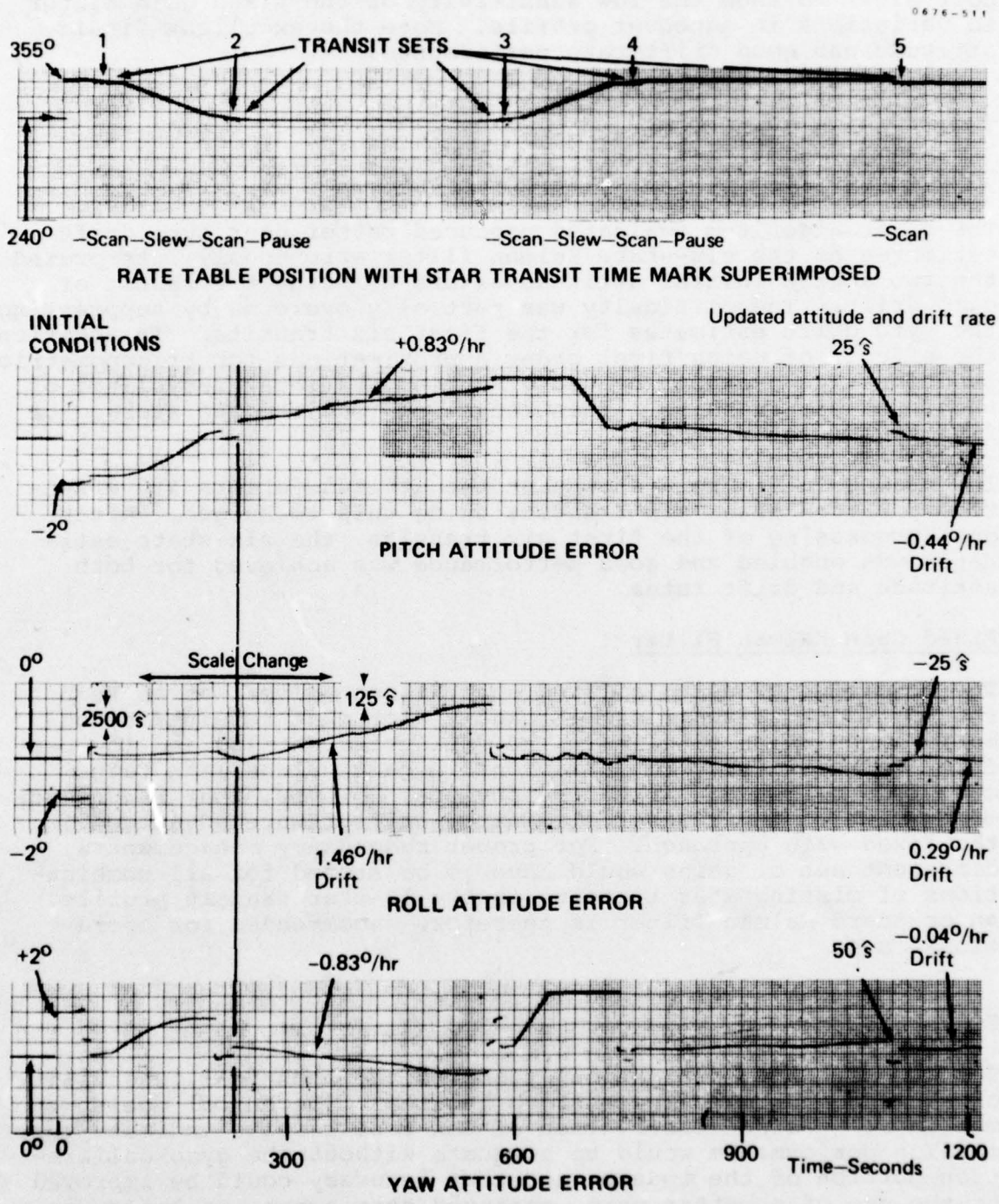


FIGURE 8. SAMPLE TEST RESULT (NO. 12)

hour slew) to show the low sensitivity of the fixed gain filter to variations in maneuver profile. Note the excellent final attitude and good drift rate performance.

TEST RESULTS EVALUATION

Convergence from Initial Attitude Error

The first algorithm evaluated produced rather poor gyro drift estimates as the six-state Kalman filter erroneously interpreted the two degree initial attitude errors as being the result of gyro drift. The difficulty was partially overcome by suppressing the gyro drift estimates for the first six transits. In addition the effects of using first order approximations for trigonometric functions was overcome by use of a "computational recycling" of the first six transits. This recycling required the storage of five transition matrices.

The traces in Figure 8 show that the attitude errors are effectively killed after six transits using this technique. After dual processing of the first six transits, the six-state estimator was enabled and good performance was achieved for both attitude and drift rates.

Fixed Gain Kalman Filter

The objective of using a fixed gain Kalman filter was to reduce the in-flight software significantly from that required by on-board calculation of gains. The small star catalog and low performance sensitivity to variations in gain values with rates make this possible. It became obvious, however, that redundancy management of the scanner eliminated any software advantage in the fixed gain approach. For proper redundancy management a different set of gains would have to be stored for all combinations of missing star transits in the 16-star transit profile. An on-board Kalman filter is therefore recommended for operational use.

CONCLUSIONS

The demonstration realistically showed the technical feasibility of stellar update in upper stage boosters. Technical goals were met in all tests. Observation of the test results indicate that mission performance would be adequate without the gyro calibration portion of the update, and that accuracy could be improved by the use of a better gyro, repeated star scans, or longer update timelines.

During the first 190 seconds used to scan stars 1 and 2 and kill attitude, the IMU gyros are, in fact, drifting. This drift, ignored by the mechanization, does decrease the accuracy of the attitude update after the first six transits. If a better gyro drift were present, the attitude accuracy would increase as shown by test 2 in Table 5 where lower drift values were present initially.

Repeated star scans would also increase accuracy. This was verified in test bed by results within measurement accuracies when using good initial attitude and drifts such as would be present after a completed profile. The results are not shown as they only illustrate that a good system remains good.

The last technique to improve accuracy is to use longer update timelines. This can be done in two ways. The first is to recognize that updates could be done every hour or so during the coast to synchronous altitude. The Kalman filter could easily discern the greatly increased propagation of gyro drift into attitude. Drift calibrations of less than 0.005 degree/hour could be done with one hour wait periods. The second alternative is simply to increase the wait periods in the present profile to give drift propagation greater weight. While these improvements are interesting, they would not effect the overall upper stage accuracy shown in Table 1 unless other error sources were also reduced. The demonstrated accuracies are already sufficient to satisfy known requirements.

From an operational viewpoint, stellar update makes the IMU attitude performance independent of mission duration. This allows long, multiple payload deployment missions with several phasing orbits and the successful completion of missions in which reconfiguration of the system due to a failure has extended mission times well beyond the capability of pure inertial guidance systems.

APPENDIX

A full explanation of the Kalman filter processing has been given in references 2, 3 and 4. It is summarized in Table 7. This filter is the result of SAMSO-sponsored programs on the Space Precision Attitude Reference System (SPARS) and the Defense Meteorological Satellite Program (DMSP). The intent here is to give the reader an intuitive understanding of the process.

A functional view of the star scanner used in this demonstration is shown in Figure 9. A transit pulse is produced when the image of a star moves across a detecting slit. The basic sensor measurement is the time when the star transit occurs. This transit time provides measurement of vehicle attitude independent of IMU data.

The measured transit time is a scalar function of the vehicle attitude. The dot product between the normal vector that defines the plane containing the detecting slit, $\underline{N}$, and the LOS vector to star image $\underline{S}$, is the attitude error measure.

$$y = \underline{N} \cdot \underline{S} \tag{1}$$

Geometrically, the dot product is the angular miss distance between the vector $\underline{S}$ and the plane of N, as depicted in Figure 9.

At the time of star transit t_t, the ideal geometrical condition requires:

$$y = \underline{N} \cdot \underline{S} \equiv 0 \tag{2}$$

At this time the on-board algorithm evaluates the dot product corresponding to the target star and slit transited using the equation

$$y = (\underline{\bar{N}}^B)^T \, T_{BI}\Big|_{t_t} \, (\underline{\bar{S}}^I) \tag{3}$$

where

$(\underline{\bar{N}}^B)$ = body frame coordinates of $\underline{N}$

$(\underline{\bar{S}}^I)$ = inertial-frame coordinates of the LOS to star, $\underline{S}$

$T_{BI}\Big|_{t_t}$ = body attitude matrix at time of transit, T_{BI} is the I to B transformation matrix

TABLE 7. KALMAN FILTER PROCESSING

Function	Equation	Form	Purpose
Covariance Propagation	$\dot{P} = AP_T + P_TA^T + Q$	6x6 - $\begin{bmatrix} \text{Attitude Cov} & \text{Cross Cov} \\ \text{Cross Cov} & \text{Drift Cov} \end{bmatrix}$	Used to propagate P(t) because of maneuvers and rates
At Star Transit Compute Geometry Matrix	H(t) = function of S, N, body to inertial transform	1x6 $\begin{bmatrix} - \\ - \\ - \\ 0 \\ 0 \\ 0 \end{bmatrix}$	Used to resolve errors and compute gain
Compute Gain	$K = P(t)H^T/(HPH^T + R)$	K - 6x1 $HPH^T + R \rightarrow$ 1 by 1 A scaler	Used to compute error state
Compute Error State	$\hat{X} = KY$	K = 6x1	Used to apply measurements into attitude
Compute New Attitude	$\hat{T}_{BI} = T_{BI}\ [I-X]$	$X = \begin{bmatrix} 0 & & \Delta\theta\text{'s} \\ & 0 & \\ \Delta\theta\text{'s} & & 0 \end{bmatrix}$	$\hat{X}$ converted to small angle matrix to correct attitude
Compute New Covariance Matrix	$\hat{P}(t) = [I-KH]\ P(t)OLD$	P(t) = 6x6 KH = 1x1 scaler	Use to determine statistics of measurements

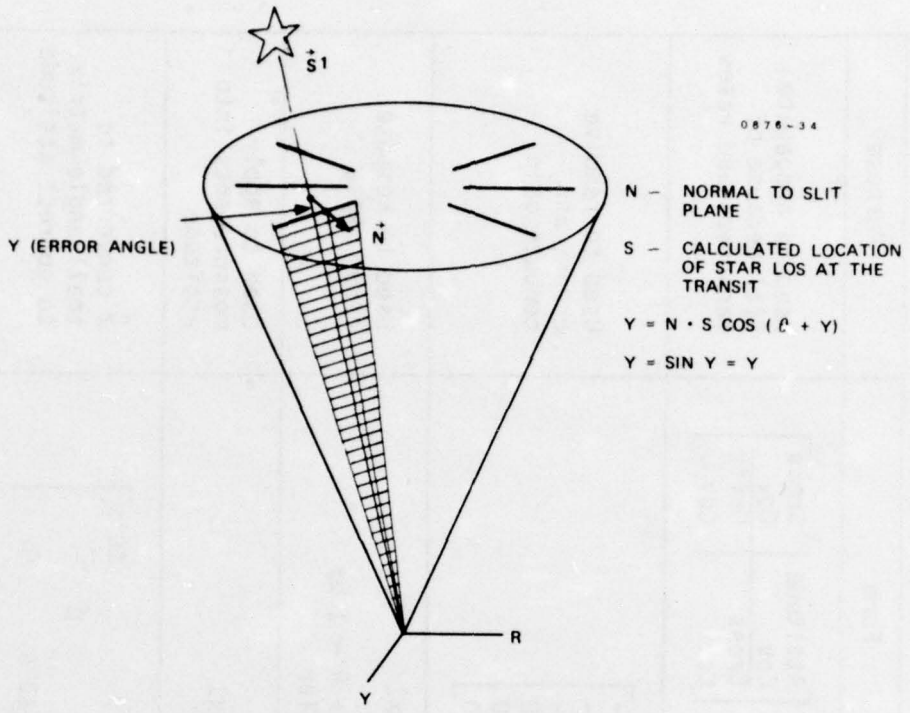


FIGURE 9. DOT PRODUCT GEOMETRY

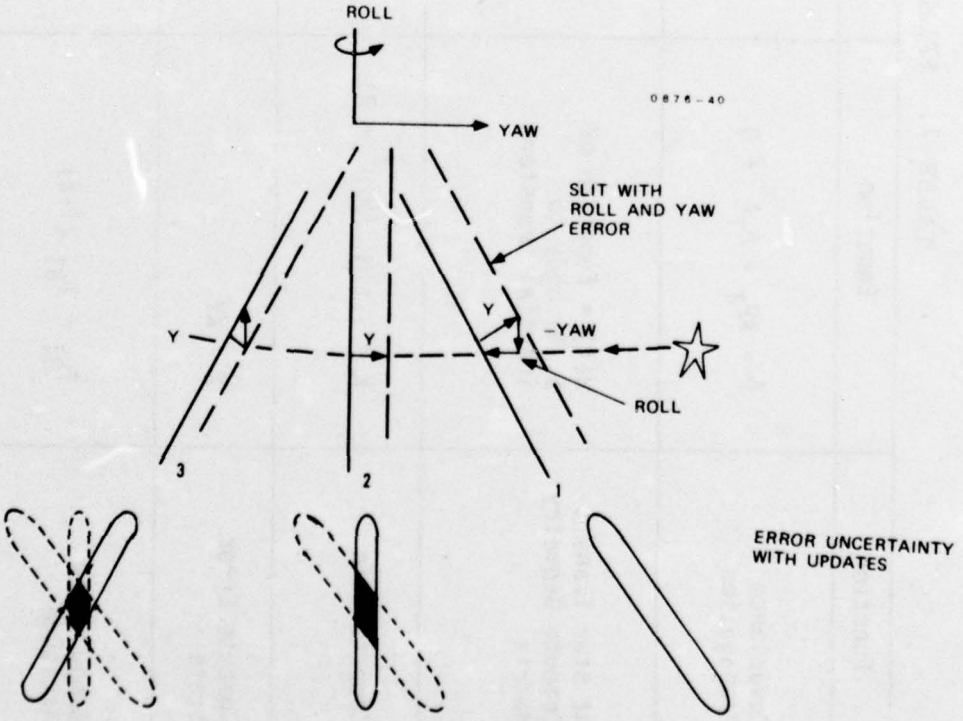


FIGURE 10. STELLAR UPDATE PROCESSING

The basic measurement, y, is shown schematically in Figure 10. From the first star transit measurement and the geometry, the error can be resolved into yaw and roll components. This reduces the net error normal to slit 1 to the accuracy of the measurement. However, there is no information as to the error along the slit. Thus, the remaining uncertainty is illustrated by a long narrow ellipse along the slit.

At the second star transit, the measurement y is almost solely due to roll error. We can see this on Figure 10. The Kalman filter knows this sensitivity through the covariance propagation and geometry matrix. It therefore applies most of the error to correcting roll. The effect is to reduce net error to the smaller area shown under slit 2 in Figure 10.

At the third star transit, the Kalman filter applies most of the correction to yaw, as it remembers it has killed the roll error at transit 2. The effect is to further reduce the error elipse as shown under slit 3 in Figure 10.

The process just described can also be seen in Figure 8. The roll and yaw errors are small after the transits on star one. The pitch error remains large and would be out of the paper if illustrated in Figure 10.

To eliminate pitch error, the vehicle must be rotated. This transfers pitch error into the yaw axis where it can be observed through scanner measurements. The transfer of pitch error to yaw can be seen in Figure 8 during the maneuver from star 1 to star 2. Continued measurements and processing serve to further reduce the attitude errors, and through covariance matrix coupling, the gyro drift errors.

It is hoped that this brief explanation will give the reader an intuitive feeling of the update processing employed in this demonstration. More depth is provided by the previously cited references.

REFERENCES

1. Update Strategy for a Strapdown Stellar Inertial Navigation System; paper by S. P. Kau and S. S. Steadman presented at 1976 IEEE Conference on Decision and Control Theory; Clearwater Beach, Florida; December 1976.

2. High Altitude Attitude Reference Study, Final Report, Report Number TR75-43, Air Force Contract F04701-74-C-0064; December 1974.

3. SPARS Algorithms and Simulation Results; paper by D. C. Paulson, D. B. Jackson, and D. C. Brown for the Symposium on Spacecraft Attitude Determination; presented at Aerospace Corporation, 30 September, 1-2 October 1969.

4. SPARS - A Completely Strapdown Concept for Precise Determination of Satellite Vehicle Attitude; paper by William R. David and Joseph A. Miller for Symposium on Spacecraft Attitude Determination; presented at Aerospace Corporation, 30 September, 1-2 October 1969.

5. Performance Predictions for Gyro Based Satellite Attitude Control Systems at Geosynchronous Altitude; paper by Michael F. Barrett and Gunter Stein; presented at AIAA Guidance and Control Conference, 16-18 August 1976.

EIGHTH BIENNIAL GUIDANCE TEST SYMPOSIUM

NEW METHODS AND RESULTS IN HIGH ACCELERATION TERMINAL HOMING GUIDANCE AND CONTROL SYSTEM'S TESTING

AUTHORS: Dr Harold L. Pastrick
Jess B. Huff

US ARMY MISSILE COMMAND
REDSTONE ARSENAL, ALABAMA

NEW METHODS AND RESULTS IN HIGH ACCELERATION TERMINAL HOMING GUIDANCE AND CONTROL SYSTEMS TESTING

JESS B. HUFF and HAROLD L. PASTRICK
Guidance and Control Directorate
Technology Laboratory
US Army Missile Research and Development Command

Abstract

The cannon launched guided projectile is launched from a 155mm howitzer and in its terminal phase is guided by tracking reflected energy from a target illuminated by a remote laser designator. Efforts to validate the cannon launched guided projectile guidance and control system included tests of projectile aerodynamics, aircraft captive flights and air drop tests to exercise seeker acquisition characteristics, g-hardened survivability and soft recovery tests, laboratory emulated flights by means of hardware-in-the-loop simulations, and full-up gun launched flights. The predictions of the hardware-in-the-loop simulation and other US Army Missile Research and Development Command generated data are compared to the results of the flight test program.

I. Introduction

The Army's Cannon Launched Guided Projectile (CLGP) is a relatively new concept in accurate munitions delivery. The CLGP, currently in engineering development, is designed around a shell which is fired from an M109A1 155mm howitzer at targets within the range of 4 to 16 km. The CLGP guidance and control (G&C) scheme mechanizes a proportional navigation and guidance law using a laser detector mounted on a free gyro in the nose of the projectile. A rear section houses the control actuation system and stabilizing fins. Figure 1 shows its primary features.

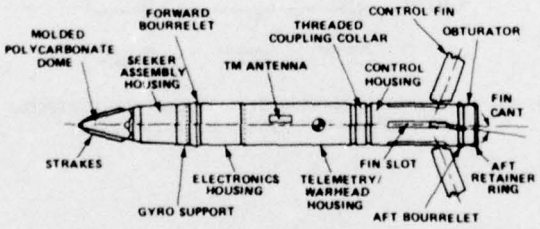


Figure 1. Features of Advanced Development Phase CLGP, Martin Marietta Design

As part of an advanced development (AD) program, an evaluation effort was initiated at the US Army Missile Research and Development Command (MIRADCOM) and directed toward identification of potential problem areas within the mechanization of this concept to delineate approaches to their solution. The effort was initially implemented by development of a full six-degree-of-freedom digital simulation to focus on the effects upon performance of variations in autopilot design during the evolution of the projectile's configuration.[1] Further simulation work was related to the choice of a G&C system and autopilot mechanization. As test results from initial design components became available, they were factored into the six-degree-of-freedom simulation to enhance the overall model and to determine the impact on system performance.[2] Continuing efforts to further validate the G&C system were directed to a time frame immediately after all design freezes were made and prior to initial flight tests of the weapon. A real-time hybrid computer simulation with hardware-in-the-loop (HWIL) was the method chosen to accomplish this important milestone.[3]

To place the CLGP AD program into perspective and for completeness, the testing which has been designed and accomplished to verify the CLGP will be described. Thus, Section II will briefly summarize the overall test program. The remainder of the paper will be oriented to emphasize the main objectives, i.e., to summarize the various test methods, and to compare the results of these testing methods with the predictions of six-degree-of-freedom simulations, results of aircraft drop tests, and actual cannon firings.

II. CLGP AD Program Summary

The purpose of the AD program was to prove that the CLGP could be used to increase the effectiveness of standard artillery against point targets. The problems in providing this proof were many and severe. The CLGP system with its precise and sensitive electrooptical components had to be designed to withstand the same high-g firing environment as a standard artillery round. The system, with no information provided to the round other than that sensed by the seeker, had to acquire and guide itself to a designated target with extreme accuracy. Moreover, the system had to be compatible with the practical world of artillery. It could not be simply a delicate laboratory device. Ultimately, the system must be producible in large quantities at reasonable prices.

AD was a two-phase program in which a period of 18 months was allotted to component/subsystem development and 19 months to prototype projectile demonstration. Phase I was concerned primarily with development and implementation of the design, inspection, and test methods needed to harden previously proven guidance, control, and telemetry components and subsystems to 9000 g and all-up projectiles to 7200 g. Phase II was dedicated to proving the CLGP concept through flight test evaluations. The emphasis on performance and hardening, combined with the extensive test program, had to produce a practical projectile that would meet or exceed all AD performance requirements.

For these reasons, the Army initiated the CLGP AD program in February 1972 with the award of two contracts, one to Martin Marietta and one to Texas Instruments. The two-contractor concept was chosen to provide a competitive atmosphere between the contractors within the realm of the differing design philosophies each was advocating. The resulting

effort by both culminated in the award of an engineering development phase contract to Martin Marietta in July 1975. For this reason, the remainder of this paper will highlight the AD phase activities as they related to the Martin Marietta approach. As will be seen in the sequel, both failures and successes will be presented.[4]

III. AD Phase I Component Development

The design and development objectives of the Phase I AD program (Figure 2) were to relate cannon launch environments to tangible design and laboratory test criteria, and to prevent the recurrence of problems and failures. The objectives were met through a series of developmental iterations involving design, laboratory test, and canister and projectile firings. Stressing these objectives, Phase I evolution of the CLGP AD design progressed through a sequence of component and subsystem development and testing. This enabled application of proven guidance, control, telemetry, and aerodynamic technology to a fully-hardened, laser-guided projectile early enough to impact design of the first Phase II CLGP round.

Component Canister Tests

A canister test program to evaluate the capability of selected CLGP components to survive the cannon launch environment was initiated early in AD. Seven canisters were fired from cannons located at Barbados and MIRADCOM. The tests consisted of firing water-flotation and parachute-recovery canisters from 155 mm and 8-in. cannons at accelerations up to 12,500 g; recovering the contents; and performing post-firing inspections, performance tests, and detailed analyses. Although two of the water-flotation canisters were lost, the remaining payloads uncovered structural problems on hybrids, integrated circuits, relays, detectors, roll gyro, and wire routing and splicing techniques. Components were redesigned and techniques were changed as required. Retesting verified the integrity of the fixes. These early component hardening tests preceded the subsystem level of development.

Subsystem Canister Tests

An extensive canister test program for ruggedized subsystems was conducted from February 1973 through February 1974. Three ruggedized guidance, control, and telemetry subsystems were fabricated for 8-in. canister firing (8,000 to 12,000 g) at MIRADCOM and returned for test and analysis. Figure 3 shows a typical mission profile of the MIRADCOM launch. The data from these firings

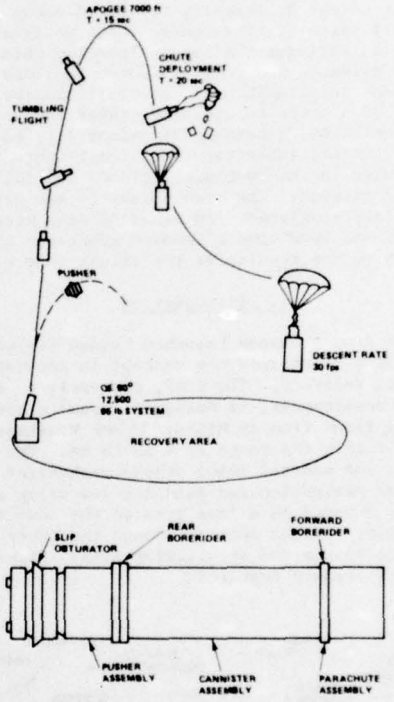


Figure 3. Typical Mission Profile for the MIRADCOM Soft Recovery System Canister Tests

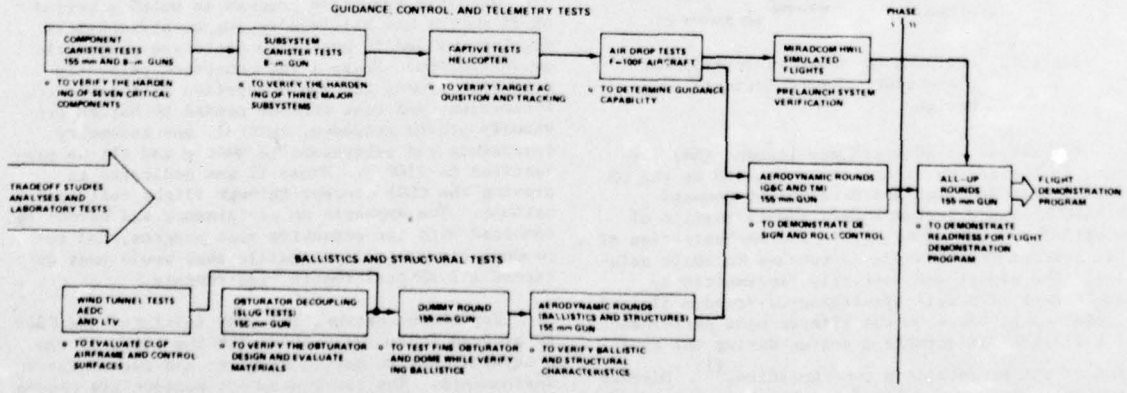


Figure 2. Objectives of Phase I AD Program

resulted in a number of design changes which included improved hybrid fabrication techniques, wire bonding and routing changes, gyro spring starter shimming, improved detector assembly to primary lens bonding, and control actuator flange design strengthening. The canister data also increased the in-plant component screening level on the centrifuge, and introduced a pull test on the hybrid ball bonds during fabrication.

Wind Tunnel Tests

The initial aerodynamic evaluation of CLGP which began in May 1972, was conducted in the LTV high speed wind tunnel and in the Arnold Engineering Development Center (AEDC) propulsion wind tunnel. Test conditions extended over a Mach range of 1.4, an angle-of-attack range of 28°, and a free stream Reynolds number of 3.9 million/ft. The data accumulated midway through these tests resulted in a modification to the seeker dome (strakes) and the control fins. The final AEDC test emphasized that the aerodynamic stability and control of the modified configuration was satisfactory over the desired dynamic range.

Obturator Decoupling Tests (Slug Tests)

Obturator decoupling tests were conducted at Ballistic Research Laboratories (BRL), Aberdeen, Maryland in November and December 1972. Ten test slugs, weighing approximately 150 lb each and simulating the ruggedized CLGP roll inertia, were test fired from a 155 mm tube. The tests were to verify the obturator design and evaluate several candidate materials and slug finishes which would withstand the CLGP operational temperature environment. After the third test, the retaining ring was redesigned and its material changed from 1020 untreated steel of 60,000 to 90,000 psi ultimate strength to heat-treated steel. After the fourth firing, the XM119 change weight for maximum pressure was increased by adding more M6 propellant. The net effect of these changes and test analyses caused the elimination of nylon as an obturator material and Teflon as a slug finish. The remaining tests demonstrated that a polypropylene obturator material riding on a properly lubricated bare steel surface would produce acceptable muzzle exit roll rates. This was the breakthrough required to begin ballistic evaluation of the CLGP design in the cannon environment.

Dummy Rounds

Two of the first CLGP dummy rounds with tail fins, obturator, and dome were fired at BRL in late December 1972. The first round was fired at maximum charge; Fastax camera data showed no aerodynamic instability. With stability assured, the second round was fired at maximum charge down the transonic spark tunnel which provided detailed instrumented coverage of the first 700 ft of travel. Post-firing analysis of the flow characteristics, supersonic blowby, aerodynamic drag, stability, structural integrity, and fin monitoring gave confidence that the CLGP ballistic characteristics were acceptable for flight.

Aerodynamic Rounds (Ballistic and Structural)

Two aerodynamic CLGP rounds with dome, pop-out fins, obturator, and designed mass and balance properties were fired from the M109A1 at White Sands in December 1972. These tests verified minimum and maximum ballistic range capability of the CLGP design; no major problems were encountered. The obturator came off the second round at muzzle exit as anticipated. Post-flight data analysis verified that projectile motion for both rounds was smooth and stable; dispersions were very low.

Captive Flight

Helicopter captive flight tests were successfully flown with CLGP Initial Design (ID-1) at MIRADCOM in February 1973. ID-1 was the first all-up operational round. The purpose of the tests was to verify acquisition and tracking of a laser-designated tank target. A total of seven range closures and ten acquisition passes were made with various laser output energies. Acquisition was accomplished on all of the passes.

Air Drop Tests

The CLGP program required that two projectiles, ID-1 and ID-2, be air dropped from an aircraft to demonstrate guidance capability during Phase I. An F-100F aircraft was provided by the US Air Force, Kirtland Air Force Base, Albuquerque, New Mexico to perform the drop mission. An aircraft safety certification program, involving ground and airborne ejection of five dummy CLGP, was performed from July through December 1972, prior to the dummy air drop program. The ID-1 mission required target acquisition before the projectile was ejected from the aircraft and then guidance to a ground-designated tank target following separation. The ID-2 mission required acquisition after release from the aircraft. The two missions are displayed in Figure 4.

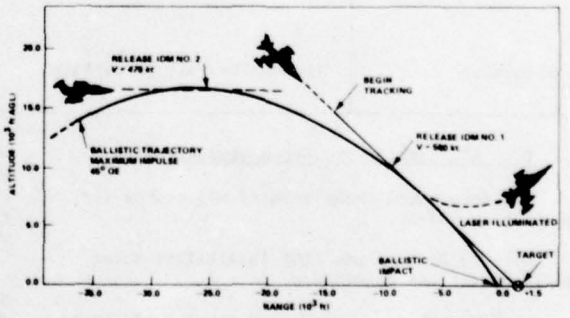


Figure 4. CLGP Air Drop Trajectories for Guidance System Validation

Both projectiles were air dropped in May 1973; neither was successful. The ID-1 failure was attributed to false target acquisition prior to separation which resulted in the seeker gyro hitting the gimbal stops after ejection, causing the projectile to tumble. ID-2 separated safely and flew ballistically for the perscribed 14 sec. However a series

of faults including shorted battery insulation were uncovered. These were subsequently corrected though they impacted fuzing procedures to a limited extent.

Cannon Firing of Phase I Projectile

Martin Marietta chose to fire their third CLGP programmed initially for air drop tests. It did not impact within the desired CFP due to sequencer problems and poor roll control. However, it did show by means of telemetry, post flight recovery, and analysis of the round that the launch shock was survivable and major portions of the G&C unit were operable.

In summary, Phase I proved that the components for the G&C system could be fabricated to meet the harsh environment of a high-g gun launch. Table 1 summarizes the problems and actions which were successful in correcting them.

Table 1. Summary of Phase I AD

Element	Problem	Action
Hybrids	Bond and substrate failures	Pull all bond and support substrates
Actuator	Structure (flange) failure at 9000 g	Redesigned for 12,500 g
Harness	Broken wires in aerodynamic flight tests	Eliminated heat shrinkable tubing and supported wire bundle every 6 in.
ARG	Bond joint released	Positive mechanical reinforcement incorporated
Roll stability	Lost roll control	Simulated failure after thorough review of aerodynamic data and modified autopilot with fix to control roll loop gain
Aft retainer ring	Ring jumped thread	Increased strength
Seeker gyro	Squib wire shorted against gotcha teeth	Increased squib wire to gotcha teeth clearance
Battery	11 V supply shorted to -30 V buss	Added fusible resistor between 11 V supply and -30 V battery initiator squib
Obturator	Inadequate roll decoupling	Changed material to polypropylene

IV. AD Phase II Prototype Demonstration

The Army cited three primary objectives for the AD test phase:

a) To demonstrate CLGP feasibility under quasi-operational conditions.

b) To obtain accuracy and other qualitative and quantitative data which would assist in selecting an engineering development contractor.

c) To identify components and/or subsystems requiring improvement in the engineering development program.

These test objectives were expanded into a comprehensive operational suitability and performance demonstration plan. The main thrust of operational suitability testing was to sample the performance envelope and evaluate user reaction and adaptability to guided projectile technology. The main thrust of performance demonstration testing was to assess the ability of the laser guided projectile to acquire and guide itself to a designated target with extreme accuracy using standard handling, loading, targeting, and gunlaying procedures for unguided ordnance. The only special procedures were limited guidance and control and telemetry confidence checks based on the White Sands Missile Range Acceptance Test Plan to assure round operability prior to delivery to the gun crew for cannon launch.

Before shipment, each test round had to complete successfully the sequence of confidence tests. The MIRADCOM HWIL guidance simulation provided a firm data base for performance verification and anomaly and failure investigations. This simulation included flight dynamics, trajectory characteristics, and terminal accuracy predictions for each launch. Figure 5 shows an overview of the HWIL simulation characteristics. The close correlation of simulation predicted impact accuracy and flight test results are shown in Table 2.

Ten Martin Marietta CLGP were tested at White Sands Missile Range during the competitive Phase II fly-off program, which began on 28 March 1974 and was successfully completed on 3 April 1975. Six of the ten CLGP rounds fired not only survived the severe cannon launch environment, but achieved direct hits on tanks operating over a full array of target scenarios. The target locations were as close as 4 km, demonstrating short range capability, and as far as 16 km, exercising the aerodynamic and component performance envelope of the AD CLGP design. The virtual immunity of armor to indirect artillery fire ended when CLGP accurately hit tanks moving at 10 and 20 mph. All operational objectives required

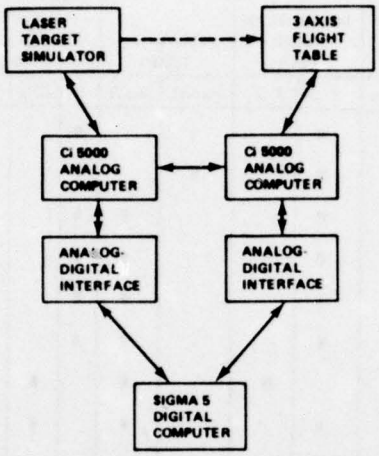


Figure 5. Block Diagram of the Simulation Facility and Information Flow

Table 2. Comparison between HWIL simulation prediction and flight test

CLGP No.	Simulation Runs	HWIL Prediction* (ft)	Flight Test Results
4	147	2.85	Direct hit
5	130	4.90	Direct hit
7	155	6.25	Direct hit
8	106	4.60	Direct hit
9	28	3.00	Direct hit
10	346	5.70	Direct hit

Total simulation runs (CLGP 1 through 10): 1165.
*Mean miss distance: 8.75 ft.
*Standard deviation of miss distance: 7.15 ft.
*Note: Values are normalized by CEP.

by the Army's proposed test program were satisfied at least once during the six successful firings. Table 3 summarizes the results.

V. Operational Proof of Principle Flights

Two outstanding successes were achieved with the CLGP using laser designation data provided by a remotely piloted vehicle (RPV) and an airborne target acquisition and fire control system (ATAFCS). The basic objectives of the demonstrations were:

a) To prove that friendly personnel need not be exposed to hostile fire during a target engagement.

b) To prove RPV and heliborne laser designators can illuminate targets sufficiently for engagement by CLGP.

c) To prove that CLGP is compatible with the two remote designators and can achieve accuracy comparable to that derived from ground designators at night as well as by day.

On 3 October 1975, an Aeronutronic-Ford Prairie IIA miniature RPV made a series of preliminary passes at a stationary tank target positioned at White Sands Missile Range 8 km from an Army self-propelled M109A/1 howitzer. After a series of check runs, the Prairie acquired the tank through its TV camera and data linked the image to the ground station operator. The operator designated the target with a laser spot while the CLGP was on its downward terminal glide. The CLGP scored a direct hit on top of the tank turret.

The ATAFCS is a complete, self-contained system capable of tracking and designating tank-size targets under both day and night conditions. The system is configured in a turret arrangement for mounting on the nose of the AH-IG (Cobra) helicopter. The design is also adaptable to a pod arrangement for carriage on the outboard stores rack. ATAFCS contains a laser, laser rangefinder, optical system, sightline stabilization unit, TV camera, forward looking infrared (FLIR) system, autotracker, laser spot detector, and the associated controls, displays, and electronics for system operation.

On 26 February 1976, at 2203 MST, CLGP was launched against a tank moving perpendicular to the projectile flight path at a range exceeding 7000 m. The ATAFCS system was in a hover mode at a range of 3000 m from the target and to the left of the CLGP flight path. ATAFCS used its on-board FLIR to acquire and "autotrack" the target as it moved away from ATAFCS while a laser boresighted with the FLIR-provided designation. Approximately 30 sec after launch, CLGP achieved a direct hit on the tank and ultimately lodged in the tank's engine compartment under the rear of the turret. The tank was disabled by the impact and subsequently stopped and caught fire.

VI. Technology Achievement Summary

The primary thrust of the AD CLGP design work was to apply scientific and technical ingenuity to overcome volume, weight, and environment constraints. As a result, significant advances were made in materials research, hybrid technology, high-acceleration components and structures, and gun barrel dynamics. To make the CLGP AD design successful, design solutions had to be found for many challenging problems. Techniques had to be developed to allow gyros, hybrids, and wire bundles to survive the high-acceleration firing environment. An obturator had to be designed to prevent blowby while successfully decoupling the projectile from the high roll rate imparted by the rifling of the gun. A method had to be devised to keep the fins retracted until the projectile left the gun and then to deploy them rapidly and positively to ensure aerodynamic stability. The validity of the design solutions shown in Table 4 were proven by Phase I canister test firings and verified by the Phase II flights.

VII. Conclusions

In summary, the CLGP AD program met all required objectives. The program demonstrated that:

a) CLGP can engage targets equally well under nighttime or daylight conditions.

Table 3. Summary of Phase II flight tests

	Acceleration Level (g)			Target Range (km)				Target Speed (mph)			Direction of Target Motion Relating to Line of Sight		Designator Range (km)		Target Types		Ballistic Aimpoint Offset (m)		
Round	1500	3000	7100	4	8	12	16	0	10	20	Across	Towards	1.5	3.2	Panel	Tank	0	250	2000
MGP-1*		●			●			●					●		●		●		
MGP-2*		●			●			●					●		●		●		
MGP-3*		●			●			●					●			●	●		
MGP-4		●			●			●					●			●	●		
MGP-5		●			●				●			●	●			●	●		
MGP-6*		●			●					●	●		●			●	●		
MGP-7			●			●		●						●		●		●	
MGP-8	●			●				●					●			●		●	
MGP-9	●			●						●	●		●			●		●	
MGP-10			●				●	●						●		●			●

*Note: These systems did not achieve planned objectives.

Table 4. Technology achievements

Problem	Achievement
Gyro survival in gun firing environment	Designed and tested a gotcha that cradles the gyro during the firing acceleration transient, and later retracts and latches in milliseconds allowing the gyro freedom to spin up and operate. Load transfer bearings were also added to aid gyro survival
Roll decoupling	Designed and tested an obturator which yielded a projectile muzzle exit roll rate less than 20 rps
Fin deployment	Designed and proved a technique for successful fin deployment after exit fin muzzle brake without scoring the gun barrel
Hybrid substrates	Developed processes to fabricate and screen candidates for cannon environment
Detector seal	Developed technique to seal detector to base hermetically to provide long storage life
Wire survival of gun fire environment	Developed techniques to route and bundle wires to survive high acceleration firing environment
High-strength structural design	Developed analytical models and fabrication processes that resulted in cannon firing reliability beyond expectation
Deliberate fin-induced roll during ballistic flight	Alleviates fin fabrication and tolerance problems and reduces ballistic dispersions

b) A helicopter designation system such as ATAPCS or an RPV can acquire and track moving targets sufficiently for accurate engagement by CLGP.

c) The CLGP was a reliable and accurate concept as evidenced by a success record in which eight of the last nine rounds achieved direct hits on targets under a broad spectrum of conditions.

As stated on more than one occasion, the CLGP may be the most significant weapon to enter the military arsenal in the past two hundred years.

VIII. References

1. Pastrick, H. L., "Terminal Guidance for the Army's 155 mm Cannon Launched Guided Projectile (CLGP)," Proceeding of AIAA Guidance and Control Conference, Stanford, California, August 1972.

2. Pastrick, H. L., York, R. J., and Jolly, A. C., "System Performance Prediction by Modeling Test Data in Digital Simulations," AIAA Guidance and Control Conference, Paper No. 73-880, Key Biscayne, Florida, August 1973.

3. Pastrick, H. L., Will, C. M., Jolly, A. C., Hazel, L. H., and Vinson, R. J., "Hardware-in-the-Loop Simulation: A Guidance System Optimization Tool," AIAA Mechanics and Control of Flight Conference, Paper No. 74-929, Anaheim, California, August 1974.

4. Cannon Launched Guided Projectile Advanced Development Program Final Report, Martin Marietta Aerospace Report No. OR 13759, May 1975.

EIGHTH BIENNIAL GUIDANCE TEST SYMPOSIUM

A NEW TECHNIQUE FOR DETECTING GUIDANCE COEFFICIENT INSTABILITIES

AUTHORS: EDWARD M. DUIVEN
CHARLES M. ERMER
KEVIN S. TAIT
C. JULIAN VAHLBERG

THE ANALYTIC SCIENCIES CORPORATION
READING, MASSACHUSETTS

A NEW TECHNIQUE FOR DETECTING GUIDANCE SYSTEM INSTABILITIES

by

Edward M. Duiven
Charles M. Ermer
Kevin S. Tait
C. Julian Vahlberg

The Analytic Sciences Corporation
Reading, Massachusetts 01867

ABSTRACT

A technique to be used to detect the presence of inertial guidance system instrument instabilities, from flight test data, is described in this paper. The technique is applied to the processing of Minuteman III telemetry and radar data resulting from the FLY-2 flight test program. Included in this paper are an introduction to the coefficient shift detection methodology, an assessment of projected detection algorithm performance, and an overview of the post flight analysis software being developed using a detailed system level simulation of the Minuteman III guidance system, the Western Test Range radars, and the FLY-2 measurement generation process.

INTRODUCTION

The question as to whether there are shifts and/or ramps in certain Minuteman III guidance system instrument error coefficients, during missile powered flight, has been of concern for a number of years. The instabilities, that may be caused by thermal effects, vehicle vibration, staging transients, etc., have heretofore not been identifiable during post-flight data analysis. The Western Test Range (WTR) radars may not provide measurement data of sufficient quality to support the recovery of time-varying guidance coefficients. However, the FLY-2 flight tests, associated with the Minuteman III Guidance Improvement Program, may develop data of sufficient quality that the instrument stability question can be answered.

Unique about the FLY-2* concept, Fig. 1, is that the test missiles (a total of six flights are currently planned) carry two Inertial Measurement Units (IMU's). The primary IMU is the weapon systems NS-20 used to generate the navigation data from which vehicle guidance commands are developed. (Ref. 1 provides good background information about the Minuteman III weapon system and its navigation system, the NS-20). In addition to the primary IMU, a second navigation system (also an NS-20) is contained in a special section (wafer) of the missile inserted between the primary weapon system and the reentry vehicles. The wafer also contains power supplies and a telemetry system to support the secondary IMU.

The azimuthal alignment of the platforms with respect to the target are different for the two IMU's, their orientation selected for "optimal" guidance coefficient recovery. On the test flights integrated specific force measurements (velocity data) will be collected from each of the IMU's, time tagged†, and transmitted, via the telemetry unit, to the ground for post flight analysis. Radar measurement data covering the uprange, midrange, and terminal phases of the test flights will also be available for processing post flight. The velocity data will be differenced post flight and the accuracy of these difference measurements will be approximately 0.01 fps.

---

*The first FLY-2 flight occured on 12 November 1976.

†Time tagging of the velocity data is required to minimize the impact of quantization on measurement accuracy.

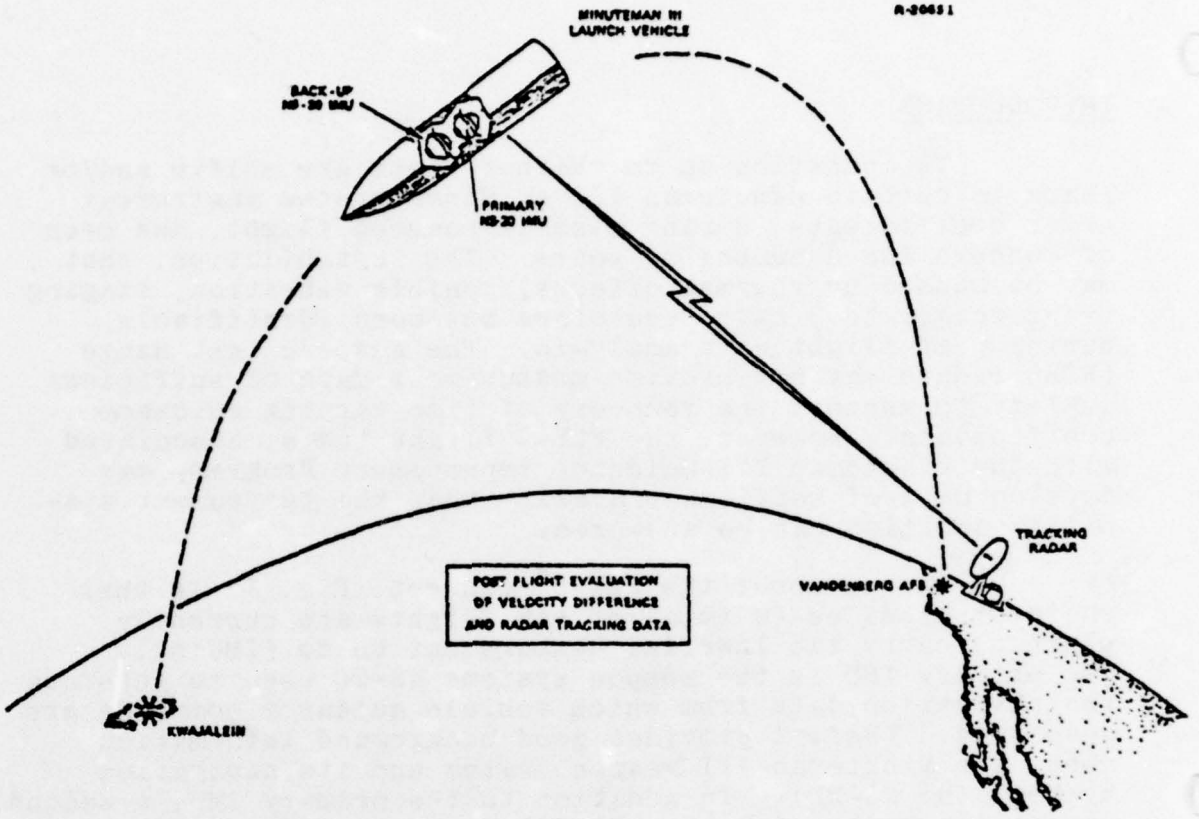


Figure 1 The FLY-2 Concept

The recovery of potential time-varying guidance coefficients, from the velocity difference and radar data, requires special analysis techniques not currently being employed in the post-flight processing of test data. TASC has developed such a technique based on Generalized Likelihood Ratio (GLR) test procedures. This approach extends the conventional GLR test procedure (Ref. 2) to allow for jump and/or ramp detection and identification in linear systems. Reference 3 develops the new GLR test in a rigorous manner.

The following sections of this paper describe the coefficient shift detection methodology developed by TASC for application to the Minuteman III flight test problem, the results of a number of simulation studies directed towards assessing both detection and identification performance of the GLR test procedures in the FLY-2 environment, and the structure of the Post Flight Analyzer being generated by TASC to perform post flight evaluation studies using FLY-2 data. A brief discussion of the Minuteman III error model used in these studies is also presented herein.

COEFFICIENT SHIFT DETECTION METHODOLOGY

The GLR test procedure selected for the detection and identification of time-varying guidance coefficients is a direct extension of techniques currently used in post-flight regression analysis. The dual NS-20 telemetry data and radar range data are used, post flight, as inputs to a filter (in this case a Kalman filter) as shown in Fig. 2. Outputs from the filter include estimates of the platform alignment errors and guidance system instrument error coefficients. The filter also generates an estimate of the measurement sequence using the platform alignment error and instrument error coefficient estimates. It is well known (Ref. 4) that the sequence of measurement residuals (i.e., the difference between the measured quantities and the filter's estimate of them) will be a zero mean white noise sequence if the filter models the process correctly.

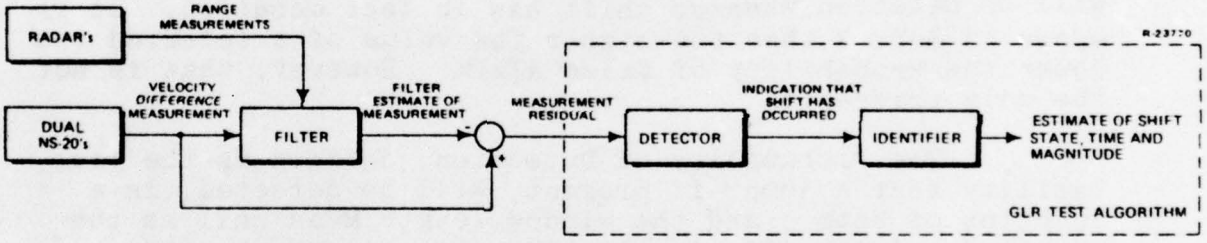


Figure 2 Functional Block Diagram of the GLR Test Procedure

The current NS-20 error model assumes that the principal instrument errors are biases, over the period of powered flight. Thus, if certain coefficients display sudden shifts or ramping characteristics the model is incorrect and the measurement residuals will not be of zero mean. It is important to note that the NS-20 error model, in the absence of guidance instrument coefficient shifts, is assumed to model the error dynamics to such a degree that the filter residual sequence would be both zero mean and white.

The function of the GLR test algorithm is two-fold. The first function is to determine whether a shift in one of the coefficients has taken place. This is referred to in the sequel as the detection process. Detection is performed by forming a weighted sum of the last M* measurement residuals

*The quantity M is referred to as the GLR detection window length.

and using this quantity as a test statistic in a binary hypothesis test. If the test statistic is greater than a specified threshold, ε, a shift is detected and if it is smaller than ε no shift is assumed to be present.

The second function is the identification process. The formulation of the GLR test described in Ref. 3 results in an algorithm that generates an estimate of which state shifted, the time of the shift, and the shift magnitude. Under the assumption of no a priori knowledge about the jump characteristics the GLR estimate is "optimal". It is the capability to estimate the jump characteristics that makes the GLR test more attractive than other residual based detection processes that do not provide the identification function (Ref. 5).

The critical parameters upon which the GLR test design is based are the Probability of False Alarm (P_F) and the Probability of Detection (P_F). The Probability of False Alarm is defined as the probability that a shift will be detected when no shift has in fact occurred. It is shown in Ref. 3 that the higher the value of ε selected the lower the Probability of False Alarm. However, that is not the only trade-off.

The Probability of Detection, defined as the probability that a jump, if present, will be detected, is a function of both ε and the window length M as well as the magnitude of the jump itself (Ref. 3). As may be seen by reference to Fig. 3, the longer the detection window the higher the Probability of Detection for a given false alarm

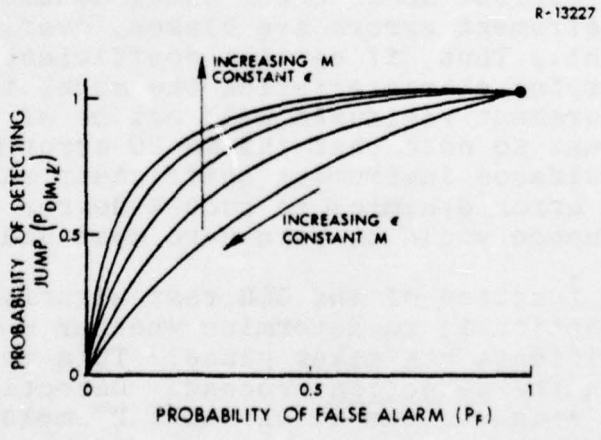


Figure 3 General Relationship Between P_D and P_F as a Function of M and ε

rate. However, the length of the window is limited by the missile flight time, computation capabilities of the post-flight software, and the fact that additional jumps may exist during the flight. The design values of ε and M for typical Minuteman III FLY-2A flights and their associated P_F's and P_D's are discussed in the performance assessment portion of this paper.

GUIDANCE SYSTEM SIMULATION

Evaluation of the GLR test methodology, the results of which are presented in the following section, is based on a 114-state model describing the velocity error growth in the dual NS-20's and WTR radar range measurement errors. The error states contained in the model are summarized in Table 1. As shown, the system errors include position, velocity, and alignment errors for the Primary NS-20 IMU. System errors for the MEW NS-20 are not directly modeled. For convenience differential, Primary minus MEW, system position, velocity, and alignment errors are modeled. This approach is analytically attractive since the key measurement variable, velocity difference, appears directly as an error state.

Returning to Table 1, it is seen that the system errors also include initial alignment errors. These errors are required to account for that portion of the accelerometer bias error which becomes correlated with platform tilt during the periodic rebiasing of the accelerometers.

The classical error sources included in the baseline NS-20 error model are also listed in Table 1. These consist of accelerometer, gyro, and Q-matrix* calibration errors for both NS-20 IMU's. The accelerometer errors include uncorrelated bias, and second order input axis nonlinearities. The gyro errors include bias, mass unbalance, anisoelastic effects, spin axis compliance, and fourth-order acceleration dependent drifts. The WTR radar error states include bias, scale factor, and random errors in addition to site survey errors and measurement noise.

In order to evaluate the GLR test methodology a detailed simulation program, consisting of three segments, was developed, see Figure 4. The first segment, is a standard

*The Q-matrix in Minuteman III notation is a matrix that relates accelerometer (PIGA) input axes to platform axes. PIGA scale factors are also included in the Q-matrix.

TABLE 1

NS-20 MODEL SUMMARY FOR FLY-2 ERROR ANALYSIS

T-0197b

ERROR OR ERROR SOURCE NAME	NUMBER OF ERRORS/STATES	DESIGNATION
Primary		
Position Errors	3	δP_{1i}
Velocity Errors	3	δV_{1i}
Alignment Errors	3	$\delta \psi_{1i}$
Initial Alignment Errors	3	$\delta \psi_{01i}$
Primary-MEW		
Differential Position Errors	3	δP_{2i}
Differential Velocity Errors	3	δV_{2i}
Differential Alignment Errors	3	$\delta \psi_{2i}$
Differential Initial Alignment Errors	3	$\delta \psi_{02i}$
Primary Errors Sources		
Accelerometers		
Uncorrelated Bias	3	b_{11}, b_{12}, b_{13}
Input Axis g^2 Nonlinearity	3	F_{1i}
Q-Matrix Calibration Errors	9	q_{1ij}
Gyros		
Bias	3	A_{21}, B_{21}, A_{11}
Mass Unbalance	4	C_{1i}, D_{1i}
Anisoelasticity	4	B_{1i}, E_{1i}
Spin Axis g^2	2	F_{1i}
Gyro g^4	8	$R_{1i}^{1si}, P_{1i}, N_{1i}, J_{1i}$
MEW Error Sources		
Accelerometers		
Uncorrelated Bias	3	b_{21}, b_{22}, b_{23}
Input Axis g^2 Nonlinearity	3	F_{2i}
Q-Matrix Calibration Errors	9	q_{2ij}
Gyros		
Bias	3	A_{22}, B_{22}, A_{21}
Mass Unbalance	4	C_{2i}, D_{2i}
Anisoelasticity	4	B_{2i}, E_{2i}
Spin Axis g^2	2	F_{2i}
Gyro g^4	8	$R_{2i}^{2si}, P_{2i}, N_{2i}, J_{2i}$
WTR Radar Errors (3)		
Bias	3	b_{ri}
Scale Factor	3	s_{ri}
Correlated Random Error	3	m_{ri}
Survey Errors	9	
TOTAL	114	

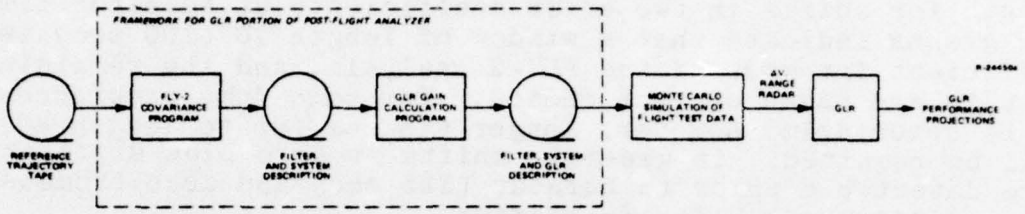


Figure 4 FLY-2/GLR Simulation

error covariance program that outputs the Kalman filter state transition and optimal gain matrices (Ref. 4). The second segment computes the GLR test gain and information matrices (Ref. 3). The third segment is a monte carlo simulation program. This segment, using initial condition and measurement noise values (selected from a pseudo random number generator), simulates the propagation of the errors through the system model. The simulation program has the capability of introducing jump and/or ramp discontinuties into the system states at selected times during the FLY-2 mission. Measurements are processed in accordance with the GLR algorithm to determine if these known jumps can be detected and identified.

GLR PERFORMANCE ASSESSMENT

The projected performance of the GLR algorithm presented in this paper is obtained by covariance analysis. In the development of the algorithm an information matrix (inverse error covariance matrix) is calculated for the GLR jump estimate at each time. Given this matrix together with the true jump time, state, and magnitude the probability of detection, P_D, for a specified false alarm rate, P_F, is determined from statistical tables (Ref. 3). In the following evaluation P_F is chosen to be 0.05 and, for each time and state the minimum jump magnitude that will yeild a specified probability of detection, say 0.50 is calculated. This gives a convenient way to display jump detectability and to assess algorithm performance.

Initial calculations were made to determine the optimum window length, M, for the GLR test procedure. Figures 5 and 6 show the variation in detectability with window length for shifts in two error coefficients at selected times. The graphs indicate that a window of length 20 (100 sec) is sufficient for most of the FLY-2 analysis, and the remaining results are based on that choice. For some jump occurances to be detectable, however, longer windows (up to length 40) will be required. In general, shifts in gyro bias drift are more detectable prior to burnout (185 sec) and accelerometer bias coefficient shifts thereafter.

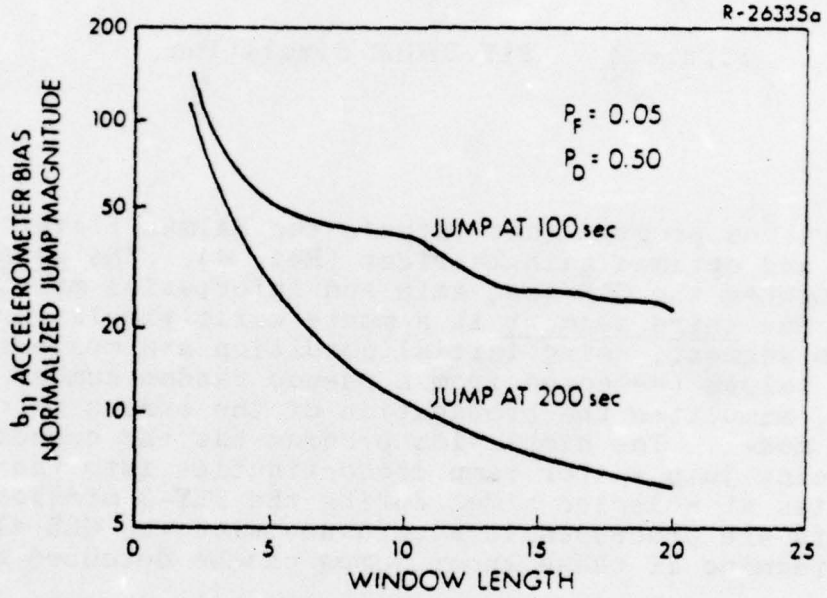


Figure 5 Accelerometer Bias Jump Required for P_D=0.50 vs Window Length

The detectability of shifts in selected guidance coefficients as a function of time is presented in Figs. 7, 8, and 9. Only one plot is shown for accelerometer bias since the other coefficients give results within 10% of those shown. Two gyro bias drifts are plotted with the A_1 and B_1 axes for the Number 1 gyro displaying almost identical characteristics. The results demonstrate that prior to burnout accelerometer jumps must be relatively large to be detected, especially in the first 100 sec of the flight. Jumps in the Number 1 gyro coefficients are reasonably detectable over the entire flight history, with best detection occuring prior to burnout. The single axis for the Number 2 gyro has

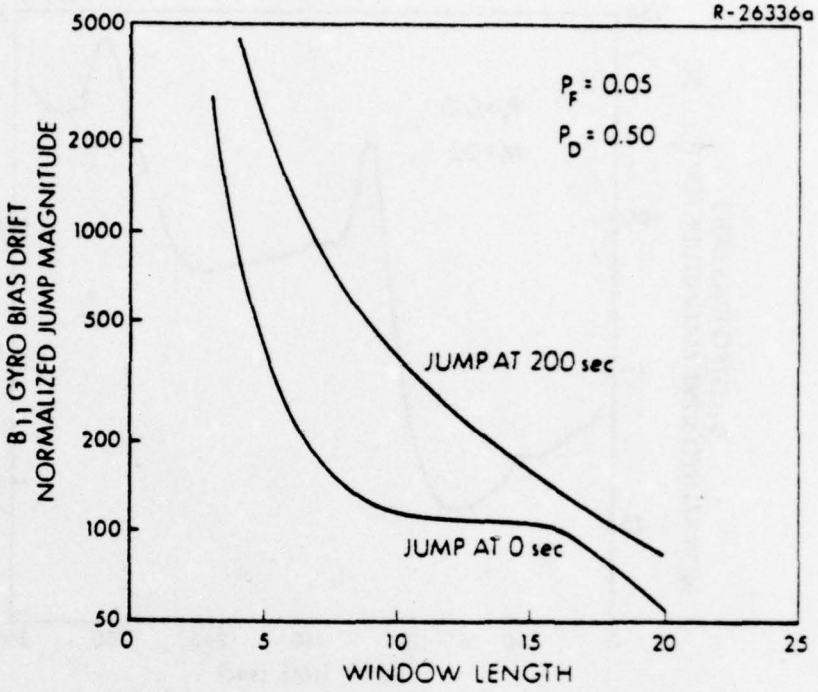


Figure 6 Gyro Bias Drift Jump Required for P_D=0.50 vs Window Length

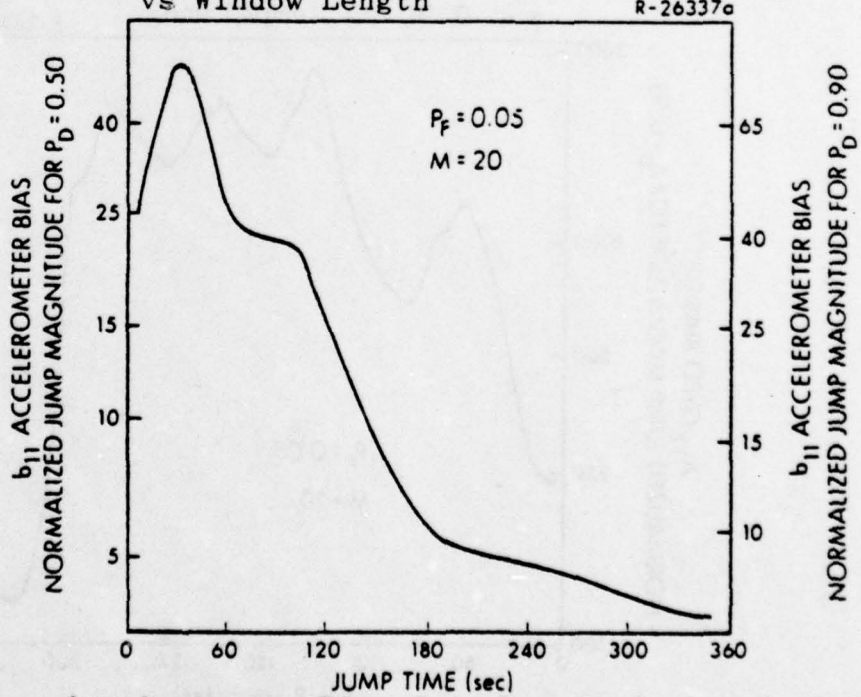


Figure 7 Accelerometer Bias Jump Magnitude for P_D=0.50 and 0.90 vs Jump Time

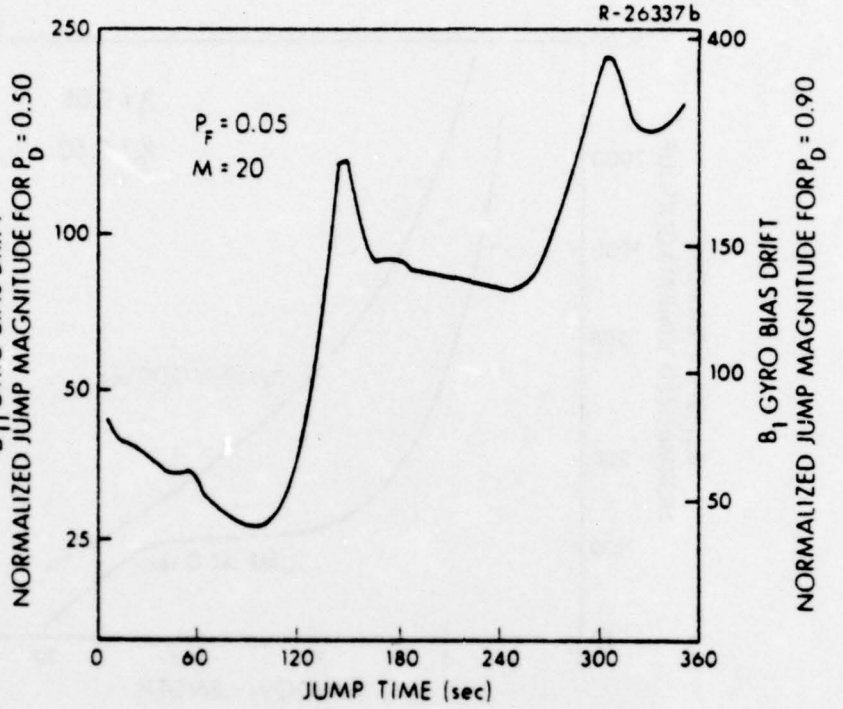


Figure 8 Gyro Bias Drift Jump Magnitude for P_D=0.50 and 0.90 vs Jump Time

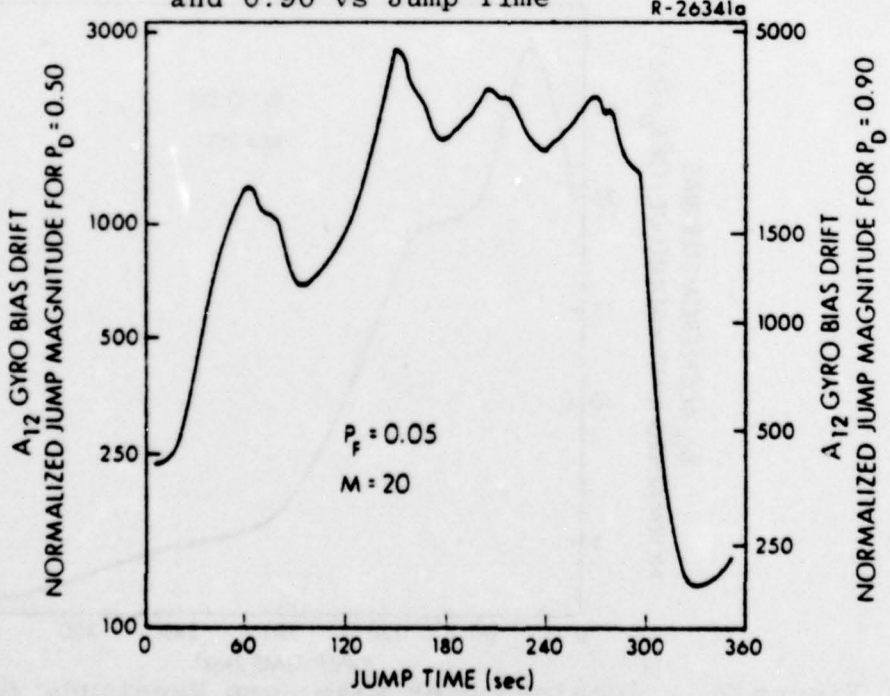


Figure 9 Gyro Bias Drift Magnitude Required for P_D=0.50 and 0.90 vs Jump Time

very poor observability. Jumps in this coefficient must be sizeable for detectability over most of the flight, with an exception occuring very early or late in the trajectory.*

The qualitative performance described above is easily interpreted in terms of the system geometry and dynamics. The large forces present during powered flight cause the g and g^2 dependent errors to dominate and suppress accelerometer bias errors prior to burnout. Since gyro bias drift enters the velocity error as the crossproduct of the small angle platform-to-computer misalignment vector with specific force ($\underline{\psi} \times \underline{f}$) it is most observable in a high acceleration environment. An exception occurs with the A_2 gyro coefficient since this axis (oriented at 30 deg to the horizontal) is nearly parallel to the specific force vector for the major part of the trajectory.

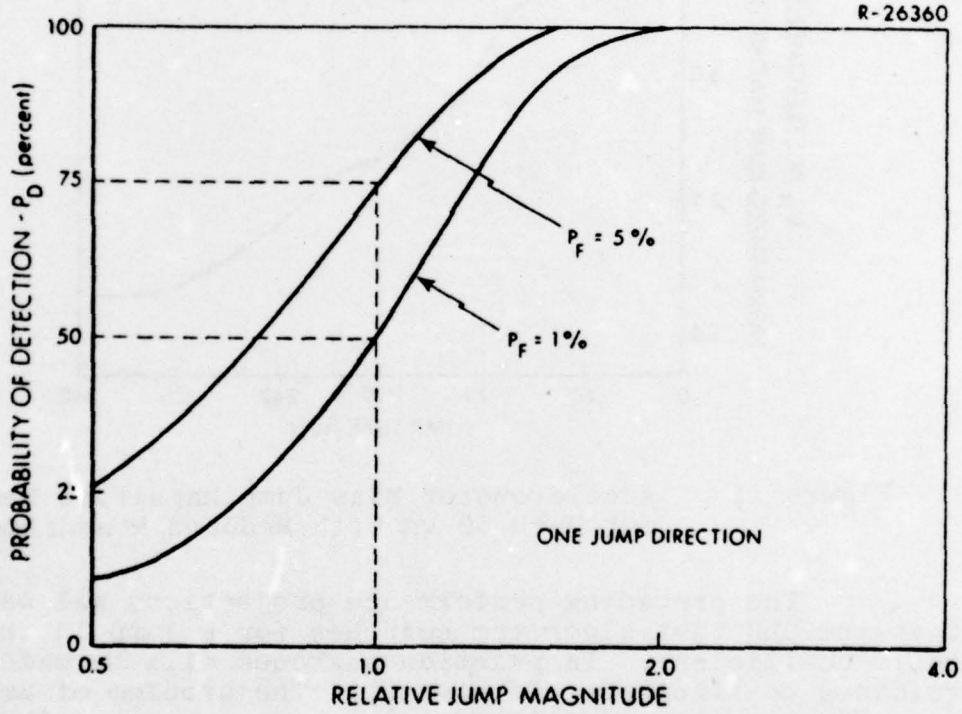


Figure 10 Probability of Detection vs Relative Jump Magnitude for Two False Alarm Rates

*Although the jump magnitudes quoted are for a 0.50 detection probability, the appropriate values for other choices of P_D are easily obtained from Fig. 10. For example twice the 0.50 value yields better than 0.90 detectability.

The sensitivity of detection performance to the measurement noise level is evaluated in Figs. 11 and 12. In these plots the velocity measurement error is reduced by $1/\sqrt{10}$ from its previous value of 0.01 fps rms. Overall detectability is improved by a factor of about 2.

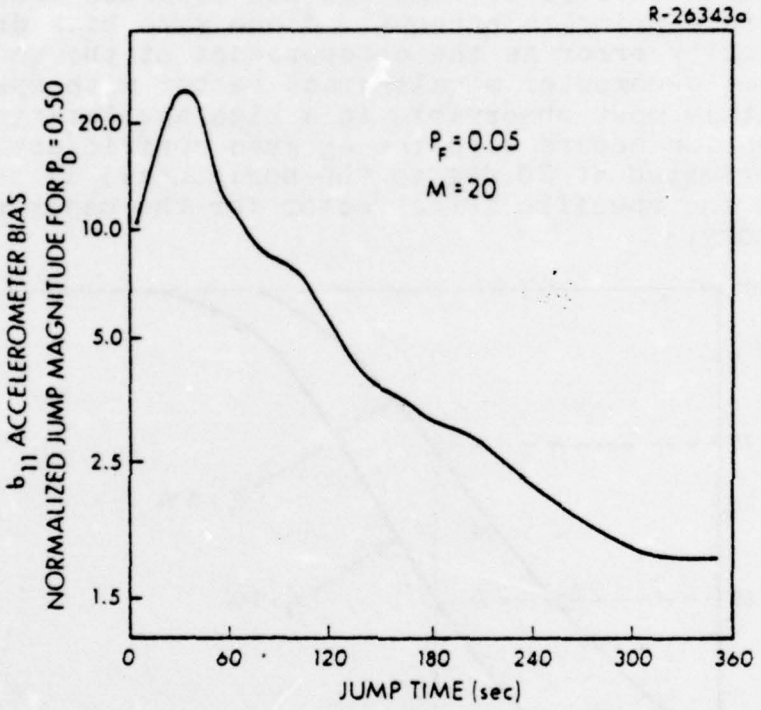


Figure 11 Accelerometer Bias Jump Magnitude Required for P_D=0.50 vs With Reduced Measurement Noise

The preceding performance projections all assume that the GLR test algorithm searches for a jump in the correct shift coefficient. In practice searches will be made in all guidance coefficients of interest. The problem of ambiguity, or incorrect jump identification, occurs when the GLR algorithm attempts to estimate a shift in a state which is not the actual jump state. The extent of this problem is assessed by considering the correlations in the jump estimate error covariance matrix (or alternatively its inverse, the information matrix). A measure of the degree of correlation is obtained from the determinants of various diagonal submatrices of the information matrix corresponding to selected subsets of states. In what follows these determinants are normalized so that a value of one denotes statistical independence (zero correlations) and a value of zero denotes inter-dependence of one or more jump state estimates.

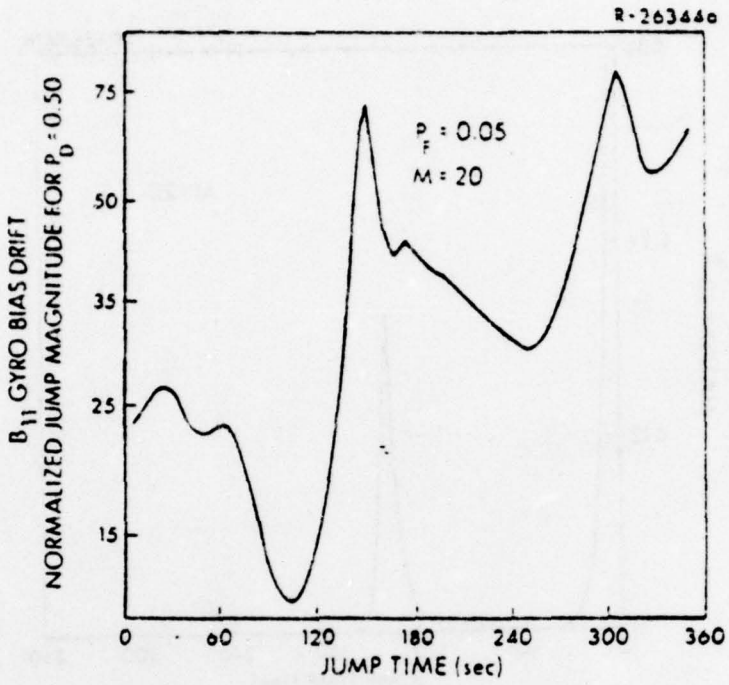


Figure 12 Gyro Bias Jump Magnitude Required for P_D=0.50 With Reduced Measurement Noise

Figs. 13 through 16 summarize the ambiguity problem for the FLY-2 flight scenario. There are three gyro bias drifts and three accelerometer bias errors for each NS-20 system for a total of 12 states to be tested by the GLR technique. The first plot demonstrates the difficulty associated with trying to effectively separate the two systems. A bias coefficient shift in the primary IMU cannot be distinguished from the same shift in the secondary IMU. Since only velocity differences are being used this is not surprising. Refined analysis may be possible with independent telemetery data on thermal transients, etc.

By restricting the search to a single IMU the system ambiguity is bypassed and the remaining ambiguity can be evaluated. It is seen that the combined six accelerometer and gyro bias states are separable during powered flight but not thereafter. The last two plots show the inter-accelerometer and inter-gyro ambiguities in isolation. The accelerometers are separable except in the vicinity of burnout, while the gyro axes are almost uncorrelated at 300 sec and reasonably separable everywhere except during the last 60 sec. Additional results, not shown, indicate that the ambiguity becomes rapidly worse for smaller window lengths. On the other hand, the identification problem is relatively insensitive to measurement noise levels.

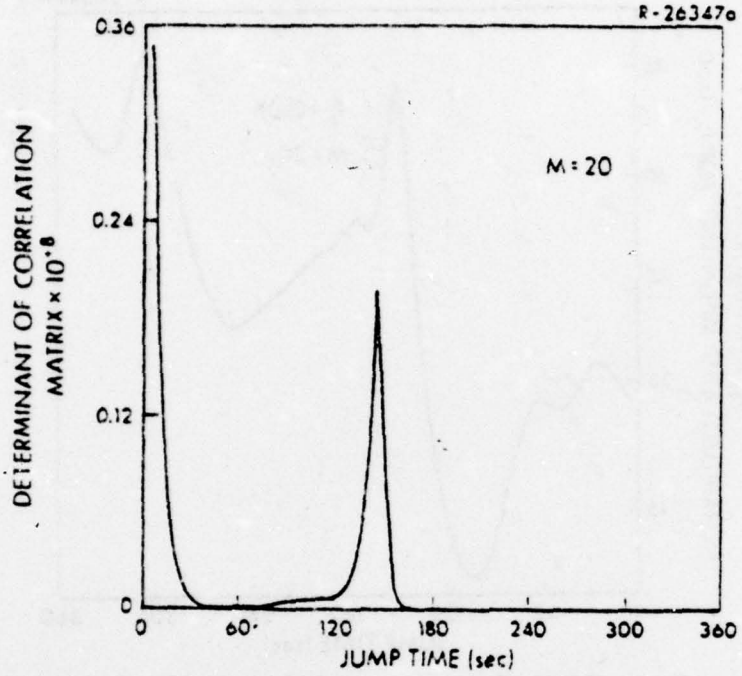


Figure 13 Determinant of Primary and MEW Gyro Bias Correlation Matrix

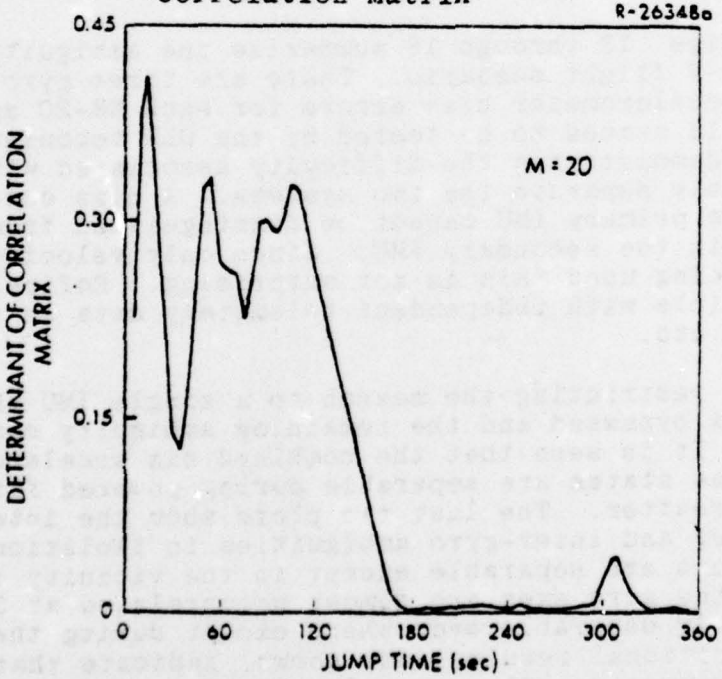


Figure 14 Determinant of Primary Accelerometer and Gyro Bias Correlation Matrix

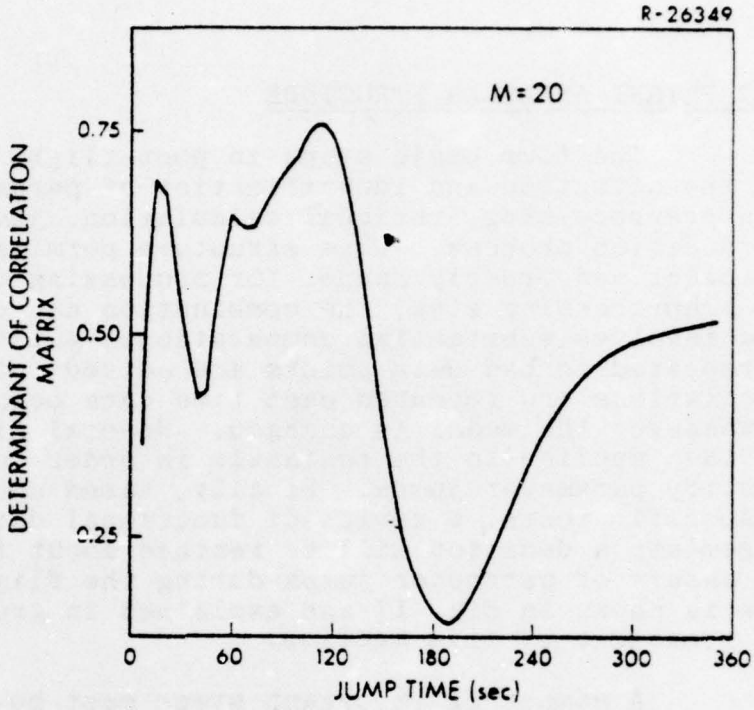


Figure 15 Determinant of Primary Accelerometer Bias Correlation Matrix

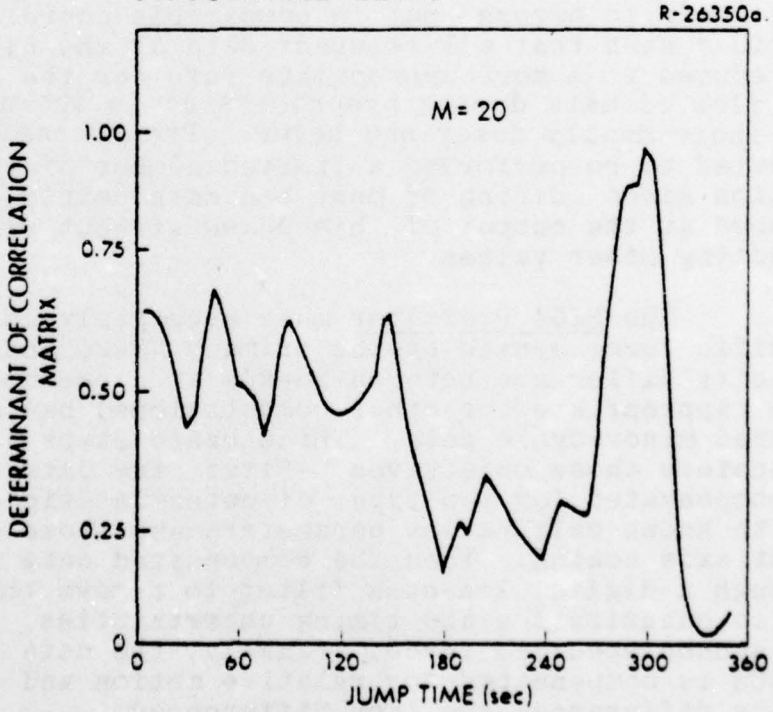


Figure 16 Determinant of Primary Gyro Bias Correlation Matrix

POST FLIGHT ANALYZER STRUCTURE

The four basic steps in post-flight data analysis for the detection and identification of parameter jumps are: data preprocessing, residual calculation, jump detection, and the decision process. This structure permits a computationally efficient and orderly manner for processing the data. In the preprocessing step, the combination and compression of data involves substantial computations, yet does not need to be repeated as bad data points are edited out. The residual calculations are repeated each time data points are removed, or whenever the model is changed. Several different tests are then applied to the residuals in order to detect and identify parameter jumps. Finally, based upon the results of specific tests, a review of functional data, and engineering judgement, a decision will be reached about the time, magnitude, and nature of parameter jumps during the flight. The flow of data is shown in Fig. 17 and explained in greater detail in the remainder of this section.

A number of important steps must be taken to prepare the raw recorded data so that it can be efficiently and accurately analyzed using the advanced analysis tools described herein. The data from two NS-20s and several radars must be sorted, time synchronized, compensated for deterministic errors, put in comparable coordinate frames and combined such that all relevant data at the high raw data rate is reduced to a more appropriate rate for the analysis tools. The flow of data during preprocessing is shown in Fig. 18 and individually described below. Preprocessing of the data is expected to be performed a limited number of times for each mission since editing of most bad data points can be accomplished at the output of this phase without significantly affecting other values.

The PIGA Prefilter must accurately calculate the specific force sensed by the primary NS-20 and the indicated-velocity difference between NS-20s at a pseudo-major cycle rate (appropriate for other computations) based upon telemetered minor-cycle data. Three basic steps are required to achieve those objectives. First, the data from each NS-20 is compensated for two types of deterministic errors, those due to known calibration parameters and those due to PIGA input axis coning. Then the compensated data is passed through a digital low-pass filter to remove the random errors due to quantization and timing uncertainties, and to estimate the sensed specific force. Finally, the data from the two NS-20s is compensated for relative motion and telemetry timing differences and then differenced.

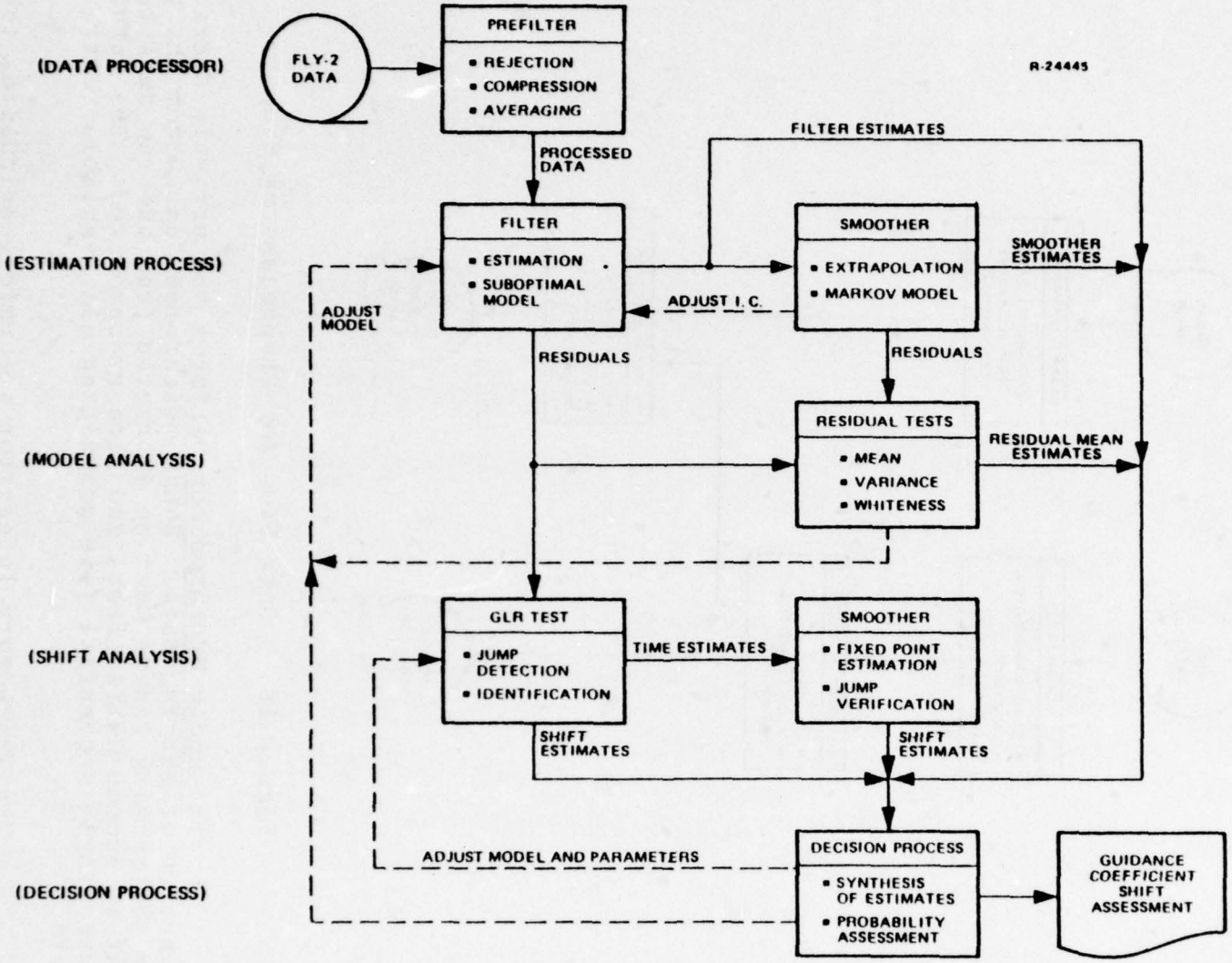


Figure 17 Post Flight Analyzer Data Flow

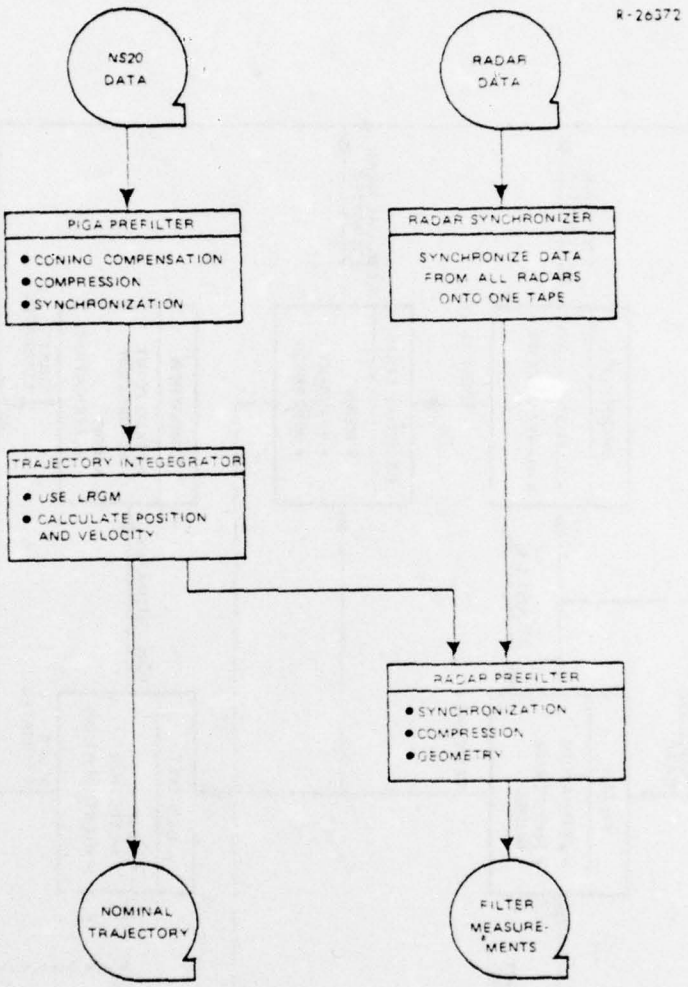


Figure 18 Data Flow for Preprocessing Step

The Radar Synchronizer performs the strictly clerical function of merging data. Range measurement data from the ten or so tracking radars must be extracted from the raw data tapes, put in common units (feet) and time synchronized. The result is a single sequential file containing all available radar data.

The Trajectory Integrator accurately calculates the position and velocity of the missile based upon the best

available model for gravity* and the specific force sensed by the primary NS-20. To allow refinements of the trajectory (as bad data is removed and errors are estimated) without repeating the long integration required by this program the total gravity gradient matrix is also calculated. The velocity differences between NS-20's are not used in this program, and are passed along unchanged.

The Radar Prefilter calculates the difference between the measured radar ranges and the value expected based upon the NS-20 indicated position. The large uncertainty in each measurement is then reduced by averaging all range differences (from each radar) over the entire pseudo major cycle interval. The geometry of each measurement is also calculated so that the filter can properly weight the one-dimensional range difference measurements in the estimation of three-dimensional position. As with the Trajectory Integrator, the NS-20 velocity differences are not used, and are passed forward unchanged since they, along with the range differences make up the measurements for the residual calculations.

The residual calculations take the sequence of range difference (radar) and velocity difference (between NS-20s) measurements and calculate the best estimate of NS-20 and radar errors based upon an a priori error model. The residual difference between the measurements and estimates are the basis for tests described in succeeding paragraphs. The basic flow of data is shown in Fig. 19. These computations are divided into two separate programs for computational efficiency since they will be repeated several times as bad data is removed and as different error models are tried. The Gain Calculation process is based on the straightforward, although lengthy, calculation of Kalman gains using the nominal trajectory, the system error model, and the measurement sequence.

The Residual Calculation uses the gains to interpret the measurements from the data preprocessor. During preliminary data editing the relatively simple residual calculations can be made many times using the same set of gains without significant loss of accuracy. The more lengthy gain calculations can then be repeated only after most of the bad data is removed or whenever the error model is changed.

---

*The WGS-72 gravity model in combination with the DMAAC Launch Region Gravity Model (LRGM) for Vandenberg AFB is used.

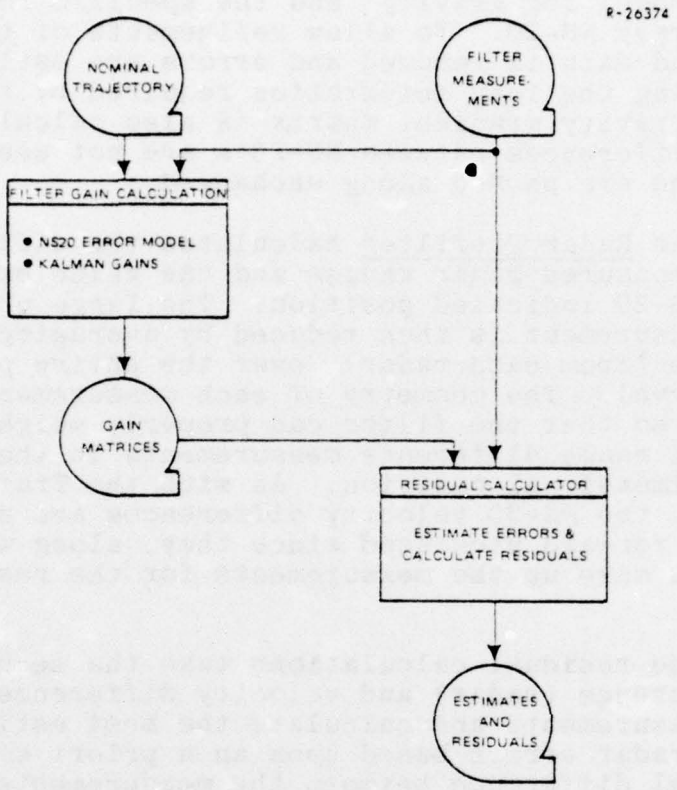


Figure 19 Data Flow for Residual Calculation

The primary jump detection will be performed using the Generalized Likelihood Ratio (GLR) test on the filter residuals. However, there are a number of other tests and procedures which will be used to support the GLR test. They include a variety of statistical tests on the residuals (e.g., mean, variance) and both fixed-point and fixed-interval smoothers. The basic flow of information is shown in Fig. 17 and described below.

The GLR Test routines use the gain matrices to determine whether the filter residuals are consistent with the model. In the event of an inconsistency, the time and identity of a parameter(s) which changed (jumped) is estimated. These jump estimates can then be used to change the model and the residual calculations can be repeated.

Two forms of Smoother may be used. The fixed-point smoother allows the computationally efficient estimation of a limited number of smoothed states at selected times. This is particularly attractive if only certain candidates are being considered. Fixed-interval smoothing allows the

smoothed estimation of all parameters but requires more computations. Both have a place however in the search for unmodelled parameter changes.

Various Residual Tests can be performed on both the filter and smoother residuals. If models are all correct, the residuals will be zero mean, uncorrelated and have the variance predicted by the model. Thus the simple mean and variance calculations provide a measure of whether the model is valid. An autocorrelation or power spectral density on the residuals can provide some clues as to the nature of modelling errors.

CONCLUSIONS

TASC is under contract to process Minuteman III telementry and radar data for the FLY-2 flight tests. The purpose of the processing effort is to detect and identify the presence of potential instabilities in specific NS-20 guidance instrument coefficients. The detection and identification process will be accomplished using the Generalized Likelihood Ratio (GLR) test developed by TASC. This paper describes preliminary results of a study directed towards assessing the performance of the GLR test in the FLY-2 environment. The major findings of the study are:

- Shifts of sufficient magnitude in both accelerometer biases and gyro bias drifts will be detectable using the GLR test procedure.

- Detection of shifts in the gyro bias drift coefficients is best obtained during missile powered flight whereas shifts in accelerometer biases are most readily detected during free-fall.

- Identification of which particular instrument coefficient shifted will be limited by both instrument coefficient observability and primary/MEW system ambiguities. Thus, the interpretation of additional telemetry data (e.g., gyro wheel speeds, thermal environment information, etc.) will be necessary to identify specific instrument coefficient shifts.

The paper also presents an overview of the post flight software required to process the FLY-2 data. As was demonstrated, the GLR test methodology is a direct extension of current flight test data processing techniques.

ACKNOWLEDGEMENT

The work described in this paper was performed for the Air Force Space and Missile Systems Organization under Contract Number F04704-76-C-0039. The authors wish to express their appreciation to Capt. Robert Warzynski and Capt. Eugene Justin of the Minuteman Project Office for their guidance and support. In addition, the technical support provided by Dr. Harold L. Jones and the programmer dedication given by Messrs. Larry R. Brown, Donald F. Piette, and John W. VanderMeer is greatly appreciated. Discussions with personnel from TRW and Rockwell International/Autonetics Group have also been beneficial in the generation of this paper.

REFERENCES

1. Wuerth, J.M., "The Evaluation of Minuteman Guidance and Control," Journal of the Institute of Navigation, Vol. 23, No. 1, pp. 64-75, Spring 1976.

2. Van Trees, H.L., Detection, Estimation, and Modulation Theory, Part I, Wiley and Sons, 1968.

3. Willsky, A.S., and Jones, H.L., "A Generalized Likelihood Ratio Approach to the Detection and Estimation of Jumps in Linear Systems," IEEE Trans. Automa. Contr., Vol, AC-21, pp. 108-112, February 1976.

4. Gelb, A., ed., Applied Optimal Estimation, M.I.T. Press, Cambridge, Massachusetts, 1974.

5. Willsky, A.S., Deyst, J.J., and Crawford, B.S., Adaptive Filtering and Self-Test Methods for Failure Detection and Compensation," Joint Automatic Control Converence (Austin), June 1974.

EIGHTH BIENNIAL GUIDANCE TEST SYMPOSIUM

AN ADVANCED SOFTWARE MECHANIZATION FOR CALIBRATION AND ALIGNMENT OF THE ADVANCED INERTIAL REFERENCE SPHERE (AIRS)

AUTHORS: D. J. SIFTER
V. D. HENDERSON

ROCKWELL INTERNATIONAL
AUTONETICS DIVISION
ANAHEIM, CALIFORNIA

ABSTRACT

This paper describes an advanced software mechanization that provides continuous calibration and alignment of a ballistic inertial navigation system without the use of external reference aids. The mechanization was developed by the Autonetics Division of Rockwell International for use with the Advanced Inertial Reference Sphere (AIRS), designed and built by the Charles Stark Draper Laboratory. The mechanized inertial system was successfully tested in the recent Missileborne Performance Monitoring System (MPMS) Program, completed in July of 1976.

A self-contained operational mechanization for a ballistic inertial navigation system must provide an update of inertial instrument calibration parameters to maintain weapon delivery accuracy. Typically, the calibration update has been performed in an off-line condition that penalizes the alert status of the missile system. The amount of time off-line and the frequency of the off-line update has been dictated by the stability characteristics of the inertial instruments.

The continuous calibration and alignment mechanization described herein achieves constant surveillance and correction of critical IMU error parameters, including platform alignment. This is accomplished by continuously rotating the inertial platform about vertical and level axes while processing accelerometer data with a Kalman filter. The Kalman filter is mechanized in an on-line system computer to optimize the error estimation and dynamic control of the inertial platform. This is in accordance with a priori statistics of parameter instabilities of the instruments. The strategic alert status time is maximized since the missile system can be launched at any time.

The paper briefly describes the evolution of the mechanization concept from its conception in the SABRE IMU test program (a predecessor of the AIRS IMU), through its application in the MPMS/AIRS Program, to its current implementation for the Autonetics Advanced Inertial Platform (ASP) gimbaled IMU. The latter platform also uses the same Third Generation Inertial Instruments (TGII) that were developed for the AIRS IMU.

A brief snapshot of the "First Generation" mechanization software for the SABRE IMU Program is presented. SABRE experience revealed the necessity of new approaches and methodology for calibration and alignment of a SABRE or AIRS-type IMU. The successful development, implementation and testing of this mechanization provided a proven baseline for the Second Generation mechanization which was tailored for the MPMS/AIRS IMU application.

The bulk of the presentation is devoted to describing the techniques and rationale for the Second Generation Software mechanization. In this mechanization, a number of novel and innovative techniques were developed and used to enhance performance and aid in the developmental testing and performance evaluation process. A qualitative comparison of accuracy from error analysis predictions and test results obtained on the MPMS/AIRS system is made. The resulting software mechanization and its successful test results now provide a proven baseline for Third Generation Software currently being developed for the Autonetics ASP system.

The Third Generation Software has special features tailored to the TGII, and thus, has application to both the ASP and AIRS IMU(s). A snapshot description of this mechanization and its features is presented.

An Advanced Software-Mechanization for Calibration and Alignment of the Advanced Inertial Reference Sphere (AIRS)

by

D. J. Sifter and V. D. Henderson
Rockwell International, Autonetics Division

AN ADVANCED SYSTEM-MECHANIZATION IS DESCRIBED

An advanced software mechanization that provides continuous self-contained calibration and alignment of a ballistic inertial navigation system is herein described. The mechanization was developed by the Autonetics Division of Rockwell International for use with the Advanced Inertial Reference Sphere (AIRS), designed and built by the Charles Stark Draper Laboratory. The mechanized AIRS inertial platform was successfully flight tested in the recent Missileborne Performance Monitoring System (MPMS) Program, completed in July of 1976.

System Readiness Time is Maximized

A self-contained operational mechanization for a ballistic inertial navigation system must provide an update of inertial instrument calibration parameters to maintain weapon delivery accuracy. Typically, the calibration update has been performed in an off-line condition that penalizes the alert status of the missile system. The amount of time off-line and the frequency of the off-line update has been dictated by the stability characteristics of the inertial instruments.

The continuous calibration and alignment mechanization described herein achieves constant surveillance and correction of critical IMU error parameters, including platform alignment. This is accomplished by continuously rotating the inertial platform about vertical and level axes while processing accelerometer data with a Kalman filter. The Kalman filter is mechanized in an on-line system computer to optimize the error estimation and dynamic control of the inertial platform. This is in accordance with a priori statistics of parameter instabilities of the instruments. The strategic alert status time is maximized since the missile system can be launched at any time.

The Mechanization Concept Evolved

The evolution of the mechanization concept is briefly described from its conception in the SABRE IMU test program (a predecessor of the AIRS IMU), through its application in the MPMS/AIRS Program, to its current implementation for the Autonetics Advanced Stabilized Platform (ASP) gimballed IMU. The latter platform also uses the same Third Generation Inertial Instruments (TGII) that were developed for the AIRS IMU.

A brief snapshot of the "First Generation" software mechanization for the SABRE IMU Program is presented. SABRE experience revealed the necessity of new approaches and methodology for calibration and alignment of a SABRE or AIRS-type IMU. The successful development, implementation and testing of this mechanization provided a proven baseline for the Second Generation mechanization which was tailored for the MPMS/AIRS IMU application.

The bulk of the presentation is devoted to describing the techniques and rationale of the Second Generation Software mechanization. In this mechanization, a number of novel and innovative techniques were developed and used to enhance performance and aid in the developmental testing and performance evaluation process. A qualitative comparison of accuracy from error analysis predictions and test results obtained on the MPMS/AIRS system is made. The resulting software mechanization and its successful test results now provide a proven baseline for Third Generation Software currently being developed for the Autonetics ASP system.

The Third Generation Software has special features tailored to the TGII, and thus, has application to both the ASP and AIRS IMU(s). The data from the MPMS Program provided a basis for refining the detailed TGII error models used for calibration and alignment purposes. These refinements account for errors such as those produced by motions of the gyro floats, which are very small but significant for attaining ultra-precise accuracy. They also account for trending and other long-term dynamic behavior of certain critical instrument parameters. For completeness, a brief overview of this mechanization and its features is also presented.

THE MECHANIZATION IS TAILORED TO OPERATIONAL REQUIREMENTS

The complete version of the inertial system mechanization was developed from design rationale evolving from Autonetics' involvement in the previously mentioned programs. It is called the "Advanced Inertial Mechanization" (AIM). It has been tailored to operational requirements leading toward an operational application.

The Third-Generation AIM is Described

The AIM is an integrated inertial system mechanization that provides not only self-contained calibration and alignment, but also both cruise and ballistic navigation modes. It provides for determination of the inertial instrument calibration parameters, including instrument axes misalignments, and platform axes orientation relative to a locally level (or launch-point) earth-referenced geographic frame. Velocity and position of the navigation vehicle are determined with respect to a geographic north, west, and vertical earth-referenced frame.

The multitude of calibration parameters are, with few exceptions, determined in a completely automatic, self-contained way. The orientation of platform axes relative to earth axes is also determined without the use of direct external reference aids. Only the indirect influence of earth's gravity and spin rate vectors is utilized in the calibration and alignment process. Navigation is accomplished in the ordinary manner of integrating sensed accelera-

tion, corrected for gravity and Coriolis effects, to extrapolate from a known set of initial conditions - velocity, position, etc. However, the navigation portion of the mechanization and the computational algorithms used for its implementation are unusual with regard to the methods used for providing precision accuracy while retaining simplicity and commonality with other portions of the mechanization. Integration of the velocity, relative to earth, is performed in the platform frame using a novel recursive mechanization, giving a compact real-time solution equivalent to a high-order integral series.

There are four basic system-performance operating modes provided by appropriate initialization and linkage of the basic functional building blocks comprising the mechanization. A rapid align mode is provided for IMU start-up to quickly locate the local gravity and earth's spin vectors in the platform frame. This coarse alignment precedes a rapid cal/align mode designed to provide system calibration and nominal alignment in a reasonable time following start-up. After the initial calibration and alignment is accomplished, a continuous optimum cal/align mode is entered, where platform level-axes rates are greatly reduced and precision calibration and alignment are achieved and maintained. A navigation mode provides for both aided and unaided inertial navigation.

The AIM has Special Features

The AIM utilizes a modular concept based upon functional building blocks. Many of the functional modules are common to each of the operational modes mentioned above. Thus, the integrated mechanization approach eliminates duplication of computer program coding and checkout, the use of tape fills for overlay programs, and the associated initialization and mode transition problems. Another feature of the modular concept is the ease and efficiency with which future changes and improvements can be made to the computer implementation of the mechanization. Impact of coding change and checkout is localized to the particular modules or functions being modified.

AIM differs from many of the IMU mechanizations of the past in its design to provide both calibration and alignment in a completely self-contained way, not requiring the use of externally applied reference aids. Its navigation modules also differ in many respects from past mechanizations in the methods of providing precision accuracy and the selection of coordinate frames for minimizing dynamic behavior of data in effecting solution of the differential equations for navigation.

The interrelationship among functional modules providing the cal/align and the navigation operating modes is shown in Figure 1 and Figure 2, respectively.

An ASP Version of AIM is being Implemented

Since the TGII are used in both the ASP and the Advanced Inertial Reference Sphere (AIRS), the AIM is applicable to both IMU(s). The particular implementation of AIM for the ASP IMU program is being coded in the Interdata 8/32 computer. This computer program has been given the name "ACES," an acronym for "ASP Calibration and Evaluation Software."

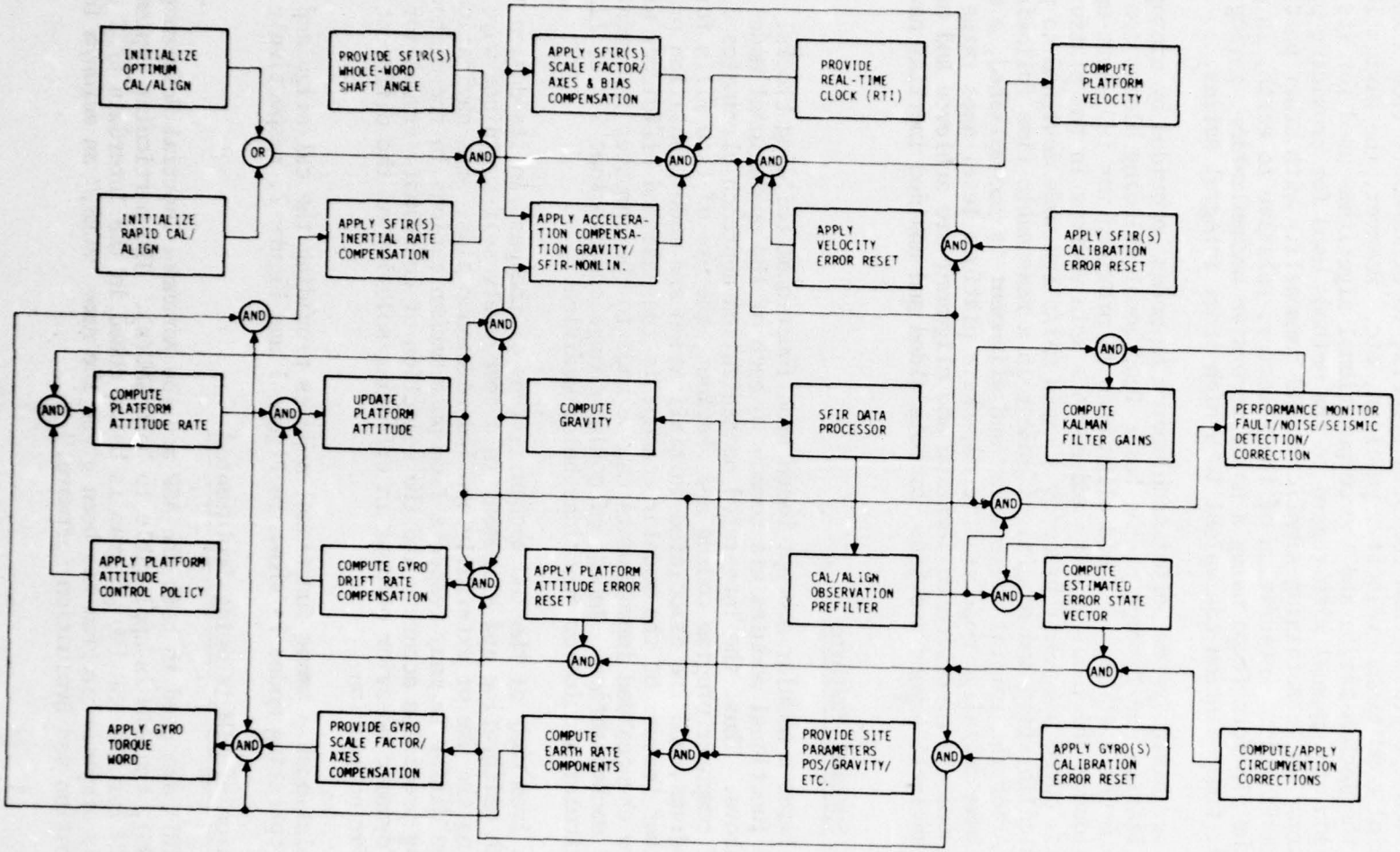


Figure 1. Optimum Continuous Cal/Align

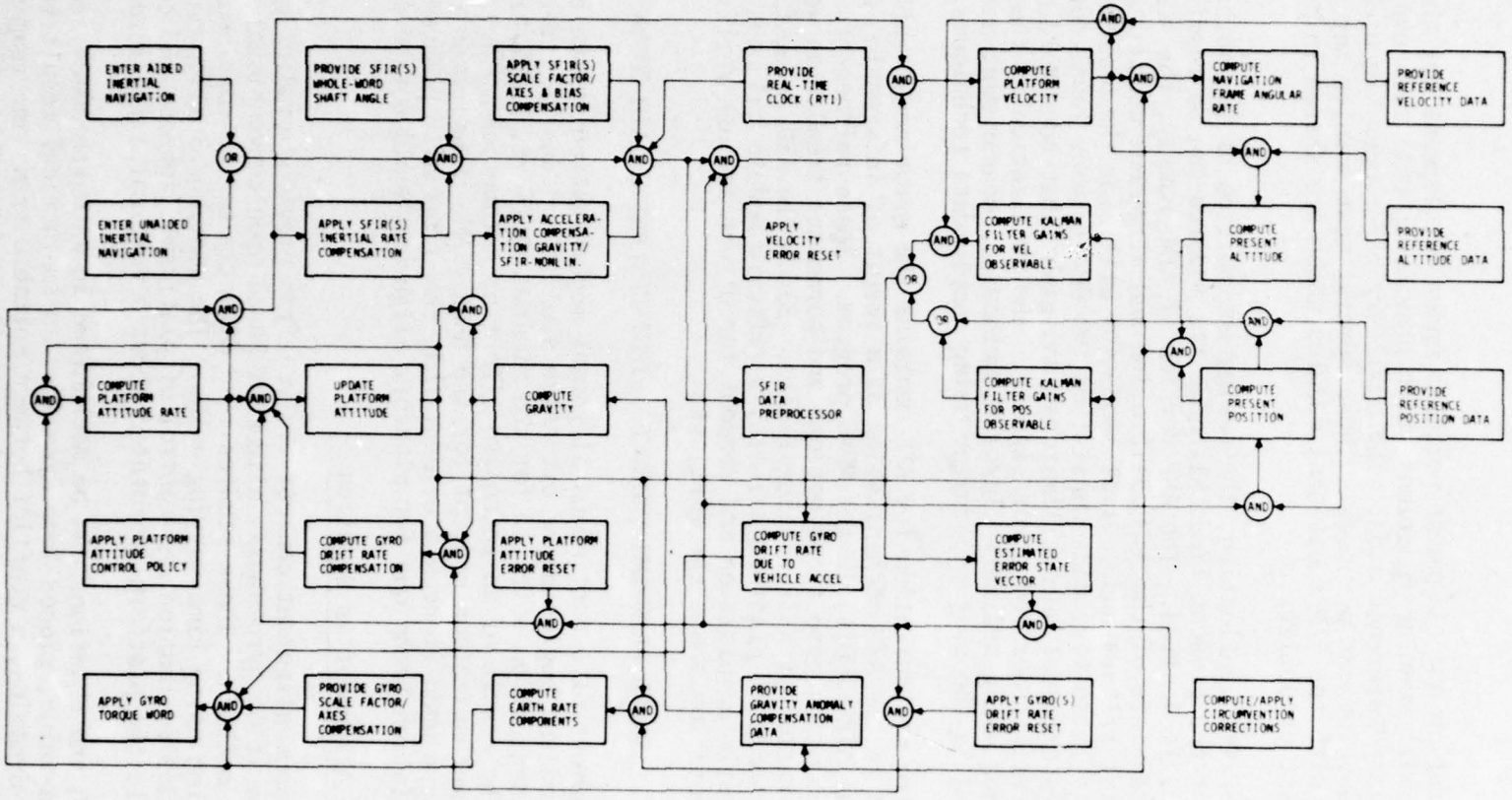


Figure 2. Aided/Unaided Cruise Navigation

The calibration and alignment portions under development for the ASP are being augmented with modular functions which provide special test capability involving auxiliary reference aids. The auxiliary references are used with ASP for hardware development purposes. These special test modules integrate very naturally with the AIM functional modules which are shared in providing the special test capability.

For the ASP IMU application, the navigation portion of the mechanization is omitted for the present time; although its modules can be readily added at a later time, if desired. The ASP version of AIM; namely, the ACES software program, consists of the AIM calibration and alignment mechanization augmented with special filters and control loops for utilizing the auxiliary reference test aids. These test aids consist of two double-axes level detectors, two double-axes external autocollimators, and gimbal bit-edge holding capability using internally derived error signals. The utilization of these aids is accomplished using ordinary classical methods of measurement and control, implemented in the system computer using sample-data techniques.

The software mechanization for ASP contains the error model refinements which were added to the AIM mechanization as a result of information gained from testing the AIRS IMU(s) in the MPMS program. These refinements include models for accommodating gyro float motions and parameter trends, as well as for on-line calibration of SFIR nonlinearities. Since the ASP is equipped to provide optical readout of platform azimuth, a software module has been added to perform automatic acquisition and readout for direct azimuth verification during platform rotation about the vertical.

SABRE PROGRAMS PRODUCED FIRST-GENERATION AIM SOFTWARE

The development of a continuous alignment mechanization, known by the acronym SCAT, marked the beginning of extensive studies and design efforts to develop system mechanization software for the floated platform, SABRE/AIRS-type IMU. SCAT was the result of an intensive effort at Autonetics to develop a viable alignment mechanization concept for the SABRE IMU. Comprehensive in-house studies began when it became evident that the originally planned gyro wheel-speed modulation technique for platform alignment would not be adequate.

Continuous Alignment is Required

The continuous alignment concept evolved from previous studies of discrete-multiple-position gyrocompass alignment based upon conventional closed-loop, fixed-gain methods. These studies lead directly to the continuous alignment mechanization using time-varying gains. The continuous alignment mechanization provides estimation and control of platform alignment and certain gyro errors while the platform is rotated about a vertical axis, relative to earth.

Even though the equations can be mechanized in an earth-space frame, with fixed eigen-value, closed-loop dynamics, an impractical result is obtained. With fixed dynamics, a conflict between suitable transient response and steady-state noise attenuation exists. An absurdly long settling time to steady-state condition typically prevails. It was quickly established that the Kalman filtering technique provides a good solution to the time-varying gain requirement,

and is essential to a useful continuous alignment mechanization.

Later studies confirmed the necessity of the continuous alignment technique for the SABRE/AIRS-type IMU design. The SCAT mechanization resulted. It consisted of a 12-state error model, using a Kalman filter formulation, which estimated and corrected level-axes gyro scale factor and axis misalignment errors, and three gyro bias drift rates, in addition to the platform attitude alignment errors. The mechanization was successfully implemented and tested on the SABRE IMU S/N-5 in 1969.

CACC Mechanization Establishes AIM Concept

It was also confirmed in the mechanization studies that addition of suitable rotations of the platform about level axes allows the remainder of the IMU calibration parameters, observable in a one-g field, to be measured. This result provided the basis for a continuous alignment continuous calibration mechanization (CACC), developed in the Missileborne Performance Instrumentation Mechanization Study (MISPIMS) program. This mechanization paved the way for the MPMS program mentioned earlier.

The CACC mechanization modeled nine of the PIGA errors, thirty-six gyro errors, and platform azimuth error in two Kalman filter formulations. The 37-state gyro and azimuth alignment filter used level-axes platform drift rates for observables. This permitted the two platform leveling-error states to be estimated and corrected independently, from PIGA data, using conventional techniques. A prefilter processed 10-msec data from the PIGA(s), providing least-squares curve-fits, which measured PIGA-sensed platform acceleration (tilt) and acceleration rate (tilt rate). These data provided the error observations for the leveling loops and the gyro estimation filter, respectively. The error in measured gravity magnitude, as determined by the total output from the three PIGA prefilters, was used for PIGA calibration. This Autonetics innovation results in an accelerometer calibration that is virtually insensitive to platform attitude errors arising from such sources as inadequacies in the gyro error models, lateral vibration or shaking of the IMU, etc.

Additional features of the CACC mechanization included dynamic acceleration compensation, where estimated components of platform acceleration were continuously computed and subtracted from those sensed by the PIGA(s). This formed acceleration error measurements that could be accurately modeled in the estimation filters, while the platform was tumbling about level axes. The estimated platform attitude data was provided by a direction-cosine algorithm which was updated by the platform alignment-error estimation and control process.

A gyro scale factor and axes alignment calibration technique called reference torquing was also utilized in the CACC mechanization. Although originally conceived and implemented by Autonetics in an unrelated IMU program in about 1962, the reference torquing application for the floated platform IMU was first established on the SABRE system. The SCAT mechanization was used. In the CACC mechanization, reference torquing greatly improved the quality of gyro calibration by improving the separability of errors and by reducing the sensitivity to measurement noise.

Also, a self-contained fault detection capability was provided in the CACC mechanization. It used the tilt-rate outputs of the PIGA data prefilter. This measurement is very sensitive to anomalous system operation. And it rapidly exhibits a distinction between such errors as spurious PIGA data noise, or transmission error, and anomalous error due to shifting of a gyro bias rate. In the first case, the filter gains were zeroed to eliminate the "wild-data" point. In the latter case, they were enhanced to properly re-bias the offending gyro.

The CACC mechanization was implemented in an IBM-1800 computer system to provide on-line calibration and alignment of the SABRE S/N-5 IMU. The mechanization was successfully tested in the SABRE laboratory at Autonetics, near the conclusion of the MISPIMS program. Thus, a sound baseline mechanization design was established for the MPMS/AIRS version of AIM which was soon to follow.

SECOND-GENERATION AIM PERFORMED IN MPMS/AIRS MISSION

The Advanced Inertial Mechanization concept, which evolved from the CACC mechanization, was applied in developing operational ground software for the MPMS/AIRS flight test mission. This effort produced the second-generation version of the AIM concept. Most of the features of the CACC mechanization that enhanced self-contained calibration and alignment performance on the SABRE IMU were retained in the MPMS/AIRS application. However, some changes in the mechanization were made to accommodate the MPMS system performance specifications and certain design characteristics peculiar to the MPMS/AIRS IMU.

Trade-off studies were performed in selected areas, to aid in determining the appropriate changes, where alternate methods existed and the best choices were not obvious. The final result was a mechanization that satisfied the MPMS mission requirements in an effective way, yielding results which were for the most part in reasonably good agreement with performance predictions. One exception to predicted performance was a deterministic bias error which resulted from an unexpected error source arising from gyro float motion. The bias error, revealed in flight, was unobservable on the ground, during the cal/align process. Changes have been made in the third-generation version of AIM that will allow observation of the error during system calibration, with the subsequent result of estimating and compensating to remove its effect.

During the MPMS program, a considerable amount of system test data was obtained. From these data, a number of error mechanisms, not catastrophic but significant in magnitude, have been identified. This has made possible the further refinement of the cal/align error models for use in the updated third-generation version of the AIM.

MPMS/AIRS Mechanization Designed Concurrently with IMU Development

The MPMS operational ground software program was developed specifically for satisfying the MPMS "performance monitoring" mission requirements. The mechanization was programmed in the Honeywell 701P flight computer (IDCU). The computer program is called the "Performance Evaluation Program" (PEP). The

MPMS program schedule required parallel and concurrent hardware and software development. This required the initial software to be developed and verified by analyses and simulations, without the benefit of an AIRS IMU.

The software mechanization had to satisfy the requirements for supporting the in-plant operations, including IMU integration, design verification and acceptance testing, and pre-launch operations at Vandenberg AFB. The cal/align portion of PEP was required to provide specified accuracy performance requirements, based upon realization of given AIRS error models and inertial instrument performance data statistics. These system descriptions, although the best available at the time, were based upon a limited amount of test data. For this reason, much attention was given to mechanization design features for minimizing the sensitivity of critical calibration parameters in a given area to error-model deficiencies in another area. A number of novel and innovative features of the mechanization are the result.

Mechanization Design Features Tailored to AIRS IMU

A number of detailed design features have resulted from experience with testing the SABRE and AIRS IMU(s). Several of the features were retained from the SABRE CACC mechanization and were incorporated in the original PEP design. Others were added later, as a result of system characteristics uncovered by data from testing the MPMS/AIRS IMU. There are further design refinements that are needed, but could not be included in the on-line PEP program due to program schedule limitations. These latter features have been incorporated in the third-generation AIM design; and were, in some cases, applied post-test or off-line to the MPMS/AIRS PEP data. Some of the more significant features originally included are listed below.

SFIR Data Prefilter Provides Measurement Data

A SFIR data prefilter provides observables for the Kalman filters used for SFIR and gyro calibration and platform alignment. The prefilter groups the propagations of all error states, observed in the SFIR data, into three categories, or composite states, modeled over a relatively short prefilter period of six minutes. These composite states are acceleration error-rate (drift rate), acceleration error (platform tilt), and velocity error. The prefilter performs least squares data fits to the velocity-error data.

The prefilter input from the SFIR(s) occurs at a rapid 100-Hz rate, while the output rate to the cal/align filters is reduced to one output each six minutes. All of the system calibration error states are modeled by the cal/align filters in terms of the composite acceleration error state. In addition to providing observables, these output data are also used in a performance-monitoring/fault-detection scheme, and to properly initialize the platform velocity at the time of launch. The initial velocity is otherwise subject to error from quantization, vibration, and SFIR readout noise. An important feature of the prefilter is its ability to filter out what would otherwise be very significant components of error in the SFIR data. These are due to various readout errors, the compensation of which would otherwise require a relatively complicated error model. The prefilter makes use of a novel least-squares algorithm consisting of a linear combination of sequential algebraic sums of the input data.

Gravity-Residual Technique Insures Precision SFIR Calibration

In a self-contained calibration mechanization, it is necessary to isolate the accelerometer (SFIR) calibration, as much as possible, from the gyro calibration and platform alignment process. This protects the SFIR calibration from undue sensitivity to relatively small gyro-related modeling errors; which are small only from the gyro calibration accuracy point of view. This isolation is required to satisfy high precision calibration requirements of the SFIR triad, for both ballistic flight accuracy, and for providing the primary reference for detecting platform alignment and gyro calibration errors. The gravity residual accelerometer calibration technique provides this isolation.

The gravity-residual technique forms the calibration error observable from the three instrument outputs. The outputs, suitably combined and compensated, yield the vertical component of the acceleration error vector. First-order leveling error (misalignment or erroneous knowledge of the vertical direction) is only present in the level components of the acceleration error vector. Thus, the sensitivity of the vertical component of the error observation to leveling error (including all contributions due to unmodeled platform drifts, etc.) is a second-order effect. The sensitivity is only 0.5-ppm/mrad, or over 2,000 times less sensitive than the 5-ppm/$\widehat{\text{sec}}$ sensitivity which is incurred by calibrating PIGA and gyro parameters together, from the same level-axes observables. Resolving the error to vertical produces higher-order coordinate functions describing the error propagations. However, observability studies have shown that all but one of the identified SFIR parameter error-states are observable in a one-g field. This exception is independent of the mechanization technique.

The gravity residual method can be described best, geometrically, as being the determination of the distance between the surfaces of a spheroidal shell and a spherical shell of unit radius. These surfaces represent the mappings of the measured and true direction-cosines, respectively, of the vertical unit-vector. With no calibration error, the spheroid converges to a unit-sphere. With calibration errors, the surface becomes distorted. Each error affects the contour of the surface in a particular region. By rotating the platform axes, the "g-vector" probes the contoured surface, generating the error map. The PEP mechanization utilizes the gravity-residual calibration feature to insure precision SFIR calibration.

Gyro Reference Torquing Technique Calibrates Gyro Frame

The gyro reference torquing technique provides precision calibration of scale-factor and axis alignment errors. The gyro reference torquing technique can be used during calibration and/or alignment. It provides rapid calibration of the gyro frame with respect to an orthogonal acceleration reference frame. It calibrates independently of the earth-rate coupling effect normally depended upon for an observable measurement of the errors.

Perturbation torquing rates are applied to each of three orthogonal platform axes, via gyro torquers. These perturbation rates increase the signal-to-noise ratio of the measurement data with regard to gyro frame errors; and the modulation permits rapid separation of these errors from other errors that produce

platform drift rate. When a perturbation rate is applied to the ith axis, the ith axis torquing scale factor error causes a drift rate about the ith axis. Also, drift rates occur about the jth and kth axes when ith axis is torqued and the jth and kth axes are misaligned about each other.

The advantages of using the technique can be better appreciated when one considers the gyro calibration observability problem in some detail. Briefly, there are five classical categories of platform drift rate to be calibrated. There are three scale-factor errors, six axis misalignments, three bias drift rate errors, twenty-four acceleration sensitive parameters (nine g-sensitive and fifteen g^2-sensitive), and platform azimuth alignment error. Without reference torquing, there are only two references, viz., the earth-rate and gravity vectors. Thus, the platform tumbling rate (mobility rate) must be such as to allow these vectors to "probe" or pass along many directions in the platform frame so that distinguishing features for the various error propagations can be established. Since the magnitude of the mobility rate is limited (for practical reasons), considerable time is required in rotating the platform. During much of this time, errors are being observed with very low signal-to-noise ratio measurements. With reference torquing, an additional reference vector is supplied which produces observations having relatively high signal-to-noise ratios.

On-Line Feedback Control Technique Provides Advantages

An important feature for supporting special investigative testing is the MPMS PEP mechanization's unusual design for data acquisition, on-line utilization, and logging. While the on-line processing provides real-time calibration and alignment, the feedback control is not used to constrain the IMU platform. Rather, it adapts the computer mechanized model to match the IMU dynamics, via parameter estimation. Thus, raw SFIR data, unaltered by on-line control, can be recorded for independent off-line processing and interpretation, should it be necessary or desirable to do so.

This mechanization design feature was developed for the PEP version of AIM in anticipation of modeling problems and other anomalous operation typically present in design phases of a developmental IMU. It has been retained in AIM as an operational tool, providing recorded or otherwise stored data for off-line self-test, diagnostic, and fault location purposes. Signatures, or symptoms, of abnormal system operation are not garbled by the on-line control.

The chosen method of on-line processing is designed around a precision direction cosine computation routine that keeps the computational platform axes (or computer axes) precisely updated with respect to the earth axes. During alignment, the computer axes are positioned collinear with the physical platform axes. The error parameters determined during calibration are used to compute the platform drift rate which is applied real time to the computer axes direction cosine solution. This process causes the computational representation of the platform axes (computer axes) to follow the real physical platform axes which are being driven along the calibration trajectory via gyro torquing rates from the trajectory control routine.

Since the error compensation is applied to the "computational IMU" rather than the physical IMU, the raw data from the platform accelerometers are unaffected. They can be recorded and analyzed off-line with the results being completely independent of the on-line process.

Also, another important feature of the above arrangement is the alignment control for updating level and azimuth errors. Normally, these corrections are administered to the physical platform via a torquing rate applied during some portion of the estimation filter computational time interval. Because of this delay in applying control, it is necessary to perform costly extrapolation or propagation of portions of the estimated error state vector. With the error update being applied to the computational platform, level and azimuth errors, as well as all other estimated errors, are corrected instantly, for all practical purposes, in a whole-value form. This would correspond to applying impulses of error correction rates, when making an analogy to control of a physical system. Since there is no delay, there no longer is a need for cumbersome and costly extrapolation of the control. Thus a significant simplication and reduction of computer requirements result.

Direction Cosine Solution Yields High Precision with Low Duty Cycle

The direction cosine solution required in providing the method of calibration and alignment feedback control, previously described, is an innovation. The dynamic acceleration compensation, also previously discussed, requires accurate direction cosine data at a 10-msec interval. In order to minimize the computer computational load in providing these data, difference equation techniques for interpolating over each 6-min computational period are used. This results in a very minimal influence upon computer duty-cycle, but it requires that direction cosines for the next upcoming time interval be computed in advance. Since the gyro drift rates are functions of components of gravity in the platform frame (i.e., direction cosines of the vertical unit-vector), and they are also input driving functions of the direction cosine equations, a system of nonlinear differential equations results.

The direction cosine algorithm provides a compact iterative solution of these nonlinear equations, requiring three passes for convergence to accuracy beyond that required for the MPMS application. The algorithm was developed and proven, in an Autonetics IMU development program, for use on the precision ESGN inertial navigator for marine system application. The developed computational algorithm was adaptable to the MPMS/AIRS application with relatively little change. Both angle and rate tracking errors are well below those satisfying MPMS requirements.

Given the direction cosines at the beginning of a six-minute period, whole-values are computed at two intermediate points and at the end of the interval. These are the data interpolated via a third-degree polynomial generated with difference equations. Only simple additions are needed for interpolation.

Gyro Calibration Error State Vector Expanded

A review of available information was made regarding the best description of an error model for the TGG(s) to be used in the design of the AIRS mechaniza-

tion. The minimum number of error states required to define the significant gyro accuracy performance characteristics was the same as had previously been used in Autonetics studies. In addition to these error states, modeled and estimated in the calibration mechanization, there have since been other errors discovered, such as trending of certain gyro parameters and errors induced by motions of the gyro floats. Provision has been made for modeling and compensating, in the new version of the AIM mechanization, to account for these errors.

In some of the on-line MPMS/AIRS system test results, the effects of these unmodeled errors was noticeable. However, manual calibration of trend error was possible from hand-plotted data. Provision for on-line application of the corresponding error compensation was made where necessary for alignment. In other cases, off-line post-test data corrections were made. A reasonably good overall agreement between system test results and those predicted from analyses was obtained, with the exception of a few calibration parameters having significant sensitivity to the unmodeled errors previously discussed.

MPMS/AIRS TEST RESULTS CONFIRM MECHANIZATION DESIGN

A comparison of calibration repeatability results, from typical system test data, and parameter estimation repeatability, predicted from computer analysis programs, is presented. The ratio of the estimated standard deviations from the test data to the computed standard deviations from analyses is given. The calibration repeatability data was obtained from the MPMS/AIRS Flight System #1. The data set consists of pooled data, over the three platform-mounted inertial instruments, from four test calibrations performed during October and November of 1976. The resulting sample is of size twelve.

A prediction of accuracy performance capability was obtained from results of an error variance analysis, accomplished by using the dual-state (filter/system) state-space error analysis technique. System error statistics were obtained or inferred from a limited amount of instrument test data and some of the IMU design specifications. The filter error statistics corresponded to those modeled in the on-line flight computer program. The results are tabulated in Table I.

In Table I, the entries marked with an asterisk need some additional explanation. The ratios entered for the D_I and D_S parameters were obtained after removing, ex post facto, somewhat excessive deterministic trends from their estimates. Analyses predict a significant sensitivity of gyro axes alignment errors and some of the gyro g-squared sensitive parameter errors to these inputs. The deleterious effects appear to be seen in the corresponding entries, for which no effort to effect their removal was made. A similar data set for Flight System #2 yielded results similar to those tabulated, except that SFIR ratios were slightly larger, and gyro ratios with the asterisk were somewhat smaller. This result corresponds to a generally less stable SFIR bias and substantially smaller D_I and D_S trends on Flight System #2. These characteristics were observed in test data throughout the MPMS/AIRS program.

TABLE I.

COMPARISON OF CAL/ALIGN TEST RESULTS
WITH PREDICTED RESULTS FROM ANALYSIS

Inertial Instrument Calibration Parameter Estimation Error	Ratio of Measured Std. Dev. from Test Sample to Predicted Std. Dev. from Analysis Program
ACCELEROMETERS (SFIR)	$\hat{\sigma}/\sigma$
Scale Factors	0.22
Axes Align	0.013
Bias Acceleration	0.29
GYROS (TGG)	
Scale Factors	0.84
Axes Align	2.80 *
Bias Drift Rate	0.94
GYRO G-SENSITIVITIES	
D_I (Input Axis)	1.20 *
D_S (Spin Axis)	0.92 *
D_O (Output Axis)	0.95
GYRO G^2-SENSITIVITIES	
DII	2.3 *
DSS	2.6 *
DIS	0.78
DIO	2.6 *
DOS	1.1
	*See text

In proper context, the results from system test data obtained with the PEP software mechanization are in generally good agreement with accuracy predictions based upon a best knowledge of system error statistics.

A SUMMARY DESCRIPTION OF THE AIM CAL/ALIGN IS PRESENTED

The basic mechanization concept of the calibration and alignment portion of the AIM is further illustrated with a simplified block diagram shown in Figure 3. This diagram provides a visual summary of significant features of the mechanization, which have been previously described. A summary description and discussion of the cal/align observability policy is also given.

Basic Cal/Align Mechanization Structure is Illustrated

The basic structure of the calibration and alignment portion of the AIM mechanization is depicted in the illustration given in Figure 3. The stabilized inertial platform is shown being influenced by local gravity, earth rate, and platform or gyro drift rate. The true components of sensed acceleration along platform axes are denoted by the three-vector $\underline{A}(t)$. These components of true acceleration are corrupted by acceleration errors, $\Delta\underline{A}(t)$, related to the platform mounted SFIR(s), the primary reference or measuring devices for the mechanization. The SFIR errors have components both deterministic and random in nature. The deterministic errors obey a known error model and the random errors are approximately characterized statistically from data obtained in past testing. Another corrupting error is an additive random acceleration error $\delta\underline{A}(t)$ and random errors originating on the velocity-level, not shown, which are modeled in the details of the actual mechanization.

The total SFIR measurement data is operated upon by a prefilter which attenuates or removes the high-frequency components of error or noise (SFIR readout harmonics, etc.) that cannot be modeled in a practical manner in subsequent Kalman filtering. Also, the data rate is reduced by the prefilter to practical iteration intervals for Kalman filters used to estimate the various calibration parameter errors of the SFIR(s), gyros, and related platform errors. This uncompensated or "raw data" from the SFIR(s) is recorded on magnetic tape and made available for special off-line computer processing, a very desirable feature in the development of a new IMU. This capability is provided by applying the on-line control to the computer representation of the inertial platform system, the output acceleration of which is subsequently compared with the measured acceleration to provide an error signal. This is shown in Figure 3 where SFIR data is corrected with the computer's best estimate of SFIR calibration parameters. The resulting compensated measurements are next compared with the computer's best estimate of the true acceleration components, and the error components are then resolved along earth axes, both level and vertically oriented.

The vertical component of error contains only SFIR parameter errors and measurement noise. Thus, upon suitably positioning the platform through a sequence of orientations, or a calibration trajectory, relative to the local gravity vector, the vertical component of acceleration error (or its integral) is used to calibrate the SFIR parameters. With the SFIR errors removed, the horizontal or level components of acceleration error reflect the difference

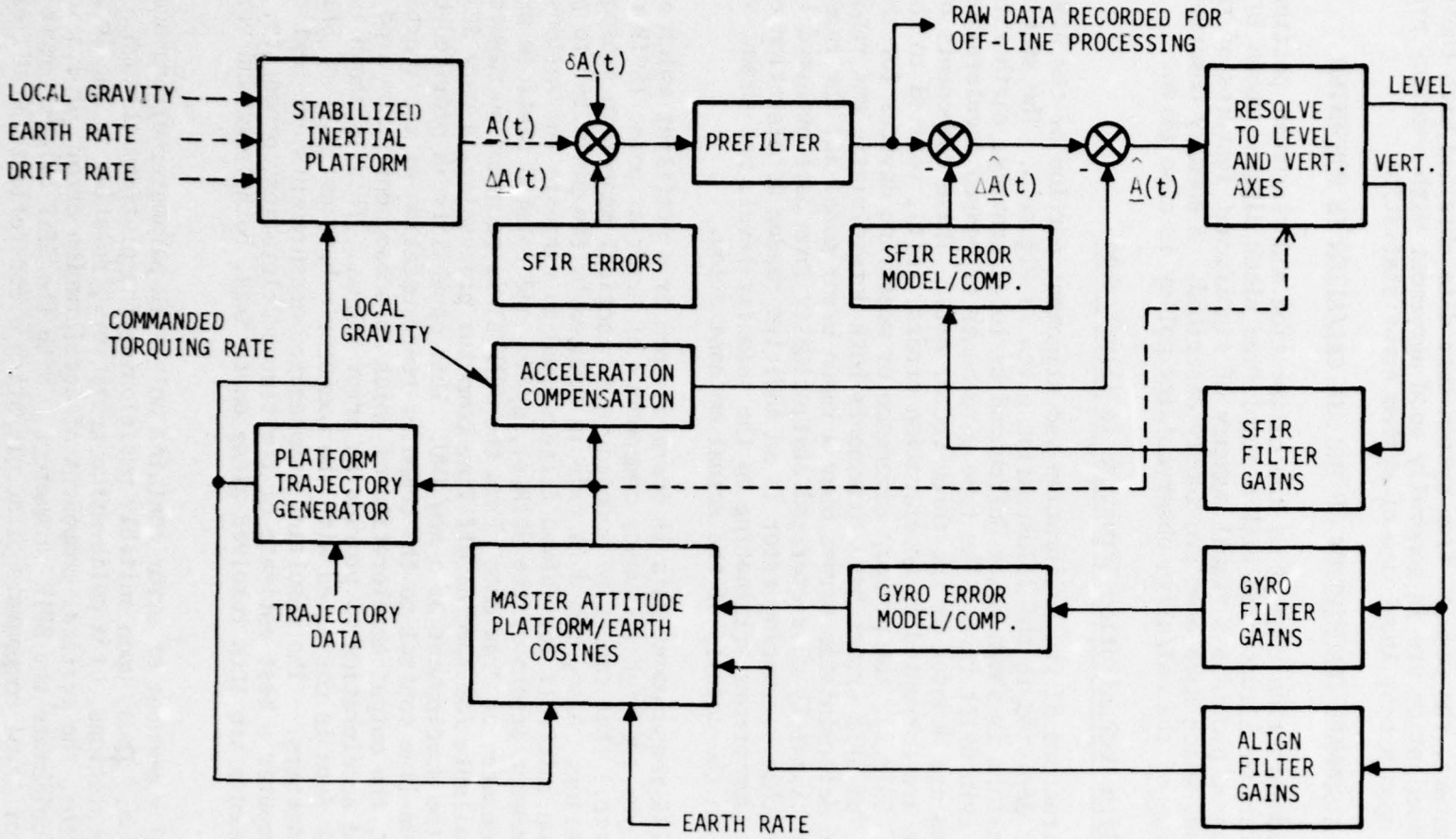


Figure 3. An Illustration of the Cal/Align Portion of the Advanced Inertial Mechanization (AIM)

between actual gyro parameter errors and those accounted for in the computer error model. Also, the level components of error reflect the misalignment of the actual platform axes and those corresponding to the computer model or computational frame.

Because the various gyro errors and platform alignment errors have distinct time propagations, or waveforms, in the level acceleration measurements, a Kalman filter modeling the dynamic error propagations can separate the errors and effect their calibration. Removing the calibration errors improves the computer's estimate of the true acceleration components and their dynamic behavior; thus reducing the error observable and ultimately converging the process to steady-state computer estimates of the calibration parameters.

The above discussion concerning the separation and calibration of parameters implies that the platform is rotated along a sequence of orientations on a trajectory path relative to earth-rate and gravity vectors such that the condition of observability of errors is achieved. Suitable trajectories for this purpose have been identified and it is generally true that a desirable trajectory for gyro calibration and alignment is also a desirable trajectory for SFIR calibration. This results from similarities in the form of the gravity-residual SFIR(s) error calibration model and that of a single-axis, floated gyro of the type used on the AIRS IMU.

It can be observed in Figure 3 that the commanded gyro torquing rate is applied to both the actual platform gyro set and to its computer modeled representation. Thus, both the platform and computer model rotate together, and the resulting error measurement reflects only the differences in relative orientation and the calibration parameters of the two. The platform can be positioned arbitrarily so long as observability is provided for the process.

One Platform Trajectory Calibrates All Errors

Near optimum SFIR and gyro calibration occur on the same observation trajectory. The platform-fixed orthogonal triad of reference axes used in defining the trajectory is independent of instrument mounting orientations and thus can be chosen arbitrarily. The only constraints imposed would be due to physical hardware characteristics. For instance, the SFIR input axes should not dwell in the level plane where the low data rate from the instrument and other corrupting influences (coning, etc.) make the data unusable. Also, it is desirable to cause only one input axis to cross the level plane during any 90-degree level rotation.

Level Mobility Rate Degrades Azimuth Accuracy

Gyrocompass azimuth alignment accuracy is degraded with increasing magnitude of the level mobility rate required for calibration. This effect results from the geometrical aspect of rotating a pseudo (or equivalent) vertical gyro away from the vertical position and toward the level plane where components of uncompensated drift rate corrupt the gyrocompassing measurement data. Drift rate along the vertical direction is always less accurately calibrated because it can be observed only through its effect on the derivative of level-axes drift rate measurements. This is a relatively low signal-to-noise ratio error observation.

The Level Mobility Rate can be Optimized

If the measurement noise is large relative to parameter instabilities, then the level mobility rate will be smaller than otherwise. This enhances the ability to align in azimuth. Measurement noise has its most adverse effect on azimuth error; the lateral impact error is highly sensitive to this error.

If the measurement noise is small relative to parameter instabilities, then the level mobility rate will be larger than otherwise. This will permit observations of all acceleration-dependent parameters on a shorter cycle-time basis, providng tighter control of these errors.

The Vertical Mobility Rate can be Optimized

The vertical mobility rate must be as large as practical. A practical rate is approximately 4 to 5 eru. The vertical mobility rate should be applied continuously at least until launch time. As the vertical mobility rate increases beyond the practical guidelines stated above, computational algorithms require higher-order accuracy than that normally provided in the past. In general, mechanization complexity and computational burden become impractical with respect to the increment of improved performance achieved. For a given gyro torque word processing interval, increasing the vertical mobility rate causes increased quantization of data in resolving earth-rate onto platform level axes.

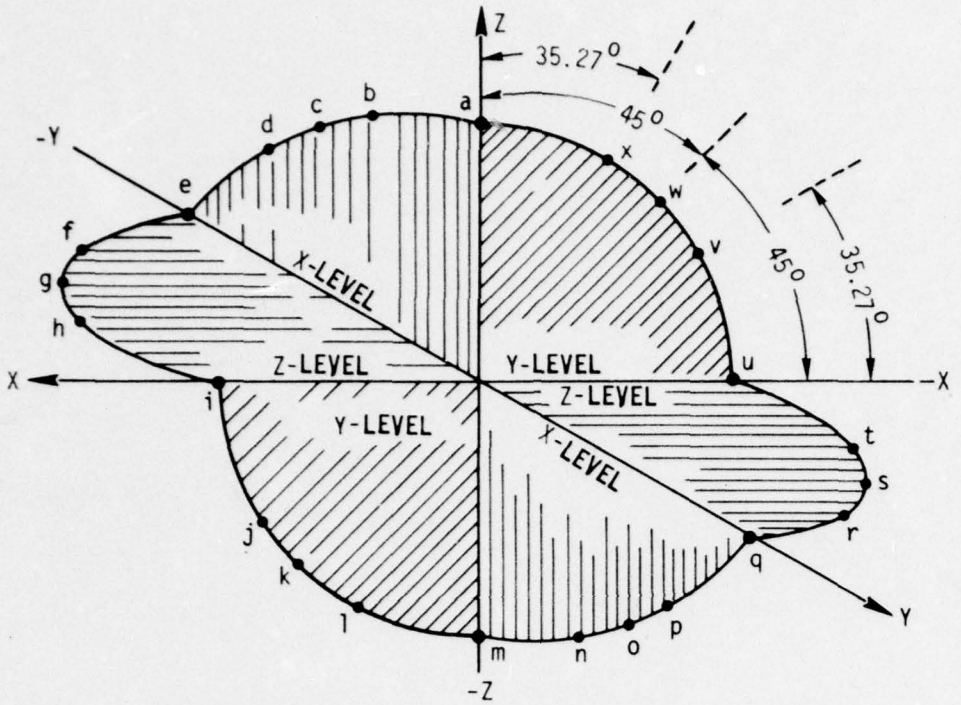
When level and vertical mobility rates are applied concurrently (cal/align), the vertical rate should be larger than the level rate, to the extent possible. Due to the previously discussed geometrical effects, azimuth alignment suffers maximum degradation when level and vertical mobility rates are equal. As the vertical rate increases, relative to the level rate, azimuth accuracy improves.

Elements of an Optimum Calibration Trajectory have been Identified

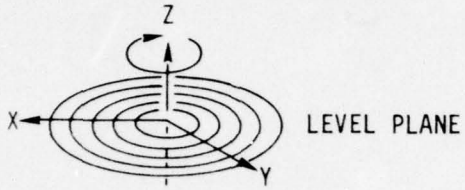
For complete observability (all error states independently calibrated) relative rotation of the stable platform with respect to earth-fixed axes must occur, sequentially, in the level plane, about each of three noncollinear platform-fixed axes. A vertical axis rotation applied either concurrently or sequentially with the level rate is also required. Optimum results are obtained with orthogonal platform-fixed reference axes, for which maximum signal-to-noise ratio error observations are obtained.

Both rapid calibration (high level-mobility rate) and optimum continuous calibration (low level-mobility rate) use the same platform trajectory. The high level-rate should be applied initially while making one pass over the closed-path trajectory. After the first pass, all parameters will be nearing steady-state calibration accuracy, but azimuth alignment will be degraded due to the high level-mobility rate. When the optimum low level-rate is applied, azimuth error will decrease, yielding a highly accurate system. Continuing in this mode will maintain all parameters in optimum calibration relative to a minimum CEP criterion.

A near-optimum trajectory consists of rotating 90-degrees about each of the three mutually orthogonal platform axes. The axis of rotation must be maintained in or near the level plane to cause each axis to assume (±) directions along the gravity vector and pairs of axes to assume 45-degree positions relative to it. A continuous rotation about the vertical axis is required. Gyro reference torquing can be used to enhance calibration of scale factors and axes misalignments if desired. A description of the cal/align trajectory currently used with AIM is given in Figure 4.



TGG, SFIR CALIBRATION ORIENTATIONS FOR OPTIMUM EXCITATION OF ERROR-STATES



ROTATION ABOUT VERTICAL PROVIDES CAL/ALIGN

Figure 4. An Optimum Continuous Cal/Align Trajectory of the Gravity Vector in the Platform Frame

EIGHTH BIENNIAL GUIDANCE TEST SYMPOSIUM

THE APPLICATION OF CS/RT TO THE OMEGA 2041 SOURCE SELECTION

AUTHORS: CAPT PAUL E. RONAN
HAROLD W. UNDERWOOD

AERONAUTICAL SYSTEMS DIVISION
AIR FORCE SYSTEMS COMMAND
WRIGHT-PATTERSON AIR FORCE BASE, OHIO

THE APPLICATION OF CS/RT TO THE OMEGA 2041 SOURCE SELECTION

BY

PAUL E RONAN, Captain, USAF
Aeronautical Systems Division
Air Force Systems Command
United States Air Force

HAROLD W UNDERWOOD
Aeronautical Systems Division
Air Force Systems Command
United States Air Force

THE APPLICATION OF CS/RT TO THE OMEGA 2041 SOURCE SELECTION

by

Mr. Harold W. Underwood
and
Capt. Paul E. Ronan

The OMEGA 2041 Program was the first major avionics procurement within the Air Force to utilize a Combined Stress Reliability Test (CS/RT) for engineering qualification and as an evaluation tool for source selection. This paper describes the OMEGA 2041 Program--its objectives, constraints and many of the problems encountered. Further, the lessons learned by the people involved are discussed in detail. The paper addresses:

a. The CS/RT concept.

b. Establishing test objectives.

c. Determining whether the Combined Stress Reliability Test should be accomplished by a government test facility or by the equipment's manufacturer.

d. Establishing the environmental test profile.

e. Test failure definition.

f. Test scheduling.

g. Cost.

This paper is particularly timely in that CS/RT is now being considered for use in the procurement of the standardized Inertial Navigation System (INS) for the Air Force as well as other avionics equipments. Therefore, the lessons learned in the OMEGA 2041 Program should be judiciously applied to future developments.

INTRODUCTION:

The OMEGA 2041 Program was the first program within the Air Force to utilize a Combined Stress/Reliability Test (CS/RT) as a replacement for Reliability Test per MIL-STD-781B and for portions of engineering qualification testing in accordance with MIL-STD-810B. Since this program was first to use CS/RT and was also one of the first programs to be structured around the Reliability Improvement Warranty (RIW) concept, it has received a great deal of interest within both the government and industry.

The OMEGA 2041 Program was established in 1973 to develop a replacement for the LORAN A Navigation Receivers which were used by most of the Air Force and Navy cargo type aircraft for overwater navigation. This need became very pressing from a schedule standpoint when the decision was made to decommission the LORAN A ground stations beginning in December, 1977. The following is a partial list of aircraft which were included in the program at its inception: C-118, C-119, C-123, C-130, C-135, C-9 and the P-3. As the program progressed, the list was reduced to include only the C-130 aircraft.

In order to achieve the stated goal of developing a low-cost airborne OMEGA Navigation Set (ONS) to replace the LORAN A receivers, a three (3) phase program was established and was structured as follows:

A. Data Collection Phase - This phase of the program was established in order to answer the question: Is OMEGA Navigation a viable replacement for LORAN A? During this phase, the industry was given the opportunity to loan the Air Force brassboard ONS's for an extensive flight test aboard an Air Force NKC-135 aircraft. Six (6) contractors ultimately accepted our offer and participated in the test. As a result of this test, the OMEGA Navigation concept was determined to be a viable replacement for Loran A.

B. Preproduction Phase - This period of time was allocated to the development, fabrication and test of preproduction equipments.

The objective of this phase was to develop and perform engineering qualification tests in three (3) different ONS designs which could then compete for a production contract. This task was scheduled for completion ten (10) months after contract award which occurred in July, 1975. Bendix Corporation, Dynell Electronics and TRACOR Sciences were selected.

C. Production Phase - A single contractor was selected to manufacture ONS equipment for the retrofit of the C-130 fleet and possibly other applications. The selection was based upon a Life Cycle Cost (LCC) Analysis and the contractors' production proposal. The LCC analysis was performed by government personnel using data provided by each of the competing contractors.

This paper will discuss the test and the analysis which were accomplished on each of the three competing ONS designs during the preproduction phase. The key issues which were to be addressed during the test program included:

A. Assuring that each delivered item of equipment had a reasonable chance of performing for an extended time period without a reliability type failure.

B. Verifying that each of the ONS designs met their performance requirements.

C. Developing realistic estimates of the equipment's reliability through field and laboratory testing.

D. Qualifying the equipment for operation in all anticipated airborne environments.

E. Evaluating the operational effectiveness and suitability of each ONS design.

An attempt was made to reduce the risk to the government that an equipment would fail shortly after receipt by the Air Force by imposing the requirement for a Pro-

duct Reliability Verification Test (PRVT). This test involved approximately 112 hours of testing under temperature/altitude and sinusoidal vibration environments. Further, the last 45 hours of testing were required to be failure free. This test was designed to reduce the problem of infant mortality during the Air Force test program and to preclude the delivery of equipment which had little chance of meeting our reliability goals.

The OMEGA 2041 Program was severly limited from a schedule standpoint (Figures 1 and 2) during the preproduction phase. This schedule constraint forced certain adjustments to be made to the normally accepted method of conducing engineering qualification in accordance with procedures stated in MIL-STD-810 and reliability qualification per MIL-STD-781. For this program, a Combined Stress/Reliability Test was chosen as a substitute for the Temperature/Altitude, Humidity and Vibration portions of the environmental qualification and as a means of estimating the field reliability of the equipment. The decision was based upon the realization that MIL-STD-781B test procedures do not adequately forecast field reliability and upon recommendations from the Air Force Flight Dynamics Laboratory (AFFDL) and Lt. Col. B. Swett's reliability test analysis.(5&6) A reliability goal was stated in the specification rather than a hard requirement for a minimum Mean Time Between Failure (MTBF). This approach was taken since we had a competitive environment between the three (3) contractors and was thought to provide a greater incentive to produce reliable equipment than a specification requirement which has in many cases been reduced when difficulty was encountered in achieving the required level of performance. Further, the accepted technique for conducting a reliability test program, as stated in MIL-STD-781, may have taken considerably more time than the schedule allowed if the test were to be accomplished with an affordable sample size and to a reasonable confidence level.

None of the contractors who competed for the OMEGA 2041 preproduction effort had an inplace Combined Environment Reliability Test (CERT) capability within the organization designated to perform the OMEGA 2041 design effort. As will be seen later, the facilities required to accomplish this type of test are costly. In view of the cost, the lead time required to procure environmental test equipment such as test chambers and random vibration shakers, and the risk to the program schedule of the test facilities not being available at the required time, the Air Force elected to accomplish

the test in-house at the Air Force Flight Dynamics Laboratory (AFFDL). This allowed the procurement of test equipment prior to the selection of the OMEGA preproduction contractors. Further, the cost of establishing a single government CERT facility was thought to be less than funding three (3) contractor facilities.

In order to assure that each of the competing designs met the performance and environmental requirements which could not be incorporated in the CS/RT, a contractor accomplished test was required to demonstrate performance under the remaining qualification test environments. The ability of the ONS to navigate accurately was evaluated by a USAF conducted flight test over two (2) radar test ranges.

The operational suitability of the preproduction OMEGA equipment and the acceptability of the OMEGA concept were evaluated by the Military Airlift Command (MAC) during their Initial Operational Test and Evaluation (IOT&E). This test addressed the man machine interfaces, reliability, maintainability, the OMEGA signal coverage and involved flights to Europe, Asia, Africa, Australia, South America, plus both arctic and anarctic regions.

The OMEGA 2041 program was structured around the Reliability Improvement Warranty (RIW) concept. This is a contractual vehicle whereby the contractor's responsibility continues for, in this case, a period of five (5) years after the initial delivery of production OMEGA sets. During this time period, the contractor is required to repair, at no additional cost to the government, any unit which fails. Also, the contractor may be required to provide other consideration, such as additional spares or cash payments if the contractual MTBF is not attained. This provides the contractor an incentive to at least maintain the level of reliability demonstrated during preproduction and, hopefully, improve upon that performance. Again, a PRV Test requirement was invoked to minimize the effects of infant mortality on field operations and demonstrate a minimum reliability prior to delivery.

The Analytical Science Corporation was on contract to the program office to collect, catagorize and establish a failure data base which could be used for performing analysis and reliability predictions. These data were used by the source selection committee in predicting field reliability which was then inputed into an LCC model. The production contractor selection was based upon lowest life cycle cost.

Having described the overall OMEGA program, philosophy and preproduction test effort, let us now proceed to examine the lessons learned in conducting the CS/RT.

Discussion

The CS/RT Concept

A Combined Stress/Reliability Test (CS/RT) involves the exposure of a test specimen simultaneously to a combination of controlled test environments; i.e., temperature, altitude, humidity and random vibration. The term "stress" implies that the equipment is being exposed to test environments which may be greater than the equipment will encounter during normal operation, but which may be experienced under emergency conditions; i.e., loss of pressurization. Reliability, at least in our particular case, does not imply the demonstration of a particular Mean Time Between Failure (MTBF) to a predetermined confidence level, but refers to the data collection task and the subsequent analysis of the test data. This analysis did result in a predicted field MTBF for each competing equipment. There are several other terms which are common in the literature: Combined Environments Reliability Test (CERT) and Combined Environments Test (CET). A conserted effort is made in structuring each of these tests to model the operational environment of the equipment as accurately as possible. Some authors omit the term reliability from the discussion because of the possible confusion with the classical reliability demonstration per MIL-STD-781 and its statistical inferences.

Test Objectives and Where the Test Should be Accomplished

As was previously stated, test facility availability and cost were the determining factors in the OMEGA 2041's program decision to accomplish the test in-house at the

Air Force Flight Dynamics Laboratory. However, when considering the more generalized case, there are other factors which should be address. The most important of these is establishing the primary test objective.

The OMEGA 2041 program had four (4) distinctly different objectives for the CS/RT Test:

1. Provide data for estimating the field reliability of the OMEGA sets which was to be used as an input to the LCC model during Source Selection.

2. Improve the reliability of the equipment by identifying failure modes and implementing corrective action.

3. Establish a MTBF requirement for inclusion in the RIW Contract Provisions.

4. Demonstrate performance in the various engineering qualification test environments.

If the first stated objective is considered primary and the data is to be used in a competitive source selection, the most advantageous way of accomplishing the test is to perform the test at either a government facility, as was done in the OMEGA 2041 program, or at a large commercial test laboratory which can handle all the competing equipment simultaneously. This will assure that the test is administered as fairly as possible.

In event the second objective is considered more important, the test can be more effectively accomplished at the contractor's facility. This is desirable since the contractor will have the test equipment and failure analysis personnel available to work the problems which are encountered during the test and implement corrective action. During the OMEGA 2041 program, this objective was only partially successful--a number of failure indications were observed at various points in the environmental profile, but were self-correcting as the test progressed in time. Unfortunately, the equipment was not accessable during the test for trouble shooting. Since the contractor did not have test facilities which could duplicate the test environment where the failure

occurred, nor sufficient spare test specimens, he was unable to positively identify several failure modes and, thus, take appropriate corrective action.

In our particular instance, we were unable to establish a firm requirement for MTBF for inclusion in the RIW provisions. This was impractical since there were very little data available at the time the Request for Proposal was being prepared, and there was concern that one or more of the participants might be eliminated from the competition by an arbitrarily selected number. Therefore, each of the contractors were asked to propose the specific number to which they were willing to commit themselves as a part of their proposal.

Later discussion will provide rationale for not considering environmental qualification as the primary objective of a CS/RT and, therefore, this has little bearing on where the test is conducted.

Failure censoring

During the CS/RT, the Air Force made provision for the censoring of test failures for reliability assessment purposes when a fix had been proposed and its effectiveness demonstrated. As might be expected, the contractors took a rather liberal interpretation of this provision. A concerted effort should be made by the procuring activity in order to assure a fair and equitable administration of this contractual provision.

For example, using this contractual provision, a very simple method was discovered to defeat the intent of the test. A contractor could, for various reasons, delay incorporation of ECP's until it is too late for evaluation during the preproduction CS/RT. That is, the production proposals would be submitted containing proposed changes which, the contractor would contend, eliminated the cause of various failures encountered during the test. This approach requires the government source selection evaluators to assess the probability of success or failure for each of the proposed fixes without the benefit of test data. In the source selection environment, the contractor is usually given the benefit of any doubt. The result of all this could be that the contractor will be given credit for reliability improvements which may not be realized in his production equipment.

The government should insist that all changes for reliability improvement, which are alledged to eliminate the cause of know failures, be verified by test data. This may require that the CS/RT be terminated in time to allow the data to be accumulated prior to submission of the production proposal. This data may or may not be CS/RT data. However, it should support the contractor's contention that the cause of the failure has been corrected.

Environmental Profile

The CS/RT environmental profile (Figure 3) for the OMEGA preproduction test was designed to encompass the worst case of environmental conditions which have historically been demonstrated during the environmental qualification test. These consisted of a tropic takeoff, climb to 50,000 feet, a landing in the desert, a takeoff from the desert with turn-on at 160°F, landing in the arctic, and an arctic takeoff and, again, landing in the desert. These tests encompassed the maximum limits of temperature/altitude and humidity which have historically been verified during environmental qualification test, but they do not reflect the normal usage of the equipment in an operational aircraft.

The vibration spectrum which was employed was a composite of the vibration spectrum which would be encountered in both propeller and turbine driven aircraft simultaneously (Figure 4). This particular spectrum excited the test specimens with more energy than would be experienced while operating on either type of aircraft.

The test facility which was used during the CS/RT was designed to accommodate six (6) sets (two (2) from each vendor) of OMEGA equipment on a single vibration table. The vibration was measured by six (6) accelerometers located at various places on the table in accordance with test practices outlined in Procedure 514 of MIL-STD-810C. These outputs were then averaged together and recorded. The random vibration shaker was then adjusted so the output of the six (6) accelerometers averaged together matched the vibration requirement stated in the specification. This approach was taken even though a slight variation between the various equipment locations was unavoidable.

Early in the test program, it became obvious that some of the ONS's were experiencing a much greater incidence of failure and what appeared to be additional failure modes which were not being experienced on either the C-130 or NKC-135 aircraft. As a result a complete vibration survey of the shaker table was made. A significant vibration was found in the input vibration levels to the various units under test. Therefore, the vibration test levels were reduced to a point where no units experienced vibration inputs above the specification limits. This resulted in a greatly reduced failure rate for the test specimens.

It is recommended that future CS/RT's not use composite vibration environments. Rather, the actual environment of the intented aircraft should be simulated as closely as practical if the field and CS/RT data are to be correlated. Data seemed to indicate that use of qualification environmental levels produced failure modes not seen in day to day usage.

Failure Definition

Prior to the start of tne OMEGA preproduction test, a concerted effort was made to describe in detail what constituted a failure. However, each of the contractors, the AFFDL and MAC later attempted to redefine a failure. In each case, the contractors reverted to the original contract definition as a result of Air Force applied contractual pressure. This was absolutely necessary since the data being generated was being used as an input to the Life Cycle Cost (LCC) Model, which in turn was being used in the Source Selection process. This was required if each of the offers was to be treated fairly.

The contract defined a failure as the occurance of any of the following conditions:

a. Equipment not meeting its specified performance requirements.

b. A fracture or permanent deformation of any LRU, SRU, component or piece part.

c. Any fixed part or assembly coming loose.

d. Any movable part coming loose or sluggish in operation.

e. Any movable control being shifted in setting, position or adjustment.

f. The need for any electrical or mechanical adjustment in order to meet the specified performance requirements.

In the CS/RT, the AFFDL prepared test report separated the failures into the following catagories:

a. Relevant failure - any failure that occurred in the CS/RT cycle which was not attributed to improper test facility operation. (This follows the contractual definition closely.)

b. Significant failure - a relevant failure that would probably be written up by the flight crew.

c. Nuisance failure - other relevant failures such as the illumination of a "failure" lamp, which would not normally be written up by the flight crew.

d. C-130 significant failures were all significant failures except those that occurred during environmental stresses not present in the C-130.

The IOT&E Test Report considered any condition which would result in the unit being removed from the aircraft for maintenance as a failure.

While there is considerable merit in each of the above definitions, a single definition should be established in the preproduction Request for Proposal (RFP) and adhered to throughout all test programs. In our particular case the rank order of the various equipments' reliability could be altered depending upon which failure definition was selected.

It was noted that the MTBF's demonstrated by the various equipment correlated quite closely between the CS/RT and the limited flight test when the contractual failure definition was employed. However, there was an order of magnitude difference between the MTBF's

observed during CS/RT using the contractual definition and that reported in the IOT&E Test Report. This difference is believed to be attributed to the differences in failure definition.

Test Scheduling

The OMEGA CS/RT was timed to begin approximately one (1) week after the scheduled delivery of the hardware and was to continue on a twenty-four (24) hour day, seven (7) day per week basis until the contractors' production proposals were submitted. This very stringent test schedule was established in the field reliability for each competing design within schedule constraints.

Several problems were encountered which precluded the test from starting as scheduled. There were slippages in the delivery of test specimens, the completion of the chamber modification was delayed, chamber start-up problems were encountered, the test specimens had incompatibilities with the simulation and often times the test specimens failed shortly after installation in the test chamber. All of these difficulties resulted in about a one and one-half (1½) month delay in the acquisition of meaningful test data. The testing was then continued until the very day the offerors' proposals were to be submitted to the Air Force for evaluation.

The established schedule was soon modified to eliminate weekend operations. This was necessary since the manpower requirements for test chamber operation and data taking had been significantly underestimated. In retrospect, the problems associated with the accomplishment of the CS/RT were significantly underestimated.

Generally, the first one and one-half (1½) months of the test program expired before the test chambers were operating properly, the infant mortality and major repetitive failure modes of the test specimens were corrected, and test data which might be considered representative of field operation was being obtained. Further, the final two (2) weeks of test had very little utility because the contractors' proposal preparation deadline prevented the analysis and correction of any

failure modes which were encountered during that time period. This essentially left the OMEGA 2041 Program with one and one-half (1½) months of test data which could be used in assessing the equipment's reliability.

Therefore, we conclude that, when a CS/RT is to be used in the preproduction phase of a program, a minimum of four (4) months of testing and two (2) months of analysis should be scheduled prior to the receipt of production proposals. If this time period is not available because of ther program constraints, the elimination of CS/RT should be considered.

In event a CS/RT were to be used as part of a production Reliability Improvement Program backed up by a Reliability Improvement Warranty, the schedule can be considered far less constraining from the government's point of view. Here, the potential for the contractors' increased profits or reduced loss will provide incentive for the contractor to identify and correct failure modes early in the program. The cost of accomplishing the test per unit of time and the money available will probably be the driving consideration.

Cost

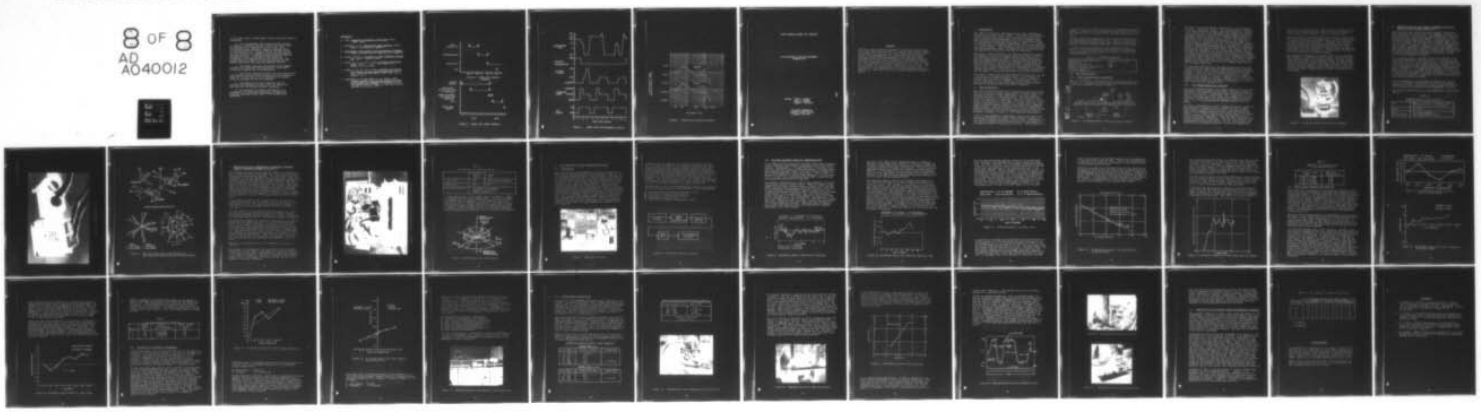
The identifiable costs to the government for accomplisning the OMEGA 2041 CS/RT was $868.2K. This figure does not include the cost of test specimens, contractor support for their installation and repair nor test failure reporting. This cost did include $637.7k for the modification of an environmental test chamber which was located at the AFFDI. This modification included the purchase of a random vibration generator, the fabrication of the unique test fixtures and the refurbishment of the existing temperature/altitude/humidity control systems. The test facility was manned by technicians under a contract to a local firm for $74.0K. The OMEGA Signal Simulator was provided by the Naval Electronics Laboratory Center for a cost of $156.5K.

CS/RT should not be considered a panacea which will alone solve the Air Force's avionics reliability problems. However, it can be a very useful part of a comprehensive test and reliability growth program. Unfortunately, there are certain pitfalls which must be avoided in its application. The following is a summary

AD-A040 012 ARMAMENT DEVELOPMENT AND TEST CENTER EGLIN AFB FLA F/G 17/7
PROCEEDINGS OF THE BIENNIAL GUIDANCE TEST SYMPOSIUM (8TH) HELD --ETC(U)
MAY 77

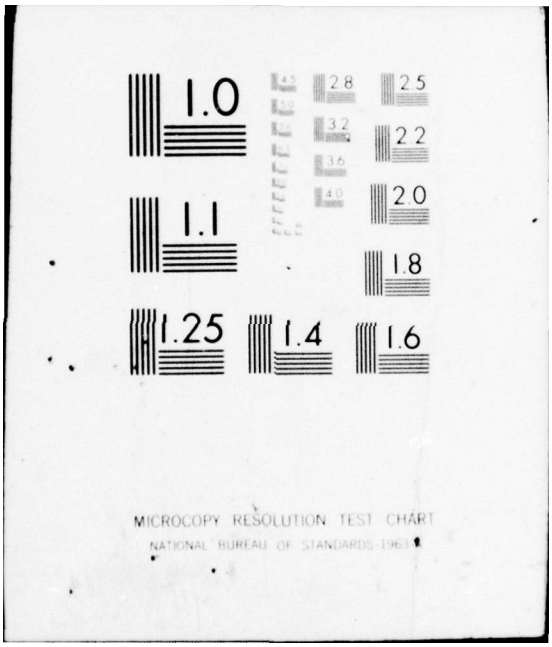
UNCLASSIFIED ADTC-TR-77-3-VOL-1 NL

8 OF 8
AD
A040012



END

DATE
FILMED
6-77


1.0
1.1
1.25
1.4
1.6
2.8
3.2
3.6
4.0
2.5
2.2
2.0
1.8
MICROCOPY RESOLUTION TEST CHART
NATIONAL BUREAU OF STANDARDS 1963

of the major point in this paper in their relative order of importance.

a. The environmental test profile should reflect as closely as possible the day to day environment which the equipment will experience in the field. This environment should include a vibration spectrum which is representative of a single class of aircraft at any one time rather than a composite vibration representing multiple aircraft. Differing vibration spectra used on alternating cycles is one method that should be considered if the application is multi-aircraft. No attempt should be made to include engineering qualification test limits into the environmental profile.

b. Sufficient time must be allowed in the program schedule for conducting and analyzing the CS/RT data if the test results are to be meaningful.

c. The failure definition which is to be used for the test should be very carefully defined and fairly administered if the test data is to be meaningful for source selection purposes or for LCC estimates.

d. The concept of failure censoring must be carefully administered to insure that the results of the CS/RT are not diluted by paper proposals.

e. The question of whether CS/RT should be a government or a contractor conducted test should be carefully analyzed in the light of the primary test objective.

REFERENCES

1. TASC, Technical Information Memorandum 747-6, 1 Jan., 1976.

2. Burkhart, A. H., OMEGA CS/RT Test Analysis, AFFDL Report (Preliminary), undated.

3. Preliminary Final Report OMEGA Navigation Equipment IOT&E, Military Airlift Command (MAC), undated.

4. Klass, Philip J., Reliability Test Procedure Changes Set, AW&ST, 19 April, 1976.

5. Swett, B. H., Lt. Col., USAF, Avionics Reliability Study, Phase 1 - July, 1973; Phase 11 - March, 1974, Hq. AFSC.

6. Swett, B. H., Lt. Col., USAF, Avionics Reliability, The Journal of Environmental Sciences, Sept./Oct., 1975, and Nov./Dec., 1975. Vol. XVIII, Issues 5 & 6.

7. Underwood, H. W. and Ronan, P. E., Capt., USAF, Lessons Learned from the Application of CS/RT to the OMEGA 2041 Program, Proceedings of the 10th Annual Data Exchange for Inertial Guidance Systems, 15-19 Nov., 1976.

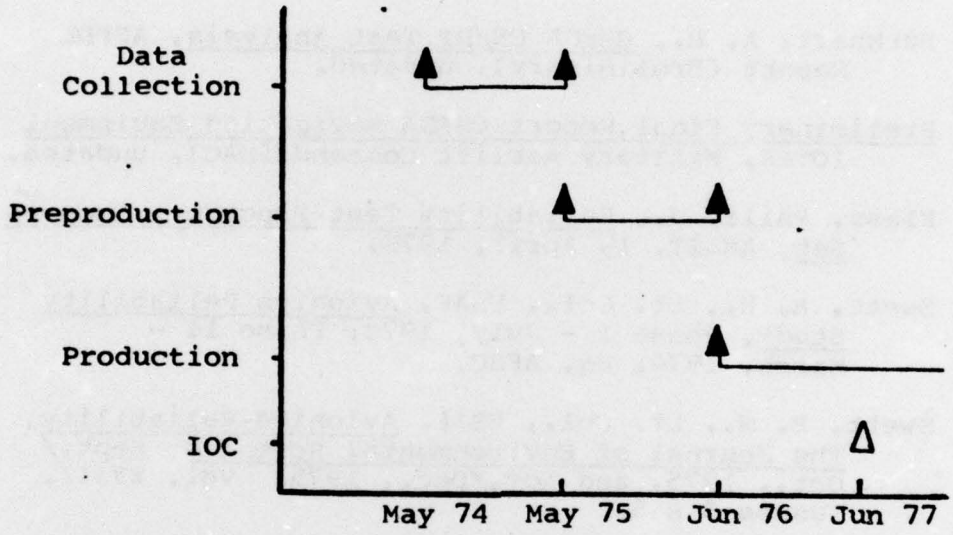


Figure 1 - OMEGA 2041 Program Schedule

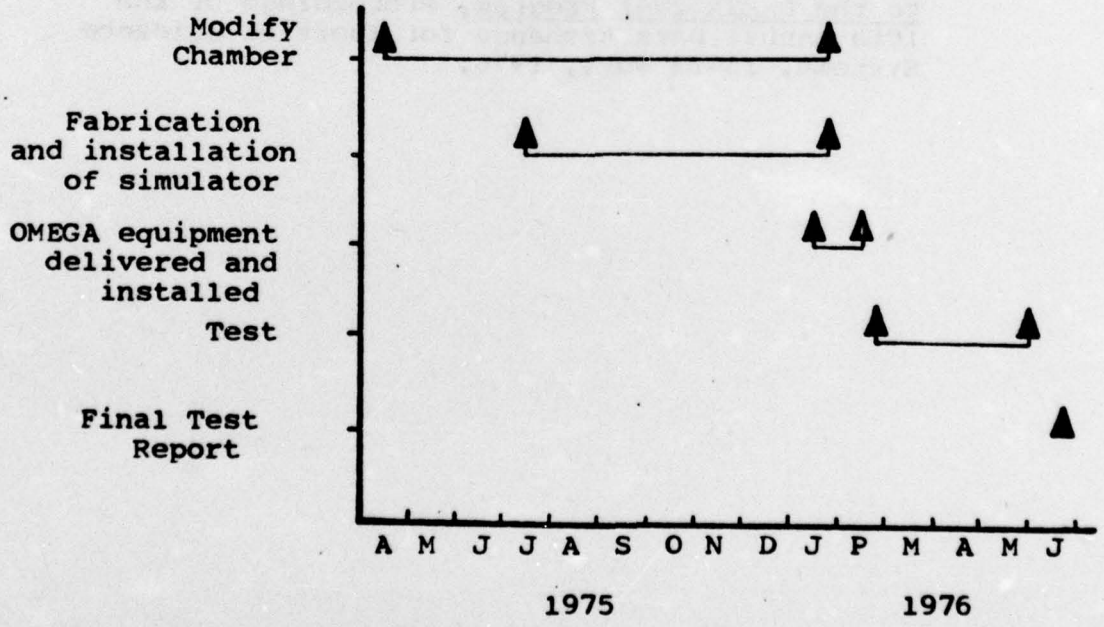


Figure 2 - OMEGA 2041 CS/RT Schedule

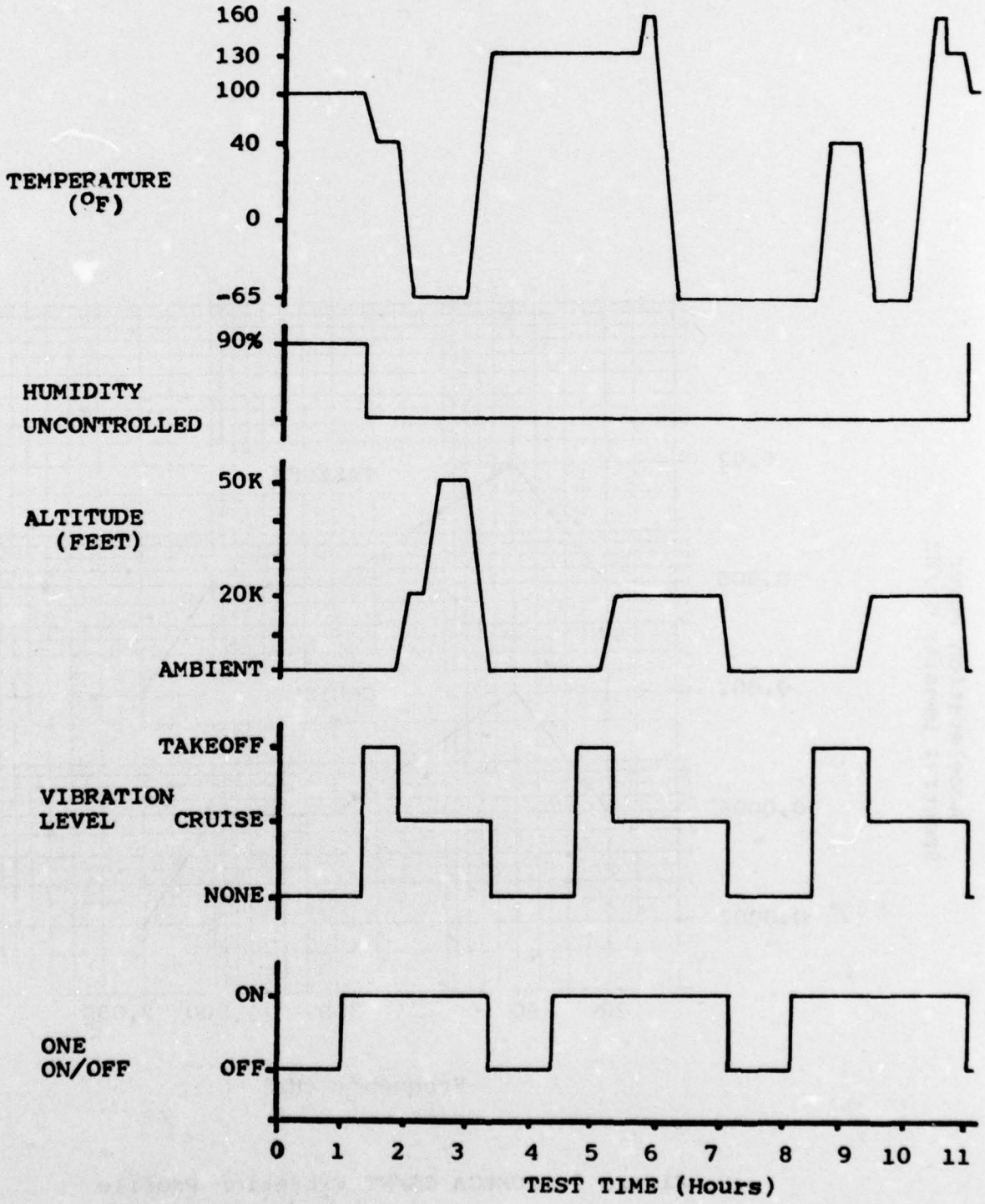


Figure 3 OMEGA CS/RT Environmental Profile

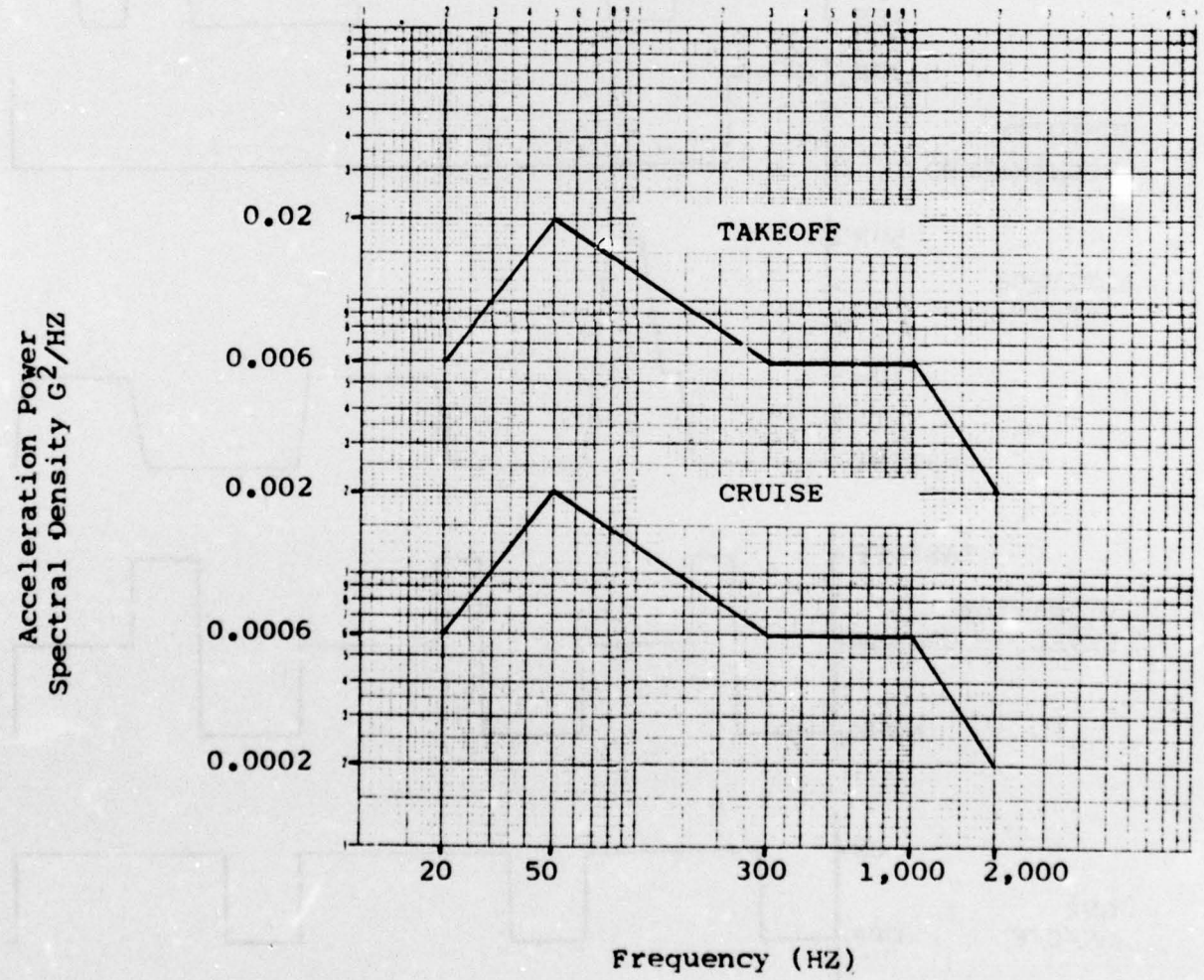


Figure 4 OMEGA CS/RT Vibration Profile

EIGHTH BIENNIAL GUIDANCE TEST SYMPOSIUM

TEST EVALUATION OF TWO HIGH PERFORMANCE STRAPDOWN IMU'S

AUTHORS: JOSEPH C. BLONDIN
JAMES A. JENNINGS
STEWART P. WEINSTEIN

THE BENDIX CORPORATION
GUIDANCE SYSTEMS DIVISION
TETERBORO, NEW JERSEY

ABSTRACT

Attitude control system requirements for recent spacecraft missions have emphasized the need for strapdown IMU's which combine the capability to provide a precision three-axis attitude reference with long mission life. This paper provides a brief description and evaluation summary for two high performance strapdown IMU's which utilize single axis gyroscopes operated with pulse rebalance servo electronics as the inertial sensors. The IMU's discussed have recently completed their qualification test programs for two scientific spacecrafts: a six sensor IMU developed for the International Ultraviolet Explorer; and, a modular two sensor IMU developed for the High Energy Astronomy Observatory. Both IMU's will be in orbital operation within six months.

I. INTRODUCTION

Both IMU's discussed in this paper utilize the 64 PM RIG gas bearing gyro as the inertial sensor. The gyro is operated in a binary (forced-limit-cycle) pulse rebalance mode which uses quantized pulse-width-modulation of the gyro torquing signal. This technique has been demonstrated to be eminently suitable for applications requiring a high dynamic range, i.e., a relatively high ratio of maximum torquing rate to attitude quantization (pulse weight). The packaging techniques utilized to minimize IMU weight and volume, including the use of custom-design hybridized microelectronics, are briefly described.

The specific IMU performance test results summarized include environmental testing to simulate spacecraft launch vibration and shock associated with launch vehicle stage separation as well as thermal/vacuum testing to simulate orbital operation. Detailed performance evaluation is provided for the stability and noise content of the attitude reference furnished by the IMU for time periods ranging from 100 milliseconds to hours, scale factor linearity and stability, repeatability of alignment through environments, and sensitivity to external disturbances such as magnetic fields and spacecraft bus voltage variations.

Test data is examined which demonstrates the ability of the IMU to maintain an attitude reference within 1.0 arc-second for time periods exceeding 30 minutes, scale factor linearity of 50 ppm, and scale factor randomness of several ppm. Also, briefly described are the highly specialized test techniques utilized to establish these performance parameters.

II. GYRO DESCRIPTION

The size 64 Permanent Magnet Rate Integrating Gyroscope (64 PM RIG) is an inertial grade single-degree-of-freedom sensor containing an advanced ceramic hydrodynamic gas bearing wheel assembly driven by a synchronous motor. The wheel and motor stator are mounted in a hermetically-sealed cylindrical float which is filled with an inert gas. The float, which is also of ceramic construction, is enclosed in a sealed outer case which houses a microsyn signal generator and a dual-scale permanent-magnet torquer. The outer case is filled with a high-density high-viscosity flotation fluid which, at the gyro operating temperature, provides the float with damping and nearly neutral buoyancy, tending to isolate it from extraneous disturbances.

A pair of electromagnetic suspensions, one at each end of the gyro and comprised of an 8-pole high-permeability laminated stator and a tapered cylindrical ferrite rotor, compensates for any error in buoyancy and stabilizes the axial and radial relationships between the gyro float and case. The suspension ex-

citation circuitry, which is basically an inductance-capacitance bridge, is operated at the upper half-power point on its resonant characteristic to obtain nearly optimum stiffness and linearity.

Internal thermistors immersed in the flotation fluid are used for temperature monitoring and active control of the heater assembly wrapped around the gyro case. Bellows at both ends of the gyro allow for thermal expansion of the flotation fluid.

A listing of basic parameters of the 64 PM RIG is given in Table 1. Life data, previous flight history, and vibration test results for this gyro type is available in a paper published by Bendett, et. al.[1].

Table 1. 64 PM RIG Parameters

Cylindrical Dimensions (in.)	2.5 dia. x 4.0 long
Weight (lbs.)	1.70
Wheel Power (watts)	3.6
Angular Momentum (dyne-cm-sec)	430K
Torquing Capability at 40 mA (deg/sec)	7

III. RATE SENSOR DESIGN

IIIa. PULSE REBALANCE LOOP ELECTRONICS

When the 64 PM RIG is operated with pulse rebalance loop electronics, it is designated a Rate Sensor and a simplified functional block diagram is shown in Figure 1.

BEST AVAILABLE COPY

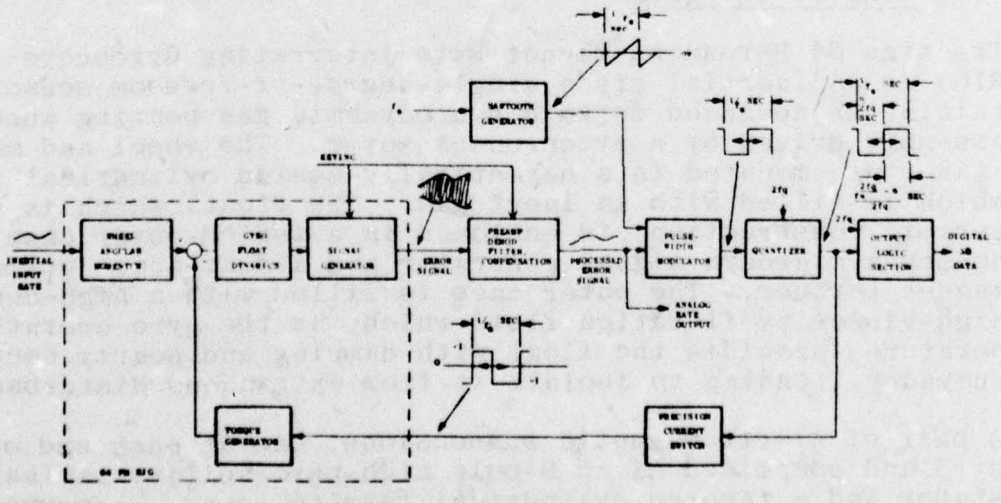


Figure 1. 64 PM Rate Sensor, Functional Block Diagram

The servo electronics consist essentially of two processing sections: analog and digital. The analog section is made up of an error amplifier, a phase sensitive demodulator, and an active filter stage that implements signal amplification and frequency shaping to provide the requisite dynamic response. The digital section is made up of a pulse-width modulator, a quantizer, and a precision current switch. The function of this section is to digitize and synchronize the signal received from the analog section into a bi-directional variable-width rectangular-current waveform, to be applied to the gyro torquer. The modulation mechanization employs two frequencies derived from the same reference clock. The lower of the two, the sawtooth frequency, f_s, is the torquing frequency and determines the period of the pulse width applied to the torquer. The higher or quantizing frequency, 2fq, determines the number of discrete modulation states that can be assumed by the torquer current waveform. When the input is zero, the torquer current waveform is characterized by a fifty percent duty cycle; for inputs other than zero, the duty cycle changes proportionally with the input amplitude.

In the Output Logic Section, the quantizing pulse train, 2fq, is gated with the same quantized PWM waveform used in generating the torquing signal, thereby obtaining data pulses corresponding to positive torquing commands and negative torquing commands. These data pulses are accumulated in an up/down counter whose content is a digital representation of the net angular motion sensed by the gyro. Bendett, et. al.,[1] provide a detailed description of the design considerations for this pulse rebalance loop mechanization.

IIIb. RATE SENSOR MECHANICAL PACKAGING

Due to the stringent weight and volume restrictions of the two strapdown IMU's described in this paper, the pulse rebalance electronics functionally described above are packaged into six hybrid microcircuits. In addition, three types of drive electronics functions (gyro wheel drive, gyro temperature control, and power inverter drive) are packaged into hybrid microcircuits. All of these devices are designed and fabricated by Bendix.

The hybrid microcircuits consist of nine (9) distinct types exhibiting power dissipations up to 850 mW with an attendant power density as high as 2.2 watts/in^2, chip populations as high as 50 elements, and with a rated operating temperature range of -15 to +95°C. The hybrid circuits consist of silicon active elements in chip form, as well as thin film chip resistors and ceramic capacitors. Both thin and thick film technology is used for the substrate. Die and chip bonding is accomplished by either gold-silicon eutectic, electrically conductive and non-conductive epoxies, in various combinations.

Electrical interconnections are performed with aluminum-silicon wire using ultrasonic welding. The circuits are packaged in hermetically sealed packages of 16-pin or 28-pin sizes.

The six hybrid microcircuits which constitute the pulse rebalance loop electronics are packaged into a single assembly which is mounted to one end of the gyro. Mounting this assembly to the gyro affords the advantages of providing close physical proximity between the gyro microsyn signal generator and the error amplifier; and, providing thermal control for these performance-critical electronics. Figure 2 shows the Rate Sensor with its top cover removed to allow viewing of the hybridized pulse rebalance electronics assembly.

The mechanical alignment of the Rate Sensor to its strapdown IMU housing is controlled by two precision locating pins which are accepted by the sensor mounting flange. The Rate Sensor mechanical attachment to the housing is made at three thermal isolators which are screwed and epoxied into the housing and then drilled and tapped to accept mounting screws. The use of thermal isolators increases power efficiency by causing most of the gyro heater energy to heat the gyro itself rather than the housing.

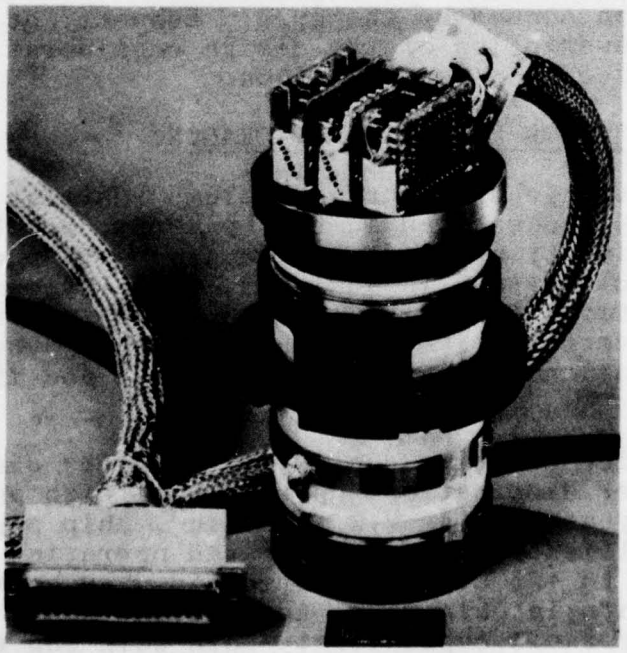


Figure 2. 64 PM Rate Sensor With Top Cover Removed

IV. DESCRIPTION OF THE HIGH ENERGY ASTRONOMY OBSERVATORY/ REFERENCE GYRO ASSEMBLY (HEAO/RGA)[2,4]

The High Energy Astronomy Observatory program, sponsored by NASA, involves the launching of three unmanned scientific observatories into low earth orbit. The spacecraft payload includes scientific experiments capable of detecting, locating and characterizing high energy X-ray, γ-ray and cosmic ray celestial sources. The Reference Gyro Assembly (RGA) forms a part of the spacecraft Attitude Control and Determination Subsystem (ACDS). As shown in Figure 3, the RGA is composed of two separate subassemblies designated as the Rate Sensor Unit (RSU) and the Electronics Control Unit(ECU). The RSU houses two 64 PM Rate Sensors and an optical reference cube. Support and interface electronics are provided in the ECU for the two electrically independent channels.

The coordinate frame of the RSU is depicted in Figure 4 and illustrates the sensor input axis with a 31.7 degree inclination with respect to the mounting surface. When arranged appropriately, a set of three RGA assemblies (six gyros) provides a non-orthogonal strapdown inertial reference system with input axis corresponding to the regular dodecahedron configuration shown in Figure 4. The HEAO A and C spacecrafts utilize two RGA Systems for a tetrahedron sensor deployment. In the case of HEAO B, the redundancy of the sensor complement is increased for mission reliability reasons and a set of three RGA Systems are employed as described above.

Digital information is provided by the RGA in the form of a 16 bit word with a quantization of 0.1 arc-second and a bandwidth of 15 Hz. Analog rate output is also provided for rates between $\pm$2.5 degrees/sec with a bandwidth of 0.4 Hz.

The physical characteristics of the HEAO/RGA are summarized in Table 2.

Table 2

HEAO/RGA Physical Characteristics

Size	RSU 6 in. x 8 in. x 5.125 in. high ECU 8 in. x 5 in. x 7 in. high
Weight	22.0 lbs.
Power (Steady State)	11.0 watts/channel (Excluding Heater Power)

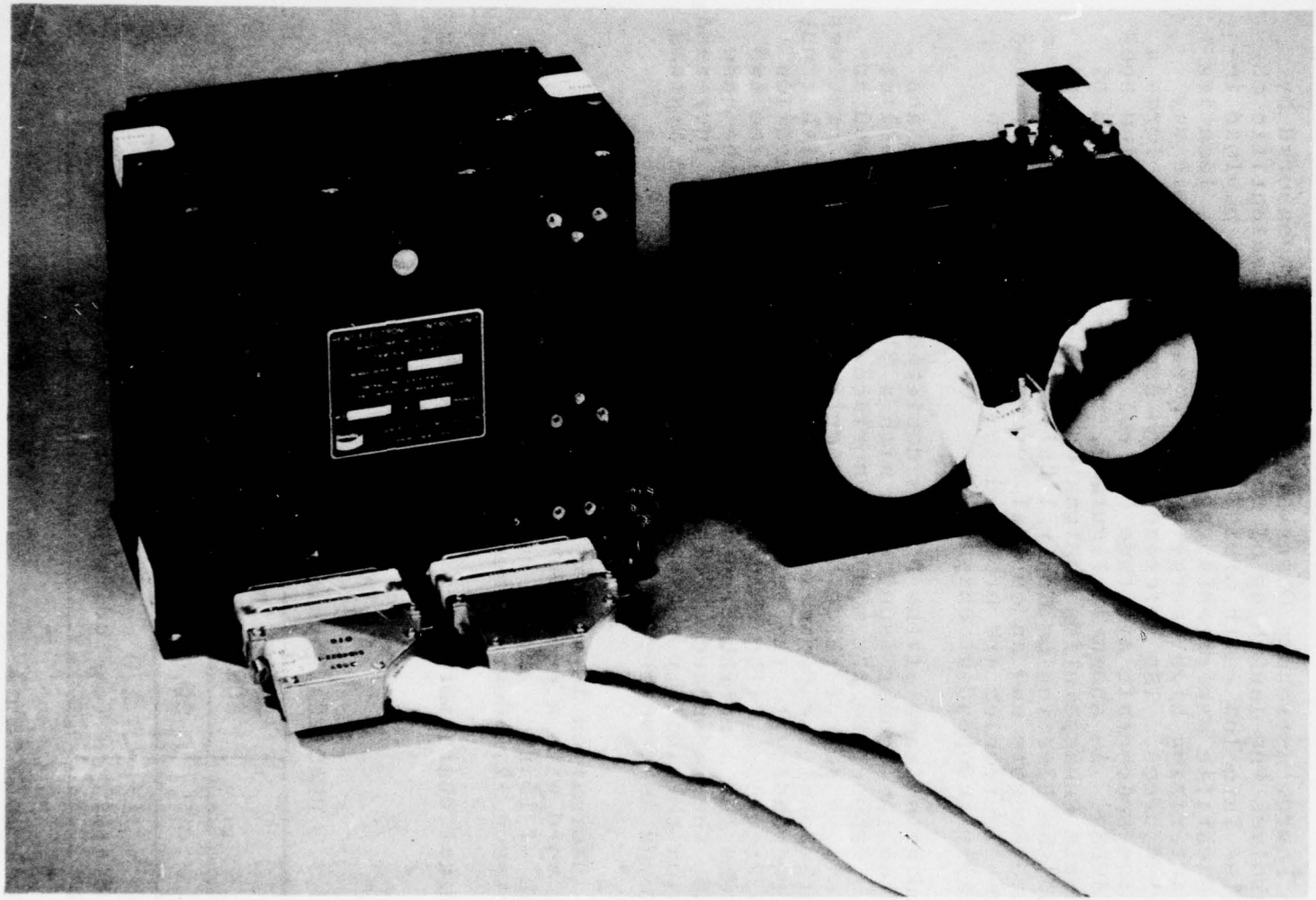
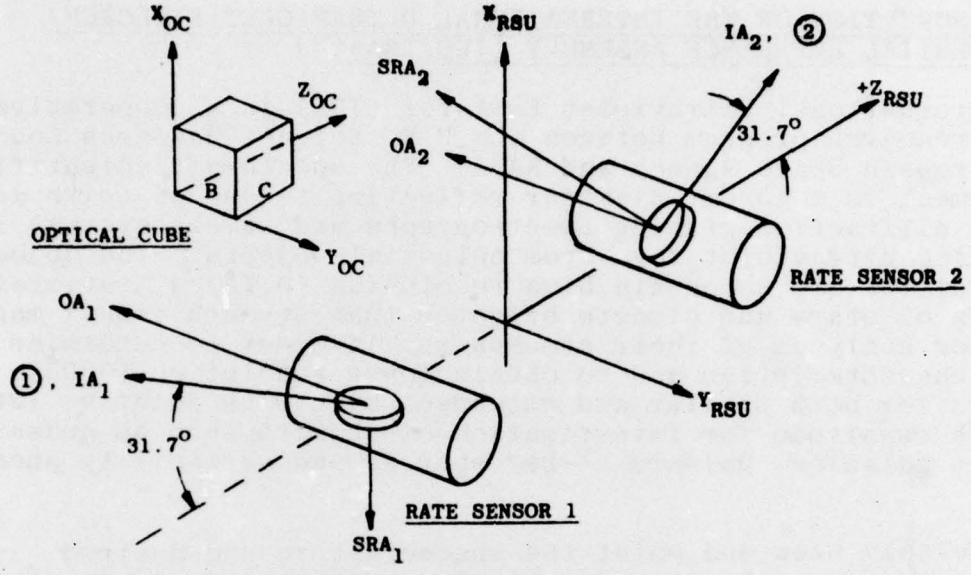
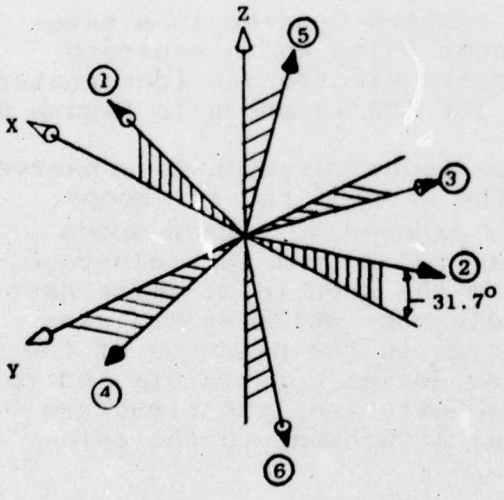
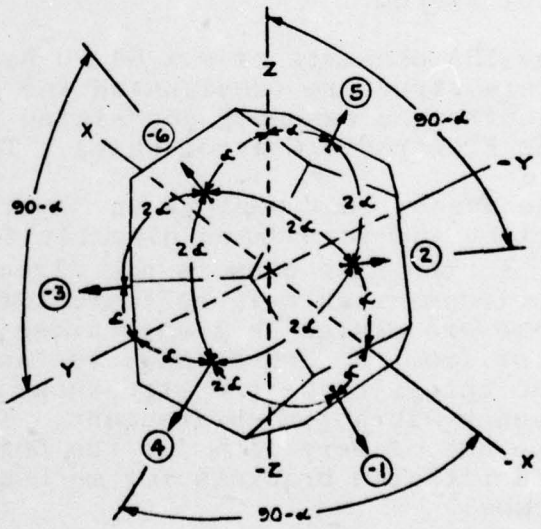


Figure 3. The HEAO/RGA System



HEAO/RGA COORDINATE FRAME DEFINITION





HEAO-A	HEAO-B
• 2 RGA SYSTEMS	• 3 RGA SYSTEMS
• 4 RATE SENSORS	• 6 RATE SENSORS

Figure 4. HEAO Input Axes Orientation Relative to The Instrument Frame Triad and the Dodecahedron

V. DESCRIPTION OF THE INTERNATIONAL ULTRAVIOLET EXPLORER/ INERTIAL REFERENCE ASSEMBLY (IUE/IRA)[3]

The International Ultraviolet Explorer (IUE) is a cooperative space research program between the U.K. Science Research Council, the European Space Agency and NASA. The spacecraft scientific instrument is a 45 cm. diameter reflecting telescope (with associated diffraction grating spectrographs and camera system) for gathering ultraviolet rays from celestial objects. The objectives of IUE are to obtain high resolution (0.1Å) ultraviolet spectra of stars and planets brighter than seventh visual magnitude for analyses of their atmospheres in order to determine their characteristics and to obtain lower resolution (6.0Å) spectra for both stellar and extended objects as faint as 12th to 15th magnitude for investigation of objects such as quasars, Seyfert galaxies, pulsars, X-ray sources and variability phenomena.

To precisely slew and point the spacecraft to the desired sources requires the use of a highly accurate and stable attitude control system. The IUE Inertial Reference Assembly (IUE/IRA) is the prime guidance sensor for this attitude control system.

The IRA consists of six 64 PM Rate Sensors mounted in a baseplate structure (designated the Sensor Unit) and a separate electronics assembly containing support electronics (designated the Electronic Control Unit). The IUE/IRA is shown in Figure 5.

The Sensor Unit employs an "open box" configuration to conserve weight and is mounted directly to the side of the telescope. Thus, the Rate Sensors are directly exposed to a deep space environment as well as thermal reflections from the telescope. A severe design challenge arose from the need to minimize heat flow from the Sensor Unit to the telescope while maintaining the integrity of the structural design in the presence of the launch vibration environment. These design constraints led to the use of beryllium for the Sensor Unit baseplate structure and titanium brackets for mechanical attachment to the telescope.

The physical characteristics of the IUE/IRA are listed in Table 3.

The IUE/IRA is configured so that any three of the six independent Rate Sensor channels can support the mission which has a life goal of five years. The Sensor Unit input axis definition is shown in Figure 6. The use of all Rate Sensor channel outputs offers a performance advantage through the use of information filtering techniques.

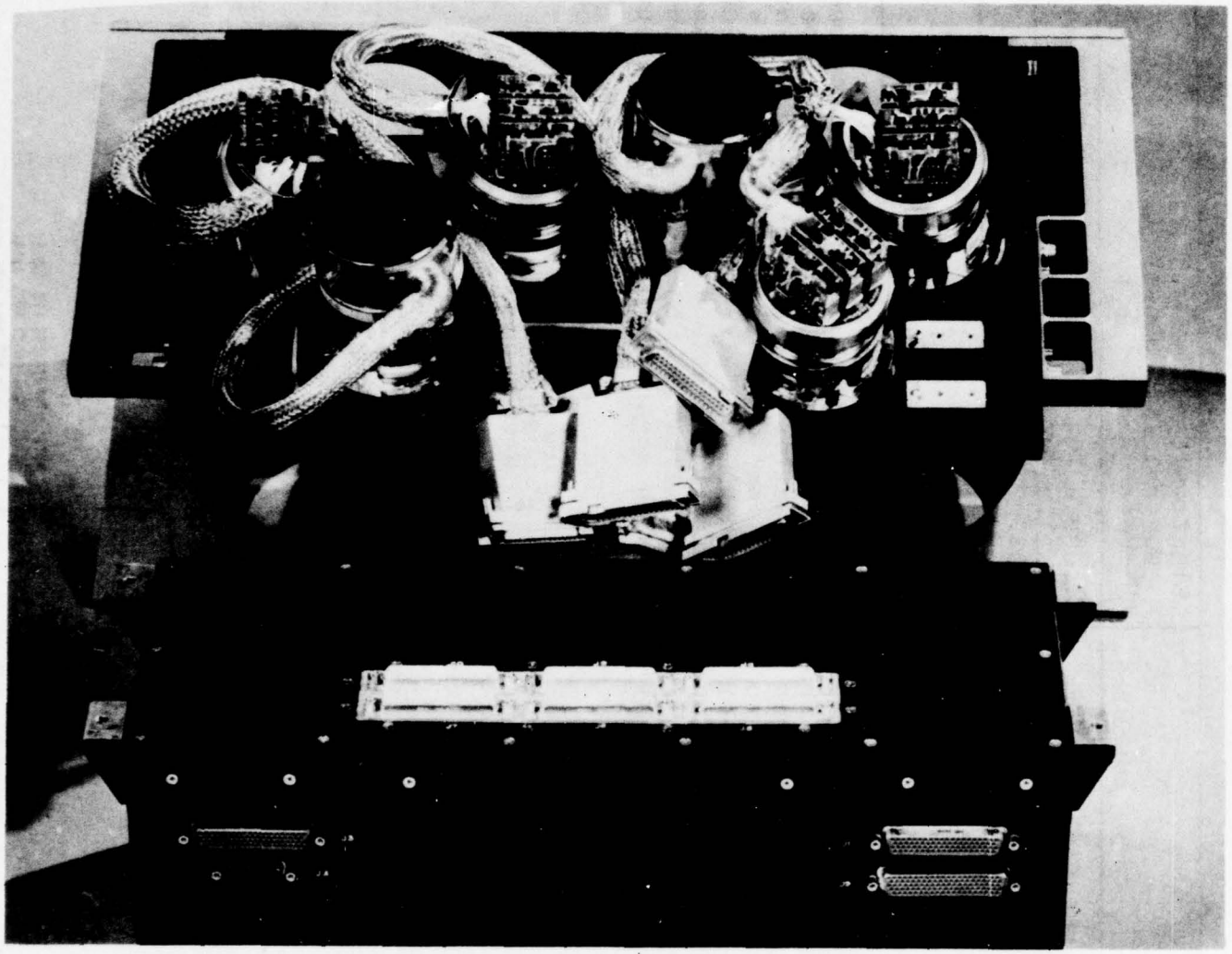


Figure 5. The IUE/IRA System (With Top Covers Removed)

Table 3

IUE/IRA Physical Characteristics

	Electronics Control Unit	Sensor Unit
Volume (in^3)	633	1507 (outer envelope)
Weight (lbs)	22.0	26.1
Power (Total System)	75.0 watts, six channel operation, stabilized orbital operation	

The Rate Sensors have a dual range capability which is commandable through the spacecraft command link. A ±5 deg/sec rebalance range (with an attendant attitude quantization of 0.3 arc-sec/bit) is used to support final despin of the spacecraft after orbital insertion and high-rate slew maneuvers. A ±600 arc-sec/sec rebalance range (with an attendant attitude quantization of 0.01 arc-sec/bit) allows for both high precision attitude stabilization and high accuracy low-rate slew maneuvers.

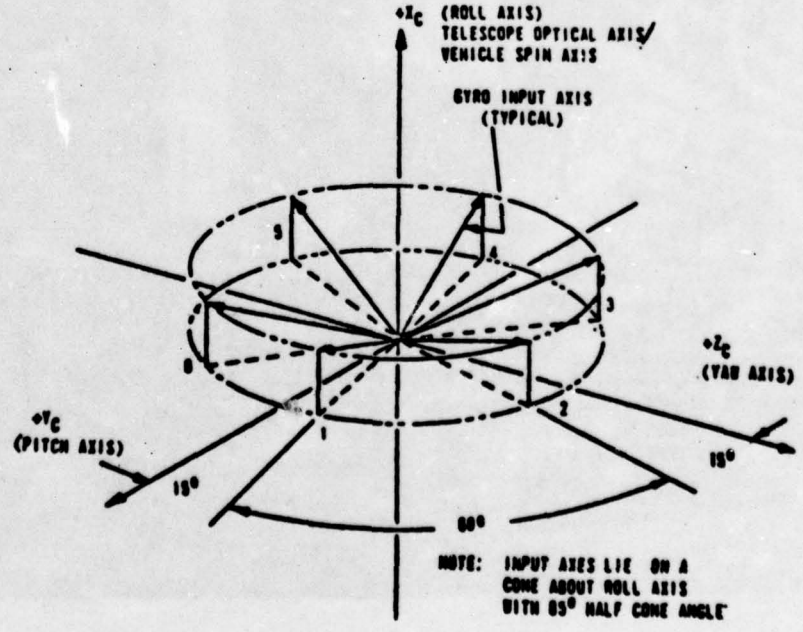


Figure 6. IUE/IRA Input Axis Configuration

VI. TEST EVALUATION OF THE HEAO/RGA AND IUE/IRA

VIa. INTRODUCTION

Design verification (performed by system test evaluation of these IMU's) represents as severe a challenge as does the initial design and development of these systems. Assuring that the resultant test data is to a large measure representative of the IMU capability rather than being corrupted by external influences (e.g., base motion) requires extreme care in the design of test facilities and techniques. All performance testing of these IMU's is conducted in a temperature and humidity-stabilized facility housing large stable piers which are isolated from the building foundation. Precise and stable turntables for sub arc-second positioning of the IMU and rate tables which can impart rates about the IMU with ppm accuracy are utilized. IMU output data is compiled by a general purpose test computer that operates under conversational teletype command from the test conductor. Figure 7 is a photo which illustrates a typical test setup for the HEAO/RGA and includes a rate table, a custom-design test station, and a test computer.

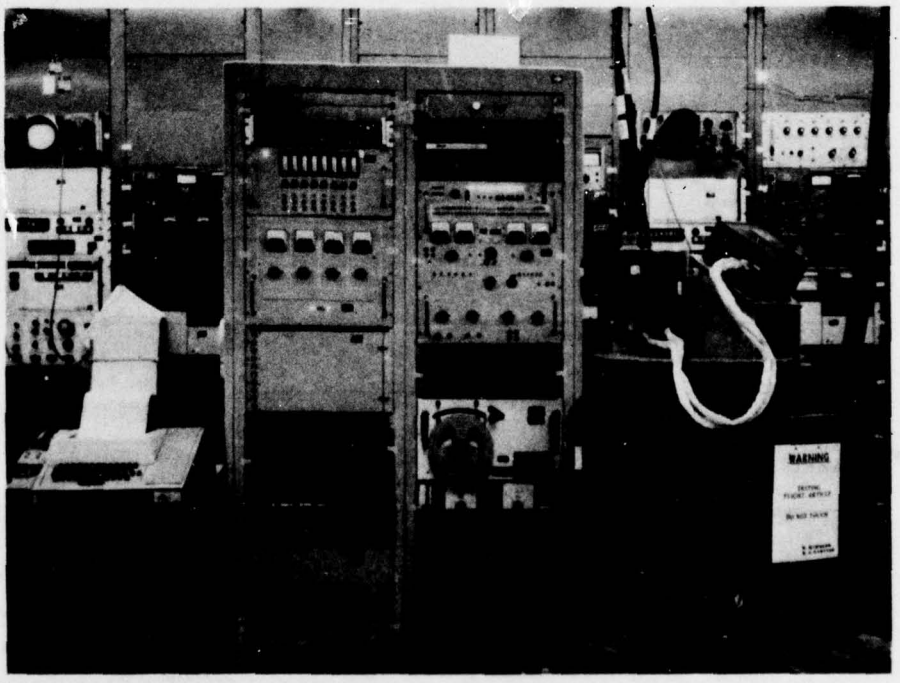


Figure 7. HEAO/RGA Test Setup

A generalized test sequence for design verification of these IMU's is shown in Figure 8. The sequence simulates the vibration and shock exposures which accompany vehicle launch and staging followed by the thermal/vacuum conditions existing in orbital operation. The pre and post-environmental functional test provides detailed performance evaluation of the IMU before and after its environmental exposures and thus enables a determination as to any effect of these environments upon performance. The operational functional test between the vibration and thermal/vacuum environments is used to assure that the IMU is fully operational following the vibration exposure.

Representative data from the HEAO/RGA and IUE/IRA test programs in the following categories of performance are presented below:

- Attitude Reference Stability Characterization
- Scale Factor Linearity and Stability
- Sensitivity to External Disturbances
- Environmental Verification
- Stability of Alignment through Environments

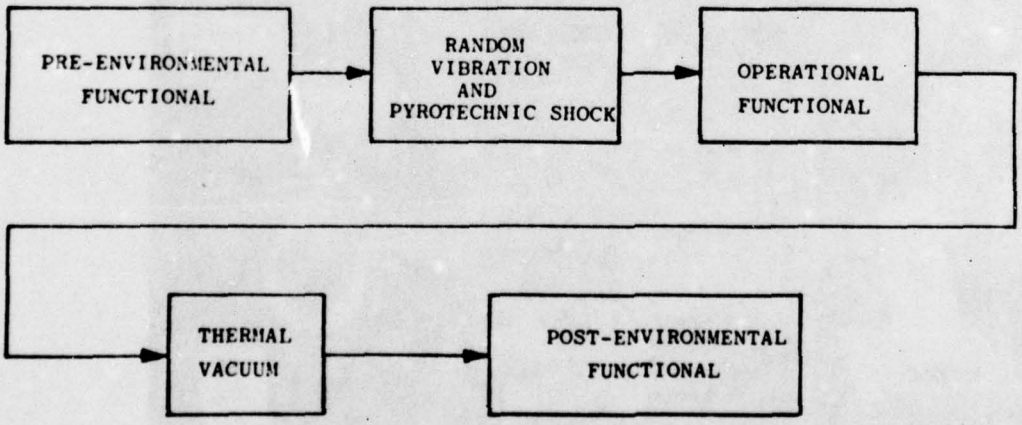


Figure 8. Generalized IMU Test Sequence

VIb. ATTITUDE REFERENCE STABILITY CHARACTERIZATION

In the HEAO and IUE applications the gyro drift rate is periodically calibrated and software compensated using other vehicle sensors. Consequently, it is the stability of the drift rate, over time periods between calibration updates or during experiment-pointing intervals which is of most interest (rather than the absolute magnitude of gyro drift rate). This section examines the stability of the attitude reference, i.e. the variability of drift rate, furnished by these IMU's, using several data gathering and reduction techniques.

The simplest representation of drift rate stability is a direct time-history record of sensor drift. Shown in Figure 9 is an example of this data obtained from one channel of the IUE/IRA with a 28-minute data averaging time over 20 hours. This data is derived by the accumulation of sensor output pulses for consecutive 28-minute averaging times, conversion of the summed output pulses to an average drift rate over each 28-minute period, and removal of the fixed component of gyro drift rate so as to examine drift rate variability. Two measures of the drift rate variability are the slope of a best-fit line through this data, termed the drift rate ramp, and the maximum deviation of the 28-minute averages. The data shown in Figure 9 has a drift rate ramp of 1.02×10^{-6} deg/hr^2 and a maximum deviation of 4.0×10^{-4} deg/hr.

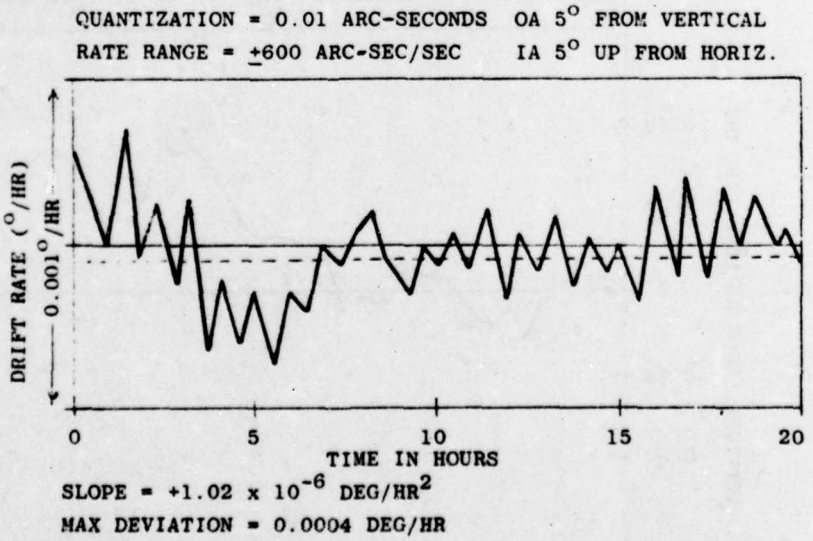


Figure 9. 64 PM Rate Sensor, 20-Hour Drift Rate Run

The drift rate ramp criteria described above is generally applied to data taken over a period of 10 hours or longer and is useful in determining the frequency with which orbital calibration updates of the gyros are required. Typical celestial-experiment observation durations, however, are significantly shorter, e.g. 30 minutes, and thus data reduction techniques which allow an assessment of the attitude error buildup attributable to the IMU for these experiment-pointing durations are also utilized and are described below.

The technique used in testing the IUE/IRA to determine its attitude error buildup for a typical experiment duration proceeds as follows: The IUE/IRA is oriented so as to minimize the g-sensitive error term of the gyros; output pulses of the Rate Sensor channels are recorded at 100 millisecond accumulation intervals (the IUE spacecraft computer interrogation rate) and then summed to form consecutive one minute data points for a total data record of 45 minutes; the first 15 minutes of the data record is used to establish the nominal least squares drift rate of each channel which is then removed from the following 30 minutes of data; and, finally the fixed-drift compensated 30 minute interval of data is integrated to form the accumulated attitude error buildup. An example of this data for one channel of the IUE/IRA is shown in Figure 10 and shows that the attitude reference is maintained within 0.5 arc-second over the 30 minute test period.

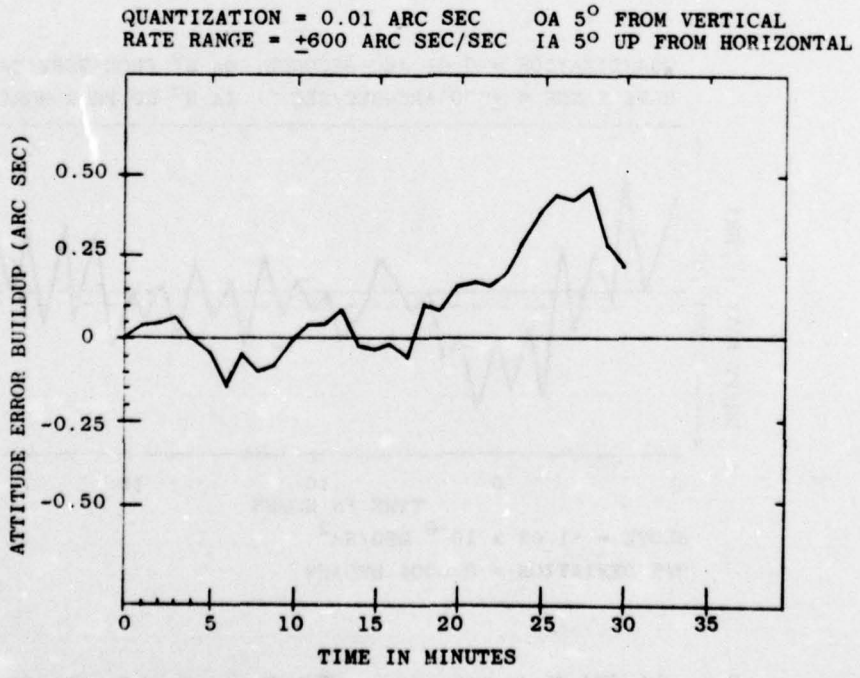


Figure 10. 64 PM Rate Sensor Attitude Error Angle Vs. Time

The test described above enables evaluation of the attitude error buildup of the IUE/IRA over a typical experiment duration. Of equal importance for experiment-pointing performance evaluation is the point-to-point attitude variation of the IMU output data when gathered at the interrogation rate of the spacecraft computer. This is designated "attitude jitter" and is evaluated in the following manner: the data is gathered by recording the channel output at 100 millisecond accumulations for a period of 45 minutes. The fixed drift rate characteristic is removed from the data and the residual plotted as attitude angle. The "attitude jitter", the deviation in attitude between consecutive 100 millisecond data accumulations, is plotted for a typical 60 second segment in Figure 11. The "attitude jitter" is seen to be well under 0.1 arc-seconds.

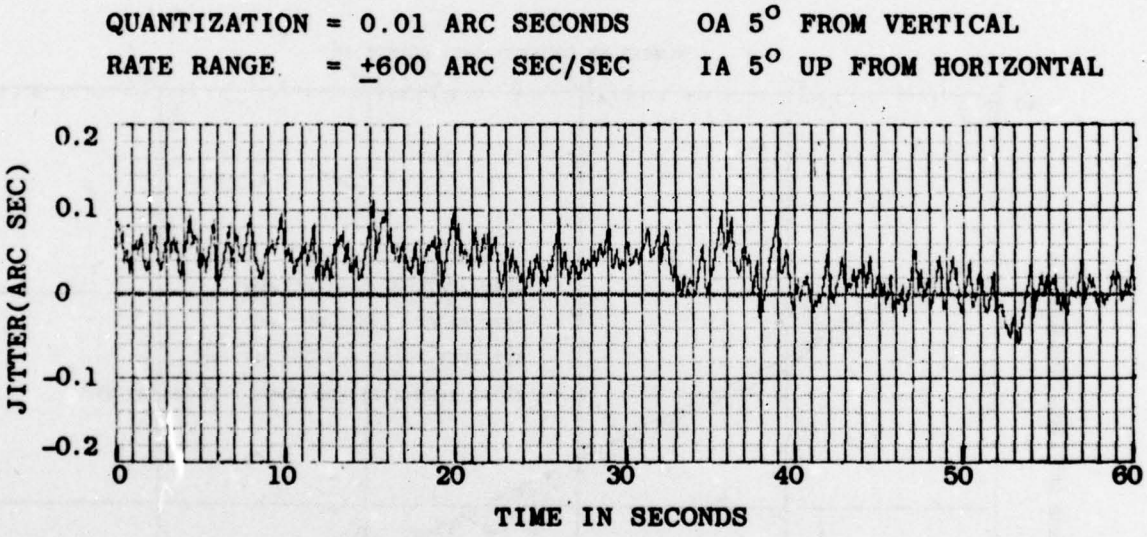


Figure 11. 64 PM Rate Sensor, Attitude Jitter

An alternative technique for determining the point-to-point attitude variation of the IMU output data when gathered at the interrogation rate of the spacecraft computer is used in testing the HEAO/RGA and proceeds as follows: The gyro output axis is oriented vertical and input axis east to minimize drift, the Rate Sensor channel output is recorded for consecutive 320 millisecond accumulation periods (HEAO spacecraft computer interrogation rate) for a total data record 32 minutes in duration. A straight line fit to the data is made and "attitude

noise" is defined as the standard deviation of the departure of the data points from the line. "Short term attitude noise" is defined as the variation in departure of any three successive data points from the line.

Additional information is obtained from the total data set by grouping the data points into larger time increments and then recomputing the attitude noise as defined above. A typical 32 minute HEAO/RGA data record reduced in this manner is shown in Figure 12 with integration times ranging from 0.32 seconds to 640 seconds. The straight line drawn through the data depicts the theoretical characteristic for a random variable when grouped in N increments of the original data points.

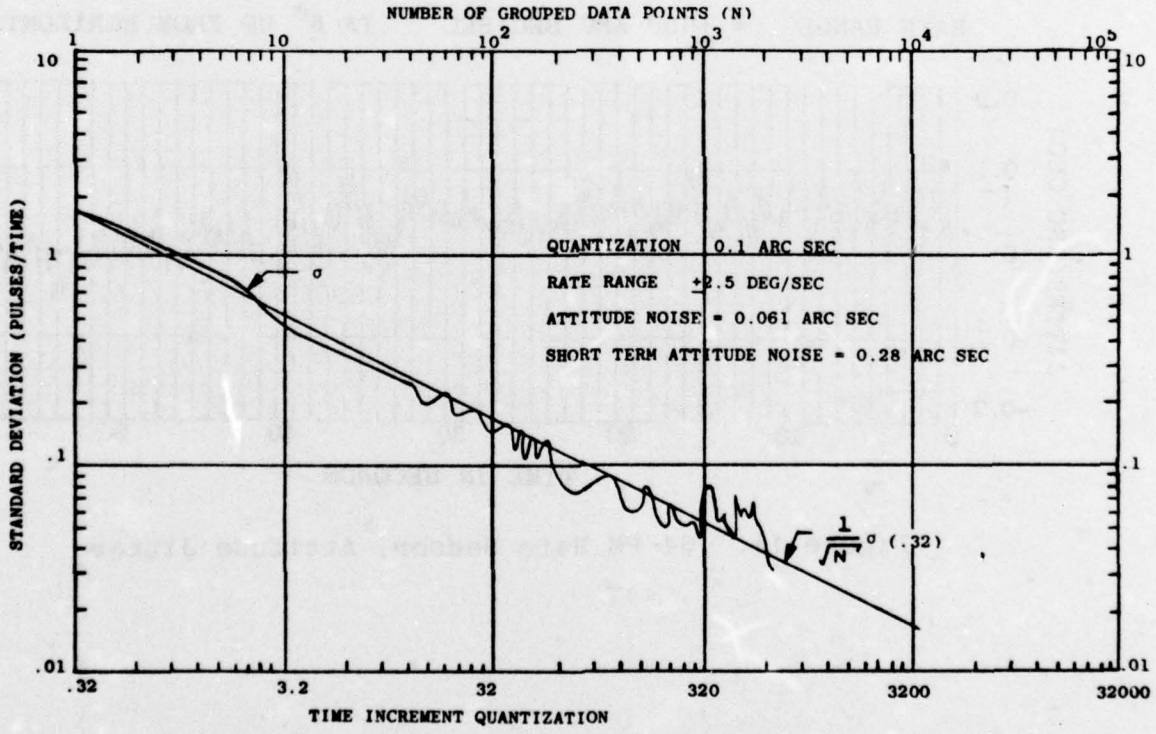


Figure 12. 64 PM Rig Rate Sensor, Attitude Noise Vs. Integration Time

The techniques described above for characterizing the attitude reference furnished by the IMU involves test data reduction exclusively in the time domain. Additional useful information can be obtained by utilizing a frequency domain evaluation of IMU output data, namely its Power Spectral Density (PSD). The manner in which the PSD is calculated using consecutive test data accumulation intervals gathered over a finite record length is described by Bendett, et al.[1]

The PSD is particularly useful when analyzing an overall vehicle control system in which the gyro drives a control loop sensitive to only a narrow frequency band. In such cases, the rms gyro drift rate, which is the integral under the entire PSD curve, is not a very revealing measure of IMU performance.

A HEAO/RGA PSD characteristic based on a 20 second duration data record and using 20 millisecond accumulation periods is shown in Figure 13. The rms drift rate for various frequency lands can be found by taking the square root of corresponding areas under the PSD curve. The results are shown in Table 4.

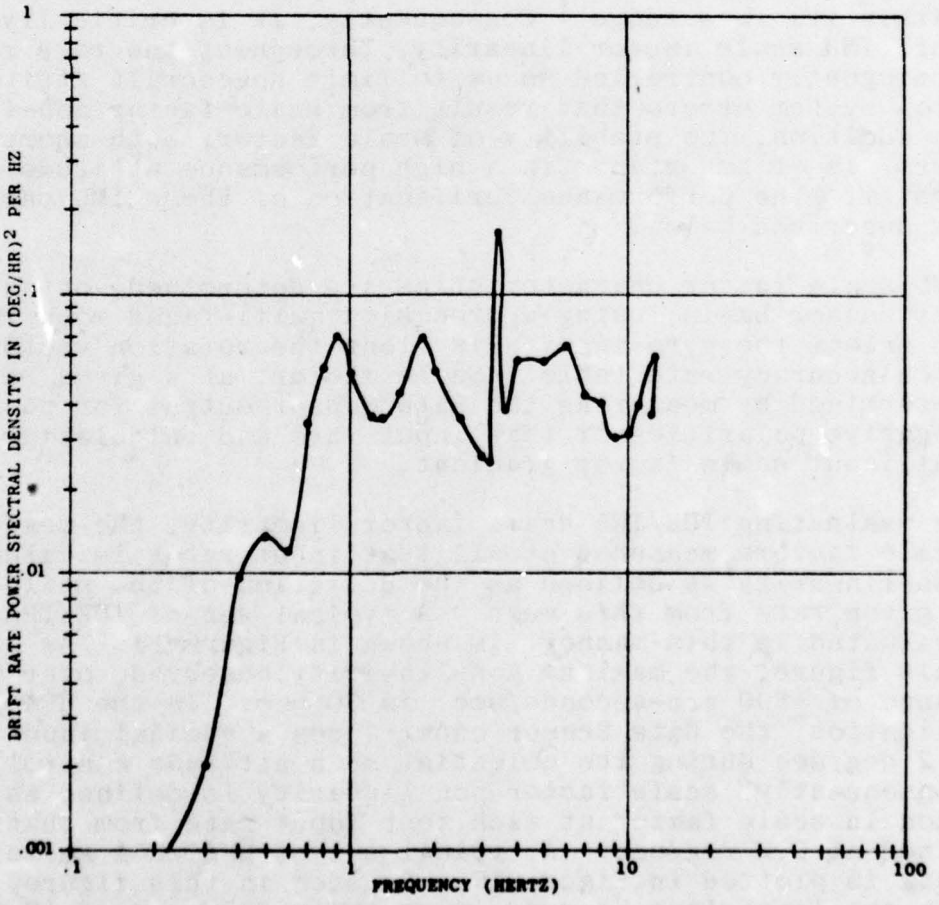


Figure 13. 64 PM Rate Sensor, Drift Rate Power Spectral Density

TABLE 4

RMS Noise vs Frequency Band
for 64 PM Rate Sensor

Frequency Band (Hz)	RMS Noise (Deg per Hour)
0.125 to 1.25Hz	0.19
0.125 to 3.13Hz	0.35
0.125 to 6.25Hz	0.52
0.125 to 12.50Hz	0.71

VIc. SCALE FACTOR LINEARITY AND STABILITY

IMU output data is processed by the spacecraft computer using a scale factor (arc-seconds/bit) determined by calibration test of each IMU channel. A single numerical scale factor is assumed, independent of the actual operating point of the Rate Sensor within its rate range. Consequently, it is critically important that IMU scale factor linearity, throughout the rate range, be stringently controlled so as to limit spacecraft attitude control system errors that result from scale factor non-linearities. In addition, the stability of scale factor, both short and long term, is of importance in a high performance attitude control system. The performance verification of these IMU parameters is described below.

IMU scale factor characteristics are determined, on an individual sensor basis, using a precision multi-faced mounting fixture to orient the gyro input axis along the rotation vector of a high accuracy rate table. Scale factor, at a given rate, is determined by measuring the Rate Sensor output for positive and negative polarities of that input rate and calculating the output/input scale factor gradient.

In evaluating IUE/IRA scale factor linearity, the mean of the scale factors measured at all test input rates is calculated and non-linearity is defined as the deviation of the scale factor at a given rate from this mean. A typical set of IUE/IRA data, evaluated in this manner, is shown in Figure 14. As seen in this figure, the maximum non-linearity observed, over the rate range of $\pm$600 arc-seconds/sec, is 30 ppm. In the HEAO/RGA application, the Rate Sensor experiences a nominal input rate of 0.2 deg/sec during the celestial scan attitude control mode. Consequently, scale factor non-linearity is defined as the deviation in scale factor at each test input rate from that determined at 0.2 deg/sec. A typical set of HEAO/RGA scale factor data is plotted in Figure 15. As seen in this figure, the maximum non-linearity observed, over the rate range of $\pm$2.5 deg/sec, is 55 ppm.

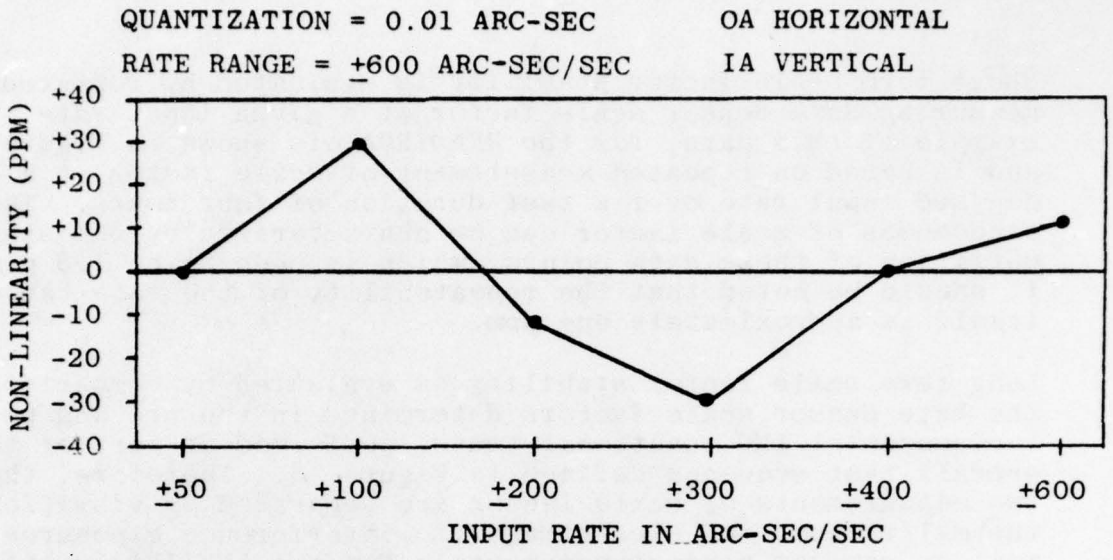


Figure 14. 64 PM RIG Scale Factor Linearity, ±600 Arc-Sec/Sec Range

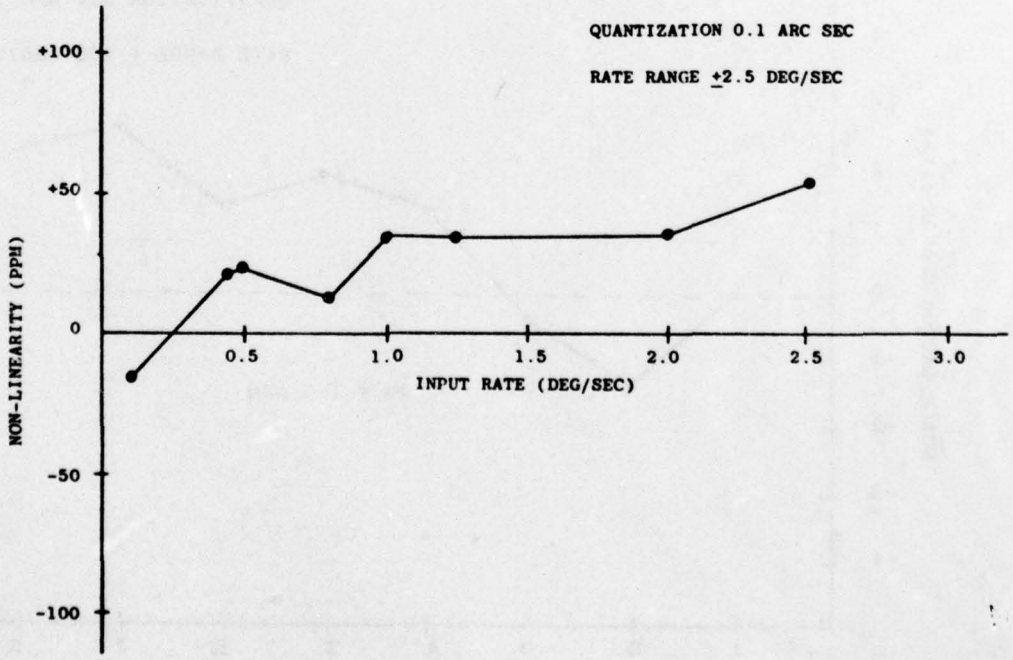


Figure 15. 64 PM Rate Sensor Scale Factor Linearity, ±2.5 Deg/Sec Range

Short term scale factor stability is evaluated by repeatedly measuring Rate Sensor scale factor at a given input rate. An example of this data, for the HEAO/RGA, is shown in Figure 16 and is based on repeated measurement of scale factor at a 0.2 deg/sec input rate over a test duration of four hours. The randomness of scale factor can be characterized by the standard deviation of these data points, which is seen to be 1.3 ppm. It should be noted that the repeatability of the rate table itself is approximately one ppm.

Long term scale factor stability is evaluated by comparison of the Rate Sensor scale factors determined in the pre and post-environmental IMU functional tests, performed as part of the overall test sequence defined in Figure 8. Therefore, the two measurements of scale factor are separated by vibration, thermal/vacuum, and electromagnetic interference exposures as well as various performance tests. For the IUE/IRA qualification unit these two scale factor tests were separated by a time period of 85 days.

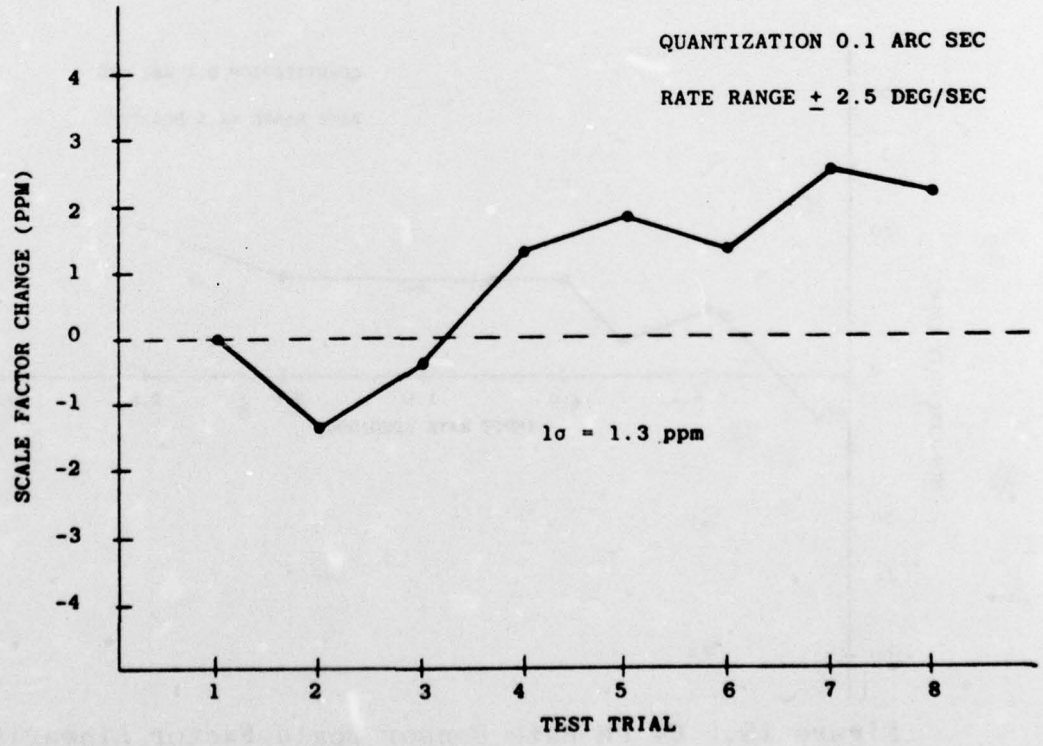


Figure 16. 64 PM Rate Sensor Stability, Short Term

Table 5 summarizes a representative sample of the change in measured mean Rate Sensor scale factor for the IUE/IRA qualification unit. The measurements were performed in the ±600 arc-seconds/sec low rate range with a nominal attitude quantization of 0.01 arc-seconds/bit. The observed time rate of change of Rate Sensor scale factor is seen to be approximately one ppm per day.

Table 5

Long Term Scale Factor Stability

Sensor	Sample Period (days)	Mean Scale Factor (arc-seconds/bit)	Change in Mean Scale Factor (ppm)
1	85	0.01011871	36
2	85	0.01003235	88
3	85	0.01010341	32

VId. SENSITIVITY TO EXTERNAL DISTURBANCES

The IMU performance testing described thus far in this paper is conducted in the benign environment of an inertial guidance test facility. In assessing the overall performance of the IMU, it is equally important to determine the IMU sensitivity to external disturbances that it will experience in orbital operation. These external disturbances include spacecraft bus voltage variations, magnetic fields, and electromagnetic fields; and, their influence on IMU performance is discussed below.

In some spacecraft applications (IUE), the IMU is supplied with a tightly regulated spacecraft bus, whereas in others (HEAO), the bus voltage supplying the IMU changes considerably as the solar panel sunlight exposure varies cyclically. Thus, in the HEAO application, the sensitivity of critical performance parameters to this bus voltage variation is precisely determined. The sensitivity of the Rate Sensor drift rate is of special interest because of its direct influence on the IMU attitude reference. The measured drift rate sensitivity of a typical HEAO/RGA channel to input power supply voltage variation is shown graphically in Figure 17, with a best fit straight line through the data defining the average sensitivity. This average sensitivity is seen to be 0.0014 deg/hr/volt. This data is taken with the gyro output axis vertical to eliminate g-sensitive drift terms.

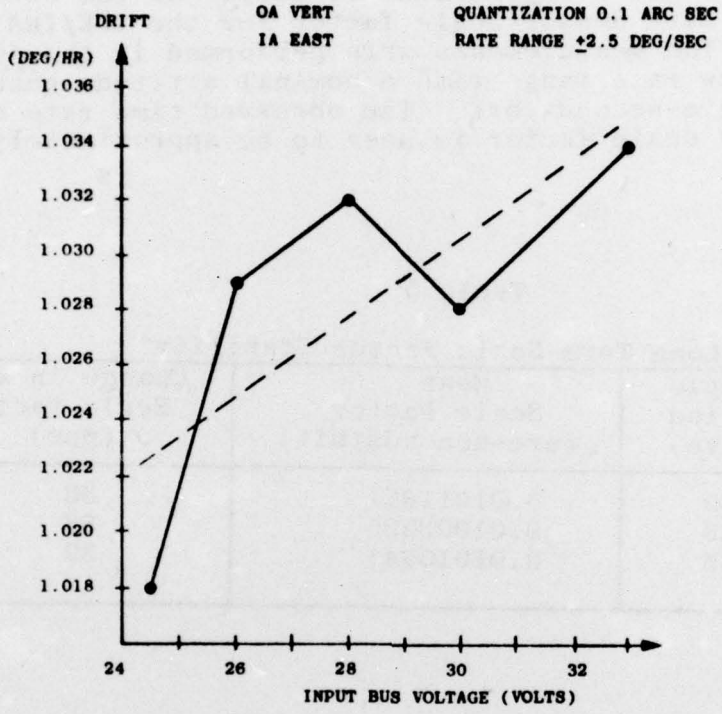


Figure 17. 64 PM Rate Sensor Drift Rate Voltage Sensitivity

Additional tests to determine the effects of voltage variations on scale factor and alignment demonstrated the following typical sensitivites:

- Scale Factor: 3 ppm/volt
- Alignment: 1 arc-second/volt

During spacecraft operation, the IMU may be subjected to varying magnetic fields generated by other onboard equipment (e.g., magnetic torquers). The sensitivity of the IMU is determined by exposing it to a magnetic field produced by a current carrying coil. The IMU is oriented with the magnetic field vector along the input, output, and spin axes of the gyro to determine worst case orientation sensitivity. Figure 18 depicts worst case HEAO/RGA sensitivity of Rate Sensor drift rate to a ± 5 Gauss magnetic field variation.

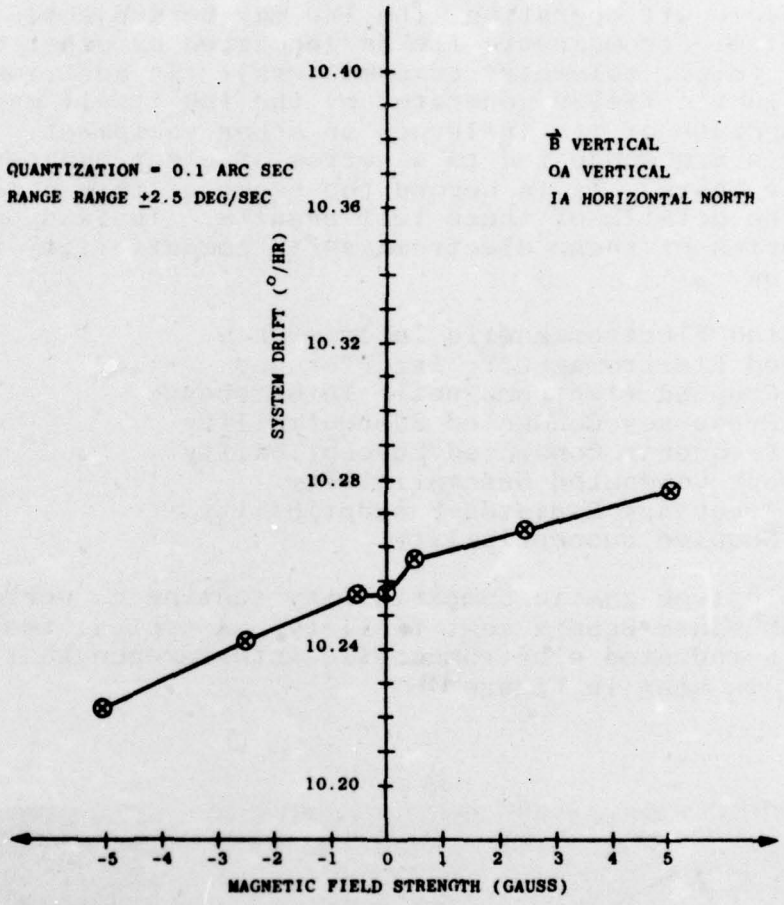


Figure 18. 64 PM Rate Sensor, Drift Rate Magnetic Field Sensitivity

Additional tests to determine magnetic field sensitivity of scale factor and alignment demonstrated the following typical parameter variations for a change of ±5 Gauss in magnetic field strength:

- Scale Factor: 20 ppm
- Alignment: 1 arc-second

During spacecraft operation, the IMU may be subjected to a variety of electromagnetic fields generated by other onboard equipment (e.g., telemetry transmitters). In addition, electromagnetic fields generated by the IMU itself may be of concern because of its influence on other equipment. Therefore, these IMU's are subjected to a series of electromagnetic compatibility tests. It is beyond the scope of this paper to present the details of these test results. Instead, a listing of categories of these electromagnetic compatibility tests is given below:

- Conducted Electromagnetic Interference
- Radiated Electromagnetic Interference
- Cable Coupled Electromagnetic Interference
- Audio Frequency Conducted Susceptibility
- Radio Frequency Conducted Susceptibility
- Transient Conducted Susceptibility
- Radio Frequency Radiated Susceptibility
- Cable Coupled Susceptibility

All IMU electromagnetic compatibility testing is performed in a totally shielded Bendix test facility. A typical test setup (showing a radiated electromagnetic interference test of the HEAO/RGA) is seen in Figure 19.

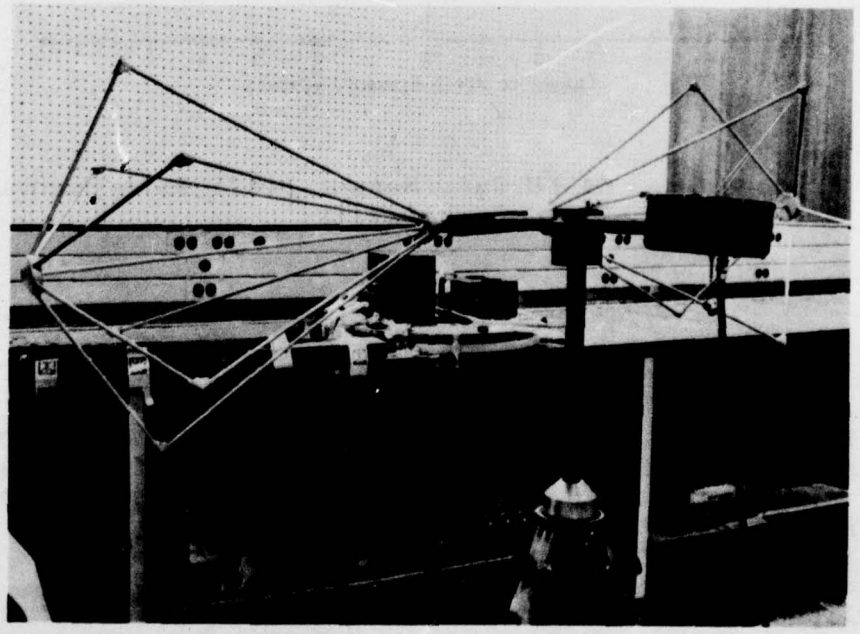


Figure 19. HEAO/RGA Radiated Electromagnetic Interference Test

VIe. ENVIRONMENTAL VERIFICATION

In operation, the strapdown IMU experiences a variety of environments, associated with both vehicle launch and orbital operation, which it is required to withstand without performance degradation. In qualification testing, environmental levels somewhat higher than those anticipated in actual usage are specified to assure a positive design margin. To verify this capability, the IMU is subjected to an extensive series of environmental tests as detailed below.

The need to maintain precise alignment through launch environments precludes the use of vibration isolation techniques in high performance applications. Consequently, the HEAO/RGA and IUE/IRA experience substantial vibration levels during launch vehicle liftoff. The IUE/IRA system, in particular, raised special design concerns due to the cantilevered arrangement of its Sensor Unit support brackets and the resultant amplification of input vibration energy.

Shown in Figure 20 is the IUE/IRA Sensor Unit installed on a vibration table which is used for sine and random vibration testing. The profiles used for sine and random vibration qualification testing are given below:

SENSOR UNIT QUALIFICATION - SINE VIBRATION

THRUST AXIS - X

Freq. (Hz)	Levels (g.0-pk)	Sweep Rate
5 - 10.8	0.50" D.A.	
10.8 - 15	3.0	
15 - 21	9.0	
21 - 35	5.0	
35 - 60	13.5	2 oct/min.
60 - 200	2.3	

LATERAL AXIS - Y, Z

Freq. (Hz)	Levels (g.0-pk)	Sweep Rate
5 - 17	6.0	
17 - 25	3.0	
25 - 45	6.0	2 oct/min.
45 - 200	1.5	

SENSOR UNIT QUALIFICATION-RANDOM VIBRATION

Frequency Range (Hz)	PSD (g^2/Hz)
20 - 300	0.05
300 - 900	+1.5 dB/oct
900 - 1500	0.08
1500 - 2000	-46 dB/oct
Overall = 10.5 grms 2 minutes/axis	

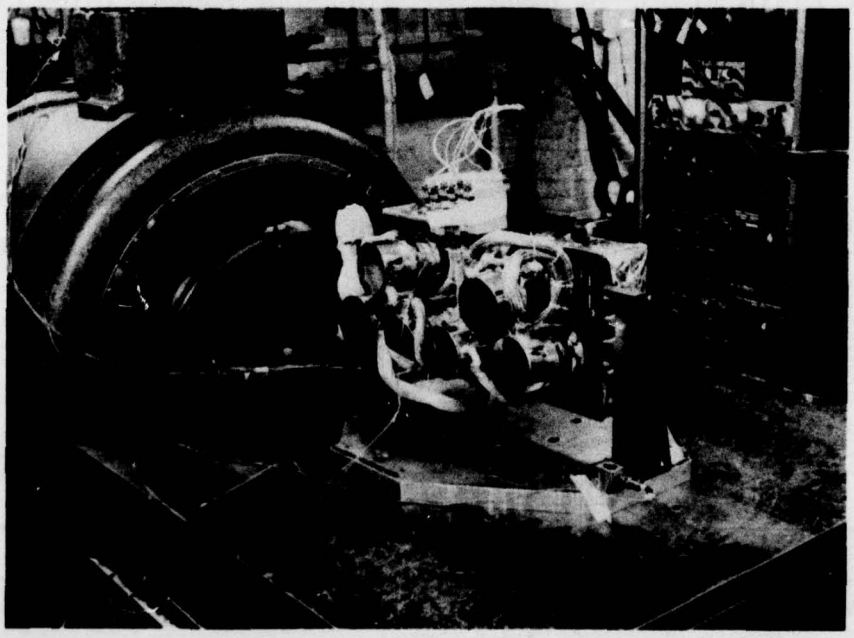


Figure 20. IUE/IRA Sensor Unit Undergoing Vibration Testing

The primary resonances, observed during sine vibration testing, occurred at 95, 110 and 240 Hz for the three axes of the unit and were accompanied by an amplification factor (Q) of approximately 24. During random vibration testing, the acceleration level experienced by the Rate Sensors was estimated to be 112 g's peak. During this vibration test of the Sensor Unit, only the gyro heaters were energized (simulating the IUE launch condition). Tests conducted prior to and following this vibration exposure demonstrated no apparent performance degradation of the IUE/IRA. The titanium support brackets performed as designed, fulfilling the stringent requirements of both a structural member and a thermal interface isolator.

Due to the firing of pyrotechnics, which accompanies stage separation of the launch vehicle, high-g high-frequency shock energy is imparted to the IMU. This pyrotechnic shock is simulated, in HEAO/RGA qualification testing, by the fixture shown in Figure 21. The shock imparted by this fixture results from a hammer being dropped along a length of rod and impacting a mass-loaded spacecraft equipment bay housing the IMU. The angle of attack of the rod and the length through which the weight is dropped is based on measurements made at the spacecraft level during actual firing of separation pyrotechnics.

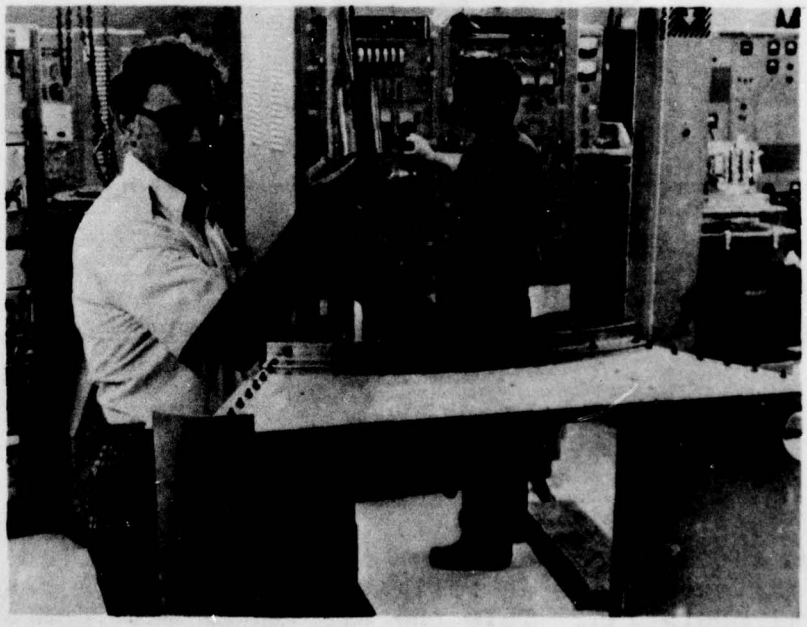


Figure 21. HEAO/RGA Pyrotechnic Shock Test Setup

During HEAO/RGA pyrotechnic shock qualification testing, the system was fully operational with the exclusion of the gyro wheels (simulating the HEAO launch condition). The response spectrum of the imparted shock is seen in Figure 22. Detailed tests confirmed that no performance degradation occurred as a result of this environmental exposure. For IUE/IRA pyrotechnic shock qualification testing, a sine equivalent vibration spectrum was utilized.

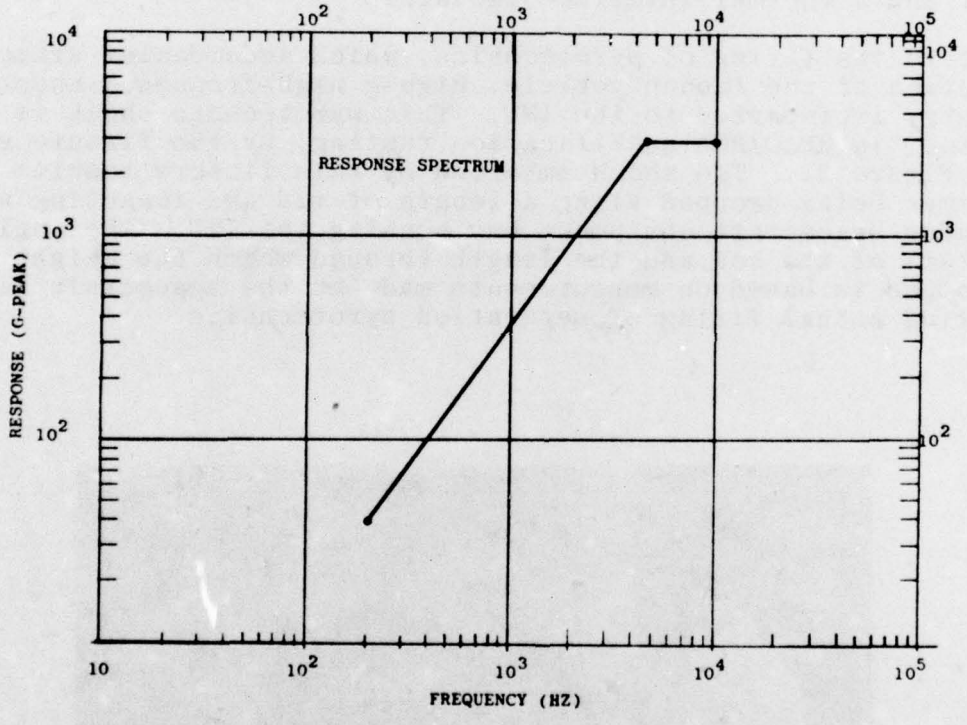


Figure 22. HEAO/RGA Pyrotechnic Shock Spectrum

In the HEAO and IUE applications, the IMU is subjected to ambient thermal excursions as well as the hard vacuum associated with orbital operation. This thermal/vacuum environment is simulated as part of IMU qualification testing. The IUE/IRA thermal/vacuum test is particularly interesting due to the manner of attachment of the IMU to the spacecraft and the con-

sequent test complexity. The IUE/IRA qualification thermal/vacuum test is described below.

During the thermal/vacuum test, both the IUE/IRA Sensor Unit and the Electronic Control Unit were tested as an integral system but located in separate compartments of the test chamber. This was done to simulate the different environments experienced by the two units in orbital operation. The Sensor Unit was mounted to a platen thermally controlled to -40°F (simulating the spacecraft telescope) and continuously exposed for four days to a cyrogenic shroud operated at -200°F (simulating deep space). The Electronics Control Unit was contained within an enclosure separate from the shroud and platen to simulate the interior of the spacecraft. The Electronics Control Unit enclosure was thermally controlled to the profile shown in Figure 23. Installation of the IUE/IRA in the test chamber is shown in Figures 24 and 25. The chamber pressure was reduced to below 1 x 10^{-5} Torr and maintained during the four day exposure.

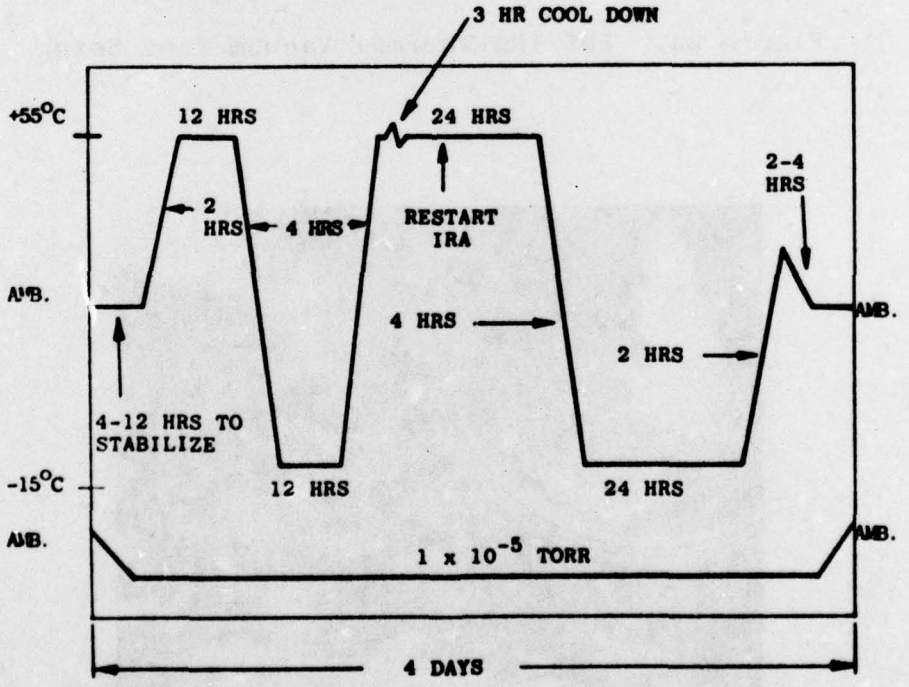


Figure 23. Electronics Control Unit Thermal Profile

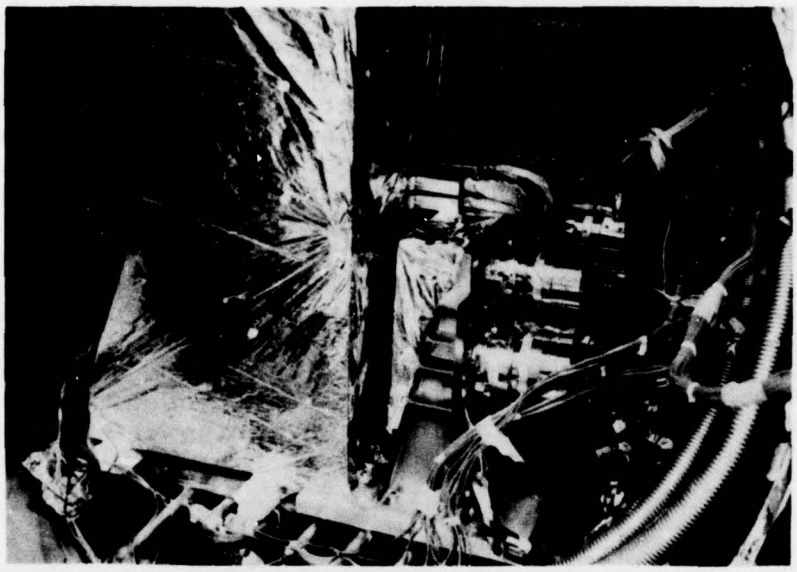


Figure 24. IUE/IRA Thermal Vacuum Test Setup

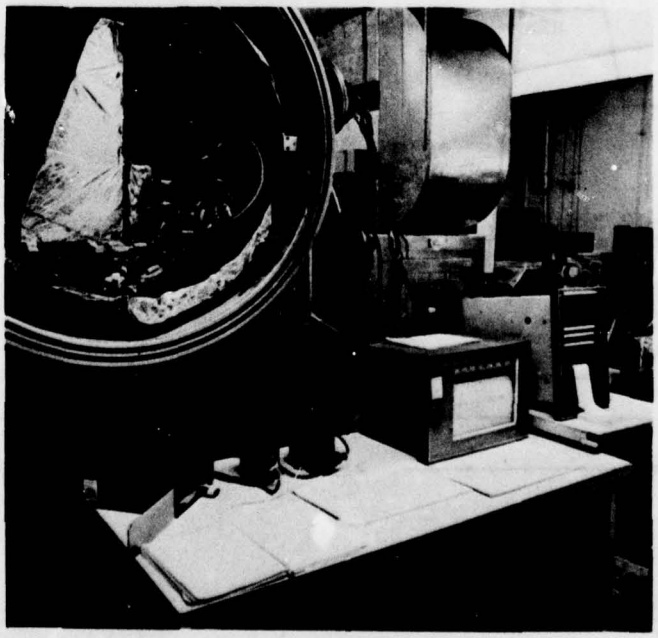


Figure 25. IUE/IRA Thermal Vacuum Instrumentation

Both the Sensor Unit and Electronic Control Unit were extensively instrumented with thermal probes so as to validate such design parameters as thermal isolator resistance, surface emissivity, and various component temperatures. The Rate Sensors were cycled on/off and exercised through all operational modes during the four day test period. Total system power, cool-down and warm-up rates, Rate Sensor heater duty cycles, and heat transfer to the mounting structure were verified.

VIf. STABILITY OF IMU ALIGNMENT ACROSS ENVIRONMENTAL EXPOSURES

The alignment stability of sensor input axes with respect to the mathematical coordinate reference axes established in the spacecraft computer is of particular concern in strapdown IMU applications. Being hard-mounted to the vehicle, the strapdown IMU experiences substantial vibration and shock levels during vehicle launch and staging as well as the thermal excursions and hard vacuum condition associated with orbital operation. To verify the ability of these IMU's to preserve sensor alignment after exposure to these environments, the detailed testing described below is performed.

Measurement of sensor input axis alignment (with respect to the coordinate axes of the mounting structure) is accomplished by determination of the individual rotational alignments of the gyro Input Axis (IA) about its Output Axis (OA) and the gyro IA about its Spin Reference Axis (SRA). These two rotational alignments are summed vectorially to determine the spatial relationship of an individual sensor IA with respect to the mounting structure. A multi-faced calibrated fixture that allows IMU positioning such that the primary axes of each gyro can be sequentially placed parallel to the rotation vector of a rate table is utilized. Each gyro of the IMU is individually rotated about its nominal IA and SRA. Monitoring of the sensor output during this rotation allows a determination as to the actual alignment of the gyro axis with respect to the rotation vector of the rate table and the mounting structure itself. Stability of alignment is determined by performing these measurements during each of the three IMU functional tests conducted as part of the overall test sequence defined in Figure 8.

Tabulated in Table 6 are the results of these alignment measurements for three HEAO/RGA systems. Typically, an alignment shift of 13 arc-seconds was observed. Also of interest is the short term repeatability of alignment which is determined by repetitive alignment measurements in a benign laboratory environment. Typically, a short term alignment repeatability of one arc-seconds was observed.

Table 6. Test Sequence Alignment Time History

RATE SENSOR TEST SAMPLE	FUNCTIONAL TEST PHASE-MISALIGNMENT (ARC-MIN)					
	PRE-ENVIRONMENTAL		OPERATIONAL		POST ENVIRONMENTAL	
	α	β	α	β	α	β
1	1.7	-0.7	1.4	-0.2	1.5	-0.1
2	-0.9	-0.3	-0.7	-1.0	-0.7	-0.3
3	-0.9	-0.3	-0.7	-0.4	-0.4	-0.8
4	1.1	-1.1	1.1	-1.1	0.7	-0.6
5	0.5	1.1	0.5	1.0	0.4	1.0
6	-0.7	0.4	-0.7	C.1	-0.6	0.2

$\alpha \triangleq$ IA ABOUT OA

$\beta \triangleq$ IA ABOUT SRA

ACKNOWLEDGEMENT

The HEAO/RGA data summarized in this paper is based on contractual activity (Contract No. A19141 RMA) conducted for TRW Systems acting as prime contractor to the NASA/Marshall Space Flight Center. The IUE/IRA data summarized in this paper is based on contractual activity (Contract No. NAS5-20081) conducted for the NASA/Goddard Space Flight Center.

Publication of this paper does not constitute approval by NASA or TRW Systems of its contents. It is published for the exchange and stimulation of ideas.

REFERENCES

1. R. Bendett, H. Kleine, S. Weinstein and D. A. Zomick, "Test Evaluation of a High Performance Pulse Rebalance Gyro for Strapdown IMU Applications", NAVIGATION: Journal of the Institute of Navigation, Volume 23, No. 1, Spring 1976.

2. J. Gilmore, "A Non-Orthogonal Multi-Sensor Strapdown Inertial Reference Unit", Instrumentation Laboratory Massachusetts Institute of Technology Cambridge, Massachusetts, A69-13211, 1968.

3. J. V. Moore, "Precision Pointing of the International Ultraviolet Explorer (IUE) Scientific Instrument Using a Gyroscopic and Stellar Reference", Goddard Space Flight Center, Greenbelt, Maryland.

4. D. Hoffman, "HEAO Attitude Control Subsystem--A Multimode/Multimission Design", TRW Defense and Space Systems Group Redondo Beach, California.